Homo- and Mixed-valence [2 × 2] Grid Complexes

Dissertation

For the award of the degree

"Ph.D., Division of Mathematics and Natural Sciences"

of the Georg-August-Universität Göttingen

Within the doctoral program

Chemistry

of the Georg-August University School of Science (GAUSS)

Submitted by

Jin Tong

from Jiangxi, VR China

Göttingen 2016

Thesis Committee

Prof. Dr. F. Meyer, Institute of Inorganic Chemistry, Georg-August University Göttingen

Dr. I. Siewert, Institute of Inorganic Chemistry, Georg-August University Göttingen

Members of the Examination Board

Reviewer: Prof. Dr. F. Meyer, Institute of Inorganic Chemistry, Georg-August University Göttingen

Second Reviewer: Dr. I. Siewert, Institute of Inorganic Chemistry, Georg-August University Göttingen

Further members of the Examination Board

Prof. Dr. S. Schneider, Institute of Inorganic Chemistry, Georg-August University Göttingen

Prof. Dr. D. Stalke, Institute of Inorganic Chemistry, Georg-August University Göttingen

Prof. Dr. T. Waitz, Institute of Inorganic Chemistry, Georg-August University Göttingen

Jun.-Prof. Dr. S. Demir, Institute of Inorganic Chemistry, Georg-August University Göttingen

Date of the oral examiniation: 06.04.2016

Table of Contents

2,6-dibromopyridine **a**

1*H*-pyrazole, 3,5-dimethyl-1*H*-pyrazole, 3,4,5-trimethyl-1*H*-pyrazole **b**

2-bromo-6-(1*H*-pyrazol-1-yl)pyridine **c1**

2-bromo-6-(3,5-dimethyl-1*H*-pyrazol-1-yl)pyridine **c2**

2-bromo-6-(3,4,5-trimethyl-1*H*-pyrazol-1-yl)pyridine **c3**

6-(1*H*-pyrazol-1-yl)picolinonitril **d1**

6-(3,5-dimethyl-1*H*-pyrazol-1-yl)picolinonitrile **d2**

6-(3,4,5-trimethyl-1*H*-pyrazol-1-yl)picolinonitrile **d3**

2-bromo-6-(1-methyl-1*H*-imidazol-2-yl)pyridine **e**

6-(1-methyl-1*H*-imidazol-2-yl)picolinonitrile **f**

pyridine-2,6-dicarboxylic acid **g**

dimethyl pyridine-2,6-dicarboxylate **h**

6-(1*H*-pyrazol-1-yl)picolinate **I**

1-(6-(1*H*-pyrazol-1-yl)pyridin-2-yl)ethanone **II**

1,3-bis(6-(1*H*-pyrazol-1-yl)pyridin-2-yl)propane-1,3-dione **III**

1,3-bis(6-(1*H*-pyrazol-1-yl)pyridin-2-yl)propane-2-methyl-1,3-dione **IV**

1-(6-(3,5-dimethyl-1*H*-pyrazol-1-yl)pyridin-2-yl)ethanone **V**

Methyl-6-(3,5-dimethyl-1*H*-pyrazol-1-yl)picolinate **VI**

1,3-bis(6-(3,5-dimethyl-1*H*-pyrazol-1-yl)pyridin-2-yl)propane-1,3-dione **VII**

1-(6-(3,4,5-trimethyl-1*H*-pyrazol-1-yl)pyridin-2-yl)ethanone **VIII**

1-(6-(3,5-dimethyl-1*H*-pyrazol-1-yl)pyridin-2-yl)-3-(6-(3,4,5-trimethyl-1*H*-pyrazol-1-yl)pyridin-2-yl)propane-1,3-dione **IX**

1-(6-(1-methyl-1*H*-imidazol-2-yl)pyridin-2-yl)ethanone **X**

Methyl-6-(1-methyl-1*H*-imidazol-2-yl)picolinate **XI**

1,3-bis(6-(1-methyl-1*H*-imidazol-2-yl)pyridin-2-yl)propane-1,3-dione **XII**

1,3-bis(6-(1-methyl-1*H*-imidazol-2-yl)pyridin-2-yl)propane-2-Methyl-1,3-dione **XIII**

Methyl-6-(hydroxymethyl)picolinate **XIV**

1-(6-(hydroxymethyl)pyridin-2-yl)ethanone **XV**

1,3-bis(6-(hydroxymethyl)pyridin-2-yl)propane-1,3-dione **XVI**

(6,6'-(1*H*-pyrazole-3,5-diyl)bis(pyridine-6,2-diyl))dimethanol **XVII**

6,6'-(1*H*-pyrazole-3,5-diyl)dipicolinaldehyde **XVIII**

1-(2,2'-bipyridin-6-yl)ethanone **XIX**

3,3'-(pyridine-2,6-diyl)bis(1-(6-(1*H*-pyrazol-1-yl)pyridin-2-yl)propane-1,3-dione) **XX**

3,3'-(pyridine-2,6-diyl)bis(1-(6-(1-methyl-1*H*-imidazol-2-yl)pyridin-2-yl)propane-1,3-dione) **XXI**

3,3'-(pyridine-2,6-diyl)bis(1-(2,2'-bipyridin-6-yl)propane-1,3-dione) **XXII**

3,5-bis(6-(1*H*-pyrazol-1-y)pyridin-2-yl)pyrid-2-yl)pyrazole $\mathbf{HL^{Pz}}$

4-Methyl-3,5-bis(6-1*H*-pyrazol-1-y)pyrid-2-yl)pyrid-2-yl)pyrazole $\mathbf{HL^{Me\text{-}Pz}}$

3,5-bis(6-(3,5-dimethyl-1*H*-pyrazol-1-yl)pyridin-2-yl)pyrid-2-yl)pyrazole $\mathbf{HL^{Me4\text{-}Pz}}$

2-(3,5-dimethyl-1*H*-pyrazol-1-yl)-6-(3-(6-(3,4,5-trimethyl-1*H*-pyrazol-1-yl)pyridin-2-yl)-1*H*-pyrazol-5-yl)pyridine $\mathbf{HL^{Me5\text{-}Pz}}$

1,3-bis(6- (1-methyl-1*H*-imidazol-2-yl)pyridin-2-yl)pyrazole $\mathbf{HL^{Me\text{-}Im}}$

4-methyl-1,3-bis(6-(1-methyl-1*H*-imidazol-2-yl)pyridin-2-yl)pyrazole $\mathbf{HL^{Me\text{-}MeIm}}$

1,3-bis(6-(1*H*-imidazol-2-yl)pyridin-2-yl)pyrazole $\mathbf{HL^{Im}}$

2,6-bis(3-(6-(1*H*-pyrazol-1-yl)pyridin-2-yl)-1*H*-pyrazol-5-yl)pyridine $\mathbf{H_2L^{Pz}}$

2,6-bis(3-(6-(1-methyl-1*H*-imidazol-2-yl)pyridin-2-yl)-1*H*-pyrazol-5-yl)pyridine **$H_2L^{Me\text{-}Im}$**

2,6-bis(3-(2,2'-bipyridin-6-yl)-1*H*-pyrazol-5-yl)pyridine **H_2L^{Py}**

$[Fe^{II}_4L^{Pz}_4](BF_4)_4$ **1**

$[Fe^{II}_4L^{Me\text{-}Pz}_4](BF_4)_4$ **2**

$[Fe^{II}_4L^{Me4\text{-}Pz}_4](BF_4)_4$ **3**

$[Fe^{II}_4L^{Me5\text{-}Pz}_4](BF_4)_4$ **4**

$[Fe^{II}_3Fe^{III}L^{Pz}_4](BF_4)_5$ **5**

$[Fe^{II}_4L^{Me\text{-}Im}_4](ClO_4)_4$ **6**

$[Fe^{II}_3Fe^{III}L^{Me\text{-}Im}_4](ClO_4)_5$ **7**

$[Fe^{II}_2Fe^{III}_2L^{Me\text{-}Im}_4](ClO_4)_6$ **8**

$[Fe^{III}_2(Ag^{I}_2)_2L^{Me\text{-}Im}_4](ClO_4)_6$ **9**

$[Fe^{II}_4L^{Me\text{-}MeIm}_4](BF_4)_4$ **10**

$[Co^{II}_4L^{Pz}_4](BF_4)_4$ **11**

$[Co^{II}_4L^{Me\text{-}Pz}_4](BF_4)_4$ **12**

$[Co^{II}_4L^{Me\text{-}Im}_4](BF_4)_4$ **13**

$[Co^{II}_4L^{Py}_4](BF_4)_4$ **14**

$[Co^{II}_2Co^{III}_2L^{Pz}_4](BF_4)_6$ **15**

$[Co^{II}_2Co^{III}_2L^{Me\text{-}pz}_4](BF_4)_6$ **16**

$[Co^{II}_2Co^{III}_2L^{Me\text{-}Im}_4](BF_4)_6$ **17**

$[Co^{II}_2Co^{III}_2L^{Py}_4](BF_4)_6$ **18**

$[Fe^{II}_3(HL^{Pz})L^{Pz}_3](BF_4)_3$ **19**

$[Fe^{II}_3(HL^{Me\text{-}Pz})L^{Pz}_3](BF_4)_3$ **20**

$[Fe^{II}_3(HL^{Me\text{-}Im})L^{Me\text{-}Im}_3](ClO_4)_3$ **21**

1. Introduction

1.1. Molecules as Electrical Components

Molecular electrical components are a new type of material, which use molecular organic functional materials to build a variety of electronic circuit components, such as molecular switches, molecular rectifiers, molecular transistors, and so on. The electro-optical characteristics of these molecular scale components are also of great interest. Professor Alan Heeger, one of the winners of the Nobel Prize in chemistry in 2000, said "the 20th century was the century of inorganic semiconductors, but the 21st century will be an organic half conductor – p-type molecular electronics century".

According to Moore's Law, inorganic semiconductor for applications in integrated circuits will reach their development limit in 2020. If the control of electron mobility in a region of organic molecules is possible, molecular electrical components with some special function could be constructed from molecular polymers.[1] There is the possibility to break the limitations of current materials and vastly improve the integration level of electricial circuitry and the working speed of computers.[2] Therefore scientists have recently dedicated more attention to molecular electronics, and will continue to do so.[3,4]

1.2. Supramolecular Chemistry

Supramolecular chemistry has been defined by Jean-Marie Lehn, one of the leading proponents, who won the Nobel Prize for his work in 1987, as the "chemistry beyond the molecular assemblies and of the intramolecular bond".[5] Originally, however, supramolecular chemistry was defined in terms of the non-covalent interaction between a 'host' and a 'guest' molecule. The interaction used by chemists to hold molecules together to construct supramolecules is non-covalent, and there are a number of such interactions. They include:

(a) electrostatics (ion-ion, ion-dipole and dipole-dipole);

(b) hydrogen bonding;

(c) $\pi - \pi$ stacking interactions;

(d) dispersion and induction forces (van der Waals forces);

(e) hydrophobic or solvatophobic effects.

The bond energy of a typical single covalent bond ranges from 350 to 942 kJ/mol. The strength of most non-covalent interactions used by supramolecular chemists are generally much weaker; for instance, dispersion force typocally range from 0 to 200 kJ/mol and ion-ion interactions from 200 – 300 kJ/mol. Tuning these interactions allow strong and selective recognition of specific guests to be achieved.[6]

Because the molecular components interact, resulting in functional architectures with novel physical properties, supramolecular chemistry is an interdisciplinary field of research with many applications.[7] In synthetic chemistry, self-aggregation, the so-called self-assembly, combines organic ligands in the presence of metals to produce small superstructures with new features.[8] The bonds in metal complexes are, although partly covalent, mostly non-covalent interactions (ion-dipole or ion-ion interactions as previously mentioned). Coordination compounds are particularly valuable for their diverse geometry and controllable physical properties, which leads to determination of structure-function relationships. Some of the many possible applications of supramolecular chemistry include ion transport,[9] template reactions for catalysis,[10,11] host-guest systems as sensors,[12] and single-molecule magnets (SMMs).[13]

Metallosupramolecular chemistry is an actively pursued area of research in supramolecular chemistry, which takes advantage of the interaction between organic ligands and metal ions to construct multicomponent and multinuclear coordination architectures. The metal ions herein are used to direct the assembly of polyfunctional metallosupramolecular entities, which has reached a high level of sophistication over the past three decades.[14,15,16,17] These architectures include helicates,[15,16,17,18] grids,[19] racks[20] and a variety of remarkable cavity-containing species.[21]

1.2.1. [2 × 2] Grid Complexes

The metallogrid structures herein are oligonuclear metal complexes in which the metal ions are essentially planar and each metal ion can be considered a point at the corners of a square or rectangular structure (Figure 1.1).

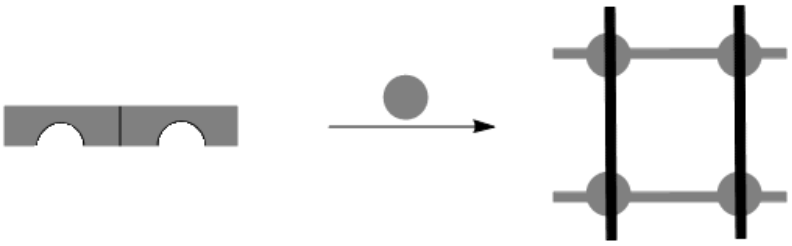

Figure 1.1. Schematic representation of the formation of [2 × 2] metallogrid complexes from a planar, ditopic ligand.

The design of grid-like metal ion arrays is based upon metal ion coordination geometry and orientation of ligand coordination sites, with the ligand planes at each metal center perpendicularly arranged. In such a coordination environment around the metal centers, the linear and rigid extension of the ligand system will automatically cause a grid-like two-dimensional coordination network with a regular array of metal centers. This construction requires that the ligands contain either bidentate or tridentate binding subunits, with metal ions which must possess tetrahedral or octahedral coordination geometry, respectively. Thus far, the most commonly used ligands for the preparation of [2 × 2] grid-like structures are listed in Figure 1.2.[22,23,24]

Ligands with nitrogen donors, such as those containing pyridine, pyrimidine, imidazole or pyrazole are the most common, but ligands with oxo- and sulfur-bridging subunits are also used. All chelating ligands shown in Figure 1.2 may result in cooperative effects during the self-assembly process due to the increased preorganization and stronger binding of ligands. Additionally, all these ligands contain rigid aromatic ring systems (mostly pyridine groups), which could be used to produce the kinetically labile intermediates as well as thermodynamically stable end products with many M^{I}, M^{II} and some M^{III} metal ions. The rigidity of these aromatic ring systems and their ability to participate in $\pi - \pi$ interactions are further stabilizing factors for the grid-type architecture formation.

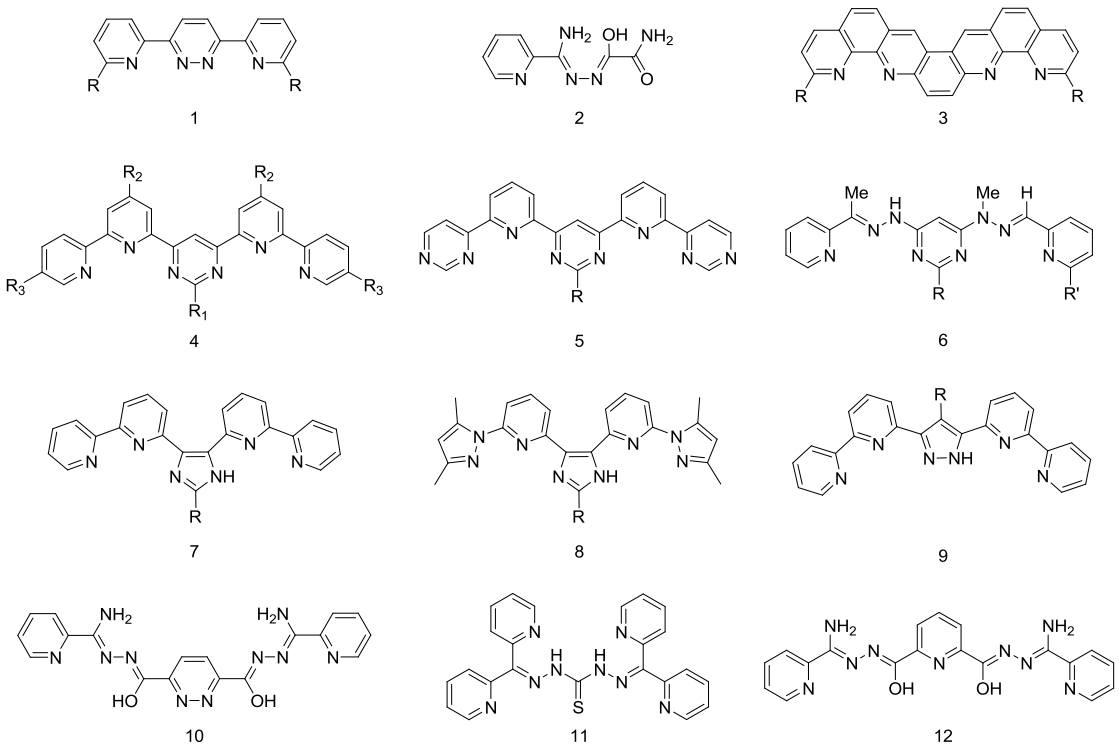

Figure 1.2. Selected ligands used in self-assembly of [2 × 2] grid.[22,23,24]

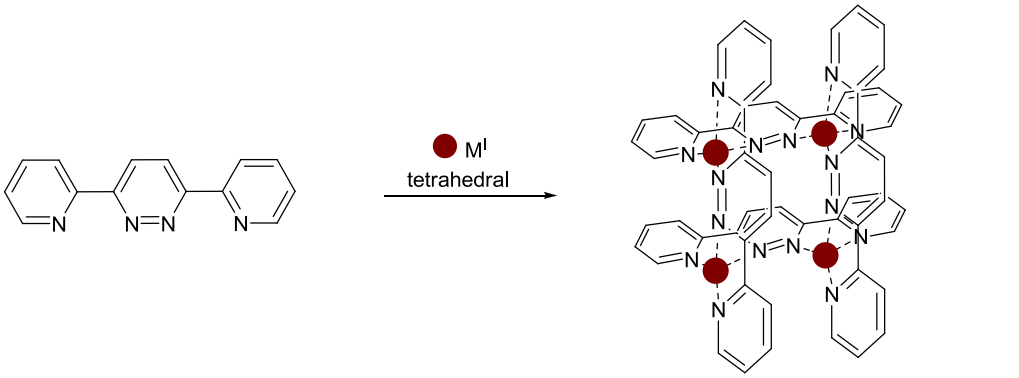

Figure 1.3. Schematic representation of the self-assembly process of a bis(bidentate) ligand and tetrahedrally coordinating metal ions (M = Ag^{I}, Cu^{I}) leading to a [2 × 2] metallogrid $[M^{I}_{4}L_{4}]^{4+}$.[22]

The first report on the formation of a [2 × 2] metallogrid architecture based on tetrahedral coordination geometry involved four ditopic ligands (3,5-Bis(2-pyridyl)-pyridazin, **1**) arranged around four metal ions (M^{I}) in a tetrahedral $\{N_4\}$ environment, wherein there are two ligands parallel to each other and perpendicular to the second ligand pair (Figure 1.3).[22] Both Cu^{I} and Ag^{I} grid structures assemble spontaneously when the metal and ligand components are mixed in a 1:1 ratio.[22,23]

Cyclic voltammetry studies of the copper complex showed that there are four reversible one-electron oxidations of copper ions. The redox properties of grid complexes were studied further[25] and can also be correlated with major structural changes.[26]

A [2 × 2] $Cu^{II}_4L_4$ metallogrid structure was obtained with the flexible ligand N,N'-imidopicolinyloxamylhydrazine (**2**). The cluster consists of four copper(II) ions at the vertices of a flattened tetrahedron. Each copper(II) ion is coordinated by four donor atoms originating from two deprotonated ligands, thereby forming a distorted square planar CuN_3O chromophore.[24]

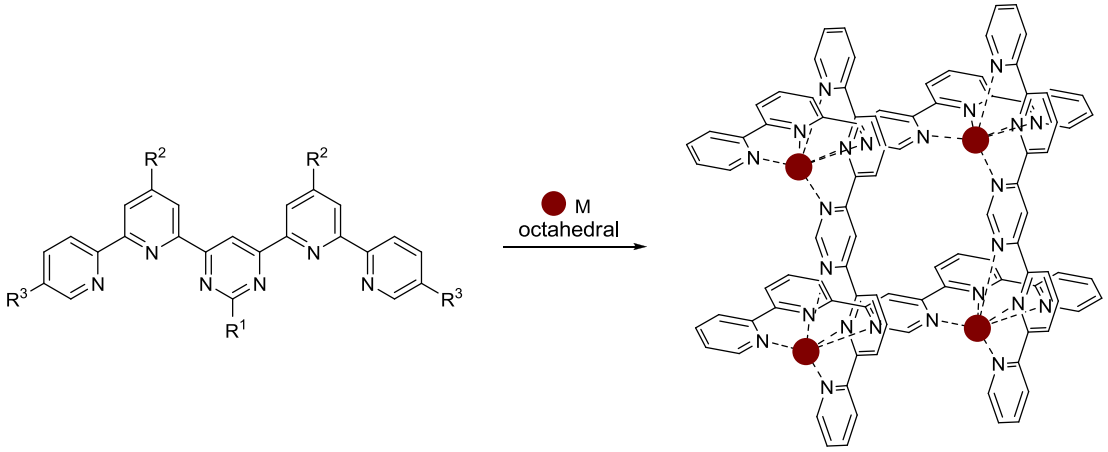

Figure 1.4. Schematic representation of the self-assembly of a [2 × 2] grid structure $[M_4L_4]$ from bis(terpyridine) ligands **4** and octahedrally coordinating metal ions.[27,28,29,30]

Other ligand systems containing terpyridine-like coordination sites enable the arrangement of octahedrally coordinating metal ions. A number of later first- and second-row transition metal ions (e.g., Fe^{II}, Co^{II}, Ni^{II}, Mn^{II}, Cu^{II}, Zn^{II}, Cd^{II}) as well as some main group metal ions (e.g., Pb^{II}), have been introduced into grid-type structures.[27,28,29,30] The range of transition metals that can coordinate to ligand systems such as substituted 4,6-di(2,2'-bipyridin-6-yl)pyrimidine (**4**) gives access to a wide variety of optical, electrochemical, photophysical, and magnetic properties. Furthermore, by using ligand system **4**, these properties can be tuned by the choice of substituents R^1, R^2 and R^3 (Figure 1.4).[27,28,29,30]

It is of great interest to control the introduction of different metal ions at specific

locations in grid architecture. Mixed metal ion [2 × 2] grid architectures were obtained via two routes: 1) a one-pot reaction using symmetrical ligands with different coordination geometries and two different metal ions (see route 1 in Figure 1.5);[31] and 2) synthesis of an intermediate so-called corner complex, in which two ligands coordinate a metal center, which in turn can be reacted with a second metal ion to form a grid (see route 2 in Figure 1.5).[32]

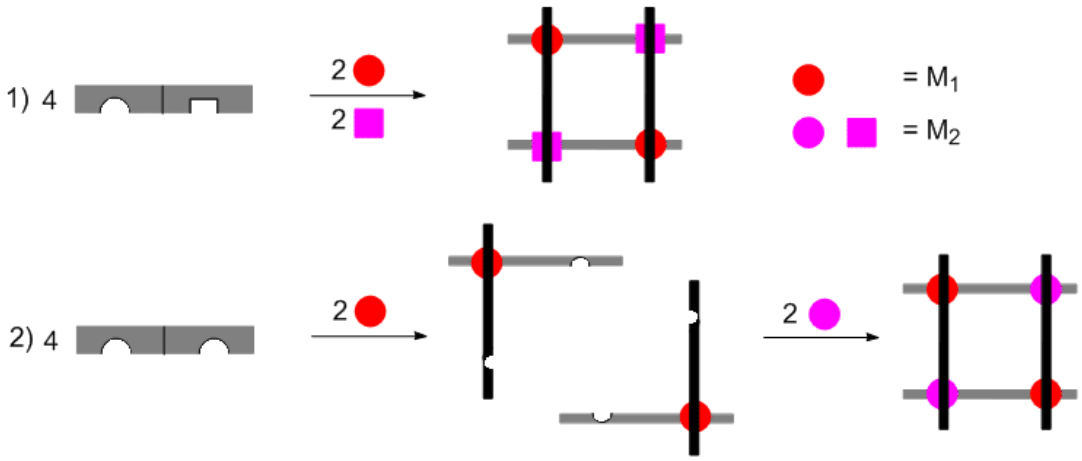

Figure 1.5. Routes for synthesizing a hetero-metallic grid. 1) using ditopic ligands with different coordination geometries; 2) via the corner complex.[31,32]

In the first route, previous examples of well-defined supramolecular structures containing different metal ions relied on the use of different binding sites, with each binding site adapted to a particular metal ion.[33] The combination of binding sites and their spatial arrangement can be viewed as a molecular program, which can be read out by the metal ions through their coordination features during the self-assembly process. It relies on the use of metal ions that possess different coordination geometries coupled to the use of specially designed ligands to direct the self-assembly process.

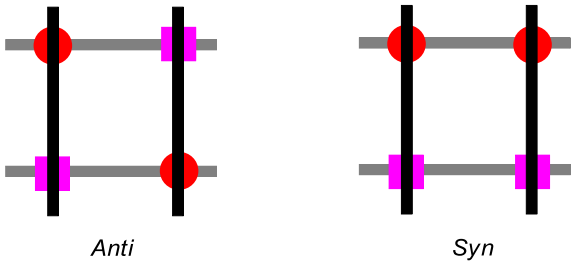

Figure 1.6. Schematic representation of the heterometallic [2 × 2] *anti* and *syn* topoisomers.

It is known that the incorporation of two different metal ions during the step by step assembly processes produces grid-type structures that may exist as either *anti* or *syn* topoisomers (localization isomers) (Figure 1.6).[34] The second novel methodology for the generation of [2 × 2] heterometallic grid-type architectures based on a stepwise process has been reported to avoid the mixture of *anti* and *syn* isomers. Ligand systems such as substituted 4-(1-methyl-2-(pyridin-2-ylmethylene)hydrazinyl)-6-(2-(1-(pyridin-2-yl)ethylidene)hydrazinyl)pyrimidine (**6**) bearing acidic protons open the way to ionizable grid structures (Figure 1.7).[35]

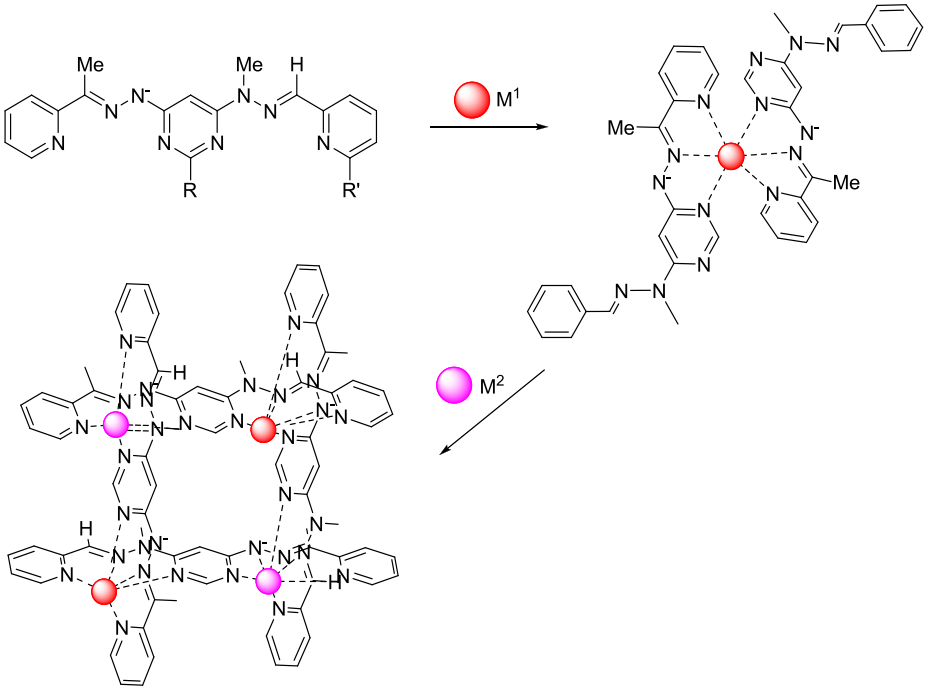

Figure 1.7. Schematic representation of the heterometallic [2 × 2] grid-type complexes $[M^1{}_2M^2{}_2L_4]$ (bottom) via the corner-type precursors $[M^1L_2]$ (top).[35]

The monometallic corner complexes ($[M^1L_2]^{2+}$) were constructed by using cobalt(III) or iron(II) ions containing two free binding sites. The $[M^1L_2]^{2+}$ complexes are subsequently combined with a second type of metal ion to assemble the $[M^1{}_2M^2{}_2L_4]^{8+}$ heterometallic grids exclusively as the anti-topoisomer. These metallogrids are capable of exhibiting multistable redox behavior.[34d,35]

Overall, the formation of gridlike structures depends on three factors which influence the self-assembly of metallogrid architectures in general:[36] 1) a robust set of coordination instructions that impose the correct geometry and drive the process based on the principle of maximum, optimally full, binding site occupancy;[37a] 2) internal orienting effects, such as steric factors that hinder the formation of undesired entities, or stabilizing interactions (e.g., stacking) that guide assembly to the desired product;[37b] 3) external factors such as binding of solvent molecules, counter ions, or other species present in the environment. In addition to the energetic parameters, entropy favors the formation of the largest number of product molecules.[37c]

Besides the assembly parameters mentioned above, ligand substitutions offer the possibility to adjust inherent functional properties (e.g., electronic, optical, magnetic etc.). These also provide the opportunity to introduce a second coordination site on the ligand backbone, to make the self-assembly process programmable.

In conclusion, the formation of [2 × 2] grid-type architectures involves a subtle interplay of steric, enthalpic, and entropic effects, concerning both the ligands and the metal ions. The ligand can cause the formation of different supramolecular coordination entities, and self-assembly may lead to several stable products partitioned under thermodynamic equilibrium. Only carefully designed systems of appropriate ligands and metal ions will provide the self-assembly of [2 × 2] gridlike metal structures in a “programmed” fashion.[36]

1.2.2. Molecular Square

Apart from the above-described [2 × 2] grid-type complexes, a number of molecular squares,[38] showing similar solid structure, have been published that have equally

fascinating properties: the switching capability of both redox and/or spin states.

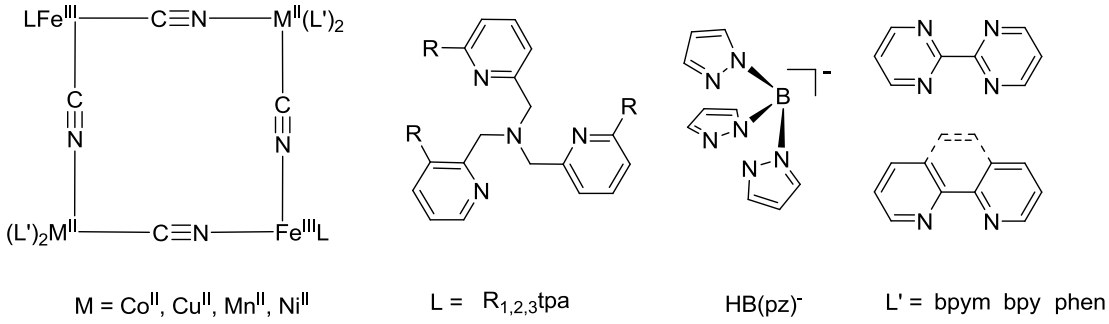

Figure 1.8. Schematic representation of heterometallic square-type tetranuclear complexes.[39]

Among the widespread variety of multinuclear coordination compounds with paramagnetic transition metal ions, the cyanide-bridged square architectures have attracted particular attention of several research groups, due to the ambidentate character of the cyanide ligand which allows the straightforward synthesis of hetero-metallic compounds and also efficiently mediates magnetic exchange coupling.[39]

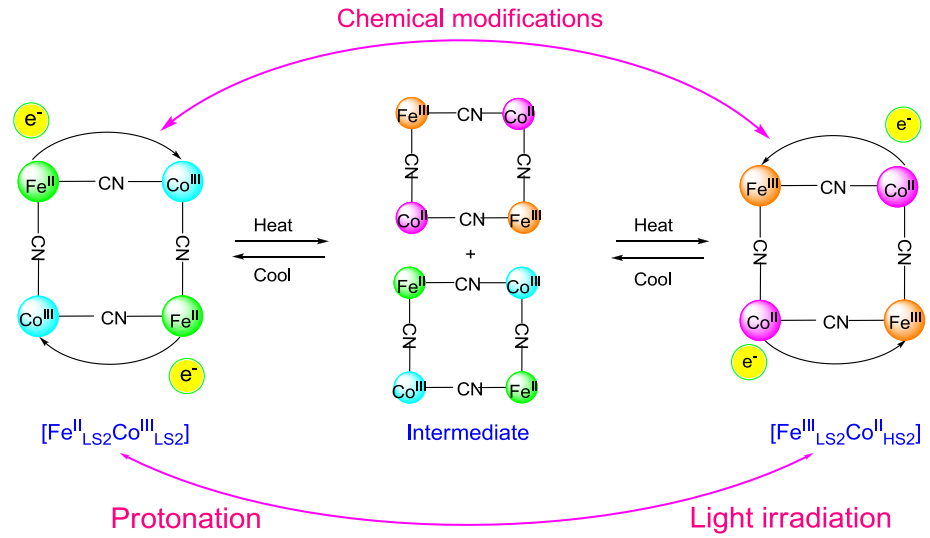

Figure 1.9. Schematic representation of a electron transfer coupled spin transitions (ETCST).[40]

The metal ions in the square structure may be four Fe^{II} centers or alternatively, some mixed metallic variants are known, in which usually two diagonal iron ions are frequently replaced by Co^{II}, Cu^{II}, Mn^{II} or Ni^{II} (Figure 1.8).[40] The mixed-valence square $2Fe^{III/II}$-$2Co^{II/III}$ in particular displays electronic variety in the form of temperature-, photo- or light-induced electron transfer and electron transfer coupled spin transitions (ETCST).[41,42] In the mixed-valence Fe–CN–Co ETCST systems

(Figure 1.9), there are two accessible electronic states of [LS Fe^{III} (t_{2g}^5)−CN−HS Co^{II} ($t_{2g}^5e_g^2$)] and [LS Fe^{II} (t_{2g}^6)−CN−LS Co^{III} (t_{2g}^6)] in the high and low temperature phase, respectively, which are generated by electron transfer between the iron t_{2g} and the cobalt e_g orbitals.

1.2.3. [3 × 3] Grid Complexes

As has been discussed in section 1.2.1 and 1.2.2, [2 × 2] grid complexes and molecular square are in principle capable of displaying multiredox processes and spin-transition phenomena, which could be used as a bi- or multi-stable molecular memory devices, quantum cellular automata (QCA) or SMMs. The study of polynuclear transition-metal clusters is an area of great interest owing to the potential of such compounds to exhibit architecture-dependent behavior, such as molecular magnetism, mixed-metal, mixed-valence and multistep Spin Crossover (SCO) properties. The [3 × 3] grid-type complexes (Figure 1.10) are a good example of the artificial alignment of metal ions, which can have many stable states because of the large number of metal ions, each of which has the potential to change the electronic state and spin sate, bringing about the fascinating overall properties.[43]

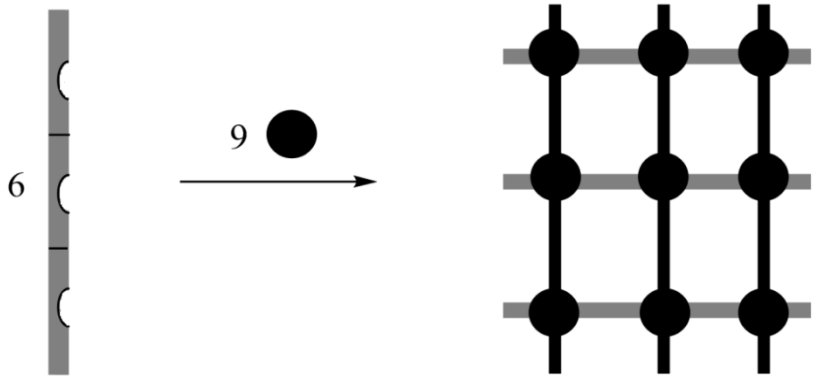

Figure 1.10. Schematic representation of the formation of [3 × 3] metallogrid complexes from planar, tritopic ligand.

The design of [3 × 3] grid-like metal ion arrays is similar to the [2 × 2] grid-type structures, except for the use of tritopic ligands instead of the ditopic ligands mostly used in latter. This construction requires the ligand to contain multidentate binding

subunits connected to metal ions possessing either tetrahedral or octahedral coordination geometry, respectively. Ligands used for preparation of [3 × 3] grid structures thus far are rare and are listed in Figure 1.11.

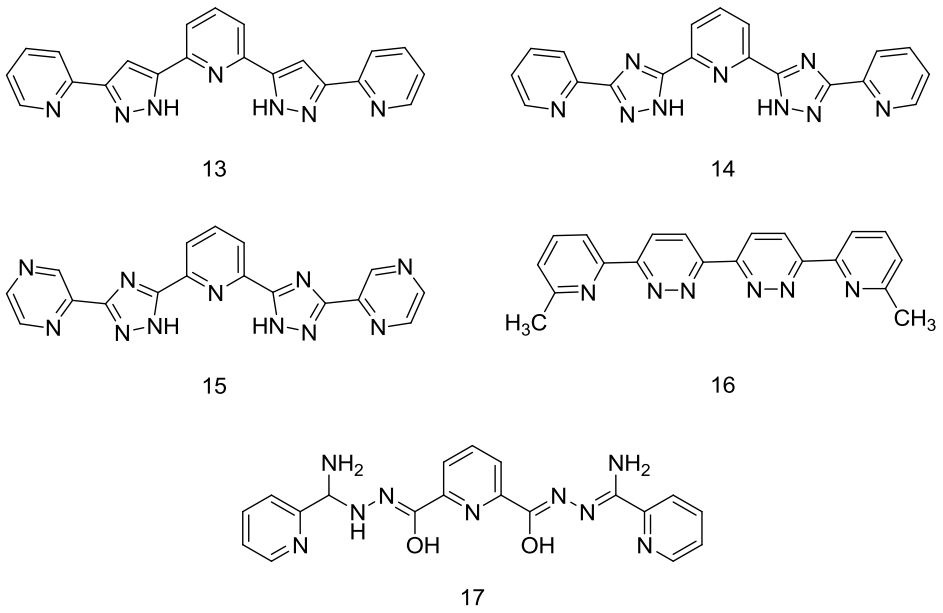

Figure 1.11. Selected ligands used in self-assembly of [3 × 3] grid.[43]

Ligand systems containing pyridine-like coordination sites enable the arrangement of octahedrally coordinating transition metal ions (Fe^{II}, Co^{II}, Ni^{II}, Mn^{II}, Cu^{II}), and have been introduced into [3 × 3] grid-tpye structures.[43] In 1994, Lehn et al. prepared a [3 × 3] silver grid-like structure,[43a] Oshio et al. investigated [3 × 3] cobalt SMMs,[43c] a multiredox active copper grid[43f] and hetero-metallic clusters (from helix to grid)[43d] by using the multidentate ligand 2,6-bis(5-(2-pyridinyl)-1*H*-pyrazol-3-yl)pyridine (**13**). More recently, Tong et al. reported the synthesis and magnetic properties of hetero-metallic grids [$M^{II}Cu^{II}_4Cu^{I}_4$] (M = Fe, Ni, Cu, and Zn) *via* programmed self-assembly by using ligand 2,6-bis(3-(pyridin-2-yl)-1*H*-1,2,4-triazol-5-yl)pyridine (**14**),[43e] while Hou et al. studied the ion-sensing and metal-exchange properties of copper grid $[Cu^{II}_5Cu^{I}_4L_6](I)_2$ with the ligand 2,6-bis(3-(pyrazin-2-yl)-1*H*-1,2,4-triazol-5-yl)pyridine (**15**).[43g] Thompson et al. reported mixed-valence Mn^{II} / Mn^{III} [3 × 3] grid complexes[43b] and oligonuclear Fe complexes (Fe, Fe_4, $Fe_{6,}$ Fe_9)[43h] derived from

(2Z,6Z,N'^{6}Z)-N'^{2}-(amino(pyridin-2-yl)methyl)-N'^{6}-(amino(pyridin-2-yl)methylene)pyridine-2,6-bis(carbohydrazonic) acid (**17**).

The synthesis of [3 × 3] metallogrid arrays is an area of intense research, as the incorporation of different metals or the same metal with different charge states in a cluster can lead to drastic changes in the physical properties, such as the spin state and redox activity, through the alteration of the overall magnetic and electronic interactions.

1.3. Molecules as Information Carriers

1.3.1. Quantum Cellular Automata (QCA)

Quantum cellular automata (QCA) is a system for molecular electronics in which information is transmitted and processed through electrostatic interactions between charges in a structure of quantum dots, which means the molecules in QCA do not act as current switches but as structured charge containers.[44] QCA wires, majority gates, clocked cell operation, and true power gain between QCA cells have been displayed in a metal-dot prototype system. Molecular QCA provides high density devices, low power dissipation, and ways to directly integrate sensors with QCA logic and memory elements.

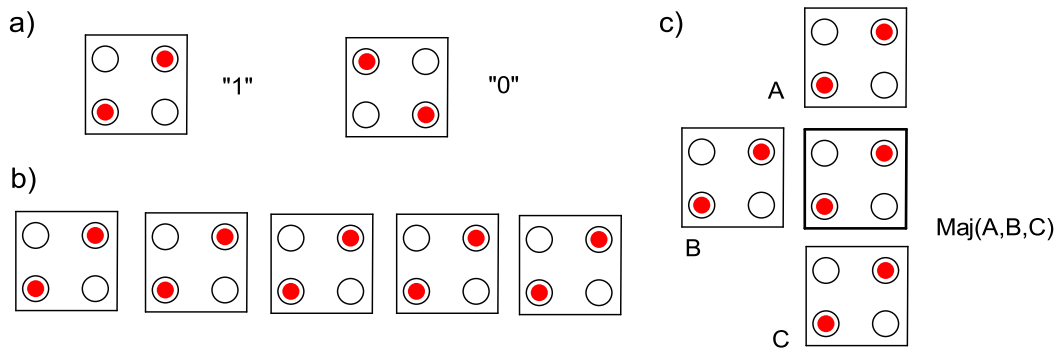

Figure 1.12. Schematic representation and working principle of "cellular automata". a) Coulomb repulsion keeps the electron density (red) at antipodal sites resulting in the degenerate "1" and "0" state. b) A wire of "cellular automata" can be formed by a one-dimensional arrangement of cells. The intercellular Coulomb interactions force all units into the same state. c) Working principle of a majority logic gate consisting of three inputs (A, B, C) which converge to an output (Maj(A; B; C)).[45]

A schematic diagram of an idealized four-dot QCA cell is shown in Figure 1.12. The cell consists of four quantum dots positioned at the corners of a square. The electrons naturally occupy opposite sites. The cell contains two extra mobile electrons, which can tunnel between neighboring sites of the cell. So a single-molecule implementation of a QCA cell requires a molecule in which charge is localized on specific sites and can tunnel between those sites.[46] The role of the dots is then played by redox sites, with tunneling paths offered by bridging ligands. The electrostatic interaction of two neighboring cells (arranged in one, two, or three dimensions) lifts the given degeneracy and results in "1" or "0" states.

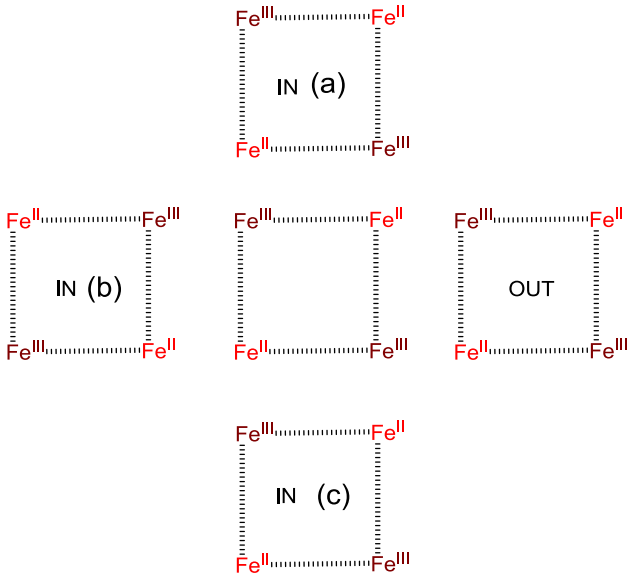

Figure 1.13. Schematic drawing of a molecular majority logic gate based on five tetranuclear di-mixed-valence complexes of iron with three cells as input, one as a central comparator, and one as the output (illustrated is one configuration of the truth table with inputs of (a) "1", (b) "0", and (c) "1" and an output of "1").[47]

Four-metal systems are well represented, but it is the square structure that fulfills one of the important criteria of molecular QCA; i.e., the di-mixed-valence state must be 2-fold degenerate. That is to say the rectangular structures are no better than dinuclear systems for QCA purposes, and tetrahedral arrays are useless as well. Placing four metal centers in a symmetric, covalently bound square structure is only the first step leading to a four-metal QCA cell. The metal ions used to build the

square must have two stable, accessible oxidation states, and there must be sufficient interaction between these redox centers such that the four-metal complex in the di-mixed-valence state can be isolated as a pure compound without being labile with respect to charge disproportionation. A logical next step is the development of a four-metal molecular QCA cell because such molecule would be a more multifunctional building block for constructing logic units than a two-metal cell. Figure 1.13 illustrates a simple majority logic gate that may be constructed from several four-dot cells or four-metal square molecules.[47]

1.3.2. Spin Crossover (SCO)

Spin Crossover (SCO), sometimes referred to as spin transition behavior, is a phenomenon that occurs in some transition metal complexes wherein the spin state of the complex changes because of external stimuli such as a variation of temperature, pressure, light irradiation or an influence of a magnetic field.[48] SCO occurs in octahedral complexes of $3d^4$ to $3d^7$ transition metal ions (most commonly Fe^{II}) when there is only a small energy difference between the electron pairing energy and the splitting of the t_{2g} and e_g orbitals.[49]

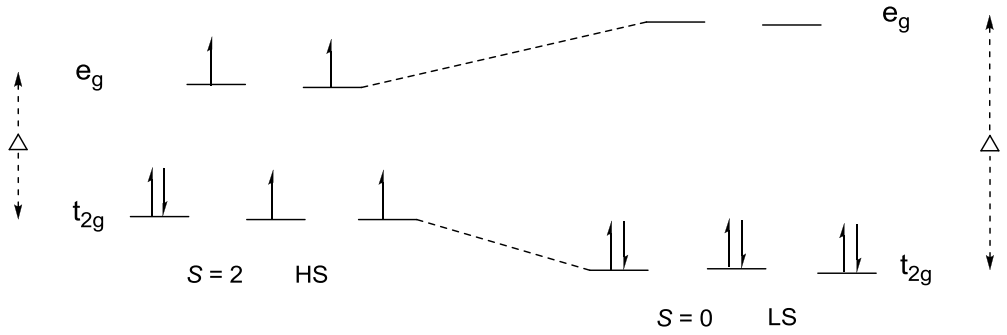

Figure 1.14. Diagram illustrating the dependence of the HS or LS state on energy gap (Δ) of the octahedral ligand field splitting and the corresponding d^6 electron configuration.

Figure 1.14 is a simplified illustration of the d orbital splitting of a d^6 metal ion in the presence of an octahedral ligand field. A large splitting between the t_{2g} and e_g atomic orbitals requires a substantial amount of energy for the electrons to overcome the energy gap (Δ) to comply with Hund's Rule. With regard to the ligand field and

ligand field theory, the change in spin state is a transition from a low spin (LS) ground state electron configuration to a high spin (HS) ground state electron configuration of the metal's atomic d orbitals, or vice versa. The magnitude of the ligand field splitting along with the pairing energy of the complex determines whether it will have a LS or HS electron configuration. A LS state occurs because the ligand field splitting (Δ) is greater than the pairing energy of the complex (which is an unfavorable process).[50]

Taking Fe^{II} as an example to illustrate the SCO phenomenon, in an octahedral ligand field the metal with the electron configuration d^6 can exist in either LS or HS state, (Figure 1.14). In a strong octahedral ligand field the electrons fill the lower energy t_{2g} orbitals completely ($t^6_{2g}e^0_g$, LS, $^1A_{1g}$), which results in the diamagnetic LS Fe^{II} ion. In contrast, the weak octahedral spin pairing energy is greater than the ligand field splitting energy, which according to Hund's rule, a $t^4_{2g}e^2_g$ ($^5T_{2g}$) configuration (HS) follows. By using various ligand systems with strong or weak ligand field strength, transition metal complexes with HS or LS metal centers display SCO or not. Simultaneously, the Co^{II} ion with the electron configuration d^7 displays the LS state $t^6_{2g}e^1_g$ (^4T_g) and the HS state $t^5_{2g}e^2_g$ (^2E_g) in strong or weak octahedral ligand field, respectively, as shown in Figure 1.15.

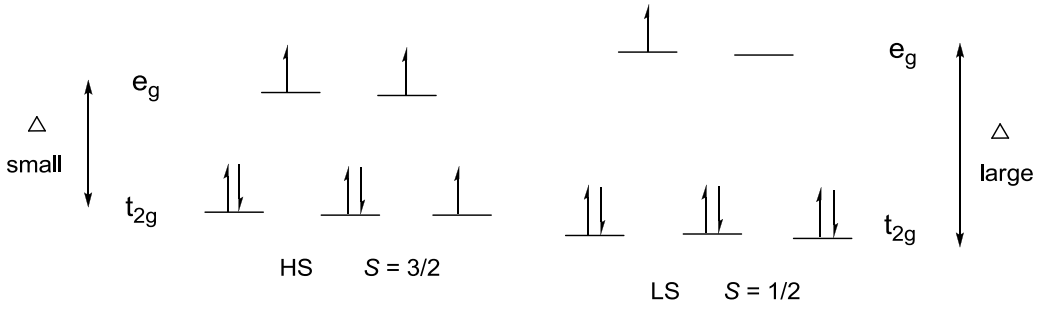

Figure 1.15. Diagram illustrating the corresponding d^7 electron configuration of the HS and LS state in the case of octahedral ligand field splitting.

A spin transition curve is obtained from a plot of the HS fraction (γ_{HS}) as a function of temperature. Such curves can be divided into different types, which are highly informative and take a number of forms for systems in the solid state. The most

typical of these are illustrated in Figure 1.16. The variety of manifestations of a transition evident in this figure arises from a number of sources but the most important is the degree of cooperativity associated with the transition. This refers to the extent to which the effects of the spin change, especially the changes in the metal-donor atom bond distances, are spread throughout the solid structure and is determined by the grid properties. The gradual transition displayed in Figure 1.16a is perhaps the most common and is observed when cooperative interactions are relatively weak. This is the course of a transition observed for a system in solution where essentially a Boltzmann distribution of the molecular states is operative. The abrupt transition shown in Figure 1.16b results from the presence of strong cooperativity. Obviously, situations intermediate between (a) and (b) exist. When the cooperativity is particularly high, hysteresis may result, as shown in Figure 1.16c. The appearance of hysteresis, usually accompanied by a crystallographic phase change associated with a spin transition, has come to be recognized as one of the most significant aspects of the whole spin crossover phenomenon. This confers bistability on the system and thus a memory effect. The potential for exploitation of this aspect of SCO in storage, memory and display devices was highlighted by Kahn and Martinez[51] and this has driven much of the recent research in the area. The quest for stable systems which display a well-defined, reasonably broad hysteresis loop spanning room temperature and an understanding of the factors which lead to such behavior is continuing. Despite the relative lack of predictability, the number of systems now known to display a spin transition curve of type (c) is remarkably high, and highest for iron(II) where,[52] significantly, the change in intramolecular dimensions is the greatest for the ions for which SCO is relatively common (Fe^{II}, Fe^{III}, Co^{II}). The transitions of type (c) are defined by two transition temperatures, one for decreasing ($T_{1/2}\downarrow$), and one for increasing temperature ($T_{1/2}\uparrow$).

Two step transitions (Figure 1.16d), first reported in 1981 for an iron(III) complex of 2-bromo-salicylaldehyde-thiosemicarbazone,[53] are relatively rare and have their origins in several sources. The retention of a significant HS fraction (Figure 1.16e)

at low temperatures may also arise from various sources. For instance, a fraction of the complex molecules may be in a different lattice site in which the field strength is sufficiently reduced to prevent the formation of low spin species.

In such complexes, the change, HS ↔ LS, is accompanied by changes in magnetism, structure, and color of the complexes, and therefore SCO active compounds may lead to potential technological applications in molecular switches, displays, sensors and memory devices.[54] The SCO phenomenon was discovered by Cambi and Szegö in 1931 in a series of *tris*(N,N-disubstituted-dithiocarbamato)-iron(III) complexes.[55] Since then, a variety of iron(III) complexes undergoing SCO between the HS (S = 5/2) and LS (S = 1/2) states have been reported.

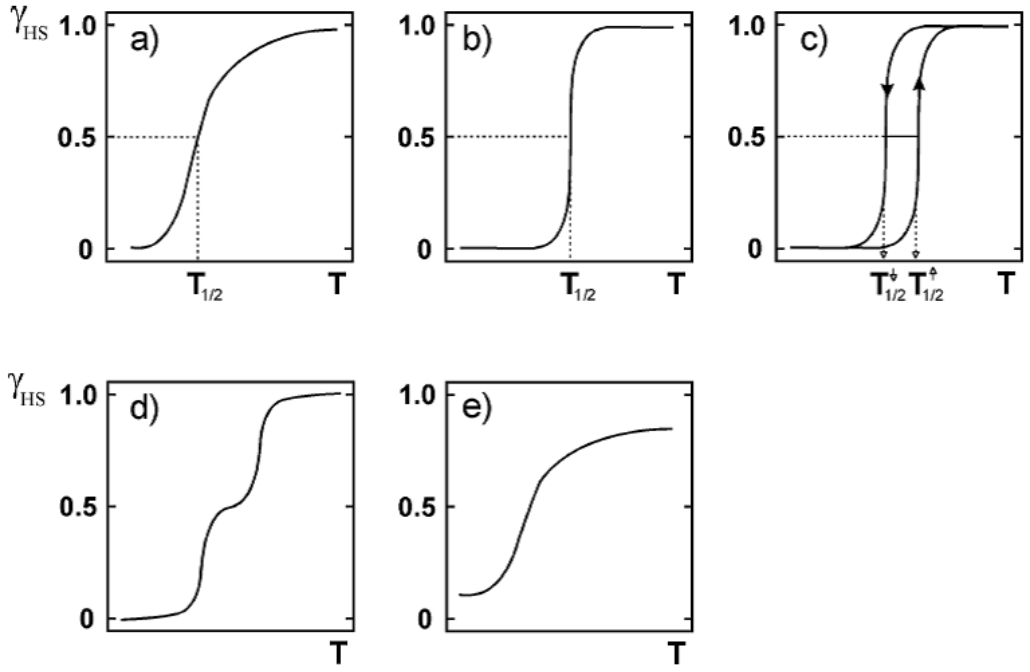

Figure 1.16. Representation of the principal types of spin transition curves (high spin fraction (γ_{HS}) (y axis) vs temperature (T) (x axis): a) gradual; b) abrupt; c) with hysteresis; d) two-step; e incomplete.[56]

Based on these research results, the field developed enormously, and since then the spin-crossover effect has been more deeply understood and has entered more sophisticated applications. Spin crossover compounds were synthesized as described in numerous review articles[57,58,59,60] and book chapters.[61,62] The largest number of SCO examples is found concerning the metal ions which do show typical behavior;

metal centers with a d^6 configuration (e.g. iron(II)) account for the vast majority of these. In these complexes, the ligand field is weaker and hence spin pairing is not so strongly favored and it is possible to obtain relatively stable high spin or low spin complexes from a broad range of ligands. For the smaller iron(III) ion (d^5), the low spin configuration is again relatively favored, but not to the extent observed for Co^{III}, partly because of the relatively LS pairing energy and higher ligand field stabiliZation energy of the latter. Thus the occurrence of SCO is much more widespread for Fe^{III} than for Co^{III}. However, conditions are less favorable than for Fe^{II}, partly because of the tendency of high spin Fe^{III} complexes to be readily hydrolyzed.

In the cases of iron and cobalt metal complexes, Mössbauer and EPR spectroscopies as well as measurements of the molecular magnetic moment via NMR spectroscopy and magnetic susceptibility as a function of temperature, $\chi(T)$, have always been the principal techniques for characterization of SCO phenomena. The former technique (Mössbauer spectroscopy), although powerful, is essentially limited to Fe and may require ^{57}Fe enrichment, whereas the short relaxation time of LS Fe^{III} (10^{-13} – 10^{-11} s), HS Fe^{II} (10^{-13} – 10^{-12} s) and HS Co^{II} (5×10^{-13} – 10^{-12} s) may lead to barely detectable EPR lines. In contrast (but due to the same reasons), ^{1}H NMR spectra of paramagnetic iron and cobalt complexes are fairly easy to obtain to estimate the magnetic moment. Thermal SCO in solid transition metal compounds is always accompanied by significant changes in the metal coordination environment, which may lead to significant positional changes in the crystal lattice as revealed by X-ray structural studies.

As Figure 1.17 shows, spin crossover in a supramolecular [2 × 2] Fe_4^{II} grid can be triggered by temperature, light and pressure.[63] Indications of SCO behavior in solution were obtained in the course of ^{1}H NMR investigations at variable temperature in a range of 228 K to 308 K. Measurements of the magnetic susceptibility $\chi(T)$ on solid samples display the transition from the 3HS-1LS state to the 1HS-3LS state with a more or less drastic change in the magnetic susceptibility. The isomer shift, δ, and the quadrupole splitting, ΔE_Q, two of the most important

parameters derived from a Mössbauer spectrum,[64] differ significantly for the HS and LS states of both Fe^{II} and Fe^{III} ions.

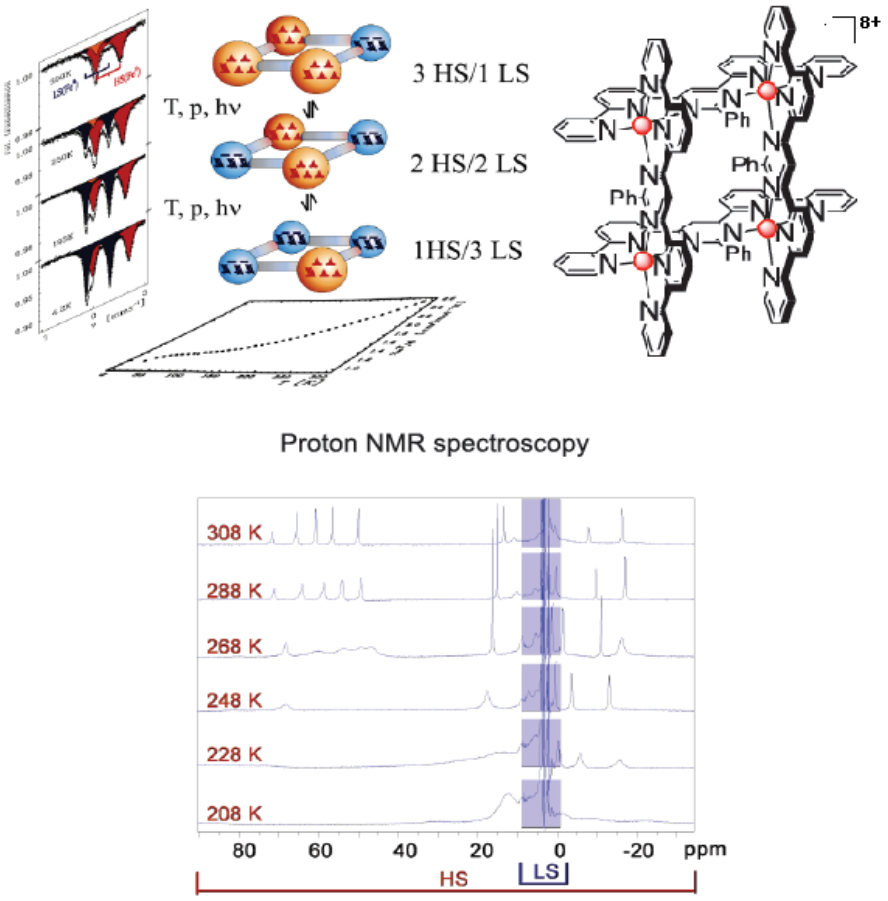

Figure 1.17. Spin state changes observable for a [2 × 2] grid of Fe(II) complex.[63]

At the same time, some chemical influences could also perturb SCO systems. Firstly, substitution within a ligand may drastically alter the spin state of a system, as a result of steric or electronic effects.[65] Secondly, a more subtle chemical influence is the variation of the anion associated with a cationic spin crossover system, or of the nature and degree of solvation of salts or neutral species.[66] Furthermore, insight comes from metal dilution. The effect of dilution of spin transition complexes into the lattice of isostructural species which do not or cannot show SCO has proved to be very diagnostic of the function of cooperative interactions in influencing the nature of spin crossover transitions in solids.[67]

1.3.3. Single Molecule Magnets (SMMs)

Single molecule magnets (SMMs) are mainly inorganic molecules that have one or

several metal centers with unpaired electrons. These metal complexes are surrounded by organic ligands and show slow relaxation of the magnetization of purely molecular origin. They can be magnetized by a magnetic field, and under a certain blocking temperature could remain magnetized even after switching off the magnetic field. No interaction between the molecules is necessary for this phenomenon to occur. This is a property of the molecule itself. The molecules possessing these characteristics are considered to be potential candidates for use in data storage, spintronics, and quantum computing devices.[68]

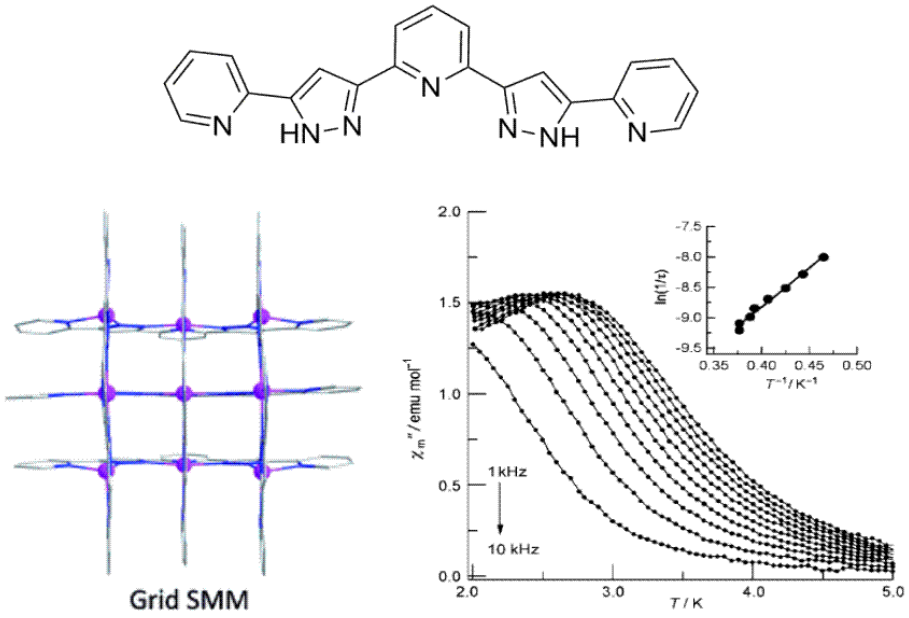

Figure 1.18. The structure and out-of-phase of components of the alternating current susceptibility for a [3 × 3] grid of cobalt complex.[69]

The field of SMMs, or molecular nanomagnets, started with the mixed-valence complex $[Mn_{12}O_{12}(OAc)_{16}(H_2O)_4]\cdot 2HOAc\cdot 4H_2O$. Variable field magnetization and high-frequency electron paramagnetic resonance (HF-EPR) data indicate that the mixed-valence complex has an S = 10 ground state. The large spin ground state arises from antiferromagnetic interactions between the S = 3/2 spins of Mn^{IV} ions and the S = 2 spins of Mn^{III} ions, and the axial zero field splitting parameter D = 0.50 cm^{-1}. This complex was first published by Lis in 1980 and subsequently studied in more detail around 10 years later,[70] which lead to the establishment of a new class of materials called single molecule magnets (SMMs).

The general approach for new SMMs is to aim for systems with large ground spin states (*S*) and enhanced negative raising (or easy axis) magnetoanisotropy (*D*).[71,72] In 3d metal chemistry the coordination compounds of Fe^{I}[73], Fe^{II}[74], Fe^{III}[75], Co^{II}[76,77], Ni^{I}[78], and Mn^{III}[79] were extensively studied as SMMs in the absence of direct current (dc) field or under an applied dc field in the past few years.[80] Most examples of SMMs are mono or multinuclear compounds. In order to be able to control the magnetic properties of SMMs, we need control over many aspects of the composition and structure of polynuclear complexes. The fact that these complexes are often synthesized and crystallised straight from a one-pot reaction, in one step, means that often we have little synthetic control. This is especially important when using a multidentate ligand, with many binding sites and many different binding modes.

However, the number of [n × n] grid metal-based complexes displaying SMMs behavior is very small. Until currently, very few examples of grids with 3d transition-metal ions displaying zero-field slow relaxation have been reported.

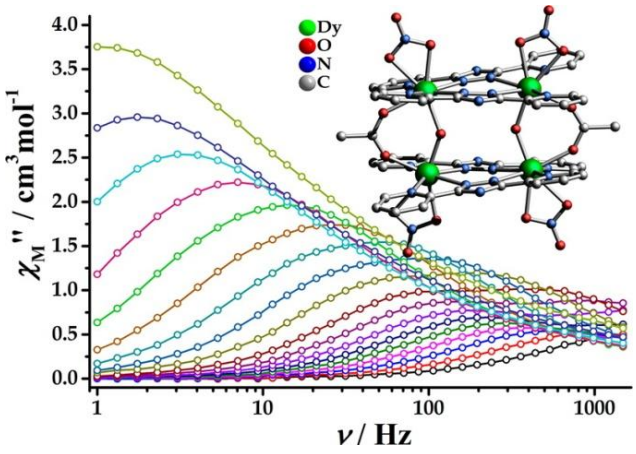

Figure 1.19. The out-of-phase of components of the alternating current susceptibility for [2 × 2] grid of Dy^{III} complex.[81]

The [3 × 3] grid-like structure ($[Co^{II}_8Co^{III}L_6](BF_4)_7$) consists of Co^{II} and Co^{III} ions coordinated to hepta-dentate polypyridine ligands (Figure 1.18, left). The Co^{II} ions in the structure show both LS (*S* = 1/2) and HS (*S* = 3/2) states. The frequency dependent out-of-phase signals of this grid compound show the peak maxima shifted to a lower temperature as the ac frequency decreased (Figure 1.18, right).[69] The

alternating current (ac) magnetic susceptibility data confirms that the structure is the first example of a grid complex SMM. However, no [2 × 2] grid transition metal complexes showing SMM behavior has been reported, except for a [2 × 2] grid Dy^{III}_4 cluster which has been proven to behave as a SMM as shown in Figure 1.19.[81] The bpt^{-}-bridged [2 × 2] complexes, with four noninteracting Dy^{III} ions (S = 5/2), exhibits SMM behavior with a remarkably high energy barrier (143 cm^{-1}).

Overall, there is still much to learn about the parameters that control slow relaxation in SMM systems, and only by synthesizing more examples and probing their low temperature behavior in greater depth can we start to understand and hence, improve their magnetic properties.

1.4. Mixed-valence Complexes

The term 'mixed valence' is one of several names, such as 'mixed oxidation state' or 'non-integral oxidation state', used to describe inorganic or metal-organic compounds in which one metal is present in more than one oxidation state.[82] Mixed-valence chemistry has a long and rich history which is characterized by a strong interplay of experimental, theoretical and computational studies.[83] The first mixed-valent inorganic compound, Prussian Blue, is a complex Fe^{II}/Fe^{III} cyanide discoved in 1704 and subsequently employed as a paint pigment.[84] In the late 1960s, molecular mixed-valence systems began to attract great interest because of new properties exhibited due to significant electron coupling between donor and acceptor sites is present and because of the relationship between optical properties and electron transfer rates of the species.[85] Mixed-valence molecules contain donor and acceptor sites separated by a bridging ligand (BL).

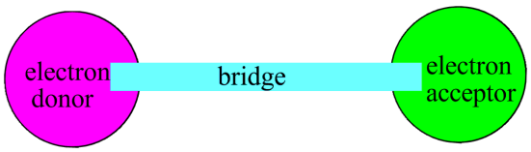

In the following discussion, binuclear compounds with formula $[L_xM^n(BL)M^nL_x]$ are considered, as shown in Figure 1.20. They contain two metals (M) in the oxidation

state (n) connected by a BL and further coordinated by additional ligands (L_x). Mixed-valent complexes can be prepared by single oxidation or reduction of these complexes. They can be formulated in two extreme scenarios, namely the fully localized form, $[L_xM^n(BL)M^{n+1}L_x]$, and the fully delocalized form, $[L_xM^{n+0.5}(BL)M^{n+0.5}L_x]$, which shows valence averaging. In the case of noninnocent bridging ligands, a radical complex, $[L_xM^n(BL^{\cdot+})M^nL_x]$, has to be considered as well.

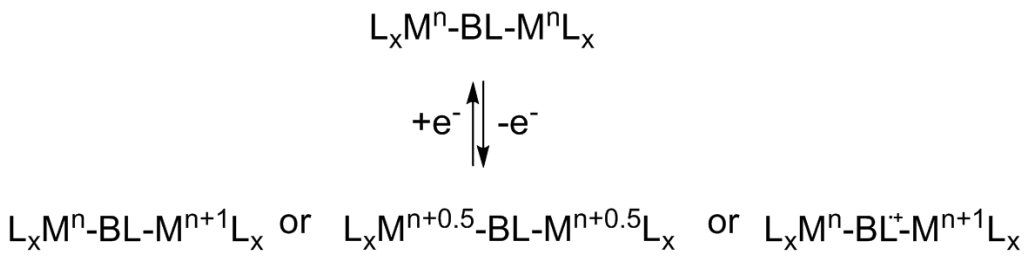

Figure 1.20. Formation of mixed valent complex by oxidation of a M^n_2 species (L_x = ligand, BL = bridging ligand).

The first comprehensive study of mixed-valence compounds was made by Robin and Day in 1967. Robin and Day, they proposed an organization of mixed-valence compounds into three categories, classes I, II, and III (Figure 1.21).[86] In class I mixed-valence compounds, no electron transfer occurs. There is no electronic coupling (H_{ab} = 0) when two bridged metal centers are far apart or when their interaction is symmetry or spin forbidden, meaning there are two completely decoupled redox states and fully localized redox centers. In class II mixed-valence compounds, two metal centers have detectable electronic interaction and electron transfer is occurring between two metal centers. The moderate electronic coupling between the centers leads to a double-well adiabatic ground-state potential-energy curve with partly localised charges and a barrier for thermal electron transition (ET) (the electronic coupling, $2H_{ab}$, is smaller than the Marcus reorganisation energy, λ). In class III mixed-valence compounds, two metal centers have such strong electronic interaction that delocalization occurs and the formal charge on each metal center is averaged, $M^{n+0.5} – M^{n+0.5}$, for example. The strong coupling with $2H_{ab} \geq \lambda$ leads to a single ground-state minimum without an ET barrier and with symmetric charge delocalization over both redox centers, making Class III mixed-valence compounds

distinct from class II compounds. In addition to the Robin-Day classification, a number of recent studies have reported more complicated systems exhibiting an intermediate behavior between class II and class III, which is now categorized as borderline class II-III.[87]

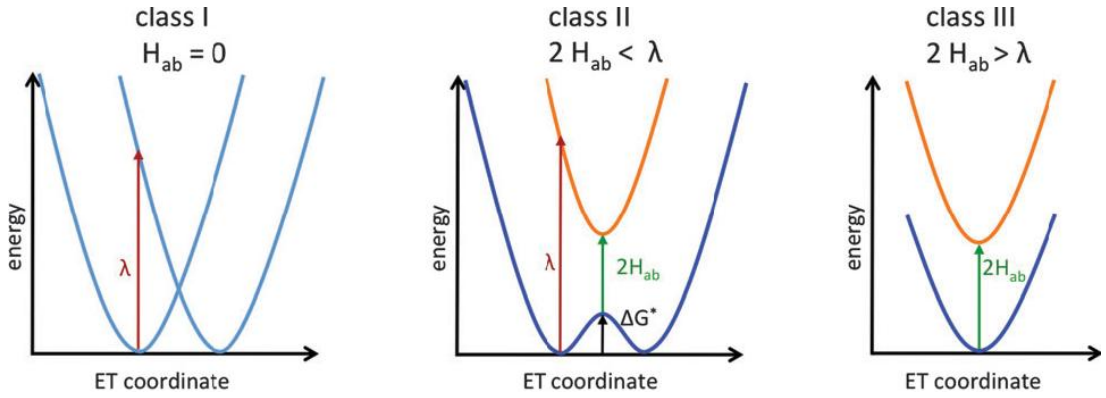

Figure 1.21. Potential curves for the three primary Robin-Day classes: class I (left), class II (middle) and class III (right).[88]

To investigate the extent of electronic interaction between two redox centers, absorption in the visible or near-infrared region is of diagnostic importance. Although class I mixed-valence compounds show no absorption, called an intervalence charge transfer (IVCT) band, class II compounds generally exhibit a broad ($\Delta\nu \geq 2000$ cm^{-1}) and weak ($\varepsilon \leq 5000$ L mol^{-1} cm^{-1}) absorption, which originates from a light-driven process from one redox site to the other (from M^n to M^{n+1}, for example). In contrast, class III mixed-valence compounds show a narrow ($\Delta\nu \leq 2000$ cm^{-1}) and intense ($\varepsilon \geq 5000$ L mol^{-1} cm^{-1}) absorption, which is historically called an IVCT band, but arises from a transition between delocalized electronic levels rather than from intramolecular charge transfer. Analysis of the IVCT bands by Marcus-Hush theory gives parameters that define the thermal electron transfer barrier.[88]

The frequently used term "coupling", used to describe the metal-metal interaction in mixed-valent compounds, can have different meanings, on the basis of either electrochemical (i), spectroscopic (ii), or magnetic measurements (iii).

(i) The very existence of any mixed-valent "intermediate" state is quantified by the

comproportionation constant, K_c, according to eq. 1.[89]

$$K_c = 10^{\Delta E/59\,\mathrm{mV}} = \frac{[M^{(n-1)}]^2}{[M^n][M^{(n-2)}]} \qquad M^n + M^{(n-2)} \rightleftharpoons 2\ M^{(n-1)} \quad \text{(eq. 1)}$$

The comproportionation constants K_c gives a measure of the stability of mixed-valence species relative to the homo-valence species. K_c can range from 4, the statistical value,[89] to more than 10^{15}.[90]

(ii) A different measure of metal-metal interaction uses information from absorption spectroscopy, specifically the energies and intensities of characteristic long-wavelength bands. For mixed-valent systems with similar or identical electron-transfer sites, these IVCT transitions in a valence-localized situation (Class II compounds) may be reformulated, e.g., as π→π* or σ→σ* transitions in a fully delocalized model (Class III situation).[89a,91]

The electronic coupling (H_{ab}) can be calculated from the energy position of the maximum of the IVCT band (ν_{max}), the transition dipole moment (μ_{12}) and the effective charge transfer distance (r_{ab}), and the unit electron charge (e) (eq. 2):[92]

$$H_{ab} = \frac{|\mu_{12}|}{r_{ab}} \nu_{max} \quad \text{(eq. 2)}$$

The transition dipole moment (μ_{12}) is experimentally accessible from the integrated intensity of the IVCT band. Calculation of the electronic coupling according to eq. 2 does not take into consideration the shape of the IVCT band. For IVCT bands with a Gaussian shape, the parameters of the IVCT band can be used for determination of the integrated intensity. By additionally inserting natural constants and conversion factors, eq. 3 is derived. It can be used to calculate H_{ab} directly from the position of the maximum (ν_{max} in cm^{-1}), the peak width at half height ($\Delta\nu_{1/2}$ in cm^{-1}) and the extinction coefficient at the absorption maximum (ε_{max} in L mol^{-1} cm^{-1}) of the IVCT band together with the effective charge transfer distance (r_{ab} in Å). For r_{ab}, the distance between the two metals (d in Å) is used as a rough estimate.[92a,93]

$$H_{ab} = \frac{2.06\times10^{-2}(\nu_{max}\varepsilon_{max}\Delta\nu_{1/2})^{1/2}}{r_{ab}} \quad \text{(eq. 3)}$$

The position, form and intensity of the IVCT band together with its behavior in different solvents gives a rough indication of the classification of a mixed-valent system. A detailed analysis of the IVCT band provides insight into the electronic structure by determination of the coupling constant (H_{ab}).

(iii) Finally, the terms "interaction" and "coupling" are also used to describe magnetic exchange in coordination compounds. Mixed-valent species can involve more than one paramagnetic metal center, such as the HS Fe^{II}-Fe^{III} sites in proteins.[94]

Compounds with two or more centers of mixed valence in a similar or identical settings have become the focus of recent research for a number of reasons. These include their role in biochemistry (e.g., $Fe^{II}Fe^{III}$, $Mn^{III}Mn^{IV}$, $Cu^{I}Cu^{II}$, or $Co^{II}Co^{III}$ centers),[82b, 95] their model character for intramolecular electron transfer,[96] their unusual spectroscopic properties,[82,95,97] their potential in molecular electronics,[98] and their function as test systems for theoretical approaches.[97,99] These studies are relevant in the development of molecular-scale functional materials in which electron transfer or transport plays a key role.[98]

The species which have been the most prominant in investigations of mixed valence complexes are bimetallic complexes in which two metal ions are connected by a bridging ligand (BL). The mixed valent state is typically accessed by the one-electron oxidation of a bis-M^{II} (M = Ru, Fe, Co) complex (Figure 1.20).[100] Such complexes may exhibit a change of the spin state of the metal ions after oxidation and therefore offer further fascinating magnetic properties. The study of mixed-valence compounds has developed into a field with multinuclear complexes displaying various oxidation states.[43] In particular, compounds of iron and cobalt have been widely studied.[101,102] It is worth while to mention that the metal oxidation states in mixed valence [2 × 2] tetranuclear grid-like compounds are usually arranged as shown in Figure 1.22, in which neighboring metals display different oxidation states, but the two metal atoms located at diagonal vertices of the grid exhibit the same oxidation state.

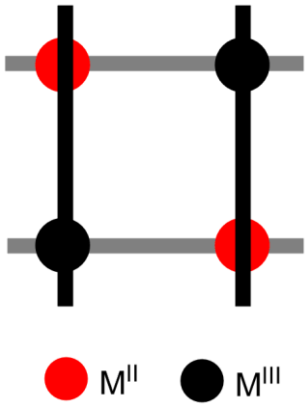

Figure 1.22. Mixed valence [2 × 2] tetranuclear grid-like architecture.

It is known that those multinuclear complexes with one or more oxidation states of the metal ions are produced accidentally and it is often difficult to predict the solid structure. The one-pot reaction used to yield the normal homo-valence [2 × 2] grid complexes could also produce the pronounced thermodynamically stable mixed-valence fragment, by introducing two metal ions of different valence during the self-assembly (Figure 1.23). [103] The ligand bis(phenyl(2-pyridyl)methanone)thiocarbohydrazone (**11**) is reacted with an Fe^{II} salt to yield the mixed-valence [2 × 2] tetranuclear compound, with two oxidized Fe^{III} located at diagonal positions of the grid structure. The di-mixed-valence molecular square ($Fe^{II}_2Fe^{III}_2$) with two extra mobile electrons occupying the opposite corners is achieved via self-assembly as a pure phase with remarkable stability for molecular expression of quantum cellular automata (QCA).

A controlled method to prepare mixed valence compounds displaying pronounced stable structures and fascinating properties has recently attracted particular attention. As discussed in section 1.2.1, the stepwise, controlled route 2 (Figure 1.5) was employed, not only to construct hetero-metallic [2 × 2] grid-type architectures by introducing different metal ions, but also to provide mixed-valence [2 × 2] gridlike structures by introducing a second metal ion of different valence.[35] The key intermediates in the synthesis of mixed-valence [2 × 2] grids by using ligand system **6** are the Co^{III} corner complexes. The metal cobalt(III) was selected in order to prepare grids with a $Co^{III}_2Co^{II}_2$ or $Co^{III}_2Fe^{II}_2$ mixed-valence structure (Figure 1.7).

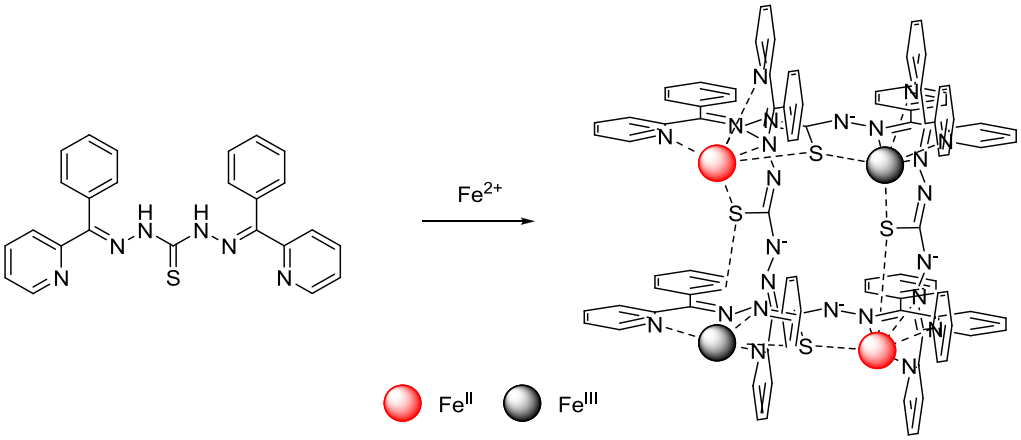

Figure 1.23. Schematic representation of the mixed-valence [2 × 2] grid-type complex $[Fe^{II}_2Fe^{III}_2L_4]^{2+}$ via a one-pot reaction.[103]

Another new method was found to controllably prepare mixed-valence [2 × 2] complexes by using chemical oxidation from the homo-valence [2 × 2] complexes (Figure 1.24).[25,104] This type of complex has been vary rarely reported. The ligand systems 2-phenyl-4,5-bis{6-(3,5-dimethyl-1*H*-pyrazol-1-yl)pyrid-2-yl}-1*H*-imidazole (**8**) and 3,5-bis{6-(2,2'-bipyridyl)}pyrazole (**9**), containing the six-member ring pyridine and five-membered ring pyrazole or imidazole as tridentate donors, are used to initiate chemical oxidation to construct the mixed-valence [2 × 2] grids. The properties of these complexes are influenced by both the ligand substituents and metal ions.

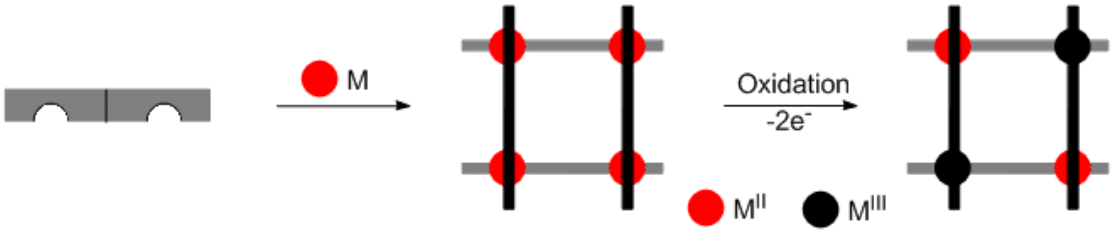

Figure 1.24. Schematic representation of the mixed-valence [2 × 2] grid-type complex via oxidation from a homo-valence [2 × 2] grid-type complex.

In these mixed-valence grid-type structures, the metal atoms used to construct the mixed-valence grid *via* oxidation of the homo-valence grid structure are Fe^{II} ions. In contrast, mixed-valence [2 × 2] cobalt grids produced *via* homo-valence compound after twice oxidation are rather rare, though there are several homo-valence [2 × 2]

grids produced using Co^{II} or Co^{III}. However, in section 1.3.3 there is one example of a [3 × 3] mixed-valence cobalt grid-type compound which displays the fascinating magnetic properties as a grid SMM.[43c]

The rational assembly of metal complexes opens the door for exploring molecular squares with mixed-valence states.[105, 106] However, the development of mixed-valence molecular squares exhibiting promising electrochemical behaviors and thermodynamic stability associated with charge disproportionation, and kinetic stability to degradation still remain substantial challenges.

2. Outline

2.1. Project Outline

There are three fascinating features of great interest resulting from grid-like architectures:

1) appearance of novel properties because of multifunctionality (multi-ligand, multi-nuclear, multi-valence);

2) generation of hetero-valence and hetero-nuclear species in a single operation;

3) access to sequential self-organization *via* the inter-grid interaction implemented by means of multivalence.

Thus, the multifunctionality features of metallogrids are clearly apparent from their electrochemistry, where not only the metal centers but also the ligands provide redox activities, as well as their magnetism in which the spin state may be influenced not only by interactions between the metal centers but also by physical factors as discussed in chapter 1. On the other hand, the potentially valuable features of grid-type structures as supramolecular entities include their use as platforms to which multiple external substituents can be attached, then making the multi-valent interactions possible.

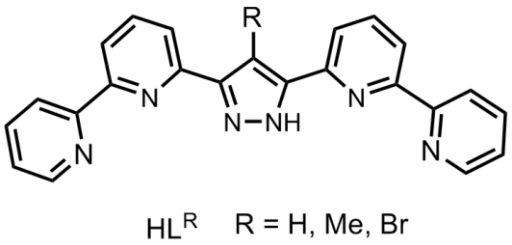

Figure 2.1. Pyrazolate-bridged binucleating proligands HL^R.

We recently developed some robust, air- and moisture-stable [2 × 2] metallogrids based on a set of substituted 3,5-bis(bipyridyl)-pyrazole ligands.[107] The Fe_4 grid of the parent proligand HL^R (Figure 2.1) exhibited multistability with respect to spin and redox states.[108] The all-ferrous complex $[Fe^{II}{}_4L^H{}_4](BF_4)_4$ featured gradual but incomplete two-step thermal SCO from the [4HS] to the [2HS-2LS] state. The di-mixed-valence species $[Fe^{II}{}_2Fe^{III}{}_2L^H{}_4](BF_4)_6$ could be produced by chemical

oxidation. In contrast, the derivative $[Fe^{II}_4L^{Me}_4](BF_4)_4$ that was obtained from the slight modification of the HL^{Me} ligand bearing a methyl substituent in the backbone C-4 position of the central pyrazolate (Figure 2.1) was shown to stabilize the dimixed-spin [2HS-2LS] state over a wide temperature range.[109] Because of its sought-after [HS-LS-HS-LS] configuration, with identical spin states at diagonally opposed vertices of the grid (*trans*-[2HS-2LS]), the latter system appeared particularly suited for potential use in QCA devices. The new compartmental proligand 4-bromo-3,5-bis{6-(2,2'-bipyridyl)}pyrazole (HL^{Br}) was developed to construct a series of $[Fe^{II}_4L^{Br}_4](X)_4$ with various counteranions ($X^- = PF_6^-$, ClO_4^-, BF_4^-, Br^-). Variations in spin-state for the crystalline material range from the [4HS] *via* the [3HS-1LS] to the [2HS-2LS] forms, with some grids showing thermal SCO, which allowed us to establish experimentally well-grounded correlations between structural distortion of the $\{FeN_6\}$ coordination polyhedron, quantified by using continuous shape measures, and the grid's spin-state pattern.[110] Additionally, a novel type of oligonuclear SCO system is reported, namely the defect-grid Fe^{II}_3 complex, which exhibits a sharp and complete SCO from the 1HS-2LS to the 2HS-1LS state with wide hysteresis near room temperature. It mediates a dramatic, yet reversible, response to the uptake of exogenous solvent molecules leading to silencing of the SCO. High sensitivity towards the guest molecules (H_2O, MeOH, EtOH, MeCN, acetone, and benzene), short response time upon exposure, and smooth reversibility of guest binding are favorable characteristics for future sensing applications, introducing a new motif to the field of grid-type coordination chemistry.[111]

2.1.1. [2 × 2] Grid Complexes

Inspired by the well established [2 × 2] tetranuclear grid and trinuclear defect-grid complexes based on the pyrazolate-bridged terpyridine ligands,[112] a series of new pyrazole-bridged compartmental ligand systems can be designed as shown in Scheme 2.1. These two similar kinds of pyrazole-bridged binucleating ligand systems have two substituted five-membered pyrazoles or imidazoles instead of pyridines as

peripheral heterocycles of the bis(tridentate) ligand strands. Then the new ligand systems should have the ability to form tetranuclear and trinuclear grid complexes that support HS Fe^{II} or / and LS HS Fe^{II} ions and have the possibility of displaying fascinating redox and magnetic properties.

Additionally, these ligand systems can be functionalized with electron donating or electro withdrawing groups at different positions of the ligands in order to examine the steric and electronic effects of various substituents on the structure and properties of the [2 × 2] Fe^{II}_4 and Co^{II}_4 grid complexes, such as SCO, and to get a better understanding of these compounds. In view of further functionalization to extended ligand systems, the attention of the synthesis will be paid on methyl group substituent bounded to the central pyrazole or side-arm pyrazole rings of ligands. Another type of [2 × 2] matrix-like iron and cobalt complexes can be also a good choice to study the SCO because of the host–guest chemistry by van der Waals interactions, hydrogen bonds, π→π interactions, or structural changes.

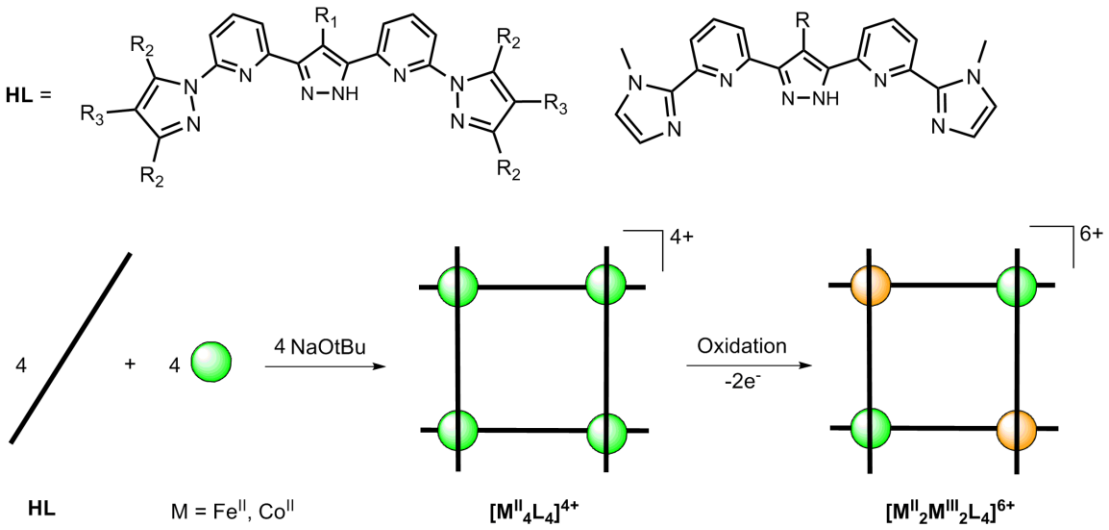

Scheme 2.1. Schematic representation of the synthesis of [2 × 2] grid and defect-grid complexes prepared with ligand **HL**.

2.1.2. [3 × 3] Grid Complexes

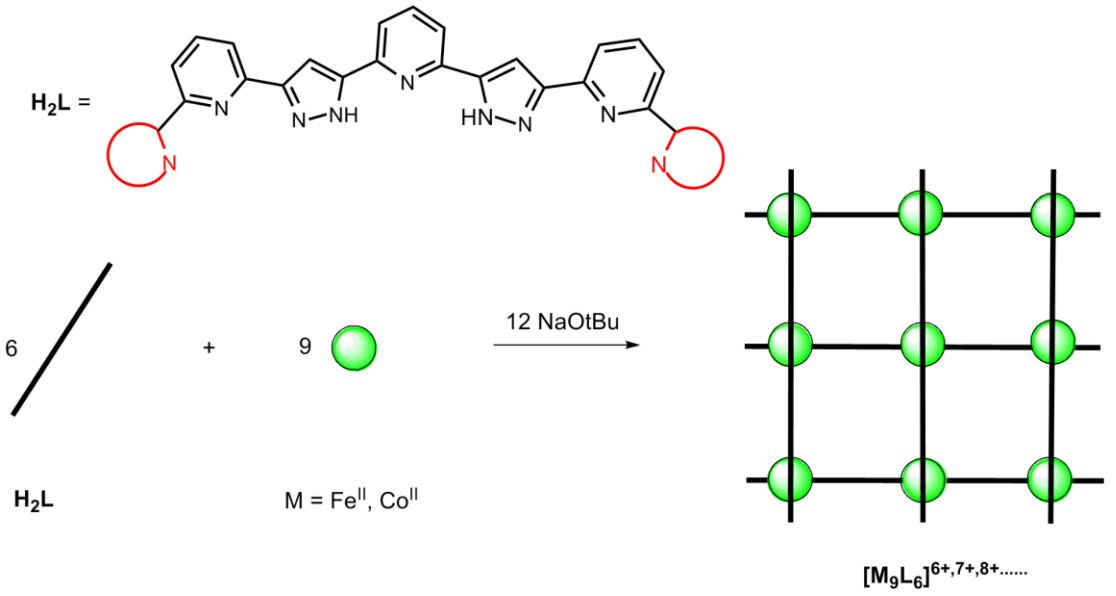

Scheme 2.2. Schematic representation of the synthesis of [3 × 3] grid complexes prepared from ligand **H_2L**.

The multinuclear grid complexes with different metal ions or the same metal ions in different oxidation states can be achieved by expanding the chelating side-arm of the two tridentate ligands to the three tridentate ligand systems by two further pyridyl units. This kind of ligands (H_2L) consists of three pyridine moieties linked by two pyrazole groups and two terminal six-member rings or five-member rings as peripheral heterocycles to give three tridentate sites coordinating environment (Scheme 2.2). By using these tritopic ligands (**H_2L**), several [n × n] grid complexes with variable numbers of metal centers ($[M_mL_n](X)_x$, M = Fe, Co; X = ClO_4^-, BF_4^-; m = 4 – 9; n = 4, 6; x = 6, 7, 8 ⋯⋯) may be produced by self-assembly.

All these designed iron and cobalt grid compounds, the spin state of the metal centers can be generally assessed by SQUID measurement in the solid state, by measuring the molecular magnetic moment *via* NMR spectroscopy in solution state, and the redox properties can be studied by cyclic voltammetry (CV) and square wave voltammetry (SWV).

2.2. Project Challenges

The first challenge is to synthesize appropriate ligands containing two tridentate N

donor subunits based on a bridging pyrazole via multistep procedures. Early studies of grid systems were largely based upon ditopic grid-forming ligands consisting of rigid aromatic ring systems, such as pyridine, pyrimidine, pyrazole or imidazole. These ligands in general are relatively difficult to synthesize. Considerably simple to synthesize, the isotypic ligands involving pyrazole-bridged sites, with pyridine, pyrazole or imidazole rings as side-arms are chosen to construct [2 × 2] grid-type architectures (Scheme 2.1). The pyrazole-bridged sites, arising from a ring-closing condensation of 1,3-diketone with hydrazine, can be obtained with a wide variety of substituents and the side arm units can also be substituted by different organic groups at different positions. Therefore a family of [2 × 2] tetrametallic grid and trimetallic defect-grid complexes successfully produced. Furthermore, the ligands with more pyridine and pyrazole rings are designed as tritopic building block to generate [3 × 3] decametallic grid structures.

The preparation of homo-valence [2 × 2] grids ($[M^{II}_4L_4]^{4+}$), defect-grid structures ($[M^{II}_3(HL)L_3]^{3+}$), and the controlled introduction of metal ions at specific locations in the grid array are of great interest because of the fascinating magnetic properties which may result from the presence of a different number of metal ions in the entity. Therefore, the ratio of the starting materials (ligand, metal salt and base) of the reaction to produce grid or defect-grid structures has to be strictly controlled. Otherwise it is easy to produce a mixture of $[M^{II}_4L_4]^{4+}$ and $[M^{II}_3(HL)L_3]^{3+}$. Because of the large size of the tritopic ligands with more aromatic rings, solubility is a prevailing problem. The solubility of [3 × 3] grids ($[M_9L_6]^{n+}$, n = 6, 7, 8 ……) make it difficult to get crystals suitable for X-ray diffraction and for the study of redox and magnetic properties.

To prepare the mixed-valence [2 × 2] grid complexes, the third stage of the project focuses on the double oxidation of homo-valence tetranuclear grid complexes. In order to determine the oxidation potential of each metal center in the homo-valence grid structure, electrochemistry measurements are necessary. The choice of oxidant and solvent based on the electrochemistry data are not only important but also

difficult to produce the pinpont mixed-valence species ($[M^{II}_2M^{III}_2L_4]^{6+}$) successfully.

Finally, the magnetic properties of the homo- and mixed-valence grid complexes are investigated. Mössbauer and SQUID measurements are analyzed to assign the spin state and charge of the metal centers in the solid state. Paramagnetic NMR spectra in solution are complicated by line broadening of the paramagnetic shifts at "unpredictable" resonance frequencies. Therefore, the integrated intensities of 1D spectra, the comparison of homonuclear and heteronuclear 2D NMR spectra, or spectra of selectively labeled isotopomers, may be the sole ground against which the spectra – if available at all – are interpreted.

3. [2 × 2] Iron Grid Complexes Based on Substituted 3,5-bis(6-(1*H*-pyrazol-1-y)pyridin-2-yl)pyrid-2-yl)pyrazole Ligands

3.1. Synthesis of Ligands

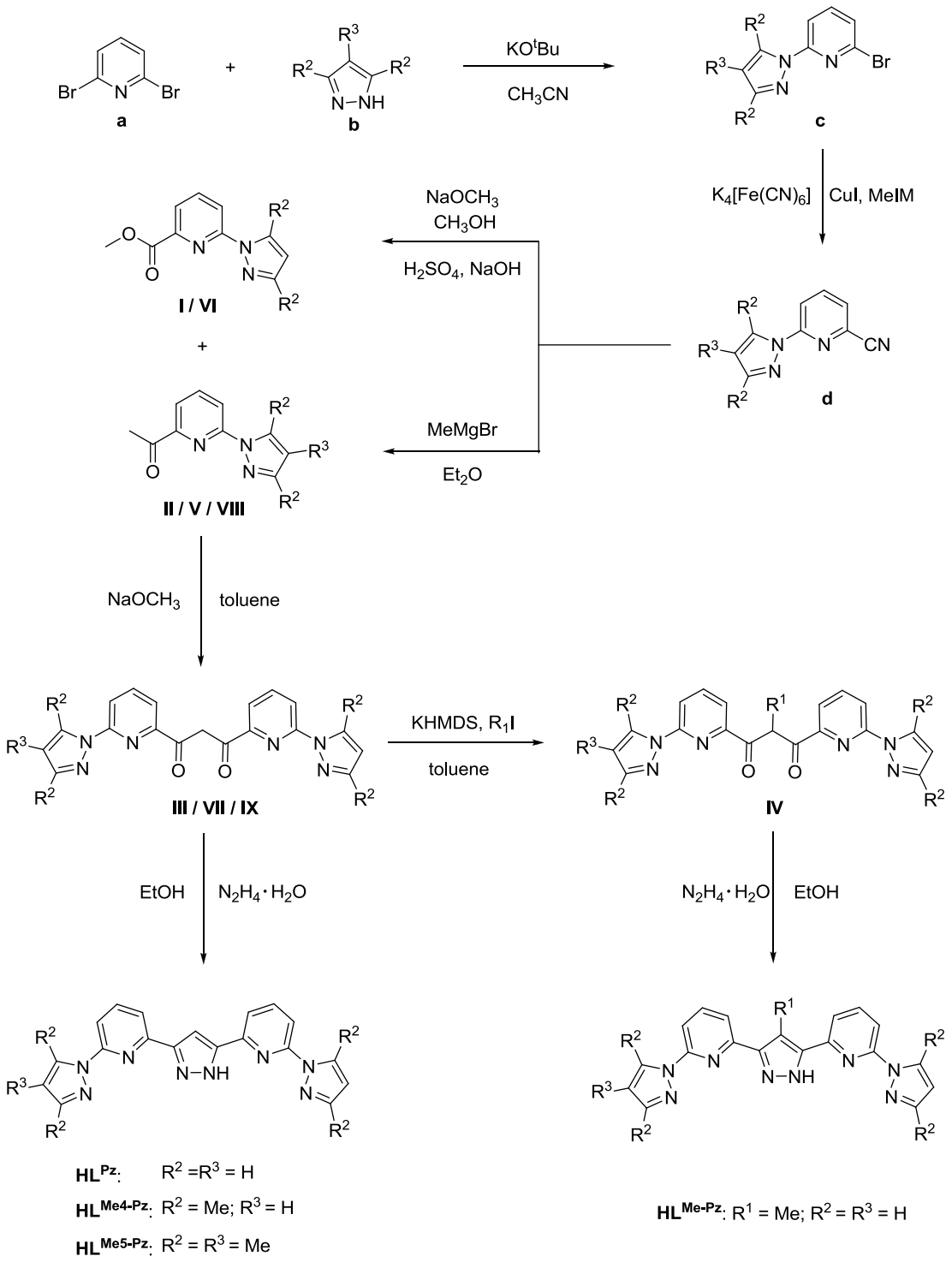

Scheme 3.1. Synthesis of ligands **HL^{Pz}**, **HL^{Me-Pz}**, **HL^{Me4-Pz}** and **HL^{Me5-Pz}**.

The synthesis of ligands used in this chapter $\mathbf{HL^{Pz}}$, $\mathbf{HL^{Me\text{-}Pz}}$, $\mathbf{HL^{Me4\text{-}Pz}}$ and $\mathbf{HL^{Me5\text{-}Pz}}$, which contain a central pyrazole bridging-unit with two substituted-pyrazolyl rings as side arms, is based on the starting material of 2,6-dibromopyridine and follows a multistep process (Scheme 3.1). Pyrazole and substituted pyrazoles are used in these reactions. We intended to synthesize the monosubstituted 2-bromo-6-(1*H*-pyrazol-1-yl)pyridine (**c**) from the reactions of 2,6-dibromopyridine (**a**) with pyrazole or substituted pyrazoles (**b**) in a molar ratio of 1:1 in the presence of base (KO^tBu) in dry 1.4-dioxane,[113] but disubstituted compounds as side-products were produced at the same time even though we controled the ratio of starting materials. In the case of pyrazole, the disubstituted compound 2,6-di(1*H*-pyrazol-1-yl)pyridine was obtained as the major product and the monosubstituted product 2-bromo-6-(1*H*-pyrazol-1-yl)-pyridine was collected as the minor product. However, in the cases using substituted pyrazoles, only the monosubstituted product was formed in high yield. The results discussed above likely result from different steric hindrance caused by the substituent(s) on the corresponding pyrazolyl ring (1*H*-pyrazole < 3,5-dimethyl-1*H*-pyrazole < 3,4,5-trimethyl-1*H*-pyrazole).[113] Copper-catalyzed C−N coupling was employed to synthesize the intermediate pyrazole substituted cyanopyridine (**d**).[114] Copper-catalyzed cyanation of **c** with $K_4[Fe(CN)_6]$ in N-methylimidazole (MeIM) in the presence of CuI formed **d**, which was then functionalized in two different ways to form both substituted methyl-6-(1*H*-pyrazol-1-yl)picolinate (**I** and **VI**) and 1-(6-(1*H*-pyrazol-1-yl)pyridin-2-yl)ethanone (**II**, **V** and **VIII**).[115, 116] Pyrazole-bridged ligands were obtained as white powders from the pseudo-Claisen condensation of **I**/**VI** and **II**/**V**/**VIII** using $NaOCH_3$ base in dry toluene and subsequent acidic workup to 1,3-diketones **III**, **VII** and **IX**,[117] followed by a ring-closing condensation with hydrazine in EtOH to produce the desired compounds $\mathbf{HL^{Pz}}$, $\mathbf{HL^{Me4\text{-}Pz}}$ and $\mathbf{HL^{Me5\text{-}Pz}}$. The ligand $\mathbf{HL^{Me\text{-}Pz}}$ was synthesized via a modified procedure. Instead of the pseudo-claisen condensation of the correspongding ketone and ester compounds, an alternative synthetic route was developed that builds on the already established synthesis of $\mathbf{HL^{Pz}}$. Hydrazine condensation, methylation of **III**

leads to the designed ligand **HL^{Me-Pz}**.

These four symmetrical or asymmetrical pyrazole-bridged binucleating ligands, varying in substitution at the 4-position of the central pyrazole ring (R^1 = H, Me) and at the 3,4,5-positions of side-arm pyrazoles (R^2, R^3 = H, Me), provide two tridentate binding pockets. These ligands differ in solubility in organic solvent such as $CHCl_3$, CH_3CN and CH_3OH, due to substitution of hydrogen atoms by methyl groups, with solubility decreasing as the number of methyls increases. All ligands have been fully characterized by ^{1}H NMR, ^{13}C NMR, ESI-MS and elemental analysis (see Experimental Section and Figures 10.1 – 10.13).

It is of interest to discuss the NMR spectra of the asymmetrical ligand **HL^{Me5-Pz}**. In theory there maybe two isomers exhibited because the exchange of N−H proton between the two nitrogen atoms of the central pyrazole ring. At room temperature, all spectra show only two signals corresponding to two methyl groups bound to the 3-positions of the side-arm pyrazolyl rings due to rapid interconversion of the two isomers. The assignment of all proton resonances is based on a ^{1}H-^{1}H COSY experiment.

The ^{1}H NMR spectrum of **HL^{Me5-Pz}** in DMSO-d_6 at 298 K will be given as an example for the assignment of all proton signals (Figure 3.1). There are eleven proton resonances observed at 13.73 ppm, 7.99 – 8.05 ppm, 7.83 – 7.90 ppm, 7.72 – 7.77 ppm, 7.40 ppm, 6.15 ppm, 2.75 ppm, 2.66 ppm, 2.21 ppm, 2.16 ppm and 1.95 ppm with integral intensities 1:2:2:2:1:1:3:3:3:3:3. The signals at 13.73 ppm, 7.40 ppm and 6.15 ppm can readily be assigned to protons N-H, H^7 and $H^{2'}$, respectively. Additionally, the proton resonance at 1.95 ppm could be identified as H^2 by comparison with the ^{1}H NMR spectrum of ligand **HL^{Me4-Pz}** (Figure 10.11).

The ^{1}H-^{1}H COSY spectrum of the DMSO-d_6 solution is shown in Figure 3.2. The broad signal at δ = 7.99 – 8.05 ppm shows cross peaks to the δ = 7.83 – 7.90 ppm and 7.72 – 7.77 ppm resonances, which can thus be assigned to $H^{5/5'}$. The signal at 2.21

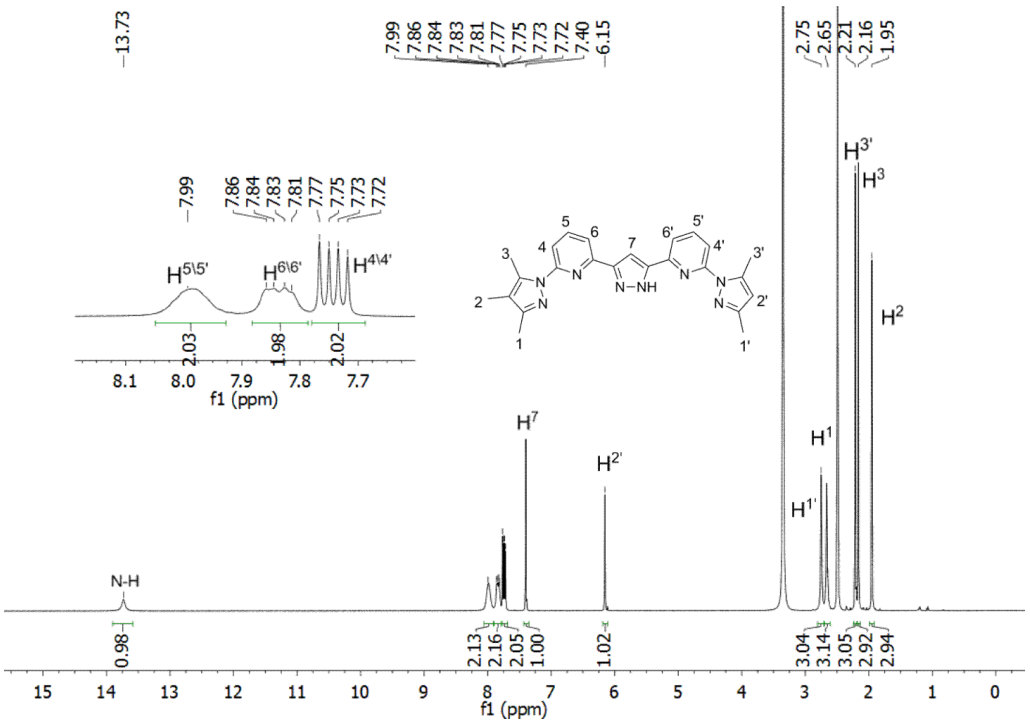

Figure 3.1. ^{1}H NMR spectrum (400 MHz, DMSO-d$_6$, 298 K) of **HL$^{Me5\text{-}Pz}$**.

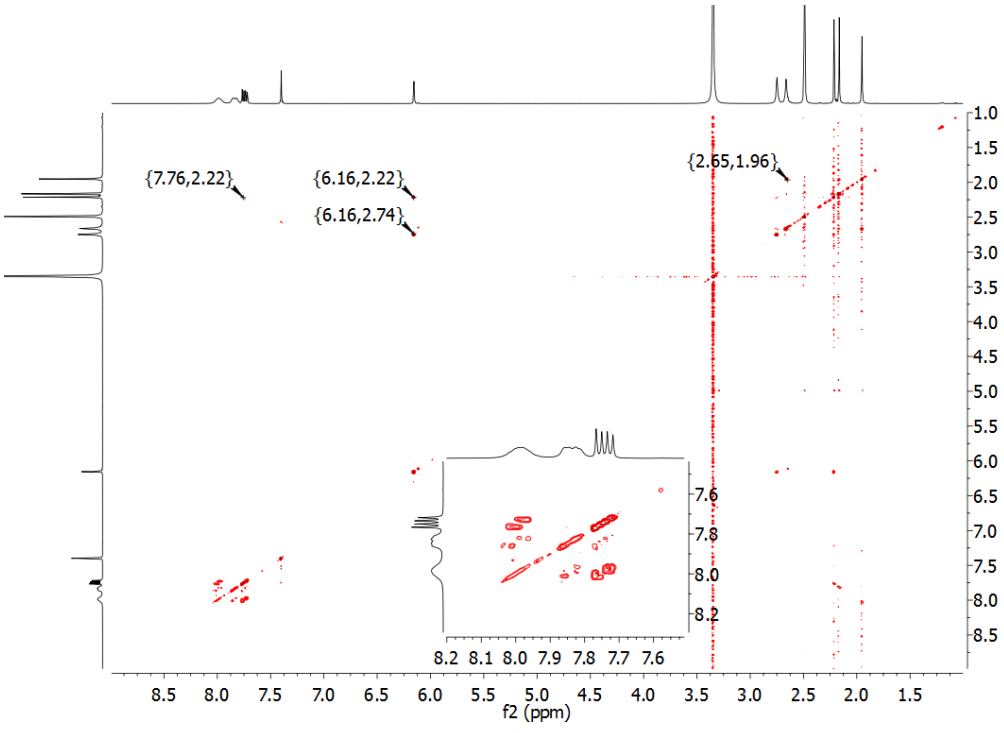

Figure 3.2. ^{1}H-^{1}H COSY spectrum (DMSO-d$_6$, 298 K) of **HL$^{Me5\text{-}Pz}$**.

ppm shows two cross peaks to the resonances at δ = 6.15 ppm and 7.72 – 7.77 ppm, and is assigned intuitively to H$^{3'}$, while the signal at 7.72 – 7.77 ppm is due to the H$^{4/4'}$. Undoubtably, the signal at δ = 7.83 – 7.90 ppm arises from H$^{6/6'}$. Meanwhile

there is one cross peak observed between the signals at δ = 6.15 ppm and 2.74 ppm, in which the signal at 2.74 ppm can be assigned to $H^{1'}$. The signal of H^2 at δ = 1.95 ppm shows a cross peak to 2.65 ppm, which can be attributed to H^1 based on the assignment of $H^{1'}$. The last signal at δ = 2.16 ppm then originates from H^3.

Upon increasing the temperature of the DMSO-d_6 solution to 348 K, the interconversion of the two isomers is faster on the NMR time scale (Figure 3.3), therefore no change of chemical shift is observed. In Figure 3.3 the peak at 2.50 ppm was cut in order to make the signals of the methyl group protons more clearly visible. On lowering the temperature in DMF-d_6 from 298 K (three solvent signals at 2.75 ppm, 2.92 ppm, 8.03 ppm and one unknown at 2.10 ppm), the signals of H^4, H^5 and H^6 become broad, and there is a small change observed for the signals of $H^{1/1'}$ due to the transformation between two isomers.

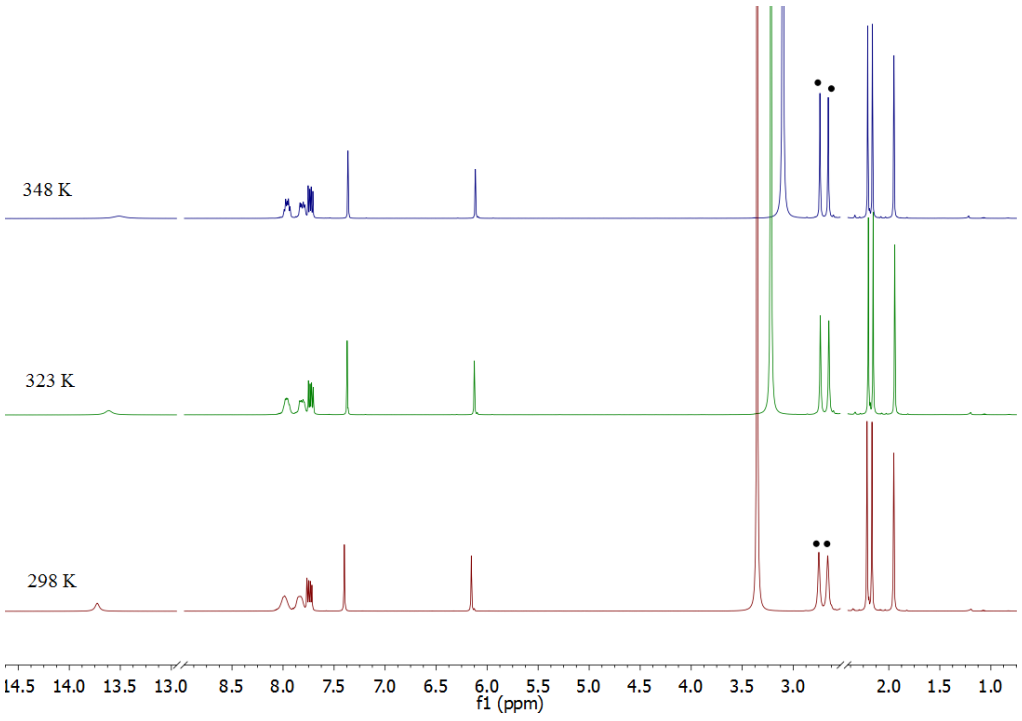

Figure 3.3. ^{1}H NMR spectra (400 MHz, DMSO-d_6) of $\mathbf{HL^{Me5\text{-}Pz}}$ at different temperatures (black dot •: signals of methyl groups).

At the lowest possible temperature (223 K), the conformer interconversion is still too fast on the NMR time scale to observe more signals for methyl group protons (Figure 3.4). The proton resonances of $H^{3/3'}$ of the methyl group at the 5-positions and $H^{1/1'}$

of -CH_3 at the 3-positions of side-arm pyrazole rings always are shown as two separate singlets.

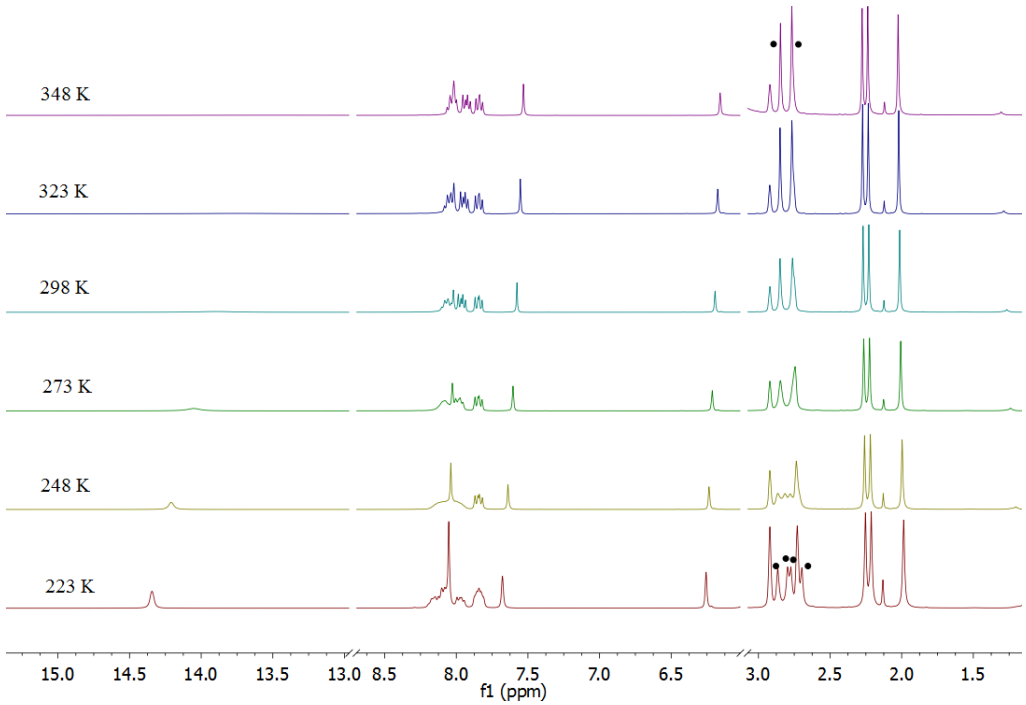

Figure 3.4. ^{1}H NMR spectra (400 MHz, DMF-d_6) of $\mathbf{HL^{Me5\text{-}Pz}}$ at different temperatures (black dot ⋅: signals of DMF-d_6).

3.2. Synthesis of [2× 2] Fe^{II}_4 Grid Complexes

Under inert conditions, ligand $\mathbf{HL^{Pz}}$ was deprotonated with NaO^{t}Bu as the base in degassed MeOH and was subsequently reacted with one equivalent of the iron salt $Fe(BF_4)_2 \cdot 6H_2O$ (Scheme 3.2). The color of the solution changed from yellow to red-brown after stirring overnight at room temperature. The crude product $[Fe^{II}_4L^{Pz}_4](BF_4)_4$ (**1**) could be obtained by adding a large quantity of Et_2O to the reaction mixture and the resulting red-brown powder was subsequently dried in vacuo. Three other [2 × 2] metallogrid complexes: $[Fe^{II}_4L^{Me\text{-}Pz}_4](BF_4)_4$ (**2**), $[Fe^{II}_4L^{Me4\text{-}Pz}_4](BF_4)_4$ (**3**) and $Fe^{II}_4L^{Me5\text{-}Pz}_4](BF_4)_4$ (**4**) could be synthesized from a procedure similar to that used for preparing complex **1**. The precipitation of voluminous red, red-orange and orange materials were observed during the reaction with ligands $\mathbf{HL^{Me\text{-}Pz}}$, $\mathbf{HL^{Me4\text{-}Pz}}$ and $\mathbf{HL^{Me5\text{-}Pz}}$, respectively. The elemental analyses of **1** – **4** indicate a 1:1 ligand-to-metal ratio.

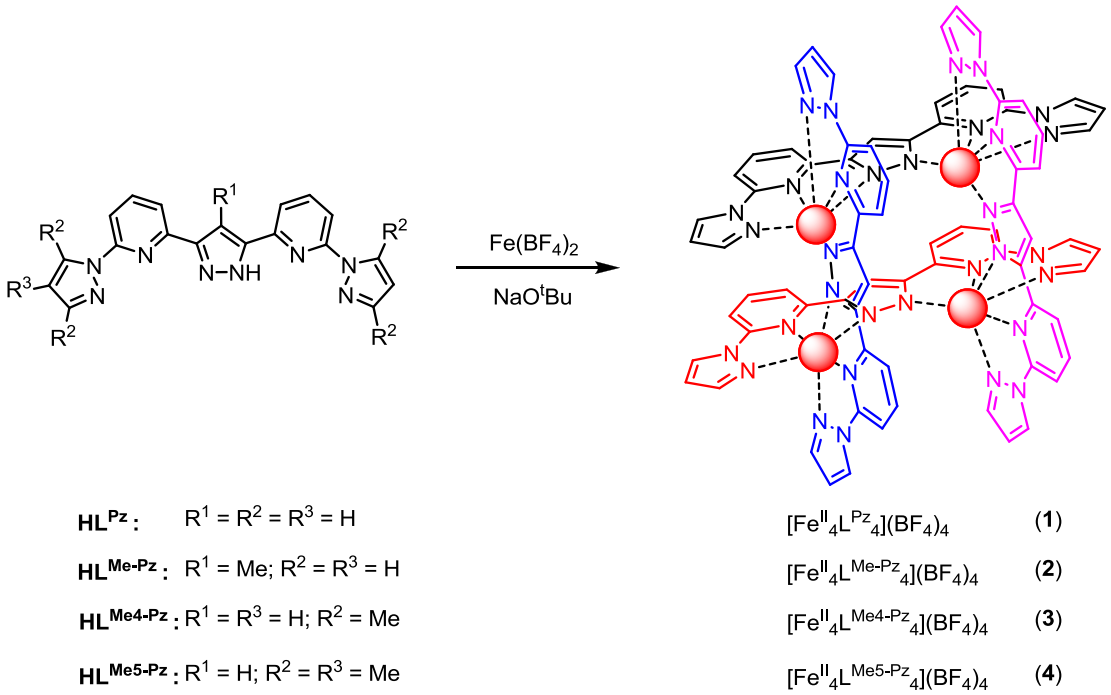

Scheme 3.2. Schematic representation of the synthesis of [2 × 2] Fe^{II}_4 grid complexes **1** – **4**.

3.3. Solid State Investigations

Structural Characterization

Single crystals suitable for X-ray diffraction have been obtained for each $[Fe^{II}_4L_4](BF_4)_4$ (L = $\mathbf{L^{Pz}}$, $\mathbf{L^{Me\text{-}Pz}}$, $\mathbf{L^{Me4\text{-}Pz}}$ and $\mathbf{L^{Me5\text{-}Pz}}$) complex by slow diffusion of diethyl ether into acetonitrile solution of crude compounds **1** – **4**. Single crystal X-ray diffraction analyses revealed the expected [2 × 2] grid-type molecular structures in all cases. Complexes **1**, **3** and **4** crystallize in the triclinic space group *P*–1, while complex **2** crystallizes in the tetragonal space group $P4_{2/n}$. It is worth mentioning that for the crystal structure of **1** there are at least 6.5 CH_3CN molecules found in the unit cell, while for structures of **2**, **3** and **4** no lattice solvent molecules were found. The model molecular structure of the [2 × 2] grid $[Fe^{II}_4L_4]^{4+}$ cation is shown in Figure 3.5.

Structural analyses show that these four [2 × 2] Fe^{II}_4 grid structures **1** – **4** share a similar coordination mode with different ligands: each Fe^{II} center displays a distorted $\{N_6\}$ octahedral environment at each grid corner, bound to two N_3-tridentate binding sites from perpendicular deprotonated ligands $(L)^-$ (L = $\mathbf{L^{Pz}}$ for **1**, $\mathbf{L^{Me\text{-}Pz}}$ for **2**, $\mathbf{L^{Me4\text{-}Pz}}$

for **3** and $\mathbf{L^{Me5\text{-}Pz}}$ for **4**). Four BF_4^- anions in the crystal structure balance the charge of the $[Fe^{II}_4L_4]^{4+}$ species. The Fe–N bonds are divided into three different groups according to the type of donor N atom with d(Fe-$N^{pz\text{-}b}$) < d(Fe-N^{py}) < d(Fe-$N^{pz\text{-}t}$), where $N^{pz\text{-}b}$ refers to the bridging pyrazole ring, N^{py} refers to the pyridine rings, while $N^{pz\text{-}t}$ refers to the terminal pyrazole rings. All complexes **1** – **4** display similar connectivity in their structures. The slight difference in pertinent metric parameters arises from the substrate from hydrogen atoms to methyl groups of ligand.

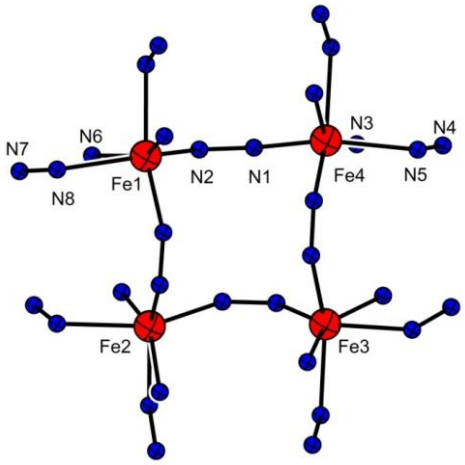

Figure 3.5. Model molecular structure of [2 × 2] grid $\mathbf{[Fe^{II}_4L_4]^{4+}}$ cations (hydrogen and carbon atoms are not included for the sake of simplicity).

Table 3.1. Mean Fe−N Bond Lengths and Continuous Symmetry Measures (CSM) for **1** – **4**.

Complex		d_{mean}/Å [a]	$S(O_h)$ [b]	S(itp) [b]	Spin state [a]
1:$[Fe^{II}_4L^{Pz}_4](BF_4)_4$	$Fe^{II}1$−N	2.18	7.35	6.66	HS
	$Fe^{II}2$−N	2.18	7.87	7.07	HS
	$Fe^{II}3$−N	2.19	6.97	8.19	HS
	$Fe^{II}4$−N	2.20	7.87	7.07	HS
2: $[Fe^{II}_4L^{Me\text{-}Pz}_4](BF_4)_4$	Fe^{II}−N	2.17	7.68	6.25	HS
3: $[Fe^{II}_4L^{Me4\text{-}Pz}_4](BF_4)_4$	$Fe^{II}1$−N	2.19	5.41	9.65	HS
	$Fe^{II}2$−N	2.23	10.62	4.47	HS
	$Fe^{II}3$−N	2.18	5.28	9.42	HS
	$Fe^{II}4$−N	2.20	9.61	4.07	HS
4: $[Fe^{II}_4L^{Me5\text{-}Pz}_4](BF_4)_4$	$Fe^{II}1$−N	2.19	6.25	7.46	HS
	$Fe^{II}2$−N	2.21	8.83	4.70	HS
	$Fe^{II}3$−N	2.19	6.33	6.98	HS
	$Fe^{II}4$−N	2.19	7.24	5.71	HS

[a] At 133 K. [b] The smaller this value (0 – 100) the closer the polyhedron is to the ideal geometry.

The average Fe−N bond lengths range from 2.17 Å to 2.23 Å for all Fe^{II} ions. To capture this quantitatively, the Continuous Symmetry Measures (CSM) method is used here.[118] This is obtained from the X-ray structural analysis, where a numerical value of $S(O_h)$ is between 0 and 100, with a value of 0 indicative of an ideal octahedron and its value reflects deviation from the ideal octahedron. The remarkably high value for $S(O_h)$ (corresponding to a lower S(itp)) in the CSM for all these complexes clearly indicates that at the temperature of measurement (133 K) all Fe^{II} ions are in the HS state with overall configuration [HS-HS-HS-HS] of the grid (Table 3.1).[119,120,121]

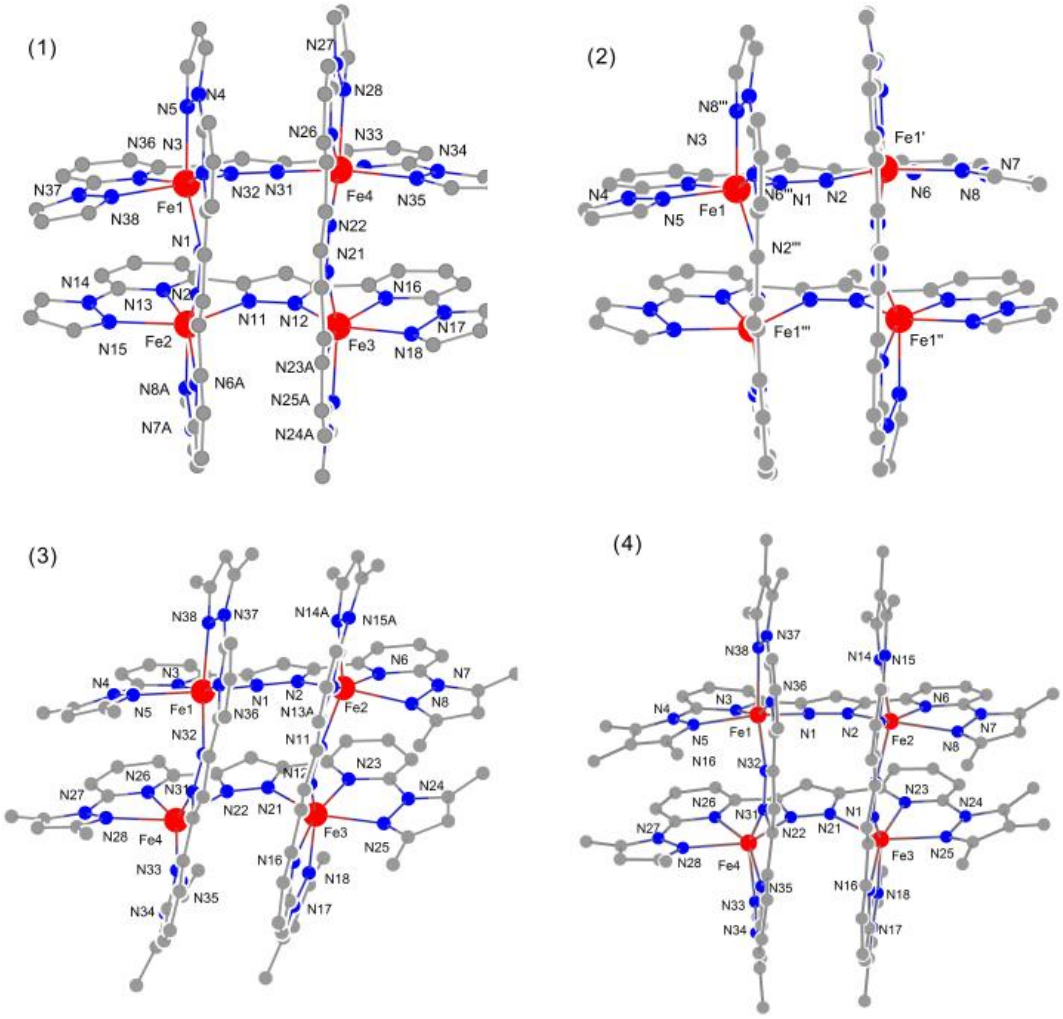

Figure 3.6. Molecular structure of the cations $[Fe^{II}_4L_4]^{4+}$ of the [2 × 2] grid complexes **1** – **4** (hydrogen atoms are not included for simplicity).

For complexes **1**·6.5CH_3CN, **3** and **4** the four different and crystallographically independent iron ions (Fe1, Fe2, Fe3 and Fe4) are not perfectly coplanar, while the

crystallographically imposed symmetry in the solid state structure of **2** yields only one crystallographically independent Fe^{II} ion and ligand (Figure 3.6). The adjacent Fe···Fe distance and separation of the diagonal Fe ions are listed in Table 3.2. Each Fe^{II} ion in the grid structures exhibits distorted octahedral coordination, provided by two central pyrazole, two pyridine and two side-arm pyrazole nitrogen atoms. The iron coordination site exhibits the longest bonds to the terminal pyrazole donor atoms, shorter bonds to the pyridine nitrogen sites, with the shortest bonds to the bridging pyrazole ring nitrogen atoms. These differences in bond lengths result in an overall axial distortion of the $\{N_6\}$ coordination octahedron. The Fe−N bond lengths confirm that all Fe^{II} ions are in the HS state and that spin configuration of grids **1** – **4** is [HS-HS-HS-HS].

Compared to the structures of **1** and **2**, longer Fe–N bond lengths corresponding to the 3,5-dimethyl-substituted pyrazole rings and smaller N–Fe–N bite angles are observed in the structure of **3**. This could be due to t the sterical demands imparted by the methyl groups which prevent the Fe^{II} center from binding to these substituted pyrazoles at a shorter distance.[122] From the superimposed structures of **1**, **2** and **3** (Figure 3.7), we can see that **3** is significantly distorted compared to the other two complexes.

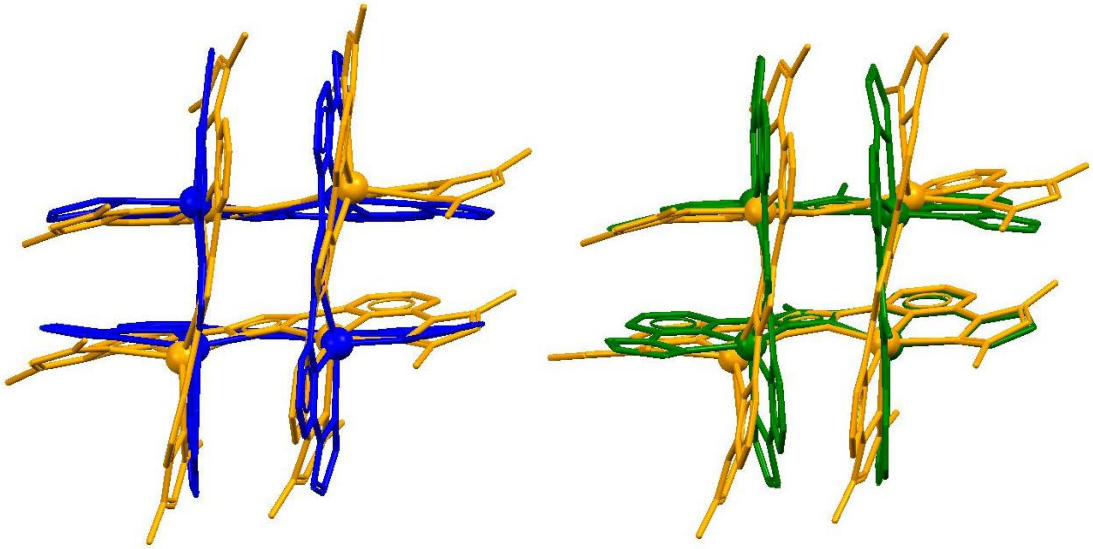

Figure 3.7. Overlay of structures on **1** (blue), **2** (green) and **3** (orange).

Table 3.2. Selected Bond Distances (Å) for **1 - 4**.

	$Fe^{II}_4L^{Pz}_4](BF_4)_4$ **1**	$Fe^{II}_4L^{Me\text{-}Pz}_4](BF_4)_4$ **2**	$Fe^{II}_4L^{Me4Pz}_4](BF_4)_4$ **3**	$Fe^{II}_4L^{Me5Pz}_4](BF_4)_4$ **4**
Fe···Fe				
Fe···Fe[a]	4.348(8) - 4.476(8)	4.262(5)	4.533(9) - 4.588(13)	4.555 (13) - 4.571(15)
Fe···Fe[b]	5.989(9) - 6.267(9)	5.936(5)	5.556(9) - 7.224(12)	6.200(15) - 6.629(13)
$Fe–N^{pz\text{-}b}$				
Fe1–N	2.119(4) 2.131(3)	2.112(13) 2.114(13)	2.151(5) 2.159(4)	2.140(5) 2.145(5)
Fe2–N	2.119(3) 2.121(4)		2.147(6) 2.171(5)	2.175(5) 2.178(5)
Fe3–N	2.120(3) 2.156(4)		2.145(4) 2.154(4)	2.137(5) 2.167(5)
Fe4–N	2.136(4) 2.155(4)		2.149(4) 2.160(4)	2.132(5) 2.155(5)
$Fe–N^{py}$				
Fe1–N	2.160(4) 2.162(4)	2.147(14) 2.153(14)	2.119(5) 2.142(4)	2.132(5) 2.140(5)
Fe2–N	2.147(7) 2.152(3)		2.270(10) 2.153(6)	2.148(5) 2.153(5)
Fe3–N	2.137(11) 2.156(4)		2.127(4) 2.133(4)	2.130(5) 2.136(6)
Fe4–N	2.165(4) 2.166(4)		2.141(4) 2.149(4)	2.132(5) 2.138(5)
$Fe–N^{pz\text{-}t}$				
Fe1–N	2.238(4) 2.287(4)	2.218(15) 2.259(14)	2.279(5) 2.281(4)	2.247(6) 2.320(5)
Fe2–N	2.254(4) 2.258(14)		2.349(8) 2.318(6)	2.248(5) 2.375(6)
Fe3–N	2.258(10) 2.285(4)		2.257(4) 2.284(4)	2.279(6) 2.303(6)
Fe4–N	2.244(4) 2.320(4)		2.277(4) 2.301(5)	2.269(5) 2.306(6)

[a] Adjacent Fe···Fe distance, [b] Diagonal Fe···Fe distance. $N^{Pz\text{-}b}$: Bridging pyrazole N atom; $N^{Pz\text{-}t}$: Terminal pyrazole N atom.

Usually, in a non-distorted [2 × 2] grid structure, the four ligands should be planar, perpendicular to the adjacent ligands and parallel to the opposite ligands. The four Fe^{II} ions occupy the four corners of a grid. To describe the overall distortion of the individual ligand strands in the four crystal structures of **1** – **4**, the angle between the

planes defined by the bridging pyrazolate ring and by the terminal pyrazole rings has been determined (gray values in Figure 3.9).

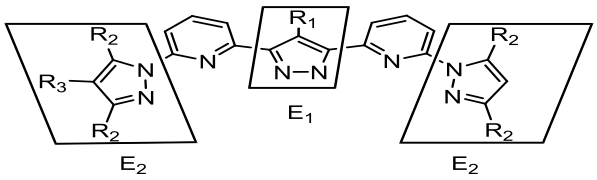

Figure 3.8. To determine the distortion of the ligand, the torsion angle between the plane of the bridging pyrazole ring (E_1) and the planes of the terminal pyrazole rings (E_2) is measured.

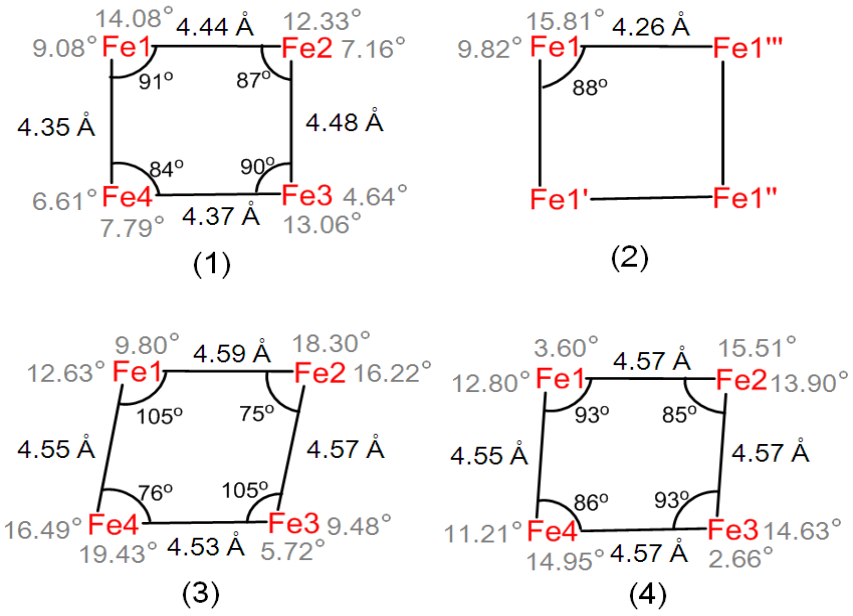

Figure 3.9. Fe···Fe distances, Fe-Fe-Fe angles (black) and torsion of the bridging pyrazole rings against terminal pyrazole rings in the same ligand (gray) of complexes **1** – **4**.

All [2 × 2] grid molecules contain HS e^{II} ions arranged likely in an square at 133 K. As reflected by the CSM parameters the coordination polyhedron is significantly distorted from octahedral. Both compounds **1** and **4** contain four crystallographically distinct Fe^{II} ions in the HS state. The HS Fe^{II} ions have $S(O_h)$ values between 6.25 and 8.83, indicating that the coordination polyhedron are closer to ideal trigonal prism (itp) than an octahedron. Unlike **1** and **4** , compound **2** features only one crystallographically independent HS Fe^{II} ion arranged in an almost perfect square. The HS Fe^{II} ion has $S(O_h)$ value around 8 and is therefore

somewhere toward an itp situation. The ligands are twisted at angles ranging from 9.8° to 15.8°. The four metal ions in **3** are arranged as a rhomb (Fe-e-e angles 75° and ~105°). While two HS Fe^{II} have a moderately distorted octahedral environment ($S(O_h)$ 5.41 and 5.28) the other two are severely distorted toward an itp situation ($S(O_h)$ 10.62 and 9.61). All ligands in **3** are highly twisted, deviating from planarity to a greater extent than the ligands in **1** and **2**.

Magnetic Properties

Since all the [2 × 2] iron grid complexes described herein possess four HS Fe^{II} centers connected through substituted pyrazole-based bridges, we carried out temperature dependent magnetometric measurements on complexes **1** – **4**. Magnetic susceptibilities were measured on powder samples of **1** – **4**, as well as on a sample of **1** covered with MeCN solvent. The samples of **1** will be referred to as "dry" and "wet", respectively, in the following discussion.

At high temperature, the $\chi_M T$ value is 15.70 $cm^3mol^{-1}K$ for the wet sample (**1**·6.5CH_3CN), collected from freshly crystallized material (Figure 3.10). In agreement with the crystallographic data, this indicates a [4HS] spin configuration (typical room temperature $\chi_M T$ values for HS Fe^{II} ions are in the range of 3.3 – 3.8 m^3Kmol^{-1}).[123] Upon decreasing the temperature, $\chi_M T$ remains almost constant until 50 K. Below this temperature, a rapid decrease in $\chi_M T$ can be seen with a minimum value of 3.21 $cm^3mol^{-1}K$ at 2 K.

The desolvated dry sample **1** can be obtained under vacuo overnight. The dry sample **1** shows a minor change of partly HS Fe^{II} ions characterized by a slightly decrease of $\chi_M T$ from 15.96 to 15.54 $cm^3mol^{-1}K$upon decreasing temperature to 100 K. The $\chi_M T$ value remained nearly constant at 15.54 $cm^3mol^{-1}K$ as temperature was decreased to 20 K. Before 2 K, a rapid decrease in $\chi_M T$ is observed until minimum value is reached at 5.28 $cm^3mol^{-1}K$ at 2 K. The behavior of the dry sample of **1** is slightly different from the wet sample and maybe a minor spin state transition from HS to LS species is happened. The magnetic properties of the dry sample **1** is also

confirmed by Mössbauer spectroscopy (see below). The slight change of the spin state of HS Fe^{II} ions from dry sample is interpreted in terms of the increased structural disorder and decreased crystallinity caused by the loss of the interstitial solvent molecules in the dry sample. The loss of solvent molecules is shown by elemental analysis (see Experimental Section).

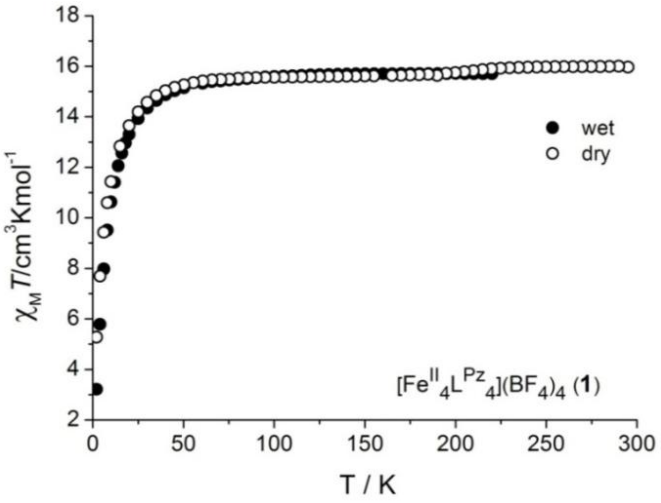

Figure 3.10. Temperature dependence of $\chi_M T$ for the wet (solid circles) and dry (open circles) samples of $[Fe^{II}_4L^{Pz}_4](BF_4)_4$ (**1**).

Magnetic susceptibility plots of **2** – **4** are shown in Figure 3.11. At room temperature, the $\chi_M T$ values are 15.94 m^3Kmol^{-1} for **2**, 13.65 $cm^3mol^{-1}K$ for **3** and 13.62 $cm^3mol^{-1}K$ for **4**, which closely matches the value expected for four S = 2 iron(II) centers in the absence of exchange coupling between the Fe^{II} ions. On decreasing the temperature, the $\chi_M T$ decreases slightly until 50 K for **2** – **4**. Below these temperatures, a rapid decrease in $\chi_M T$ can be observed with minimum values of 2.70, 7.40 and 3.47 $cm^3mol^{-1}K$ at 2 K for **2**, **3**, and **4**, respectively.

These SQUID data are consistent with four systems that remain in the HS state at all temperature ranges studied, and with the molecular structure as resolved through single-crystal X-Ray diffraction studies. Magnetic measurements for complexes **1** – **4** were simulated using a Heisenberg-Dirac-van-Vleck Hamiltonian (*HDvV*, eq. 1)[124] that includes terms for Zeeman and zero-field splitting, where D is the axial anisotropy (zero field splitting) parameter (we thus neglect here any rhombicity):

$$\hat{H} = -2J(\hat{S}_1\hat{S}_2 + \hat{S}_2\hat{S}_3 + \hat{S}_3\hat{S}_4 + \hat{S}_1\hat{S}_4) + \sum_{i=1}^{4} \hat{D}_i(\hat{S}_{zi} - \frac{1}{3}\hat{S}_i(\hat{S}_i + 1)) + g\mu_B\vec{B}\sum_{i=1}^{4}\hat{S}_i$$

(eq. 1)

The best fit leads to $|D|$ = 8.6 cm^{-1} and g =2.31 for **1**, $|D|$ = 0 cm^{-1} and g = 2.32 for **2**, $|D|$ =10.5 cm^{-1} and g = 2.13 for **3**, and $|D|$ = 0 cm^{-1} and g = 2.14 for **4**. The intramolecular coupling between all metal centers is also is also taken into account for the magnetic properties of these four grids.

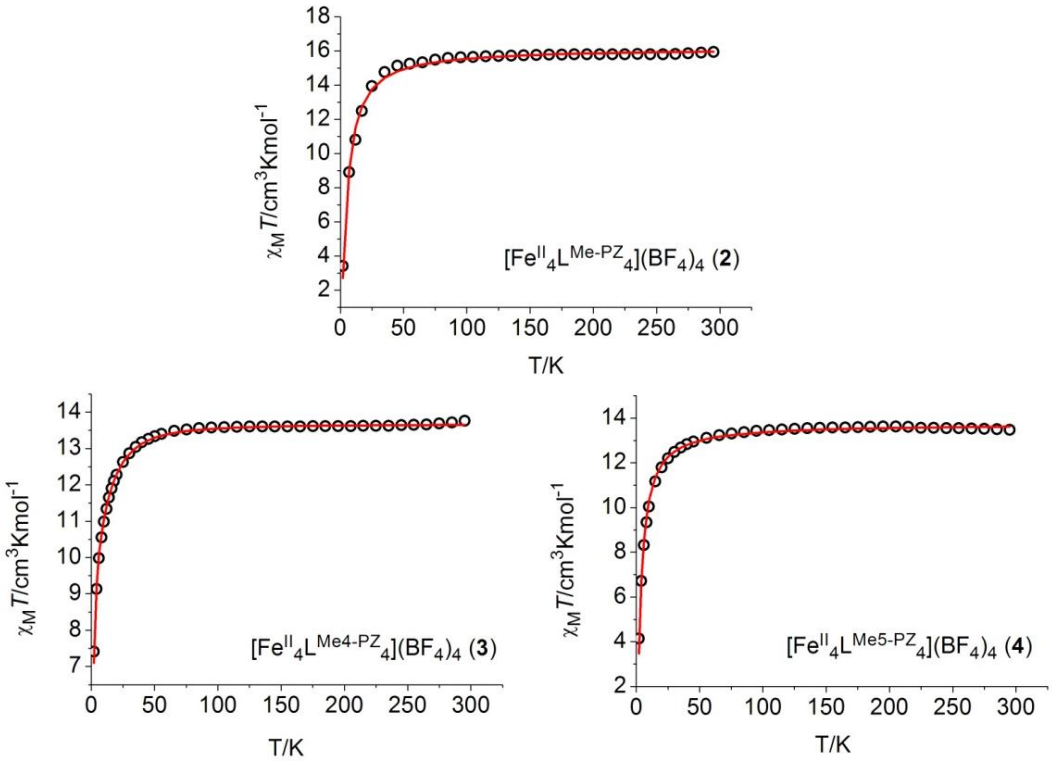

Figure 3.11. Temperature dependence of $\chi_M T$ for dry samples of $[Fe^{II}_4L^{Me\text{-}Pz}_4](BF_4)_4$ (**2**), $[Fe^{II}_4L^{Me4\text{-}Pz}_4](BF_4)_4$ (**3**) and $[Fe^{II}_4L^{Me5\text{-}Pz}_4](BF_4)_4$ (**4**). Red line is the best simulation for data points.

All SQUID data discussed below show a decrease of $\chi_M T$ below 50 K due to zero-field splitting of the HS Fe^{II} (S = 2) ions present in every compound, but this low-temperature feature will not be specifically mentioned in each case.[125]

The decrease of the curve at low temperature also provides evidence that in complexes **1**, **2** and **4** antiferromagnetic coupling (J = –0.191 cm^{-1} for **1**, –0.348 cm^{-1} for **2**, –0.245 cm^{-1} for **4**) exists between the HS Fe^{II} ions in the [HS-HS-HS-HS] form.

For complex **3**, the weak ferromagnetic coupling (J = 0.063 cm^{-1}) between the HS Fe^{II} ions does not show obviously effect on the $\chi_M T$ value with the decreasing temperature.

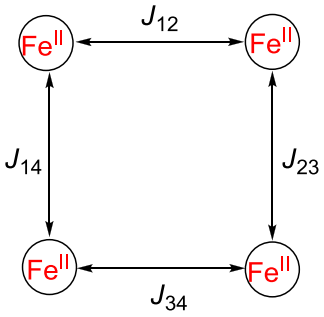

Figure 3.12. Magnetic coupling scheme of [2 × 2] Fe_4 grid complexes **1** – **4**.

Mössbauer Spectroscopy

^{57}Fe Mössbauer spectroscopy is a valuable tool for assessing spin and charge states of iron ions.[126] The ^{57}Fe Mössbauer spectra of a fresh crystalline sample of **1**·6.5CH_3CN and powder samples of **2** – **4** have been measured (Figure 3.13 and Table 3.3).

The spectra of $[Fe^{II}_4L^{Pz}_4](BF_4)_4$ (**1**) and $[Fe^{II}_4L^{Me4\text{-}Pz}_4](BF_4)_4$ (**3**) feature two different quadrupole doublets with equal area fractions, red subspectrum 1: δ_1 = 1.09 mm/s, ΔE_{Q1} = 1.67 mm/s, red subspectrum 2, δ_2 = 1.09 mm/s, ΔE_{Q2} = 2.36 mm/s for **1**; red subspectrum 1, δ_1 = 1.09 mm/s, ΔE_{Q1} = 1.85 mm/s, red subspectrum 2, δ_2 = 1.12 mm/s, ΔE_{Q2} = 3.72 mm/s for **3**, that is, parameters that compare with those reported for S = 2 HS-Fe^{II} ions in a series of $[FeN_6]$[108,127] compounds (δ = 0.92 – 1.21 mm/s and ΔE_Q = 1.30 – 2.99 mm/s), a system of [2 × 2] grids including bi-tridentate ligand. These results exhibit the presence of two types of HS Fe^{II} centers in both grids **1** and **3**. Only one quadrupole doublet with parameters typical for HS-Fe^{II} is observed for $[Fe^{II}_4L^{Me\text{-}Pz}_4](BF_4)_4$ (**2**) and $[Fe^{II}_4L^{Me5\text{-}Pz}_4](BF_4)_4$ (**4**): red subspectrum δ = 1.07 mm/s, ΔE_Q = 2.66 mms/s for **2**, red subspectrum δ = 1.09 mm/s, ΔE_Q = 3.32 mm/s for **4**.

The quadrupole splitting values for $[Fe^{II}_4L_4](BF_4)_4$ become greater with the increasing number of methyl groups on the ligand, either in the 4-position of central pyrazole or in the 3-, 4- and 5-positions of the side-arm pyrazolyl rings.

Table 3.3. Mössbauer Parameter of the Crystalline Samples of **1** − **4**.

Complex		δ / mm/s	ΔE_Q / mm/s	A / %
1·6.5CH_3CN[a]	HS-Fe^{II}	1.09	1.67	50
	HS-Fe^{II}	1.09	2.36	50
1·6.5CH_3CN[b]	HS-Fe^{II}	1.10	1.89	50
	HS-Fe^{II}	1.09	2.47	50
1[c]	HS-Fe^{II}	1.08	2.45	69
	HS-Fe^{II}	1.10	1.82	19
	LS-Fe^{II}	0.39	0.62	12
2[c]	HS-Fe^{II}	1.07	2.66	100
3[c]	HS-Fe^{II}	1.09	1.85	50
	HS-Fe^{II}	1.12	3.72	50
4[c]	HS-Fe^{II}	1.09	3.32	100
1[d]	HS-Fe^{II}	1.09	2.55	67
	LS-Fe^{II}	0.39	0.60	33
2[d]	HS-Fe^{II}	1.09	2.32	83
	LS-Fe^{II}	0.40	0.53	17
1[e]	HS-Fe^{II}	1.09	2.58	83
	LS-Fe^{II}	0.39	0.53	17

[a] the fresh crystalline sample **1** at 80 K; [b] the fresh sample **1** at 7 K; [c] the powdered polycrystalline samples **1 – 4** at 80 K; [d] the DMF solution sample **1** and **2** at 80 K; [e] the CH_3CN solution sample **1** at 80 K.

The higher quadrupole splitting values for **2 – 4** are typical of that expected for iron(II) in a highly distorted pseudooctahedral coordination environment.[128] This may be an effect of the somewhat greater distortion in the Fe coordination sphere due to the methyl substituents. These results are in accordance with structural and magnetic susceptibility data which confirm the presence of the [HS-HS-HS-HS] species for complexes **1 – 4**.

Upon cooling to 7 K, the Fe^{II} ions in **1**·6.5 CH_3CN remain in the HS state, while the parameters for the HS doublet change significantly: the isomeric shift increases slightly to δ_1 = 1.10 mm/s, δ_2 = 1.09 mm/s at 7 K, while the quadrupole splitting

increases considerably to ΔE_{Q1} = 1.89 mm/s, ΔE_{Q2} = 2.47 mm/s. Thus, the doublets superimpose more upon decreasing temperature (Figure 3.14 and Table 3.3).

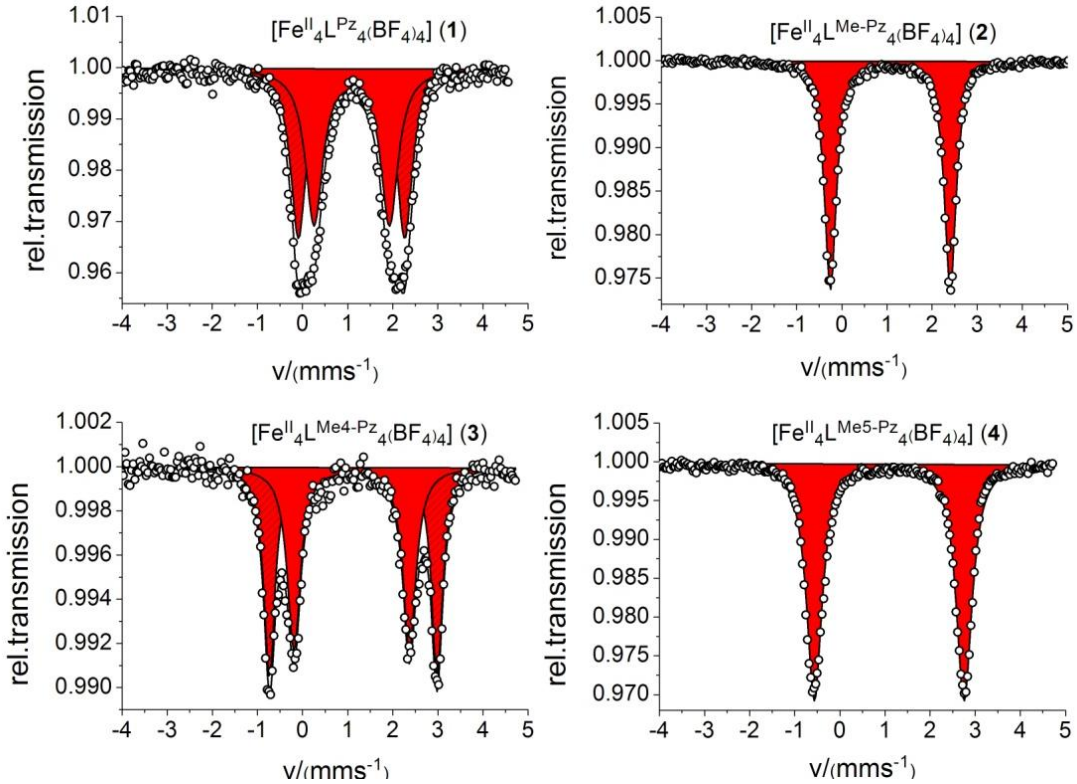

Figure 3.13. Zero-field ^{57}Fe Mössbauer spectra for fresh crystalline sample **1**·6.5 CH_3CN and powder crystalline sample **2** – **4** at 80 K. Lines represent simulations with Lorentzian doublets for HS Fe^{II}.

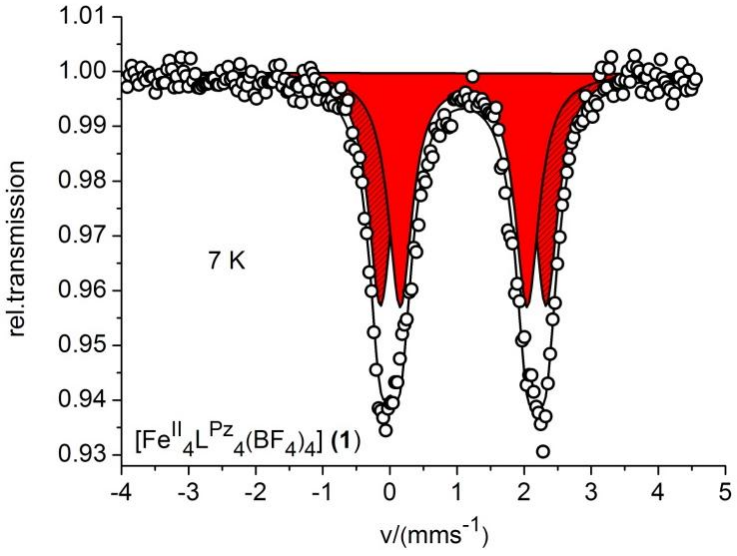

Figure 3.14. Zero-field ^{57}Fe Mössbauer spectra for fresh crystalline sample **1**·6.5 CH_3CN at 7 K. Lines represent simulations with Lorentzian doublets for HS-Fe^{II}.

^{57}Fe Mössbauer spectroscopy was also used to further understand the minor change of the spin state of Fe^{II} ions in the powder sample of **1**. The 80 K Mössbauer spectrum of a dry sample of **1** (Figure 3.15 and Table 3.3) shows three quadrupole doublets. Two of these doublets have parameters characteristic of HS-Fe^{II}, namely isomer shift/quadrupole splitting $\delta/\Delta E_Q$ = 1.08/2.45 mm/s (red subspectrum) and 1.10/1.82 mm/s (green subspectrum), respectively, and represent ~69% and ~19% of all HS-Fe^{II} ions in the dry sample. The third doublet has Mössbauer parameters $\delta/\Delta E_Q$ = 0.39/0.62 mm/s (blue subspectrum), which are typical for S = 0, LS Fe^{II} compound (δ = 0.27 – 1.38 mm/s and ΔE_Q = 0.26 – 1.01 mm/s),[127] and this represents ~12% of the LS Fe^{II} ions in the dry sample.

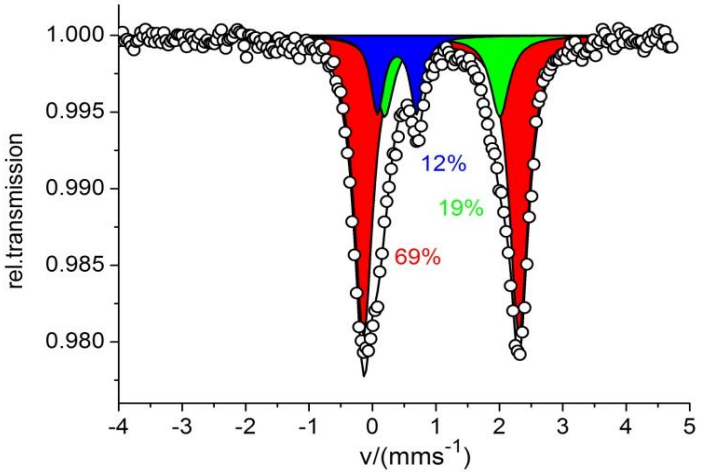

Figure 3.15. Zero-field ^{57}Fe Mössbauer spectra for powder crystalline sample of **1** at 80 K. Lines represent simulations with Lorentzian doublets for HS-Fe^{II} (red and green doublet); LS-Fe^{II} (blue doublet).

Comparison between $[Fe_4L^{Pz}{}_4]_4(BF_4)_4$ (1) and $[Fe_4L^{Py}{}_4]_4(BF_4)_4$

The previously reported compound **$[Fe_4L^{Py}{}_4]_4(BF_4)_4$**, synthesized by B. Schneider, and complex $[Fe_4L^{Pz}{}_4]_4(BF_4)_4$ (**1**) show the same spin configuration of [4HS] at high temperature. Complex $[Fe_4L^{Pz}{}_4]_4(BF_4)_4$ (**1**) exhibits almost no SCO over the SQUID measurement range of 2 – 300 K, but with 12% LS and 88% HS Fe^{II} at 80 K from Mössbauer spectroscopy, while compound **$[Fe_4L^{Py}{}_4]_4(BF_4)_4$** exhibits step-by-step thermal SCO and generates configuration of 34% LS and 66% HS Fe^{II} at 80 K.

Comparison of both molecular structures shows how distorted they are according to the twist of ligands, Fe···Fe distances and Fe-Fe-Fe angles (Figure 3.16).

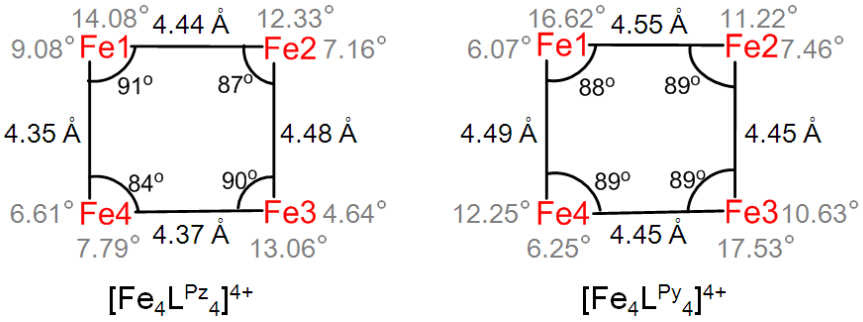

Figure 3.16. Fe···Fe distances, Fe-Fe-Fe angles (black) and torsion of the central pyrazole against side-arm pyrazolate or terminal pyridine in the ligands (gray) of $[Fe_4L^{Pz}{}_4]^{4+}$ and $[Fe_4L^{Py}{}_4]^{4+}$.

A more accurate description of the distortion is given by the CSM method. The data from the structure analysis of $[Fe_4L^{Pz}{}_4]_4(BF_4)_4$ (**1**), with $S(O_h)$ for the octahedron and S(itp) (itp means ideal trigonal prism) for the trigonal prism are listed in Table 3.4. **$[Fe_4L^{Py}{}_4](BF_4)_4$** is included for comparison. The higher values for $S(O_h)$ (corresponding to a lower S(itp)) of iron atoms in $[Fe_4L^{Pz}{}_4](BF_4)_4$ (**1**) suggests the coordination polyhedron is significantly more distorted from octahedral, compared with **$[Fe_4L^{Py}{}_4](BF_4)_4$**. Therefore the HS Fe^{II} ions in $[Fe_4L^{Pz}{}_4](BF_4)_4$ (**1**) have a stronger tendency to remain in that HS state due to their greater distortion from ideal octahedral geometry. This comparison shows clearly that a strong correlation exists between magnetic properties of $Fe^{II}{}_4$ grids and their solid-state structures.

Table 3.4. Mean Fe−N Bond Lengths and Continuous Symmetry Measures (CSM) for $[Fe^{II}{}_4L^{Pz}{}_4](BF_4)_4$ (**1**) and **$[Fe^{II}{}_4L^{Py}{}_4](BF_4)_4$**.

Complex	Center	d_{mean}/Å	$S(O_h)$	S(itp)	Spin state
1:$[Fe^{II}{}_4L^{Pz}{}_4](BF_4)_4$	$Fe^{II}1$	2.18	7.35	6.66	HS
	$Fe^{II}2$	2.18	7.87	7.07	HS
	$Fe^{II}3$	2.19	6.97	8.19	HS
	$Fe^{II}4$	2.20	7.87	7.07	HS
$[Fe^{II}{}_4L^{Py}{}_4](BF_4)_4$	$Fe^{II}1$	2.18	6.23	7.36	HS
	$Fe^{II}2$	2.16	5.57	7.57	HS
	$Fe^{II}3$	2.18	6.63	7.25	HS
	$Fe^{II}4$	2.18	6.35	7.32	HS

Additionally, Mössbauer spectra of **1** and **2** were recorded in frozen solution at 80 K in DMF and CH_3CN (Figure 3.17 and Table 3.4). ^{57}Fe Mössbauer measurements of frozen solutions of **1** and **2** in DMF reveal the presence of both LS Fe^{II} ions and HS Fe^{II} ions at 80 K with two characteristic quadrupole doublets, respectively. The characteristic subspectra for LS Fe^{II} ions (blue subspectrum) and HS Fe^{II} ions (red subspectrum)) for **1,** and LS Fe^{II} ions (blue subspectrum) and HS Fe^{II} ions (red subspectrum)) for **2** are displayed in Table 3.3. The ratio of HS and LS is 67:33 in the spectrum of **1** and 83:17 in **2**, respectively (compared to 100% HS Fe^{II} in the solid sample), which suggests that there is a mixture of spin configurations of [2HS-2LS] and [3HS-1LS] for **1** and [3HS-1LS] and [4HS] for **2** existing together. The Mössbauer spectrum of a frozen solution of **1** in CH_3CN displays a different ratio of HS and LS as 83:17 (δ = 0.39 mm/s, ΔE_Q = 0.53 mm/s for LS Fe^{II} (blue subspectrum); δ = 1.09 mm/s, ΔE_Q = 2.58 mm/s for HS Fe^{II} (red subspectrum)). The percent of LS state in frozen CH_3CN is lower than in the frozen DMF sample for compound **1**. A decrease in solvent donor number (DN) from DN = 19.1 (DMF) to DN = 14.1 (CH_3CN) causes a shift percent of LS Fe^{II} from 33% to 17%, which suggests that in solvent with a higher DN value the LS state is favored. While a preference for the LS state in solutions of donor solvents such as MeCN and DMF is documented and has been attributed to H-bonding between the ligands and solvent molecules or to some dissociation equilibria,[129,130] the effect of equilibrium reactions is not expected to take place in frozen solution for these grid complexes. It is likely that hydrogen bonds between the substituted pyrazolate-bridged ligands and the DMF or CH_3CN solvent molecules effect the spin state of the iron(II) ions in these [2 × 2] grid complexes in solution state.

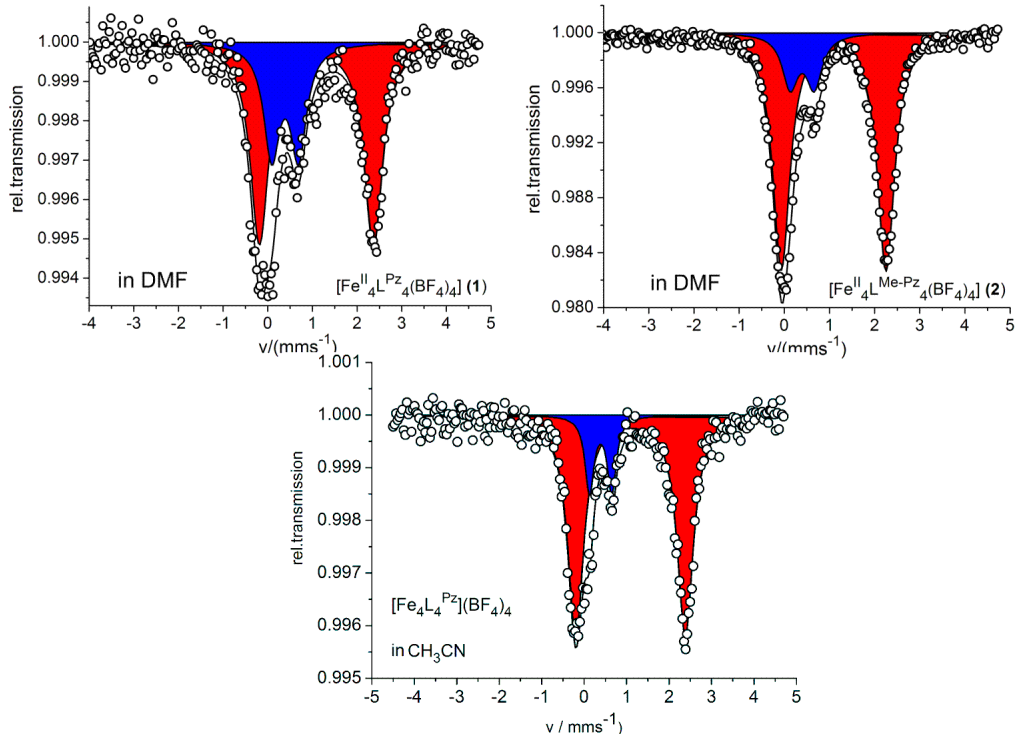

Figure 3.17. Zero-field ^{57}Fe Mössbauer spectra for **1** and **2** (top) in frozen DMF solution and **1** (bottom) in frozen CH_3CN solution at 80 K. Lines represent simulations with Lorentzian doublets for HS-Fe^{II} (red doublet) and LS Fe^{II} (blue doublet).

3.4. Solution State Investigations

Mass Spectrometry

Complexes **1** – **4** have been characterized by ESI mass spectrometry in CH_3CN solution. ESI mass spectrometry of all complexes show three prominent peaks characteristic of the different charged ions $[Fe^{II}_4L_4]^{4+}$, $[Fe^{II}_4L_4(BF_4)]^{3+}$ (or $[Fe^{II}_4L_4(F)]^{3+}$) and $[Fe^{II}_4L_4(BF_4)_2]^{2+}$. Isotope patterns matched those simulated and peak separations were consistent with the charges. This evidence unequivocally confirms the [2 × 2] Fe^{II}_4 grid species in solution, and suggests the high stability of grid-type structures in solution. The ESI-MS of **2** as is shown as an example in Figure 3.18. Three main signals can be detected, deriving from $[Fe^{II}_4L^{Me\text{-}Pz}_4]^{4+}$ combined with 0 – 2 BF_4^- counterions (m/z = 423.1 $[Fe^{II}_4L^{Me\text{-}Pz}_4]^{4+}$, 570.5 $[Fe^{II}_4L^{Me\text{-}Pz}_4(BF_4)]^{3+}$ and 933.2 ($[Fe^{II}_4L^{Me\text{-}Pz}_4(BF_4)_2]^{2+}$).

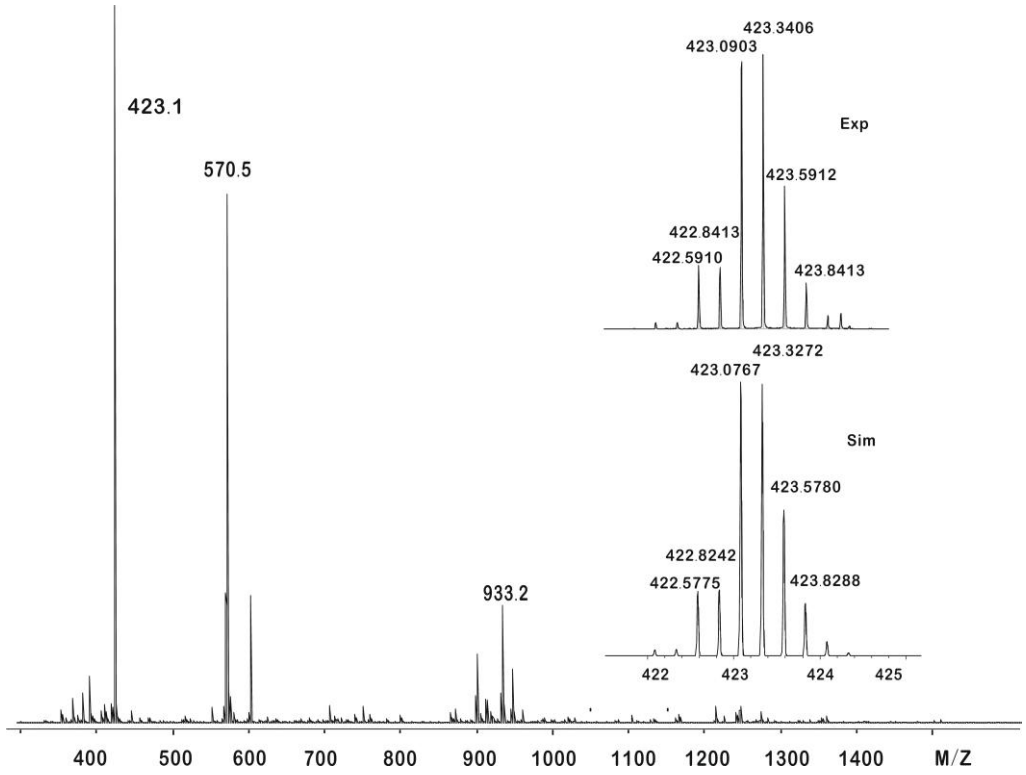

Figure 3.18. ESI–MS (MeCN) of $[Fe^{II}_4L^{Me\text{-}Pz}_4](BF_4)_4$ (**2**); (inset) experimental (upper) and simulated (lower) isotopic distribution pattern for the peak pattern around m/z = 423.1 characteristic for the $[Fe^{II}_4L^{Me\text{-}Pz}_4]^{4+}$ ion.

NMR Spectroscopy

Iron(II) possesses a d^6 electron configuration that corresponds to HS $t_{2g}^4e_{g2}^2$ and LS t_{2g}^6 arrangements within the O_h point group. All complexes containing HS Fe^{II} ions will possess four unpaired electron and present paramagnetism. It is well known that the ^{1}H NMR spectrum of paramagnetic iron complexes is fairly easy to obtain[131] and can be used to estimate the magnetic moment due to the short relaxation time of HS Fe^{II} (10^{-12} s). However, the interpretation of such ^{1}H NMR spectra is complicated due to line broadening and paramagnetic chemical shifts at "unpredictable" resonance frequencies. Therefore, the integrated intensities, or the spectra of selectively labeled isotopomers, may be the sole ground against which the spectra – if available at all – are interpreted.[131]

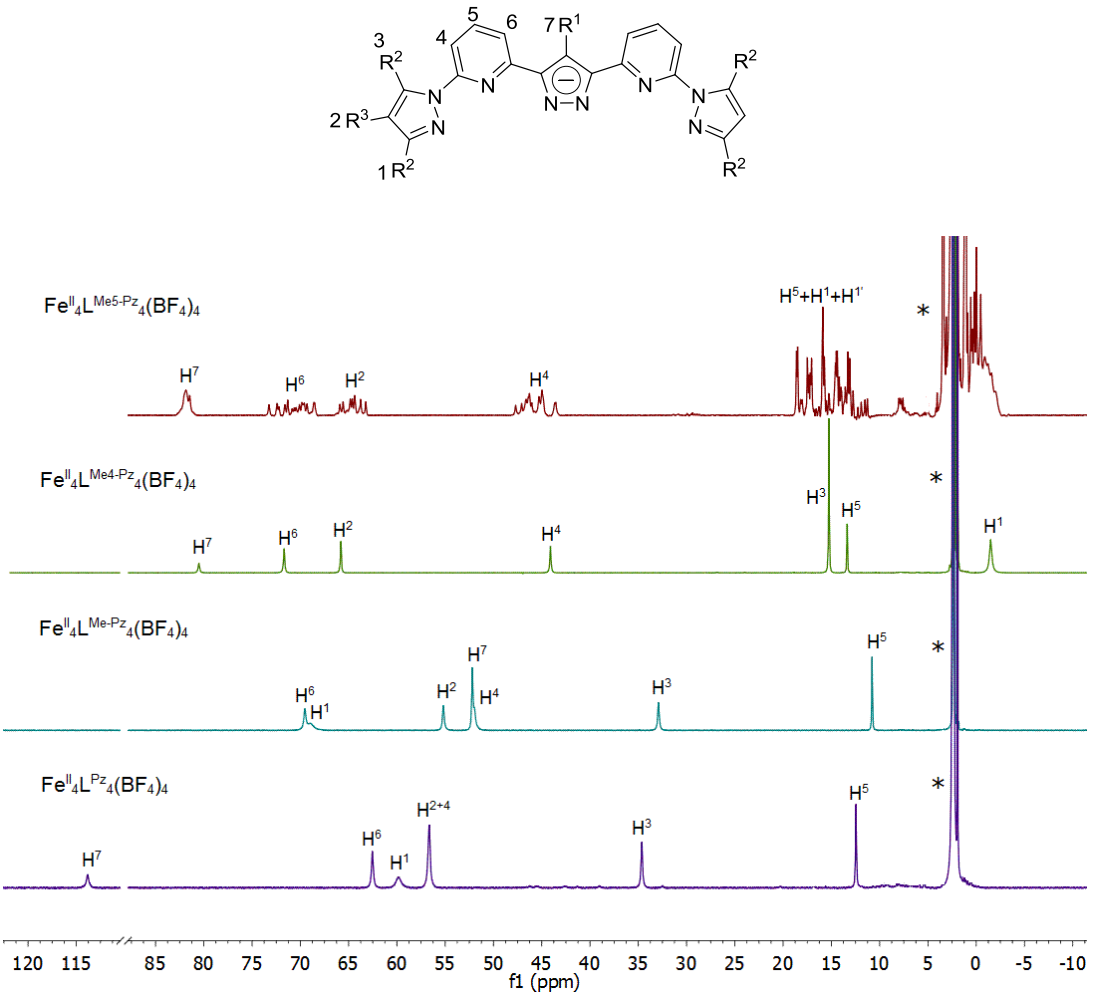

Figure 3.19. ^{1}H NMR spectra (500 MHz, CD_3CN, 298 K) of **1** – **4**.

^{1}H NMR measurements of complexes **1** – **4** confirm that the HS state of the Fe^{II} ions, as deduced from the crystal structure analyses and magnetic measurements in the solid state, are also retained in solution, with partly broad and paramagnetically shifted resonances, as shown in Table 3.5 and Figure 3.19.

The grid complexes **1** – **3** exhibit similarities in their ^{1}H NMR spectra: 1) only one set of broad, paramagnetically shifted peaks over a large chemical shift range (δ = 0 – 115 ppm (**1**), 0 – 70 ppm (**2**), −5 – 80 ppm (**3**)), attributed to the influence of the paramagnetic HS-Fe^{II} ion on the local magnetic field and proton relaxation rate;[132] 2) the number of signals observed, showing little variation in chemical shift, coincides in the three cases with the expected number of signals of the respective, symmetrically coordinated ligands. The ^{1}H NMR spectra of three grids were analyzed by

two-dimensional homonuclear experiments ^{1}H-^{1}H COSY and by comparison with the fully assigned spectra of related systems.

Table 3.5. ^{1}H chemical shift δ (ppm) of protons in complexes **1 – 4** in CD_3CN at 298 K.

Complex	H^1	H^2	H^3	H^4	H^5	H^6	H^7
1:$[Fe^{II}_4L^{Pz}_4](BF_4)_4$	60.1	56.5	34.7	56.5	12.5	62.7	113.8
2: $[Fe^{II}_4L^{Me\text{-}Pz}_4](BF_4)_4$	68.9	55.2	32.9	51.9	10.8	69.6	52.5
3: $[Fe^{II}_4L^{Me4\text{-}Pz}_4](BF_4)_4$	−1.5	65.8	15.3	44.1	13.4	71.7	80.5
4: $[Fe^{II}_4L^{Me5\text{-}Pz}_4](BF_4)_4$	11.1 – 15.8	56.8 – 58.8	0.2 – 1.0	42.4 – 43.5	11.1 – 15.8	60.9 – 63.8	74.9 – 75.2

The seven proton resonances of ^{1}H NMR spectrum of grid **1** attribute to three pyridines, three terminal pyrazoles, and one bridging pyrazole H-atoms arranged in a highly symmetric structure as shown in Figure 10.30. The peak at δ = 113.8 ppm, mostly shifted at lowest field, can immediately be assigned to the proton H^7 on the basis of the integral. The strongly broadened low-field signal at δ = 60.1 ppm is attributed to H^1 due to the close to the paramagnetic HS-Fe^{II} center. The remaining proton resonances are assigned based upon the ^{1}H-^{1}H COSY spectrum (Figure 10.31). The signal at δ = 12.5 ppm shows cross peaks to the signals at δ = 62.7 ppm and δ = 56.5 ppm. It follows that the δ = 12.5 ppm signal is due to H^5, although the assignment of H^4 and H^6 remains ambiguous. However, the signals at δ = 62.7 ppm and δ = 56.5 ppm are assigned to the H^6 and H^4 protons, respectively, on the basis of a slightly longer distance to metal for the latter, as seen in the solid structure.[133] Although there is no cross peak between signals H^2 and H^3 in the homonuclear 2D NMR spectrum, the assignment of both signals could be finished by comparison with the ^{1}H NMR spectra of other methyl substituted complexes **2** and **3**.

By comparison with the ^{1}H NMR spectrum of complex **1**, there are no noticeable difference shown in ^{1}H NMR spectra of $[Fe^{II}_4L^{Me\text{-}Pz}_4](BF_4)_4$ (**2**) and $[Fe^{II}_4L^{Me4\text{-}Pz}_4](BF_4)_4$ (**3**) (Table 3.5, Figures 10.33 and 10.38). The assignments of all protons are also based on the ^{1}H-^{1}H COSY experiments (Figures 10.34 and 10.39).

Finally, the only one set signals observed in the ^{1}H NMR spectrum strongly supports

that the geometry around the metal center found in the solid is also retained in solution at least on the NMR time scale.

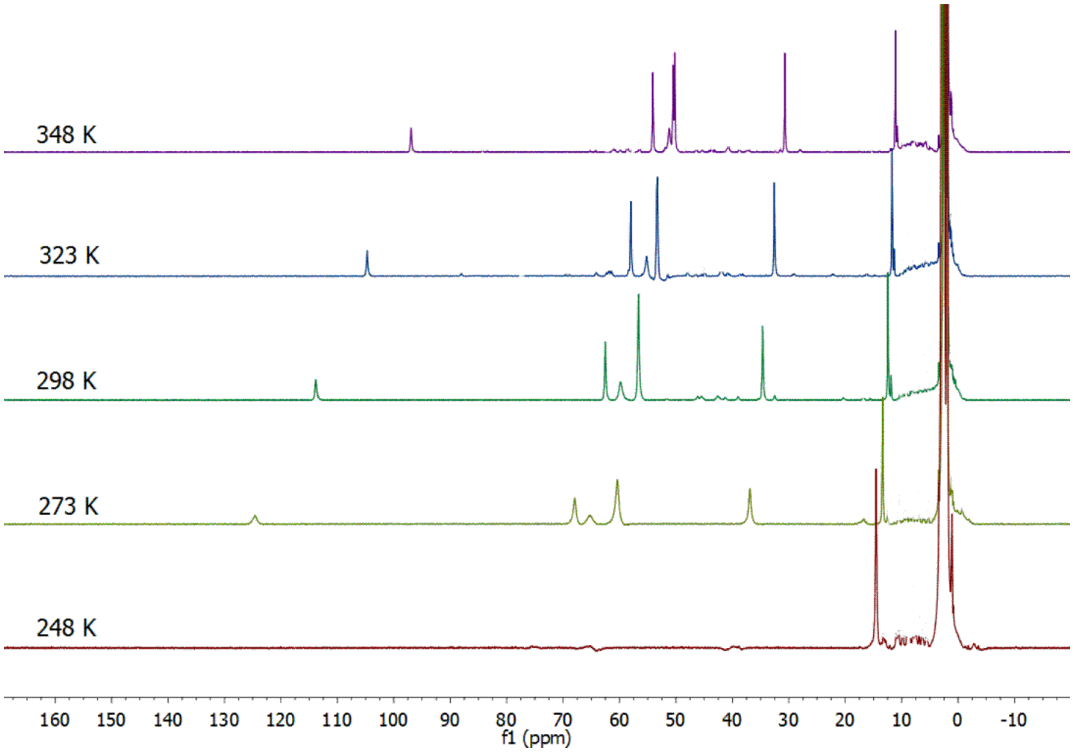

Figure 3.20. Variable-temperature ^{1}H NMR spectra (500 MHz, CD_3CN) of $[Fe^{II}_4L^{Pz}_4](BF_4)_4$ (**1**).

In the ^{1}H NMR spectra these three metal complexes **1 – 3** display Curie behaviour in solution over the studied temperature range of 248 – 348 K (Figures 3.20, 10.35 and 10.40). The Curie plot of the proton chemical shifts illustrates the minor changes under varying temperature and shows the expected linear correlation between chemical shifts and inverse temperature (Figures 3.21, 10.36 and 10.41). Spectrometer and solvent limitations prohibited the examination of a broader temperature interval.

It is worth mentioning that there is always only one set signals with paramagnetic chemical shift found from the ^{1}H NMR spectra at different temperature, which indicate the spin state of all Fe^{II} ions is kept in HS state and there is no SCO observed in soltion samples at least in the temperature range from 248 to 348 K.

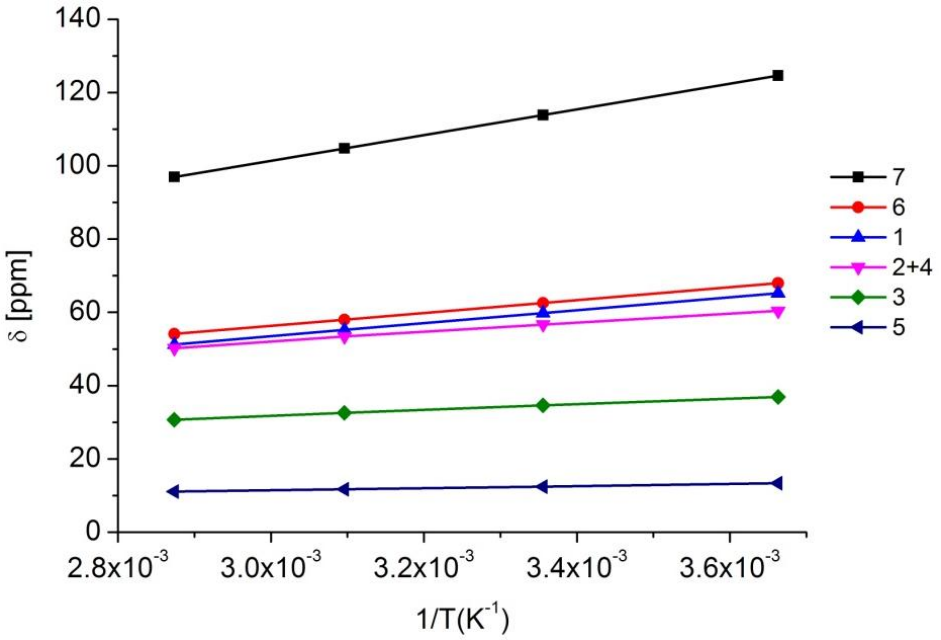

Figure 3.21. Curie plot showing the linear dependence of ^{1}H resonance shifts on the inverse temperature of $[Fe^{II}{}_4L^{Pz}{}_4](BF_4)_4$ (**1**).

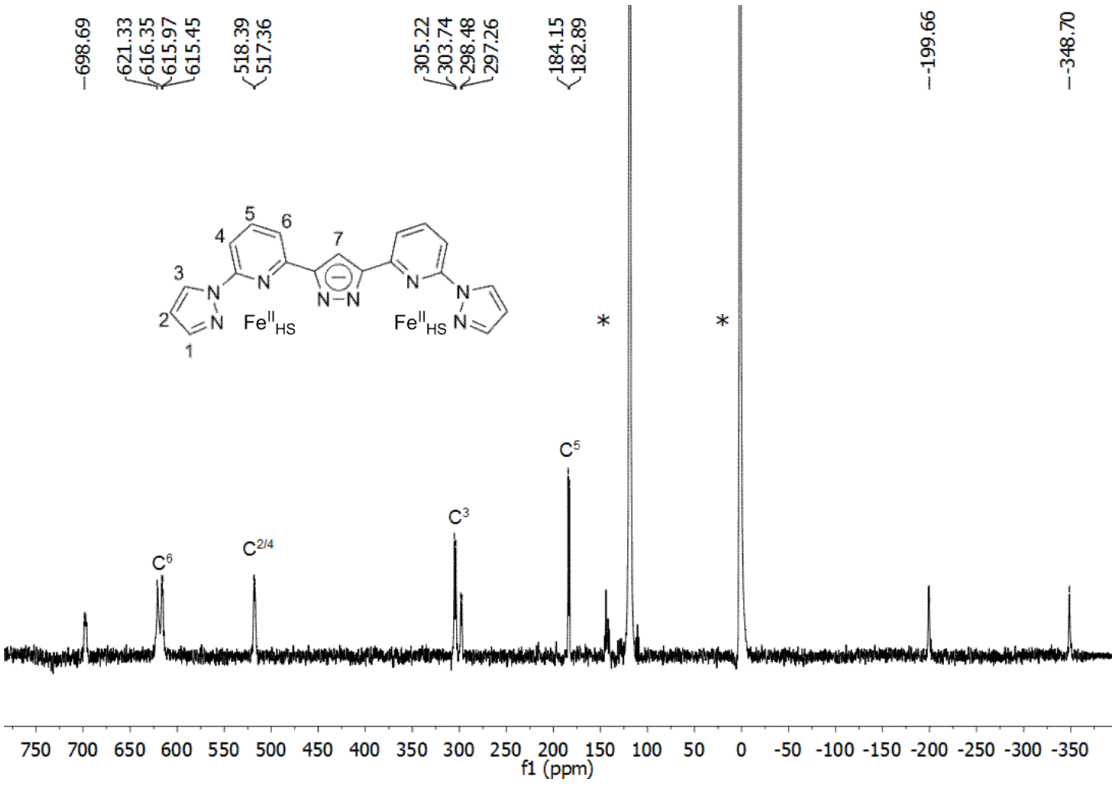

Figure 3.22. ^{13}C NMR spectrum (125MHz, CD_3CN, 298 K) of $[Fe^{II}{}_4L^{Pz}{}_4](BF_4)_4$ (**1**) (*CH_3CN).

The ^{13}C NMR spectra of complexes **1 – 3** also could be obtained with large range of paramagnetic chemical shift. All spectra displays several carbon resonances as

doublets and singlets at 298 K, which all arise from carbon atoms of the symmetrical molecule as depicted in Figures 3.22, 10.37 and 10.42. Some carbon signals are not detected due to their close vicinity to the paramagnetic Fe^{II} center. The the carbon atoms show doublets in the ^{13}C NMR spectra can be easily assigned to carbons with direct connection to proton atoms based on the ^{1}H-^{13}C correlation experiment (^{1}H-^{13}C HMQC, Figures 10.32 and 10.43), and the remaining singalets are attributed to quarternary ^{13}C atoms.

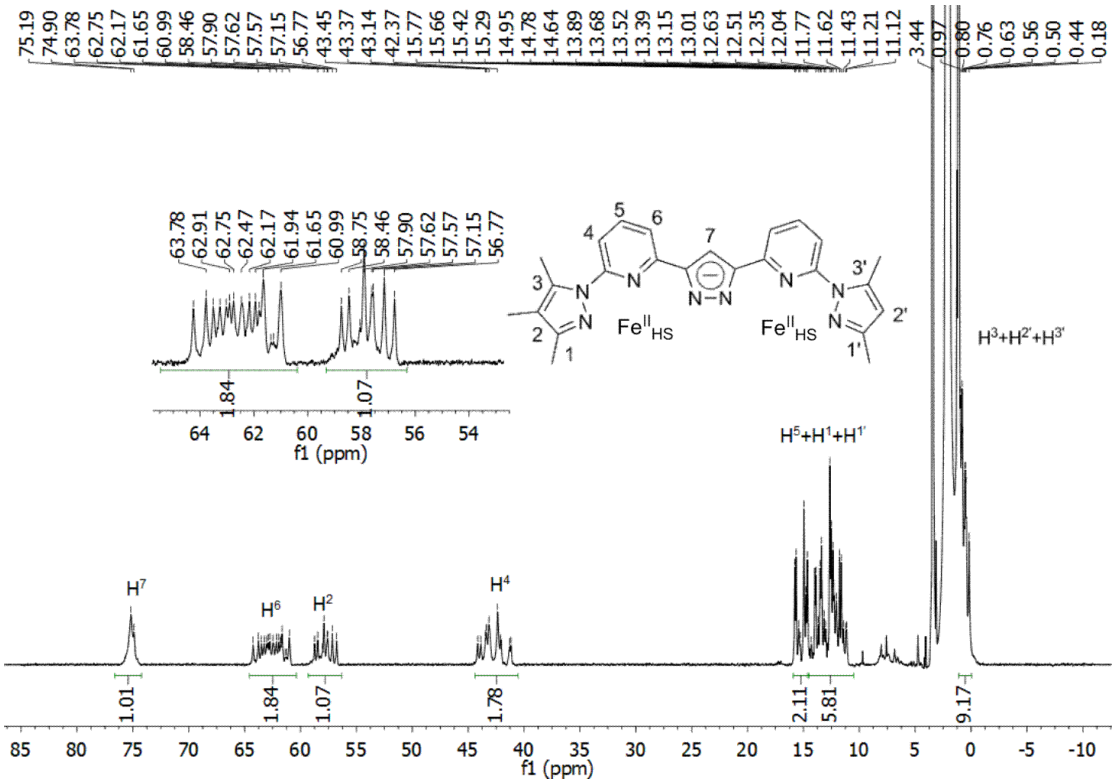

Figure 3.23. ^{1}H NMR spectrum (500 MHz, CD_3CN, 298 K) of $[Fe^{II}_4L^{Me5\text{-}Pz}_4](BF_4)_4$ (**4**).

In the case of $[Fe^{II}_4L^{Me5\text{-}Pz}_4](BF_4)_4$ (**4**) the ^{1}H NMR spectrum is more complicated than the spectra of the former three iron grid complexes (Figure 3.23). More peaks detected in a range from −5 ppm to 90 ppm suggest the presence of isomers, owing to the asymmetry of ligand $\mathbf{HL^{Me5\text{-}Pz}}$. The most shifted signals at chemical shift δ = 74.9 – 75.2 ppm can immediately be assigned to H^7, which is closest to the paramagnetic HS Fe^{II} ion. The signals at around 56.8 – 57.6 ppm are assigned intuitively to $H^{2'}$ on the basis of the integral intensity. Other four group signals would be assigned by comparison with the ^{1}H NMR spectrum of complex **3**. The

variable-temperature ^{1}H NMR spectra of **4** in CD_3CN over the temperature range 248 – 348 K shows the similar chemical shift with the increasing temperature, but the Curie behavior could not be observed due to the multiple-peaks of these proton atoms (Figure 10.44). Again the ^{13}C NMR spectrum of complex $[Fe^{II}_4L^{Me5\text{-}Pz}_4](BF_4)_4$ (**4**) is also difficult to be identified because of the isomers existed together in solution sample, which makes the assignment of the carbon atoms impossible (Figure 10.45).

Electrochemistry

The electrochemical properties of **1** – **4** were examined by cyclic voltammetry (CV) and square wave voltammetry (SWV) in CH_3CN. The presence of redox-active bridging ligands, together with four redox-active iron centers makes complexes **1** – **4** ideal candidates for investigating their redox properties.

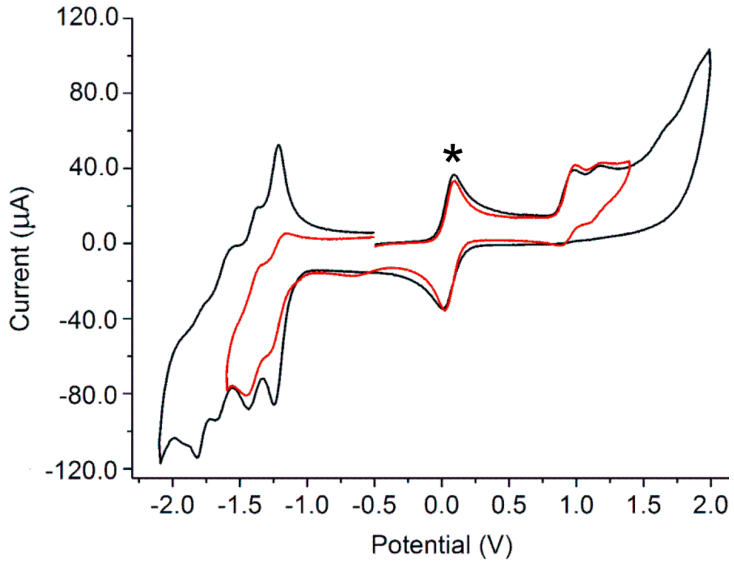

Figure 3.24. Cyclic voltammograms of $[Fe^{II}_4L^{Pz}_4](BF_4)_4$ (**1**) over the potential range –2.3 V to +2.3 V (CH_3CN/0.1M Bu_4NPF_6, scan rate 0.1 V/s, *$Me_{10}Fc/Me_{10}Fc^{+}$).

All grid complexes gave well-defined CVs showing pairs of stepwise one-electron transfers. Analyses of peak shapes and characteristics at different scan rates show similar oxidative properties attributed to the Fe^{II}/Fe^{III} redox couples and reductive process based on pyrazolate-bridged ligands. Table 3.6 summarizes the redox behavior of grid complexes **1** – **4**. Closer inspection of the redox potentials of complexes **1** – **4** in CH_3CN exhibits, a slight dependence of the electrochemical

behavior on the ligand substitutions.

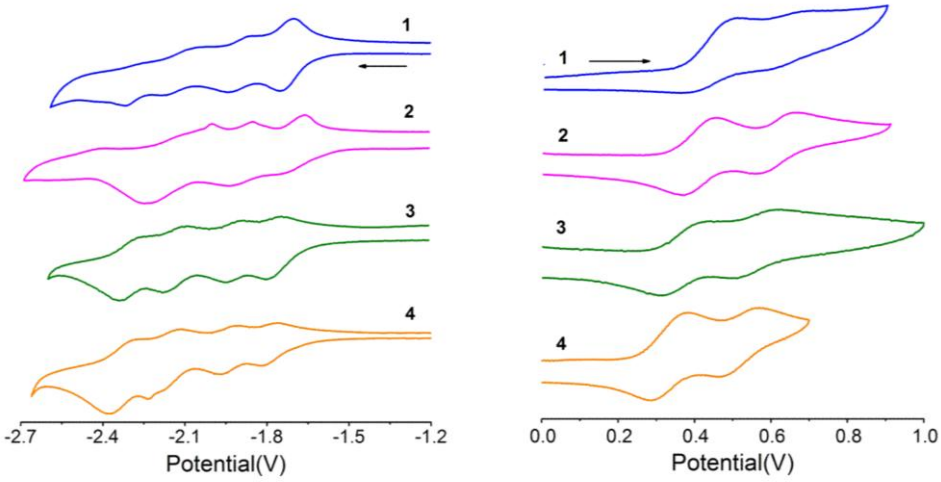

Figure 3.25. Cyclic voltammograms of **1** – **4** at the potential range –2.7 V to –1.2 V (left) and 0.4 V to −1.6 V (right) in CH_3CN/0.1M Bu_4NPF_6, scan rate 0.1 V s^{-1} vs Fc/Fc^+.

Reduction Processes

CV and SWV of complexes **1** – **4** reveal multiple single-electron reduction processes with quasi-reversibility for each compound and the reduction waves with a slight potential shift from hydrogen to methyl substrates correspond to the gradual reduction of the four ligands in grid structure (Figure 3.35 (left)).

Table 3.6. Electrochemical data, $E_{1/2}$ (ΔE_p), for complexes **1** – **4** in CH_3CN/0.1 M Bu_4NPF_6). $E_{1/2}$ in V and ΔE_p in mV vs Fc/Fc^+(Fc: ferrocene).

Complex	Fe^{II}-Fe^{III}				Ligand-reduction			
	I	II	III	IV	I	II	III	IV
$[Fe^{II}_4L^{Pz}_4](BF_4)_4$	0.42	0.63	1.08	1.60	–1.72	–1.89	–2.14	–2.29
(**1**)	(104)	(94)	(161)	[b]	(142)	(120)	(121)	(80)
$[Fe^{II}_4L^{Me\text{-}Pz}_4](BF_4)_4$	0.39	0.59	0.99	1.39	–1.73	–1.92	–2.14	–2.30
(**2**)	(82)	(78)	(268)	[b]	(207)	(234)	(176)	(192)
$[Fe^{II}_4L^{Me4\text{-}Pz}_4](BF_4)_4$	0.33	0.52	no[a]	no	–1.76	–1.93	–2.13	–2.29
(**3**)	(114)	(98)			(61)	(61)	(77)	(67)
$[Fe^{II}_4L^{Me5\text{-}Pz}_4](BF_4)_4$	0.32	0.51	no	no	–1.77	–1.96	–2.17	–2.32
(**4**)	(74)	(84)			(66)	(89)	(81)	(102)

[a]: not observed; [b]: anodic peak potential of irreversible wave.

For complex $[Fe^{II}_4L^{Pz}_4](BF_4)_4$ (**1**) there are four one-electron reduction steps displayed in the CV and SWV in CH_3CN solution ($E_{1/2}$ = –1.72, –1.89, –2.14 and –2.29 V vs. Fc/Fc^+) (Figures 3.25 and 3.26). Typically in grid complex the reduction processes could be observed due to the bridging ligands or the metal centers. The separation between the first two reductions is relatively small ($\Delta E_{1/2}$ = 170 mV), while the separation between the second and third processes ($\Delta E_{1/2}$ = 250 mV) is larger. The reduction potential of the third and fourth ones are separated by $\Delta E_{1/2}$ = 150 mV, which is similar to the first pair reduction.

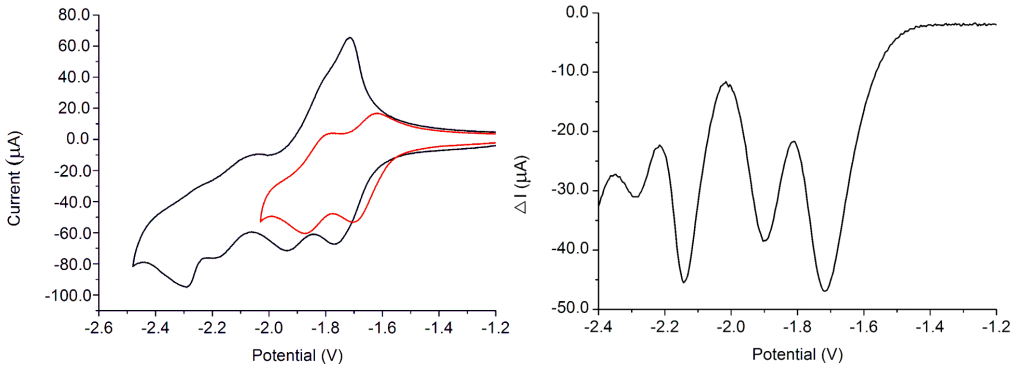

Figure 3.26. Cyclic voltammograms of $[Fe^{II}_4L^{Pz}_4](BF_4)_4$ (**1**) over different potential ranges of –2.02 V to –1.20 V (left, red) and –2.48 V to –1.20 V (left, black) and square wave voltammogram in a range of –2.40 V to –1.20 V (right) (CH_3CN/0.1M Bu_4NPF_6, scan rate 0.1 V s^{-1}, vs Fc/Fc^+).

The first and second reductions occur at similar potentials to the reduction of iron(II) in mononuclear complex such as $[Fe(tpy)_2]^{2+}$[134], which suggest these reduction processes may be corresponding to both the reduction of each ligand or Fe^{II} center in the [2 × 2] Fe^{II}_4 grid. It is not clear at this time on the assignment of these reduction steps. Further work to figure out the reduction processes is in progress. The introduction of methyl groups per ligand causes the reduction potential shift to less negative (Figures 10.79 – 10.81). However, for these three substituted grid compounds, the problem of assigning the reduction steps is still unsolved.

Oxidation Processes

The CV and SWV of [2 × 2] Fe^{II}_4 grid complexes **1** – **4** display pairs of one-electron oxidation waves, assigned to Fe^{II}/Fe^{III} redox couples on non-interacting iron centers

from +0.3 to +1.6 V vs. Fc/Fc^+ (Figure 3.25, right and Table 3.6). There are different oxidation steps and potential ranges exhibited in complexes **1** – **4**.

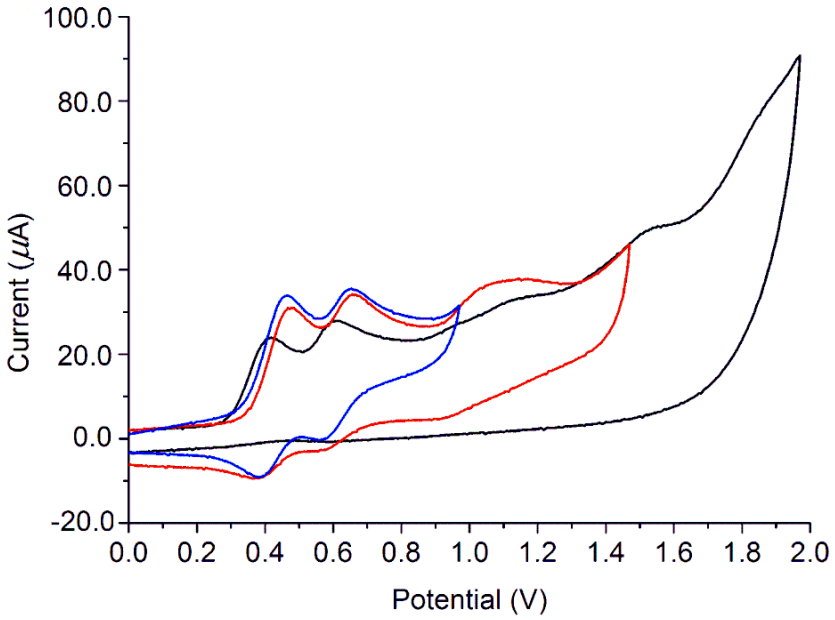

Figure 3.27. Cyclic voltammogram of $[Fe^{II}_4L^{Pz}_4](BF_4)_4$ (**1**) over the potential range 0.0 V to 2.0 V (CH_3CN/0.1M Bu_4NPF_6, scan rate 0.1 V s^{-1}, vs Fc/Fc^+).

For both complexes $[Fe_4L^{Pz}_4](BF_4)_4$ (**1**) and $[Fe_4L^{Me\text{-}Pz}_4](BF_4)_4$ (**2**), there are four oxidation processes observed (Figures 3.30 and 10.82). The first three one-electron transfers are quasi-reversible, and the remaining one-electron transfer is irreversible. Although the oxidation waves concerning the first two Fe^{II} centers of complexes **1** and **2** display a similar peak shape, the oxidation potentials exhibit a dependence upon the charge of the bridging ligand. Complex **1** displays one pair of quasi-reversible, one-electronic metal-centered oxidations at $E_{1/2}^{oxi1}$ = 0.42 V and $E_{1/2}^{oxi2}$ = 0.63 V (vs. Fc/Fc^+). In contrast to **1**, the oxidation potential is slightly less positive when the Fe^{II} center is coordinated by $\{N_6\}$ from the methyl-substrate into 4-position of the central pyrazole bridging ligands of complex **2** ($E_{1/2}^{oxi1}$ (**1**) – $E_{1/2}^{oxi1}$ (**2**) = +30 mV and $E_{1/2}^{oxi2}$ (**1**) – $E_{1/2}^{oxi2}$ (**2**) = +40 mV). Such a shift can be expected from simple electropositive arguments considering the replacement of methyl group in **2**, thus the electron-donating effect of methyl group would lower the Fe^{II} oxidation potential.

The introduction of more electron-donating methyl groups per ligand into the

3,4,5-positions of pyrazole side-arms, yields complexes $[Fe_4L^{Me4\text{-}Pz}{}_4]^{4+}$ (**3**) and $[Fe_4L^{Me5\text{-}Pz}{}_4]^{4+}$ (**4**). The CVs and SWVs of these two complexes display only two well-defined quasi-reversible oxidation processes (0.33 V and 0.52 V vs. Fc/Fc^+ for **3**; 0.32 V and 0.51 V vs. Fc/Fc^+ for **4**) and larger positive shift of the oxidation potentials relative to the oxidation of complex **1** (Figures 10.83 and 10.84).

The electronic effect of methyl groups is further confirmed by the CVs of complexes **3** and **4**. The substitution of protons on the position of side-arm pyrazole rings in **1** by electron-donating methyls to form grid structures **3** and **4** is reflected in a more decrease of oxidation potentials.

In theory, the larger number of methyl groups of complexes **3** and **4** could bring greater effect on the oxidation potential could shift the oxidation potential to less positive values. The average oxidation potential of the first and second oxidation waves is slightly less positive in **4** compared to those in **3** ($E_{1/2}{}^{oxi1}$ (**1**) – $E_{1/2}{}^{oxi1}$ (**3**) = +90 mV and $E_{1/2}{}^{oxi2}$ (**1**) – $E_{1/2}{}^{oxi2}$ (**3**) = +110 mV; $E_{1/2}{}^{oxi1}$ (**1**) – $E_{1/2}{}^{oxi1}$ (**4**) = +100 mV and $E_{1/2}{}^{oxi2}$ (**1**) – $E_{1/2}{}^{oxi2}$ (**4**) = +120 mV). Fewer oxidation steps are observed when more methyl groups are present on the ligands. These results can be expected due to the methyl-methyl steric repulsion, which would lengthen the Fe−N bonds between the iron center and pyrazole side-arm moieties in the grid structure, and therefore decrease the oxidation potential slightly and destabilize Fe^{III} relative to Fe^{II}.[135,136]

UV/Vis Spectroscopy

The investigation of the spectroscopic properties of **1** – **4** was carried out on different concentrated solutions in CH_3CN in the range 200 – 1200 nm (Figure 3.34).

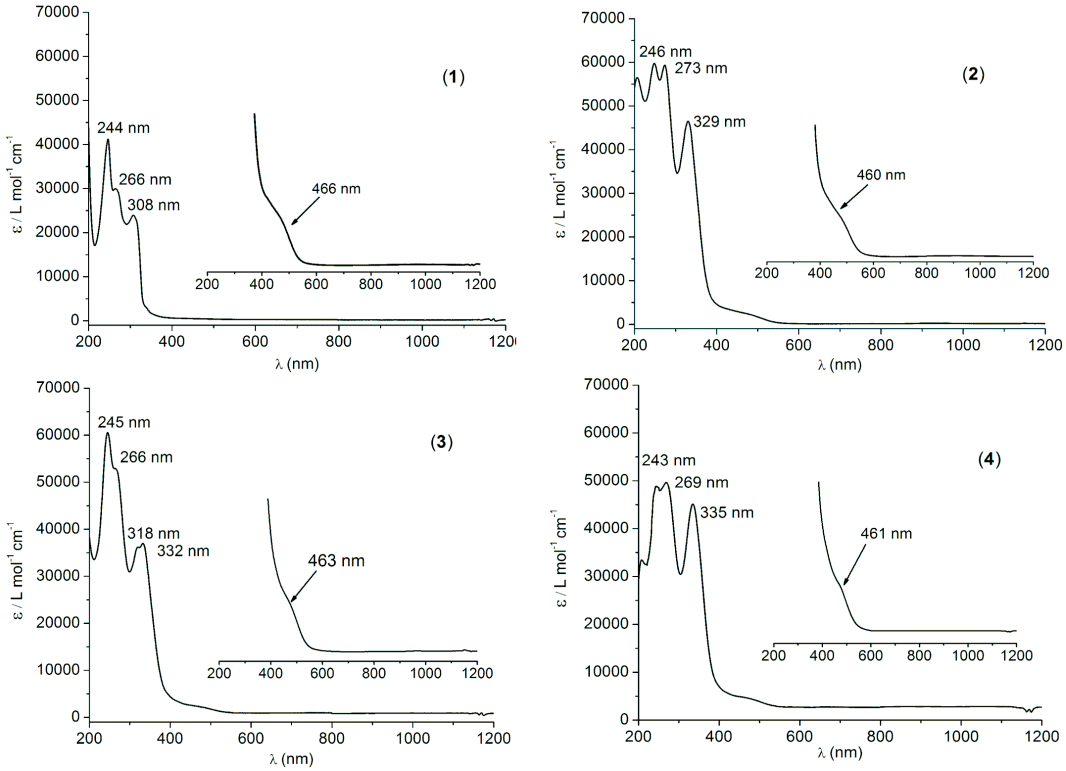

Figure 3.28. UV/Vis spectra of **1** – **4** (c = 5×10^{-5} M) in CH_3CN.

For complex **1** there are three intense bands at 244 nm (ε = 41174 L mol^{-1} cm^{-1}), 266 nm (ε = 29857 L mol^{-1} cm^{-1}) and 308 nm (ε = 24113 L mol^{-1} cm^{-1}) and one more shoulder at 462 nm (ε = 373 L mol^{-1} cm^{-1}). The former three intense bands are likely π→π* transitions on the ligand, while the shoulder at 462 nm is likely a metal-to-ligand charge transfer (MLCT) transition. It is known that the π→π* and MLCT transitions could display blue shift in the UV/Vis spectrum with the adding of methyl substituents as electro donating groups. From the UV/Vis spectra of **2** – **4**, there are several similar absorption bands with however small shift obversed (Figure 3.34). The results evidence no significant effect induced by the methyl substituents as electron donating groups bound to the 4-positions of the central pyrazole rings or 3, 4, 5- positions of the peripheral pyrazole rings of ligands in the grid compounds.

Spectroelectrochemistry

The UV/Vis absorbance of **1** – **4** during chemical oxidation was examined by spectroelectrochemistry. Controlled potential UV/Vis measurements were conducted on a solution of **1** – **4** in CH_3CN/0.1 M NBu_4PF_6 at room temperature. Since the

first two oxidation steps are hardly separated from each other, the experiment began directly with the two-electron oxidation at a potential of 0.8 V vs Fc/Fc^+ for **1** – **4** and wavelength range between 200 and 1000 nm (Figure 3.35).

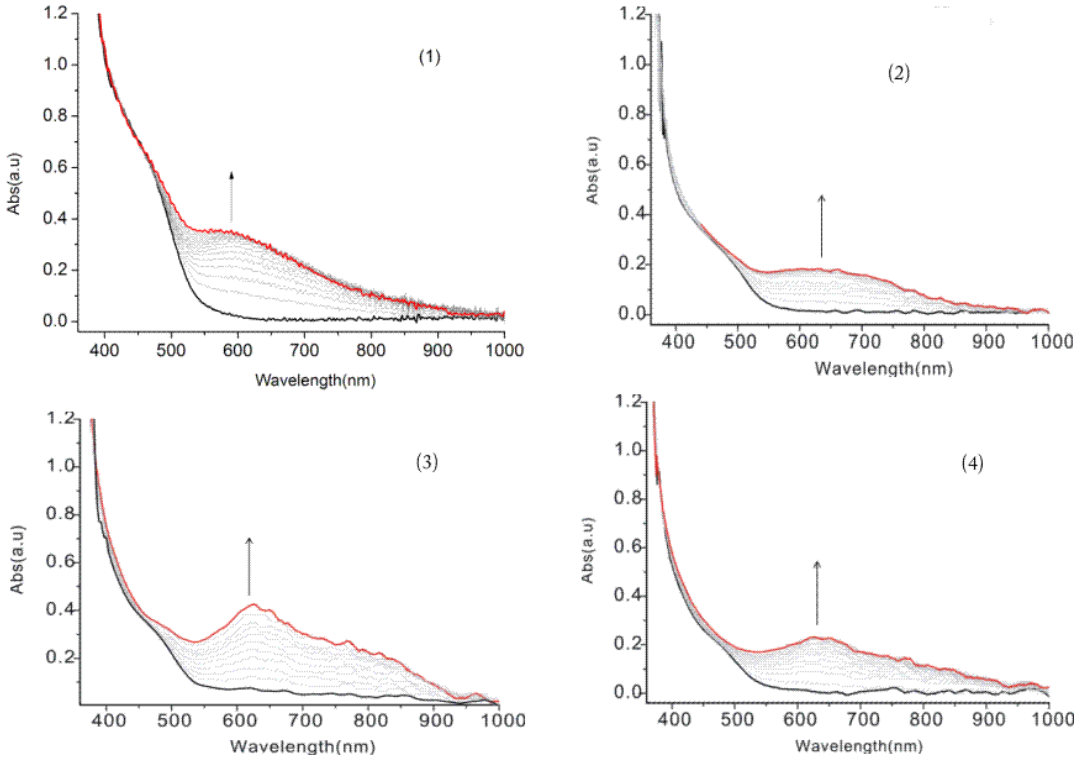

Figure 3.29. Electrochemical oxidation in CH_3CN/0.1 M Bu_4NPF_6 at a potential of 1.6 V for **1**; 1.5 V for **1**; 1.2 V for **3** and 1.2 V for **4**. The course of oxidation was followed by UV/vis spectroscopy.

Two-electron oxidations from $[Fe^{II}_4L_4]^{4+}$ to $[Fe^{II}_2Fe^{III}_2L_4]^{6+}$ under applied potential caused the Fe^{II} to ligand charge transfer (MLCT) band (λ_{max} = 466 nm for **1**, 460 nm for **2**, 463 nm for **3** and 461 nm for **4**) to weaken, while a new broad band at 600 nm (**1**), 612 nm (**2**), 629 nm (**3**) and 646 nm (**4**), respectively, corresponding to a ligand-to-Fe^{III} charge transfer (LMCT) transition was observed and increases in intensity. Since the oxidation steps in complexes reported herein are metal centered (see discussion above), there is no description about the change in the position and intensity of the bands of bridging-ligand centered $\pi \rightarrow \pi^*$ transition. Hence, the two-electron oxidized species is best described as $[Fe^{II}_2Fe^{III}_2L_4]^{6+}$. The $\pi \rightarrow \pi^*$, LMCT and MLCT bands of $[Fe^{II}_4]^{4+}$ and $[Fe^{II}_2Fe^{III}_2L_4]^{6}$ for complexes **1** – **4** are red

shifted with increasing methyl electron-donating substituents at the side arm and bridging pyrazoles of the ligands.

3.5. Conclusion

An extended family of homo-valence $[Fe^{II}_4L^R_4]^{4+}$ (**HL^{Pz}**, **HL$^{Me\text{-}Pz}$**, **HL$^{Me4\text{-}Pz}$** and **HL$^{Me5\text{-}Pz}$**) [2 × 2] grid complexes **1** – **4** has been prepared by using substituted pyrazole-bridging ligand systems. The substituents (R) bounded at different positions of the central-pyrazole or side-arm pyrazole rings have a slight effect on complex geometry and influence both the electrochemical and magnetic behavior of the systems. Mössbauer spectra and SQUID experiments confirm HS Fe^{II} ions in all cases with no SCO observed. Solution state ^1H and ^{13}C NMR spectra of paramagnetic **1** – **4** confirm that the Fe^{II}_4 grids are spin-localized on the NMR time scale.

4. Mixed-spin and Mixed-valence in Pyrazole-bridged Tetranuclear [2 × 2] Iron Grid Complexes

4.1. Synthesis of Ligands

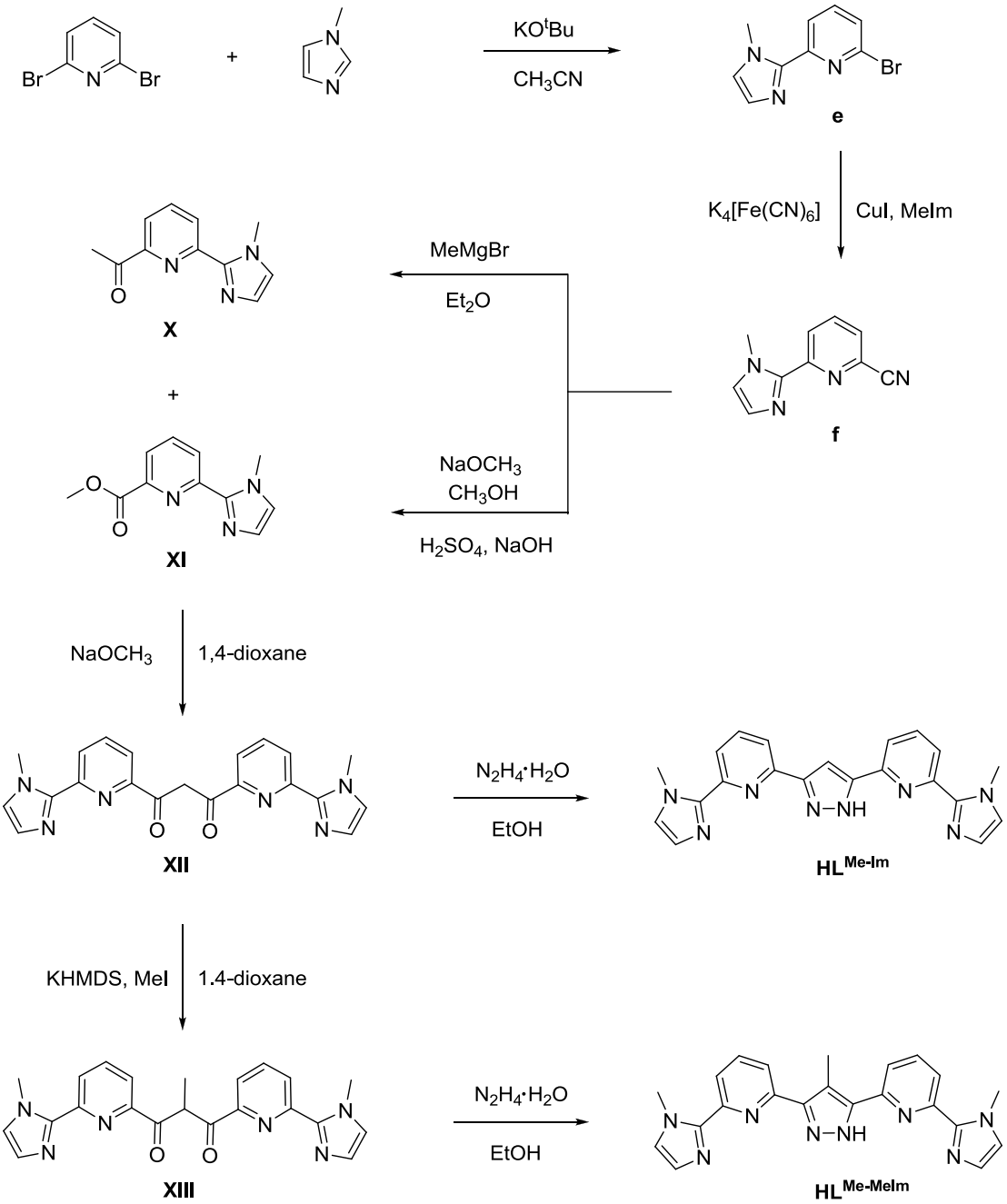

Scheme 4.1. Synthesis of ligands $\mathbf{HL^{Me\text{-}Im}}$ and $\mathbf{HL^{Me\text{-}MeIm}}$.

The new ligands used in this chapter were designed based upon the ligands discussed in chapter 3, which are 3,5-bis(6-(1-methylimidazole-2-yl)pyrid-2-yl)pyrazole

(**HL**$^{\mathbf{Me\text{-}Im}}$) and 4-methyl-3,5-bis(6-(1-methylimidazole-2-yl)pyrid-2-yl)pyrazole (**HL**$^{\mathbf{Me\text{-}MeIm}}$). In comparison with ligand **HL**$^{\mathbf{Pz}}$ used in chapter 3, ligand **HL**$^{\mathbf{Me\text{-}Im}}$ contains two 1-methyl-1*H*-imidazole groups instead of pyrazole rings as side arms, and therefore one of the starting materials for the first synthetic step was changed to methylimidazole, instead of the substituted pyrazole compounds (Scheme 4.1). The key intermediate 6-cyano-2-(1-methylimidazol-2-yl)pyridine (**f**), prepared in two steps from 2,6-dibromopyridine and 1-methyl-1*H*-imidazole (see Experimental Section), was functionalized in two different ways to form both 6-acethyl-2-(1-methylimidazol)pyridine (**X**) and 6-methylcarboxy-2-(1-methylimidazol)pyridine (**XI**).[137] The 1,3-diketone **XII** could be obtained *via* pseudo-claisen condensation of **X** and **XI** and the ligand **HL**$^{\mathbf{Me\text{-}Im}}$ was then prepared as a white powder by a ring-closing condensation with hydrazine. Additionally, the 1,3-diketone **XII** was methylated and the resulting diketone **XIII** was then condensed with hydrazine to yield ligand **HL**$^{\mathbf{Me\text{-}MeIm}}$.

The synthesis of the other new ligand 1,3-bis(6-(1*H*-imidazol-2-yl)pyrid-2-yl)pyrazole (**HL**$^{\mathbf{Im}}$) is different from the former two ligands and the starting material of the first synthetic step is pyridine-2,6-dicarboxylic acid (**g**). The key intermediate methyl-6-formylpicolinate (**h**) (see Experimental Section), was functionalized to form methyl-6-(1*H*-imidazol-2-yl)picolinate (**XIV**) and then further modified to produce 1-(6-(hydroxymethyl)pyridin-2-yl)ethanone (**XV**). The 1,3-diketone **XVI** could be obtained *via* pseudo-claisen condensation of compounds **XIV** and **XV** and the pyrazole-bridged dimethanol compound **XVII** was then produced by a ring-closing condensation with hydrazine, which is similar to the synthesis of other pyrazole-bridged ligands. The dimethanol compound was oxidized to dialdehyde and then reacted with glyoxal and ammonia in MeOH to obtain the ligand **HL**$^{\mathbf{Im}}$.

The three ligands have been characterized by ^{1}H NMR and ^{13}C NMR spectroscopies, ESI-MS and elemental analyses (Figures 10.14 – 10.20 and see Experimental Section).

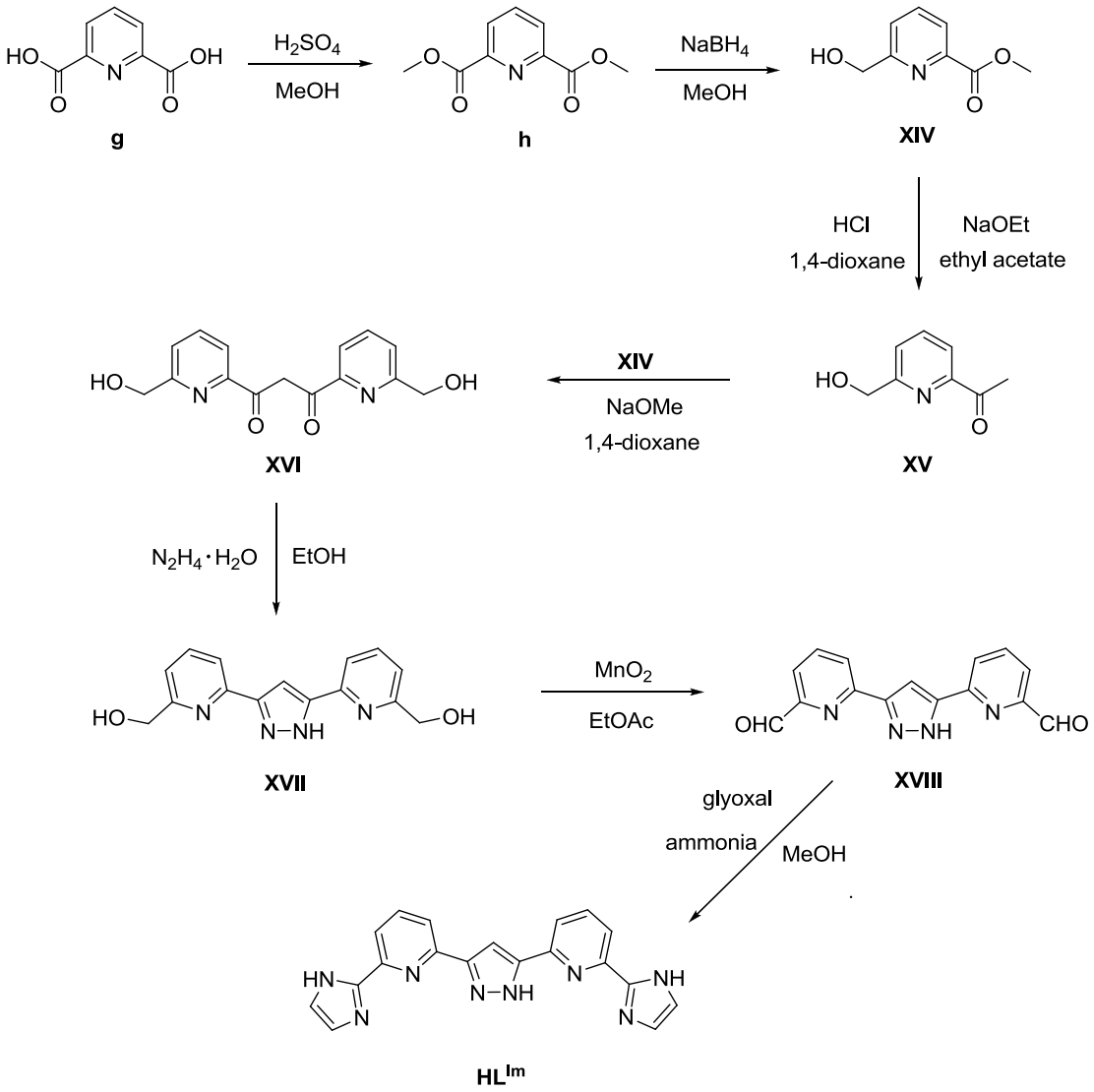

Scheme 4.2. Synthesis of ligand $\mathbf{HL^{Im}}$.

4.2. Homo-valence [2 × 2] Fe_4 Grid Complexes

4.2.1. Synthesis of [2 × 2] Fe^{II}_4 Grid Complexes

For the synthesis of the all-ferrous grid complexes, ligand $\mathbf{HL^{Me\text{-}Im}}$ or $\mathbf{HL^{Me\text{-}MeIm}}$ is dissolved in dry MeOH together with NaO^tBu base. Addition of solid $Fe(ClO_4)_2 \cdot 6H_2O$ gave a deep-red solution (Scheme 4.3). After purification by extraction and recrystallization by using a large quantity of Et_2O, crystalline material of $[Fe^{II}_4L^{Me\text{-}Im}_4](ClO_4)_4$ (**6**) was collected by slow diffusion of Et_2O into a solution of crude complex in MeOH, while the complex $[Fe^{II}_4L^{Me\text{-}MeIm}_4](BF_4)_4$ (**10**) was obtained

by slow diffusion of Et_2O into a solution of the crude complex in CH_3CN.

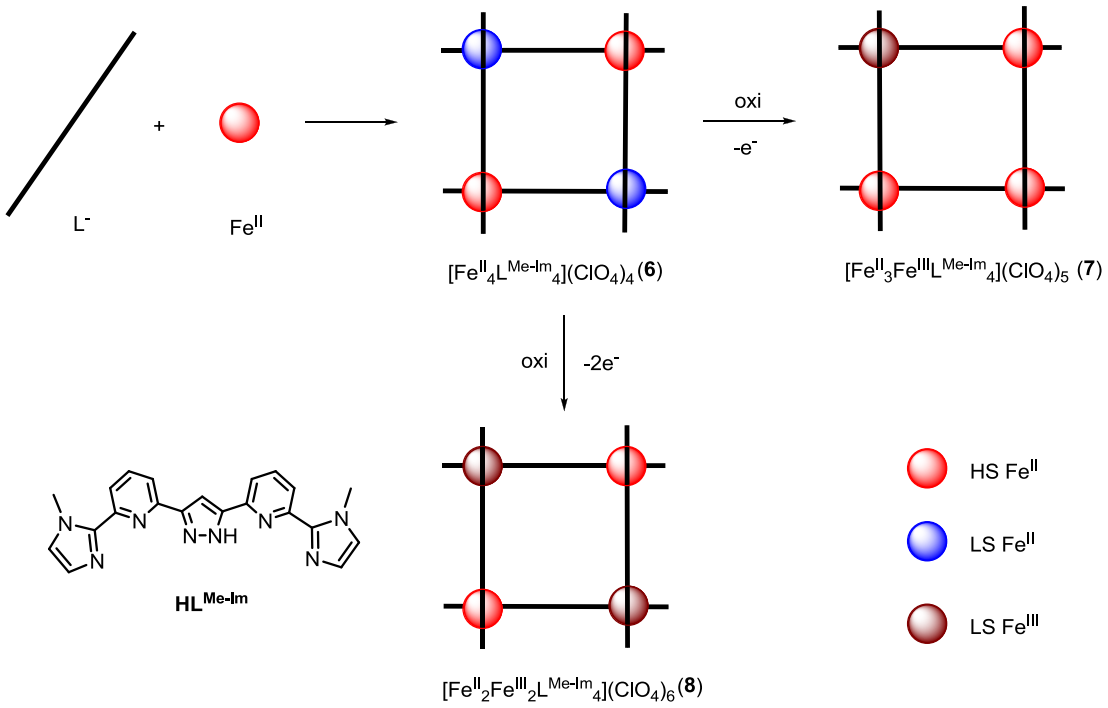

Scheme 4.3. Schematic representation of the synthesis of [2 × 2] Fe_4 grid complexes **6**, **7** and **8**.

4.2.2. Solid State Investigations

Structural Characterization

Compounds **6** and **10** are air-stable and the molecular structures were characterized by single X-ray crystallography. The all-ferrous grid complexes consist of four crystallographically independent Fe^{II} ions and four bridging ligands $(L^R)^-$ (**HL** = **HL$^{Me\text{-}Im}$** for **6** and **HL$^{Me\text{-}MeIm}$** for **10**). The four iron atoms are bridged by ligands. The ligands in the [2 × 2] grid adopt bi-tridentate coordination modes through their central pyrazole rings. Each of the four Fe^{II} centers is coordinated to six nitrogen atoms from two neighboring ligands (two side-arm 1-methyl-1-*H*-imidazole N, two pyridine N, and two central pyrazolate N atoms). Four ClO_4^- or BF_4^- anions in both grid structures balance the charge of the $[Fe^{II}_4L_4]^{4+}$ species.

The four metal ions (Fe1, Fe2, Fe3, Fe4) in [2 × 2] $[Fe^{II}_4L^{Me\text{-}Im}_4]^{4+}$ cation of **6** are not perfectly coplanar (interior Fe-Fe-Fe angles 80°, 99°, 82° and 98° and the four ligands divide into two sets, with one pair situated above and the other below the Fe^{II}_4 mean plane as shown in Figure 4.1. Inspection of the Fe–N bond lengths helps

distinguishing between HS Fe^{II} and LS Fe^{II}.[138] The average bond lengths *d*(Fe–N) for the four Fe^{II} ions are 1.95 Å (Fe1–N), 2.17 Å (Fe2–N), 1.98 Å (Fe3–N) and 2.18 Å (Fe4–N), which therefore can infer that Fe1 and Fe3 are in the LS state and Fe2 and Fe4 were in HS state ions.

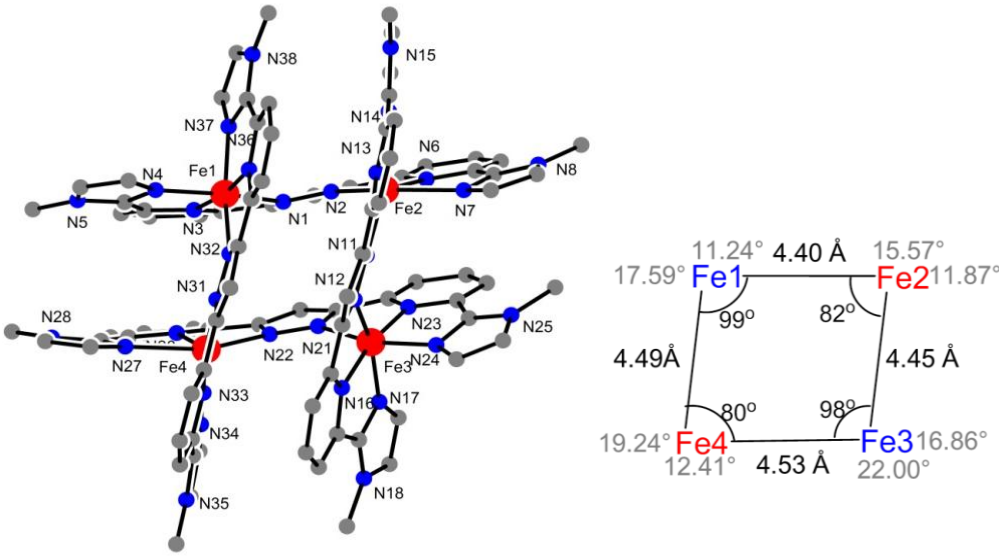

Figure 4.1. Molecular structure of the cation $[Fe^{II}_4L^{Me\text{-}Im}_4]^{4+}$ of the [2 × 2] grid complex **6** (hydrogen atoms are not included for simplicity) (left); Fe···Fe distances, Fe-Fe-Fe angles (black) and torsion of the central pyrazole against side-arm methylimidazole in same ligand (gray) (right, HS-Fe^{II} (red); LS-Fe^{II} (blue)).

As a result, pairs of metal atoms of the same spin state are located at diagonally opposing corners of the rectangular complex. The adjacent Fe^{II}···Fe^{II} distance range from 4.40 Å to 4.53 Å, and diagonal Fe^{II} ions are separated by 5.81 Å (Fe1···Fe3) and 6.78 Å (Fe2···Fe4) (Figure 4.2). The geometry around the Fe^{II} ions is distorted octahedral and the distortion of the {FeN_6} coordination polyhedron from idealized octahedral (O_h) or trigonal prismatic symmetry (D_{3h}) can be described accurately by using the CSM. The coordination polyhedron of Fe^{II} atoms in the HS state shows a higher distortion from a perfect octahedron (O_h) than the LS Fe^{II} ions. On the other hand the deviation from trigonal prism (tp) is more pronounced in the case of the LS Fe^{II} ions. The results of the CSM are summarized in Table 4.1. A remarkably high value for *S*(O_h) and low value *S*(itp) suggest that Fe2 and Fe4 centers are likely locked

in the HS Fe^{II} state and lack the ability of facile thermal switching to the LS state, while the low value for $S(O_h)$ (corresponding to a higher S(itp)) confirms the LS-Fe^{II} state of Fe1 and Fe3 centers, which clearly indicates the di-mixed-spin configuration [LS-HS-LS-HS] of grid complex **6**.

Table 4.1. Mean Fe−N Bond Lengths and Continuous Symmetry Measures (CSM) for $[Fe^{II}_4L^{Me\text{-}Im}_4](ClO_4)_4$ (**6**).

Complex		d_{mean}/A[a]	Spin state[a]	$S(O_h)$[b]	S(itp)[b]
$[Fe^{II}_4L^{Me\text{-}Im}_4](ClO_4)_4$	Fe^{II}1−N	1.95	LS	2.10	11.08
(**6**)	Fe^{II}2−N	2.18	HS	7.74	6.38
	Fe^{II}3−N	1.98	LS	2.68	10.84
	Fe^{II}4−N	2.18	HS	7.09	6.28

[a] At 133 K. [b] The smaller this value (0 – 100), the closer the polyhedron is to the ideal geometry.

The [2 × 2] $[Fe^{II}_4L^{Me\text{-}MeIm}_4](BF_4)_4$ **10** is crystallized by slow diffusion of Et_2O into MeCN solution and its structure is characterized by single crystal X-ray crystallography. Complex **10** has a similar [2 × 2] grid-type architecture to **6**, consisting of four ligands and four Fe^{II} ions and with four BF_4^- anions to counter balance the charge of the $[Fe^{II}_4L^{Me\text{-}MeIm}_4]^{4+}$ species. The adjacent $Fe^{II}\cdots Fe^{II}$ distances range from 4.29 Å to 4.38 Å, with diagonal Fe^{II} ions separated by 5.96 Å and 6.18 Å (Figure 4.2). The bond lengths of Fe-N in the complex **10** range from 2.08 Å to 2.23 Å, which is within the range of the HS Fe^{II}-N bond lengths reported in mononuclear SCO complexes.[139] The values of $S(O_h)$ and S(itp) in Table 4.2 suggest that all four Fe^{II} ions are therefore somewhere between octahedral and itp.

Table 4.2. Mean Fe−N Bond Lengths and Continuous Symmetry Measures (CSM) for $[Fe^{II}_4L^{Me\text{-}MeIm}_4](BF_4)_4$ (**10**).

Complex		d_{mean}/A[a]	Spin state[a]	$S(O_h)$[b]	S(itp)[b]
$[Fe^{II}_4L^{Me\text{-}MeIm}_4](BF_4)_4$	Fe^{II}1−N	2.14	HS	6.47	7.43
(**10**)	Fe^{II}2−N	2.17	HS	7.00	7.03
	Fe^{II}3−N	2.16	HS	6.91	7.26
	Fe^{II}4−N	2.17	HS	7.96	6.68

[a]At 133 K. [b]The smaller this value (0−100), the closer the polyhedron is to the ideal geometry.

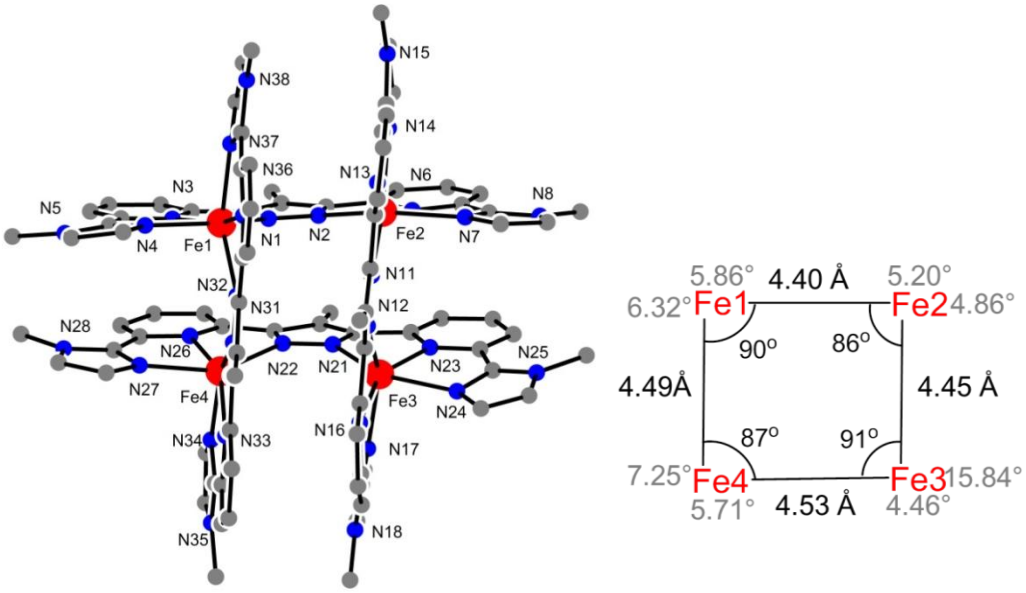

Figure 4.2. Molecular structure of the cation $[Fe^{II}_4L^{Me\text{-}MeIm}_4]^{4+}$ of the [2 × 2] grid complex **10** (hydrogen atoms are not included for simplicity) (left); Fe···Fe distances, Fe-Fe-Fe angles (black) and torsion of the central pyrazole against side-arm methylimidazole in same ligands (gray) (right, HS-Fe^{II} (red)).

Somewhat unexpectedly, however, complex **10** exhibits a different spin configuration and the two LS Fe^{II} ions in complex **6** change to HS Fe^{II} in structure **10**, due to different ligand field strengths resulting from the substituent methyl group in the 4-position of the central pyrazole ring. According to our recent report by B. Schneider,[109] the methyl substitution as an electron donating group at the 4-position of the pyrazole ring could increase the ligand field strength, which leads to LS Fe^{II}.[140] However, Fe^{II} ions in **10** prefer to be in the HS state, which is not agreement with the previous result. It is not clear at this time why there is a difference between the two systems.

Magnetic Properties

Magnetic susceptibility for a crystalline sample of complex **6** was measured at 0.5 T magnetic field in the temperature range of 2 – 220 K using a SQUID magnetometer. The SQUID measurement for compound **10** was not performed because only a small quantity of crystalline materials was obtained.

The $\chi_M T$ versus T of complex **6** shows the high temperature value of 8.42 $cm^3mol^{-1}K$ (Figure 4.3), which matches the predicted spin-only value for two S = 2.0 centers with g = 2.0, confirming the presence of two LS Fe^{II} ions (S = 0) and two uncorrelated HS Fe^{II} ions (S = 2.0) in [2 × 2] Fe^{II}_4 grid structure **6**. The $\chi_M T$ values decrease slightly with decreasing temperature to 8.28 $cm^3mol^{-1}K$ at 50 K, followed by a rapid decrease to 2.49 $cm^3mol^{-1}K$ at 2 K. This drop of $\chi_M T$ observed here is most likely due to zero-field splitting and any magnetic coupling between the diagonally opposed HS Fe^{II} spin carriers in the molecule is negligible (Figure 4.4).[141]

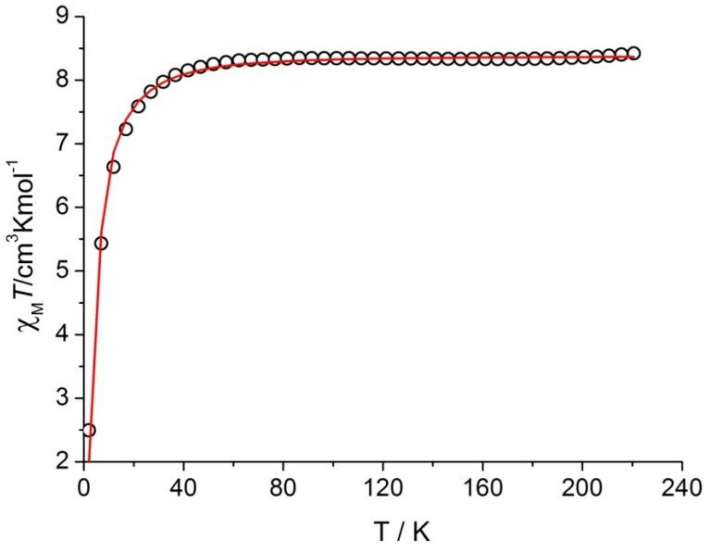

Figure 4.3. $\chi_M T$ vs. T measurement in the temperature range of 2 – 220 K at 0.5 T for crystalline sample of $[Fe^{II}_4L_4](ClO_4)_4$ (**6**). Solid lines correspond to the best fits within the spin-only formalism.

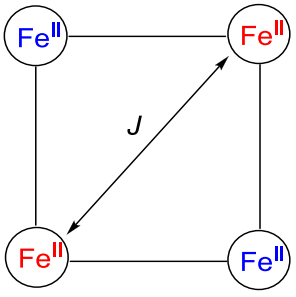

Figure 4.4. Magnetic Coupling Scheme for $[Fe^{II}_4L^{Me\text{-}Im}_4]^{4+}$ cation of **6** (HS-Fe^{II} (red), LS-Fe^{II} (blue)).

Experiment data in the range of temperatures measured were well simulated assuming two uncoupled S = 2 centers (J = 0), with an axial zero field splitting parameter $|D|$ = 11.9 cm^{-1} and Zeeman splitting g = 2.36, by using the appropriate spin Hamiltonian

given in eq. 1.[142]

$$\hat{H} = \sum_{i=1}^{2}\left(D(\hat{S}_{zi}^{2} - \frac{1}{3}S_i(S_i+1)) + g\mu_B\vec{B}\cdot\vec{S}_i \right) \qquad \text{(eq. 1)}$$

It is well known that the nature of SCO transitions is related not only to the energy of different spin states but also to supramolecular structures.[143] As Figure 4.1 shows, in $[Fe^{II}{}_4L^{Me\text{-}Im}{}_4](ClO_4)_4$ (**6**) the average angles between the planes of the central pyrazolates and side-arm methylimidazole rings are 13.7°, 15.83° (at HS $Fe^{II}2$ and HS $Fe^{II}4$ sites) and 14.1°, 19.4° (at LS $Fe^{II}1$ and LS $Fe^{II}3$ sites), which reflects much greater ligand distortion. Due to the flexibility of pyrazolate-bridged ligands reported here to interlock the metal centers, there is increased strain across the entire grid structure caused by ligand distortion away from planarity, resulting in a coordination sphere of the iron centers which is strongly distorted from ideal octahedral geometry confirmed by the $S(O_h)$ and S(itp) values in Table 4.1. The increased strain across the whole grid structure can suppress the spin transition.[143] Therefore the HS Fe^{II} ions in both grid structures have a strong tendency to remain in that spin state,[144,145] even throughout the range of temperature.

Mössbauer Spectroscopy

The specific spin states seen in the Fe^{II} ions in the grid complex $[Fe^{II}{}_4L^{Me\text{-}Im}{}_4](ClO_4)_4$ (**6**) were confirmed further by Mössbauer spectroscopy, while there is no Mössbauer spectra for **10** due to difficulty to collect crystalline material. The ^{57}Fe Mössbauer spectrum of **6** was recorded at 80 K (Figure 4.5), which shows two different signals: one quadrupole doublet with an isomer shift of δ = 1.10 mm/s and large quadrupole splitting of ΔE_Q = 2.74 mm/s (red subspectrum), that is, parameters that compare with those reported in chapter 3 for S = 2, HS Fe^{II} ions of complexes **1** – **4** and another quadrupole doublet with an isomer shift of δ = 0.42 mm/s and smaller quadrupole splitting of ΔE_Q = 0.54 mm/s (blue subspectrum), confirming the presence of two LS Fe^{II} ions in structure **6**. The two different quadrupole doublets are presented in a ratio of 1:1, as expected for two types of Fe^{II} ions. This result agrees with structural

analysis and magnetic susceptibility measurements and further confirms the presence of the [(2LS-Fe^{II})(2HS-Fe^{II})] mixed-spin state configuration of the four iron centers in [2 × 2] Fe^{II}_4 grid structure.

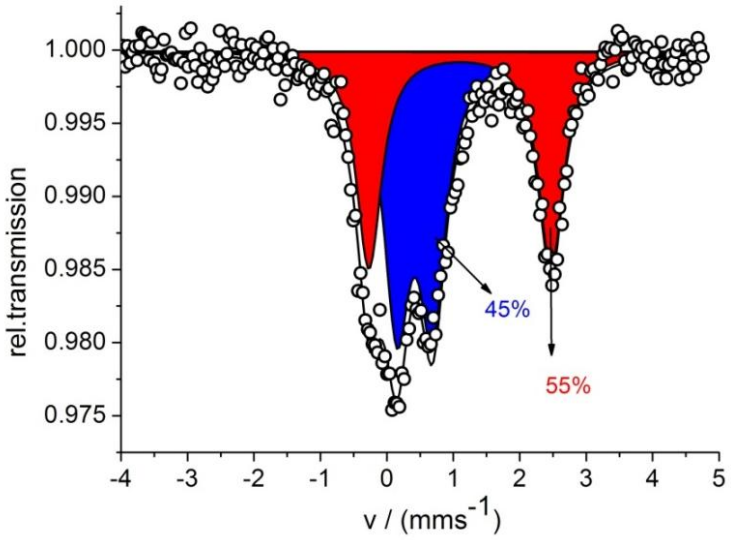

Figure 4.5. Zero-field ^{57}Fe Mössbauer spectrum for solid $[Fe^{II}_4L^{Me\text{-}Im}_4](ClO_4)_4$ (**6**) at 80K. Lines represent simulations with Lorentzian doublets for HS Fe^{II} (red doublet) and LS Fe^{II} (blue doublet).

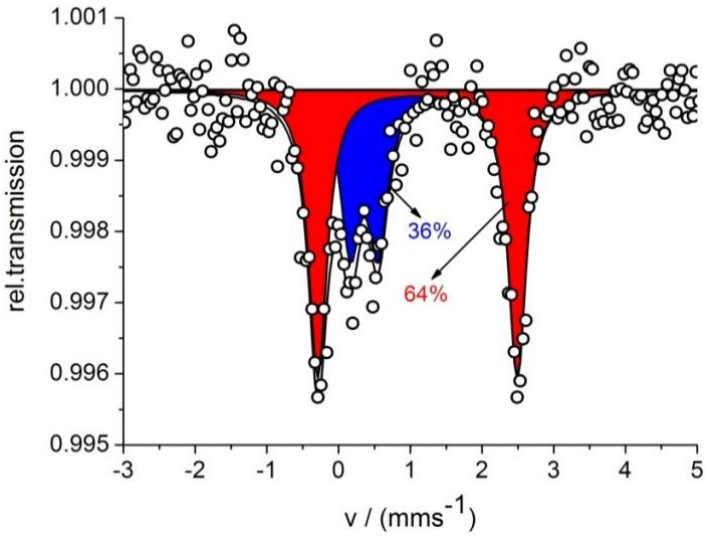

Figure 4.6. Zero-field ^{57}Fe Mössbauer spectrum for solution $[Fe^{II}_4L^{Me\text{-}Im}_4](ClO_4)_4$ (**6**) at 80K in CH_3CN. Lines represent simulations with Lorentzian doublets for HS-Fe^{II} (red doublet) and LS-Fe^{II} (blue doublet).

Additionally, a Mössbauer spectrum of frozen MeCN solution of $[Fe^{II}_4L^{Me\text{-}Im}_4](ClO_4)_4$ (**6**) was recorded at 80 K as well. The spectrum, depicted in Figure 4.6, displays a

similar characteristic subspectrum for LS Fe^{II} (δ = 0.36 mm/s and ΔE_Q = 0.39 mm/s, blue) and HS Fe^{II} (δ = 1.10 mm/s and ΔE_Q = 2.78 mm/s, red) to those found in the Mössbauer spectrum of the solid sample. However, the ratio of HS to LS is 0.64/0.36 in solution sample in frozen CH_3CN solution. Whereas it is 0.55/0.45 in the solid sample. The higher percent of HS iron ions suggests a mixture with spin configuration [3HS-LS] and [2HS-2LS] for grid $[Fe^{II}_4L^{Me\text{-}Im}_4]^{4+}$.

It is well documented that the spin states of Fe^{II} ions are different for solution samples using donor solvents such as MeCN and DMF,[146] which is usually due to hydrogen bonding between the solvent molecules and the ligands or to different dissociation equilibria.[146] For **6**, we assume that hydrogen bonding interactions between the solvent and C-H group of the ligands affect the spin state change from LS to HS. At the same time we also consider that perhaps the change of spin state results from a change of the solid structure in solution due to the motion of ClO_4^- cunterions. It is nuclear at this time why there is a higher retio of HS Fe^{II} ions in the frozen MeCN solution.

4.2.3. Solution State Investigations

Electrochemistry

Since the [2 × 2] grid complex $[Fe^{II}_4L^{Me\text{-}Im}_4](ClO_4)_4$ (**6**) possesses four redox-active Fe^{II} centers and four redox-active bridging ligands, the redox properties of **6** were investigated by means of CV and SWV in MeCN/0.1M NBu_4PF_6 at room temperature.

The CV of complex **6** displays pairs of quasi-revisible redox steps in the potential range from –2.5 V to 1.4 V vs Fc/Fc^+ (Figure 4.7). SWV spectroscopy confirms that all redox waves are one-electron processes (Figure 4.8), four of which are reduction steps at $E_{1/2}$ = –170 V, –1.85 V, –2.06 V and –2.20 V. The assignment of these reduction steps could not be performed and further work is in progress.

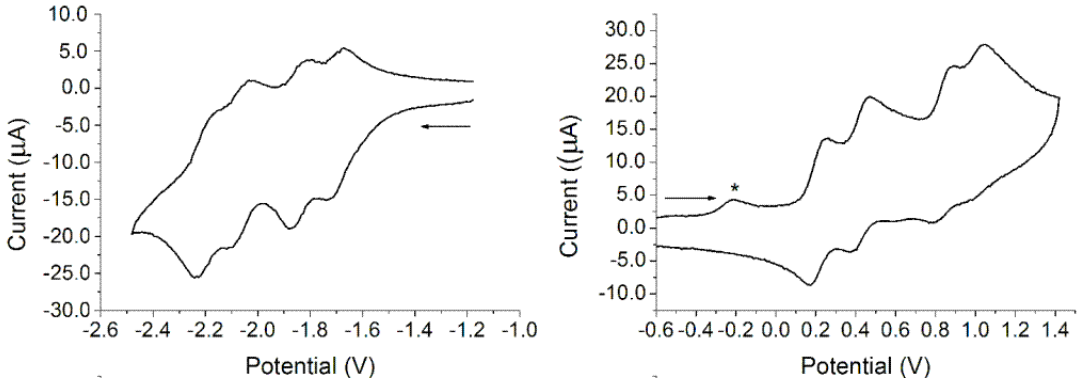

Figure 4.7. Cyclic Voltammogram curves of $[Fe^{II}_4L^{Me\text{-}Im}_4](ClO_4)_4$ (**6**) in MeCN/0.1 M Nbu_4PF_6 as an electrolyte at scan rates of 100 $mV{\cdot}s^{-1}$ vs. Fc/Fc^+ in the –2.5 V – 1.1 V and –0.6 V – 1.4 V potential range (the asterisk results from the inpurity).

The remaining four electrochemically reversible redox processes with half wave potentials $E_{1/2}$ = +0.23 V, +0.45 V, +0.87 V and +1.04 V in the potential range from 0.0 V to +1.4 V vs. Fc/Fc^+, correspond to the stepwise mono-electron Fe^{II}/Fe^{III} couples: $[Fe^{II}_4L_4]^{4+}$ ⇄ $[Fe^{II}_3Fe^{III}L_4]^{5+}$ ⇄ $[Fe^{II}_2Fe^{III}_2L_4]^{6+}$ ⇄ $[Fe^{II}Fe^{III}_3L_4]^{7+}$ ⇄ $[Fe^{III}_4L_4]^{8+}$,[147] finally leading to oxidation of the all ferrous grid to all-ferric $[Fe^{III}_4L_4]^{8+}$ (Table 4.3).

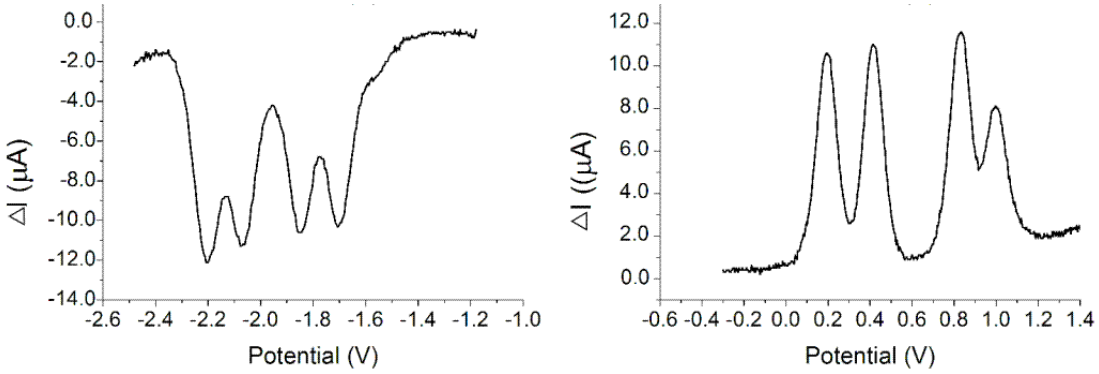

Figure 4.8. Square wave voltammogram curves of $[Fe^{II}_4L^{Me\text{-}Im}_4](ClO_4)_4$ (**6**) in MeCN/0.1 M NBu_4PF_6 as an electrolyte vs. Fc/Fc^+ in the –2.5 V – 1.1 V (left) and –0.3 – 1.4 V (right) potential range.

Following the first oxidation of one of the four identical centers, a second oxidation process is observed at a potential slightly more positive than the first one ($\Delta E_{1/2}$ = 220 mV). Because there is significant electronic interaction between metal centers connected to the same bridge in normal grid complexes,[148] it can be suggested that the second oxidation step involves the Fe^{II} center which is farthest away, in other

words, the one diagonal to the first oxidized center. The third oxidation process concerns one of the two other Fe^{II} centers. Its potential is significantly more positive than the second one ($\Delta E_{1/2}$ = 420 mV), which is a result of the presence of two nearby oxidized Fe^{III} ions. The fourth oxidation naturally involves the remaining Fe^{II} center. It is interesting to note that the separation of the third and fourth oxidation processes ($\Delta E_{1/2}$ = 170 mV) is different from the separation between the first two processes ($\Delta E_{1/2}$ = 220 mV).

Table 4.3. Electrochemical Parameters versus Fc/Fc^+ for $[Fe^{II}_4L^{Me\text{-}Im}_4](ClO_4)_4$ (**6**) obtained from CV.

	$E_{1/2}$/mV	ΔE_p/mV[a]	$E_{1/2}^{n+1} - E_{1/2}^{n}$	Oxidized species (K_c)
1	230	87	220	$[Fe^{II}_3Fe^{III}L^{Me\text{-}Im}_4]^{5+}$ (5.37×10^3)
2	450	87	420	$[Fe^{II}_2Fe^{III}_2L^{Me\text{-}Im}_4]^{6+}$ (1.31×10^7)
3	870	94	170	$[Fe^{II}Fe^{III}_3L^{Me\text{-}Im}_4]^{7+}$ (7.59×10^2)
4	1040	97		$[Fe^{III}_4L^{Me\text{-}Im}_4]^{8+}$

[a] ΔE_p denotes the separation of the anodic and cathodic peak potentials for the individual redox events ($\Delta E_p \approx 85$ mV for the internal standard Fc).

Accordingly the differentiation into two pairs is readily explained by electrostatic interaction between neighboring corners of the grid. Such a difference suggests that the electronic interaction between two redox-active sites localized at opposite corners of a [2 × 2] Fe^{II}_4 grid is a function of the oxidation state of the other redox-active sites.

The frequently used term "coupling" used to describeg the metal-metal interaction in mixed-valence compounds, can have different meanings in the context of either electrochemical, spectroscopic, or magnetic measurements.[149] According to the CV measurements, the very existence of any mixed-valence "intermediate" state is quantified by the comproportionation constant K_c according to reaction (1) (see chapter 1.4). The values of K_c of $[Fe^{II}_3Fe^{III}L_4]^{5+}$, $[Fe^{II}_2Fe^{III}_2L_4]^{6+}$ and $[Fe^{II}Fe^{III}_3L_4]^{7+}$ were determined to be 5.37×10^3, 1.31×10^7 and 7.59×10^2, respectively, which reveals the mixed-valence species $[Fe^{II}_2Fe^{III}_2L_4]^{6+}$, consisting of two ferric ions at diagonally opposed positions of the rhombic arrangement and two ferrous ions as neighbors, has pronounced thermodynamic stability. The redox properties of **6** were

studied at different scan rates as shown in Figure 4.9. With increasing scan rate, there is no significant change in the oxidation waves.

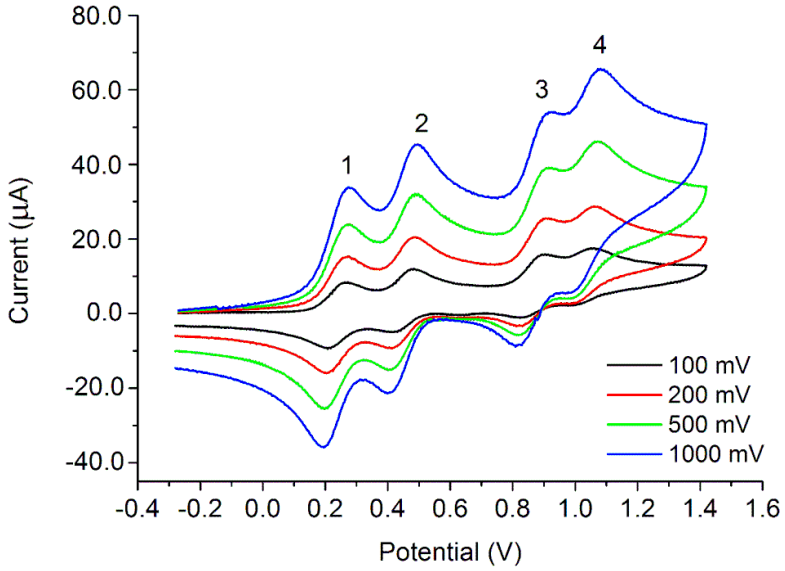

Figure 4.9. Cyclic voltammogram curves of $[Fe^{II}_4L^{Me\text{-}Im}_4](ClO_4)_4$ (**6**) in MeCN/0.1 M Nbu_4PF_6 as an electrolyte at varying scan rates of 100, 200, 500 and 1000 mV s^{-1} vs. Fc/Fc^+ in potential range of –0.3 V to 1.5 V.

4.3. Mixed-valence [2 × 2] Fe_4 Grid Complexes

The observance of four quasi-reversible oxidation steps at relatively low potential for complex $[Fe^{II}_4L^{Me\text{-}Im}_4](ClO_4)_4$ (**6**) prompted us to attempt to chemically isolate the one- and two-electron oxidized species $[Fe^{II}_3Fe^{III}]$ and $[Fe^{II}_2Fe^{III}_2]$, respectively. Gratifyingly we were able to isolate both $[Fe^{II}_3Fe^{III}L^{Me\text{-}Im}_4](ClO_4)_5$ (**7**) and $[Fe^{II}_2Fe^{III}_2L^{Me\text{-}Im}_4](ClO_4)_6$ (**8**) compounds after chemical oxidation of **6** with silver perchlorate in $MeNO_2$, which solubilizes **6**, ensuring the full oxidizing potency of the Ag/Ag^+ ion ($E_{1/2}$ = 0.67 V vs. Fc/Fc^+, see Experimental Section).[150] This is a surprising result considering the small difference in potential between the first and second oxidation processes (220 mV) for **6**. The oxidized species **7** and **8** were characterized by elemental analyses (see Experimental Section).

4.3.1. One-electron Oxidized [2 × 2] $Fe^{II}_3Fe^{III}$ Grid Complexes

4.3.1.1. Synthesis of One-electron Oxidized [2 × 2] $[Fe^{II}_3Fe^{III}L^{Me\text{-}Im}_4](ClO_4)_5$

Complexes

The once oxidized species [2 × 2] $[Fe^{II}_3Fe^{III}L^{Me\text{-}Im}_4](ClO_4)_5$ (**7**) was synthesized by mixing the starting material **6** and excess $AgClO_4$ in $MeNO_2$ at low temperature (0℃). The color of the reaction mixture changed from red to blue after stirring overnight. It was possible to obtain single crystal **7** from slow diffusion of Et_2O into the reaction solution, which was analyzed by X-ray crystallography. Compound **7** is air stable and crystallizes in the triclinic *P*−1 space group, with the general formula $[Fe^{II}_3Fe^{III}L^{Me\text{-}Im}_4](ClO_4)_5$. Although an excess of $AgClO_4$ as oxidant was used, only a single oxidation of the Fe^{II}_4 compound **7** was observed due to the reaction temperature, which is an important factor for the oxidation of Fe^{II} (see below).

4.3.1.2. Structural Characterization of One-electron Oxidized [2 × 2] $[Fe^{II}_3Fe^{III}L^{Me\text{-}Im}_4](ClO_4)_5$ Complexes

The complex cation consists of an approximately square array of one Fe^{III} and three Fe^{II} ions (average inner angles: Fe^{II}-Fe^{III}-Fe^{II} = 93°, Fe^{II}-Fe^{II}-Fe^{II} = 94°, Fe^{III}-Fe^{II}-Fe^{II} = 84° and 85°) (Figure 4.10).

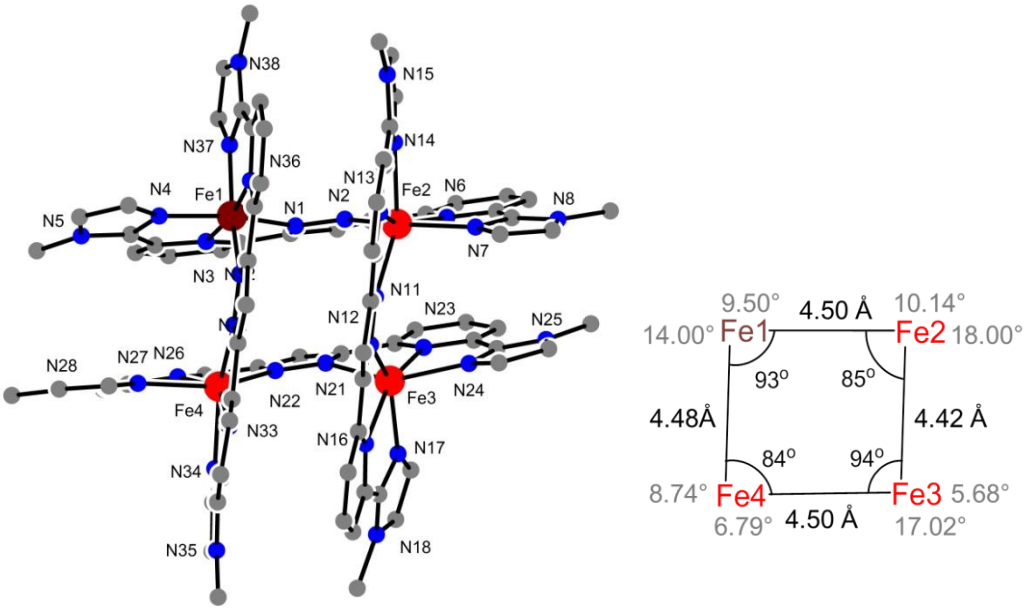

Figure 4.10. Molecular structure of the cation $[Fe^{II}_3Fe^{III}L^{Me\text{-}Im}_4]^{5+}$ of the [2 × 2] grid complex **7** (HS Fe^{II} (red), LS Fe^{III} (deep red), hydrogen atoms are not included for simplicity) (left); Fe···Fe distances,

Fe-Fe-Fe angles (black) and torsion of the central pyrazole against side-arm methylimidazole in same ligands (gray) (right).

Table 4.4. Mean Fe−N Bond Lengths and Continuous Symmetry Measures (CSM) and Bond Valence Sums (BVS) for $[Fe^{II}_3Fe^{III}L^{Me\text{-}Im}_4](ClO_4)_5$ (**7**).

Complex		d_{mean}/A[a]	Spin state[a]	(O_h)[b]	(itp)[b]	BVS[c]
$[Fe^{II}_3Fe^{III}L_4](ClO_4)_5$	Fe^{III}1−N	1.94	LS	2.04	10.74	3.80
(**7**)	Fe^{II}2−N	2.16	HS	7.18	6.89	2.07
	Fe^{II}3−N	2.19	HS	7.42	7.88	1.93
	Fe^{II}4−N	2.17	HS	7.33	6.20	2.05

[a] At 133 K. [b] The smaller this value (0−100), the closer the polyhedron is to the ideal geometry. [c] The BVS values are calculated based on a R_0 value of 1.77 Å for Fe^{II}−N and 1.82 Å for Fe^{III}−N with the formular $s_{ij} = \exp((R_0 - R_{ij})/b)$ with b = 0.37 Å. The larger BVS values correspond to R_0 = 1.82 Å. R_0 values taken from bv 2013.cif available from http://www.iucr.org/resources/data/datasets/nond-vvalence-parameters

The average Fe−N bond distances are 1.94 Å for Fe^{III}−N and 2.16 − 2.19 Å for Fe^{II}−N. The Fe^{II}−N bond lengths are significantly longer than Fe^{III}-N bonds, reflecting weaker coordinative interactions at the HS d^6 Fe^{II} ion compared with the LS d^5 Fe^{III} ion (Table 4.4). The CSM method in this case can also be used to characterize the HS and LS states of Fe^{II} ions and the bond value sums (BVS) can be used to confirm the oxidation state of the iron ions. The results suggest the spin configuration of **7** is [(LS-Fe^{III})(3HS-Fe^{II})].

Attempts to generate the once oxidized form of $[Fe^{II}_3Fe^{III}L^{Pz}_4](BF_4)_5$ (**5**) was also successful by using homo-valence compound $[Fe^{II}_4L^{Pz}_4](BF_4)_4$ (**1**) with thianthrenium tetrafluoroborate as oxidant in MeCN solvent, which allows **1** to be dissolved completely and ensures the full oxidizing potency of the [thianthrene]$^{\bullet+}$ ion ($E_{1/2}$ = 0.86 V vs. Fc/Fc^+).[150] Compound $[Fe^{II}_3Fe^{III}L^{Pz}_4](BF_4)_5$ (**5**) was crystallized from Et_2O/MeCN and its structure investigated by single X-ray crystallography. Similar to the structure of **7**, compound **5** possesses one Fe^{III} and three Fe^{II} ions (inner angles: Fe^{II}-Fe^{III}-Fe^{II} = 100°, Fe^{II}-Fe^{II}-Fe^{II} = 98°, Fe^{III}-Fe^{II}-Fe^{II} = 81°), each metal ion is coordinated in a distorted N_6 octahedral environment by two neighboring ligand fragments (Figure 4.11). The steric parameter of the Fe−N bond lengths and values

of $S(O_h)$, S(itp) and BVS are listed in Table 4.5, which suggests the spin configuration of $[Fe^{II}_3Fe^{III}L^{Pz}_4](BF_4)_5$ (**5**) as [(LS Fe^{III})(3HS Fe^{II})].

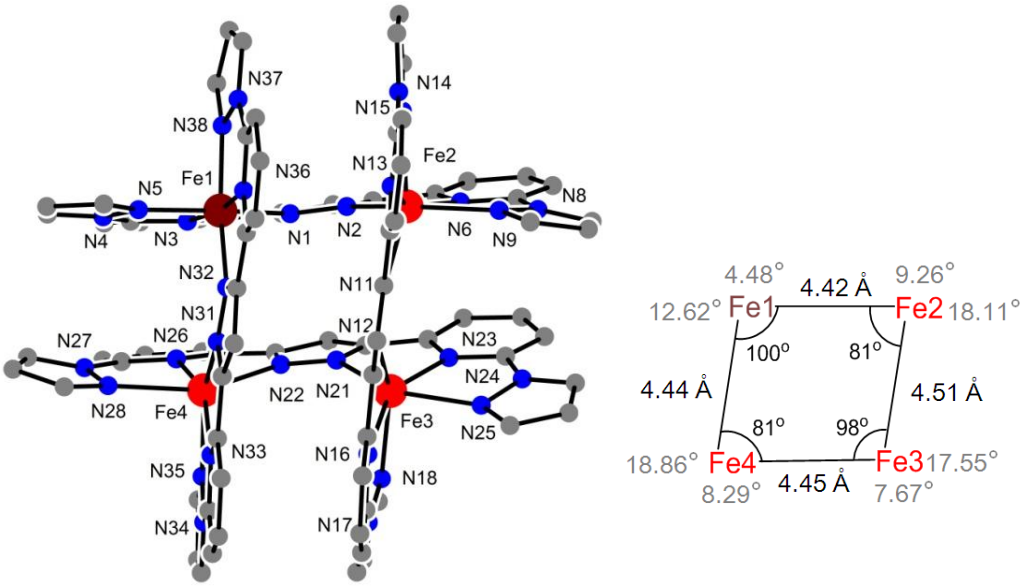

Figure 4.11. Molecular structure of the cation $[Fe^{II}_3Fe^{III}L^{Pz}_4]^{5+}$ of the [2 × 2] grid complex **5** (HS Fe^{II} (red), LS Fe^{III} (deep red), hydrogen atoms are not included for simplicity) (left); Fe···Fe distances, Fe-Fe-Fe angles (black) and torsion of the central pyrazole against side-arm methylimidazole in same ligands (gray) (right).

Table 4.5. Mean Fe−N Bond Lengths and Continuous Symmetry Measures (CSM) and Bond Value Sums (BVS) for $[Fe^{II}_3Fe^{III}L^{Pz}_4](BF_4)_5$ (**5**).

Complex		d_{mean}/A[a]	spin state[a]	(O_h)[b]	(itp)[b]	BVS[c]
$[Fe^{II}_3Fe^{III}L^{Pz}_4](BF_4)_5$	Fe^{III}1−N	1.94	LS	2.09	10.96	3.78
(**5**)	Fe^{II}2−N	2.18	HS	7.56	6.06	2.02
	Fe^{II}3−N	2.20	HS	7.67	7.70	1.87
	Fe^{II}4−N	2.17	HS	6.71	6.57	2.09

[a] At 133 K. [b] The smaller this value (0 – 100), the closer the polyhedron is to the ideal geometry. [c] The BVS values are calculated based on a R_0 value of 1.77 Å for Fe^{II}−N and 1.82 Å for Fe^{III}−N with the formular $s_{ij} = \exp((R_0 - R_{ij})/b)$ with b = 0.37 Å. The larger BVS values correspond to R_0 = 1.82 Å. R_0 values taken from bv 2013. Cif available from http://www.iucr.org/resources/data/datasets/nond-vvalence-parameters

4.3.2. Two-electron Oxidized [2 × 2] $Fe^{II}_2Fe^{III}_2$ Grid Complexes

The synthesis of twice oxidized species $[Fe^{II}_2Fe^{III}_2L^{Me\text{-}Im}_4](ClO_4)_6$ (**8**) is similar to the once oxidized compound **7**, except for the reaction temperature. In order to produce

the mixed-valence [2 × 2] $Fe^{II}_2Fe^{III}_2$ species, the reaction mixture should be heated to 50 °C for at least 2 hours in $MeNO_2$. The color of the solution changed from red to deep blue and the purified powder could be obtained by adding a large quantity of Et_2O into the solution.

4.3.2.1. Solid State Investigations

Structural Characterization

The crystals of mixed-valence [2 × 2] grid complex $[Fe^{II}_2Fe^{III}_2L^{Me\text{-}Im}_4](ClO_4)_6$ (**8**) were obtained by slow diffusion of Et_2O into MeOH solution and its structure was determined by single crystal X-ray diffraction. Compound **8** crystallizes in the monoclinic $P2_1/n$ space group and is composed of four ligands in the anticipated grid-type array of alternating Fe^{III} and Fe^{II} centers (inner angles: Fe^{II}-Fe^{III}-Fe^{II} = 102° and 103°, Fe^{III}-Fe^{II}-Fe^{III} = 78°) in an octahedral coordination geometry (Figure 4.12). This is similar to the mixed-valence $[Fe^{II}_2Fe^{III}_2L^{Py}_4](BF_4)_6$ grid with pyridine rings as side-arms of each ligand. Compounds 8 and $[Fe^{II}_2Fe^{III}_2L^{Py}_4](BF_4)_6$ display a different number of crystallographically independent iron ions.[108]

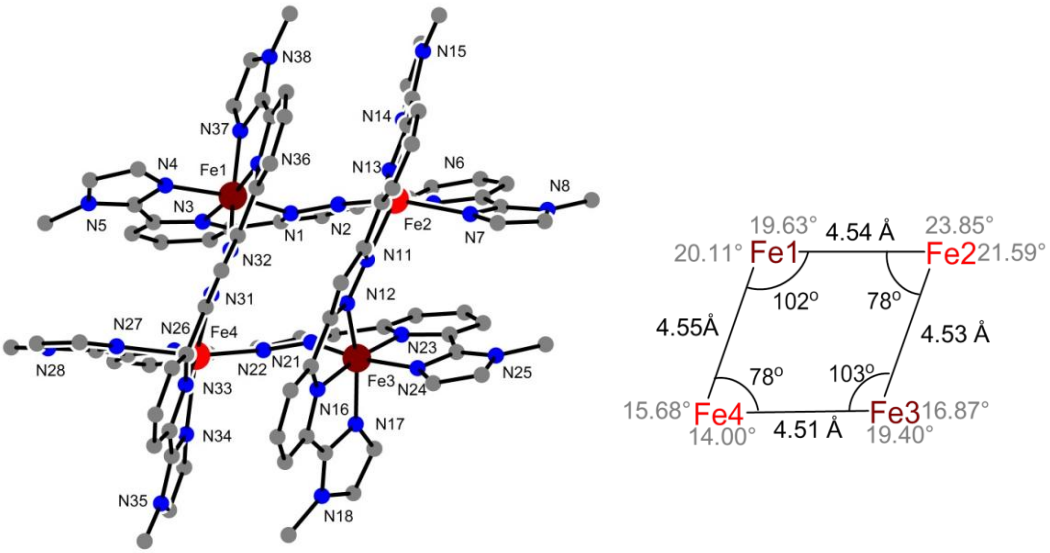

Figure 4.12. Molecular structure of the cation $[Fe^{II}_2Fe^{III}_2{}^{Me\text{-}Im}_4]^{6+}$ of the [2 × 2] grid complex **8** (HS Fe^{II} (red), LS Fe^{III} (deep red), hydrogen atoms are not included for simplicity) (left); Fe···Fe distances, Fe-Fe-Fe angles (black) and torsion of the central pyrazole against side-arm methylimidazole in same ligands (gray) (right).

Table 4.6. Mean Fe−N Bond Lengths and Continuous Symmetry Measures (CSM) and Bond Value Sums (BVS) for $[Fe^{II}_2Fe^{III}_2L^{Me\text{-}Im}_4](ClO_4)_6$ (**8**).

Complex		d_{mean}/A[a]	spin state[a]	$S(O_h)$[b]	S(itp)[b]	BVS[c]
$[Fe^{II}_2Fe^{III}_2L^{Me\text{-}Im}_4](ClO_4)_6$	$Fe^{III}1$−N	1.94	LS	1.90	12.08	3.76
(**8**)	$Fe^{II}2$−N	2.18	HS	8.42	4.78	1.99
	$Fe^{III}3$−N	1.95	LS	2.06	11.80	3.72
	$Fe^{II}4$−N	2.17	HS	7.36	6.07	2.02

[a] At 133 K. [b] The smaller this value (0 – 100), the closer the polyhedron is to the ideal geometry. [c] The BVS values are calculated based on a R_0 value of 1.77 Å for Fe^{II}−N and 1.82 Å for Fe^{III}−N with the formular $s_{ij} = \exp((R_0 - R_{ij})/b)$ with b = 0.37 Å. The larger BVS values correspond to R_0 = 1.82 Å. R_0 values taken from bv 2013. Cif available from http://www.iucr.org/resources/data/datasets/nond-vvalence-parameters

In complex **8**, there are four different crystallographically independent iron ions ($Fe^{III}1$, $Fe^{II}2$, $Fe^{III}3$ and $Fe^{II}4$), which results in slightly different Fe···Fe and Fe−N distances. The adjacent Fe^{III}···Fe^{II} distances range from 4.51 Å to 4.55 Å, and diagonal Fe ions are separated by 5.69 Å (Fe^{III}···Fe^{III}) and 7.05 Å (Fe^{II}···Fe^{II}). The Fe−N bond lengths of Fe1 and Fe3 range from 1.91 Å to 1.96 Å, which is within the range of the LS Fe^{III}−N bond lengths, and the Fe−N bond lengths of Fe2 and Fe4 range from 2.12 Å to 2.22 Å, which is within the range of the HS Fe^{II}−N bond lengths. As listed in Table 4.6, the average Fe−N bond distances, Bond Valence Sum (BVS) values and the different structural distortion parameters further confirm the spin and oxidation state of the four iron ions. The spin configuration of [2 × 2] $[Fe^{II}_2Fe^{III}_2L^{Me\text{-}Im}_4](ClO_4)_6$ (**8**) is [(LS Fe^{III})(HS Fe^{II})(LS Fe^{III})(HS Fe^{II})].

Magnetic Properties

Magnetic susceptibility measurements were performed on a crystalline sample of $[Fe^{II}_2Fe^{III}_2L^{Me\text{-}Im}_4](ClO_4)_6$ (**8**) in the temperature range of 2 – 210 K at 0.5 T.

The $\chi_M T$ versus T plot of **8** (Figure 4.13) shows a high temperature value of 9.06 $cm^3mol^{-1}K$, which is slightly larger than the spin only value of two Fe^{III} in the LS state (S = 1/2), 1.0 $cm^3mol^{-1}K$ (g = 2.0) and two Fe^{II} in the HS state (S = 2), 6.6 – 7.6 $cm^3mol^{-1}K$ (g = 2.0). $\chi_M T$ values increase gradually with decreasing temperature until reaching a maximum value of 16.32 $cm^3mol^{-1}K$ at 7 K, before dropping to 10.85

$cm^3mol^{-1}K$ at 2 K. The magnetic behavior is a result of the competitive effect of ferromagnetic coupling as well as spin-orbital interactions of the metal ions in **8**.

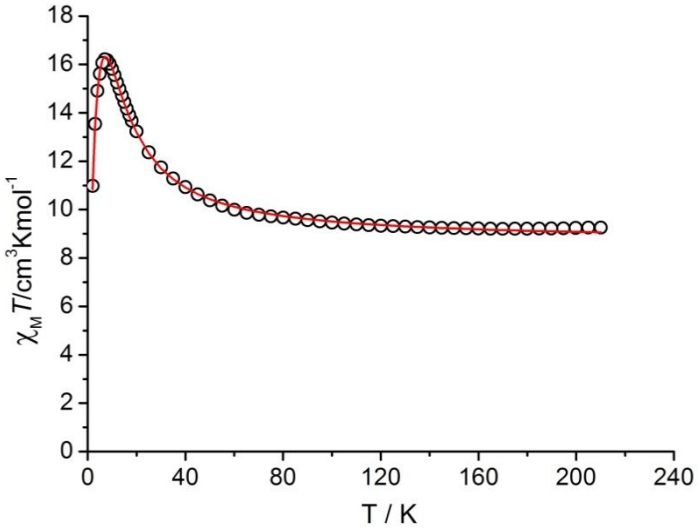

Figure 4.13. $\chi_M T$ vs. T measurement in the temperature range of 2 – 210 K at 0.5 T for crystalline samples of complex $[Fe^{II}_2Fe^{III}_2L^{Me\text{-}Im}_4](ClO_4)_6$ (**8**).

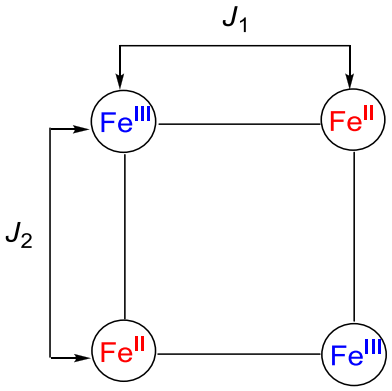

Figure 4.14. Magnetic coupling schemes for two independent coupling constants.

Considering the molecular structure of **8**, four interaction pathways exist in this case (Figure 4.14). The experimental data was simulated by using a Heisenberg-Dirac-van-Vleck Hamiltonian (*HDvV*) spin Hamiltonian that includes terms for Zeeman and zero-field splitting (eq. 2).[142]

$$\hat{H} = -2J_1(\hat{S}_1\hat{S}_2 + \hat{S}_3\hat{S}_4) - 2J_2(\hat{S}_2\hat{S}_3 + \hat{S}_1\hat{S}_4) + \sum_{i=1}^{4}\left(\hat{D}_i(\hat{S}_{zi} - \frac{1}{3}\hat{S}_i(\hat{S}_i + 1)) + g\mu_B\vec{B}\cdot\vec{S}_i\right) \qquad \text{(eq. 2)}$$

Where J is the exchange coupling constant between neighboring spins and g is the Land g factors of the Fe^{II} and Fe^{III} ions, and D is the zero-field splitting parameter. The best fit was obtained by assuming coupling parameter $|D| = 4.01$ cm^{-1} and $g_1 = 2.00$, $g_2 = 2.28$, and two subunits [(HS Fe^{II})(LS Fe^{III})] with relatively strong intrasubunit ferromagnetic coupling ($J_1 = +4.98$ cm^{-1}) and much weaker inter-subunit coupling ($J_2 = +3.05$ cm^{-1}) (Figure 4.14).

Mössbauer Spectroscopy

The specific spin states seen in the Fe^{II} and Fe^{III} centers in the mixed-valence grid **8** have also been confirmed by Mössbauer spectroscopy. A ^{57}Fe Mössbauer spectrum of **8** was recorded at 80 K (Figure 4.15).

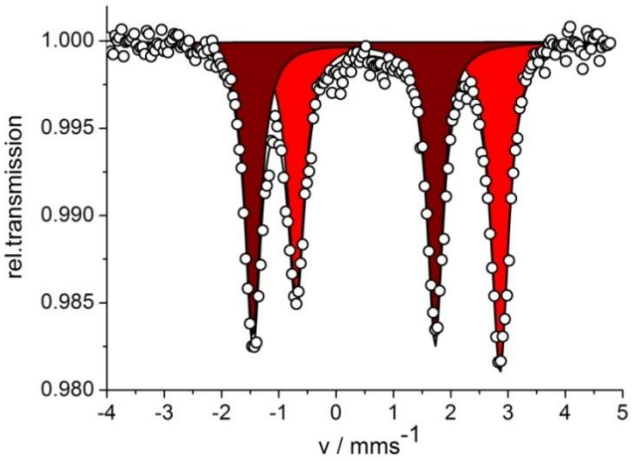

Figure 4.15. Zero-field ^{57}Fe Mössbauer spectra for solid $[Fe^{II}_2Fe^{III}_2L^{Me\text{-}Im}_4](ClO_4)_6$ (**8**) at 80K. Lines represent simulations with Lorentzian doublets for HS Fe^{II} (red doublet) and LS Fe^{III} (deep red doublet).

The spectrum exhibited two doublet peaks corresponding to HS Fe^{II} and LS Fe^{III} species, with a peak intensity ratio of HS Fe^{II}/LS Fe^{III} = 0.52/0.48. The isomer shift (δ) of 1.08 mm/s and quadrupole splitting (ΔE_Q) of 3.55 mm/s are attributed to a HS Fe^{II} species (red subspectrum) according to the parameters, whilst the corresponding parameters of another signal with the isomer shift (δ) of 0.14 mm/s and the quadrupole splitting (ΔE_Q) of 3.18 mm/s (deep red subspectrum), are comparble with the data of compound **6** and those of [$Fe^{III}N_6$] analogues in the $S = 1/2$ state ($\delta = 0.03$

– 0.19 and ΔE_Q = 2.72 – 3.49)[127] This provides evidence that the two HS Fe^{II} ions remain, while the LS Fe^{II} ions are oxidized to LS Fe^{III}. The Mössbauer spectrum of **8** confirmed the presence of two LS Fe^{III} ions and two HS Fe^{II} ions in the mixed-valence grid structure; this is a result which is consistent with the information obtained from structural analysis and SQUID measurements.

4.3.2.2. Solution State Investigations

Mass Spectrometry

Complexes **6** and **8** have been characterized by ESI mass spectrometry in MeCN solution. The ESI mass spectrometry of **6** shows three prominent peaks characteristic for the different charged ions, deriving from $[Fe^{II}_4L^{Me\text{-}Im}_4]^{4+}$ in combination with different counter ions ClO_4^- (m/z = 437.1 for $[Fe^{II}_4L_4]^{4+}$, 616.1 for $[Fe^{II}_4L_4](ClO_4)^{3+}$, 974.2 for $[Fe^{II}_4L_4(ClO_4)_2]^{2+}$) (Figure 4.16). ESI-MS results unequivocally confirm the [2 × 2] Fe^{II}_4 grid species in solution, and furthermore suggest the high stability of grid-type structure in solution.

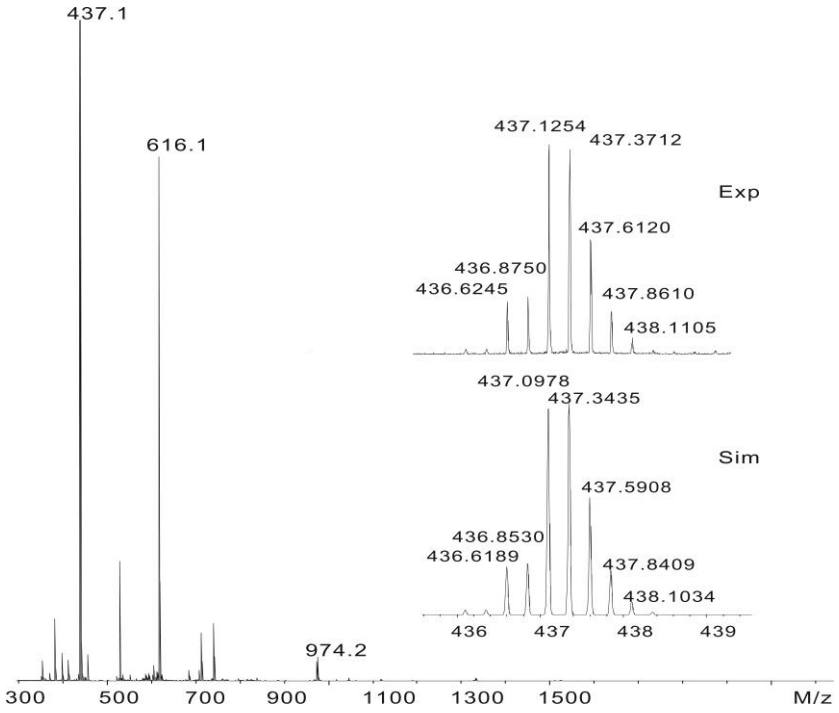

Figure 4.16. ESI-MS (MeCN) of $[Fe^{II}_4L^{Me\text{-}Im}_4](ClO_4)_4$ (**6**); (inset) experimental (upper) and simulated (lower) isotopic distribution pattern for the peak pattern around m/z = 437.1 characteristic for the $[Fe^{II}_4L^{Me\text{-}Im}_4]^{4+}$ ion.

However, the molecule $[Fe^{II}_2Fe^{III}_2L^{Me\text{-}Im}_4](ClO_4)_6$ (**8**) exihibits peaks at m/z = 349.9 $[Fe^{II}_3Fe^{III}L^{Me\text{-}Im}_4]^{5+}$, 649.4 $[Fe^{II}_3Fe^{III}L^{Me\text{-}Im}_4(ClO_4)_2]^{3+}$ and 1023.6 $[Fe^{II}_3Fe^{III}L^{Me\text{-}Im}_4(ClO_4)_3]^{2+}$ (Figure 4.17). These $[Fe^{II}_3Fe^{III}]$ species presumably arise from the reduction of the $[Fe^{II}_2Fe^{III}_2]$ in the process of undergoing ESI-MS, as a similar phenomenon has been reported in our previous work.[108] In addition, the main peak of the spectrum of $[Fe^{II}_4L^{Me\text{-}Im}_4](ClO_4)_4$ (**6**) is also observed here (m/z = 437) and there is one small fragments observed at m/z = 486.2 ($[Fe_2L_2]^{2+}$).

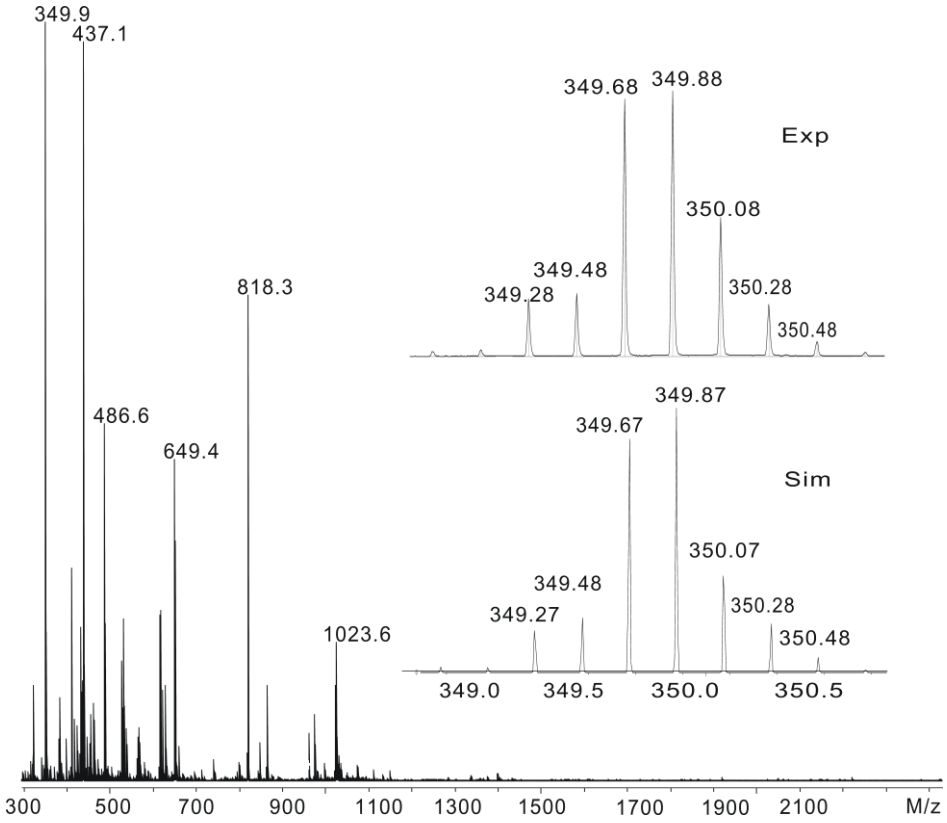

Figure 4.17. ESI-MS (MeCN) of $[Fe^{II}_2Fe^{III}_2L^{Me\text{-}Im}_4](ClO_4)_6$ (**8**); (inset) experimental (upper) and simulated (lower) isotopic distribution pattern for the peak pattern around m/z = 349.9.1 characteristic for the $[Fe^{II}_3Fe^{III}L^{Me\text{-}Im}_4]^{5+}$ ion.

NMR Spectroscopy

As discussed in chapter 3, in the cases of iron complexes the spin state could be generally assessed by measurement of the molecular magnetic moment *via* paramagnetic NMR spectroscopy. Difficult interpreting these spectra makes peak assignments difficult. In the mixed-spin and mixed-valence state complexes **6** and **8**, there are three kinds of iron ions involved (HS Fe^{II}, LS Fe^{II} and LS Fe^{III}). The

electron configurations of HS Fe^{II} and LS Fe^{III} ions have 4 or 1 unpaired electrons, respectively, confirming to the paramagnetic properties of these iron ions. LS Fe^{II} ion has no unpaired electrons and is diamagnetic behavior. The magnetic features of **6** and **8** were investigated in solution by using ^{1}H NMR spectroscopy.

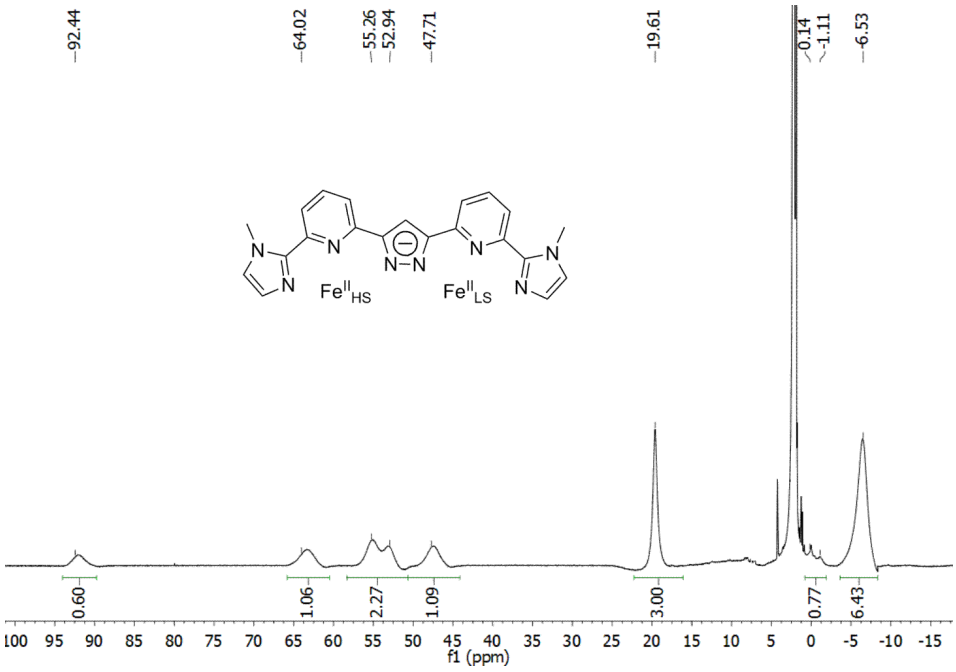

Figure 4.18. ^{1}H NMR spectrum (500 MHz, CD_3CN, 348 K) of $[Fe^{II}_4L^{Me\text{-}Im}_4](ClO_4)_4$ (**6**).

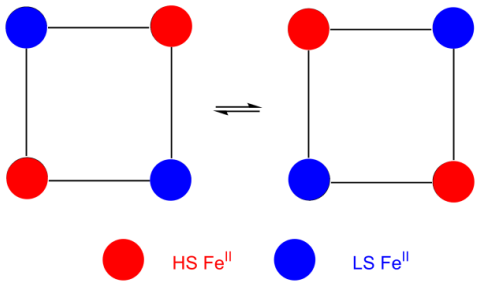

For homo-valence and mixed-spin state [2 × 2] Fe^{II}_4 grid structure **6**, there should be two sets of signals observed in the ^{1}H NMR spectrum due to the paramagnetic HS Fe^{II} and diamagnetic LS Fe^{II} ions.[151] However, unexpectedly, the 500 MHz ^{1}H NMR spectrum of a CD_3CN solution of **6** exhibits several broad and paramagnetically shifted signals in the range of −10 to 95 ppm, which arise from protons close to the paramagnetic Fe^{II} center, and there are no signals found in the region of 0 to 10 ppm (Figure 4.18), likely due to the fast exchange between the HS Fe^{II} and LS Fe^{II} centers on the NMR time scale. The chemical shifts of spectrum expand to larger region

upon cooling to 238 K, leading to broad and paramagnetically shifted proton resonances which are difficult to be detected (Figure 10.46). It is not clear at this time why there is a exchange between the two iron centers.

In contrast, the mixed-valence and mixed-spin state complex $[Fe^{II}_2Fe^{III}_2L^{Me\text{-}Im}_4](ClO_4)_6$ (**8**) contains four paramagnetic iron centers (HS Fe^{II} and LS Fe^{III}) and therefore displays a paramagnetic ^{1}H NMR spectrum with chemical shifts between 0 – 70 ppm (Figure 4.19). The 500 MHz ^{1}H NMR spectrum of a CD_3CN solution of **8** exhibits eight broadened and two sharp signals at 11.50 ppm, 16.53 ppm, 19.59 ppm, 30.38 ppm, 34.49 ppm, 40.79 ppm, 42.84 ppm, 47.57 ppm, 53.77 ppm and 67.19 ppm with integral intensities 3:3:1:1:2:1:2:1:2:1. The signals at δ = 11.50 ppm and 16.53 ppm can be assigned to methyl group protons on the basis of the integral. Other broad signals are not able to be assigned because no cross peaks were observed from the homonuclear ^{1}H-^{1}H COSY spectrum.

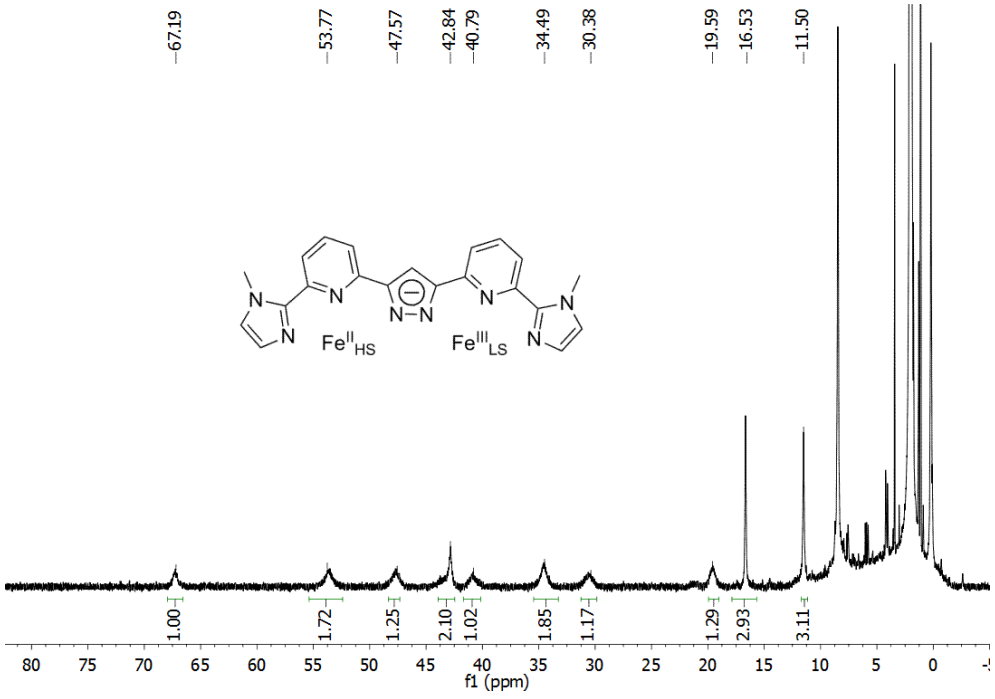

Figure 4.19. ^{1}H NMR spectrum (500 MHz, 333 K) of $[Fe^{II}_2Fe^{III}_2L^{Me\text{-}Im}_4](ClO_4)_6$ (**8**) in CD_3CN.

UV/Vis/NIR Spectroscopy

Investigation of the spectroscopic properties of complexes **6** and **8** was carried out in MeCN solutions at different concentrations in the range of 200 – 1400 nm (Figures

4.20 and 4.21).

For complex **6** there are five bands observed in the UV/Vis/NIR spectrum (Figure 4.21, left). The two intense bands on display in the high-energy range below 400 nm at λ_{max} = 269 nm and 335 nm are assigned to $\pi \rightarrow \pi^*$ transitions on the ligand. The bands in the visible range and beyond, at 498 nm (ε = 8018 L mol^{-1} cm^{-1}), 543 nm (ε = 7545 L mol^{-1} cm^{-1}) and 670 nm (ε = 1635 L mol^{-1} cm^{-1}), are likely MLCT transitions involving Fe^{II} ions.

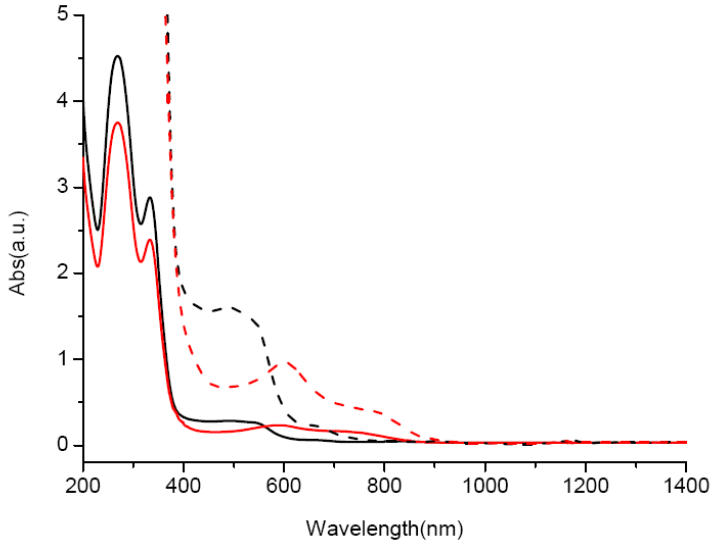

Figure 4.20. UV/Vis/NIR spectrum of $[Fe^{II}_4L^{Me\text{-}Im}_4](ClO_4)_4$ (**6**) (black) and $[Fe^{II}_2Fe^{III}_2L^{Me\text{-}Im}_4](ClO_4)_6$ (**8**) (red) in MeCN solution at two different concentrations (—$2 \cdot 10^{-5}$ M, ⋯ $2 \cdot 10^{-4}$ M).

The UV/Vis/NIR spectroscopy of **8** is similar to the spectrum of **6** (Figure 4.21, right). The position and intensity of bands, assigned to the $\pi \rightarrow \pi^*$ transitions, show no obvious change from the homo-valence $[Fe^{II}_4L^{Me\text{-}Im}_4]^{4+}$ to the mixed-valence $[Fe^{II}_2Fe^{III}_2L^{Me\text{-}Im}_4]^{6+}$. However, three new bands at 602 nm (ε = 4704 L mol^{-1} cm^{-1}), 720 nm (ε = 2258 L mol^{-1} cm^{-1}) and 792 nm (ε = 2021 L mol^{-1} cm^{-1}) are observed and have been tentatively assigned to LMCT transitions involving the Fe^{III} ions. Somewhat unexpectedly, however, no intervalence charge transfer (IVCT) band appears between hetero-valence iron ions, which could also be confirmed by spectroelectrochemistry (see below).

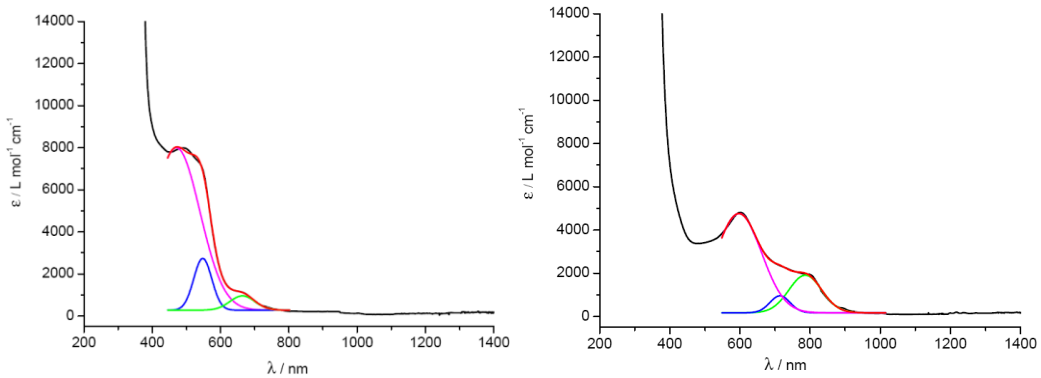

Figure 4.21. Deconvoluted vis bands with fitted Gauss curves for $[Fe^{II}_4L^{Me\text{-}Im}_4](ClO_4)_4$ (**6**) (left) and $[Fe^{II}_2Fe^{III}_2L^{Me\text{-}Im}_4](ClO_4)_6$ (**8**) (right).

Room temperature solid-state absorption spectroscopies of **6** and **8**, comparable with those obtained from solution samples, display the same absorption bands in the UV/Vis/NIR region (Figure 4.22), which confirms the species are unaltered in both solution and the solid state.

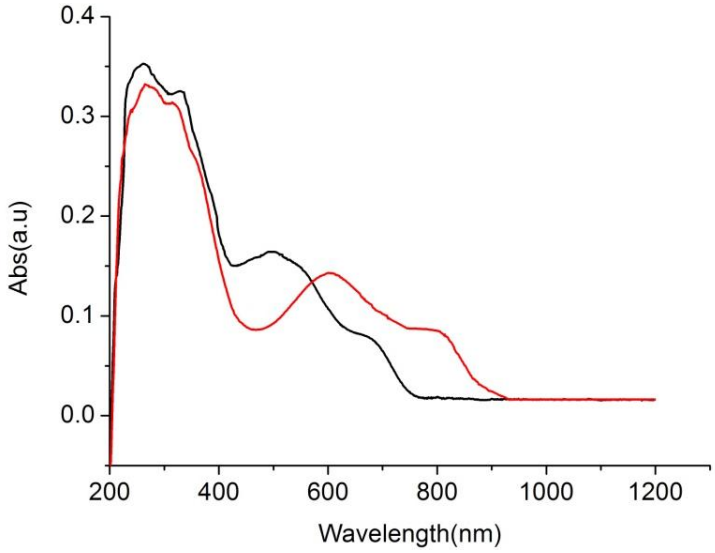

Figure 4.22. Solid-state absorption spectrum of $[Fe^{II}_4L^{Me\text{-}Im}_4](ClO_4)_4$ (**6**) (black) and $[Fe^{II}_2Fe^{III}_2L^{Me\text{-}Im}_4](ClO_4)_6$ (**8**) (red). Spectra were collected on solid samples compressed into KBr pellet and measured in transmission mode.

Spectroelectrochemistry

For further characterization of the oxidized species, the spectroscopic properties of $[Fe^{II}_4L^{Me\text{-}Im}_4](ClO_4)_4$ (**6**) were investigated during the time-resolved two-fold

electrochemical oxidation. As Figure 4.23 shows, we can observe the changes in the absorption spectrum of compound $[Fe^{II}_4L^{Me\text{-}Im}_4](ClO_4)_4$ (**6**) while potentials of 0.65 V and 1.10 V vs. Fc/Fc^+ are applied, which corresponds to a two- and four-electron oxidation. The oxidations of the first two ferrous irons from $[Fe^{II}_4L_4{}^{Me\text{-}Im}_4]^{4+}$ to mixed-valence $[Fe^{II}_2Fe^{III}_2L^{Me\text{-}Im}_4]^{6+}$ caused the Fe^{II} MLCT bands around 498 nm and 543 nm to weaken, while two new absorption bands appeared at about 602 nm and 792 nm. Meanwhile the band at 670 nm of $[Fe^{II}_4L^{Me\text{-}Im}_4]^{4+}$ increased in intensity accompanied by a shift to 720 nm during the double oxidations to $[Fe^{II}_2Fe^{III}_2L^{Me\text{-}Im}_4]^{6+}$. The bands at 602 nm, 720 and 792 nm are tentatively assigned to LMCT transitions involving the Fe^{III} ions. After the complete oxidation of the complex to the all ferric $[Fe^{III}_4L_4]^{8+}$, most bands do not show any significant changes, except for the growing intensity of the bands corresponding to Fe^{III}.

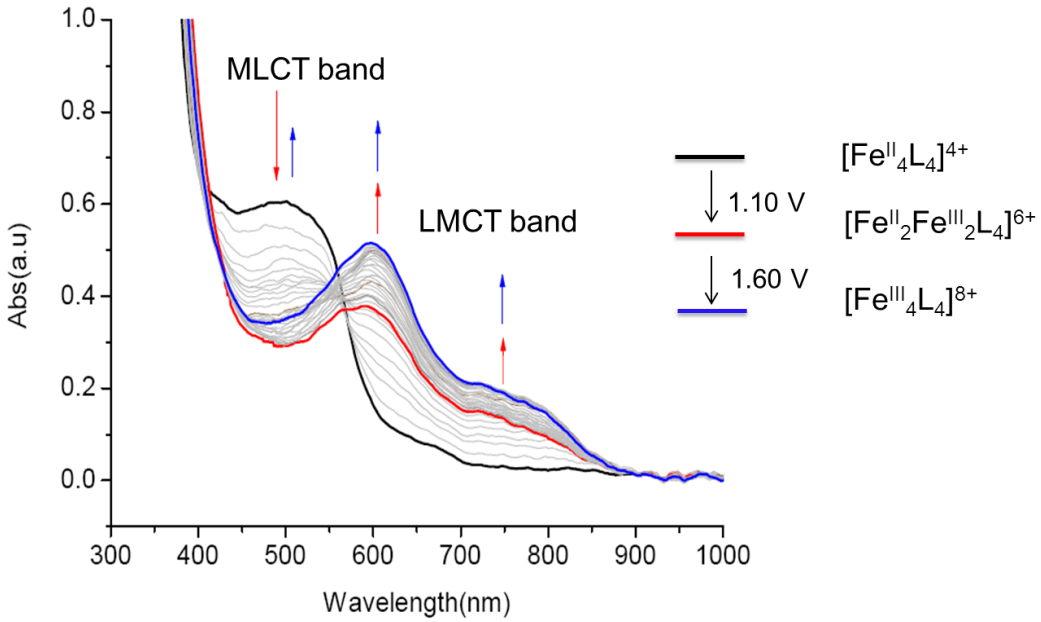

Figure 4.23. UV/Vis spectral changes of $[Fe^{II}_4L^{Me\text{-}Im}_4](ClO_4)_4$ (**6**) during the controlled potential oxidation in MeCN containing 0.1 M Bu_4NPF_6 on increasing the applied potential from 1.1 to 1.6 V (vs $Me_{10}Fc$).

4.4. Conclusion

Building upon our recent report of a robust pyrazolate-bridged Fe^{II}_4 [2 × 2] grid complex, we have now modified the pyrazolate-derived ligand scaffold to slightly

increase the ligand field strength. This has furnished a new Fe^{II}_4 [2 × 2] grid, $[Fe^{II}_4L^{Me\text{-}Im}_4](BF_4)_4$ (**6**), that has [2HS-2LS] spin configuration. The mixed-valence molecular squares $[Fe^{II}_3Fe^{III}L^{Me\text{-}Im}_4](BF_4)_5$ (**7**) and $[Fe^{II}_2Fe^{III}_2L^{Me\text{-}Im}_4](BF_4)_6$ (**8**), one or two extra mobile electrons (or holes) occupying the opposite corners, is observed as a pure phase after either one or twoe oxidations. The di-mixed-valent compound **8** displays remarkable stability for molecular expression of quantum cellular automata (QCA).

5. Hexanuclear Hetero-metallic [2 × 2] Grid and Trinuclear [2 × 2] Defect-grid Complexes

5.1. Hexanuclear Hetero-metallic [2 × 2] $Fe^{III}_2Ag^I_4$ Grid Complex

5.1.1. Synthesis of $[Fe^{III}_2Ag^I_4L^{Me\text{-}Im}_4](ClO_4)_6$

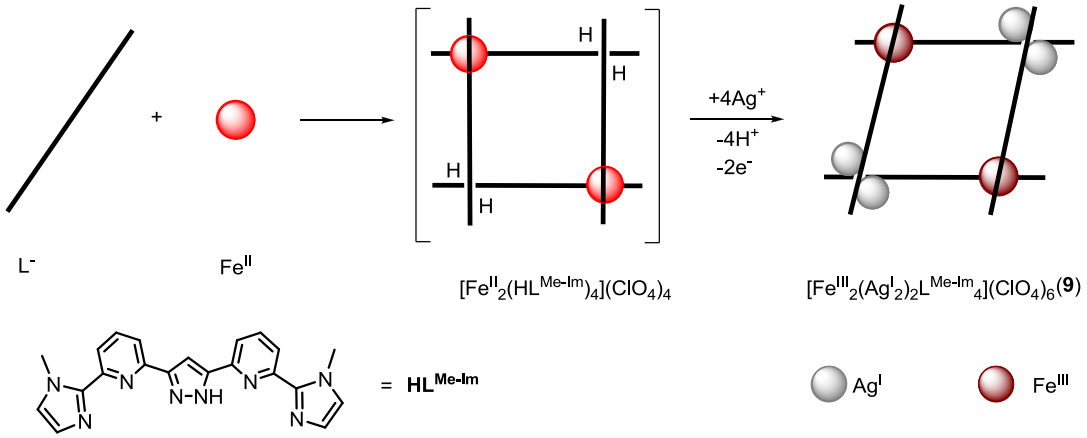

Scheme 5.1. Schematic representation of the synthesis of $[Fe^{III}_2Ag^I_4L^{Me\text{-}Im}_4](ClO_4)_6$ (**9**).

For the synthesis of complex $[Fe^{III}_2Ag^I_4L^{Me\text{-}Im}_4](ClO_4)_6$ (**9**), ligand **HL$^{Me\text{-}Im}$** was dissolved in $MeNO_2$, followed by addition of 0.5 equivalent $Fe(ClO_4)_2 \cdot 6H_2O$ salt to give a red solution containing the "corner complex" $[Fe^{II}(HL^{Me\text{-}Im})_2](ClO_4)_2$ as a key intermediate,[152] which was treated directly with an excess of $AgClO_4$, after which the color of the solution changed from red to blue (Scheme 5.1). The Ag^+ ions serve partly as an oxidant, leading to oxidation of the Fe^{II} ions. Secondly the $AgClO_4$ causes ligand deprotonation and eventually leads to incorporation of Ag^+ to give the target product. After purification by recrystallization using a large quantity of Et_2O, crystalline material of $[Fe^{III}_2Ag^I_4L^{Me\text{-}Im}_4](ClO_4)_6$ (**9**) was obtained by slow diffusion of Et_2O into a solution of the crude compound in MeCN (see Experimental Section).

5.1.2. Solid State Investigations

Structural Characterization

The molecular structure of the hexanuclear hetero-metallic grid $[Fe^{III}_2Ag^I_4L^{Me\text{-}Im}_4](ClO_4)_6$ (**9**) has been determined by X-ray crystallography. Complex **9** crystallizes in the triclinic space group *P*−1 and consists of two

crystallographically independent Fe^{III} ions, four crystallographically independent Ag^{I} ions and four ligands $(L)^{-}$, which is very similar to the structure of $[Fe^{III}_2Ag^{I}_4L^{Py}_4](BF_4)_6$ where HL^{Py} is 3,5-bis(bipyridyl)pyrazole.[152] The two iron and four silver ions are bridged by pyrazolate-bridged ligands as shown in Figure 5.1. Each of the two Fe^{III} centers is coordinated by six N atoms from two neighboring ligands (two methylimidazole N, two pyridine N, and two pyrazole N) and the Ag^{I} ion is coordinated by three N atoms from two neighboring ligands (one methylimidazole N, one pyridine N, and one pyrazole N atoms). Six ClO_4^{-} anions are present in the structure to balance the charge of the $[Fe^{III}_2Ag^{I}_4L^{Me\text{-}Im}_4]^{6+}$ species.

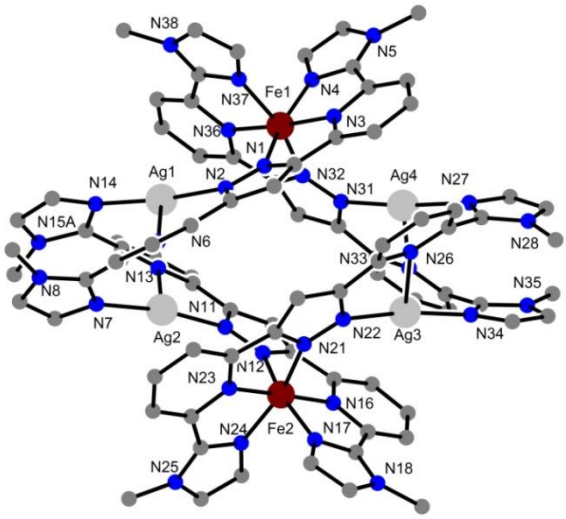

Figure 5.1. Molecular structure of the cation $[Fe^{III}_2Ag^{I}_4L^{Me\text{-}MeIm}_4]^{6+}$ of the [2 × 2] grid complex **9** (LS Fe^{III} (deep red), Ag^{I} (grey), hydrogen atoms are not included for simplicity).

The two diagonal Fe^{III} ions are separated by 7.82 Å. The geometry around the Fe^{III} ions is distorted octahedral with average angles of 161.65° (Fe1) and 162.71° (Fe2) for $N^{me\text{-}im}$–Fe–N^{pz} and 80.57° (Fe1) and 80.88° (Fe2) for $N^{me\text{-}im}$–Fe–N^{py}, which deviate from the ideal octahedron by ~10% ($N^{me\text{-}im}$ refers to the methylimidazole N atom, N^{pz} refers to the bridging pyrazole N atom, N^{py} refers to the pyridine N atom). The Fe–N bond lengths range from 1.91 Å to 1.97 Å, which is within the range of typical LS Fe^{III}–N bond lengths reported for iron complexes. A more accurate description of the distortion is given by CSM. The $S(O_h)$ and S(itp) calculations for

$[Fe^{III}_2Ag^{I}_4L^{Me\text{-}Im}_4](ClO_4)_6$ (**9**), are listed in Table 5.1, and measures for $[Fe^{III}_2Ag^{I}_4L^{Py}_4](BF_4)_6$ are included for comparison. As reflected by the CSM parameters the Fe^{II} ions are likely in the LS state.

Table 5.1. Mean Fe−N Bond Lengths and Continuous Symmetry Measures (CSM) for $[Fe^{III}_2Ag^{I}_4L^{Me\text{-}Im}_4](ClO_4)_6$ (**9**) and $[Fe^{III}_2Ag^{I}_4L^{Py}_4](BF_4)_6$.

Complex		d_{mean}/A[a]	Spin state[a]	$S(O_h)$[b]	S (itp)[b]
$[Fe^{III}_2Ag^{I}_4L^{Me\text{-}Im}_4](ClO_4)_6$	Fe^{III}1−N	1.93	LS	1.82	11.50
(**9**)	Fe^{III}2−N	1.92	LS	1.53	12.52
$[Fe^{III}_2Ag^{I}_4L^{Py}_4](BF_4)_6$	Fe^{III}1−N	1.94	LS	1.97	10.89
	Fe^{III}2−N	1.94	LS	1.92	10.79

[a] At 133 K. [b] The smaller this value (0 – 100), the closer the polyhedron is to the ideal geometry.

The other two corners of structure **9** have been replaced by four Ag^+ ions and the grid is distorted to a rhomboid. Thus, the $\{N_6\}$ pockets at those opposite corners of the rhomboid each host a Ag^{I}_2 dumbbell with Ag−Ag distances 3.17 Å for Ag1−Ag2 and 3.24 Å for Ag3−Ag4, which is longer than the Ag−Ag distances (2.93 Å for Ag1−Ag2 and 2.88 Å for Ag3−Ag4) in compound $[Fe^{III}_2Ag^{I}_4L^{Py}_4](BF_4)_6$, are still shorter than the sum of Bondi's van der Waals radii of two Ag atoms (3.44 Å), indicating $d^{10} – d^{10}$ interactions.[153]

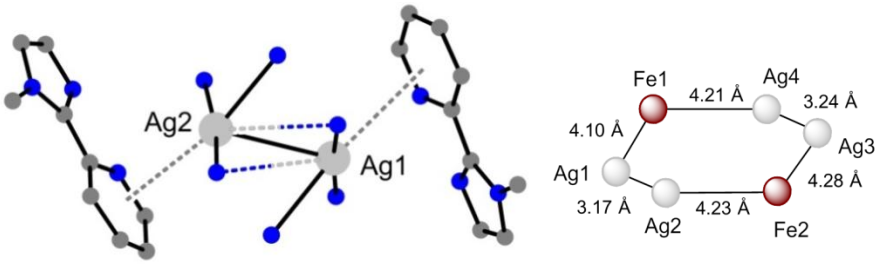

Figure 5.2. Left: Coordination environment of the Ag^{I}_2 units; right: Hexagon of metal ions in **9**.

The Ag−N distances range from 2.12 Å to 2.61 Å. When the Ag−Ag interaction is neglected, the coordination environment of the Ag^{I} ions is best described as {3+1}: three N donors are arranged almost in a plane, and one of them (pyridine N) forms a weak asymmetric bridge to the apical position of a neighboring Ag^{I}. Additional it can be seen that Ag^{I} ions appear to be stabilized by close contacts (3.39 Å and 3.72 Å) with the π system of a proximate pyridine unit that is bound to Fe^{III} center (Figure 5.2).

These distances are above the usual Ag–π interactions but below the sum of the van der Waals radii.[154,155]

Mössbauer Spectroscopy

^{57}Fe Mössbauer spectrum for a crystalline sample of $[Fe^{III}_2Ag^{I}_4L^{Me\text{-}Im}_4](ClO_4)_6$ (**9**) was collected at 80 K. Analysis of the spectrum provides information about the spin and charge states of the two iron ions presented in the hexanuclear hetero-metallic complex. The Mössbauer spectrum features two quadrupole doublets as shown in Figure 5.3. The two doublets have parameters characteristic of LS Fe^{III} centers by comparison with those discussed in chapter 4 for S = 1/2 LS Fe^{III} ions in complex **8**. The parameters of isomer shift/quadrupole splitting are $\delta/\Delta E_Q$ = 0.02/3.10 mm/s and 0.15/2.83 mm/s, respectively. The two types of Fe^{III} ions are presented in a ratio of 1:1. The two subspectra observed in the Mössbauer spectrum for the solid material may be rationalized by the presence of two crystallographically distinct Fe^{III} vertices in the crystal structure, which is also observed in the Mössbauer spectrum of compound $[Fe^{III}_2Ag^{I}_4L^{Py}_4](BF_4)_6$

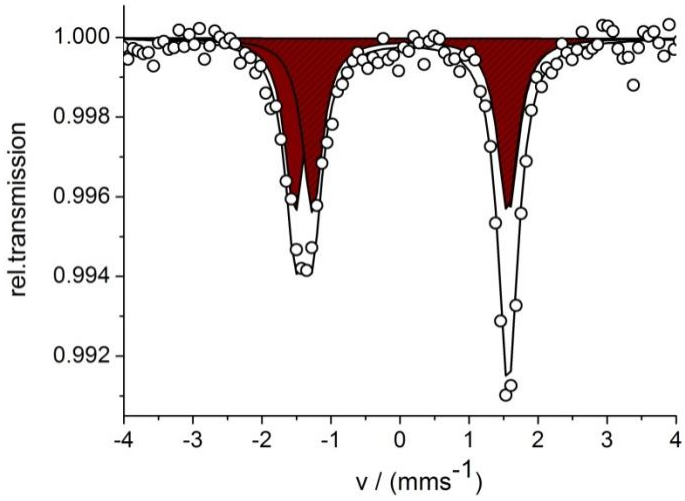

Figure 5.3. Zero-field ^{57}Fe Mössbauer spectrum for solid $[Fe^{III}_2Ag^{I}_4L^{Me\text{-}Im}_4](ClO_4)_6$ (**9**) at 80K. Lines represent simulations with Lorentzian doublets for LS Fe^{III} (deep red doublet).

5.1.3. Solution State Investigations

UV/Vis Spectroscopy

Investigation of the spectroscopic properties of $[Fe^{III}_2Ag^{I}_4L^{Me\text{-}Im}_4](ClO_4)_6$ (**9**) was carried out on different concentrated solutions in MeCN in the range 200 – 1400 nm (Figure 5.4).

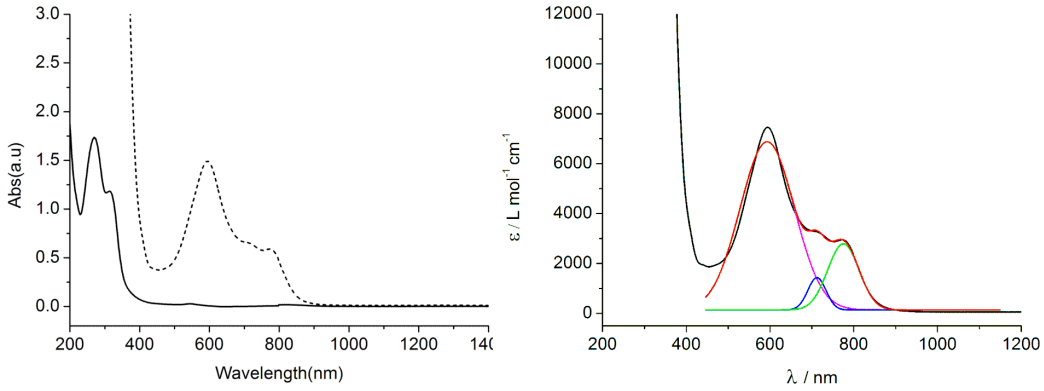

Figure 5.4. UV/Vis/NIR spectra of $[Fe^{III}_2Ag^{I}_4L^{Me\text{-}Im}_4](ClO_4)_6$ (**9**) in MeCN solution at two different concentrations (— $1{\cdot}10^{-5}$ M, ⋯ $1{\cdot}10^{-4}$ M).

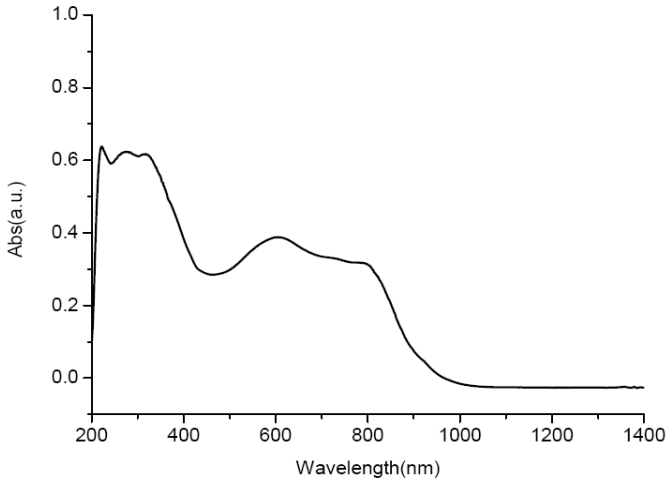

Figure 5.5. Solid-state absorption spectrum of $[Fe^{III}_2Ag^{I}_4L_4](ClO_4)_6$ (**9**). Spectra were collected on solid samples compressed into KBr pellet and measured in transmission mode.

For complex **9** there are five bands observed in the UV/Vis/NIR spectrum. The two intense bands on display in the high-energy region at 269 nm and 315 nm are likely π→π* transitions on the ligands. The bands in the visible range and beyond at 595 nm (ε = 7421 L mol^{-1} cm^{-1}), 712 nm (ε = 3306 L mol^{-1} cm^{-1}) and 780 nm (ε = 2897 L mol^{-1} cm^{-1}), are likely LMCT transitions involving the Fe^{III} ions. The UV/Vis/NIR

spectrum of **9** closely resembles the spectrum of the mixed-valence grid complex $[Fe^{II}_2Fe^{III}_2L^{Me\text{-}Im}_4](ClO_4)_6$ (**8**) (λ_{max} = 602, 720 and 792 nm) discussed in chapter 4, which supports the idea that these three absorptions of LMCT originate from the Fe^{III} chromophore. The solid state absorption UV/Vis/NIR spectrum of $[Fe^{III}_2Ag^{I}_4L^{Me\text{-}Im}_4](ClO_4)_6$ (**9**) is in good agreement with the electronic spectrum of the solution sample (Figure 5.5). Thus, the species are unaltered in solution and in the solid state.

5.2. Trinuclear [2 × 2] Fe^{II}_3 Defect-grid Complexes

5.2.1. Synthesis of $[Fe^{II}_3(HL)L_3](X)_3$ Complexes

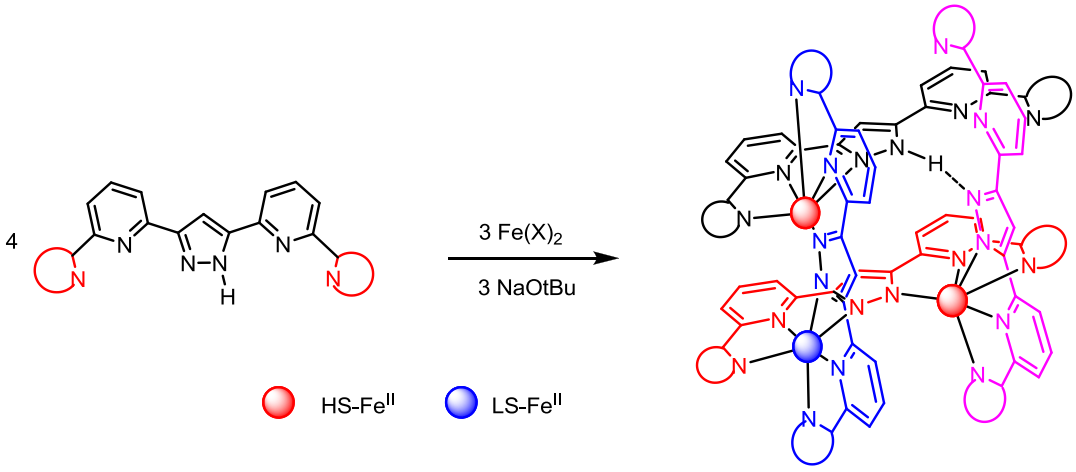

HL = HL^{Pz}	X = BF_4^-	$[Fe^{II}_3(HL^{Pz})L^{Pz}_3](BF_4)_3$	(**19**)
$HL^{Me\text{-}Pz}$	BF_4^-	$[Fe^{II}_3(HL^{Me\text{-}Pz})L^{Me\text{-}Pz}_3](BF_4)_3$	(**20**)
$HL^{Me\text{-}Im}$	ClO_4^-	$[Fe^{II}_3(HL^{Me\text{-}Im})L^{Me\text{-}Im}_3](ClO_4)_3$	(**21**)

Scheme 5.2. Schematic representation of the synthesis of $[Fe^{II}_3(HL^{Pz})L^{Pz}_3](BF_4)_3$ (**19**), $[Fe^{II}_3(HL^{Me\text{-}Pz})L^{Me\text{-}Pz}_3](BF_4)_3$ (**20**) and $[Fe^{II}_3(HL^{Me\text{-}Im})L^{Me\text{-}Im}_3](ClO_4)_3$ (**21**) grid complexes.

As shown on Scheme 5.2, the trinuclear [2 × 2] defect-grid complexes ($[Fe^{II}_3(HL)L_3](X)_3$ (X = BF_4^- or ClO_4^-)) could be obtained by a one-pot reaction of ligand, iron salt and base in a ratio of 4:3:3 in MeCN or MeOH (see Experimental Section).

In the self-assembly process, the partially deprotonated ligands (**HL** = $\mathbf{HL^{Pz}}$, $\mathbf{HL^{Me\text{-}Pz}}$, $\mathbf{HL^{Me\text{-}Im}}$) and Fe^{II} ions organize to form the matrix-like complexes $[Fe^{II}_3(HL^{Pz})L^{Pz}_3](BF_4)_3$ (**19**), $[Fe^{II}_3(HL^{Me\text{-}Pz})L^{Me\text{-}Pz}_3](BF_4)_3$ (**20**) and

$[Fe^{II}_3(HL^{Me\text{-}Im})L^{Me\text{-}Im}_3](ClO_4)_3$ (**21**). One of the four ligands remains protonated. The analytical purity of these complexes was established by elemental analyses (see Experimental Section). The [2 × 2] defect-grid complexes containing two protonated ligands by using the starting materials at a ratio of 4:3:2 (ligand, iron salt and base) were anticipated to prepare according to the work by M. Steinert.[111] However, the product $[Fe^{II}_3(HL)L_3](X)_3$ was obtained whether adding 2 or 3 equivalents of base in the reaction, which suggests the defect-grid complexes with one protonated ligand are favored.

5.2.2. Solid State Investigations

Structural Characterization

Cryrstals of defect-grid complexes **19** and **21** were obtained by slow diffusion of Et_2O into solutions and characterized by single crystal X-ray crystallography. Unfortunately, in the case of complex **20**, we were unable to obtain crystals suitable for single crystal X-ray diffraction. Various counterions, solvents and temperatures have been tried to no avail.

The molecular structure of the cation $[Fe^{II}_3(HL^{Pz})L^{Pz}_3]^{3+}$ of **19** is illustrated in Figure 5.6 (left). Four BF_4^- counter ions are not shown and at least one co-crystallized MeCN molecule is found. As expected, the structure shows a matrix-like [2 × 2] arrangement of two ligands which are perpendicular to the other two ligands. This results in four $\{N_6\}$ pockets which are occupied by three Fe^{II} ions. In the fourth case, there is one proton forming as $N^{pz\text{-}b}$–H···$N^{pz\text{-}t}$ linkage ($N^{pz\text{-}b}$ refers to the bridging pyrazole N atom, $N^{pz\text{-}t}$ refers to the terminal pyrazole N atom) between the two pyrazolate N atoms. Furthermore, the proton acts here as a protecting group, which prevents the formation of a tetranuclear [2 × 2] grid structure. The average bond lengths *d*(Fe−N) for three crystallographically unique Fe^{II} ions are 2.18 Å (Fe1−N), 2.18 Å (Fe2−N) and 1.97 Å (Fe3−N). The coordination geometry of the Fe^{II} ions deviates from an ideal octahedral coordination, reflected by the values of $S(O_h)$ (7.52 for Fe1, 7.30 for Fe2 and 3.10 for Fe3). It can be seen that the two outer metal ions

Fe1 and Fe2 are crystallographically different but nonetheless very similar. In addition, the bond lengths and distortion paremeters clearly reflect a spin configuration [HS-LS-HS] with the LS Fe^{II} ion in the center (Table 5.2).

The molecular structure of the species $[Fe^{II}_3(HL^{Me\text{-}Im})L^{Me\text{-}Im}_3](ClO_4)_3$ (**21**) are similar to **19** as shown in Figure 5.6 (right). The average bond lengths *d*(Fe−N) and the parameters of CSM of the three crystallographically different Fe^{II} ions are listed in Table 5.2, which suggests the spin configuration of the defect-grid structure **21** is [HS-LS-HS].

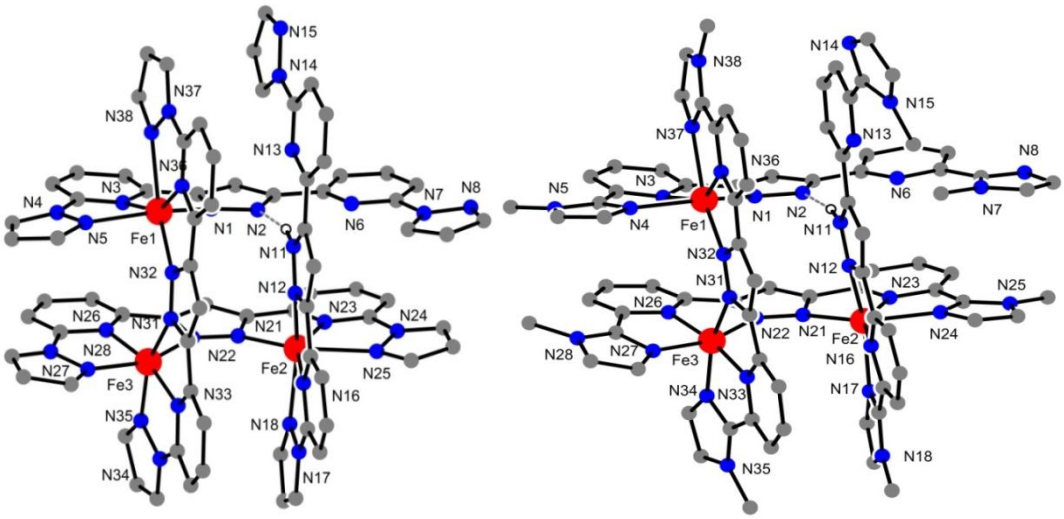

Figure 5.6. Molecular structure of the cations $[Fe^{II}_3(HL^{Pz})L^{Pz}_3]^{3+}$ of **19** (left) and $[Fe^{II}_3(HL^{Me\text{-}Im})L^{Me\text{-}Im}_3]^{3+}$ of **21** (right) (hydrogen atoms are not included for simplicity).

Table 5.2. Mean Fe−N Bond Lengths and Continuous Symmetry Measures (CSM) for complexes $[Fe^{II}_3(HL^{Pz})L^{Pz}_3](BF_4)_3$ (**19**), $[Fe^{II}_3(HL^{Me\text{-}Im})L^{Me\text{-}Im}_3](ClO_4)_3$ (**21**) and $[Fe^{II}_3(HL^{Py})_2L^{Py}_2](BF_4)_4$.

Complex		d_{mean}/A[a]	$S(O_h)$[b]	S(itp)[b]	Spin state[a]
$[Fe^{II}_3(HL^{Pz})L^{Pz}_3](BF_4)_3$	$Fe^{II}1$−N	2.18	7.52	8.09	HS
(**19**)	$Fe^{II}2$−N	2.18	7.30	8.24	HS
	$Fe^{II}3$−N	1.97	3.10	8.69	LS
$[Fe^{II}_3(HL^{Me\text{-}Im})L^{Me\text{-}Im}_3](ClO_4)_3$	$Fe^{II}1$−N	2.18	6.71	7.35	HS
(**21**)	$Fe^{II}2$−N	2.18	6.96	7.69	HS
	$Fe^{II}3$−N	1.95	2.21	10.18	LS
$[Fe^{II}_3(HL^{Py})_2L^{Py}_2](BF_4)_4$	$Fe^{II}1$−N	1.96	2.18	11.53	LS
	$Fe^{II}2$−N	1.96	2.19	11.51	LS
	$Fe^{II}3$−N	2.18	6.08	7.00	HS

[a] At 133 K. [b] The smaller this value (0 – 100), the closer the polyhedron is to the ideal geometry.

Comparison between structures $[Fe^{II}_3(HL)L_3]^{3+}$ and $[Fe^{II}_3(HL)_2L_2]^{4+}$

The previously synthesized defect-grid compound $[Fe^{II}_3(HL^{Py})_2L^{Py}_2](BF_4)_4$ by M. Steinert displayed a spin configuration of [LS-HS-LS], which is different from the spin configuration of [HS-LS-HS] of complexes $[Fe^{II}_3(HL^{Pz})L^{Pz}_3](BF_4)_3$ (**19**) and $[Fe^{II}_3(HL^{Me\text{-}Im})L^{Me\text{-}Im}_3](ClO_4)_3$ (**21**). The molecular structure of $[Fe^{II}_3(HL^{Py})_2L^{Py}_2](BF_4)_4$ exhibits a matrix-like [2 × 2] arrangement of the ligands, wherein two mutually perpendicular ligands form a coordination pocket $\{N_6\}$ environment and three of these pockets are filled with Fe^{II} ions, which is the same as the defect-grid structures of **19** and **21**.

As we know the fourth corner of $[Fe^{II}_3(HL^{Py})_2L^{Py}_2](BF_4)_4$ is protected by two protonated ligands and two interligand $N^{pz}–H\cdots N^{py}$ hydrogen bonds (N^{pz} refers to the bridging pyrazolate N atom, N^{py} refers to the bridging pyridyl N atom) are found between the N−H proton and the N^{py} atom of the bridging pyridine group (distance of $N^{pz}\cdots N^{py} \approx 2.9$ Å). For both structures **19** and **21**, the NH proton forms an interligand hydrogen bond with another central pyrzaolate N atom as $N^{pz\text{-}b}–H\cdots N^{pz\text{-}t}$. The distances of $N^{pz\text{-}b}\cdots N^{pz\text{-}t}$ between two neighboring ligands are 2.64 Å (**19**) and 2.72 Å (**21**), which is shorter than the distances of $N^{pz\text{-}b}\cdots N^{py}$ in **19** (3.37 Å) and **21** (3.85 Å). These values suggest that the hydrogen bond formed between the $N^{pz\text{-}b}\cdots N^{pz\text{-}t}$ is more stable.

To determine the distortion of these three defect-grid compounds, the torsion angles of the terminal side-arm groups to the central pyrazole rings (Figure 5.7, gray values), the Fe···Fe distances and Fe-Fe-Fe angles were calculated. The Fe···Fe distances and Fe-Fe-Fe angles in **19** and **21** are comparable to those found in compound $[Fe^{II}_3(HL^{Py})_2L^{Py}_2](BF_4)_4$, while the later [LS-HS-LS] structure shows a stronger twisting of ligands than that shown in the [HS-LS-HS] structures (Figure 5.7).

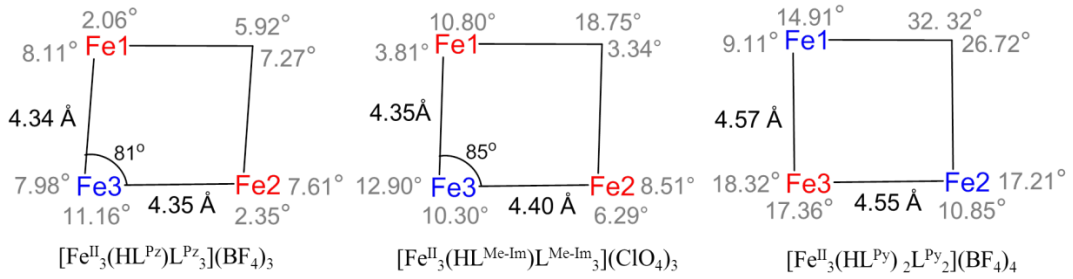

Figure 5.7. Structural comparison of $[Fe^{II}_3(HL^{Pz})L^{Pz}_3](BF_4)_3$ (**19**), $[Fe^{II}_3(HL^{Me\text{-}Im})L^{Me\text{-}Im}_3](ClO_4)_3$ (**21**) and $[Fe^{II}_3(HL^{Py})_2L^{Py}_2](BF_4)_4$. Fe···Fe distances, Fe-Fe-Fe angles (black) and torsion of the central pyrazole against side-arm methylimidazole in same ligands (gray) (right, (HS-Fe^{II} (red; LS-Fe^{II} (blue)).

Mössbauer Spectroscopy

^{57}Fe Mössbauer spectroscopy is used herein to assess the spin state and charge state of iron atoms in these defect-grid structures **19** – **21**.

The Mössbauer spectrum of a powder sample of **19** at 80 K features three doublets (one blue subspectrum and two red subspectra) as shown in Figure 5.8 (upper, left). The signal shown in blue, with isomer shift δ = 0.43 mm/s and quadrupole splitting ΔE_Q = 0.48 mm/s, has an area fraction of 15%. These values are characteristic of LS Fe^{II} ions. Another two signals shown in red, two doublets with δ_1 = 1.08 mm/s, ΔE_{Q1} = 2.69 mm/s and δ_2 = 1.10 mm/s, ΔE_{Q2} = 2.13 mm/s, having area fractions of 54% and 31%, respectively, are due to HS Fe^{II} ions. The percentage of LS Fe^{II} ions (15%) is less than the resultwe expect (33%) based on analysis of the solid state structure. In contrast, the area fraction of HS Fe^{II} (85%) is greater than the anticipated 67%. In comparison with the Mössbauer parameters (δ_1 = 1.08 mm/s, ΔE_{Q2} = 2.45 mm/s) of the powder sample of **1**, the doublet with δ_1 = 1.08 mm/s, ΔE_{Q1} = 2.69 mm/s showed in the spectrum of **19** likely arises from the normal grid $[Fe^{II}_4L^{Pz}_4]^{4+}$ species. Consequently, the difference in the area fractions observed for the HS and LS iron ions in the solid state structure and Mössbauer spectrum can be explained by the possibility of some normal grid $[Fe^{II}_4L^{Pz}_4]^{4+}$ species with a [4HS] spin configuration present in the sample, which increases the percent of HS Fe^{II} ions.

The Mössbauer spectrum of **20** displays only two quadrupole doublets (Figure 5.8

(upper, right). The parameters of one doublet (δ = 0.41 mm/s, ΔE_Q = 0.37 mm/s) are typical for LS Fe^{II} ion. This quadrupole doublet represents 17% of the total iron content. The Mössbauer paremeters of another quadrupole doublet, representing an area fraction of 83%, are observed at δ = 1.10 mm/s, ΔE_Q = 2.40 mm/s. The area fractions of the two doublets are also different from the solid state structure analysis. Similarly, by comparison with the Mössbauer paremeters (δ = 1.07 mm/s, ΔE_Q = 2.66 mm/s) of compound **2**, there may be normal grid $[Fe^{II}_4L^{Me\text{-}Pz}_4]$ species formed in the powder sample of **20**.

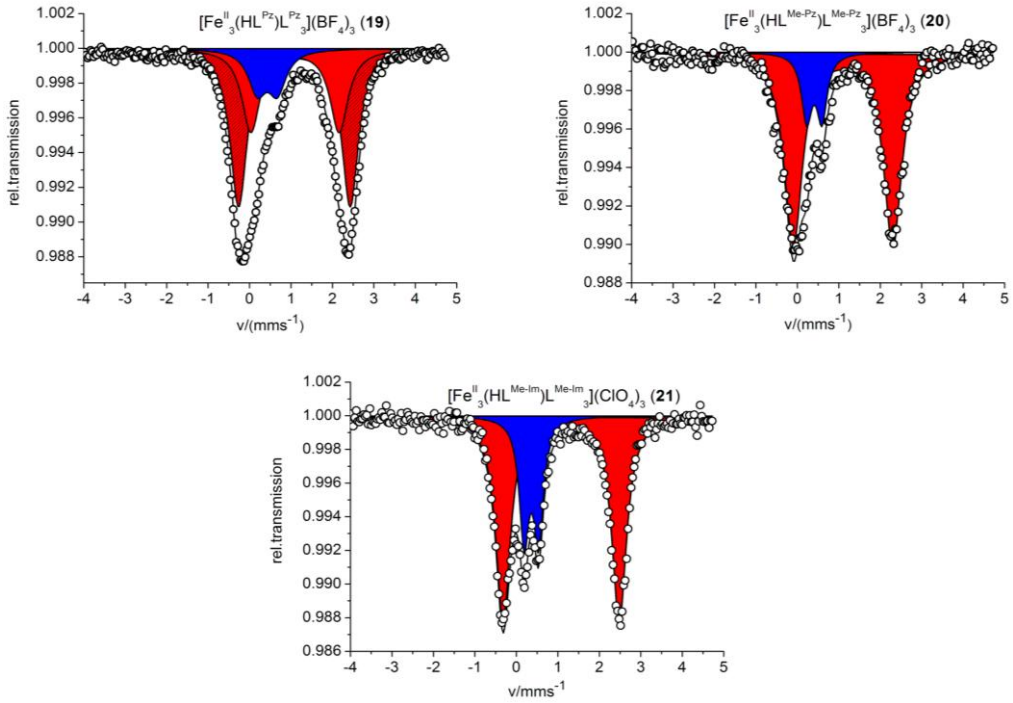

Figure 5.8. Zero-field ^{57}Fe Mössbauer spectra for powder $[Fe^{II}_3(HL^{Pz})L^{Pz}_3](BF_4)_3$ (**19**), $[Fe^{II}_3(HL^{Me\text{-}Pz})L^{Me\text{-}Pz}_3](BF_4)_3$ (**20**) and $[Fe^{II}_3(HL^{Me\text{-}Im})L^{Me\text{-}Im}_3](ClO_4)_3$ (**21**) at 80K. Lines represent simulations with Lorentzian doublets for HS-Fe^{II} (red doublet) and LS-Fe^{II} (blue doublet).

With respect to compound **21**, two quadrupole doublets are observed in the Mössbauer spectrum as well, with parameters of δ = 0.36 mm/s, ΔE_Q = 0.35 mm/s being assigned to LS Fe^{II} ion and δ = 1.08 mm/s, ΔE_Q = 2.80 mm/s corresponding to HS-Fe^{II} ion (Figure 5.8, lower). The former quadrupole doublet represents 28% and the latter 72% of the total Fe content. These values are in good agreement with the data obtained from the X-ray structure as a [LS-2HS] spin configuration.

Magnetic Properties

Magnetic susceptibility measurements in the temperature range from 2 to 400 K were performed for a crystalline sample of $[Fe^{II}_3(HL^{Me\text{-}Im})L^{Me\text{-}Im}_3](ClO_4)_3$ (**21**) using a SQUID magnetometer under a constant magnetic field of 0.5 T. No SQUID data were collected for compounds **19** and **20** because of contamination of the samples, which contain normal Fe^{II}_4 grid compound.

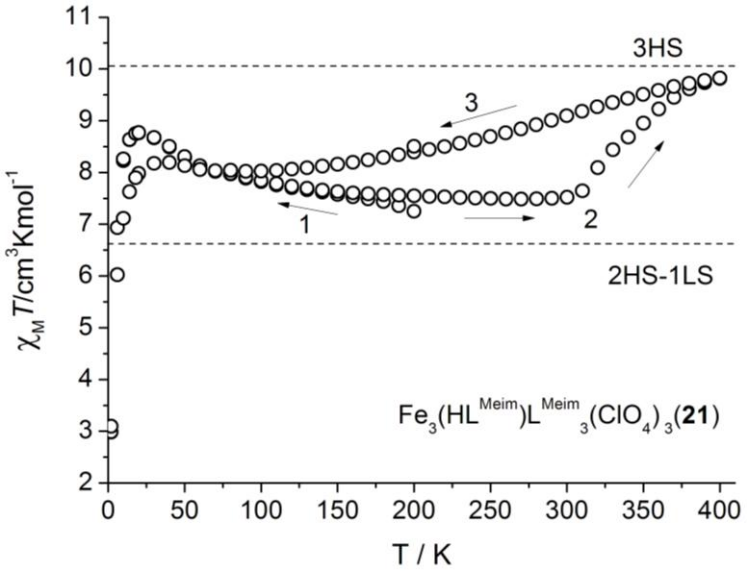

Figure 5.9. $\chi_M T$ vs. T measurement in the temperature range of 2 – 400 K at 0.5 T for crystalline sample of complex $[Fe^{II}_3(HL^{Me\text{-}Im})L^{Me\text{-}Im}_3](ClO_4)_3$ (**21**).

The $\chi_M T$ vs T curve (Figure 5.9) shows that the spin configuration of compound **21** is [2HS-1LS] in the temperature range from 2 to 200 K, consistent with the observations from single crystal X-ray diffraction and Mössbauer spectroscopy. After bringing the system to 2 K, the temperature was then raised again to 400 K. As the temperature increases, the $\chi_M T$ values remain practically constant up to nearly 300 K, where the $\chi_M T$ is 7.48 cm^{3}mol^{-1}K. Then $\chi_M T$ product starts to increase slightly as a result of a gradual change from LS to HS of Fe^{II} and causes the [3HS] spin configuration with the $\chi_M T$ increasing to 9.90 cm^{3}mol^{-1}K at 400 K, which may be a result from the loss of the co-crystallized solvent molecules or only a result of varying the temperature. On cooling down the sample back to 2 K, the $\chi_M T$ goes back to 7.95 cm^{3}mol^{-1}K at 77 K, which reflects a thermally induced gradual SCO from the

[3HS] back to [2HS-1LS] spin configuration. The changes in spin state observed for the various transformations described above demonstrate the potential of this compound as a spin-based sensor.

5.2.3. Solution State Investigations

Mass Spectrometry

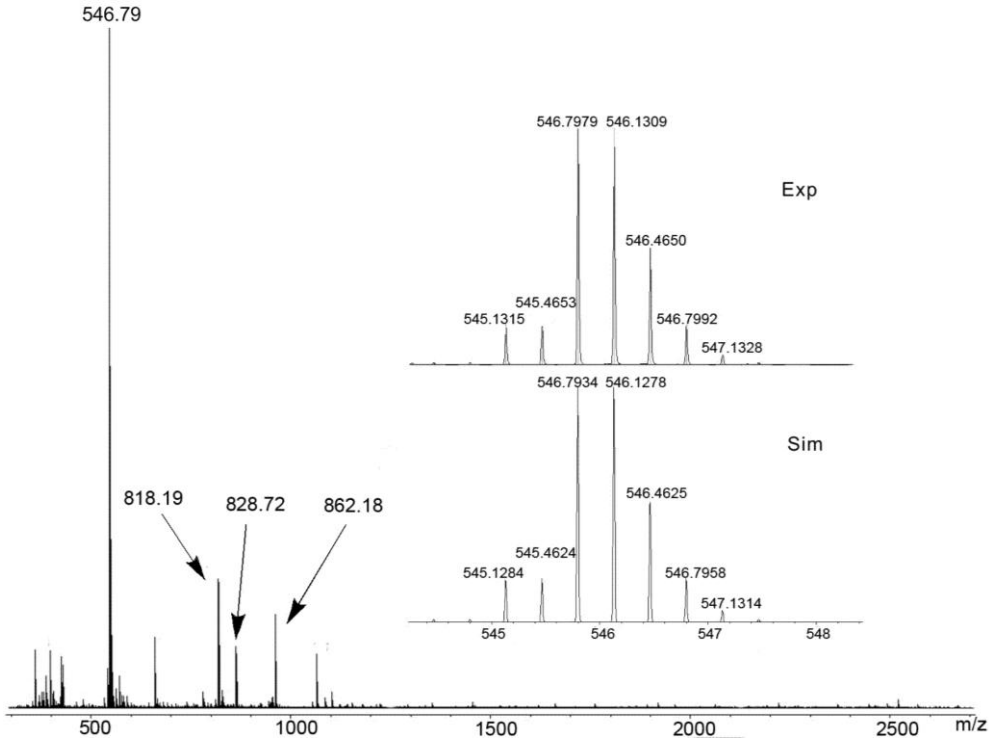

Figure 5.10. ESI-MS (MeCN) of $[Fe^{II}_3(HL^{Me\text{-}Pz})L^{Me\text{-}Pz}_3](BF_4)_3$ (**20**); (inset) experimental (upper) and simulated (lower) isotopic distribution pattern for the peak pattern around m/z = 546.79 characteristic for the $[Fe^{II}_3(HL^{Me\text{-}Pz})L^{Me\text{-}Pz}_3]^{3+}$ ion.

The ESI-MS of MeCN solutions of complexes **19** – **21** show a prominent peak characteristic of the triply charged ions $[Fe^{II}_3(HL)L_3]^{3+}$ and other peaks deriving from $[Fe^{II}_3(HL)L_3]^{3+}$. Isotope patterns matched those simulated, and peak separations were consistent with the charges, which suggest that the defect-grid-type arrays with one protonated ligand stay intact in solution with high stability.

The ESI mass spectrum of **20** is shown as an example in Figure 5.10. There are four prominent peaks characteristic of the different charged ions deriving from $[Fe^{II}_3(HL^{Me\text{-}Pz})L^{Me\text{-}Pz}_3]^{3+}$ in combinations with different counter ions BF_4^- or F^- (m/z =

546.8 for $[Fe^{II}_3(HL^{Me\text{-}Pz})L^{Me\text{-}Pz}_3]^{3+}$; 818.2 for $[Fe^{II}_3L^{Me\text{-}Pz}_4]^{2+}$; 828.7 for $[Fe^{II}_3(HL^{Me\text{-}Pz})L^{Me\text{-}Pz}_3F]^{2+}$; 862.2 for $[Fe^{II}_3(HL^{Me\text{-}Pz})L^{Me\text{-}Pz}_3(BF_4)]^{2+}$). This evidence unequivocally confirms the integrity of the [2 × 2] Fe^{II}_3 species in solution, and suggests high stability of the defect-grid-type core in solution. However, a dominant ESI-MS peak characteristic (m/z = 417.9) for the tetracation $[Fe^{II}_3(HL^{Py})_2L^{Py}_2]^{4+}$ indicates that there are two protonated ligands remaining in the defect-grid compound.

Electrochemistry

The investigation of the electrochemical properties of $[Fe^{II}_3(HL^{Me\text{-}Im})L^{Me\text{-}Im}_3](ClO_4)_3$ (**21**) was carried out on a solution of the complex in MeCN with 0.1M NBu_4PF_6 as the supporting electrolyte. No electrochemical data collected for compounds **19** and **20** because of the contaminated samples.

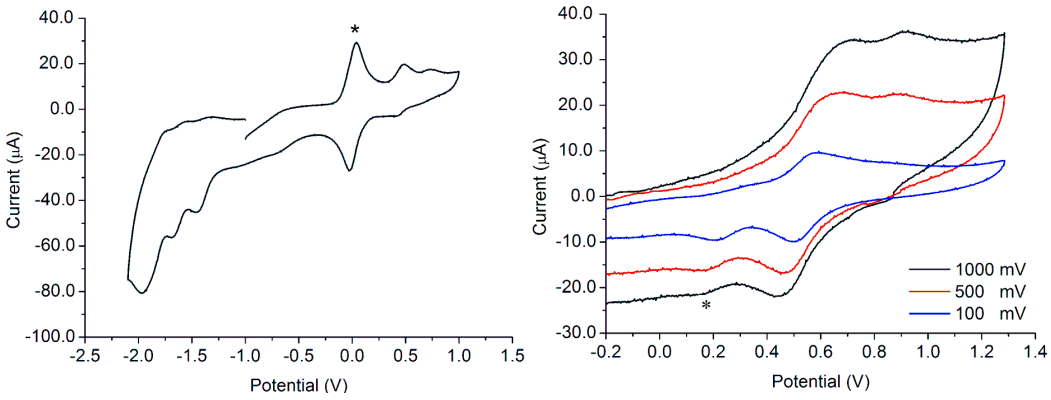

Figure 5.11. Left: Cyclic voltammetry study of $[Fe^{II}_3(HL^{Me\text{-}Im})L^{Me\text{-}Im}_3](ClO_4)_3$ (**21**) in MeCN/0.1M Bu_4NPF_6. Left: scan rate 0.1 V/s vs $Me_{10}Fc/Me_{10}Fc^+$ of about –22 to 1.2 V (asterisk means the signals of $Me_{10}Fc$); Right: Potential range of –0.2 to 1.3 V at different scan rates (asterisk means signal of inpurity).

The redox properties of defect-grid **21** were studied at different scan rates and the cyclic voltammograms are presented in Figure 5.11. There are two oxidation processes observed and the first step at $E_{1/2}$ = 570 mV is reversible (the separation of the anodic and cathodic peak potentials $\Delta E_p^{Oxi1} \approx 58$ mV) at low scan rate 0.1 V/s as shown in Figure 5.11 (left). When the scan rate is increased to 1.0 V/s, the second oxidation step at 900 mV becomes reversible ($\Delta E_p^{Oxi2} \approx 55$ mV) (Figure 5.11, right).

This reflects the shorter oxidation time. The separation between the two oxidation peaks is $\Delta E_{1/2}$ = 330 mV at the scan rate 1.0 V/s, which is significantly high and suggests the two oxidized iron ions are at diagonally opposed positions of the grid. According to the assumption that the structure of [2HS Fe^{II}-LS Fe^{II}] exists in solution (supported by mass spectrometric investigations and analyses of the solid state samples), one can assume that the two outer HS Fe^{II} ions are oxidized at almost identical potential, because they have a very similar environment. The remaining LS Fe^{II} ion is difficult to be oxidized further, due to the presence of two nearby oxidized Fe^{III} ions.

5.3. Conclusion

The pyrazolate-based ditopic ligand **$HL^{Me\text{-}Im}$** forms a strongly hydrogen-bonded corner complex dimer $[Fe^{II}(HL^{Me\text{-}Im})_2]_2(BF_4)_4$ with a [2 × 2] gridlike arrangement of four ligand strands. The two empty vertices can then be filled with $\{Ag_2\}^{2+}$ dumbbells, yielding the unprecedented diferric complex $[Fe^{III}{}_2Ag^{I}{}_4L^{Me\text{-}Im}{}_4](BF_4)_6$ (**9**), that features a rhombic-like structure with an almost planar hexagon of metal ions. A new type of [2 × 2] matrix-like complexes $[Fe^{II}{}_3(HL)L_3](BF_4)_3$ (HL = **HL^{Pz}**, **$HL^{Me\text{-}Pz}$** and **$HL^{Me\text{-}Im}$**) (**19** – **21**) with one vertex devoid of a metal ion has been selectively synthesized by using the pyrazole-bridged ligands, which exhibits dangling groups amenable to H-bonding next to the free vertex. SQUID experiments show that these [2 × 2] defect-grid complexes exhibiting fascinating magnetic properties.

6. Redox-induced Mixed-valent Single-Molecule Magnets: [2 × 2] Cobalt Grid Complexes

6.1. Homo-valence [2 × 2] Co_4 Grid Complexes

6.1.1. Synthesis of [2 × 2] Co^{II}_4 Grid Complexes

Ligands **HL^{Pz}**, **HL$^{Me\text{-}Pz}$**, **HL$^{Me\text{-}Im}$** and **HL^{Py}** varying in the peripheral groups (pyrazole or methylimidazole or pyridine) at the 6,6'-positions of the pyridine rings, were used to produce [2 × 2] Fe_4 grid complexes in chapter 3 and 4. The different terminal groups were introduced to allow functionalization of the grid-type structures for incorporation into more complex systems. These [2 × 2] Fe_4 grid complexes display fascinating redox and magnetic properties. Similarly by using these ligand systems, we intend to prepare [2 × 2] Co_4 grid complexes to study the structures and functionality.

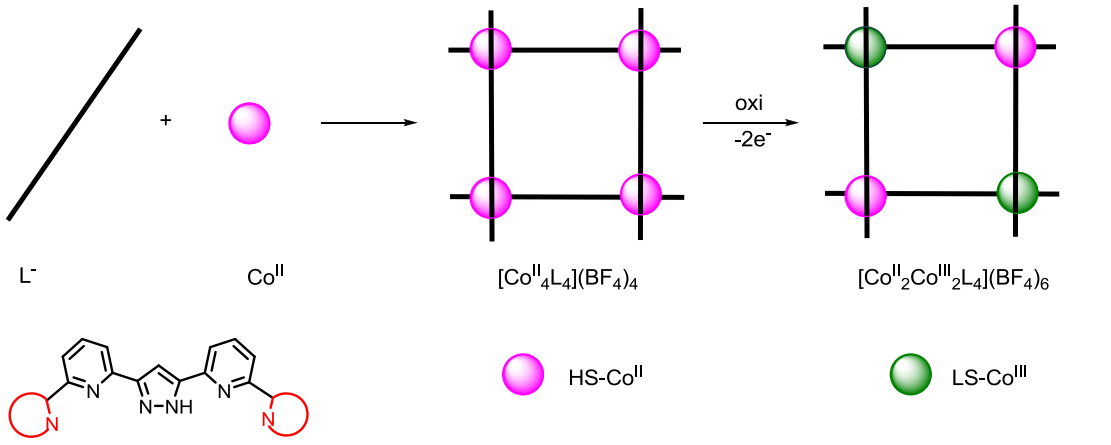

HL = **HL^{Pz}**	$[Co^{II}_4L^{Pz}_4](BF_4)_4$ (**11**)	$[Co^{II}_2Co^{III}_2L^{Pz}_4](BF_4)_6$ (**15**)
HL$^{Me\text{-}Pz}$	$[Co^{II}_4L^{Me\text{-}Pz}_4](BF_4)_4$ (**12**)	$[Co^{II}_2Co^{III}_2L^{Me\text{-}Pz}_4](BF_4)_6$ (**16**)
HL$^{Me\text{-}Im}$	$[Co^{II}_4L^{Me\text{-}Im}_4](BF_4)_4$ (**13**)	$[Co^{II}_2Co^{III}_2L^{Me\text{-}Im}_4](BF_4)_6$ (**17**)
HL^{Py}	$[Co^{II}_4L^{Py}_4](BF_4)_4$ (**14**)	$[Co^{II}_2Co^{III}_2L^{Py}_4](BF_4)_6$ (**18**)

Scheme 6.1. Schematic representation of the synthesis of [2 × 2] Co^{II}_4 grid complexes **11** – **18**.

For the synthesis of the homo-valence [2 × 2] grid complexes $[Co^{II}_4L^{R}_4]^{4+}$, ligand was dissolved in MeOH/DMF mixture with NaO^{t}Bu as the base. Mixing equimolar amounts of cobalt salt ($Co(BF_4)_4{\cdot}6H_2O$) and deprotonated ligand $[L^R]^-$(HL^R = **HL^{Pz}** for **11**, **HL$^{Me\text{-}Pz}$** for **12**, **HL$^{Me\text{-}Im}$** for **13** and **HL^{Py}** for **14**), leads to the assembly of the

[2 × 2] tetracobalt(II) complexes **11** – **14** (Scheme 6.1).

These complexes could be isolated either with BF_4^- or with ClO_4^- as counterions. For further studies of **11** – **14**, BF_4^- turned out to be the counter anion of choice because thianthrenium tetrafluoroborate and silver tetrafluoroborate were chosen as readily available oxidizing agents in subsequent steps for preparing the mixed-valent species that have only a single anion type (see section 6.2). Recrystallization of the crude products from MeCN was achieved with addition of a large quantity of Et_2O to produce pure crystalline materials **11** – **14**. While the final yield for all grid complexes $[Co^{II}_4L_4](BF_4)_4$ is not high, 58%, 65%, 45% and 42% for **11** – **14**, respectively, the preparations are reproducible. The elemental analyses of **11** – **14** indicate a 1:1 ligand-to-metal ratio in the grid formulas.

6.1.2. Solid State Investigations

Structural Characterization

Crystals of four homo-valence [2 × 2] Co^{II}_4 grid structures **11** – **14** were obtained by slow diffusion of Et_2O into saturated MeCN solution of the crude complexes. Structural analysis by single crystal X-ray diffraction shows that the four cobalt(II) grid structures share a similar coordination environment. The molecular structures consist of four cobalt ions and four monoanionic ligands in the anticipated grid architecture, with pairs of roughly parallel ligand strands. The four cobalt ions at the grid's corners are hosted in two nearly orthogonal tridentate compartments from two ligands, resulting in an overall $\{N_6\}$ coordination (two side-arm pyrazole N, two pyridine N, and two central pyrazole N atoms), with the pyrazolate bridging neighboring metal ions (Figures 6.1, 6.2, 6.4 and 6.7). Four BF_4^- anions in the grid structure balance the charge of the $[Co^{II}_4L_4]^{4+}$ species. The metal ion to ligand bonds (Co–N) are divided into three different groups according to the type of donor N atom, with different distances between cobalt ions and donor atoms. The difference in pertinent metric parameters of the Co^{II}_4 structures arises from the different backbone substituents or different side-arms of ligand systems. The average Co−N bond

lengths range from 2.13 Å to 2.15 Å and markably high values of $S(O_h)$ (corresponding to a lower S(itp)) in CSM and values of Bond Valence Sums (BVS) in all cases were observed, suggestive of an all HS configuration [HS-HS-HS-HS] for [2 × 2] Co^{II}_4 grid compounds **11** – **14** (Table 6.1).[156,157,158]

Table 6.1. Mean Co−N Bond Lengths and Continuous Symmetry Measures (CSM) and Bond Valence Sums (BVS) of complexes **11** – **14**.

Complex		d_{mean}/Å	Spin state	$S(O_h)$	S(itp)	BVS[a]
11:$[Co^{II}_4L^{Pz}_4](BF_4)_4$	$Co^{II}1$−N	2.14	HS	7.35	6.66	1.61
	$Co^{II}2$−N	2.14	HS	7.87	7.07	1.61
	$Co^{II}3$−N	2.13	HS	6.97	8.19	1.66
	$Co^{II}4$−N	2.15	HS	7.87	7.07	1.61
12:$[Co^{II}_4L^{Me\text{-}Pz}_4](BF_4)_4$	Co^{II}−N	2.13	HS	7.68	6.25	1.65
13:$[Co^{II}_4L^{Me\text{-}Im}_4](BF_4)_4$	$Co^{II}1$−N	2.14	HS	6.57	6.43	1.62
	$Co^{II}2$−N	2.14	HS	5.82	6.82	1.62
	$Co^{II}3$−N	2.14	HS	5.80	7.78	1.61
	$Co^{II}4$−N	2.14	HS	6.06	6.81	1.60
14:$[Co^{II}_4L^{Py}_4](BF_4)_4$	$Co^{II}1$−N	2.15	HS	5.63	6.78	1.49
	$Co^{II}2$−N	2.14	HS	5.31	7.30	1.61
	$Co^{II}3$−N	2.15	HS	5.51	7.00	1.59
	$Co^{II}4$−N	2.15	HS	5.76	7.08	1.57

[a] The BVS values are calculated based on a R_0 value of 1.65 Å for Co−N with the formular $s_{ij} = \exp((R_0 - R_{ij})/b)$ with b = 0.37 Å. R_0 values taken from bv2013.cif available from http://www.iucr.org/resources/data/datasets/nond-vvalence-parameters

The structure of grid complex $[Co^{II}_4L^{Pz}_4](BF_4)_4$ (**11**) was characterized by X-ray crystallography (Figure 6.1). Compound **11** crystallizes in the monoclinic space group $P2_1/c$ and consists of four Co^{II} centers coordinated to four ligands. All Co^{II} atoms are crystallographically independent (Co1, Co2, Co3 and Co4) and are not perfectly coplanar, which results in slightly different Co···Co and Co−N distances. Co···Co separations of adjacent metal ions range from 4.36 Å to 4.50 Å, and diagonally opposed cobalt(II) ions are separated by 6.01 Å and 6.29 Å (Table 6.2). The geometry around the Co^{II} ions is a distorted octahedral, as proven by the CSM parameters $S(O_h)$ (Table 6.1). The Co−N bond lengths fall into three groups according to the type of donor N atom, with the longest distances between Co^{II} and the side-arm pyrzaole moieties. The Co−N bond lengths range from 2.07 Å to 2.28

Å, which is within the range of the HS Co^{II}–N bond lengths reported in mononuclear SCO complexes (HS-Co^{II}, Table 6.1).[159]

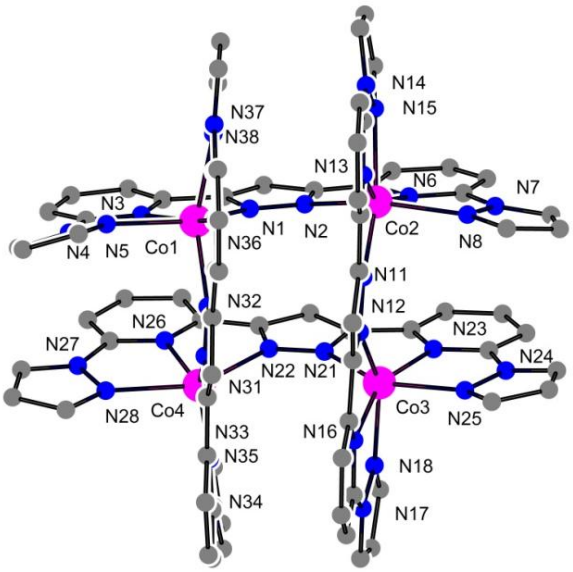

Figure 6.1. Molecular structure of the cation $[Co^{II}_4L^{Pz}_4]^{4+}$ of the [2 × 2] grid complex **11** (Co^{II} (pink), hydrogen atoms are not included for simplicity).

Compound $[Co^{II}_4L^{Me\text{-}Pz}_4](BF_4)_4$ (**12**) crystallizes in the tetragonal space group $P4_{2/n}$. The crystallographically imposed symmetry in **12** (S_4) yields only one crystallographically independent cobalt ion and one ligand (Figure 6.2). The adjacent Co···Co distance is 4.31 Å, and diagonal Co^{II} ions are separated by 6.00 Å within the molecule. The HS-Co^{II} ions are highly distorted ($S(O_h)$ around 8) resulting in coordination polyhedron closer to itp than an octahedron. Thus, the axial Co–N bond lengths to the side-arm pyrazole rings are longer than the Co–N distances to the equatorially coordinated pyridine and central pyrazole rings. The average Co–N bond distance of 2.12 Å again indicates the HS state of Co^{II} ions in complex **12**.

Structural determination shows that complexes $[Co^{II}_4L^{Pz}_4](BF_4)_4$ (**11**) and $[Co^{II}_4L^{Me\text{-}Pz}_4](BF_4)_4$ (**12**) share similar connectivities in their structures. The difference in pertinent metric parameters arises from the different functional groups (R = H, Me) on the ligand. In **11**, each central pyrazole group of four ligands possess a lone proton in the 4-position, whereas there are four methyl groups for **12**.

A comparison of the two molecular structures at 133 K is shown in Figure 6.3 (left). Although compounds **11** and **12** crystallize in different space groups, with a very small deviation from the orthorhombic system by an angle of 4°, the Co···Co distances and Co-Co-Co angles agree well with each other, and show a very strong twisting of the ligands, which is also confirmed by the superimposition of the two molecular structures (Figure 6.3, right).

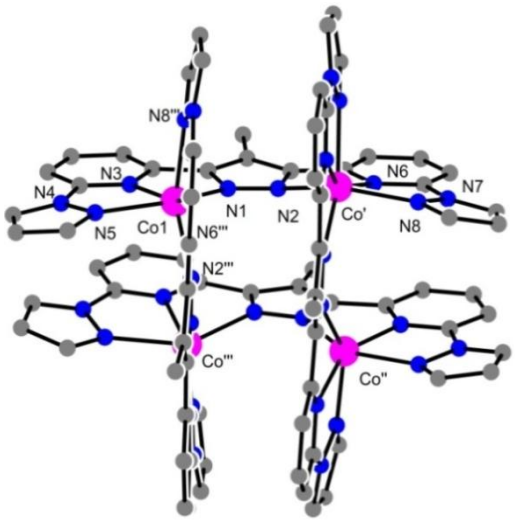

Figure 6.2. Molecular structure of the cation $[Co^{II}_4L^{Me\text{-}Pz}_4]^{4+}$ of the [2 × 2] grid complex **12** (Co^{II} (pink), hydrogen atoms are not included for simplicity).

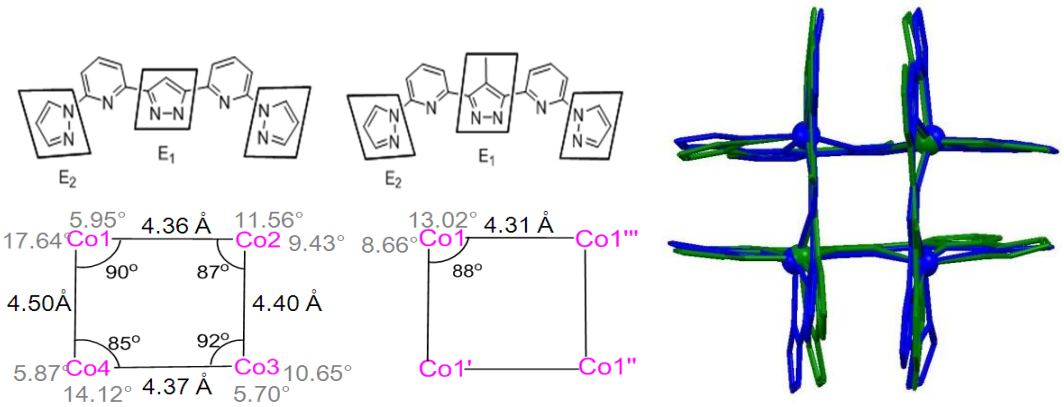

Figure 6.3. Structural comparison of cations $[Co^{II}_4L^{Pz}_4]^{4+}$ of **11** and $[Co^{II}_4L^{Me\text{-}Pz}_4]^{4+}$ of **12**. Left: Co···Co distances, Co−Co−Co angles (black) and torsion of the central pyrazoles (E_1) against side-arm pyrazoles in same ligands (E_2) (gray); Right: Overlay of structures of cations $[Co^{II}_4L^{Pz}_4]^{4+}$ of **11** (blue) and $[Co^{II}_4L^{Me\text{-}Pz}_4]^{4+}$ of **12** (green).

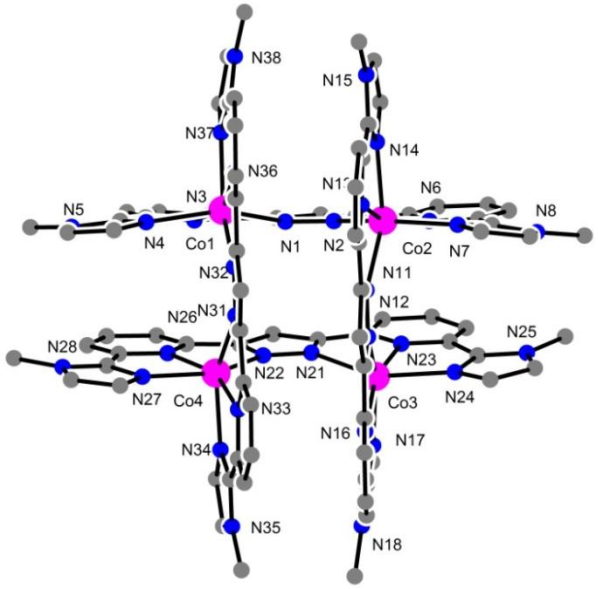

Figure 6.4. Molecular structure of the cation $[Co^{II}_4L^{Me\text{-}Im}_4]^{4+}$ of the [2 × 2] grid complex **13** (Co^{II} (pink), hydrogen atoms are not included for simplicity).

Table 6.2. Selected distances (Å) in complexes **11**, **12**, **13** and **14**.

	11	**12**	**13**	**14**
Co^{II}–N	2.073(3) – 2.276(3)	2.088(16) – 2.229(17)	2.101(2) – 2.205(2)	2.060(7) – 2.308(7)
$Co^{II}\cdots Co^{II}$ *adjacent*	4.356(9) – 4.500(7)	4.307(5)	4.437(6) – 4.503(6)	4.458(19) – 4.543(19)
$Co^{II}\cdots Co^{II}$ *diagonal*	6.008(8) / 6.291(8)	5.993(5)	6.227(7) / 6.215(5)	6.257(19) / 6.352(20)

The structures of [2 × 2] grid complex $[Co^{II}_4L^{Me\text{-}Im}_4]^{4+}$ (**13**) and $[Co^{II}_4L^{Py}_4]^{4+}$ (**14**) were also investigated by single crystal X-ray diffraction. Compounds **13** and **14** crystallize in the triclinic space group *P*–1 and monoliclic space group $P2_1$, respectively. Both structures possess four different, crystallographically independent Co^{II} ions. The distances of adjacent Co···Co and diagonal Co^{II} ions are listed in Table 6.2. Each Co^{II} ion is coordinated in a distorted $\{N_6\}$ octahedral environment by two mer-N_3 donor sets from a pair of closely perpendicularly oriented ligands (Figures 6.4 and 6.7). All the Co-N bond lengths are in accordance with the presence of HS-Co^{II} ions. The HS Co^{II} ions in crystal structures of **13** and **14** have $S(O_h)$ values between 5.31 and 6.57 and therefore the coordination polyhedron are in

between octahedral and itp.

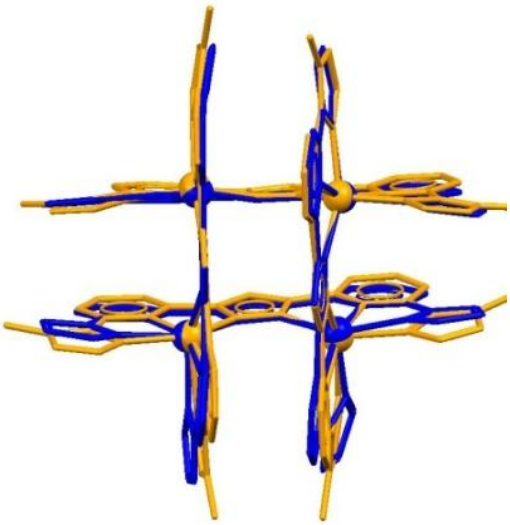

Figure 6.5. Overlay of structures of cations $[Co^{II}_4L^{Pz}_4]^{4+}$ of **11** (blue) and $[Co^{II}_4L^{Me\text{-}Im}_4]^{4+}$ of **13** (orange).

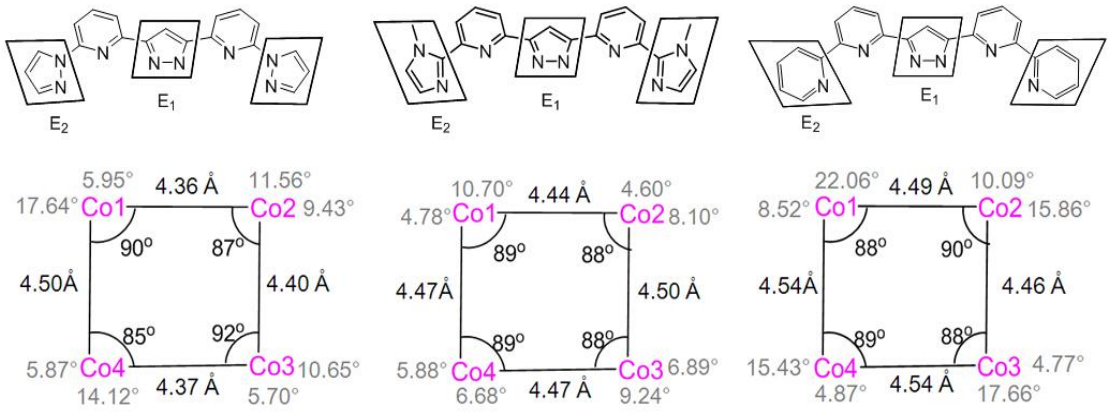

Figure 6.6. Structural comparison of cations $[Co^{II}_4L^{Pz}_4]^{4+}$ of **11**, $[Co^{II}_4L^{Me\text{-}Im}_4]^{4+}$ of **13** and $[Co^{II}_4L^{Py}_4]^{4+}$ of **14**. Co···Co distances, Co-Co-Co angles (black) and torsion of the central pyrazole (E_1) against the peripheral heterocycles as the side arms of the in same ligands (E_2) (gray).

Both [2 × 2] grid complexes $[Co^{II}_4L^{Pz}_4](BF_4)_4$ (**11**) and $[Co^{II}_4L^{Me\text{-}Im}_4](BF_4)_4$ (**13**) consist of four ligands with five-membered pyrazole and methylimidazole heterocyclic rings as the side-arm, respectively. The distortion of each ligand in both [2 × 2] grid structures varies according to the torsion angle of the central pyrazole to side-armpyrazoles of the ligand (gray values). Co···Co distances and Co−Co−Co

angles (black values) are illustrated in Figure 6.6. The results show the structure of **11** ideviates more from a square array than **13**, which is also reflected by the CSM parameters. The superimposed structures of both cations are nearly identical, except the terminal side-arm groups in **11** are twisted slightly more than **13** (Figure 6.5).

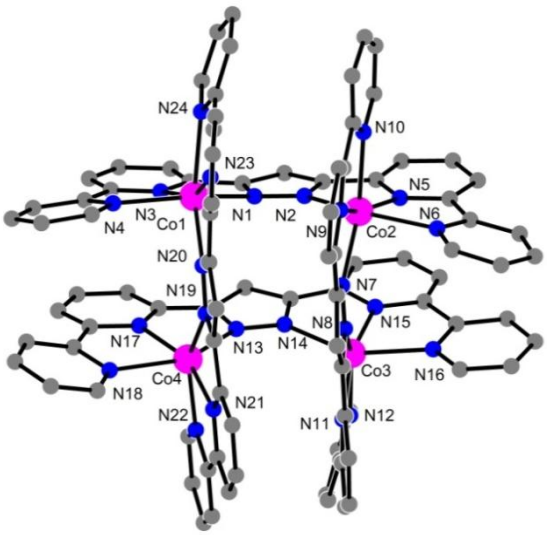

Figure 6.7. Molecular structure of the cation $[Co^{II}_4L^{Py}_4]^{4+}$ of the [2 × 2] complex **14** (Co^{II} (pink), hydrogen atoms are not included for simplicity).

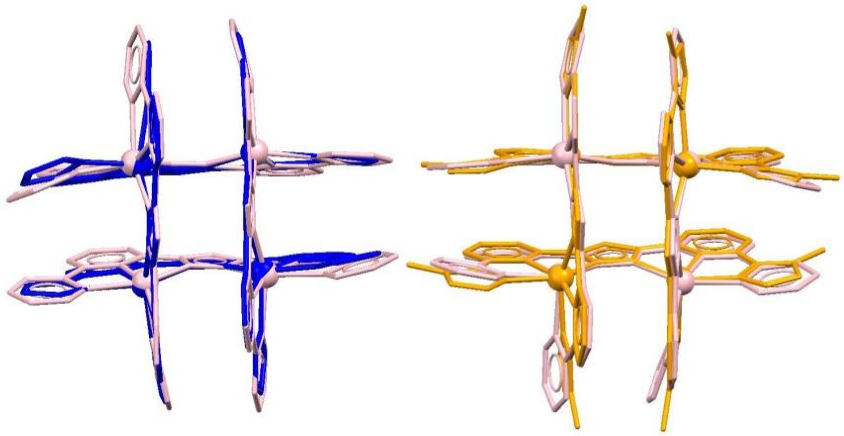

Figure 6.8. Overlay of structures of cations $[Co^{II}_4L^{Pz}_4]^{4+}$ of **11** (blue), $[Co^{II}_4L^{Me\text{-}Im}_4]^{4+}$ of **13** (orange) and $[Co^{II}_4L^{Py}_4]^{4+}$ of **14** (pink).

Interestingly, comparison of the molecular structures of $[Co^{II}_4L^{Pz}_4](BF_4)_4$ (**11**), $[Co^{II}_4L^{Me\text{-}Im}_4](BF_4)_4$ (**13**) and $[Co^{II}_4L^{Py}_4](BF_4)_4$ (**14**) at 133 K show little difference, except for a slight twisting for compound **14** (Figure 6.6). [2 × 2] grid structure **14,** with a pyridine moieties as side-arm units, displays longer Co−N bond lengths (the

donor N atom from the side-arm moieties) and relatively larger torsion angles with respect to the ligands compared to the other two derivatives with pyrazole and methylimidazole rings as side-arm in structures **11** and **13** (Figure 6.8). Introduction of two six-membered heterocycle pyridine moieties per ligand as the side-arm in **14** prevents close connection between the metal and ligand as a result of the steric bulk of the terminal pyridine moiety.

Magnetic Properties

Since the four homo-valence [2 × 2] Co^{II}_4 grid complexes possess four HS Co^{II} ions connected through bridging ligands, we carried out temperature dependent magnetometric measurements on polycrystalline samples of **11** – **14** from 2 K to 210 K with an applied magnetic field of 0.5 T. The polycrystalline sample was contained in a gel bucket, covered with a drop of low viscosity perfluoropolyether based inert oil Fomblin YL VAC 25/6 to fix the crystals, and placed in a non-magnetic sample holder. The maximum measuring temperature of 210 K was chosen because of the pour point of the oil, where the oil must be kept frozen and to avoid the orientation of the crystals parallel to the magnetic field. The $\chi_M T$ versus T plots of **11** – **14** are shown in Figure 6.9.

The observed $\chi_M T$ values at 210 K are 11.36 $cm^3mol^{-1}K$ for **11**, 10.22 cm^3Kmol^{-1} for **12**, 10.87 $cm^3mol^{-1}K$ for **13** and 9.80 $cm^3mol^{-1}K$ for **14**, where χ_M is the molar magnetic susceptibility per Co^{II}_4 unit. These values are larger than the spin-only value of four HS Co^{II} ions (S = 3/2) in the range of 8.4 – 13.6 $cm^3mol^{-1}K$, with an isotropic g value of 2.0.[160] This is a common phenomenon for Co^{II} complexes because of the significant orbital contributions of the distorted coordination phase of HS Co^{II} ions.[161] Upon lowering the temperature, the $\chi_M T$ values in all cases decrease gradually toward zero, which provides evidence that all complexes have S_T = 0 ground-state due to antiferromagnetic coupling between the cobalt(II) ions in all homo-valence [2 × 2] grid structures.

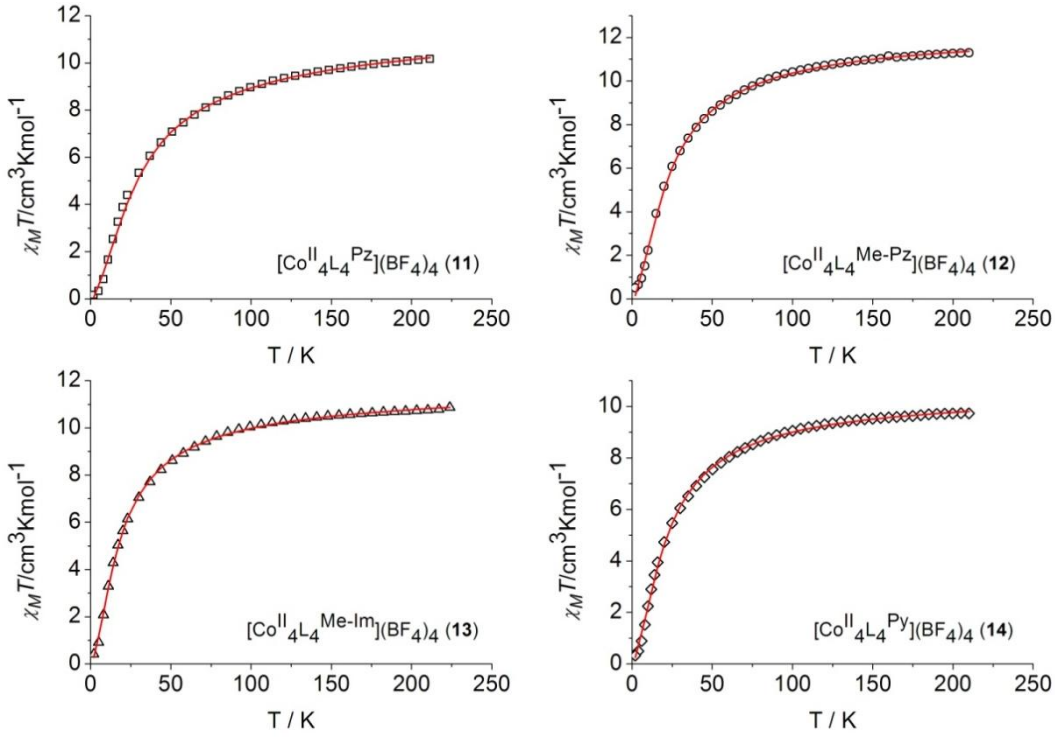

Figure 6.9. $\chi_M T$ vs. T measurement in the temperature range of 2 – 210 K at 0.5 T for crystalline samples of complexes **11** – **14**. Solid lines correspond to the best fit within the spin-only formalism.

Based on the molecular structures of **11** – **14**, four magnetic pathways are possible (Figure 6.10). Experimental data were simulated using a fitting procedure to the appropriate Heisenberg–Dirac-van-Vleck (*HDvV*) spin Hamiltonian with isotropic coupling and Zeeman splitting, assuming equal J values for all four metal-metal bridges, given in eq. 1.[162,163]

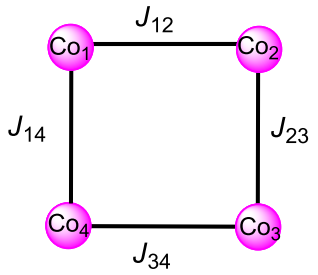

Figure 6.10. Magnetic coupling schemes for four independent coupling constants.

$$\hat{H} = -2J(\hat{S}_1\hat{S}_2 + \hat{S}_2\hat{S}_3 + \hat{S}_3\hat{S}_4 + \hat{S}_1\hat{S}_4) + g\mu_B\vec{B}\sum_{i=1}^{4}\vec{S}_i \qquad \text{(eq. 1)}$$

In all $[Co^{II}_4L_4]^{4+}$ cases, including zero-field splitting parameters D and E/D in the fitting procedure did not have any major effect on the magnitude of the J value. The best fit results were obtained for g = 2.56 and J = –2.39 cm^{-1} for **11**, g = 2.42 and J = –3.05 cm^{-1} for **12**, g = 2.25 and J = –2.45 cm^{-1} for **13**, g = 2.43 and J = –2.23 cm^{-1} for **14**. The g value significantly exceeds that of the spin only case (g = 2.0) due to non-negligible contributions of the orbitalmoment component.[164] Slightly different g values for **11** – **14** may originate from differences in distortion of the HS-Co^{II} coordination environment from octahedral symmetry. The strength of the magnetic exchange lies in the same order as for previously reported similar pyrazolate bridged grid complexes (–2.0 cm^{-1}).[107] Consequently, despite of the pronounced single-ion anisotropy of individual Co^{II} ions, the homo-valence grids **11** – **14** are magnetically non-spectacular due to antiferromagnetic exchange interaction.

6.1.3. Solution State Investigations

Mass Spectrometry

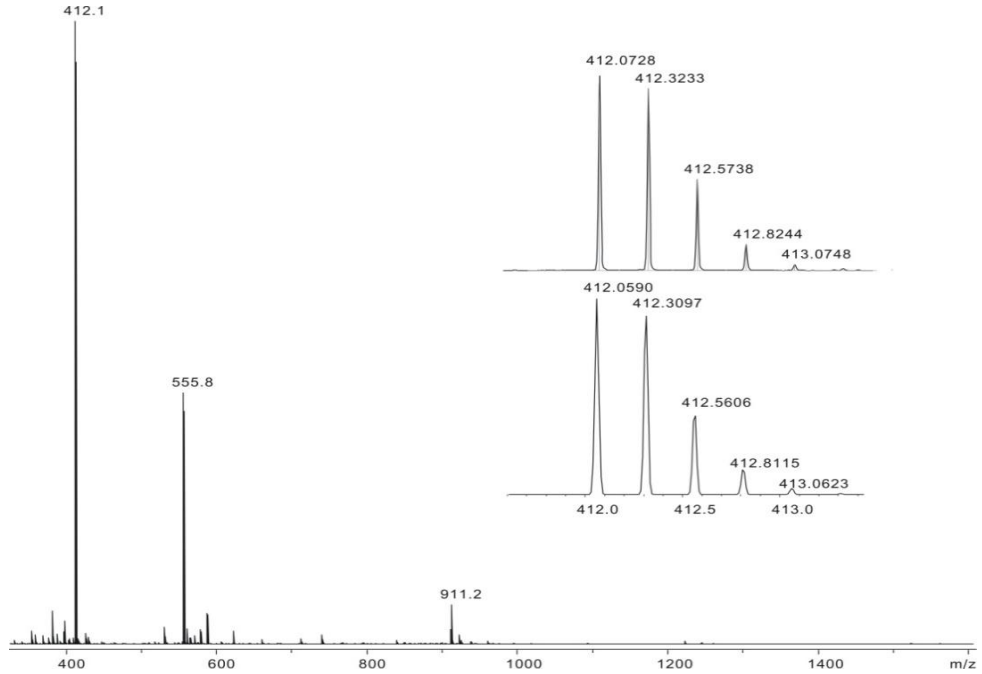

Figure 6.11. ESI-MS (MeCN) of $[Co^{II}_4L^{Pz}_4](BF_4)_4$ (**11**); (inset) experimental (upper) and simulated (lower) isotopic distribution pattern for the peak pattern around m/z = 412.1 characteristic for the $[Co^{II}_4L^{Pz}_4]^{4+}$ ion.

The ESI Mass Spectrometry of these [2 × 2] Co^{II} grid complexes **11** – **14** show only peaks from multiply charged cationic species, resulting from loss of the BF_4^- counterions. For example, the ESI-MS of $[Co_4L^{Me\text{-}Im}{}_4](BF_4)_4$ (**11**) in MeCN solution shows three main signals at m/z = 412.1 for $[Co^{II}{}_4L^{Py}{}_4]^{4+}$, 555.8 for $[Co^{II}{}_4L^{Py}{}_4(BF_4)]^{3+}$ and 911.2 for $[Co^{II}{}_4L^{Py}{}_4(BF_4)_2]^{2+}$ depicted in Figure 6.11. The ESI-MS unequivocally confirm that the grid structures are very stable in solution.

NMR Spectroscopy

Co^{II} ion shows a d^7 electron arrangement, possessing at least one unpaired electron. Within the O_h point group, this corresponding to a HS $t_{2g}{}^5e_g{}^2$ or LS $t_{2g}{}^6e_g{}^1$ configurations. The ^1H NMR spectra of the Co^{II} complexes are affected by the paramagnetic cobalt center, where the local magnetic field at the proton will be significantly different from the applied field as a result of the coupling between the electronic and magnetic spin, providing a very efficient relaxation mechanism.[165,166,167] The effect on the Co^{II} complexes causes the ^1H NMR spectra to be paramagnetically shifted over several hundred ppm. The HS six-coordinated Co^{II} complexes have short relaxation time ($5 \times 10^{-12} – 10^{-13}$ s), which makes the peaks of the paramagnetic ^1H NMR spectra reasonably sharp.

All [2 × 2] $Co^{II}{}_4$ grid complexes $[Co_4L^{Pz}{}_4](BF_4)_4$ (**11**), $[Co_4L^{Me\text{-}Pz}{}_4](BF_4)_4$ (**12**), $[Co_4L^{Me\text{-}Im}{}_4](BF_4)_4$ (**13**) and $[Co_4L^{Py}{}_4](BF_4)_4$ (**14**) are closed to the spin crossover and the spin state for all HS Co^{II} ions remain unchanged. For all complexes paramagnetic ^1H NMR and ^{13}C NMR experiments were conducted at variable temperature. The cobalt(II) complexes afforded well resolved paramagnetic NMR due to the rapid electron relaxation of the high spin d^7 systems.[168] In order to assign the peaks of the one dimensional paramagnetic NMR spectra, two dimensional homonuclear ^1H-^1H COSY and heteronuclear ^1H-^{13}C HMQC experiments were performed at room temperature.

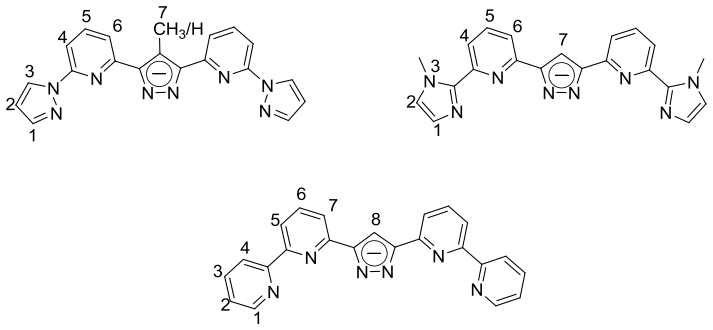

Figure 6.12. Numbering scheme for NMR assignments of complexes **11** – **14**.

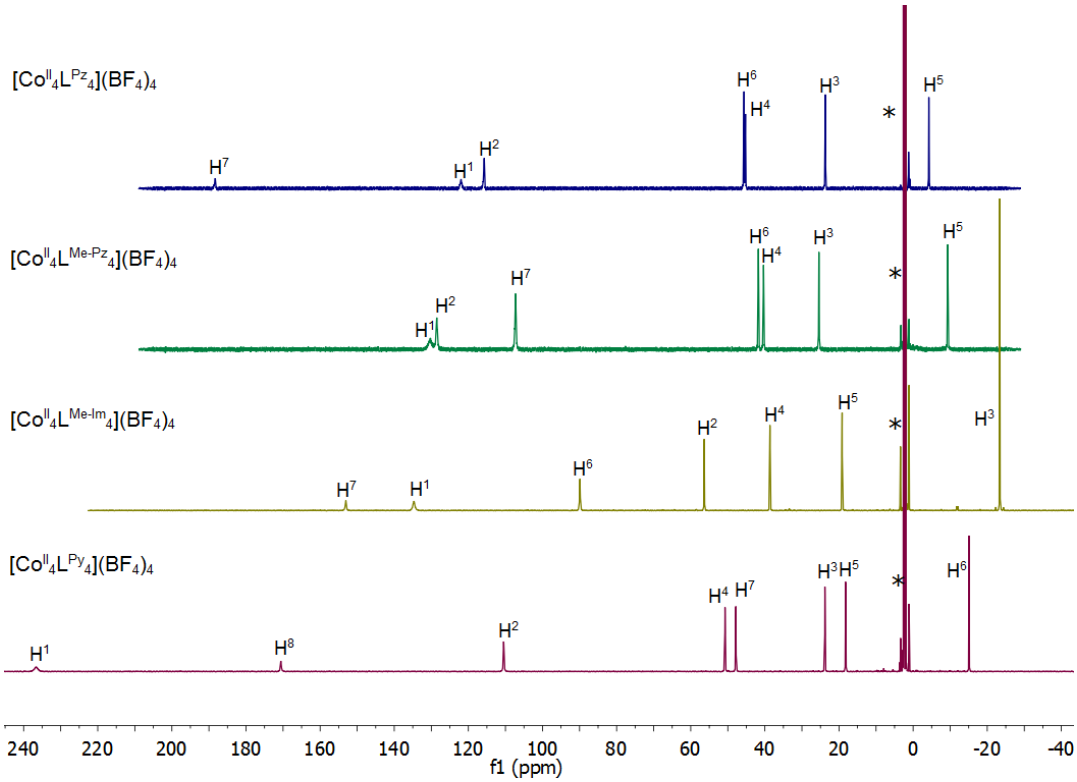

Figure 6.13. ^{1}H NMR spectra (500 MHz, CD_3CN, 298 K) of [Co$^{II}_4$L$^{Pz}_4$](BF$_4$)$_4$ (**11**), [Co$^{II}_4$L$^{Me-Pz}_4$](BF$_4$)$_4$ (**12**), [Co$^{II}_4$L$^{Me-Im}_4$](BF$_4$)$_4$ (**13**) and [Co$^{II}_4$L$^{Py}_4$](BF$_4$)$_4$ (**14**).

The number scheme for all protons of the ligands is depicted in Figure 6.12. All homo-valence [2 × 2] Co^{II} grid complexes **11** – **14** exhibited similarities in their ^{1}H NMR spectra: 1) displaying only one set of paramagnetically shifted and sharp peaks over the range of δ = –6 – 190 ppm (**11**), –9 – 140 ppm (**12**), –25 – 160 ppm (**13**), –12 – 205 ppm (**14**), indicating the HS state for all Co^{II} atoms in grid complexes;[169] 2) possessing one broad peak in the low field region (δ = 188.4 ppm (**11**), 130.6 ppm (**12**), 153.3 ppm (**13**), 204.4 ppm (**14**), which is assigned to the side-arm group proton

H^1 closest to the paramagnetic HS Co^{II} ion (Figure 6.13).[170] All signals of ^1H NMR spectra are the result of the contact and dipolar relaxation mechanisms arising from the coupling of electronic and nuclear magnetic moments,[171] the hyperfine structure is not observed in the one dimensional spectra, but a detailed analyses of two dimensional homonuclear ^1H-^1H COSY and heteronuclear ^1H-^{13}C HMQC NMR correlation spectra allow the complete assignment of all proton resonances (Tables 6.3 and 6.4).

Table 6.3 ^1H NMR chemical shifts δ (ppm) for complexes **11** – **13** and **15** – **17** in CD_3CN at 298 K.

Complex	H^1	H^2	H^3	H^4	H^5	H^6	H^7
	$H^{1'}$	$H^{2'}$	$H^{3'}$	$H^{4'}$	$H^{5'}$	$H^{6'}$	
$[Co^{II}_4L^{Pz}_4](BF_4)_4$ **11**	121.8	115.6	23.7	45.2	–4.3	45.6	188.4
$[Co^{II}_4L^{Me\text{-}Pz}_4](BF_4)_4$ **12**	130.6	128.7	23.7	40.4	–9.3	41.8	107.4
$[Co^{II}_4L^{Me\text{-}Im}_4](BF_4)_4$ **13**	134.2	56.4	23.7	–23.38	19.15	89.9	153.3
$[Co^{II}_2Co^{III}_2L^{Pz}_4](BF_4)_6$ **15**	158.5	126.3	26.0	60.5	7.4	61.9	96.9
	0.2	7.2	–14.3	–30.9	0.6	23.0	
$[Co^{II}_2Co^{III}_2L^{Me\text{-}Pz}_4](BF_4)_6$ **16**	167.3	136.0	25.7	56.7	6.3	60.6	51.6
	–0.4	7.9	–15.6	–35.1	0.12	24.1	
$[Co^{II}_2Co^{III}_2L^{Me\text{-}Im}_4](BF_4)_6$ **17**	116.2	74.9	–21.5	60.5	10.9	24.4	88.7
	–1.8	2.0	–11.9	–31.6	–4.5	16.5	

The ^1H NMR spectrum of grid **11** displays six singlets with an integral of two and one singlet with an integral of one spread over more than 100 ppm (Figure 10.47). The very strongly shifted peak at the lowest field (δ = 188.4 ppm) can immediately be assigned to H^7 on the basis of the integral. The broad signal at δ = 121.8 ppm is attributed to the proton (H^1) closest to the paramagnetic Co^{II} center. The remaining five signals (δ = –4.3 – 115.6 ppm) were fully assigned by using ^1H-^1H COSY experiment (Figure 6.14). The signal at δ = –4.3 ppm shows cross peaks to the signals at δ = 45.6 ppm and 45.2 ppm. It follows that the signal δ = –4.3 ppm is due to H^5, although the assignment of H^4 and H^6 remains ambiguous. The broaden peak of H^1 (δ = 121.8 ppm) shows no detectable cross peaks, but the signal at δ = 23.8 ppm shows cross peaks to the signals at δ = 115.6 ppm and 45.2 ppm. Therefore the

signal at δ = 23.7 ppm belongs to proton H^3, and those at 115.6 ppm and 45.2 ppm could be assigned to H^4 and H^2, respectively. Finally the last peak at 45.6 ppm corresponds to proton H^6.

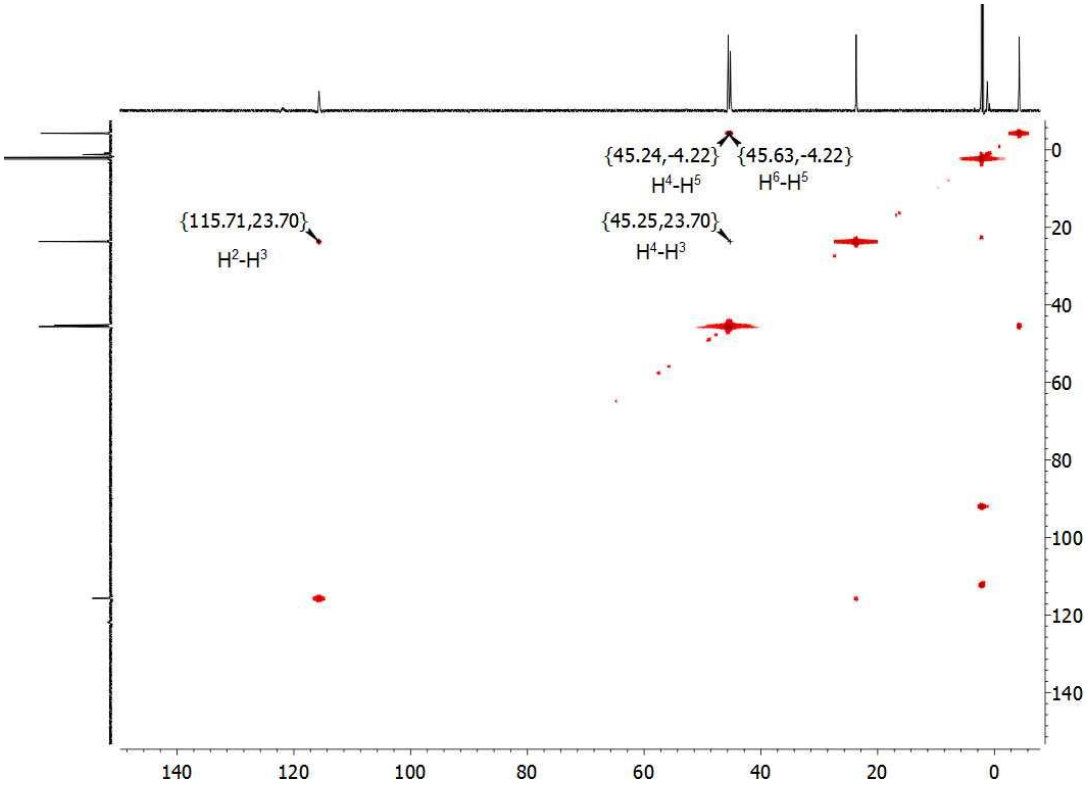

Figure 6.14. ^{1}H-^{1}H COSY spectrum (CD_3CN, 298 K) of $[Co^{II}_4L^{Pz}_4](BF_4)_4$ (**11**).

Variable temperature ^{1}H NMR was conducted on complex **11** illustrating interesting difference. For instance, increasing the temperature from 248 K to 348 K affords a significant shif from –20 – 240 ppm to a smaller range of –10 – 180 ppm (Figure 6.15, left). The linear correlation between the chemical shifts and inverse temperature (Figure 6.15, right) is characteristic of Curie behavior in solution. Spectrometer and solvent limitations prohibited the examination of a broader temperature range.

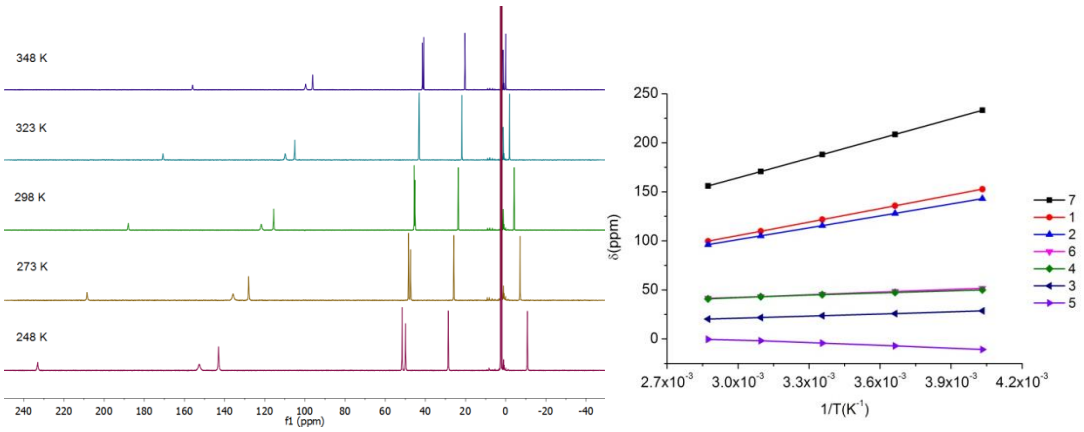

Figure 6.15. Variable-temperature ^{1}H NMR spectrum (500 MHz, CD_3CN) of $[Co^{II}_4L^{Pz}_4](BF_4)_4$ (**11**); Curie plot showing the linear dependence of ^{1}H resonance shifts with inverse temperature.

The ^{13}C NMR spectrum of complex **11** also exhibits a paramagnetic chemical shift in the range of –30 to –700 ppm. Eight carbon signals are observed, which arise from eight of the ten non-equivalent carbon atoms of the Co^{II} grid structure as depicted in Figure 6.16. Two signals were not detected, presumably due to their close vicinity to the paramagnetic metal center. Five resonances in the ^{13}C NMR spectrum can be easily assigned to the carbon atoms coupled to one proton, as the ^{1}H-^{13}C HMQC spectrum (Figure 6.17) showed (δ = 659.46/659.22 ppm, C^6; 645.29/644.48 ppm, C^2; 470.10/468.63 ppm, C^4; 287.94/286.48 ppm, C^5; 233.71/232.65 ppm, C^3), which give rise to doublets in the ^{1}H-coupled ^{13}C NMR spectrum. The remaining three quarternaru ^{13}C atoms give rise to signals without $^{1}J_{CH}$ coupling.

The introduction of a methyl group at the 4-position of the central pyrazole ring of the ligand in $[Co^{II}_4L^{Pz}_4](BF_4)_4$ (**11**) led to a change in the chemical shift corresponding to the proton atomon the 4-position of the central pyrazole fragment in $[Co^{II}_4L^{Me\text{-}Pz}_4](BF_4)_4$ (**12**), which is illustrated in Figure 10.48. In the ^{1}H NMR spectrum of **12**, the signal for H^7 at δ = 188.43 ppm corresponds to the methyl protons ($-CH_3$) based on the integral intensity. Similarly, all the signals of compound **12** could also be assigned by using the ^{1}H-^{1}H COSY spectrum (Figure 10.49) and comparison with the fully assigned spectrum of **11**. In comparison with **11**, the complex $[Co^{II}_4L^{Me\text{-}Im}_4](BF_4)_4$ (**13**) consists of 1-methylimidazole units as the side-arm

of the pyrazolate-bridged ligand **HL$^{Me\text{-}Im}$** and the ^{1}H NMR spectrum displays the same number of proton signals, but the chemical shift were shifted slightly to lower field (Figure 10.53). The assignment of the spectrum was based on integrals, ^{1}H-^{1}H COSY NMR spectroscopy, and by comparison with the fully assigned spectra of **11** and **12**.

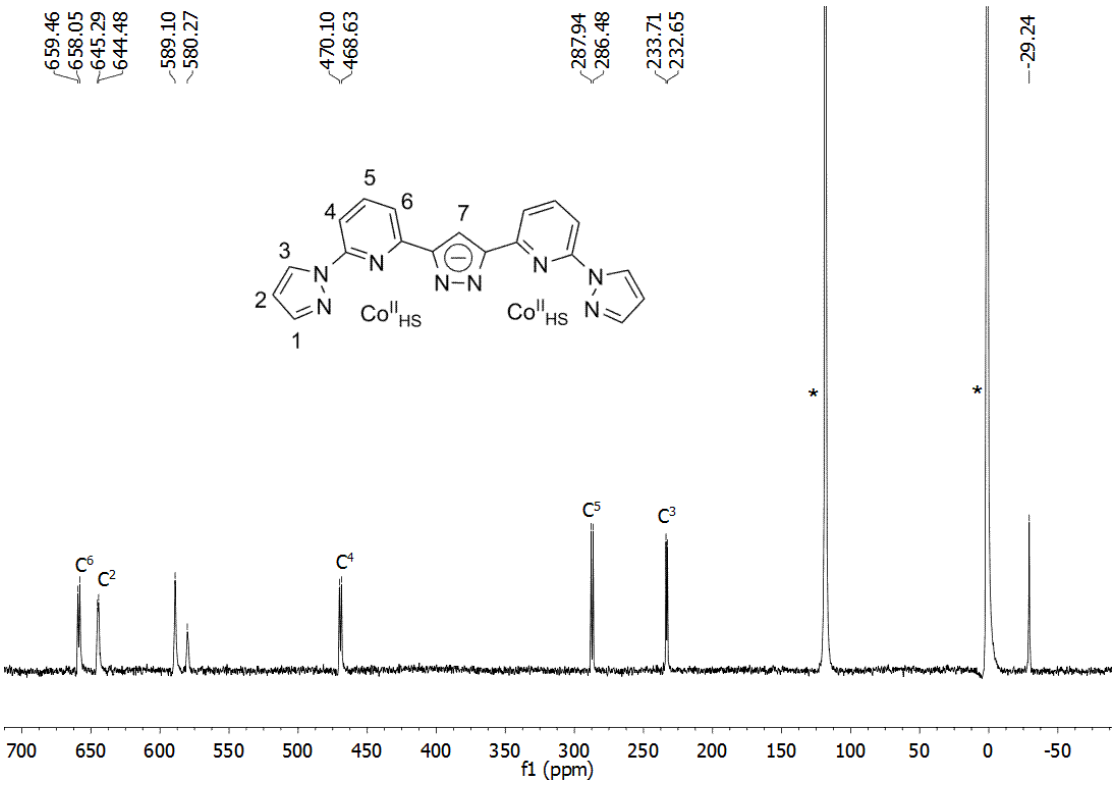

Figure 6.16. ^{13}C NMR spectrum (125 MHz, CD_3CN, 298 K) of $[Co^{II}_4L^{Pz}_4](BF_4)_4$ **11** (*MeCN).

The introduction of six-membered pyridine rings, instead of the conventional five-member pyrazole or imidazole heterocyclic moieties, as side-arm of each ligand in [2 × 2] grid structure increases the total number of protons. This is reflected by the number of signals in ^{1}H NMR spectrum of $[Co^{II}_4L^{Py}_4](BF_4)_4$ (**14**) in CD_3CN (Figure 10.56). Moreover the change of the side-arm to pyridine results in the proton resonance of H^{1} to shift to lower fields of $\delta \approx 240$ ppm. A detailed analysis of two-dimensional homonuclear ^{1}H-^{1}H correlation spectrum (Figure 10.58) allows the assignment of the eight signals as listed in Table 6.4.

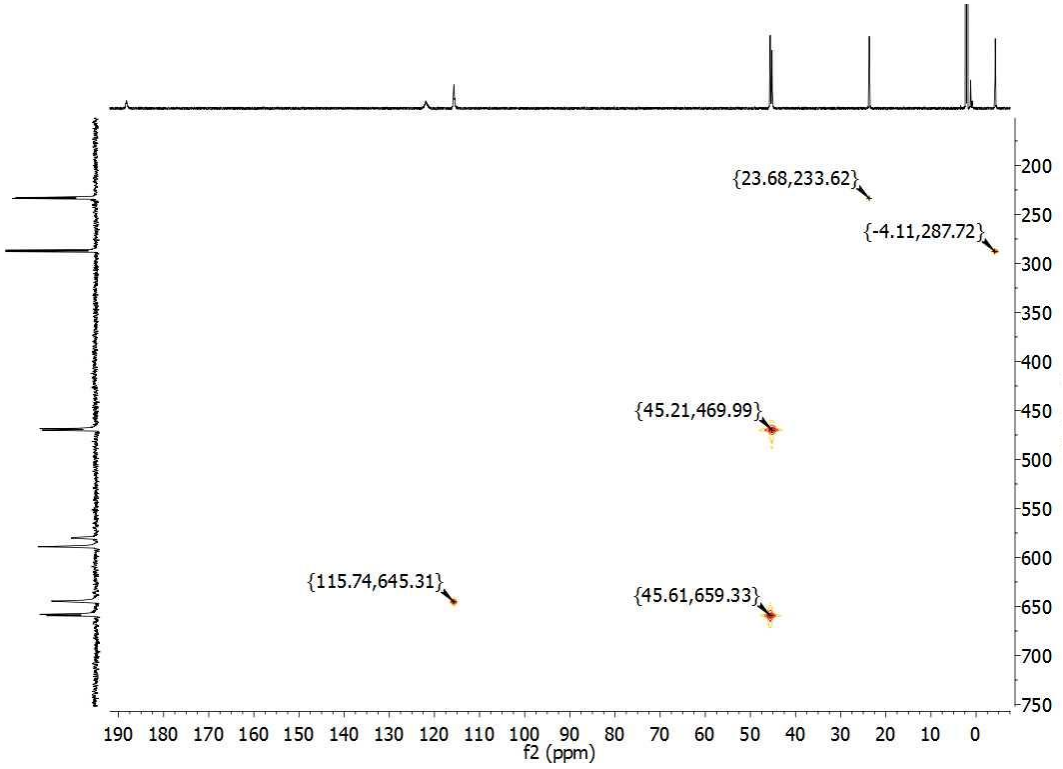

Figure 6.17. ^{1}H-^{13}C HMQC spectrum (CD_3CN, 298 K) of $[Co^{II}{}_4L^{Pz}{}_4](BF_4)_4$ (**11**).

Table 6.4. ^{1}H NMR chemical shifts δ (ppm) for complexes **14** and **18** in CD_3CN at 298 K.

Complex	H^1	H^2	H^3	H^4	H^5	H^6	H^7	H^8
	$H^{1'}$	$H^{2'}$	$H^{3'}$	$H^{4'}$	$H^{5'}$	$H^{6'}$	$H^{7'}$	
$[Co^{II}{}_4L^{Py}{}_4](BF_4)_4$ **14**	236.9	110.6	23.8	50.7	18.2	–15.1	47.8	170.1
$[Co^{II}{}_2Co^{III}{}_2L^{Py}{}_4](BF_4)_6$ **18**	130.9	30.2	70.1	31.05	8.3	–7.7	3.8	90.2
	2.0	27.0	–6.1	–27.8	–19.7	–12.8	52.94	

The variable temperature ^{1}H NMR spectra of **12** and **14** display similar Curie behavior in solution to **11** over the studied temperature range of 248 to 348 K (Figures 10.50 and 10.60). As expected for **12** – **14**, several carbon resonances are found in the ^{13}C NMR spectra (Figures 10.51, 10.55 and 10.61). The assignment of carbon atoms which display doublets in the ^{13}C NMR spectrum can be determined by the ^{1}H-^{13}C HMQC correlation experiment, while other quarternary carbons can not be assigned, displaying signals without $^{1}J_{CH}$ coupling in ^{13}C NMR spectrum (Figures 10.52, 10.56, 10.58 and 10.67).

Electrochemistry

The electrochemical behavior of complexes **11** – **14** was investigated by CV and SWV in the presence of 0.1 M NBu_4PF_6 in MeCN solution at room temperature.

Most of the grid complexes gave CVs showing pairs of multi-electrons transfer processes of ligands and one-electron or multi-electrons transfer steps of metal centers. Closer inspection of the redox potentials of complexes **11** – **14** suggests a slight dependence of the electrochemical behavior on the ligand substitutions. The electrochemical data for the Co^{II} grid complexes **11** – **14** are tabulated in Table 6.5.

Table 6.5. Redox potential *E*(V) of grid complexes **11** – **14** in MeCN/0.1 M Nbu_4PF_6, vs. Fc/Fc^+.

	$[Co_4L^{Pz}{}_4]^{4+}$(**11**)	$[Co_4L^{Me\text{-}Pz}{}_4]^{4+}$(**12**)	$[Co_4L^{Me\text{-}Im}{}_4]^{4+}$(**13**)	$[Co_4L^{Py}{}_4]^{4+}$(**14**)
E_{red}[a]	–1.82 – –2.31	–2.02 – –2.42	–1.72 – –2.02	–1.49 – –1.87
E_{oxi}[a]	0.56 – 1.2	0.42 – 1.16	0.70 – 0.98	0.47 – 0.68

[a] Multi-electron and irreversible processes. All values are from SWV measurements.

Reduction Processes

The CV of grid **11** is presented in Figure 6.18, which shows at least four reduction waves below –1.8 V (vs. Fc/Fc^+), corresponding to the reduction of ligands and Co^{II} ions in the cobalt grid and all reduction processes are all quasi-reversible. The first reduction occurs at much lower potential than in mononuclear cobalt complexes such as $[Co(terpy)_2]^{2+}$, $[Co(bipy\text{-}pz)_2]^{2+}$ or $[Co(pz\text{-}py\text{-}pz)_2]^{2+}$ (Figure 6.19),[172] likely as a result of the weaker π-acceptor properties of the pyrazole moiety compared to a pyridine substituent, and the anionic character of the pyrazolate bridge in **11**.

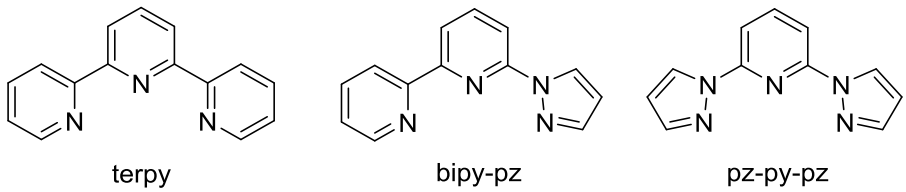

Figure 6.18. Tridentate $\{N_3\}$ ligands used in related mononuclear $Co^I/Co^{II}/Co^{III}$ complexes.

In view of the established Co^I character of reduced $[Co(terpy)_2]^+$ and related species,[173] the cathodic processes for **11** are attributed to the stepwise one-electron

$Co^{II} \rightarrow Co^{I}$ reductions in the Co_4 grid; at lower potentials these may well overlap with additional reductions of the $[L^{Pz}]^-$ ligand (Figure 6.19, left).

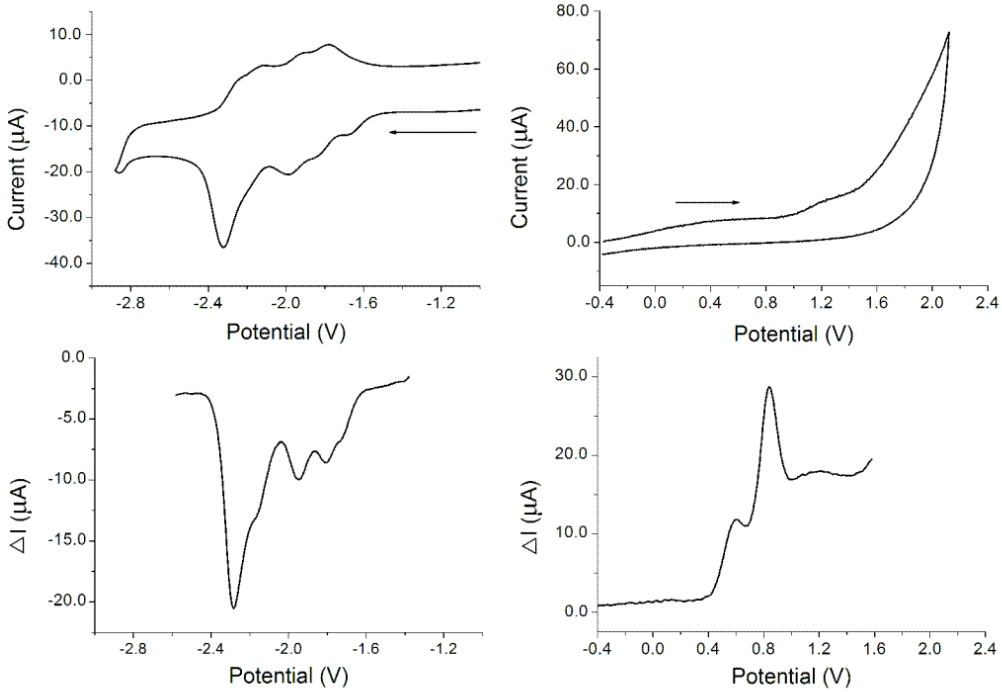

Figure 6.19. Cyclic and Square wave voltammograms of **11** in MeCN/0.1 M Bu_4NPF_6 at a scan rate of 100 mV s^{-1} vs Fc/Fc^+.

In comparison, the reduction processes of **12** are similar to **11**. The CV and SWV of **2** display a sequence of at least four cathodic processes with $E_{1/2}$ below –2.0 V (vs. Fc/Fc^+), attributed to $Co^{II} \rightarrow Co^{I}$ reductions and perhaps additional reduction of the bridging ligands at lower potentials (Figure 6.20, left). It is of interest to note that the reduction potential depends on substituent on the backbone of ligands. For instance, introduction of a methyl group into the 4-position of the central pyrazole of the ligands in **12**, the reduction potentials are shifted to less negative values (Table 6.3). Thus, substitution of the proton by a methyl group in the 4-position of central pyrazole ring causes a negative shift of the reduction potential.

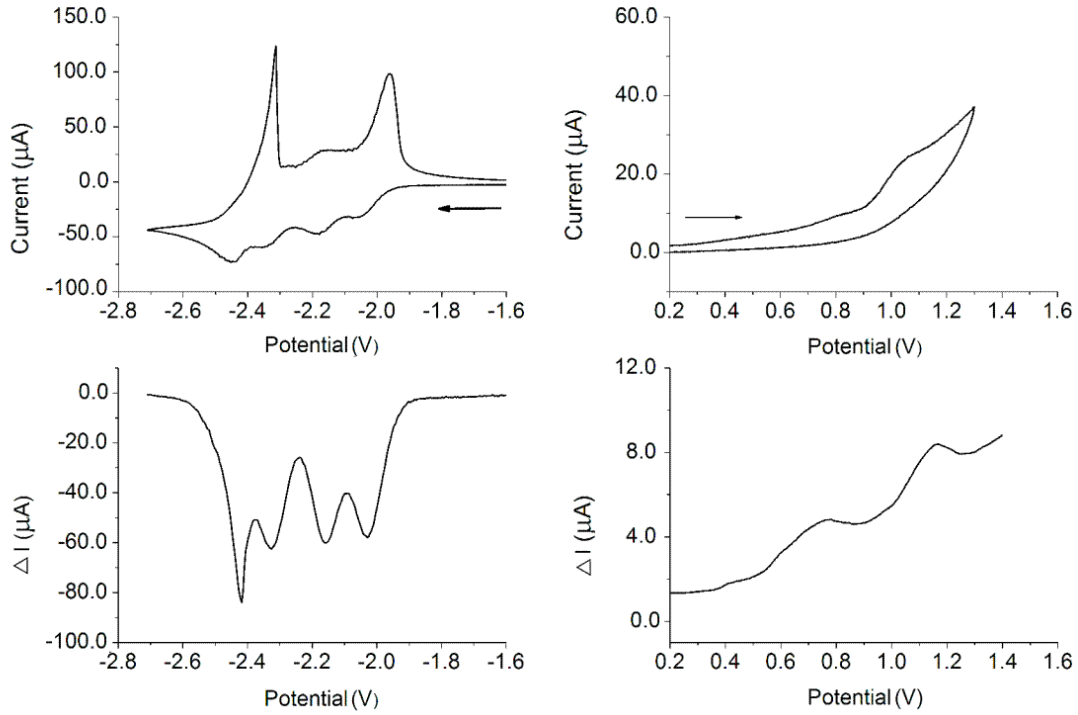

Figure 6.20. Cyclic and Square wave voltammograms of **12** in MeCN/0.1 M Bu_4NPF_6 at a scan rate of 100 mV s^{-1} vs Fc/Fc^+.

The reduction of complex $[Co_4L^{Me\text{-}Im}{}_4](BF_4)_4$ (**13**) exhibits four broad reduction steps at room temperature, but with all reduction potential slightly shifted to less negative values due to the changing of the side-arm by methylimidazole with different electron density (Figure 6.21, left). The assignment of the reduction steps could be analyzed by comparison with complexes **11** and **12**, which suggests $Co^{II} \rightarrow Co^{I}$ reductions and perhaps additional reduction of the bridging ligands in the lower potential range.

In contrast, the reduction pattern of $[Co_4L^{Py}{}_4](BF_4)_4$ (**14**) differs substantially from the other three grids **11** – **13**. Introduction of two pyridine rings for the side-arm of the ligand in the grid structure **14** give rise to eight pyridine rings than complexes **11** – **13**. The CV and SWV of **14** display a very pronounced shift of the three reduction potentials (Table 6.5), likely due to the stronger π-acceptor properties of pyridine compared to pyrazole (Figure 6.22, left). Additionally, the third reduction step is depicted as a broad wave, which can not be determined as a one- or multi-electrons reduction process. As a result, the three reduction processes for **14** may be attributed

to $Co^{II} \rightarrow Co^{I}$ and ligands reductions in Co^{II}_4 grid.

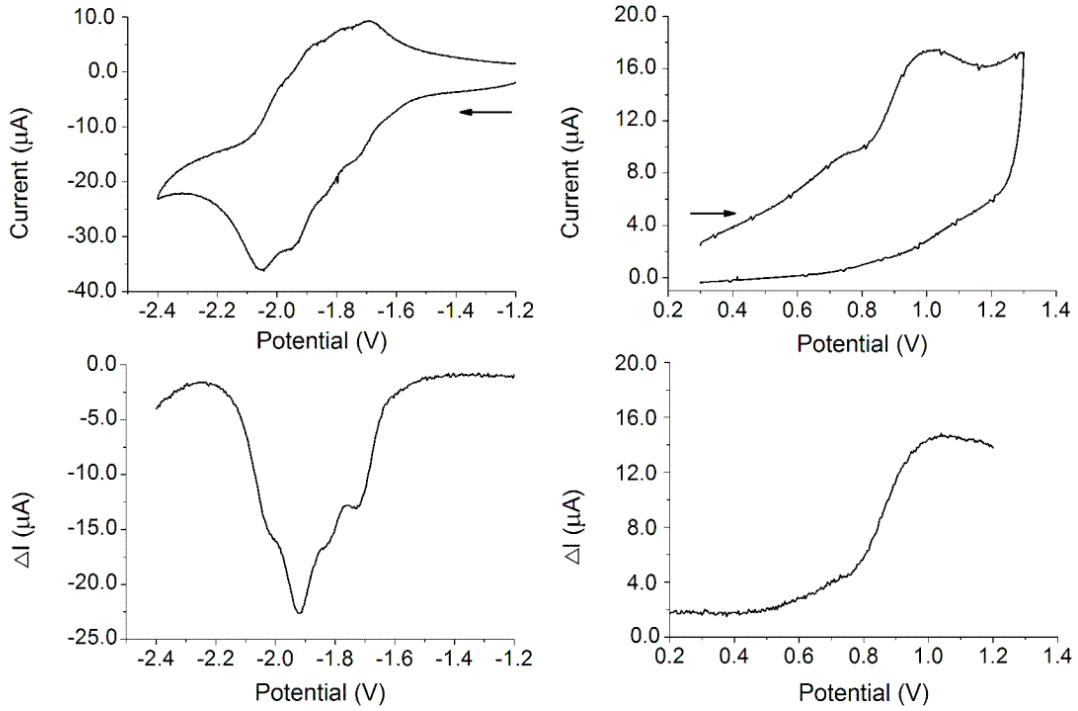

Figure 6.21. Cyclic and Square wave voltammograms of **13** in MeCN/0.1 M Bu_4NPF_6 at a scan rate of 100 mV/s vs Fc/Fc^+.

Oxidation Processes

On the other hand, the CV of **11** in the anodic regime exhibits a very broad oxidation wave above +0.4 V and a further broad and ill-defined wave around E_{pa} = +1.2 V (*vs.* Fc/Fc^+), all electrochemically irreversible. These anodic responses likely reflect a sequence of non-resolved and kinetically hindered one-electron oxidation processes, describing the oxidation of the Co^{II}_4 to the fully oxidized Co^{III}_4 grid *via* mixed-valent states, in particular via the di-mixed-valent $Co^{II}_2Co^{III}_2$ species (Figure 6.19, right). Use of the SWV technique allowed resolving the first two oxidation steps, which occur at +0.59 V and +0.84 V and are tentatively assigned to sequential one-electron oxidations of two Co^{II} centers in the grid. The electrochemical potential for the first oxidation of **11** is much higher than the Co^{III}/Co^{II} potentials for $[Co(terpy)_2]^{2+}$ and $[Co(bipy\text{-}pz)_2]^{2+}$, but similar to the one of $[Co(pz\text{-}py\text{-}pz)_2]^{2+}$.[174] The third very broad peak in the SWV of **11** occurs around +1.2 V and further anodic processes at even

higher potential can therefore be assigned to the two subsequent oxidations of the remaining Co^{II} centers, which are separated from the first two steps by a potential gap of ca. 350 mV. Such large energy gap implies a high thermodynamic stability of the di-mixed-valent $Co^{II}_2Co^{III}_2$ species, which has been confirmed by the successful isolation of $[Co^{II}_2Co^{III}_2L^{H}_4](BF_4)_6$ (**15**) by using the $[thianthrene]^{\bullet+}$ ion as an oxidant in MeCN (see below).

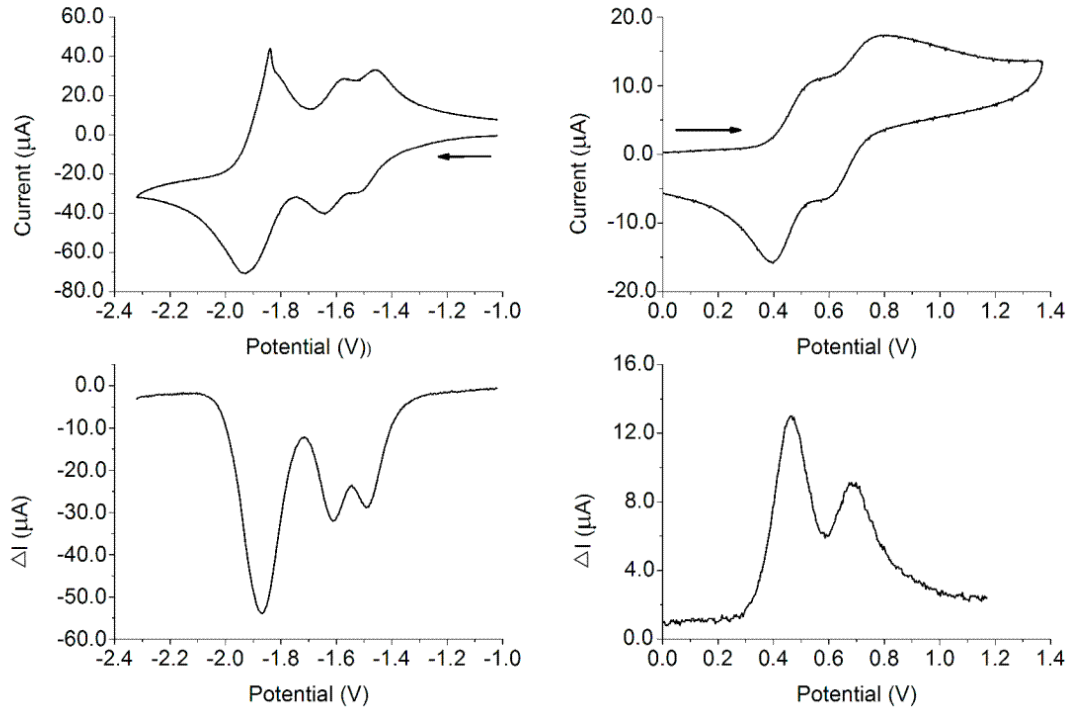

Figure 6.22. Cyclic and Square wave voltammograms of **14** in MeCN/0.1 M NBu_4PF_6 at a scan rate of 100 mV s^{-1} vs Fc/Fc^+.

Some broad and electrochemically irreversible oxidation processes of **12** are discernible in the SWV below +0.8 V with a further broad wave around +1.16 V. These potentials are slightly lower than for **11** (Figure 6.20, right), as expected because of the +I effect of the methyl substituent at the pyrazolate-C^4 position.

In comparison, the oxidation of **13** under identical conditions led to two broad and irreversible steps of CV and SWV, and with the oxidation potential slightly shifted to less positive values ($E_{pa} \approx$ +0.70 V, +0.98 V) relative to redox behavior of **11** and **12**. These two multi-electronic oxidations can only be attributed to the four electrons

transfer of Co^{II}/Co^{III} in [2 × 2] tetranuclear grid structure of **13** without any other analysis in detail.

It should be noted that electrochemical signatures with broad and electrochemically irreversible oxidation steps were reproducibly obtained when using single crystalline material of highest purity for the preparation of the solutions for CV measurements. Similar phenomena were reported also for some previously studied Co_4 grids[175] and for related mononuclear cobalt complexes[176] and have been attributed to the kinetically slow electron transfer in the Co^{III}/Co^{II} redox couple, which strongly depends on the electrode material.[176]

It is interesting to note that CV and SWV of **14** showed two separated and quasi-reversible oxidations at 0.47 V and 0.68 V vs Fc/Fc^+ (Figure 6.22, Table 6.5). These are assigned to the sequential oxidation of two Co^{II} ions in the grid, likely at opposite (diagonally disposed) corners, to give the $[Co^{III}Co^{II}_3L^{Py}_4]^{5+}$ and $[Co^{III}_2Co^{II}_2L^{Py}_4]^{5+}$ species; the one-electron of the two redox processes was confirmed by the small potential gap ($\Delta E_{1/2}$ = 210 mV). Additionlly, there is no more oxidation peaks observed even at high potential. This suggests that the di-mixed-valence species $[Co^{II}_2Co^{III}_2L_4]^{6+}$, two-electron oxidation of the homo-valence species $[Co^{II}_4L_4]^{4+}$, reveals a pronounced thermodynamic stability and it is difficult to be further oxidized. This result could be confirmed by the successful separation of the mixed-valence $[Co^{II}_2Co^{III}_2L^{Py}_4](BF_4)_6$ (**18**) grid compound.

6.2. Mixed-valence [2 × 2] Co_4 Grid Complexes

6.2.1. Synthesis of [2 × 2] $Co^{II}_2Co^{III}_2$ Grid Complexes

The observance of the first bi-electronic oxidation step at relatively low potential for homo-valence grids $[Co^{II}_4L_4]^{4+}$ (**11** – **14**) prompted us to investigate two-electrons oxidized species $[Co^{II}_2Co^{III}_2L_4]^{6+}$, where HL = $\mathbf{HL^{Pz}}$ (**15**), $\mathbf{HL^{Me\text{-}Pz}}$ (**16**), $\mathbf{HL^{Me\text{-}Im}}$ (**17**), $\mathbf{HL^{Py}}$ (**18**). After chemical oxidation of **11** and **12** with thianthrenium tetrafluoroborate in MeCN, which solubilizes **11** and **12** and ensures the full oxidizing potency of the $[thianthrene]^{\bullet+}$ ion ($E_{1/2}$ = 0.86 V vs Fc/Fc^+),[177] the mixed-valence

$[Co^{II}_2Co^{III}_2L^{Pz}_4](BF_4)_6$ (**15**) and $[Co^{II}_2Co^{III}_2L^{Me\text{-}Pz}_4](BF_4)_6$ (**16**) grids were synthesized on a preparative scale, respectively (see Experimental Section). At the same time a second oxidation of **13** and **14** is successful as well to produce the mixed-valence grid complexes $[Co^{II}_2Co^{III}_2L^{Me\text{-}Im}_4](BF_4)_6$ (**17**) and $[Co^{II}_2Co^{III}_2L^{Py}_4](BF_4)_6$ (**18**) by using silver tetrafluoroborate as the oxidant in $MeNO_2$. The color of the reaction mixture of all cases is quickly changed from orange to olive-green, and crystalline material **15** – **18** could be obtained by slow diffusion of Et_2O into an MeCN solution of the crude product. Unfortunately, in the case of complex **17**, we were unable to obtain crystals suitable for single crystal X-ray diffraction. Various counterions, solvents and temperatures have been tried to no avail. Nevertheless, analytical purity of all these complexes **15** – **18** were confirmed by elemental analyses (see Experimental Section).

6.2.2. Solid State Investigations

Structural Characterization

Crystals of the mixed-valence [2 × 2] grid cations $[Co^{II}_2Co^{III}_2L_4]^{6+}$ of complexes **15**, **16** and **18** were obtained from Et_2O/MeCN and the structures were determined by single crystal X-ray crystallography. The molecular structures of **15**, **16** and **18** are conserved although a significant distortion from a square geometry to a rhombic arrangement of the four metals is observed. Pairs of cobalt ions of the same oxidation states are located on opposite corners of the grid (Figures 6.23 and 6.24). Comparisons of Co−N bond lengths (Å), parameters of CSM and Bond Valence Sums (BVS) for all complexes are shown in Table 6.7. The Co−N bond lengths and CSM calculations can be used to characterize HS and LS states and BVS can be used to confirm the oxidation state of the cobalt ion.[178]

Compounds $[Co^{II}_2Co^{III}_2L^{Pz}_4](BF_4)_6$ (**15**) crystallizes in the monoclinic $P2_1/n$ space group and $[Co^{II}_2Co^{III}_2L^{Me\text{-}Pz}_4](BF_4)_6$ (**16**) crystallizes in the tetragonal $I4_1/acd$ space group. The complex cation $[Co^{II}_2Co^{III}_2L^{Pz}_4]^{6+}$ consists of alternating Co(III) and Co(II) ions, with each metal displaying distorted octahedral coordination to six nitrogen atoms from two bridging ligand fragments. The adjacent $Co^{II}\cdots Co^{III}$

distances range from 4.47 Å to 4.54 Å in **15** and 4.37 Å in **16**. The bdiagonal Co ions are separated by 6.80 Å ($Co^{II}\cdots Co^{II}$) and 5.87 Å ($Co^{III}\cdots Co^{III}$) for compound **15** and 6.56 Å ($Co^{II}\cdots Co^{II}$) and 5.79 Å ($Co^{III}\cdots Co^{III}$) for complex **16**, respectively (Table 6.7).

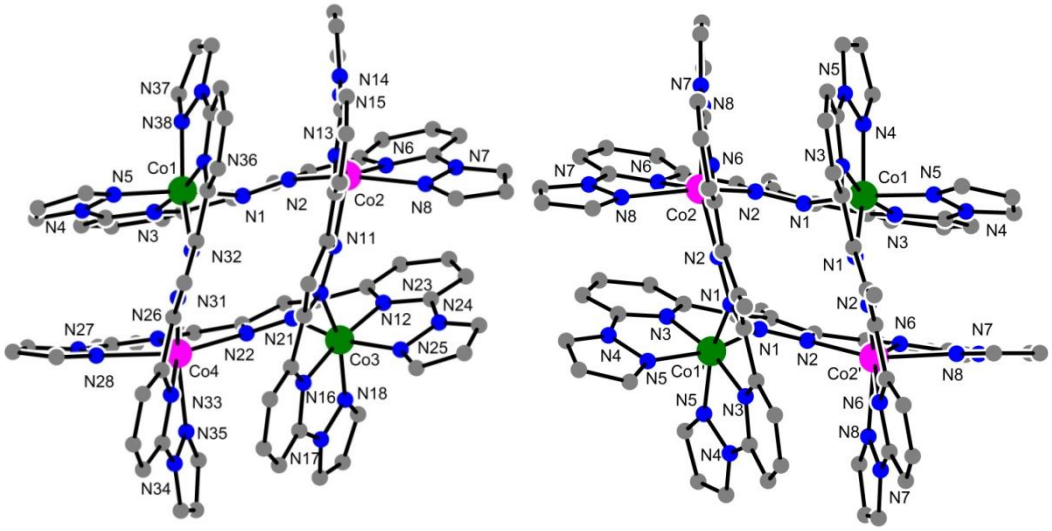

Figure 6.23. Molecular structure of cations $[Co^{II}_2Co^{III}_2L^{Pz}_4]^{6+}$ of [2 × 2] grid complexes **15** (left) and **16** (right) (Co^{II} (pink), Co^{III} (green), hydrogen atoms are not included for simplicity).

The Co−N bond lengths fall into two groups according to the valence of cobalt ion, then could be further divided into three categories depending on the type of donor N atom attached to the cobalt center, with the longest distance between Co^{II} and the side-arm pyrazole moieties. The Co^{II}–N bond lengths of **15** and **16** (2.08 Å to 2.21 Å) are comparable to those found in **11** and **12**, while the Co^{III}–N bond lengths are significantly shorter ranging from 1.87 Å to 1.97 Å. In **16**, metal ions of the same oxidation state are located on the 2-fold rotation axes resulting in a crystallographically imposed D_2 symmetry.[179]

Table 6.6. Mean Co−N Bond Lengths, Continuous Symmetry Measures (CSM) and Bond Valence Sums (BVS) of complexes **15** – **18**.

Complex		d_{mean}/Å	Spin state	$S(O_h)$	S(itp)	BVS[a]
15:$[Co^{II}_2Co^{III}_2L^{Pz}_4](BF_4)_6$	Co^{III}1−N	1.920	LS	1.97	10.77	2.90/3.80
	Co^{II}2−N	2.155	HS	7.94	4.91	1.55
	Co^{III}3−N	1.918	LS	1.86	10.96	2.91/3.82
	Co^{II}4−N	2.148	HS	6.85	5.88	1.58
16:$[Co^{II}_2Co^{III}_2L^{Me\text{-}Pz}_4](BF_4)_6$	Co^{III}1−N	1.944	LS	2.30	10.39	2.72/3.56
	Co^{II}2−N	2.136	HS	7.65	5.02	1.63
18:$[Co^{II}_2Co^{III}_2L^{Py}_4](BF_4)_6$	Co^{III}1−N	1.929	LS	1.75	11.25	2.84/3.72
	Co^{II}2−N	2.119	HS	6.13	6.25	1.52

[a] The BVS values are calculated based on a R_0 value of 1.65 Å for Co−N and 1.75 Å for Co^{III}−N with the formular $s_{ij} = \exp((R_0 - R_{ij})/b)$ with b = 0.37 Å. The larger BVS values correspond to R_0 = 1.75 Å. R_0 values taken from bv 2013.cif available from http://www.iucr.org/resources/data/datasets/nond-vvalence-parameters

To further confirm the oxidation state assignment, bond valence sum (BVS) calculations were carried out for each cobalt atom in mixed-valence grid structure **15** and **16**. With an R_0 of 1.65 Å the BVS values of 2.90 and 2.91 (**15**) and 2.72 (**16**) were obtained which correspond to Co^{III} ion. However, the tabulated R_0 for Co^{III}−N is 1.75 Å, which gives large bond valence sums of 3.80 and 3.81 for **15** and 3.56 for **16**. BVS values for the Co^{II} atoms in **15** and **16** are significantly smaller (**15**: 1.56 and 1.58; **16**: 1.63).[180,181,182] These data clearly indicate the oxidation of two metal atoms upon carrying out a two one-electron oxidations of the starting complexes.

The molecular structure of the mixed-valence species $[Co^{II}_2Co^{III}_2L^{Py}_4](BF_4)_6$ (**18**) are similar to **15** and **16**. The four cobalt ions in the grid are also coplanar and two ligands lie above the Co_4 plane and the others below the plane. The Co−N bond lengths, the adjacent $Co^{II}\cdots Co^{III}$ distances and diagonal separation of the Co ions are shown in Tables 6.4 – 6.5. In the structure of **18**, the average Co−N bond distances

indicate the presence of HS Co^{II} and LS Co^{III} ions. The small octahedral distortion parameters and larger BVS values, further confirm the oxidized Co^{III} ions is in the LS state.

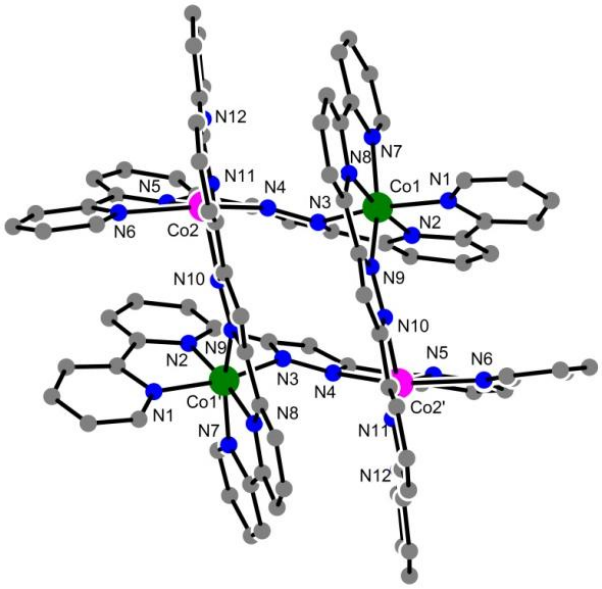

Figure 6.24. Molecular structure of the cation $[Co^{II}_2Co^{III}_2L^{Me\text{-}Pz}_4]^{6+}$ of the [2 × 2] grid complex **16** (Co^{II} (pink), Co^{III} (green), hydrogen atoms are not included for simplicity).

Table 6.7. Selected distances (Å) in complexes **15**, **16**, and **18**.

	15	**16**	**18**
Co^{II}–N	2.080(8) – 2.207(7)	2.085(4) – 2.203(4)	2.052(6) – 2.272(5)
Co^{III}–N	1.871(7) – 1.947(8)	1.901(3) – 1.971(3)	1.872(6) – 1.988(6)
$Co^{II}\cdots Co^{II}$ *diagonal*	6.7972(17)	6.5605(10)	6.869(14)
$Co^{II}\cdots Co^{III}$ *adjacent*	4.460(17) – 4.535(16)	4.374(6)	4.546(13) – 4.614(13)
$Co^{III}\cdots Co^{III}$ *diagonal*	5.871(16)	5.786(7)	6.0343(13)

By comparison with homo-valence [2 × 2] grid structures (**11**, **12** and **14**), the distortion of Co^{II} centers is strongly in mixed-valence [2 × 2] grid structures (**15**, **16** and **18**) according to the values of $S(O_h)$ (Table 6.1 and 6.7), while the three mixed-valence [2 × 2] grid structures show similar structural distortion parameters with each other. In the three compounds, the twisting of the ligand is larger on Co^{III} coordination side than those on Co^{II} corner. The Co^{III}-Co^{II}-Co^{III} and Co^{II}-Co^{III}-Co^{II}

angles are all around 82° and 97°, respectively. The superimposed structures of **15**, **16** and **18** show the ocular and obvious distortion of the grid structures, except for the terminal side-arm groups with different twisting (Figures 6.25 and 6.26).

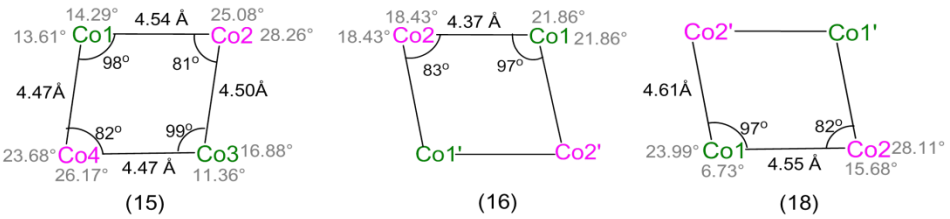

Figure 6.25. Structural comparison of cations $[Co^{II}_2Co^{III}_2L^{Pz}_4]^{6+}$ of **15**, $[Co^{II}_2Co^{III}_2L^{Me\text{-}Pz}]^{6+}$ of **16** and $[Co^{II}_2Co^{III}_2L^{Py}_4]^{4+}$ of **18**. Co···Co distances, Co-Co-Co angle (black) and torsion of the central pyrazole against side-arm pyrazolate and pyridine in same ligands (gray).

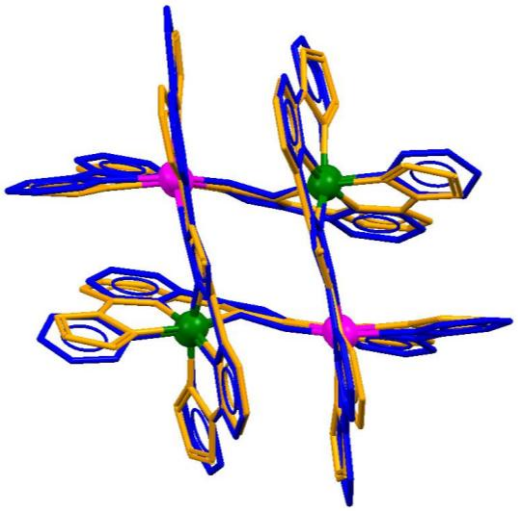

Figure 6.26. Overlay of structures of cations $[Co^{II}_2Co^{III}_2L^{Me\text{-}Pz}]^{6+}$ of **16** (orange) and $[Co^{II}_2Co^{III}_2L^{Py}_4]^{4+}$ of **18** (blue).

Magnetic Properties

The magnetic behavior of mixed-valence grids **15** – **18** are significantly different from the homo-valence grids **11** – **14**, since there is no magnetic exchange shown after replacing two paramagnetic Co^{II} ions with two diamagnetic Co^{III} ions in the tetranuclear structures. Therefore, the magnetic properties of the mixed-valence systems are determined by singe-ion properties of two remaining HS-Co^{II} ions. The direct current (dc) magnetic susceptibilities of **15** – **18** were measured between 2.0

and 210 K (H = 0.5 T), and the results are shown in Figure 6.27 as a plot of $\chi_M T$ versus T. At high temperature (210 K), the $\chi_M T$ values are 5.16 $cm^3mol^{-1}K$ for **15**; 5.87 $cm^3mol^{-1}K$ for **16**; 5.37 $cm^3mol^{-1}K$ for **17** and 5.64 $cm^3mol^{-1}K$ for **18**, where the χ_M is the molar magnetic susceptibility per Co^{II}_2 unit. The values of $\chi_M T$ fall within the range expected for two magnetically isolated HS Co^{II} ions (S = 3/2) in the range of 4.2 – 6.8 $cm^3mol^{-1}K$ (g = 2.0) and no contributions with the two LS Co^{III} ions (S = 0), located at diagonally opposing corners of the rectangular complexes. When the temperature is lowered, the $\chi_M T$ decreases substantially below 100 K to a minimum of 3.64, 4.25, 3.43 and 3.80 $cm^3mol^{-1}K$ for **15** – **18**, respectively, at 2 K.

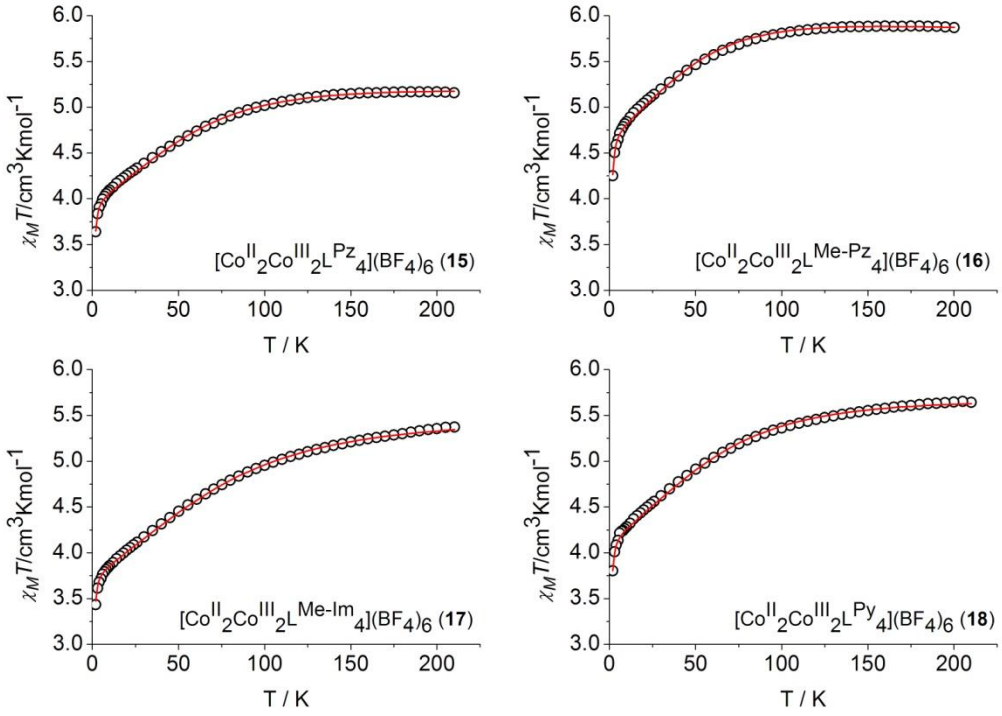

Figure 6.27. $\chi_M T$ vs. T measurement in the temperature range of 2 – 210 K at 0.5 T for crystalline samples of complexes **15** – **18**.

The Co^{III} ions in these grid structures are diamagnetic and exhibit weak exchange coupling interactions. The mixed-valence grid can be, therefore, well approximated as two uncoupled mononuclear HS Co^{II} (S = 3/2) complex (Figure 6.28). The spin Hamiltonian of these compounds has the form given in eq. 2, Where μ_B is the Bohr magneton and D, S, B represent the axial zero-field splitting (ZFS) parameter, the spin,

and magnetic field vectors, respectively. Identical Zeeman splitting and zero-field splitting (in this fit the orthorhombic ZFS parameter E was set to zero) were used:

$$\hat{H} = \mu_B(S_x g_x B_x + S_y g_y B_y + S_z g_z B_z) + D\left[\hat{S}_z^2 - \frac{1}{3}S(S+1)\right] \qquad \text{(eq. 2)}$$

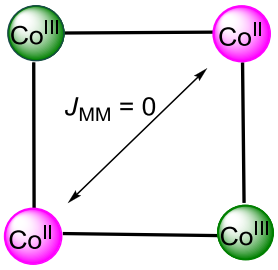

Figure 6.28. Magnetic coupling schemes for two independent coupling constants.

The best fit parameters are $g_x = g_y = 2.25$, $g_z = 2.64$; $D = -81.8$ cm^{-1} for **15**, and $g_x = g_y = 2.17$, $g_z = 2.76$, $D = -77.5$ cm^{-1} for **16**, $g_x = g_y = 2.31$, $g_z = 2.57$; $D = -96.2$ cm^{-1} for **17**, $g_x = g_y = 2.29$, $g_z = 2.70$; $D = -83.7$ cm^{-1} for **18**. Surprisingly, the low temperatures data for compounds **15** – **18** were modeled quite well according to the spin-only Hamiltonian even without the inclusion of intermolecular magnetic interactions. Moreover, the D value is comparable with those of other mononuclear cobalt(II) complexes.[183]

It is worth mentioning that, as the variations of $\chi_M T$ are in general not very sensitive to the sign of D, it is difficult to determine the absolute value of the axial ZFS parameter D only from magnetic susceptibility data derived from measurements on polycrystalline samples. However, a more sensitive probe can be used to determine D by measuring the magnetization at intermediate fields and appropriate low temperatures (M_{mol} vs. $\mu_B B/kT$). Consequently, the variable temperature and variable field (VTVH) magnetization measurements were studied over the temperature range of 0 – 2.0 K and at fields of H = 1, 3, 5 T (Figure 6.29). The M_{mol} vs $\mu_B B/kT$ data at 1.86 K for **15** – **18** show that at 5 T the magnetization is saturated, reaching values of 2.02, 2.07, 1.88 and 2.08 μ_B, respectively. The M_{mol} vs $\mu_B B/kT$ plots for **15** – **18** are not superimposed on one another at different magnetic fields.

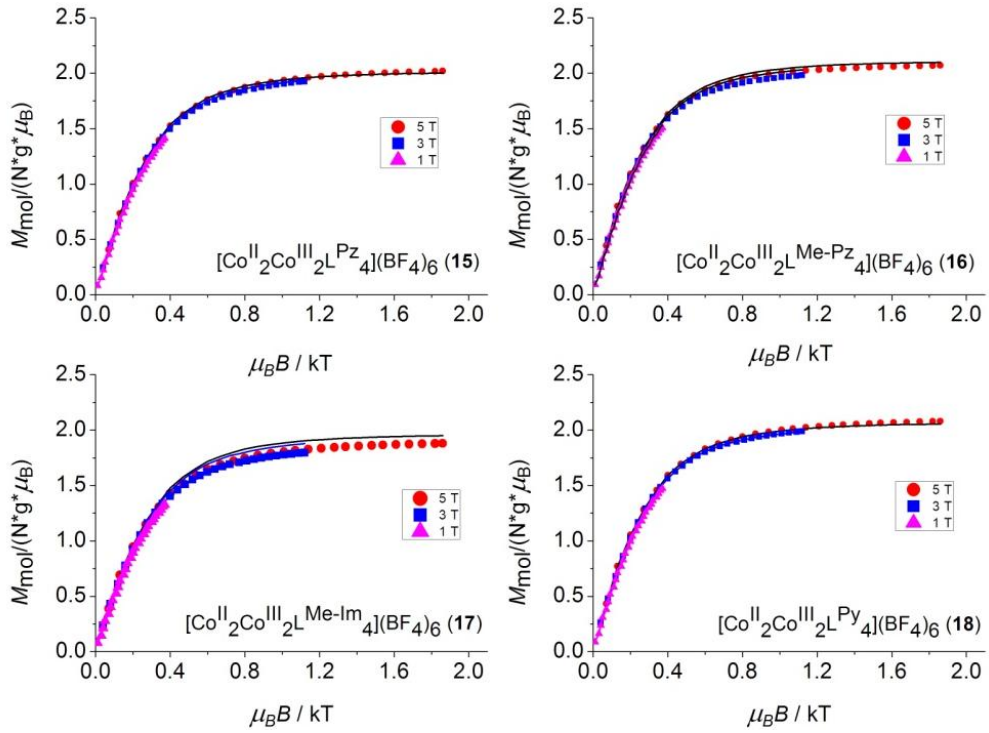

Figure 6.29. Variable temperature/variable field (VTVH) magnetization measurements at fields of 1 T, 3 T and 5 T for crystalline samples of **15** – **18**. The solid lines represent the calculated curve fits.

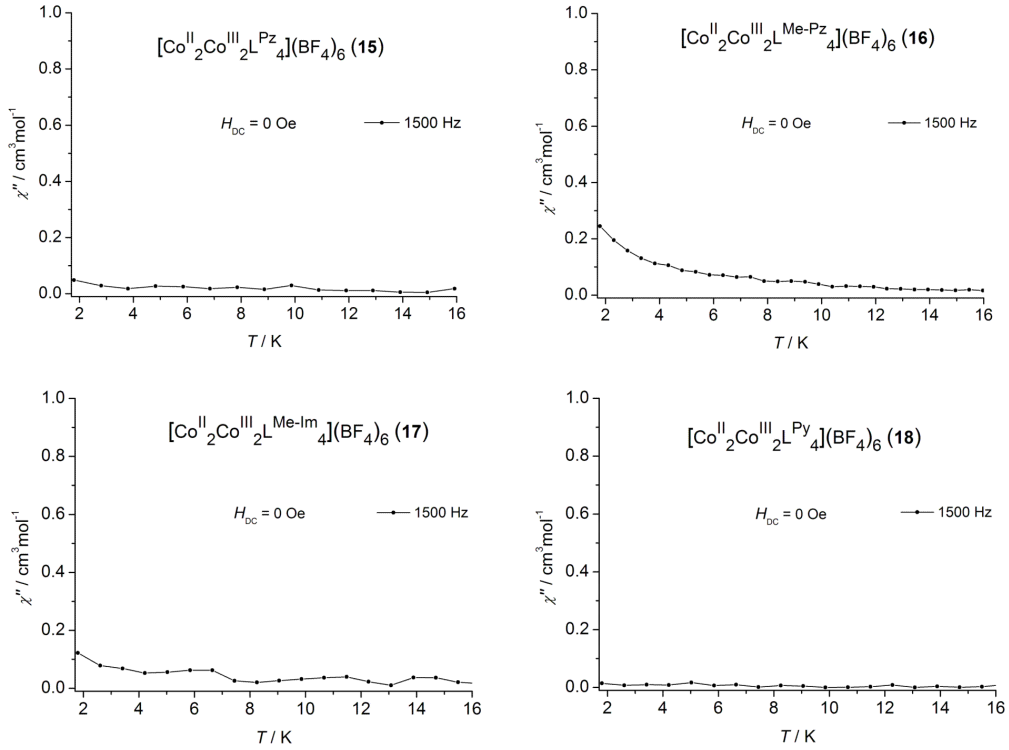

Figure 6.30. Temperature dependence of χ" of **15** – **18** without applied dc field using 1500 Hz ac frequency.

The deviations in magnetization from the saturation value and non-superimposition indicate the presence of strong zero field splitting in these mixed-valent species. These data at different fields supports the magnetic anisotropy, and a fit of the data in all cases **15** – **18** with the spin Hamiltonian given in eq. 2 yielded the *D* values, which agrees well with the calculated fit of the $\chi_M T$ data. It is known that positive *D* values stabilize the ±1/2 ground state and negative *D* values stabilize the ±3/2 ground state. The energy barriers to spin inversion between the +3/2 and –3/2 states are remarkably high ($|2D| \approx 160$ (**15**), 155 (**16**), 190 (**17**), 170 (**18**) for an Orbach process). The reasonably large and negative *D* value leads one to expect that these four mixed-valence [2 × 2] grid compounds **15** – **18** might behave as Single-Molecule Magnets (SMMs).

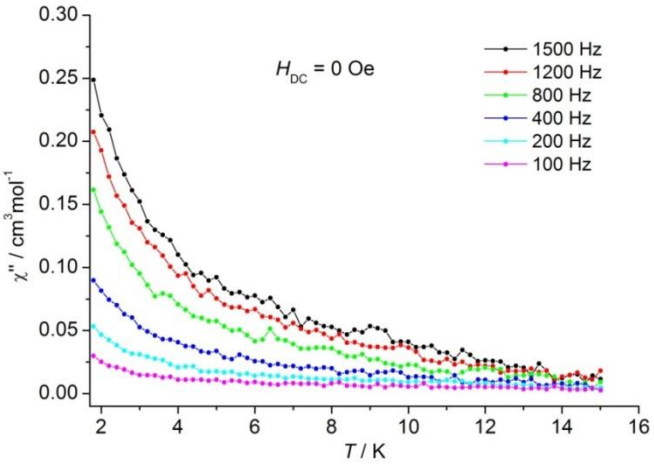

Figure 6.31. Temperature dependence of χ'' of **16** without applied dc field at different ac frequency showing no out-of-phase signals.

The alternating current (ac) magnetic susceptibilities of **15** – **18** were conducted under zero and non-zero applied static fields in the temperature range of 2 – 16 K to further investigate the dynamic magnetic behavior. The ac susceptibility measurements for complexes **15** – **18** with 0 Oe dc field for frequency 1500 Hz of the alternating field were measured over the temperature range of 1.8 – 16 K (Figure 6.30), which reveals the beginning of out-phase (χ") signals. However, no maximum value was observed until the temperature drops to 1.8 K for complexes **15**, **17** and **18**. In particular, compound **16** shows the characteristic increase of the imaginary part of the ac

magnetic susceptibility (χ″) at different frequencies (Figure 6.31).

The dependence of χ'' on the applied dc field strength (H_{dc}) was examined using 1500 Hz AC frequency (Figure 6.32). Increasing the H_{dc} the χ'', the signal rises progressively to reach its maximum value around 2000 Oe for four mixed-valent cobalt complexes. Based on these experiments, this confirms that the SMMs behavior of the four cobalt complexes depends upon the applied dc field. Using the optimal magnetic field H_{dc} = 2000 Oe, frequency dependent maxima of χ″ could then be observed for complexes **15** – **18** (Figure 6.33). The peak temperatures (Tp) in χ'' shift from 2.0 K to 6.8 K for **15**, 2.0 K to 8.8 K for **16**, 2.0 K to 7.6 K for **17** with increasing frequencies from 2 Hz to 1500 Hz. For complex **18**, the peak temperature (Tp) in χ'' shifts from 2.0 K to 4.0 K from 20 Hz to 1500 Hz. The ac magnetic susceptibility data confirms that the mixed-valence [2 × 2] grid complexes **15** – **18** behave as SMMs.

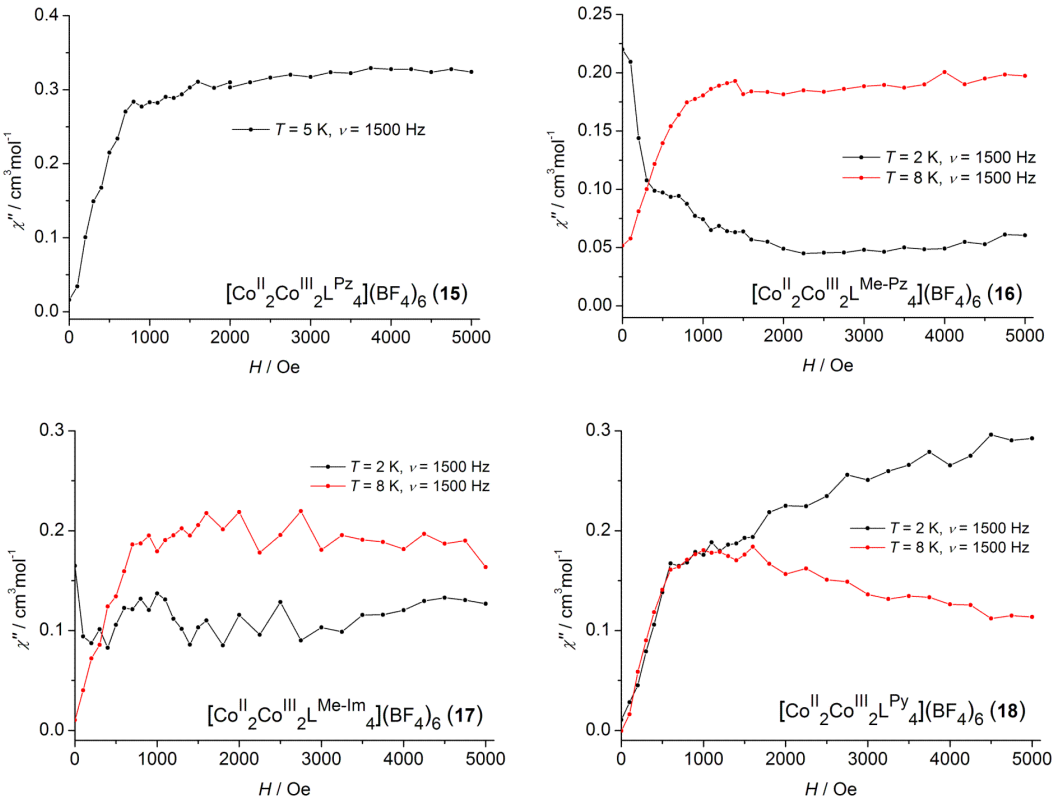

Figure 6.32. Field dependence of χ'' at 5 K for **15**, 5 and 8 K for **16** – **18** using 1500 Hz ac frequency.

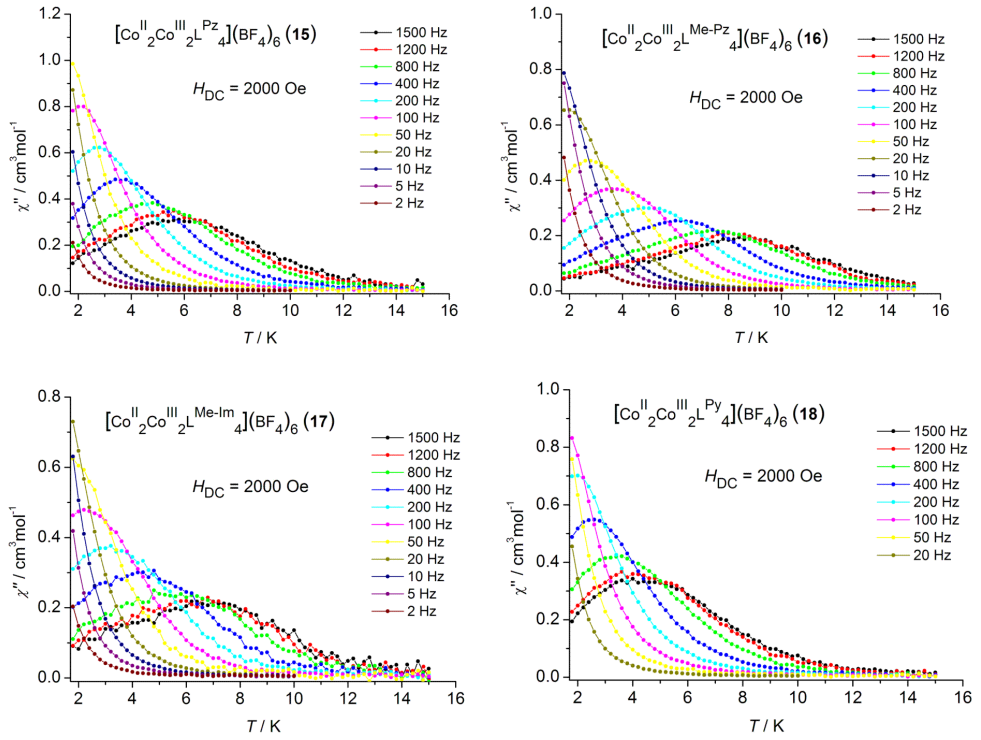

Figure 6.33. Temperature dependence of χ″ of **15** – **18** at various frequency with an applied dc field of H_{dc}= 2000 Oe. The measurements were done between 2.0 and 1500 Hz.

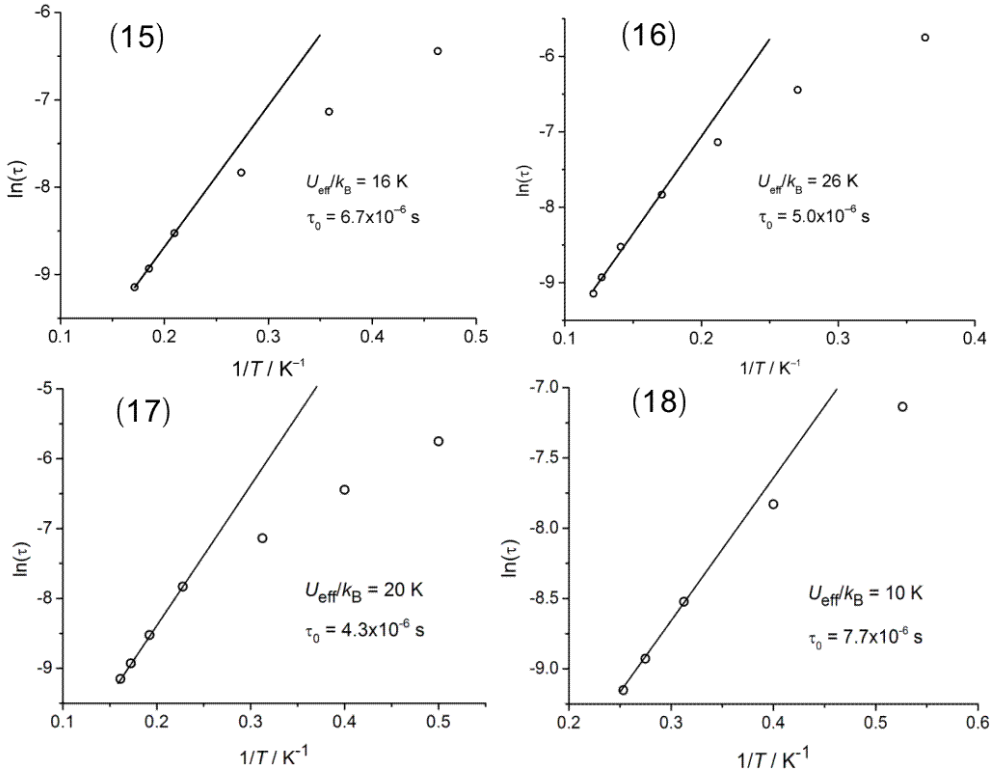

Figure 6.34. Magnetic relaxation time τ versus T^{-1} plots with the calculated straight line for s thermally activated relaxation for **15** – **18** at H_{dc} = 2000 Oe.

Analysis of the temperature dependence of the obtained relaxation times τ according to the Arrhenius law for **15** – **18** (Figure 6.34) given in eq. 3:

$$\tau = \tau_0 \cdot \exp(U_{eff}/k_BT) \text{ (eq. 3)}$$

reveals thermal energy barrier U_{eff}/k_B = 16 K ($\tau_0 = 6.7 \cdot 10^{-6}$ s) for **15**, U_{eff}/k_B = 26 K ($\tau_0 = 5.0 \cdot 10^{-6}$ s) for **16**, U_{eff}/k_B = 20 K ($\tau_0 = 4.3 \cdot 10^{-6}$ s) for **17** and U_{eff}/k_B = 10 K ($\tau_0 = 7.7 \cdot 10^{-6}$ s) for **18**. The τ_0 values observed for **15** – **18** are similar to those found for Co^{II} Single Ion Magnets (SIMs) and the U_{eff}/k_B values fall well within the range of typical Co^{II} SMMs (8.6 – 89 K). [184,185]

Although many four- and penta-coordinated Co^{II} complexes with slow relaxation are known, the six-coordinated SIMs (single ion magnets) are in quite rare.[186] In order to understand the relationship between the coordination geometry and magnetic anisotropy *D* in 3*d*-transition metal complexes, a theoretical study using CASSCF calculations have been performed. The *D* value varies with the number of 3*d*-electrons, the coordination number and the symmetry around the metal ion. It is known that for six-coordinated Co^{II} complexes, large negative *D* values are typicaly associated for molecules with a trigonal prism geometry (D^{3h}), while large positive *D* values are preferable for molecules in an octahedral environment (O_h). Indeed, experimentally observed *D* values in distorted octahedral complexes are primarly positive, [187] whereas the trigonal prismatic geometry leads to large negative anisotropy.[186,188] The magnitude of *D* in the trigonal prismatic complexes depends on the distortion from ideal D_{3h} symmetry. The angles α, β, θ, ϕ, and γ (Figure 6.35) describe the distortion in a quantitative way.[188a,189] The values α and β can be obtained from the crystal structures. The parameters θ and ϕ are calculated from the average values of α and β using (eq. 4) and (eq. 5)

$$\cos\theta = \sqrt{\frac{1+2\cos\alpha}{3}} \quad \text{(eq. 4)}$$

$$\cos\frac{\phi}{2} = \sqrt{\frac{3(1+\cos\beta)}{4(1-\cos\alpha)}} \quad \text{(eq. 5)}$$

The angle θ describes the trigonal compression (θ > 54.74°) or elongation (θ < 54.74°). The angle ϕ reflects the rotation of the base triangles to each other, *i.e.* ϕ = 0° for the trigonal prism and ϕ = 60° for an octahedron environment. The angle γ connects both parameters θ and ϕ (eq. 6) and describes the so-called "pitch", defined as the dihedral angle between the plane perpendicular to the C_3 axis and the N−Co−N plane involving nitrogen atoms that form the β angle.

$$\cos\gamma = \frac{\sin\frac{\phi}{2}}{\sqrt{\sin^2\frac{\phi}{2} + \cot^2\theta}} \quad \text{(eq. 6)}$$

The largest pitch of γ = 90° is expected for ϕ = 0° and it decreases with larger ϕ or θ (for the case $\phi \neq$ 0°) values. The small γ pitch, large ϕ and θ distorts the Co^{II} ions from an ideal D_{3h} symmetry.

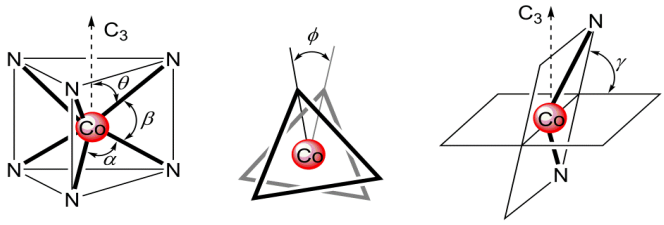

Figure 6.35. Definition of the angular parameters α, β, θ, ϕ and γ.

Table 6.8 summarizes these angular parameters of HS-Co^{II} ions in **15**, **16** and **18**. Firstly, by comparison with **11** – **14**, the $S(O_h)$ values of the HS-Co^{II} ions in **15**, **16** and **18** increase and at the same time S(itp) values decrease during the oxidation processes according to data in Table 6.2 and 6.4 and as shown in Figure 6.36. The result indicates the transformation of the Co^{II} coordination geometry towards a trigonal prism from the homo-valence to mixed-valence [2 × 2] grid structures.

Table 6.8. Selected angular parameters of HS-Co^{II} ions in **15**, **16** and **18** (in °)

Complex	Center	α	β	θ	ϕ	γ
15	$Co^{II}2$	84.3	81.7	50.8	25.1	75.1
15	$Co^{II}4$	85.2	81.7	51.4	29.0	72.6
16	$Co^{II}2$	83.8	82.3	50.4	24.6	75.5
18	$Co^{II}2$	85.4	81.8	52.5	30.1	71.3

It has recently been discussed for [2×2] Fe^{II}_4 grid complexes based on the 3,5-bis{6-(2,2'-bipyridyl)}pyrazolate ligand that a high degree of cooperativity for multi-step SCO transitions is imparted by strain effects of the rigid bridging ligands and strong elastic coupling of the four corners of the grid.[110,190] In particular, structural changes at one corner, which in case of the [2×2] Fe^{II}_4 grids are induced by SCO between HS-Fe^{II} and LS-Fe^{II} states, propagates into significant structural distortion not only at the neighboring sites, but moreover at the opposite corner, favoring a second SCO to occur at the *trans* position.[110,190] Similar ligand strain induced cooperativity favoring mixed HS/LS configurations has also been reported for dimeric and polymeric SCO systems.[191] In the case of the present Co_4 grids, twofold oxidation leads to strong structural changes at the two Co^{III} corners which translate into a more favorable geometry for SMM behavior at the neighboring Co^{II} sites, mediated by elastic communication via the bridging ligands (Figure 6.36).

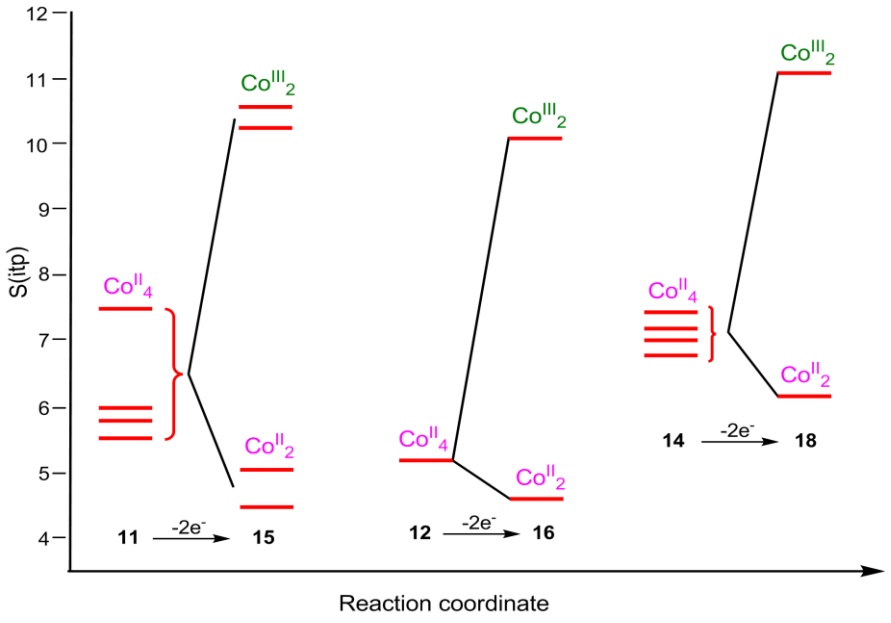

Figure 6.36. Graphical representation of the change of the *S*(itp) values for **$[Co^{II}_4L_4]^{4+}$** to **$[Co^{II}_2Co^{III}_2L_4]^{6+}$** upon two-electrons oxidation.

The observed structural parameters (γ) and energy barriers (U_{eff}/k_B) of **15**, **16** and **18** fit very well to the newly obtained correlation, where the relatively small U_{eff}/k_B values correspond to the small pitches γ, *i.e.* the literature reported energy barriers of 41 K to 54 K for pitches of 73.0° to 75.5°.

The U_{eff}/k_B values are found to be much higher (125 to 163 K) for only a minor in the pitch form 78° to 79°, indicating the high sensitivity of the energy barriers to the structural changes. The higher U_{eff}/k_B value in **18** can be attributed to the slightly higher pitch than in **15** and **16**, although the influence of the other factors, *e.g.* the asymmetry in the distortion of the trigonal prism, cannot be fully excluded.

6.2.3. Solution State Investigations

Mass Spectrometry

The four mixed-valence [2 × 2] Co_4 grid complexes **15** – **18** have been characterized by ESI mass spectrometry in MeCN solution. ESI mass spectrometry of these doubly oxidized complexes show some fragments characteristic for the different charged ions, deriving from $[Co^{II}_3Co^{III}L_4]^{5+}$ in combinations with different counter ions BF_4^- or F^-, which arise from the reduction of $[Co^{II}_2Co^{III}_2L_4]^{6+}$. The peak of the starting material homo-valence $[Co^{II}_4L_4]^{4+}$ is also observed as well. The results suggest the doubly oxidized mixed-valence [2 × 2] Co_4 grid species could be reduced during the ESI mass spectrometry measurement in solution.

For example, the ESI mass spectrum of the molecule $[Co^{II}_2Co^{III}_2L^{Py}_4](BF_4)_6$ (**18**) can be used to illustrate the change of the mixed-valence species during the ESI mass spectrometry measurement. As Figure 6.37 shown, peaks at m/z = 347.5 $[Co^{II}_3Co^{III}L^{Py}_4]^{5+}$, 443.6.4 $[Co^{III}_2L^{Py}_2(F)_2]^{2+}$, 636.8 $[Co^{II}_3Co^{III}L^{Py}_4(BF_4)_2]^{3+}$ are observed. These $[Co^{II}_3Co^{III}]$ species presumably arise by the reduction of the $[Co^{II}_2Co^{III}_2]$ species in mass spectrometry, and a similar phenomenon has been reported in our previous work on the di-oxidized mixed-valence iron complex. In addition, the main peak of the spectrum of $[Co^{II}_4L^{Py}_4](BF_4)_4$ (**14**) is also observed here (m/z = 434).

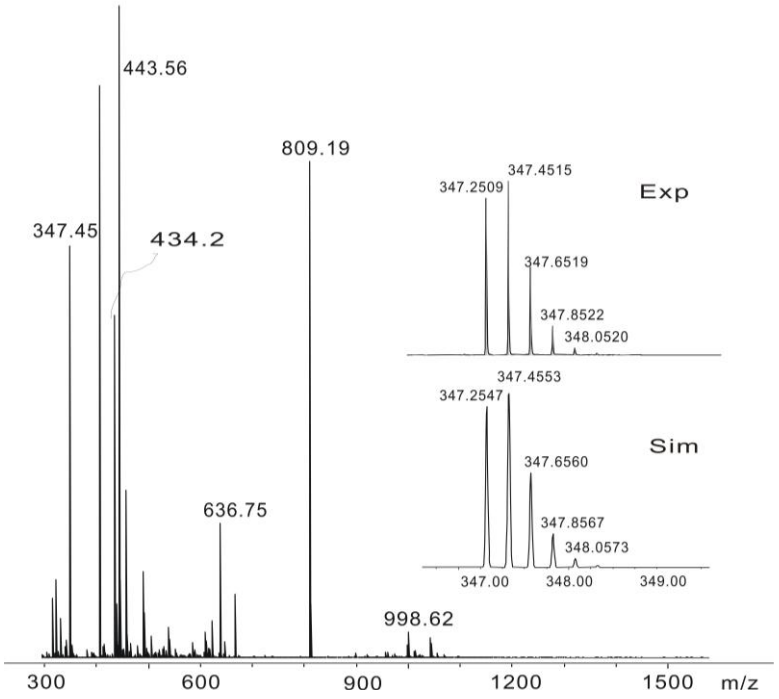

Figure 6.37. ESI-MS (MeCN) of $[Co^{II}_2Co^{III}_2L^{Py}_4](BF_4)_6$ (**18**); (inset) experimental (upper) and simulated (lower) isotopic distribution pattern for the peak pattern around m/z = 347.5 characteristic for the $[Co^{II}_3\,Co^{III}L^{Py}_4]^{5+}$ ion.

NMR Spectroscopy

The redox processes appears to change the spin states of the cobalt centers and have a profound influence on the magnetic properties of the grid complexes according to the solid state structure and magnetic susceptibility data. Co(III) ion possesses a d^6 electron configuration and within O_h point group, this corresponds to HS $t_{2g}^4e_g^2$ and LS $t_{2g}^6e_g^0$ configuration. In the mixed-valence [2 × 2] grid structure, two Co^{II} ions are remain unchanged in the HS state while the remaining Co^{II} ions are oxidized to LS Co^{III} ions, which are confirmed by the magnetic measurement. The LS Co^{III} complexes are diamagnetic and therefore can be easily characterized by ^{1}H NMR spectra.[192] Consequently, the change of the magnetic features can also be investigated in solution by means of NMR spectroscopy.

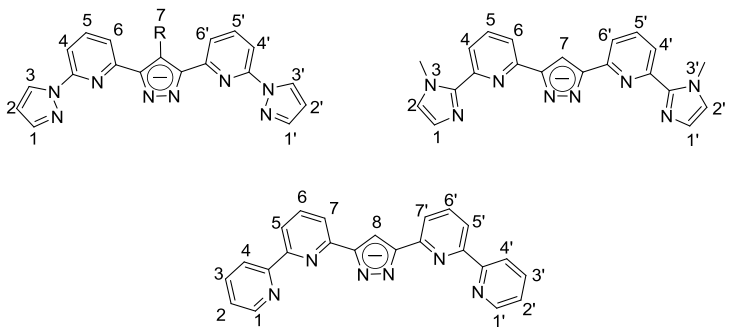

Figure 6.38. Numbering scheme for NMR assignments of complexes **15** – **18**.

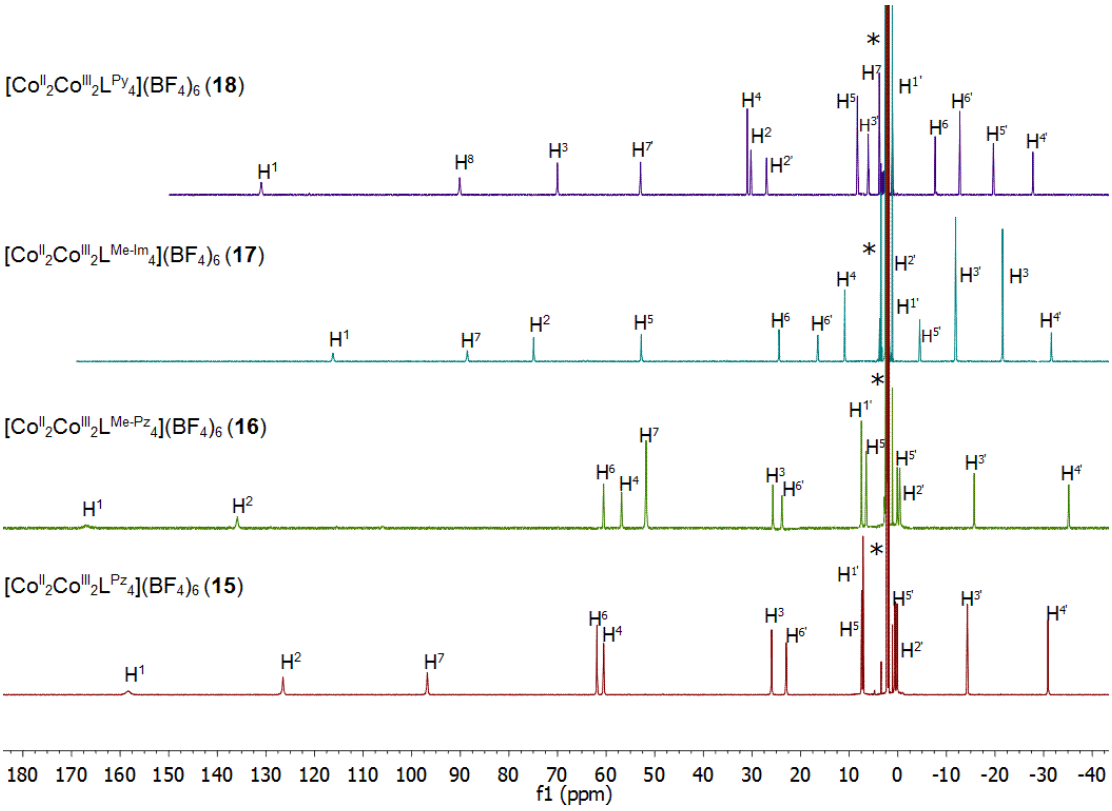

Figure 6.39. ^{1}H NMR spectra (500 MHz, CD_3CN, 298 K) of complexes **15** – **18** in the range from – 40.0 to 180 ppm.

The ^{1}H NMR spectra of mixed-valence grids **15** – **18** display several remarkable features consistent with the proposed mixed-valence species with HS Co^{II} and LS Co^{III} ions (Figure 6.39). Firstly, the change from a paramagnetically shifted ^{1}H NMR spectrum to a spectrum with aromatic signals between 10 and 0 ppm confirmed the partial change of cobalt ion from a HS d^7 to LS d^6 configuration. Secondly the total number of resonances has doubled, compared with those found in ^{1}H NMR spectra of the homo-valence grid complexes. Then all proton resonances of the

pyrazolate-bridged ligand were observed and they exhibited the expected shift and coupling. These signals could be divided into two sets that can be attributed to protons adjacent to the paramagnetic HS Co^{II} and diamagnetic LS Co^{III} sites, respectively, and are assigned using a combination of integrals, ^{1}H-^{1}H COSY experiments and the comparison with the fully assigned spectra of homo-valence systems **11** – **14**.

The ^{1}H NMR spectrum of $[Co^{II}_{2}Co^{III}_{2}L^{Pz}_{4}](BF_4)_6$ (**15**) displays thirteen singlets each with an integral of one spread from 160 ppm downfield to –30 ppm upfield (Figure 10.67). A detailed analysis of two-dimensional homonuclear ^{1}H-^{1}H COSY correlation spectrum allows the complete assignment of all the signals (Figure 6.40).

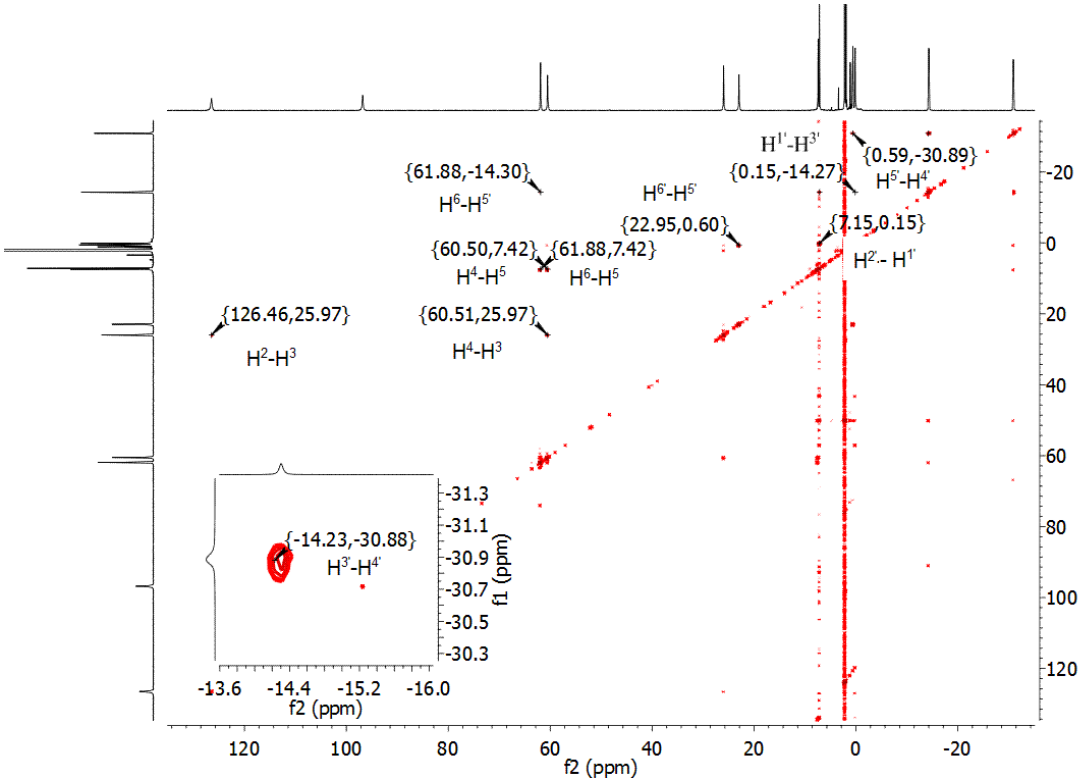

Figure 6.40. ^{1}H-^{1}H COSY spectrum (CD_3CN, 298 K) of $[Co^{II}_{2}Co^{III}_{2}L^{Pz}_{4}](BF_4)_6$ (**15**).

The six proton resonances surrounding the paramagnetic Co^{II} center are sharp and paramagnetically shifted up to 160 ppm as those in ^{1}H NMR spectrum of **11** due to the paramagnetic Co^{II} ion on the local magnetic field. In contrast, the other six peaks close to the Co^{III} site occur in the "diamagnetic region –30 – 20 ppm" at δ = –30.9 ($H^{4'}$), –15.79 ($H^{3'}$), 0.2 ($H^{1'}$), 0.6 ($H^{5'}$), 7.2 ($H^{2'}$) and 23.0 ppm ($H^{6'}$) according to

the ^{1}H-^{1}H COSY spectrum. These protons belong to diamagnetic LS Co^{III} ion coordination sphere, although the neighboring paramagnetic Co^{II} center clearly affects their chemical shifts. Interestingly, the distinct signal of the proton H^{7} bound to the 4-position of the central pyrazole resonates at δ = 96.9 ppm in **15**, which represents a shift to higher field by 91.5 ppm from δ = 188.4 ppm in the ^{1}H NMR spectrum of **11**, indicating that an additive influence of the Co^{II} ions on the isortopic shift of the proton that is located at equal distance from both metals.

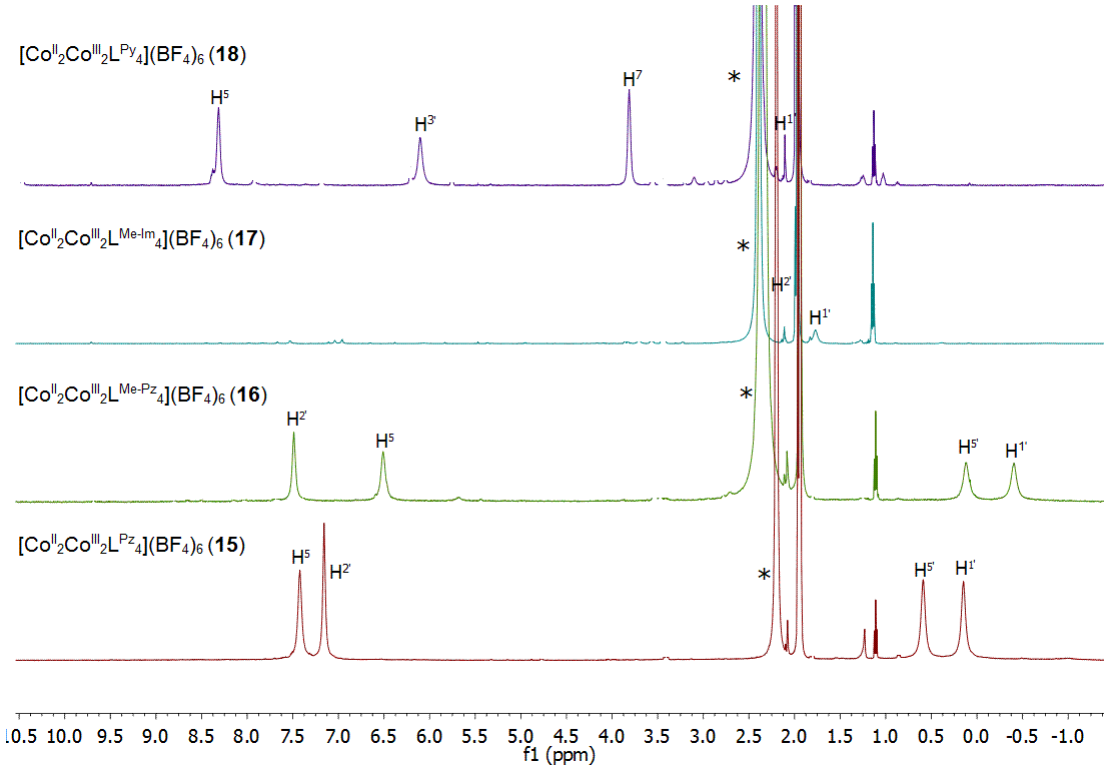

Figure 6.41. ^{1}H NMR spectra (500 MHz, CD_3CN, 298 K) of complexes **15** – **18** in the range of –1.0 – 10 ppm(*MeCN).

In the case of **15**, eighteen signals are observed in the range of 14 to 950 ppm, which arise from eighteen of the nineteen C atoms of the grid molecule as depicted in Figure 6.42. One signal was not detected, presumably due to its close vicinity to the paramagnetic HS-Co^{II} ion. The assignment of these carbon resonances is more complicated. Twelve resonances can be assigned to the CH groups by their $^{1}J_{CH}$ coupling derived from doublets in the ^{1}H-^{13}C HMQC spectra (Figure 6.43 and 6.44); the other six resonances represent quarternary ^{13}C nuclei without $^{1}J_{CH}$ coupling.

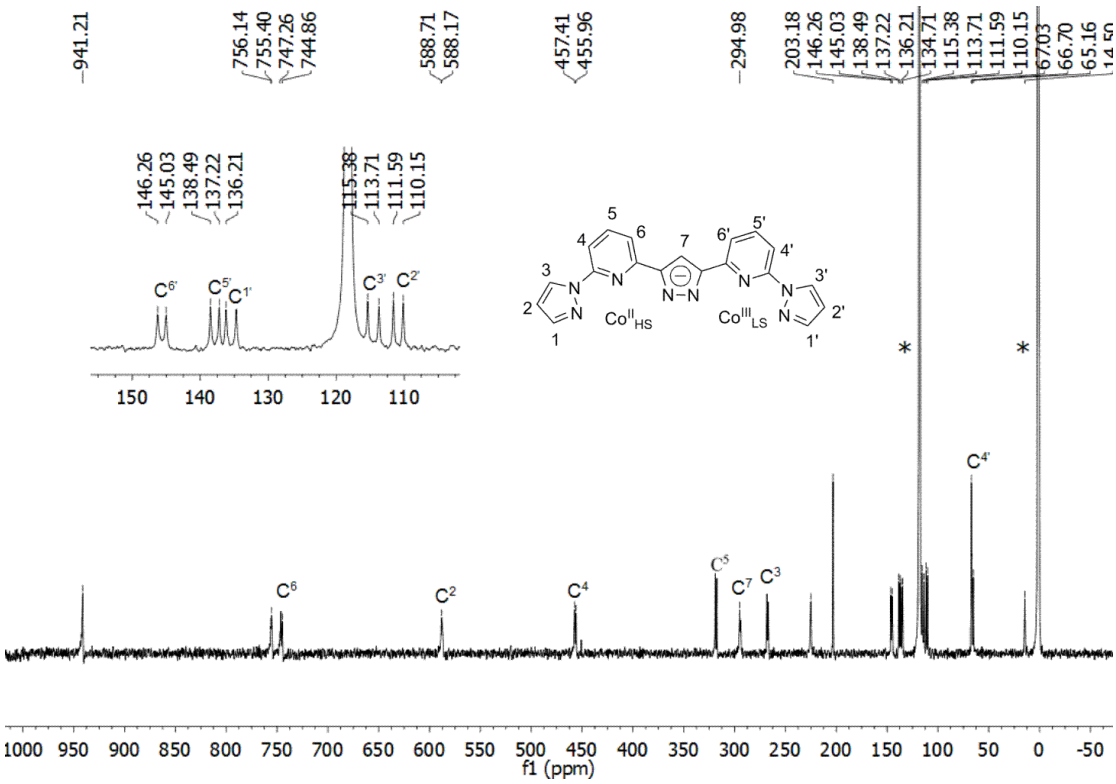

Figure 6.42. ^{13}C NMR spectrum (125 MHz, CD_3CN, 298 K) of $[Co^{II}_2Co^{III}_2L^{Pz}_4](BF_4)_6$ (**15**).

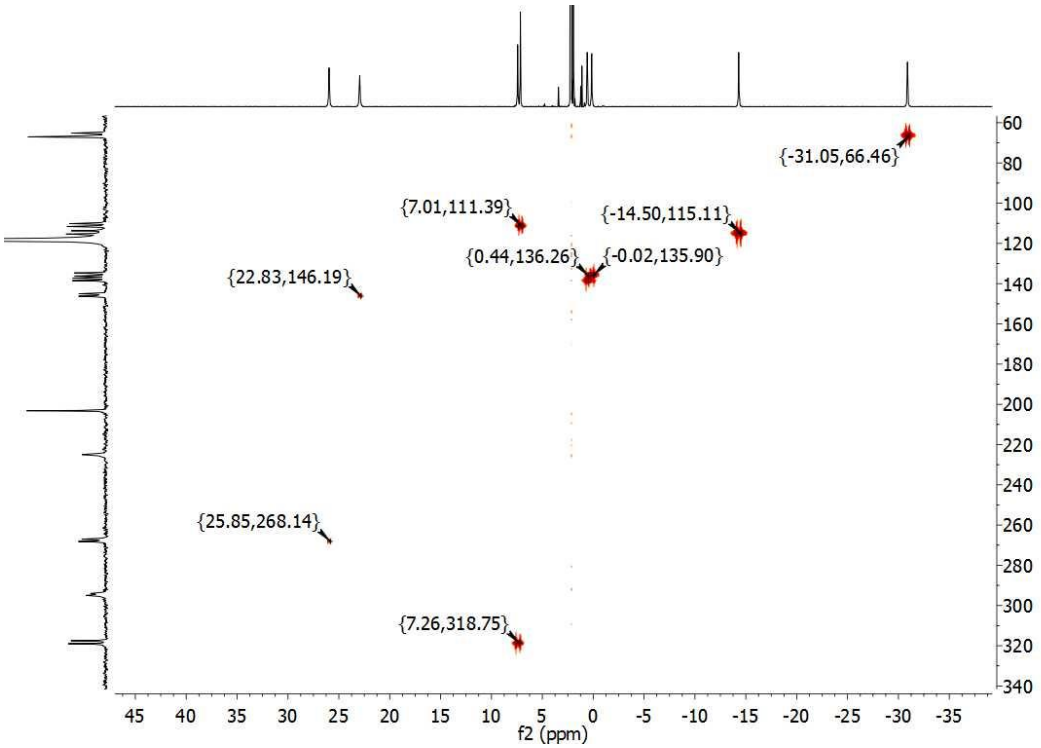

Figure 6.43. ^{1}H-^{13}C HMQC spectrum (298 K) of $[Co^{II}_2Co^{III}_2L^{Pz}_4](BF_4)_6$ (**15**) in CD_3CN (^{1}H: –35 to 45 ppm; ^{13}C: 60 to 340 ppm).

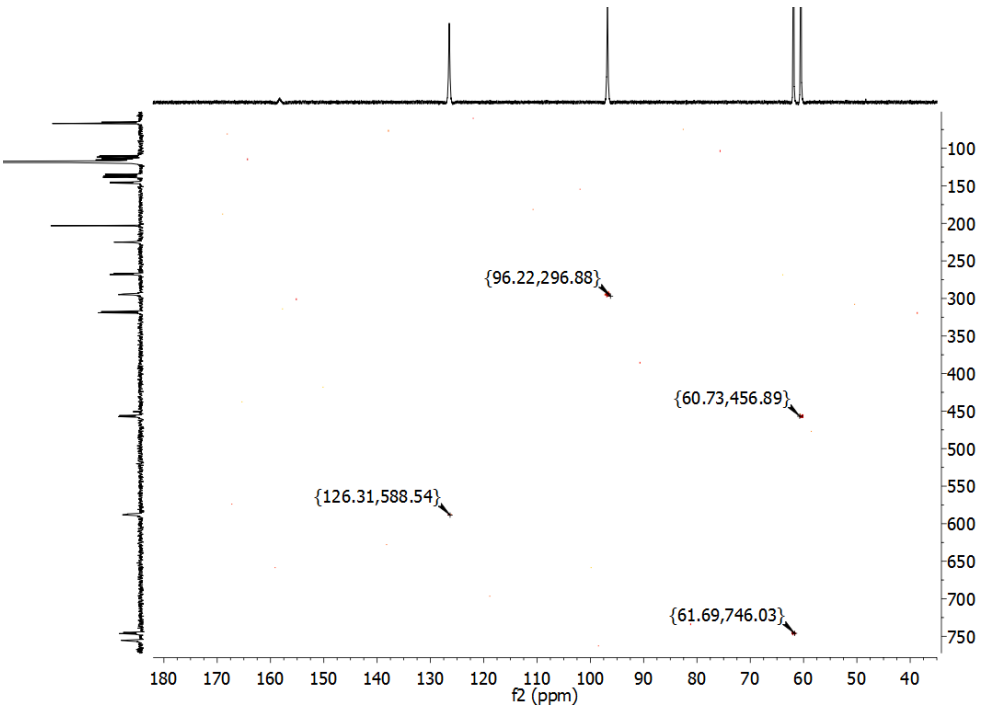

Figure 6.44. ^{1}H-^{13}C HMQC spectrum (CD_3CN, 298 K) of $[Co^{II}_2Co^{III}_2L^{Pz}_4](BF_4)_6$ (**15**) (^{1}H: 40 to 180 ppm; ^{13}C: 100 to 750 ppm).

Mixed-valence complexes $[Co^{II}_2Co^{III}_2L^{Me\text{-}Pz}_4](BF_4)_6$ (**16**), $[Co^{II}_2Co^{III}_2L^{Me\text{-}Im}_4](BF_4)_6$ (**17**) and $[Co^{II}_2Co^{III}_2L^{Py}_4](BF_4)_6$ (**18**) give similar ^{1}H and ^{13}C NMR spectra and signals are assigned based on ^{1}H-^{1}H COSY and ^{1}H-^{13}C HMQC spectra (Figures 10.64 – 10.78) as well as comparison with the spectra of homo-valence compounds **12** – **14** (Tables 6.3 and 6.4).

Electrochemistry

Redox properties of mixed-valence $[Co^{II}_2Co^{III}_2L_4]^{6+}$ grids (**15** – **18**) were investigated by CV in MeCN solution. These four grid compounds showed a set of cathodic processes in the range from –2.00 to –2.50 V (*vs.* Fc/Fc^{+}) similar to the reduction steps found for homo-valence grids (**11** – **14**). The $Co^{III} \rightarrow Co^{II}$ reduction processes are identified by broad, electrochemically irreversible waves with peak potentials E_{pc} in the range of 0.0 V – –1.20 V for **15** and **16** (Figure 6.45), and 0.0 V – –1.80 V for **17** and **18** (Figures 6.46 and 6.47).

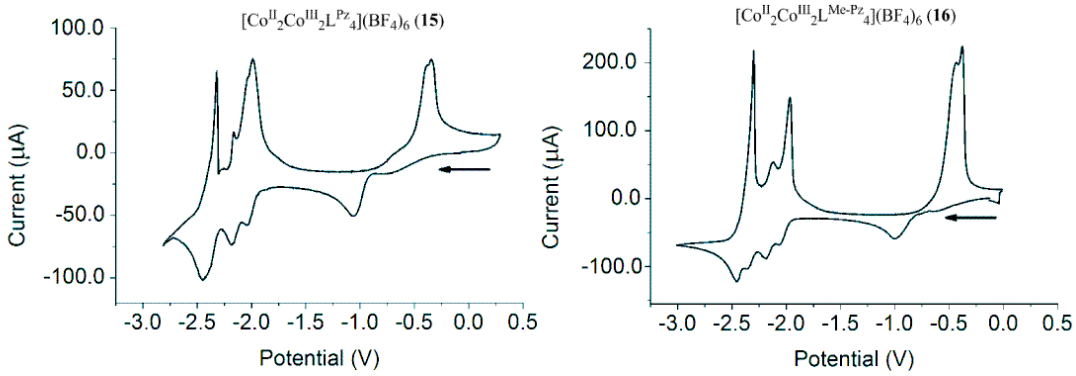

Figure 6.45. Cyclic voltammograms of $[Co^{II}_2Co^{III}_2L^{Pz}_4](BF_4)_6$ (**15**) and $[Co^{II}_2Co^{III}_2L^{Me\text{-}Pz}_4](BF_4)_6$ (**16**) in MeCN/0.1 M NBu_4PF_6 as an electrolyte at a scan rate of 0.1 V s^{-1} vs. Fc/Fc^+.

It is of interest to note the evolution of color for compounds **15** – **18** during the electrochemical studies: the olive-green color of the solutions of the oxidized species $[Co^{II}_2Co^{III}_2L_4]^{6+}$ gradually changed back to the orange color of the starting materials $[Co^{II}_4L_4]^{4+}$ during several cycles of cathodic reduction. Concomitantly the two waves of the $Co^{III} \rightarrow Co^{II}$ reductions disappeared while new broad, electrochemically irreversible waves reappeared at the same anodic potential seen or the non-oxidized Co^{II}_4 grid complexes. These results indicate that the redox interconversion between $[Co^{II}_4L_4]^{4+}$ and $[Co^{II}_2Co^{III}_2L_4]^{6+}$ grids is chemically reversible despite the sluggish electron transfer kinetics.

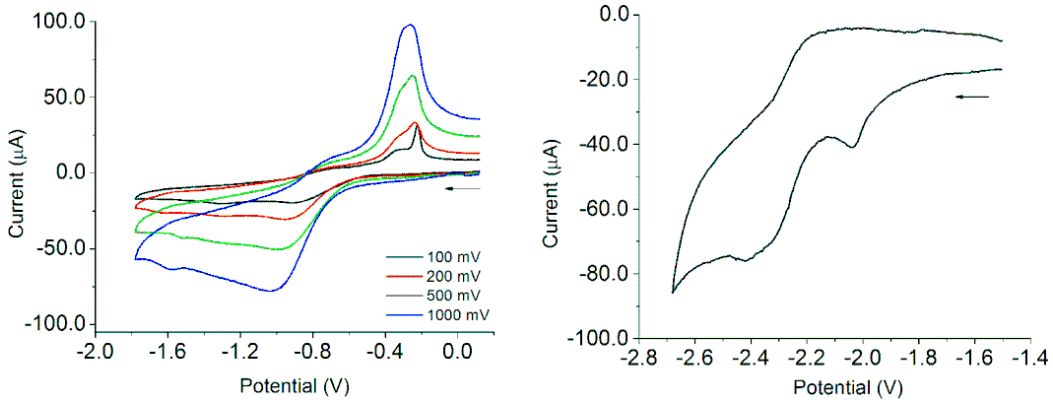

Figure 6.46. Cyclic voltammogram of $[Co^{II}_2Co^{III}_2L^{Me\text{-}Im}_4](BF_4)_6$ (**17**) in MeCN/0.1 M NBu_4PF_6 as an electrolyte at different potential range of 0 – –2.0 V (left) and –1.4 – –2.8 V (right) vs. Fc/Fc^+.

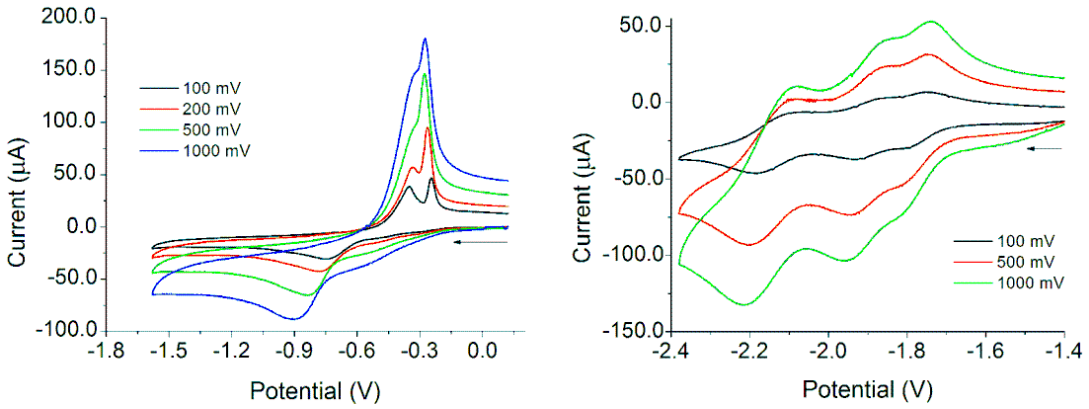

Figure 6.47. Cyclic voltammogram of $[Co^{II}_2Co^{III}_2L^{Py}_4](BF_4)_6$ (**18**) in MeCN/0.1 M Bu_4NPF_6 as an electrolyte at different potential range of 0 – –1.8 V (left) and –1.4 – –2.4 V (right) vs. Fc/Fc^+.

UV/Vis Spectroscopy and Spectroelectrochemistry

The investigations of the spectroscopic property of Co^{II}_4 complexes **11** – **14** were carried out in MeCN in the range of 200 – 1200 nm (Figure 6.48). All compounds **11** – **14** show two absorption bands in the visible region at 434 nm (ε = 478 L mol^{-1} m^{-1}) / 529 nm (ε = 128 L mol^{-1} cm^{-1}) for **11**, 438 nm (ε = 457 L $mol^{-1}\cdot cm^{-1}$) / 538 nm (ε = 123 L $mol^{-1}\cdot cm^{-1}$) for **12**, 440 nm (ε = 450 L $mol^{-1}\cdot cm^{-1}$) / 553 nm (ε = 121 L $mol^{-1}\cdot cm^{-1}$) for **13** and 490 nm (L $mol^{-1}\cdot cm^{-1}$) / 560 nm (ε = 120 $M^{-1}\cdot cm^{-1}$) for **14** detectable as shoulders in the UV/Vis spectra. Both bands are tentatively assigned to metal-to-ligand charge transfer (MLCT) transitions[193]. The position of these bands of **11** – **14** are only slightly influenced by the methyl substituents at the backbone of the bridging ligand and the different heterocyclic moieties as side-arm units.

UV/Vis spectroelectrochemical measurements were performed for **11**, **12** and **13** in MeCN / 0.1 M Bu_4NPF_6 at room temperature at an applied potential of 1.10 V, 1.30 V and 1.2 V, respectively. Upon two-electron oxidation to **15** – **17**, both bands from the starting material grow in intensity and shift slightly to 409 nm (ε = 1780 L $mol^{-1}\cdot cm^{-1}$) and 613 nm (ε = 301 L $mol^{-1}\cdot cm^{-1}$) for **15**, 412 nm (ε = 1758 L mol^{-1} cm^{-1}) and 619 nm (ε = 306 L mol^{-1} cm^{-1}) for **16**, and 426 nm (ε = 1702 L mol^{-1} cm^{-1}) and 606 nm (ε = 280 L mol^{-1} cm^{-1}) for **17**. For all mixed-valence cobalt complexes, one band with higher energy is assigned to ligand-to-metal charge transfer (LMCT) transitions involving the Co^{III} ions and another is likely originating from IVCT

transition. All complexes show a medium degree of electronic coupling and were assigned to class II by analysis of the IVCT bands and by comparison with literature data. For example the complex **15** shows a low intensity IVCT band ($\Delta\nu_{1/2}$ = 4320 cm^{-1}, ε = 301 L mol^{-1} cm^{-1}) with a maximum at 16008 cm^{-1}. From the experimental data, a coupling constant (H_{ab}) of 4421.8 cm^{-1} was determined. While in the case of **16**, the coupling constant H_{ab} was determined to be 4416.9 cm^{-1}. In general, a stronger electronic coupling was found for electron donating substituents.[194]

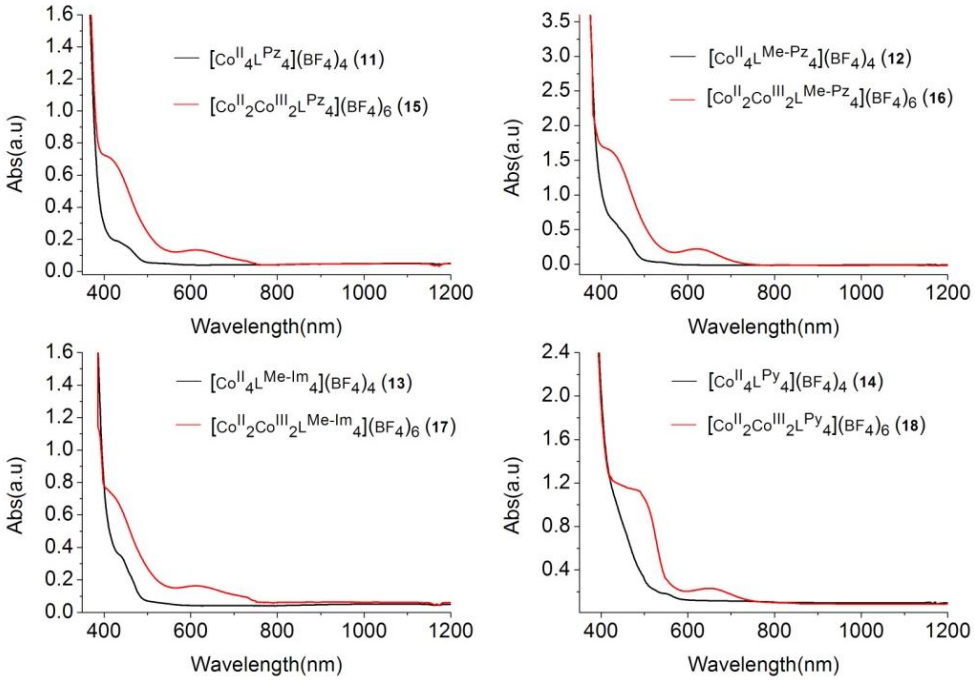

Figure 6.48. UV/vis spectra of homo-valence grids $[Co^{II}_4L^{Pz}_4](BF_4)_4$ (**11**), $[Co^{II}_4L^{Me\text{-}Pz}_4](BF_4)_4$ (**12**), $[Co^{II}_4L^{Me\text{-}Im}_4](BF_4)_4$ (**13**), $[Co^{II}_4L^{Pz}_4](BF_4)_4$ (**14**) (black) and $[Co^{II}_2Co^{III}_2L^{Pz}_4](BF_4)_6$ (**15**), $[Co^{II}_2Co^{III}_2L^{Me\text{-}Pz}_4](BF_4)_6$ (**16**), $[Co^{II}_2Co^{III}_2L^{Me\text{-}Im}_4](BF_4)_6$ (**17**), $[Co^{II}_4L^{Py}_4](BF_4)_6$ (**18**) (red) in MeCN solution.

The UV/Vis absorption spectra (200 – 1200 nm) of **11** – **18** recorded in MeCN confirmed the change of related bands in the low-energy range above 400 nm during the oxidation processes (Figure 6.50). The room temperature solid-state absorption spectra of **11**, **12**, **15** and **16** are comparable with those obtained from solution samples, indicated by the same absorption maxima in the UV/Vis region (Figure 6.51). Thus, the species are unaltered in solution and in the solid state.

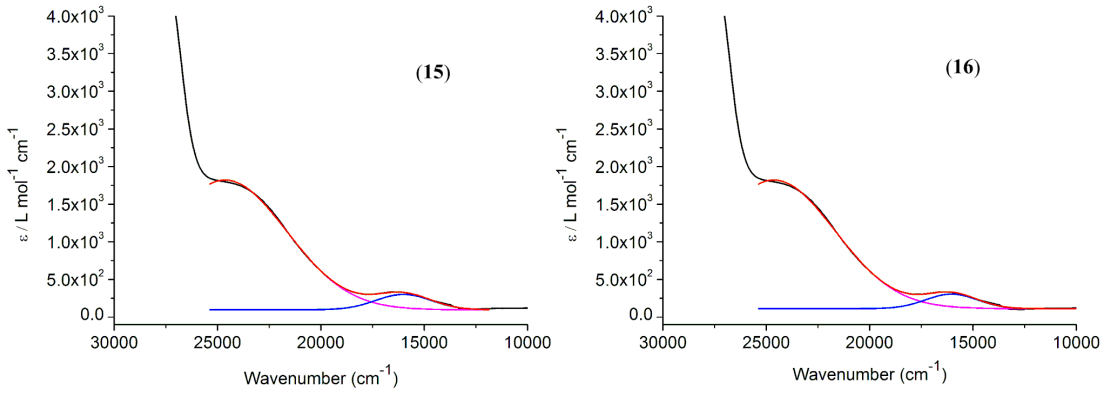

Figure 6.49. Analysis of the IVCT band of $[Co^{II}_2Co^{III}_2L^{Pz}_4](BF_4)_6$ (**15**) and $[Co^{II}_2Co^{III}_2L^{Me\text{-}Pz}_4](BF_4)_6$ (**16**) in MeCN. The experimental spectra of $Co^{II}_2Co^{III}_2$ oxidation state were treated by a Gaussian deconvolution. The experimental data (black), the simulation (red).

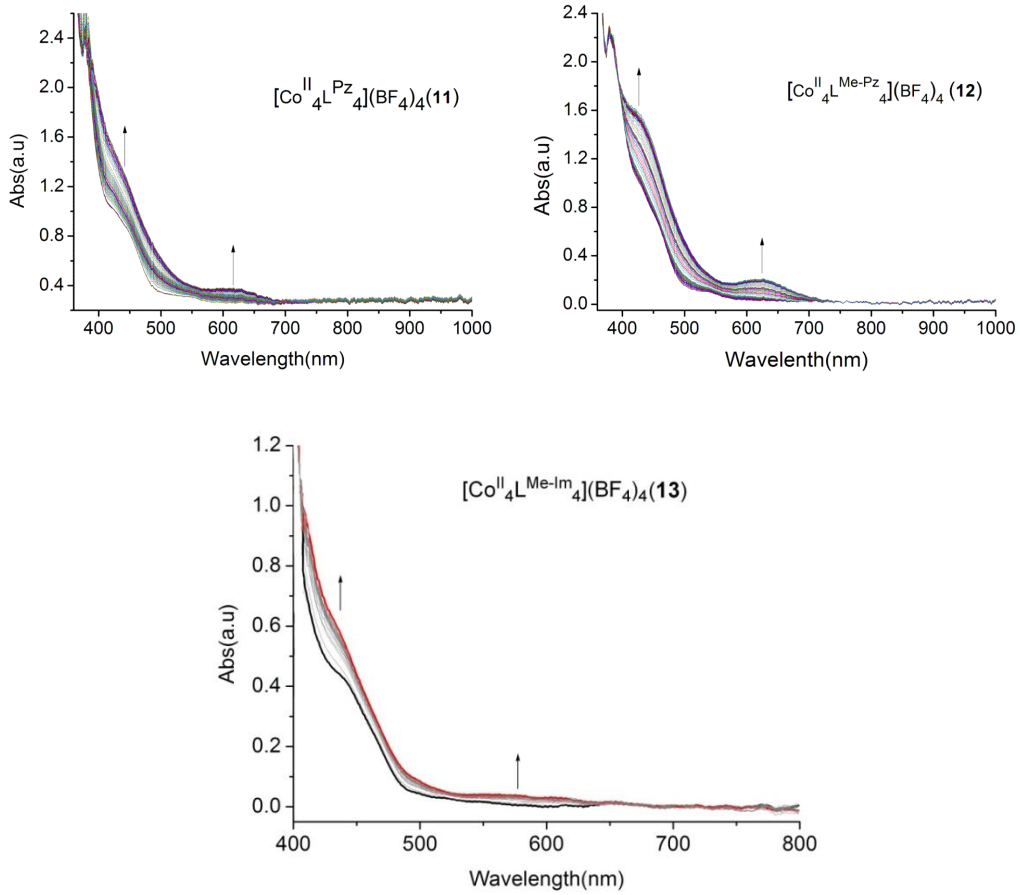

Figure 6.50. UV/vis spectral changes of **11**, **12** and **13** during the controlled potential oxidation in MeCN containing 0.1 M NBu_4PF_6 at RT on increasing the applied potential to 1.0 V.

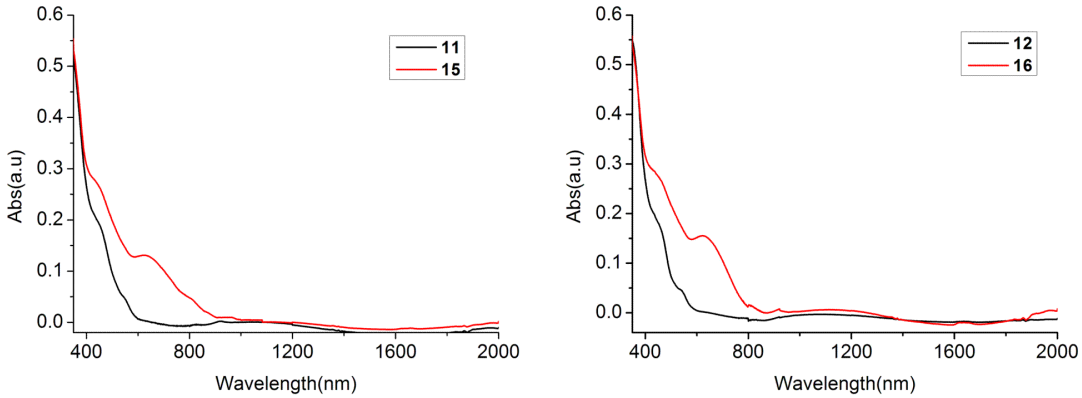

Figure 6.51. Solid-state absorption spectra of **11** (black), **15** (red) (left) and **12** (black), **16** (red) (right).

6.3. Conclusion

The homo-valence [2 × 2] Co^{II}_4 grid complexes $[Co^{II}_4L^{Pz}_4](BF_4)_4$ (**11**), $[Co^{II}_4L^{Me\text{-}Pz}_4](BF_4)_4$ (**12**), $[Co^{II}_4L^{Me\text{-}Im}_4](BF_4)_4$ (**13**) and $[Co^{II}_4L^{Py}_4](BF_4)_4$ (**14**) were synthesized and successfully characterized. Magnetic measurements revealed the HS (S = 3/2) state of the metal ions and moderate antiferromagnetic interactions to give an overall diamagnetic S_T = 0 ground state for **11** – **14**. Two-fold oxidations, electrochemically or chemically, led to the di-mixed-valence [2 × 2] Co_4 grids $[Co^{II}_2Co^{III}_2L^{Pz}_4](BF_4)_6$ (**15**), $[Co^{II}_2Co^{III}_2L^{Me}_4](BF_4)_6$ (**16**), $[Co^{II}_2Co^{III}_2L^{Me\text{-}Im}_4](BF_4)_6$ (**17**) and $[Co^{II}_2Co^{III}_2L^{Py}_4](BF_4)_6$ (**18**). Solution state ^1H and ^{13}C NMR spectra of paramagnetic **11** – **18** were obtained and confirm that the di-mixed-valent $Co^{II}_2Co^{III}_2$ grids are charge-localized on the NMR time scale. SQUID experiments show the high-spin Co^{II} to be magnetically isolated in the di-mixed-valent $Co^{II}_2Co^{III}_2$ grids, with complexes **15** – **18** displaying SMM behavior.

7. [3 × 3] Iron and Cobalt Grid Complexes Based on Pyrazole-bridged Tritopic Ligands

7.1. Synthesis of Ligands

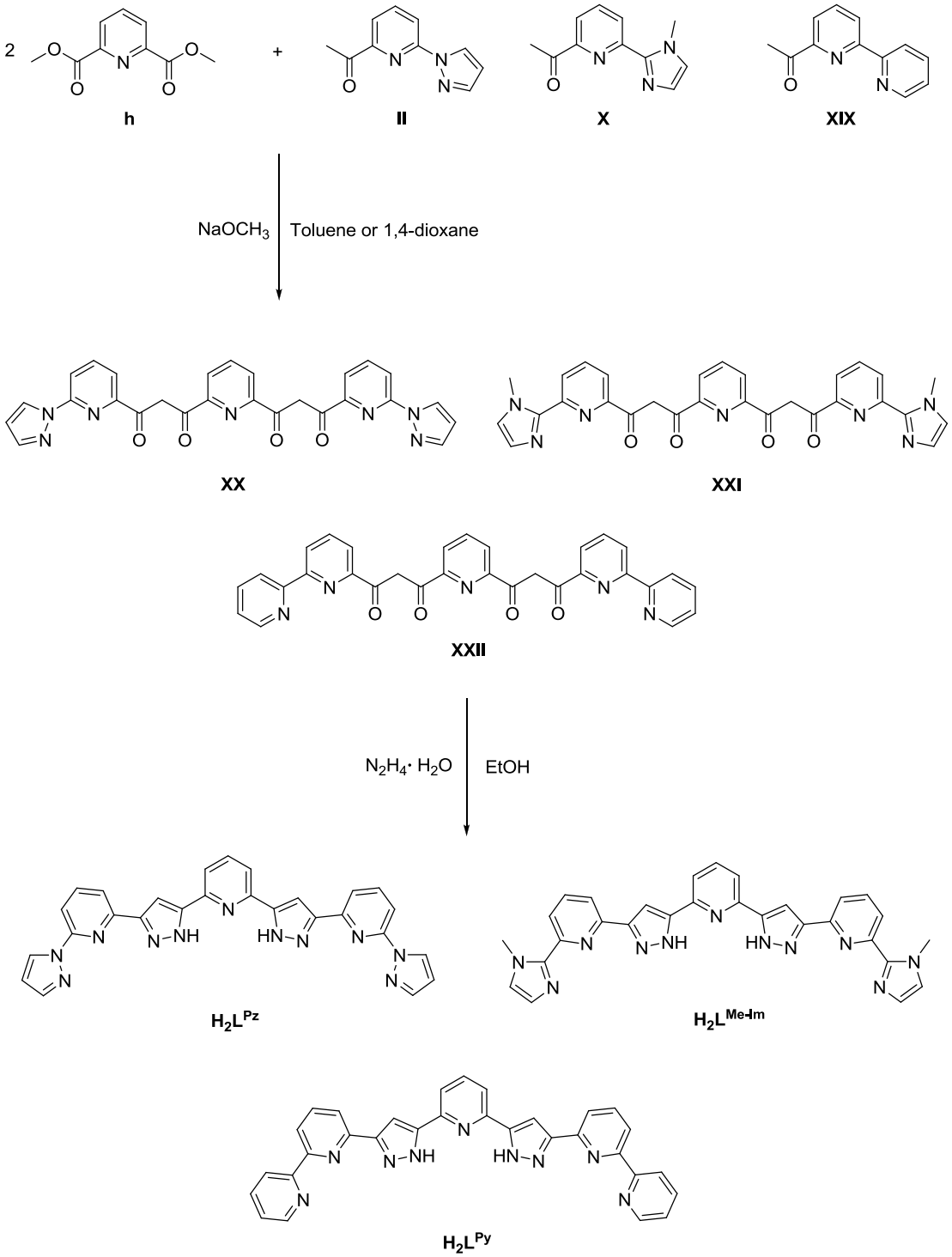

Scheme 7.1. Synthesis of ligands H_2L^{Pz}, $H_2L^{Me\text{-}Im}$ and H_2L^{Py}.

The synthesis of polypyridine ligands $\mathbf{H_2L^{Pz}}$, $\mathbf{H_2L^{Me\text{-}Im}}$ and $\mathbf{H_2L^{Py}}$ is based upon the pseudo-claisen condensation of dimethyl pyridine-2,6-dicarboxylate and ketone **II**/**X**/**XIX** using NaOMe as the base in dry toluene or 1.4-dioxane and subsequent acidic workup to 1,3-diketone **X**, **XI** and **XII** implemented, followed by a ring-closing condensation with hydrazine as shown in Scheme 7.1. These ligands consist of three pyridine groups linked by two pyrazole moieties with two pyrazole, or methylimidazle or pyridine rings as side arm, thus forming three tridentate binding sites. All of them have been fully characterized by ^{1}H NMR, ^{13}C NMR, and EI-MS (see Experimental Section and Figures 10.21 – 10.29).

7.2. Synthesis of [3 × 3] Fe_9 and Co_9 Grid Complexes

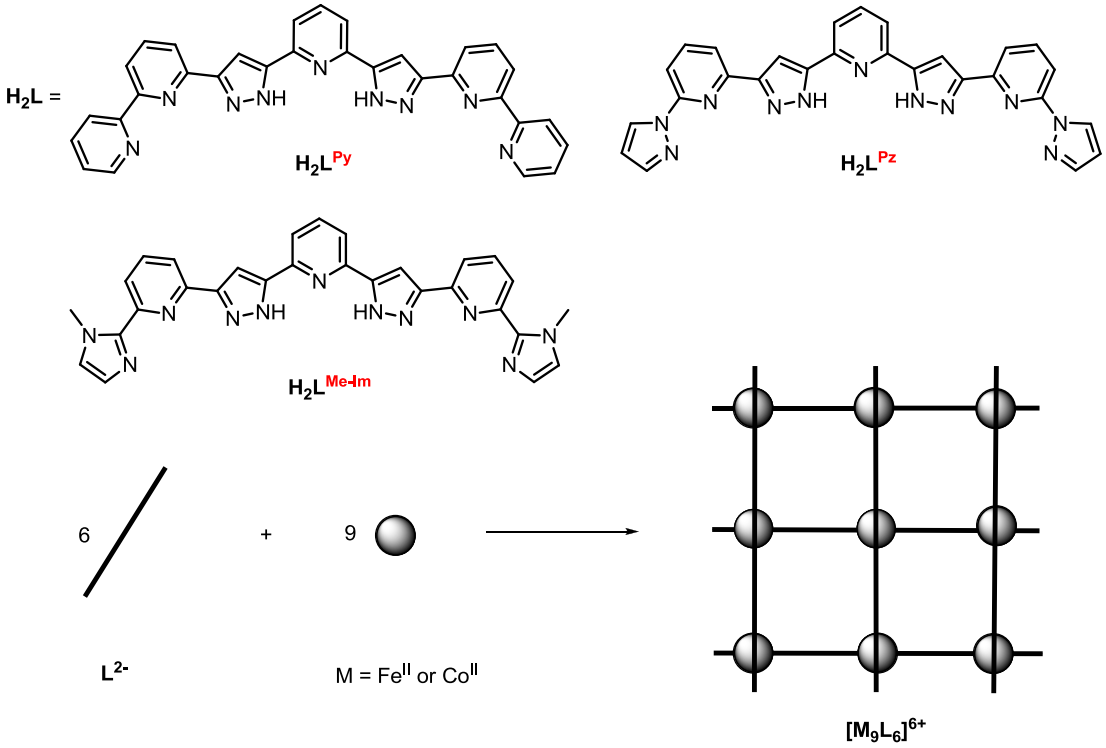

Scheme 7.2. Schematic representation of synthesis of [3 × 3] grid complexes.

Under inert conditions, ligand ($\mathbf{H_2L^{Pz}}$, $\mathbf{H_2L^{Me\text{-}Im}}$ and $\mathbf{H_2L^{Py}}$) was deprotonated with 2 equivalents NaO^tBu as the base in degassed MeCN/DMF (1:1) and was subsequently reacted with metal salt ($Fe(BF_4)_2 \cdot 6H_2O$ or $Co(BF_4)_2 \cdot 6H_2O$) (Scheme 7.2). The color of the reaction mixture changed from colourless to red and red precipitation appeared after stirring overnight at room temperature. Unfortunately, these products show bad

solubility in normal organic solvent such as $CHCl_3$, MeCN, MeOH, EtOH, acetone, toluene, DMF, DMSO and so on. No further analysis was possible during the course of this work.

8. Summary

In this work homo- and mixed-valence [2 × 2] grid-like complexes were studied in detail. Here, the multifunctionality features of these iron and cobalt grids are clearly illustrated in properties: 1) the electrochemistry of the metal centers and ligands, which provide a range of redox levels; 2) the magnetism of metal centers, in which the spin state may be influenced not only by the substitution of ligands but also by the structure of complexes; 3) the redox processes are able to change not only the oxidation state but also the spin state of the metal centers, which can enrich the functionality of grid structures. Therefore the understanding of properties in the solid state and solution state of these compounds has been improved.

In chapter 3, a series of [2 × 2] Fe^{II}_4 grid complexes (**$[Fe^{II}_4L_4](BF_4)_4$**) of substituted ligands related to 3,5-bis(6-(1*H*-pyrazol-1-y)yridine-2-yl)pyrid-2-yl)pyrazole (**HL** = **HL^{Pz}**, **$HL^{Me\text{-}Pz}$**, **$HL^{Me4\text{-}Pz}$** and **$HL^{Me5\text{-}Pz}$**), have been prepared to evaluate any significant impact of the 4-position of central (R^1) pyrazolyl and 3-, 4- and 5-positions of terminal pyrazolyl (R^2 and R^3) substitution on the electronic, magnetic and structural properties of the grid complexes. In the solid state, complexes have been characterized by X-ray diffraction, Mössbauer spectroscopy and magnetic measurements. The magnetic measurements show that the iron(II) centers of complexes remain in high spin state in the temperature range from 2 to 210 K. It is of interest to note that there is partly spin-state transition observed on the dry crystalline sample of **$[Fe^{II}_4L^{Pz}_4](BF_4)_4$** by means of Mössbauer spectroscopy and magnetic measurements, likely due to the loss of the co-crystallized solvent molecules. In solution state, the iron(II) complexes have been fully characterized by ESI mass spectrometry, paramagnetic NMR spectroscopy and cyclic voltammetry. These results of spectroscopic and structural studies show that methyl substitution at the pyrazolyl rings makes the oxidation potential of metal centers to be less positive and the reduction potential of ligands to be more negative. Additionlly, the substitution of methyl group causes a slight change of the coordination geometry of complexes, whereas the ligand field strength is not significantly influenced though the inductive

effect.

In chapter 4, by using the modified pyrazolate-derived ligand (**$HL^{Me\text{-}Im}$**) with two methylimidazole groups as peripheral side-arms to slightly increase the ligand field strength, a new [2 × 2] Fe^{II}_4 grid-type complex (**$[Fe^{II}_4L^{Me\text{-}Im}_4](ClO_4)_4$**) has been produced. In the solid state, **$[Fe^{II}_4L^{Me\text{-}Im}_4](ClO_4)_4$** adopts a di-mixed-spin configuration [HS-LS-HS-LS] over a wide temperature range (2 – 300 K), with Fe^{II} ions of the same spin state located at diagonally opposed vertices of the grid. Furthermore, **$[Fe^{II}_4L^{Me\text{-}Im}_4](ClO_4)_4$** is more easily oxidized to the 2-fold oxidized species **$[Fe^{II}_2Fe^{III}_2L^{Me\text{-}Im}_4](ClO_4)_6$**, which has favorably high stability. The sequence of redox events suggests that identical iron ions in **$[Fe^{II}_2Fe^{III}_2L^{Me\text{-}Im}_4](ClO_4)_6$**, having the same spin state and charge state, are again located at diagonally opposed vertices of the grid. Such configuration is indeed required for potential implementation in QCA devices.

In chapter 5, the unusual heterometallic grid (**$[Fe^{III}_2Ag^{I}_4L^{Me\text{-}Im}_4]^{6+}$**) and incomplete grid (**$[Fe^{II}_3(HL)L_3]^{+3}$**) complexes have been prepared selectively and fully characterized by single crystal X-ray diffraction and Mössbauer spectroscopy. The hexametallic complex **$[Fe^{III}_2Ag^{I}_4L^{Me\text{-}Im}_4]^{6+}$**, with two Fe^{III} ions and two $(Ag^{I})_2$ dumbbells on the four corners of grid, was synthesized *via* a corner complex as a key intermediate. The incomplete grid **$[Fe^{II}_3(HL)L_3]^{+3}$**, named defect-grid, is a new type of [2 × 2] matrix-like complex with one vertex devoid of a metal ion, and one hydrogen bonding instead, while there are two hydrogen bonds observed in the [2 × 2] defect-grid structure by using 3,5-bis(bipyridyl)pyrazolate ligand instead by B. Schneider and M. Steinert. The defect-grid iron complexes present the spin configuration [HS-LS-HS], which appears to be an attractive perspective as SCO systems due to the H-bonding between the vertex lack of metal ion and solvent molecules.

In chapter 6, a family of [2 × 2] Co^{II}_4 grid structures (**$[Co^{II}_4L^{R}_4](BF_4)_4$**) has been prepared, where the ligands **HL^{R}** (**HL^{Pz}**, **$HL^{Me\text{-}Pz}$**, **$HL^{Me\text{-}Im}$** and **HL^{Py}**) are the same as the ones used in chapters 3 and 4. In the solid state, complexes have been

characterized by single crystal X-ray diffraction and magnetic measurements. The magnetic measurements show that the Co^{II} ions of all these complexes remain in their HS state in the temperature range of 2 – 210 K, without any spin state changes. The paramagnetism of the Co^{II} complexes also has been studied through paramagnetic NMR spectroscopy in solution. The cyclic voltammetry curves of the cobalt grid complexes look worse than those of relevant Fe^{II} complexes considering the number and reversibility of redox waves likely because of sluggish electron transfer kinetics. These anodic responses likely reflect a sequence of non-resolved and kinetically hindered one-electron oxidation processes, describing the oxidation of the Co^{II}_4 to the fully oxidized Co^{III}_4 grid *via* mixed-valent states, in particular *via* the di-mixed-valent $Co^{II}_2Co^{III}_2$ species. As expected, the HS Co^{II} ions in homo-valence complexes (**$[Co^{II}_4L_4](BF_4)_4$**) are weakly antiferromagnetically coupled, which results in an overall diamagnetic $S_T = 0$ ground state. Oxidation of two Co^{II} ions giving the mixed-valence species **$[Co^{II}_2Co^{III}_2L_4](BF_4)_6$** with two LS Co^{III} ions located at opposite corners of the grids, leads to some interesting results. Firstly, the remaining two HS Co^{II} ions are now magnetically separated by diamagnetic LS Co^{III} ions and antiferromagnetic coupling vanishes. Secondly, due to the rigid ligand framework that enforces strong mechanical coupling between the corners of the grid, and because the LS Co^{III} ions strongly favor an octahedral coordination enviroment, distortion of the entire grid occurs upon oxidation which causes the coordination geometry of the remaining Co^{II} ions to significantly tend towards a trigonal prism. As a consequence, SMM properties of the mixed-valence complexes emerge. NMR studies in solution revealed that the Co valencies in the mixed-valence **$[Co^{II}_2Co^{III}_2L_4](BF_4)_6$** grids remain localized on the NMR time scale.

In chapter 7, there are three tritopic ligands prepared, which consist of three pyridine groups linked by two pyrazole moieties with different side arms containing N atoms as donor atom, thus forming three tridentate binding sites. By using these tritopic ligands to react with cobalt or iron salt, the red powders produced as procuct with super bad solubility. Unfortunately, no further analysis was possible during the

course of this work because of their bad solubility.

9. Experiment

9.1. Material and Methods

9.1.1. Work Techniques and Materials

General Considerations

All manipulations were carried out under an anaerobic and anhydrous atmosphere of dry nitrogen by standard Schlenk techniques. Glassware was dried at 120℃. THF was dried with potassium and sodium in the presence of benzophenone, Et_2O was dried with sodium in the presence of benzophenone; DMF and MeCN were dried with CaH_2; EtOH and MeOH were dried over Mg; dioxane was dried with anhydrous Na_2SO_4 and sodium; Toluene were used after drying over molecular sieve using a Mbraun PLC; all solvents were distilled prior to use.

Chemicals used were either present in the working group or were purchased from commercial sources or their synthesis is described below**.**

Column chromatographic purifications (63 – 200 μm particle size) were performed on silica. TLC was performed on silica gel (Macherey-Nagel, Polygram SIL G/UV254).

9.1.2. Analytics

NMR Spectroscopy

NMR spectra were recorded on Bruker Avance 300, 400 and 500 MHz spectrometers. Chemical shifts (δ) are given in ppm relative to residual solvent signals of CD_3CN, $CDCl_3$, DMF-d_6 and DMSO-d_6. And signals are labeled according to their splitting pattern as singlet (s), doublet (d), triplet (t), artet (q) or multiplet (m).

Mass Spectrometry

ESI mass spectrometry was recorded with an Applied Biosystems API 2000 and a HCT Ultra (Bruker) instrument. EI mass spectrometry was recorded with Finnigan MAT 8200.

Elemental Analysis

Elemental analyses were performed in the Analytical Laboratory of the Institute of Inorganic Chemistry at the University of Göttingen using an Elementar 4.1 Vario EL 3 instrument.

Electrochemistry

Cyclic Voltammetry (CV) and Square Wave Voltammetry (SWV) experiments were performed either on a Model 263A (PerkinElmer) or a CHI-660 (IJ-Cambria scientific) potentiostat. Glassy carbon disk electrodes (2mm diameter) were used as working, platinum wire as auxiliary and a Saturated Calomel Electrode (SCE) as reference electrode in MeCN/0.1 M NBu_4PF_6. Decamethylferrocene and ferrocene were used as the internal standard.

UV/Vis Spectroscopy

UV/Vis spectra were recorded on a Cary 50 Bio (Varian) or a Cary 5000 (Varian) using quartz cuvettes (d = 1 cm or 0.1 cm). Spectra were analyzed by Cary Win UV software.

Spectroelectrochemistry Experiments

Spectroelectrochemistry experiments were performed in SCE-C quartz glass cells (ALS, d = 0.1 cm). A platinum mash was used as working, platinum wire as auxiliary and an silver as reference electrode. All electrodes were washed with water and acetone and air dried before use. Complexes were dissolved in MeCN containing tetrabutylammoniumhexafluorophosphate (NBu_4PF_6, c = 0.1 M) as electrolyte. UV/Vis/NIR spectra were recorded on a Cary 50 Bio (Varian).

IR Spectroscopy

IR spectra of all complexes as KBr pallets were recorded on a Vertex 70 (Bruker) instrument. IR signals were analyzed according to their relative intensity as strong (s), medium (m) and weak (w).

Thermogravimetry

Thermo gravimetric measurements were performed using a Netzsch STA409PC LUXX, scan rate: 10 K/min.

Mössbauer spectroscopy

Mössbauer data were collected with a ^{57}Co source embedded in a Rh matrix using an alternating constant acceleration Wissel Mössbauer spectrometer operated in the transmission mode and equipped with a Janis closed-cycle helium cryostat. Isomer shifts are given relative to iron metal at ambient temperature. Simulation of the experimental data was performed with the Mfit program.[195]

SQUID magnetometry

Magnetic susceptibility measurements were carried out with a Quantum-Design MPMS-5S SQUID magnetometer equipped with a 5 Tesla magnet in the range from 400 to 2.0 K at a magnetic field of 0.5 T. The powdered or crystalline samples were contained in a teflon bucket and fixed in a non-magnetic sample holder. Each raw data file for the measured magnetic moment was corrected for the diamagnetic contribution of the sample holder and the teflon bucket. The molar susceptibility data were corrected for the diamagnetic contribution.

9.2. Experiment

Some of the presented syntheses are based on literature procedures (precursors **c**[196] **d** and **f**[197] and **e**[198].

9.2.1. Synthesis of Ligand Precursors and Ligands

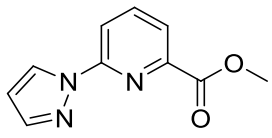

Methyl 6-(1*H*-pyrazol-1-yl)picolinate (I)

Under an atmosphere of argon NaOMe (1.67 g, 31.0 mmol) was added to a solution of 6-(1*H*-pyrazol-1-yl)picolinonitrile (3.10 g, 18.26 mmol) in anhydrous MeOH (75 mL). After stirring overnight at room temperature, AcOH (5 mL) and solid $NaHCO_3$ (4.90

g) were added, the mixture was stirred for half an hour and filtered to remove salts, and subsequently, the solvent was removed under reduced pressure. The residue was dissolved in EtOAc/sat. aq. $NaHCO_3$ (100 / 25 mL), the phases separated, the aqueous layer extracted with EtOAc (4 × 50 mL) until no change in color was observed, and the combined organic phase was washed with sat. aq $NaHCO_3$ (40 mL) and water (40 mL). After drying ($MgSO_4$) and removal of the solvent, the solid was dissolved in a mixture of MeOH (50 mL) and water (50 mL). After stirring for 30 min, 5% aq. H_2SO_4 was added to the solution drop by drop to pH 1 – 2 and further stirred overnight at RT. Then the pH of mixture adjusted to pH 8 – 9 with saturated NaOH solution (~ 60 mL), EtOAc (100 mL) was added, and the organic phase was separated. The aqueous phase was extracted with EtOAc (3 × 60 mL) and the combined organic phase was dried over anhydrous $MgSO_4$ and filtered. After evaporating the solvent, the residue was purified by column chromatography on a silica gel to give white powder.

Yield 2.12 g, 10.44 mmol, 57.2%.

Molecular Weight 204.07 g mol^{-1}.

^{1}H NMR (300 MHz, $CDCl_3$): δ = 8.69 (d, J = 2.6 Hz, 1H), 8.17 (m, 1H), 7.98 (m, 2H), 7.76 (s, 1H), 6.49 (m, 1H), 4.02 (s, 3H) ppm.

^{13}C{^{1}H} NMR (75 MHz, $CDCl_3$): δ = 164.32, 151.55, 146.52, 142.61, 139.70, 127.66, 122.68, 116.16, 108.24, 52.95 ppm.

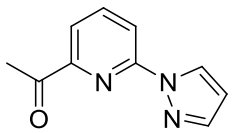

1-(6-(1*H*-pyrazol-1-yl)yridine-2-yl)ethanone (II)

To the compound 2-(2-methyl-1,3-dioxolan-2-yl)-6-(1*H*-pyrazol-1-yl)pyridine (2.68 g, 14.32 mmol) in acetone (85 mL) was added 35 mL of hydrochloric acid (2 M). The mixture was stirred in room temperature for twelve hours and then was concentrated and neutralized with a sat. aq. Na_2CO_3. The solution was extracted with CH_2Cl_2 and

the combined organic phases were collected, washed with sat. $NaHCO_3$ and brine, dried over anhydrous $MgSO_4$, and evaporated to give a pale yellow oil as crude product. The crude product was purified by column chromatography on silica gel and affording a white solid.

Yield 2.62 g, 13.93 mmol, 98%.

Molecular Weight 188.08 g mol^{-1}.

^{1}H NMR (300 MHz, $CDCl_3$): δ = 8.54 (m, 1H), 8.11 (m, 1H), 8.09 (s, 1H), 7.90–7.69 (m, 2H), 6.50 (m, 1H), 2.67 (s, 3H) ppm.

^{13}C{^{1}H} NMR (75 MHz, $CDCl_3$): δ = 199.58, 152.25, 151.20, 142.95, 140.15, 127.49, 119.54, 116.49, 108.63, 26.19 ppm.

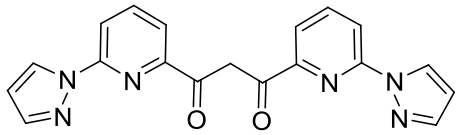

1,3-bis(6-(1*H*-pyrazol-1-yl)yridine-2-yl)propane-1,3-dione (III)

To a solution of **I** (1.20 g, 5.72 mmol) in anhydrous toluene (20 mL) under an argon atmosphere was added NaOMe (380 mg, 7.10 mmol). After heating this mixture to around 50℃, a solution of **II** (1.19 g, 5.92 mmol) in anhydrous toluene (10 mL) was added dropwise. The color of this reaction mixture changed from yellow to orange during this period. After stirring for two hours, an orange precipitate appeared, and the reaction was stirred overnight at room temperature. A precipitate was separated by filtration and washed with toluene (2 × 5 mL). The solid was slowly poured with constant and vigorous stirring into a mixture containing acetic acid (6 mL) and water (10 mL). A pale yellow solid was formed, which was filtered and washed with water. After drying, range solid was obtained, which was used without further purification.

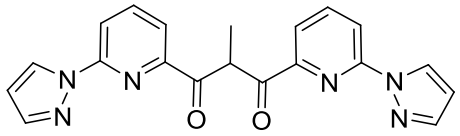

1,3-bis(6-(1*H*-pyrazol-1-yl)yridine-2-yl)propane-2-methyl-1,3-dione (IV)

Under an atmosphere of argon compound **III** (1.07 g, 3.0 mmol) and potassium bis(trimethylsilyl)-amide (0.90 g, 3.0 mmol) were suspended in toluene (60 mL). The suspension was heated to 75 ℃ and the color changed from orange to green, then methyl iodide (0.92 mL, 15.0 mmol) was added. The mixture was stirred at the refluxing temperature for 4 h and the color of the reaction mixture changed to yellow finally. The yellow precipitate was separated by filtration and washed with toluene (2 × 10 mL). The filtrate was washed with sat. aq. Na_2CO_3 (40 mL) and water (40 mL). The combined aqueous phases were extracted with chloroform (3 × 40 mL), and the combined organic phases were dried over anhydrous Mg_2SO_4. After removal of the solvent, orange solid was obtained.

Yield 0.84 g, 2.25 mmol, 75.3% (over two steps).

Molecular Weight 373.14 g mol^{-1}.

^{1}H NMR (300 MHz, $CDCl_3$): δ = 8.19 (d, J = 2.6 Hz, 2H), 8.02 – 7.94 (m, 4H), 7.78 (d, J = 6.0, 2H), 7.67 (s, 2H), 6.37 (s, 2H), 4.56 – 4.49 (m, 1H), 1.59 (d, J = 7.0 Hz, 3H) ppm.

^{13}C{^{1}H} NMR (75 MHz, $CDCl_3$): δ = 196.476, 150.65, 150.18, 142.57, 140.29, 127.91, 119.50, 115.82, 108.71, 54.00, 13.48 ppm.

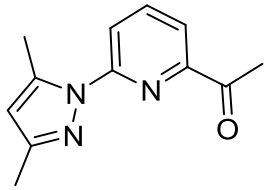

1-(6-(3,5-dimethyl-1*H*-pyrazol-1-yl)yridine-2-yl)ethanone (V)

6-(3,5-dimethyl-1*H*-pyrazol-1-yl)picolinonitrile (1.0 g. 5.05 mmol) was dissolved in dry THF (50 mL) under anhydrous conditions and cooled to c.a. –15℃ prior to

dropwise addition of MeMgBr (3 M in Et_2O, 2.6 mL). The orange solution was stirred at –15℃ for one hour and stirred overnight at RT. Sat. NH_4Cl solution (20 mL) was added slowly to the dark-red reaction mixture, followed by phase separation and extraction of the aqueous phase with THF (20 mL) and DCM (20 mL) and the dark organic phase washed with sat. NaCl solution (20 mL) and H_2O (20 mL). Combined organic phases were dried with $MgSO_4$. After filtering off the $MgSO_4$, the filtrate solvent was removed by rotary evaporation to leave red oil. The oil was purified by column chromatography (DCM / MeOH) to yield the white solid as product.

Yield 0.65 g, 3.03 mmol, 60.5%.

Molecular Weight 216.11 g mol^{-1}.

^{1}H NMR (300 MHz, $CDCl_3$): δ = 8.10 (dd, J = 7.6, 1.6 Hz, 1H), 7.86 (m, 2H), 6.01 (s, 1H), 2.69 (s, 3H), 2.63 (s, 3H), 2.27 (s, 3H) ppm.

^{13}C{^{1}H} NMR (75 MHz, $CDCl_3$): δ = 199.25, 151.28, 150.25, 141.91, 119.20, 118.51, 109.72, 26.19, 15.09, 13.47 ppm.

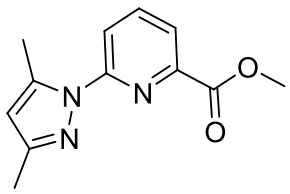

Methyl-6-(3,5-dimethyl-1*H*-pyrazol-1-yl)picolinate (VI)

6-(3,5-dimethyl-1*H*-pyrazol-1-yl)picolinonitrile (1.0 g, 5.05 mmol) and NaOMe (0.45 g, 1.66 eq.) were dissolved in dry MeOH (20 mL) under anhydrous conditions and stirred at RT. Overnight. $NaHCO_3$ (2.07 g, 2.5 eq.) and acetic acid (1.35 mL) were added and the mixture was allowed to stir for 30 minutes. The solution was filtered and the filtrate solvent was removed by rotary evaporation. The white residue was dissolved in EtOAc/sat. $NaHCO_3$ (4 : 1) solution prior to phase separation and extraction of the aqueous phase with EtOAc. The aqueous phase was washed with sat. $NaHCO_3$ solution and water prior to drying with $MgSO_4$ and, after filtration, the organic solvent was removed by rotary evaporation. The white residue was

suspended in a 1:1 MeOH / H_2O solution and H_2SO_4 was added until pH = 1 – 2. The solution was stirred for a minimum of 2 hours. NaOH solution was added to the solution until PH = 7 – 8. The solution was phase separated upon addition of EtOAc, with the aqueous phase extracted further with EtOAc. After drying with $MgSO_4$ and filtration, the organic solvent was removed to yield a white solid as product.

Yield 0.88 g, 3.81 mmol, 75.5%.

Molecular Weight 232.11 g mol^{-1}.

^{1}H NMR (300 MHz, $CDCl_3$): δ = 7.98 (d, J = 7.8 Hz, 1H), 7.82 (m, 2H), 5.92 (s, 1H), 3.89 (s, 3H), 2.64 (s, 3H), 2.20 (s, 3H) ppm.

^{13}C{^{1}H} NMR (75 MHz, $CDCl_3$): δ = 165.43, 153.29, 150.38, 145.71, 142.21, 139.09, 121.70, 118.78, 109.58, 52.74, 14.72, 13.65 ppm.

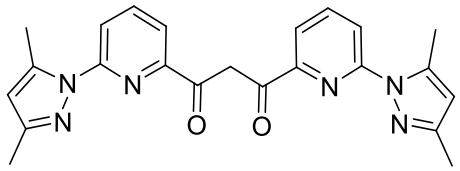

1,3-bis(6-(3,5-dimethyl-1*H*-pyrazol-1-yl)yridine-2-yl)propane-1,3-dione (VII)

Under anhydrous conditions, **VI** (0.43 g, 1.85 mmol) and NaOMe (0.11 g, 2.04 mmol) were dissolved in dry toluene (10 mL) and the solution was heated to c.a. 50℃. The solution of **V** (0.40 g, 1.86 mmol) dissolved in dry toluene (20 mL) was then added dropwise to the heated solution, causing a colour change from colourless to orange. The orange solution was heated at c.a. 50℃ for 5 hours and then left stirring at RT overnight. The resulting dark red precipitate was collected by filtration and dissolved in a minimum volume of water (8 mL). Acetic acid (2 mL) was added slowly to the aqueous solution, resulting in a brown-yellow precipitate. The solid was collected by filtration and used for next step without further purifition.

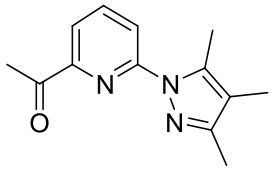

1-(6-(3,4,5-trimethyl-1*H*-pyrazol-1-yl)yridine-2-yl)ethanone (VIII)

6-(3,4,5-trimethyl-1*H*-pyrazol-1-yl)picolinonitrile (2.30 g, 10.85 mmol) was dissolved in dry THF (125 mL) under anhydrous conditions and cooled to c.a. –15℃ prior to dropwise addition of MeMgBr (5.5 mL, 3 M in Et_2O). The light red solution was stirred at –15℃ for 1 hour and stirred overnight at RT. Solution of sat. NH_4Cl (50 mL) was added slowly to the dark-red reaction mixture, followed by phase separation and extraction of the aqueous phase with THF (50 mL) and DCM (50 mL) and the organic phase washed with sat. NaCl solution (50 mL) and H_2O (100 mL). Solvent of combined organic phases were removed by rotary evaporation to leave red oil. The oil was purified by column chromatography (DCM / MeOH) to yield the white solid as product.

Yield 1.92 g, 8.36 mmol, 77.1%.

Molecular Weight 230.12 g mol^{-1}.

^{1}H NMR (300 MHz, $CDCl_3$): δ = 8.05 (dd, J = 7.7, 1.5 Hz, 1H), 7.82 (m, 2H), 2.64 (s, 3H), 2.61 (s, 3H), 2.21 (s, 3H), 1.93 (s, 3H) ppm.

^{13}C{^{1}H} NMR (75 MHz, $CDCl_3$): δ = 199.36, 151.25, 149.81, 139.24, 119.20, 118.29, 115.76, 26.17, 13.17, 11.08, 7.95 ppm.

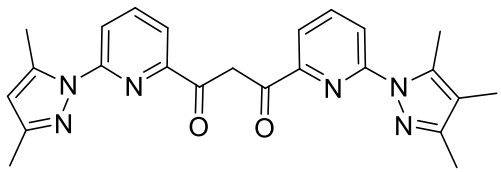

1-(6-(3,5-dimethyl-1*H*-pyrazol-1-yl)yridine-2-yl)-3-(6-(3,4,5-trimethyl-1*H*-pyrazol-1-yl)181yridine-2-yl)propane-1,3-dione (IX)

Complex **VI** (0.43 g, 1.85 mmol) and NaOMe (0.09 g, 2.04 mmol.) were dissolved in

dry toluene (10 mL) under anhydrous conditions, and the solution was heated to 50℃. The solution of **VIII** (0.43 g, 1.86 mmol) dissolved in dry toluene (20 mL) was then added dropwise to the heated solution, causing a colour change from colourless to orange. The orange solution was heated at c.a. 50℃ for 5 hours and then left stirring overnight at RT. The resulting dark red precipitate was collected by filtration and dissolved in water (8 mL). Acetic acid (2 mL) was added slowly to the aqueous solution, resulting in a brown-yellow precipitate.

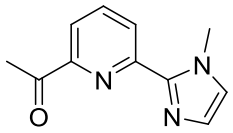

1-(6-(1-methyl-1*H*-imidazol-2-yl)yridine-2-yl)ethanone (X)

Under an argon atmosphere MeMgBr (3.95 mL, 3.0 M in Et_2O, 1.2 eq.) was added slowly to a solution of 6-(1-methyl-1*H*-imidazol-2-yl)picolinonitrile (1.82 g, 9.88 mmol) in anhydrous THF (50 mL) at –15℃. The reaction mixture was further stirred for one hour at –15 ℃ and then overnight at room temperature to give an orange solution. Slow addition of a sat. NH_4Cl solution (40 mL) was followed by phase separation. The aqueous phase was extracted with THF (40 mL) and then DCM (40 mL). The combined organic phases were washed with saturated NaCl (40 mL) and H_2O (40 mL) and then dried over $MgSO_4$. The organic phase was dried over anhydrous $MgSO_4$ and filtered. After evaporating the solvent, the residue was purified by column chromatography on a silica gel to give a crystalline white solid.

Yield 1.39 g, 6.92 mmol, 70%.

Molecular Weight 202.10 g mol^{-1}.

^{1}H NMR (300 MHz, $CDCl_3$): δ = 8.47 (d, J = 8.88 Hz, 1H), 7.98 – 7.89 (m, 2H), 7.18 (s, 1H), 7.04 (s, 1H), 4.24 (s, 3H), 2.74 (s, 3H) ppm.

^{13}C{^{1}H} NMR (75 MHz, $CDCl_3$): δ = 197.09, 159.88, 150.06, 150.02, 137.63, 128.51, 125.97, 124.94, 120.22, 36.72, 26.10 ppm.

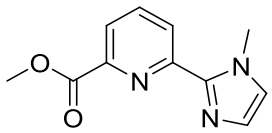

Methyl-6-(1-methyl-1*H*-imidazol-2-yl)picolinate (XI)

Under an argon atmosphere sodium methoxide (0.82 g, 15.14 mmol) was added to a solution of 6-(1-methyl-1*H*-imidazol-2-yl)picolinonitrile (1.68 g, 9.13 mmol) in anhydrous MeOH (30 mL). After stirring overnight at room temperature, AcOH (3 mL) and solid $NaHCO_3$ (2.0 g, 23.81 mmol) were added, the mixture was stirred for 30 min and filtered to remove salts, and subsequently, the solvent was removed in vacuo. The residue was dissolved in EtOAc/sat. aq. $NaHCO_3$ (100 / 25 mL), the phases separated, the aqueous layer extracted with EtOAc (4 × 50 mL), and the combined organic extracts were washed with sat. aq $NaHCO_3$ (40 mL) and water (40 mL). After drying ($MgSO_4$) and removal of the solvent in vacuo, the solid methyl imidate ester was dissolved in a mixture of MeOH (60 mL) and water (60 mL). After stirring for 30 min, the solution was acidified to pH 1 – 2 with 5% aq H_2SO_4 and further stirred overnight at RT. Then the pH of mixture adjusted to pH 8-9 with saturated NaOH solution (~ 60 mL), EtOAc (100 mL) was added, and the brown organic phase was separated. The aqueous phase was extracted with EtOAc (3 × 60 mL) and the organic phase was dried over anhydrous $MgSO_4$ and filtered. After evaporating the solvent, the residue was purified by column chromatography on a silica gel to give a crystalline white solid.

Yield 1.20 g, 5.53 mmol, 61%.

Molecular Weight 218.09 g mol^{-1}.

^{1}H NMR (300 MHz, $CDCl_3$): δ = 8.35 (d, J = 8.37 Hz, 1H), 7.97 (d, J = 8.61 Hz, 1H), 7.84 (t, J = 7.80 Hz, 1H), 7.09 (s, 1H), 6.95 (s, 1H), 4.17 (s, 3H), 3.934 (s, 3H) ppm.

^{13}C{^{1}H} NMR (75 MHz, $CDCl_3$): δ = 160.65, 153.66, 146.79,146.49, 137.55, 128.47, 125.54, 124.96, 123.53, 52.69, 30.46 ppm.

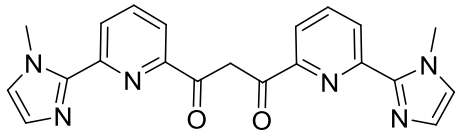

1,3-bis(6-(1-methyl-1*H*-imidazol-2-yl)yridine-2-yl)propane-1,3-dione (XII)

Under a argon atmosphere NaOMe (0.38 g, 7.10 mmol) was added to a solution of **XI** (1.20 g, 5.72 mmol) in anhydrous 1.4-dioxane (20 mL). After heating this mixture to around 50℃, a solution of **X** (1.19 g, 5.92 mmol) in anhydrous 1.4-dioxane (10 mL) was added dropwise. The color of this reaction mixture changed from yellow to red during this period. After stirring for 5 hours, an orange precipitate appeared, and the reaction was stirred overnight at room temperature. A precipitate was separated by filtration and washed with 1.4-dioxane (2 × 5 mL). The solid was slowly poured with constant and vigorous stirring into a mixture containing acetic acid (6 mL) and H_2O (10 mL). A pale yellow solid was formed, which was filtered and washed with H_2O (2 × 10 mL). After drying, a bright yellow solid was obtained, which was used without further purification.

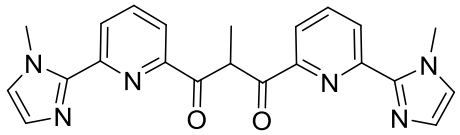

1,3-bis(6-(1-methyl-1*H*-imidazol-2-yl)yridine-2-yl)propane-2-Methyl-1,3-dione (XIII)

Under an atmosphere of argon compound **XII** (1.16 g, 3.0 mmol) and potassium bis(trimethylsilyl)-amide (0.90 g, 3.0 mmol) were suspended in toluene (60 mL). The suspension was heated to 75 ℃ and the color changed from orange to green, then methyl iodide (0.92 mL, 15.0 mmol) was added. The mixture was stirred at the refluxing temperature for 4 hours and the color of the reaction mixture changed to yellow finally. The yellow precipitate was separated by filtration and washed with toluene (2 × 10 mL). The filtrate was washed with sat. aq. Na_2CO_3 (40 mL) and water (40 mL). The combined aqueous phases were extracted with chloroform (3 ×

40 mL), and the combined organic phases were dried over anhydrous Mg_2SO_4. After removal of the solvent, orange solid was obtained.

Yield 0.42 g, 1.06 mmol, 35.3% (over two steps).

Molecular Weight 400.4 g mol^{-1}.

^{1}H NMR (300 MHz, $CDCl_3$): δ = 8.26 (d, *J* = 9.06 Hz, 2H), 7.91 (d, *J* = 8.91 Hz, 2H), 7.82 (t, *J* = 7.80 Hz, 2H), 7.03 (s, 2H), 6.82 (s, 2H), 3.72(s, 3H), 3.44 – 3.37 (m, 1H), 1.16 (m, 3H) ppm.

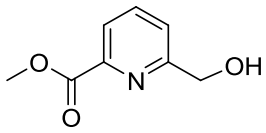

Methyl-6-(hydroxymethyl)picolinate (XIV)

$NaBH_4$ (3.65 g, 96 mmol) was added to a stirred solution of dimethyl-pyridine-2,6-dicarboxylate (5.0 g, 25.64 mmol) in MeOH (200 mL) at 0 ℃. The solution was stirred for 3 hours at 0 ℃ and then poured into a saturated $NaHCO_3$ aqueous solution (100 mL). The bulk of the methanol was evaporated, and the resulting aqueous solution was extracted with $CHCl_3$ (5 × 100 mL). The combined organic phases were dried over $MgSO_4$ and evaporated to dryness to get white powder.

Yield 3.01 g, 18.00 mmol, 70%.

Molecular Weight 167.20 g mol^{-1}.

^{1}H NMR (300 MHz, $CDCl_3$): δ = 7.97 (d, *J* = 7.68 Hz, 1H), 7.81 (t, *J* = 7.74 Hz, 2H), 7.54 (d, *J* = 7.80 Hz, 1H), 4.83 (s, 2H), 3.93 (s, 3H), 2.12 (s, 1H) ppm.

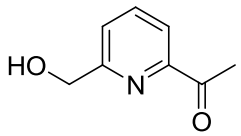

1-(6-(hydroxymethyl)yridine-2-yl)ethanone (XV)

Under nitrogen atmosphere, added 100 mL anhydrous EtOAc and 5 mL 1.4-dioxane to the dry NaOEt (9.5 g, 140.50 mmol). After stirring about 3 hours, added a solution of **XV** (3.34 g, 20.00 mmol) in 1.4-dioxane to the above reaction solution with stirring to afford a yellowish mixture, which was refluxed for 12 hours and stirred at RT overnight. Most of the solvent was evaporated, and 50 mL HCl (1.0 M, 20 mL) was added. Then the mixture was refluxed for 16 hours. After the mixture was cooled to RT, it was concentrated under reduced pressure. The residual aqueous phase was extracted with EtOAc (3 × 150 mL). The combined extracts were washed with a saturated aqueous solution of $NaHCO_3$, dried over anhydrous $MgSO_4$ and filtered, and the solvent was finally evaporated. The desired compound **XV** was obtained after purification by column chromatography.

Yield 0.97 g, 6.40 mmol, 32%.

Molecular Weight 151.20 g mol^{-1}.

^{1}H NMR (300 MHz, $CDCl_3$): δ = 7.88 (d, J = 1.26 Hz, 1H), 7.78 (t, J = 7.68 Hz, 2H), 7.40 (d, J = 1.26 Hz, 1H), 4.77 (s, 2H), 3.80 (s, 1H), 2.65 (s, 3H) ppm.

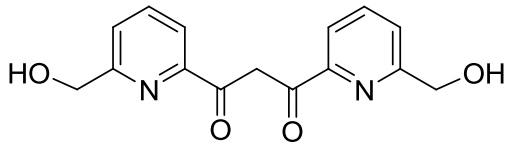

1,3-bis(6-(hydroxymethyl)yridine-2-yl)propane-1,3-dione (XVI)

To a solution of **XIV** (962.10 mg, 5.72 mmol) in anhydrous toluene (20 mL) under an argon atmosphere was added NaOMe (380 mg, 7.10 mmol). After heating this mixture to around 50℃, a solution of **XV** (895.10 mg, 5.92 mmol) in anhydrous toluene (20 mL) was added dropwise. The color of this reaction mixture changed from yellow to orange during this period. After stirring for two hours, an orange-red precipitate appeared, and the reaction was stirred overnight at RT. A precipitate was separated by filtration and washed with toluene (2 × 5 mL). The solid was slowly poured with constant and vigorous stirring into a mixture containing acetic acid (6 mL) and water (10 mL). A pale yellow-red solid was formed, which was filtered and

washed with water. After drying, yellow-red solid **XVI** was obtained which was used without further purification.

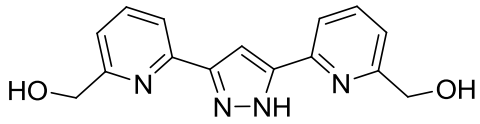

(6,6'-(1H-pyrazole-3,5-diyl)bis(pyridine-6,2-diyl))dimethanol (XVII)

Crude compound **XVI** (652.76 mg, 2.28 mmol) was suspended in ethanol (25 mL) and hydrazine hydrate (0.6 mL) was added. The mixture was heated to reflux for 5 hours and continued to stir overnight at RT. A red precipitate was collected by filtration and washed with a small amount of H_2O (2 × 10 mL) to give white solid as product **XVII**.

Yield 529.30 mg, 1.87 mmol, 82%.

Molecular Weight 282.30 g mol^{-1}.

^{1}H NMR (300 MHz, $CDCl_3$): δ = 7.93 (m, 4H), 7.50 (m, 2H), 5.51 (s, 2H), 4.72 (s, 4H), 3.38 (s, 2H) ppm.

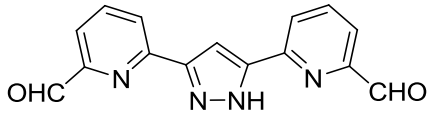

6,6'-(1H-pyrazole-3,5-diyl)dipicolinaldehyde (XVIII)

An excess of activated MnO_2 (1.30 g, 15.0 mmol) and **XVII** (424.5 mg, 1.50 mmol) were refluxed with stirring for 3 days in 50 mL of EtOAc. After colling to RT, the mixture was passed through a bed of celite and eluted with additional volumes of EtOAc. The solvent was evaporated in vacuo, and the residue was purified by column chromatography to afford **XVIII**.

Yield 208.30 mg, 0.75 mmol, 50%.

Molecular Weight 278.30 g mol^{-1}.

^{1}H NMR (300 MHz, $CDCl_3$): δ = 10.11 (s, 2H), 8.08 (m, 2H), 7.90 (m, 4H), 7.55 (s, 1H) ppm.

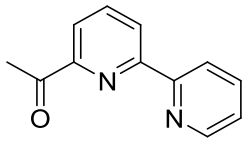

1-(2,2'-bipyridin-6-yl)ethanone (**XIX**)

To a solution of 6-Cyano-2,2'-Bipyridin (2.89 g, 16.0 mmol) in dry THF (100 mL) was added slowly MeMgBr (3.0 M in Et_2O, 6.3 mL, 19.1 mmol) at –15 °C. The reaction mixture was further stirred for 1 hour at –15 °C and then for 2 hours at RT to give an orange-red solution. Slow addition of a saturated NH_4Cl solution (70 mL) was followed by phase separation. The aqueous phase was extracted with THF (70 mL) and then CH_2Cl_2 (70 mL). The combined organic phases were washed with saturated NaCl (70 mL) and H_2O (70 mL) and then dried over $MgSO_4$. Evaporation of the filtrate in vacuo left a reddish oil. Extraction with hexane (3 × 50 mL) and removal of the solvent in vacuo yielded **XIX** as an off-white solid.

Yield 1.97 g, 9.93 mmol, 62%.

Molecular Weight 195.20 g mol^{-1}.

^{1}H NMR (300 MHz, $CDCl_3$): δ = 8.69 – 8.65 (m, 1H), 8.59 (dd, *J* = 7.7, 1.2 Hz, 1H), 8.50 (d, *J* = 7.9 Hz, 1H), 8.02 (dd, *J* = 7.5, 1.3 Hz, 1H), 7.91 (t, *J* = 8.2 Hz, 1H), 7.83 (dt, *J* = 7.9, 1.2 Hz, 1H), 7.32 (ddd, *J* = 8.2, 3.8, 0.9 Hz, 1H), 2.79 (s, 3H) ppm.

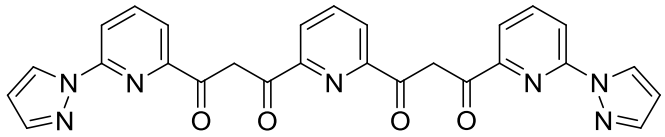

3,3'-(pyridine-2,6-diyl)bis(1-(6-(1*H*-pyrazol-1-yl)yridine-2-yl)propane-1,3-dione) (**XX**)

Under an atmosphere of argon dimethyl pyridine-2,6-dicarboxylate (728.20 mg, 3.73 mmol) and NaOMe (830.40 mg, 12.20 mmol) were dissolved in toluene (60 mL). After heating this mixture to around 50°C, a solution of **II** (1.59 g, 8.50 mmol) in toluene (30 mL) was added dropwise to the heated solution, causing a colour change from colourless to orange. Then orange solution was heated at 50°C for 5 hours and

then left stirring at RT overnight. The resulting orange precipitate was collected by filtration and dissolved in H_2O (16 mL). Acetic acid (4 mL) was added slowly to the aqueous solution, resulting in a brown-yellow precipitate, which was filtered and washed with water. After drying, yellow-red solid **XX** was obtained, which was used without further purification.

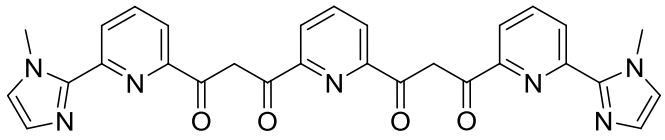

3,3'-(pyridine-2,6-diyl)bis(1-(6-(1-methyl-1H-imidazol-2-yl)yridine-2-yl)propane-1,3-dione) (**XXI**)

The synthesis of **XXI** is the same as **XX** by using **X** instead of **II**.

Under an atmosphere of argon dimethyl pyridine-2,6-dicarboxylate (728.20 mg, 3.73 mmol) and NaOMe (830.40 mg, 12.20 mmol) were dissolved in 1.4-dioxane (60 mL). After heating this mixture to around 50°C, a solution of **X** (1.70 g, 8.50 mmol) in dioxane (30 mL) was added dropwise to the heated solution, causing a colour change from colourless to orange.

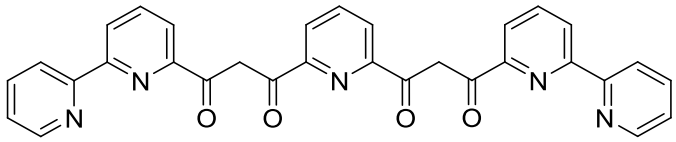

3,3'-(pyridine-2,6-diyl)bis(1-(2,2'-bipyridin-6-yl)propane-1,3-dione) (XXII)

The synthesis of **XXII** is the same as **XX** by using **XIX** instead of **II**.

Under an atmosphere of argon dimethyl pyridine-2,6-dicarboxylate (728.20 mg, 3.73 mmol) and NaOMe (830.40 mg, 12.20 mmol) were dissolved in toluene (60 mL). After heating this mixture to around 50°C, a solution of **XIX** (1.68 g, 8.50 mmol) in toluene (20 mL) was added dropwise to the heated solution, causing a colour change from colourless to orange.

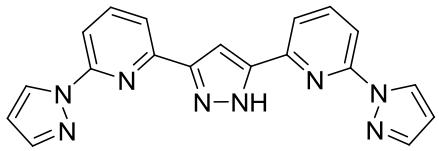

3,5-bis(6-(1*H*-pyrazol-1-y)yridine-2-yl)pyrid-2-yl)pyrazole (HL^{Pz})

Crude compound **III** (0.88 g, 2.28 mmol) was suspended in EtOH (15 mL) and hydrazine hydrate (0.6 mL) was added. The mixture was heated to reflux for five hours and continued to stir overnight at room temperature. A white precipitate was collected by filtration and washed with a small amount of H_2O (2 × 10 mL) to give white solid as product.

Yield 0.83 g, 2.34 mmol, 44.1%.

Molecular Weight 355.14 g mol^{-1}.

^{1}H NMR (500 MHz, $CDCl_3$): δ =8.67 (s, 2H), 7.92 (m, 2H), 7.85 (s, 2H), 7.78 (m, 4H), 7.44 (s, 1H), 6.49 (s, 2H) ppm.

$^{13}C\{^1H\}$ NMR (125 MHz, $CDCl_3$): δ = 151.12, 148.13, 142.19, 139.60, 126.99, 117.39, 111.61, 107.83, 102.21 ppm.

EI-MS m/z (%): 355 (100) $[M]^+$.

Anal. Calcd (%) for **HL^{Pz}** ($C_{19}H_{14}N_8$): C, 64.38; H, 3.98; N, 31.63. Found: C, 64.52; H, 3.77; N, 31.71.

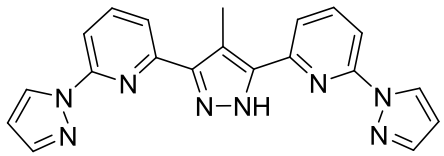

4-Methyl-3,5-bis(6-1*H*-pyrazol-1-y)pyrid-2-yl)pyrid-2-yl)pyrazole ($HL^{Me\text{-}Pz}$)

Solid **IV** (0.74 g, 2 mmol) was suspended in EtOH (30 mL) and hydrazine hydrate (0.50 mL, 10 mmol) was added. The mixture was heated to reflux for 5 hours and continued to stir overnight at RT. A white precipitate was collected by filtration and washed with a small amount of H_2O (2 × 20 mL) to give white solid.

Yield 0.59 g, 1.60 mmol, 70.5%.

Molecular Weight 369.16 g mol^{-1}.

^{1}H NMR (500 MHz, $CDCl_3$): δ = 8.65 (s, 2H), 8.00–7.91 (m, 4H), 7.80 (s, 4H), 6.53 (s, 2H), 2.87 (s, 3H) ppm.

^{13}C{^{1}H} NMR (125 MHz, $CDCl_3$): δ = 151.22, 142.26, 139.56, 127.10, 118.66, 117.44, 111.65, 111.05, 107.88, 102.29, 11.26 ppm.

EI-MS m/z (%): 369 (100) $[M]^+$.

Anal. Calcd for **HL$^{Me\text{-}Pz}$** ($C_{20}H_{16}N_8$): C, 65.19; H, 4.38; N, 30.42. Found: C, 64.88; H, 4.35; N, 30.76.

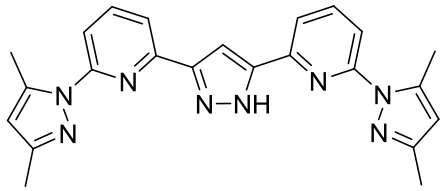

3,5-bis(6-(3,5-dimethyl-1*H*-pyrazol-1-yl)yridine-2-yl)pyrid-2-yl)pyrazole (HL$^{Me4\text{-}Pz}$)

Solid **VII** (0.42 g, 1.02 mmol) was suspended in EtOH (10 mL). $N_2H_4 \cdot H_2O$ (0.5 mL) was added and the reaction mixture was refluxed at 80℃ for four hours prior to stirring overnight at RT. The resulting white precipitate was collected by filtration and washed with a small amount of EtOH to yield the desired ligand.

Yield 0.34 g, 0.83 mmol, 45.5% (over two steps).

Molecular Weight 411.20 g mol^{-1}.

^{1}H NMR (300 MHz, $CDCl_3$): δ = 7.88 – 7.83 (m, 4H), 7.75 – 7.71 (m, 2H), 7.31 (s, 1H), 6.05 (s, 2H), 2.76 (s, 6H), 2.33 (s, 6H) ppm.

^{13}C{^{1}H} NMR (75 MHz, $CDCl_3$): δ = 153.17, 150.07, 141.34, 139.23, 116.60, 114.81, 109.37, 102.06, 15.04, 13.66 ppm.

EI-MS m/z (%): 411 (100) $[M]^+$.

Anal. Calcd (%) for **HL$^{Me4\text{-}Pz}$** ($C_{23}H_{22}N_8$): C, 67.28; H, 5.41; N, 27.31. Found: C, 67.98; H, 5.87; N, 26.15.

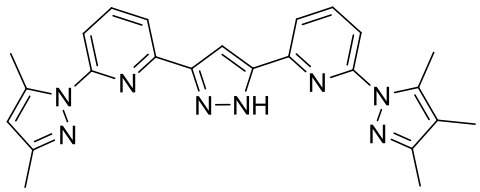

2-(3,5-dimethyl-1*H*-pyrazol-1-yl)-6-(3-(6-(3,4,5-trimethyl-1*H*-pyrazol-1-yl)pyridin-2-yl)-1*H*-pyrazol-5-yl)pyridine (HL$^{Me5\text{-}Pz}$)

Solid **IX** (0.68 g, 2.2 mmol) was collected by filtration and suspended in a minimum volume of EtOH. $N_2H_4 \cdot H_2O$ (0.5 mL) was added and the reaction mixture was refluxed at 80℃ for 4 hours prior to stirring overnight at RT. The resulting white precipitate was collected by filtration and washed with EtOH to yield the desired ligand.

Yield 0.45 g, 1.06 mmol, 57.3% (over two steps).

Molecular Weight 425.22 g mol^{-1}.

^{1}H NMR (300 MHz, $CDCl_3$): δ = 7.64 – 7.81 (m, 6H), 7.25 (s, 1H), 5.99 (s, 1H), 2.71 (s, 3H), 2.61 (s, 3H), 2.27(s, 6H), 1.95(s, 3H) ppm.

^{1}H NMR (400 MHz, DMSO-d6): δ = 13.73 (s, 1H,NH), 7.99-8.05 (br, 2H，H^5), 7.83 – 7.90 (br, 2H, H^4), 7.72 – 7.77 (q, *J* = 8.0 Hz, 2H， H^6), 7.40 (s, 1H, H^7), 6.15 (s, 1H， H$^{2'}$), 2.75 (s, 3H， H$^{1'}$), 2.66 (s, 3H, H1), 2.21 (s, 3H， H$^{3'}$), 2.16 (s, 31H, H^3), 1.95 (s, 3H， H^2) ppm.

^{1}H NMR (400 MHz, DMF-d6): δ = 13.91 (s, 1H), 8.04 – 8.10 (q, *J* = 8.0 Hz, 2H), 7.941 – 7.99 (q, *J* = 8.0 Hz, 2H), 7.82 – 7.87 (q, *J* = 8.0 Hz, 2H), 7.580 (s, 1H， H^7), 6.195 (s, 1H), 2.85 (s, 3H), 2.76 (s, 3H), 2.27 (s, 3H), 2.23 (s, 3H), 2.01 (s, 3H) ppm.

^{13}C{^{1}H} NMR (100 MHz, DMSO-d6): δ = 152.97, 152.76, 151.80, 149.93, 148.72, 145.72, 143.12, 141.14, 139.71, 137.14, 118.08, 116.22, 114.90, 114.04, 132.26 ppm.

EI-MS m/z (%): 425 (100) [M]$^+$.

Anal. Calcd (%) for **HL$^{Me5\text{-}Pz}$** ($C_{24}H_{24}N_8$): C, 67.89; H, 5.70; N, 26.41. Found: C, 67.98; H, 5.87; N, 26.15.

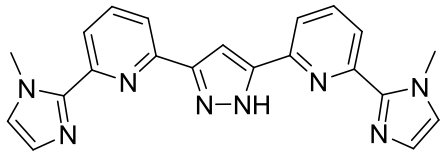

1,3-bis(6- (1-methyl-1*H*-imidazol-2-yl)yridine-2-yl)pyrazole (HL$^{Me\text{-}Im}$)

Complex **XII** (1.32 g, 35.1 mmol) was suspended in ethanol (20 mL) and hydrazine hydrate (2 mL) was added. The mixture was heated to reflux for 5 hours and continued to stir overnight at room temperature. A white precipitate was collected by filtration and washed with a small amount of H_2O (2 × 10 mL) to give white solid.

Yield 1.05 g, 27.56 mmol, 78.8%.

Molecular Weight 381.17 g mol^{-1}.

^{1}H NMR (500 MHz, $CDCl_3$): δ = 8.15 – 8.13 (m, 2H), 7.827 – 7.82 (m, 4H), 7.34 (s, 1H), 7.17 (s, 2H), 7.03(s, 2H), 4.24 (s, 6H) ppm.

^{13}C{^{1}H} NMR (125 MHz, $CDCl_3$): δ = 150.32, 144.68, 137.65, 128.41, 124.547, 122.10, 118.62, 101.63, 36.52 ppm.

EI-MS m/z (%): 383 (100) $[M]^+$.

Anal. Calcd (%) for **HL$^{Me\text{-}Im}$** ($C_{21}H_{18}N_8$): C, 65.94; H, 4.74; N, 29.31. Found: C, 65.98; H, 4.87; N, 29.04.

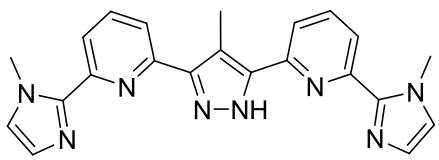

4-methyl-1,3-bis(6-(1-methyl-1*H*-imidazol-2-yl)yridine-2-yl)pyrazole (HL$^{Me\text{-}MeIm}$)

Complex **XIII** (0.42 g, 1.06 mmol) was suspended in ethanol (10 mL) and hydrazine hydrate (0.2 mL) was added. The mixture was heated to reflux for 5 h and continued

to stir overnight at room temperature. A white precipitate was collected by filtration and washed with a small amount of H_2O (2 × 5 mL) to give white solid.

Yield 0.34 g, 0.85 mmol, 80.0%.

Molecular Weight 396.4 g mol^{-1}.

^{1}H NMR (300 MHz, $CDCl_3$): δ = 7.15 (d, J = 7.86 Hz, 2H), 7.86 (t, J = 7.86 Hz, 2H), 7.76 (d, J = 7.83 Hz, 2H), 7.17 (s, 2H), 7.02(s, 2H), 4.19 (s, 6H), 2.73 (s, 3H) ppm.

^{13}C{^{1}H} NMR (125 MHz, $CDCl_3$): δ = 150.25, 144.95, 137.65, 128.41, 124.41, 121.73, 120.28, 113.19, 36.92, 10.99 ppm.

EI-MS m/z (%): 397 (100) $[M]^+$.

Anal. Calcd (%) for **HL$^{Me\text{-}MeIm}$** ($C_{22}H_{20}N_8$): C, 66.64; H, 5.09; N, 28.28. Found: C, 65.98; H, 5.17; N, 28.85.

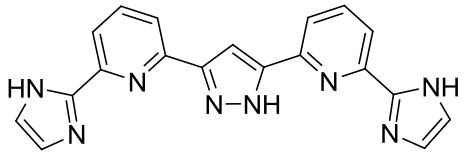

1,3-bis(6-(1*H*-imidazol-2-yl)yridine-2-yl)pyrazole (HL^{Im})

To a solution of **XVIII** (208.30 mg, 0.75 mmol) in 20 mL MeOH was added glyoxal trimer dehydrate (125.0 mg, 0.59 mmol) followed by slow addition of 0.05 mL of 7 N ammonia (MeOH solution). After stirring 12 hours at RT, the solvent was evaporated in vacuo, and the residue was dissolved H_2O (20 mL) and DCM (20 mL). The aqueous phase was extracted with DCM (2 × 20 mL). The combined extracts were dried to yield red solid as **HL^{Im}**.

Yield 208.30 mg, 0.75 mmol, 50%.

Molecular Weight 354.40 g mol^{-1}.

^{1}H NMR (300 MHz, DMSO-d_6): δ = 13.77 (s, 1H), 12.79 (s, 2H), 8.02 – 7.57 (m, 7H), 7.23 – 7.09 (m, 4H) ppm.

EI-MS m/z (%): 355 (100) $[M]^+$.

Anal. Calcd (%) for **HL^{Im}** ($C_{19}H_{14}N_8$): C, 64.38; H, 3.98; N, 31.63. Found: C, 64.21; H, 4.17; N, 21.62.

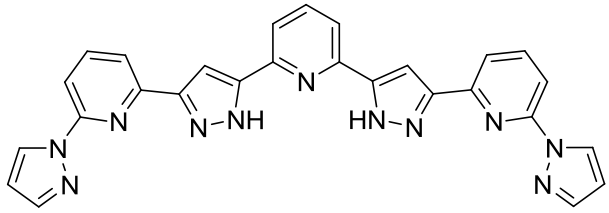

2,6-bis(3-(6-(1*H*-pyrazol-1-yl)yridine-2-yl)-1*H*-pyrazol-5-yl)pyridine (H$_2$L^{Pz})

Crude compound **XX** (1.05 g, 2.28 mmol) was suspended in EtOH (25 mL) and $N_2H_4{\cdot}H_2O$ (0.6 mL) was added. The mixture was heated to reflux for 5 hours and continued to stir overnight at RT. The precipitate was collected by filtration and washed with a small amount of water (2 × 5 mL) to give white solid as product.

Yield 775.32 mg, 1.56 mmol, 68.4%.

Molecular Weight 497.5 g mol^{-1}.

^{1}H NMR (500 MHz, DMSO-d_6): δ = 8.17 – 8.02 (m, 2H), 7.99 – 7.83 (m, 2H), 6.65 (s, 2H) ppm.

^{13}C NMR (125 MHz, DMSO-d_6): δ = 167.40, 162.45, 161.91, 150.53, 150.50, 150.47, 149.00, 142.56, 142.34, 140.93, 140.35, 139.35, 139.00, 137.62, 127.85, 127.55, 123.69, 122.76, 121.99, 120.66, 120.44, 117.26, 116.98, 110.36, 108.14, 108.11, 103.28, 102.74 ppm.

EI-MS m/z (%): 497(100) $[M]^+$.

Anal. Calcd (%) for **H$_2$L^{Pz}** ($C_{27}H_{19}N_{11}$): C, 65.17; H, 3.85; N, 30.98. Found: C, 65.21; H, 3.77; N, 31.98.

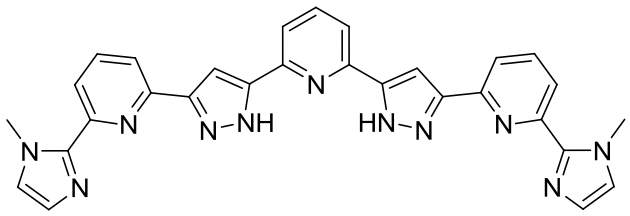

2,6-bis(3-(6-(1-methyl-1*H*-imidazol-2-yl)yridine-2-yl)-1*H*-pyrazol-5-yl)pyridine ($H_2L^{Me\text{-}Im}$)

Crude compound **XXI** (1.22 g, 2.28 mmol) was suspended in ethanol (25 mL) and hydrazine hydrate (0.6 mL) was added. The mixture was heated to reflux for 5 hours and continued to stir overnight at RT. The precipitate was collected by filtration and washed with a small amount of H_2O (2 × 5 mL) to give white solid as product.

Yield 840.32 mg, 1.60 mmol, 70.2%.

Molecular Weight 525.2 g mol^{-1}.

^{1}H NMR (500 MHz, DMSO-d_6): δ = 8.06 – 7.90 (m, 10H), 7.52 (s, 1H), 7.37 (d, 2H), 7.06 (d, 2H), 4.24 (d, 2H) ppm.

^{13}C NMR (125 MHz, DMSO-d_6): δ = 167.63, 150.13, 143.81, 137.86, 137.50, 127.78, 125.35, 122.76, 120.94, 118.61, 117.91, 102.28, 36.39, 36.27 ppm.

EI-MS m/z (%): 525 (100) $[M]^+$.

Anal. Calcd (%) for **$H_2L^{Me\text{-}Im}$** ($C_{29}H_{23}N_{11}$): C, 66.26; H, 4.41; N, 29.33. Found: C, 65.21; H, 3.77; N, 31.98.

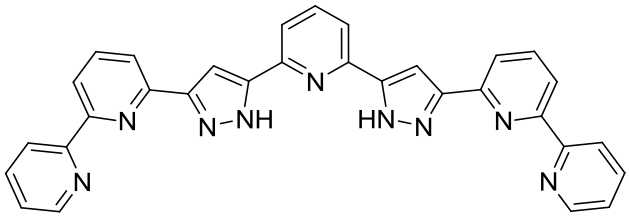

2,6-bis(3-(2,2'-bipyridin-6-yl)-1*H*-pyrazol-5-yl)pyridine (H_2L^{Py})

Crude compound **XXII** (1.20 g, 2.28 mmol) was suspended in ethanol (25 mL) and hydrazine hydrate (0.6 mL) was added. The mixture was heated to reflux for 5 hours and continued to stir overnight at RT. The precipitate was collected by filtration and washed with a small amount of H_2O (2 × 5 mL) to give white solid as product.

Yield 972.19 mg, 1.87 mmol, 82.0%.

Molecular Weight 519.6 g mol^{-1}.

^{1}H NMR (300 MHz, DMSO-d_6): δ = 8.70 – 8.80 (m, 2H), 8.39 – 8.33 (m, 2H), 8.11 – 7.99 (m, 9H), 7.85 – 7.88 (m, 2H), 7.85 – 7.88 (m, 2H), 7.53 – 7.47 (m, 2H) ppm.

EI-MS m/z (%): 519 (100) $[M]^+$.

Anal. Calcd (%) for $\mathbf{H_2L^{Py}}$ ($C_{31}H_{21}N_9$): C, 71.65; H, 4.08; N, 24.27. Found: C, 65.21; H, 3.77; N, 31.98.

9.2.2. Synthesis of Complexes

$[Fe^{II}_4L^{Pz}_4](BF_4)_4$ (1)

The ligand $\mathbf{HL^{Pz}}$ (280 mg, 0.8 mmol) together with NaO^tBu (80 mg, 0.88 mmol) was in dry MeOH (4 mL) for one hour, resulting in bright-yellow solution, after which was added dropwise to a solution of $Fe(BF_4)_2 \cdot 6H_2O$ (320 mg, 0.96 mmol) in degassed and dry MeOH (4 mL). The solution gradually turned red-brown and was stirred overnight at room temperature. The reaction solution was filtered and the majority of the filtrate solvent was removed by rotary evaporation. The remaining reaction mixture was then poured into stirred diethyl ether (300 mL) and further stirred for 30 min. After sedimentation, the main part of the solvent was decanted. The residue was washed repeatedly in the same way. The resulting red-brown powder was subsequently dried in vacuo, which was finally crystallized by diffusion of diethyl ether into a solution of the crude complex in MeCN.

Yield 320 mg, 0.16 mmol, 80%.

Molecular Weight 1984.0 g mol^{-1}.

^{1}H NMR (500 MHz, CD_3CN): δ = 113.82 (s, 1H), 62.68 (s, 2H), 60.05 (br, 2H), 56.51 (s, 4H), 34.12 (s, 2H), 12.22(s, 2H) ppm.

^{13}C NMR (125 MHz, CD_3CN): δ = 698.69, 621.33, 615.97, 518.39, 305.22, 298.48, 184.15, –199.66, –348.70 ppm.

IR (KBr pellet, cm^{-1}): 743.9 (w), 798.2 (s), 955.8 (m), 989.5 (m), 1020.8 (s), 1054.5 (s), 1079.9 (s), 1124.4 (m), 1173.8 (m), 1214.6 (w), 1241.2 (w), 1292.8 (w), 1310.9

(s), 1347.0 (w), 1401.2(m), 1445.8 (m), 1474.6 (s), 1520.3 (w), 1540.8 (m), 1572.1 (m), 1614.2 (m), 3080.3 (w), 3423.5 (s).

ESI-MS (MeCN): m/z (%) = 409.1 $[Fe_4L_4]^{4+}$, 551.8 $[Fe_4L_4(BF_4)]^{3+}$, 905.2 $[Fe_4L_4(BF_4)_2]^{2+}$.

UV/vis (CH_3CN): λ_{max} = 244, 266, 308, 462 nm.

Anal. Calcd for $[Fe_4(C_{19}H_{13}N_8)_4(BF_4)_4]$: C 46.00, H 2.64, N 22.59. Found: C 45.93, H 2.74, N 21.83.

$[Fe^{II}_4L^{Me\text{-}Pz}_4](BF_4)_4$ (2)

By a procedure similar to that used for preparing complex **1**, complex **2** was obtained by using **$HL^{Me\text{-}Pz}$** (297.2 mg,0 .81 mmol) instead of **HL^{Pz}**, and dry DMF (1 mL) was added in the MeOH solution. The precipitation of a voluminous red-brown material was observed after stirring overnight at room temperature. The resulting red-brown powder was washed with diethyl ether and subsequently dried in vacuo, which was finally crystallized by diffusion of diethyl ether into a solution of the crude complex in CH_3CN.

Yield 340 mg, 0.17 mmol, 84%.

Molecular Weight 2040.1 g mol^{-1}.

^{1}H NMR (500 MHz, CD_3CN): δ = 69.56 (s, 2H), 68.94 (br, 1H), 55.195 (s, 2H), 52.19 (s, 3H), 51.88 (s, 1H), 32.93 (s, 2H), 10.78 (s, 2H) ppm.

^{13}C NMR (125 MHz, CD_3CN): δ = 719.46, 623.02, 589.88, 512.12, 372.48, 286.08, 201.10, 188.87, –169.91 ppm.

IR (KBr pellet, cm^{-1}): 701.4 (w), 758.8 (m), 804.8 (m), 954.4 (m), 990.8 (w), 1035.8 (s), 1066.6 (w), 1086.7 (s), 1127.0 (m), 1167.2 (m), 1210.5 (w), 1220.4 (w), 1263.7 (w), 1305.3 (m), 1345.6 (w), 1380.2 (w), 1406.0 (m), 1472.1 (s), 1506.6 (w), 1524.9 (m), 1576.71 (m), 1609.2 (m), 3083.3 (w), 3423.4 (s).

ESI-MS (CH_3CN): m/z (%) = 423.1 $[Fe_4L_4]^{4+}$, 570.5 $[Fe_4L_4(BF_4)]^{3+}$, 933.2 $[Fe_4L_4(BF_4)_2]^{2+}$.

UV/vis (CH_3CN): λ_{max} = 246, 272, 330, 475 nm.

Anal. Calcd for $[Fe_4(C_{20}H_{15}N_8)_4(BF_4)_4]$: C 47.09, H 2.96, N 21.97. Found: C 46.69, H 3.02, N 21.64.

$[Fe^{II}_4L^{Me4\text{-}Pz}_4](BF_4)_4$ (3)

Complex **3** was produced by a procedure similar to that used for preparing complex 2, except **$HL^{Me4\text{-}Pz}$** (327.4 mg, 0.78 mmol) was employed instead of **$HL^{Me\text{-}Pz}$**, and dry DMF (1.5 mL) was added. The resulting red-brown powder was obtained.

Yield 350 mg, 0.16 mmol, 82%.

Molecular Weight 2208.5 g mol^{-1}.

^{1}H NMR (500 MHz, CD_3CN): δ = 73.97 (s, 1H), 62.92 (s, 2H), 58.39 (s, 2H), 41.45 (s, 2H), 13.13 (s, 6H), 12.24 (s, 2H), –1.44 (s, 6H) ppm.

^{13}C NMR (125 MHz, CD_3CN, 298 K): δ = 634.29, 586.25, 583.36, 520.00, 400.38, 242.12, 197.69, 64.54, –251.66 ppm.

IR (KBr pellet, cm^{-1}): 669.6 (w), 718.8 (w), 752.2 (w), 844.9 (s), 985.8 (w), 1031.8 (w), 1058.6 (w), 1086.7 (s), 1126.6 (m), 1176.0 (w), 1263.5 (w), 1315. 9 (w), 1385.6 (w), 1423.4 (w), 1446.4 (m), 1472.9 (m), 1506.6 (w), 1545.4 (w), 1578.2 (m), 1610.2 (m), 2925.3 (w), 3461.5 (s).

ESI-MS (CH_3CN): m/z (%) = 465.4 $[Fe_4L_4]^{4+}$, 626.8 $[Fe_4L_4(BF_4)]^{3+}$, 1017.2 $[Fe_4L_4(BF_4)_2]^{2+}$.

UV/vis (CH_3CN): λ_{max} = 248, 270, 319, 334, 480 nm.

Anal. Calcd for $[Fe_4(C_{23}H_{21}N_8)_4(BF_4)_4]$: C 50.03, H 3.83, N 20.30. Found: C 49.63, H 3.98, N 20.58.

$[Fe^{II}_4L^{Me5\text{-}Pz}_4](BF_4)_4$ (4)

Using ligand **$HL^{Me5\text{-}Pz}$** (349.7 mg, 0.81 mmol) instead of **$HL^{Me\text{-}Pz}$**, complex **4** was obtained by a procedure similar to that used for preparing complex **2**, and dry DMF (2 mL) was added. The resulting red-brown powder was obtained.

Yield 380 mg, 0.17 mmol, 84%.

Molecular Weight 2264.6 g mol^{-1}.

^{1}H NMR (500 MHz, CD_3CN): δ = 74.90 – 75.19 (br, 1H, H^7), 57.90 – 63.78 (m, 2H, H^6), 56.77 – 57.62 (m, 1H, H^2), 42.37 – 43.45 (m, 2H, H^4), 11.12 – 15.77 (m, 8H,), 0.18-0.97 (m, 9H) ppm.

IR (KBr pellet, cm^{-1}): 663.6 (w), 755.8 (m), 792.2 (m), 832.9 (w), 953.0 (w), 989.8 (m), 1023.9 (s), 1084.4 (s), 1108.6 (w), 1126.7 (m), 1171.6 (m), 1248.3 (w), 1278.9 (w), 1321.9 (m), 1355.6 (m), 1391.4 (m), 1418.2 (m), 1448.9 (s), 1473.4 (s), 1540.9 (m), 1562.2 (s), 1612.7 (s), 3067.3 (w), 3412.5 (s).

ESI-MS (CH_3CN): m/z (%) = 479.4 $[Fe_4L_4]^{4+}$, 645.5 $[Fe_4L_4(BF_4)]^{3+}$, 1045.3. $[Fe_4L_4(BF_4)_2]^{2+}$.

UV/vis (CH_3CN): λ_{max} = 250, 268, 336, 486 nm.

Anal. Calcd for $[Fe_4(C_{24}H_{23}N_8)_4(BF_4)_4]$: C 50.92, H 4.09, N 19.79. Found: C 51.11, H 3.86, N 20.04.

$[Fe^{II}_3Fe^{III}L^{Pz}_4](BF_4)_5$ (5)

Complex **1** (50.0 mg, 0.025 mmol) and thianthrenium tetrafluoroborate (80.0 mg, 0.25 mmol) were dissolved in CH_3CN (10 mL) and stirred for overnight. The solution turned deep purple and was then filtered under ambient conditions. The black crystalline material was obtained by layering the CH_3CN solution containing the crude product with Et_2O.

Yield 30.0 mg, 0.012 mmol, 48.20%.

Molecular Weight 2071.0 g mol^{-1}.

$[Fe^{II}_4L^{Me\text{-}Im}_4](ClO_4)_4$ (6)

NaO^tBu (8.1 mg, 0.08 mmol, 1.1 eq.) was added to a solution of **$HL^{Me\text{-}Im}$** (30.0 mg, 0.076 mmol) in MeOH (5.0 mL) under an inert atmosphere of argon. After 0.5 hour, this solution was added dropwise to a solution of $Fe(ClO_4)_2 \cdot 6H_2O$ (33.1 mg, 0.09 mmol) in MeOH (2 mL). The reaction mixture was stirred overnight and then filtered under ambient conditions. Slow diffusion of diethyl ether into the filtrate resulted in the formation of black block crystals.

Yield 34.0 mg, 0.016 mmol, 84.2%.

Molecular Weight 2150.9 g mol^{-1}.

IR (KBr pellet, cm^{-1}): 627.3 (m), 696.3 (w), 721.2 (w), 803.9 (m), 939.0 (w), 1016.4 (w), 1043.9 (w), 1090.4 (s), 1112.6 (w), 1123.7 (w), 1179.6 (w), 1231.3 (w), 1256.4 (m), 1286. 9 (w), 1314.3 (w), 1347.4 (w), 1380.2 (w), 1424.9 (w), 1468.8 (m), 1529.9 (m), 1565.2 (m), 1606.7 (m), 3420.9 (s).

ESI-MS (CH_3CN): m/z (%) = 437.1 (100) $[Fe_4L_4]^{4+}$, 615.8 (70) $[Fe_4L_4(ClO_4)]^{3+}$, 974.1 (8) $[Fe_4L_4(ClO_4)_2]^{2+}$.

UV/vis (CH_3CN): λ_{max} = 270, 377, 498, 553, 670 nm.

Anal. Calcd (%) for ($[(C_{21}H_{18}N_8)_4Fe_4(ClO_4)_4 \cdot (H_2O)_2]$): C, 45.98; H, 3.46; N, 20.15. Found: C, 46.23; H, 3.33; N, 20.55.

$[Fe^{II}_3Fe^{III}L^{Me\text{-}Im}_4](ClO_4)_5$ (7)

Solution of complex **6** (34.0 mg, 0.016 mmol) in $MeNO_2$ (5.0 mL) was added excess $AgClO_4$ (15.5 mg, 0.075 mmol). The mixture was stirred overnight at RT. The precipitate (silver) was removed by filtration. Upon adding a large amount of Et_2O into this solution, the resulting powder appeared and repeatedly washed with Et_2O. The residue was re-dissolved in CH_3CN (5 mL). Slow diffusion of diethyl ether into the filtrate resulted in the formation of black block crystals $[Fe^{II}_2Fe^{III}_2L_4](ClO_4)_5$, which were collected by filtration.

Yield 10.35 mg, 0.0046 mmol, 28.7%

Molecular Weight 2250.3 g mol^{-1}.

$[Fe^{II}_2Fe^{III}_2L^{Me\text{-}Im}_4](ClO_4)_6$ (8)

Excess $AgClO_4$ (15.5 mg, 0.075 mmol) was added to a $MeNO_2$ (5.0 mL) solution of **6** (34.0 mg, 0.016 mmol). The mixture was stirred for one hour at 60℃, cooled to room temperature, and the precipitate (silver) was removed by filtration. Upon adding a large amount of Et_2O into this solution, the resulting powder appeared and repeatedly washed with Et_2O. The residue was re-dissolved in CH_3CN (10 mL). Slow diffusion of diethyl ether into the filtrate resulted in the formation of black block crystals, which were collected by filtration.

Yield 18.2 mg, 0.006 mmol, 48.7%.

Molecular Weight 2349.8 g mol^{-1}.

IR (KBr pellet, cm^{-1}): 627.3 (m), 636.3 (w), 688.2 (w), 697.9 (w), 727.6 (w), 744.4 (w), 763.8 (w), 802.2 (s), 865.1 (w), 940.7 (w), 972.4 (w), 1047.3 (w), 1092.4 (s), 1142. 9 (m), 1259.3 (m), 1300.4 (w), 1353.2 (w), 1388.2 (w), 1419.8 (w), 1482.9 (s), 1567.8 (m), 1611.7 (m), 3436.9 (s).

ESI-MS (CH_3CN): m/z (%) 349.9 (100) $[Fe_4L_4]^{5+}$, 486.2 (50) $[Fe_2L_2]^{2+}$, 649.4 (45) $[Fe_4L_4(ClO_4)_2]^{3+}$, 818.3 (65) $[FeL_2]^{+}$, 1023.6 (20) $[Fe_4L_4(ClO_4)_3]^{2+}$.

UV/vis (CH_3CN): λ_{max} = 270, 377, 602, 6703,792 nm.

Anal. Calcd. (%) for ($[Fe_4(C_{21}H_{17}N_8)_4(ClO_4)_6]$): C, 43.04; H, 2.93; N,19.13. Found: C, 42.99; H, 2.64; N, 19.41.

$[Fe^{III}_2(Ag^{I}_2)_2L^{Me\text{-}Im}_4](ClO_4)_6$ (9)

$Fe(ClO_4)_2 \cdot 6H_2O$ (13.8 mg, 0.038 mmol, 0.5 eq.) and **$HL^{Me\text{-}Im}$** (30.0 mg, 0.076 mmol) were dissolved in CH_3NO_2 (10 mL) and the solution immediately turned to a deep red color. After stirring for two hours, $AgClO_4$ (63 mg, 0.304 mmol, 4.0 eq.) was added, which resulted in the mixture color changing to blue. During 6 hours of stirring, a precipitate (silver) was removed by filtration. Upon adding a large amount of Et_2O into the solution, the resulting powder appeared and repeatedly washed with Et_2O. The residue was worked up with the same way as in the last step. Black block crystals were collected by filtration.

Yield 0.023 g, 0.008 mmol, 45%.

Molecular Weight 2349.8 g mol^{-1}.

IR (KBr pellet, cm^{-1}): 628.3 (m), 657.6 (w), 5 687.2 (w), 697.9 (w), 725.6 (w), 745.9 (w), 762.8 (w), 802.2 (m), 928.1 (w), 941.9 (w), 978.3 (w), 1087.3 (s), 1149.4 (s), 1247.9 (w), 1293.3 (m), 1357.4 (w), 1391.2 (w), 1421.2 (w), 1480.5 (s), 1570.9 (m), 1593.8 (w), 1618.7 (m), 3436.9 (s).

UV/vis (CH_3CN): λ_{max} = 268, 315, 593, 716, 776 nm.

Anal. Calcd (%) for $[Fe_2Ag_4(C_{21}H_{17}N_8)_4(ClO_4)_6])\cdot(CH_3CN)_2$: C, 37.92; H, 258; N,16.85. found: C, 38.00; H, 3.03; N, 16.79.

$[Fe^{II}{}_4L^{Me\text{-}MeIm}{}_4](BF_4)_4$ (10)

Under an inert atmosphere of argon ligand **$HL^{Me2\text{-}Im}$** (31.71 mg, 0.08 mmol) together with NaO^tBu (8.0 mg, 0.088 mmol) was 203yridine203 in MeOH (10 mL) for one hour. This solution was added dropwise to a solution of $Fe(BF_4)_2\cdot 6H_2O$ (33.0 mg, 0.088 mmol) in MeOH (5 mL). The solution gradually turned orange red and was stirred overnight and then filtered under ambient conditions. Most solvent was removed by rotary evaporation and the remaining reaction mixture was then poured into stirred Et_2O (50 mL) and further stirred for 30 min. After sedimentation, the main part of the solvent was decanted. The residue was washed repeatedly in the same way. The orange red crystalline material was obtained by layering the CH_3CN solution containing the crude product with Et_2O.

Yield 19.37 mg, 0.009 mmol, 45.1%.

Molecular Weight 2152.4 g mol^{-1}.

$[Co^{II}{}_4L^{Pz}{}_4](BF_4)_4$ (11)

Ligand **HL^{Pz}** (280 mg, 0.8 mmol) together with NaO^tBu (80 mg, 0.88 mmol) was 203yridine203 in CH_3CN (50 mL) for one hour under an inert atmosphere of argon. This solution was added dropwise to a solution of $Co(BF_4)_2\cdot 6H_2O$ (270 mg, 0.88 mmol) in CH_3CN (20 mL). The solution gradually turned deep orange and was stirred overnight and then filtered under ambient conditions. The yellow orange crystalline material was obtained by layering the CH_3CN solution containing the crude product with Et_2O.

Yield 230 mg, 0.12 mmol, 58.1%.

Molecular Weight 1996.4 g mol^{-1}.

^{1}H NMR (500 MHz, CD_3CN): δ = 188.05 (s, 1H), 121.76 (s, 2H), 116.17 (s, 2H), 45.62 (s, 2H), 45.22 (s, 2H), 23.67 (s, 2H), –4.25 (s, 2H) ppm.

^{13}C NMR (125 MHz, CD_3CN): δ = 658.2, 643.39, 589.08, 579.55, 470.18, 470.09,

287.94, 286.48, 233.71, 232.65, –29.24 ppm.

IR (KBr pellet, cm^{-1}): 756.9.9 (w), 797.3 (s), 955.5 (w), 989.9 (w), 1018.3 (w), 1036.5(w), 1056.8(w), 1085.1 (s), 1170.3 (w), 1121.6(w), 1263.5 (w), 1316.1 (w), 1349.3 (w), 1401.5(m), 1445.9 (w), 1475.6 (s), 1522.9 (w), 1537.1 (w), 1574.2 (s), 1614.1 (s), 3422.4 (s).

ESI-MS (CH_3CN): m/z (%) = 412.1 (100) $[Co_4L_4]^{4+}$, 555.8 (40) $[Co_4L_4(BF_4)]^{3+}$, 911.2 (10) $[Co_4L_4(BF_4)_2]^{2+}$.

UV/vis (CH_3CN): λ_{max} = 242, 277, 334, 434, 529 nm.

Anal. Calcd. (%) for $[Co_4(C_{19}H_{13}N_8)_4(BF_4)_4]$: C 45.68, H 2.63, N 22.45; found: C 45.34, H 2.901, N 22.20.

$[Co^{II}_4L^{Me\text{-}pz}_4](BF_4)_4$ (12)

Complex **12** was obtained by a procedure similar to that used for preparing complex **11**, except $\mathbf{HL^{Me\text{-}Pz}}$ (289.0 mg 0.8 mmol) was employed instead of $\mathbf{HL^{Pz}}$.

Yield 270 mg, 0.13 mmol, 65%.

Molecular Weight 2052.5 g mol^{-1}.

^{1}H NMR (500 MHz, CD_3CN): δ = 130.00 (s, 2H), 128.40 (s, 2H), 107.40 (s, 3H), 41.76 (s, 2H), 40.35 (s, 2H), 25.45 (s, 2H), –9.34 (s, 2H) ppm.

^{13}C NMR (125 MHz, CD_3CN): δ = 668.13, 663.63, 630.55, 598.47, 467.53, 271.19, 240.37, 16.00 ppm.

IR (KBr pellet, cm^{-1}): 760.8 (w), 805.2 (s), 953.4(w), 1034.9(s), 1084.4 (s), 1172.5 (w), 1260.4 (m), 1307.8 (w), 1346.3(w), 1382.9(w), 1402.2 (m), 1473.1 (s), 1507.5 (w), 1524.6 (s), 1574.0 (s), 1610.5 (s), 3429.3 (s).

ESI-MS (CH_3CN): m/z (%) = 426.3 (100) $[Co_4L_4]^{4+}$, 574.4 (36) $[Co_4L_4(BF_4)]^{3+}$, 939.2 (12) $[Co_4L_4(BF_4)_2]^{2+}$.

UV/vis (CH_3CN): λ_{max} = 242, 279, 336, 438, 535 nm.

Analy. Calcd. (%) for $[(C_{20}H_{15}N_8)_4Co_4(BF_4)_4]$: C 46.77, H 2.94, N 21.83; found: C 46.83, H 3.09, N 21.61.

$[Co^{II}_4L^{Me\text{-}Im}_4](BF_4)_4$ (13)

$HL^{Me\text{-}Im}$ (68.0 mg, 0.18 mmol) and NaO^tBu (9.72 mg, 0.18 mmol) were dissolved in MeOH (20 mL). After stirring for one hour, a solution of $Co(BF_4)_2 \cdot 6H_2O$ (61.2 mg, 0.18 mmol) in $MeCH_3OH$ (5 mL) was added. The resulting mixture was stirred overnight at rt. Any precipitate was filtered off and the filtrate was added to large quantity Et_2O. The new precipitate was separated by filtration, washed with Et_2O and dried in vacuo. The crude product was obtained as a brown powder. Crystalline material suitable for further characterization could be obtained by slow diffusion of Et_2O into a solution of the crude product in CH_3CN.

Yield 34.92 mg, 0.02 mmol, 45%.

Molecular Weight 1724.3 g mol^{-1}.

^{1}H NMR (500 MHz, CD_3CN): δ = 153.30 (s, 1H), 134.24 (s, 2H), 89.92 (s, 2H), 56.36 (s, 2H), 38.64 (s, 2H), 19.15 (s, 2H), –23.38 (s, 6H) ppm.

^{13}C NMR (125 MHz, CD_3CN): δ = 1127.21, 623.151, 612.75, 495.11, 447.15, 336.77, 197.41, 91.12, 88.88, –52.44 ppm.

IR (KBr pellet, cm^{-1}): 653.9 (w), 688.0 (w), 699.8 (w), 726.0 (w), 740.0 (w), 767.3 (w), 802.5 (s), 920.2 (w), 940.1 (w), 1039.5 (s), 1084.8 (s), 1121.6 (w), 1061.1 (w), 1170.3 (w), 1227.1 (w), 1258.5 (w), 1282.7 (m), 1310.3 (w), 1341.8 (m), 1397.9 (w), 1415.6 (w), 1574.9 (w), 1533.1 (w), 1564.2 (s), 1613.1 (s), 3104.5 (s), 3422.4 (s).

ESI-MS (CH_3CN): m/z (%) = 440.6 (100) $[Co_4L_4]^{4+}$, 615.8 (100) $[Co_4L_4(BF_4)]^{3+}$, 967.2 (75) $[Co_4L_4(BF_4)_2]^{2+}$.

UV/vis (CH_3CN): λ_{max} = 272, 308, 330, 383, 438 nm.

Analy. Calcd. (%) for $[Co_4(C_{23}H_{15}N_6)_4(BF_4)_4]$: C 52.97, H 2.90, N 16.12; found: C 52.83, H 3.09, N 15.61.

$[Co^{II}_4L^{Py}_4](BF_4)_4$ (14)

HL^{Py} (40.0 mg, 0.11 mmol) and NaO^tBu (10.4 mg, 0.126 mmol) were dissolved in CH_3CN (20 mL) and DMF (2 mL) at room temperature under an inert atmosphere of argon. $Co(BF_4)_2 \cdot 6H_2O$ (30.8 mg, 0.12 mmol) in CH_3CN (10 mL) was then added to give a yellow solution and stirred for overnight. Filtration and removal of solvent in

vacuo from the yellow filtrate left a yellow solid. Slow diffusion of Et_2O into a solution of the crude product in CH_3CN yielded red orange crystals.

Yield 20.8 mg, 0.01 mmol, 42%.

Molecular Weight 2084.6 g mol^{-1}.

^{1}H NMR (500 MHz, CD_3CN): δ = 204.41 (s, 2H), 148.83 (s, 1H), 96.94 (s, 2H), 47.76 (s, 2H), 42.83 (s, 2H), 21.45 (s, 2H), 19.18 (s, 2H), –11.86 (s, 2H) ppm.

^{13}C NMR (125 MHz, CD_3CN): δ = 1151.59, 582.41, 464.88, 404.79, 251.94, 221.53, 142.90, 47.49 ppm.

IR (KBr pellet, cm^{-1}): 626.0 (m), 655.0 (w), 701.3 (m), 777.5 (s), 825.2 (m), 976.1 (m), 1000.3 (s), 1057.1 (s), 1083.5 (s), 1245.7 (m), 1277.7 (w), 1311.8 (m), 1444.4 (s), 1458.6 (m), 1489.9 (w), 1535.1 (m), 1568.2 (s), 1603.1 (s), 3048.5 (s), 3421.4 (s).

ESI-MS (CH_3CN): m/z (%) = 434.3 (100) $[Co_4L_4]^{4+}$, 606.8 (36) $[Co_4L_4(BF_4)]^{3+}$, 955.2 (12) $[Co_4L_4(BF_4)_2]^{2+}$.

UV/vis (CH_3CN): λ_{max} = 238, 279, 336, 438, 546 nm.

Analy. Calcd. (%) for $[(C_{23}H_{15}N_6)_4Co_4(BF_4)_4]$: C 52.97, H 2.90, N 16.12; found: C 52.83, H 3.09, N 15.61.

$[Co^{II}_2Co^{III}_2L^{Pz}_4](BF_4)_6$ (15)

Complex **11** (100 mg, 0.05 mmol) and thianthrenium tetrafluoroborate (320 mg, 1.0 mmol) were dissolved in CH_3CN (20 mL) and stirred for overnight. The solution turned deep purple and was then filtered under ambient conditions. T he black crystalline material was obtained by layering the CH_3CN solution containing the crude product with Et_2O

Yield 70 mg, 0.03 mmol, 67.8%.

Molecular Weight 2170.0 g mol^{-1}.

^{1}H NMR (500 MHz, CD_3CN): δ = 158.51 (s, 1H), 126.26 (s, 1H), 96.92 (s, 1H), 61.89 (s, 1H), 60.51 (s, 1H), 25.96 (s, 1H), 22.95 (s, 1H), 7.42 (s, 1H), 7.16 (s, 1H), 0.59 (s, 1H), 0.15 (s, 1H), –14.30 (s, 1H), –30.88 (s, 1H) ppm.

^{13}C NMR (125 MHz, CD_3CN): δ = 941.16, 755.22, 745.56, 744.83, 588.44, 456.67,

318.25, 267.51, 222.23, 203.18, 145.65, 137.85, 135.46, 114.55, 110.85, 67.03, 65.16, 14.51 ppm.

IR (KBr pellet, cm^{-1}): 763.8 (w),804.2 (m), 987.2 (w), 1021.2 (w), 1036.9(w), 1063.8(w), 1083.7 (s), 1123.62(w), 1173.7 (m), 1261.7 (w), 1312.8 (m), 1351.1 (w), 1402.1(m), 1444.7 (w), 1478.1 (s), 1523.5 (w), 1541.9 (w), 1574.5 (s), 1619.2 (s), 3422.4 (s).

ESI-MS (CH_3CN): m/z (%) = 274.7 (90) $[Co_2L_2]^{3+}$, 329.7 (50) $[Co_4L_4]^{5+}$, 412.1 (20) $[Co_4L_4]^{4+}$.

UV/vis (CH_3CN): λ_{max} = 242, 277, 334, 409, 613 nm.

Analy. Calcd. (%) for $[Co_4(C_{19}H_{13}N_8)_4(BF_4)_6]$: C 41.98, H 2.51, N 20.63; found: C 41.64, H 2.90, N 20.52.

$[Co^{II}_2Co^{III}_2L^{Me\text{-}pz}_4](BF_4)_6$ (16)

Complex **16** was obtained in the same manner as **15**, using **12** (86.5 mg, 0.04 mmol) in place of **11**.

Yield 80 mg, 0.03 mmol, 71.2%.

Molecular Weight 2226.1 g mol^{-1}.

^{1}H NMR (500 MHz, CD_3CN): δ = 167.27 (s, 1H), 135.99 (s, 1H), 60.63 (s, 1H), 56.73 (s, 1H), 51.60 (s, 3H), 25.70 (s, 1H), 24.11 (s, 1H), 7.87 (s, 1H), 6.26 (s, 1H), 0.12 (s, 1H), –0.41 (s, 1H), –15.64 (s, 1H), –35.09 (s, 1H) ppm.

^{13}C NMR (125 MHz, CD_3CN): δ = 912.21, 762.24, 750.63, 592.35, 454.15, 341.27, 301.65, 277.26, 195.12, 138.73, 135.31, 131.90, 128.29, 113.59, 111.28, 61.13, 57.60, 52.94 ppm.

IR (KBr pellet, cm^{-1}): 770.3 (w), 805.9 (m), 952.5(w), 1032.0(s), 1058.5(w), 1084.4 (s), 1174.7(w), 1211.4 (w), 12620.3 (w), 1307.2 (m), 1347.9(m), 1386.8(w), 1400.9 (m), 1476.4 (m), 1496.8 (w), 1525.2 (m), 1570.2 (w), 1613.7 (m), 3408.1 (s).

ESI-MS (CH_3CN): m/z (%) = 284.1 (50) $[Co_2L_2]^{3+}$, 340.9 (28) $[Co_4L_4]^{5+}$, 426.1 (100) $[Co_4L_4]^{4+}$, 793.2 (15) $[CoL]^{+}$.

UV/vis (CH_3CN): λ_{max} = 242, 277, 334, 412, 619 nm.

Analy. Calcd. (%) for $[Co_4(C_{20}H_{15}N_8)_4(BF_4)_6]$: C 44.13, H 3.09, N 19.62; found: C 44.28, H 2.83, N 20.02.

$[Co^{II}_2Co^{III}_2L^{Me\text{-}Im}_4](BF_4)_6$ (17)

Complex **13** (34.5 mg, 0.02 mmol) and solid $AgBF_4$ (40.0 mg, 10 eq.) were dissolved in $MeNO_2$ and the mixture was stirred overnight at RT. The precipitated Ag was filtered off. $MeNO_2$ solvent was removed and the residue was redissolved in CH_3CN (5 mL). The solution was added a large quantity of Et_2O. The resulting green powder was repeatedly washed with Et_2O. Crystalline material suitable for further characterization could be obtained by slow diffusion of Et_2O into a solution of the crude product in CH_3CN.

Yield 32.0 mg, 0.014 mmol, 70.8%.

Molecular Weight 2258.2 g mol^{-1}.

^{1}H NMR (500 MHz, CD_3CN): δ = 130.87 (s, 1H), 90.23 (s, 1H), 70.05 (s, 1H), 52.94 (s, 1H), 30.97 (s, 1H), 30.22(s, 1H), 27.01 (s, 1H), 8.31 (s, 1H), 6.12 (s, 1H), 3.81 (s, 1H), 1.99 (s, 1H), -7.69 (s, 1H), –12.75 (s, 1H), –19.66 (s, 1H), –27.79 (s, 1H) ppm.

^{13}C NMR (125 MHz, CD_3CN): δ = 903.46, 581.42, 570.95, 408.383, 289.77, 274.05, 272.86, 259.27, 227.36, 217.37, 156.67, 144.92, 143.68, 136.55, 1357.105, 134.41, 1324.89, 129.02, 127.80, 127.27, 125.82, 108.41, 102.31, 100.94, 82.75, 81.26, 79.50 ppm.

IR (KBr pellet, cm^{-1}): 664.0 (w), 690.8 (w), 702.1 (w), 743.5 (w), 762.8 (w), 807.7 (m), 943.2 (w), 979.2 (w), 1039.1 (s), 1087.5 (s), 1120.7 (s), 1177.3 (w), 1256.8 (w), 1289.9 (w), 1307.6 (w), 1400.9 (w), 1475.1 (s), 1569.2 (m), 1611.1 (m), 3080.5 (s), 3412.4 (s).

ESI-MS (CH_3CN): m/z (%) = 347.45 (50) $[Co_4L_4]^{5+}$, 433.56 (78) $[Co_2L_2F]^{2+}$, 636.76 (20) $[Co_4L_4(BF_4)_2]^{3+}$, 809.19 (60) $[CoL_2]^{+}$.

UV/vis (CH_3CN): λ_{max} = 242, 308, 330, 419, 613 nm.

Analy. Calcd. (%) for $[(C_{19}H_{13}N_8)_4Co_4(BF_4)_6]$: C 42.02, H 2.41, N 20.65; found: C 41.64, H 2.90, N 20.52.

$[Co^{II}_2Co^{III}_2L^{Py}_4](BF_4)_6$ (18)

Complex **14** (41.68 mg, 0.02 mmol) and $AgBF_4$ (39.0 mg, 10 eq.) were dissolved in $MeNO_2$ (10 mL) and stirred for overnight. The solution turned olive-green and was then filtered under ambient conditions. Crystalline material suitable for further characterization could be obtained by slow diffusion of Et_2O into a solution of the crude product in CH_3CN.

Yield 31.9 mg, 0.014 mmol, 70.0%.

Molecular Weight 2282.2 g mol^{-1}.

^{1}H NMR (500 MHz, CD_3CN): δ = 116.24 (s, 1H), 88.65 (s, 1H), 74.92 (s, 1H), 52.78 (s, 1H), 24.44 (s, 1H), 16.46 (s, 1H), 10.90 (s, 1H), 1.99 (s, 1H), 1.77 (s, 1H), –4.53 (s, 1H), –11.90 (s, 3H), –21.54 (s, 3H), –31.59 (s, 1H) ppm.

^{13}C NMR (125 MHz, CD_3CN): δ = 922.10, 747.00, 609.29, 486.57, 461.157, 287.11, 240.19, 202.38, 171.23, 138.73, 131.10, 129.75, 1203.10, 108.54, 91.29, 90.71, 89.51, 88.24, 71.71, 66.66, 21.40, –19.08 ppm.

IR (KBr pellet, cm^{-1}): 612.3 (w), 629.3 (w), 650.0 (m), 687.0 (w), 703.3 (w), 747.3 (w), 775.5 (m), 818.2 (w), 975.1 (m), 1026.3 (s), 1054.3 (s), 1083.3 (s), 1126.1 (w), 1046.5 (w), 1249.7 (w), 1311.7 (m), 1340.8 (mw), 1440.4 (m), 1454.6 (m), 1485.9 (w), 1497.1 (w), 1568.2 (m), 1611.1 (m), 3072.5 (s), 3404.4 (s).

ESI-MS (CH_3CN): m/z (%) = 293.40 (100) $[Co_2L_2]^{3+}$, 449.59 (450) $[Co_2L_2F]^{2+}$, 821.25 (5) $[CoL_2]^+$.

UV/vis (CH_3CN): λ_{max} = 238, 279, 336, 452, 596 nm.

Analy. Calcd. (%) for $[Co_4(C_{21}H_{17}N_8)_4(BF_4)_6]$: C 44.16, H 3.00, N 19.63; found: C 44.64, H 2.90, N 20.02.

$[Fe^{II}_3(HL^{Pz})L^{Pz}_3](BF_4)_3$ (19)

The ligand **HL^{Pz}** (37.6 mg, 0.106 mmol) and NaO^tBu (5.30 mg, 0.55 mmol, 0.50 eq) was dissolved in CH_3CN (10 mL) under an inert atmosphere of dry argon. After stirring for 1 hour this solution was added to a solution of $Fe(BF_4)_2 \cdot 6H_2O$ (26.70 mg, 0.790 mmol) in CH_3CN (5 mL). The reaction mixture was stirred overnight and then

filtered under ambient conditions. The reaction solution was filtered and the majority of the filtrate solvent was removed by rotary evaporation. Crystalline material suitable for further characterization could be obtained by slow diffusion of Et_2O into a solution of the crude product in CH_3CN.

Yield 26.36 mg, 0.018 mmol, 67.3%.

Molecular Weight 1478.2 g mol^{-1}.

ESI-MS (CH_3CN): m/z (%) = 527.1 (100) $[Fe_3(HL)L_3]^{3+}$, 790.2 (12) $[Fe_3L_4]]^{2+}$, 800.2 (32) $[Fe_3(HL)L_3(F)]^{2+}$, 834.2 (40) $[Fe_3(HL)L_3(BF_4)]^{2+}$.

$[Fe^{II}_3(HL^{Me\text{-}Pz})L^{Me\text{-}Pz}_3](BF_4)_3$ (20)

Using ligand **$HL^{Me\text{-}Pz}$** (38.9 mg, 0.106 mmol) instead of **HL^{Pz}**, complex **20** was obtained by a procedure similar to that used for preparing complex **19**.

Yield 24.68 mg, 0.016 mmol, 60.7%.

Molecular Weight 1534.3 g mol^{-1}.

ESI-MS (CH_3CN): m/z (%) = 545.8 (100) $[Fe_3(HL)L_3]^{3+}$, 818.2 (36) $[Fe_3L_4]]^{2+}$, 828.7 (20) $[Fe_3(HL)L_3(F)]^{2+}$, 862.2 (12) $[Fe_3(HL)L_3(BF_4)]^{2+}$.

$[Fe^{II}_3(HL^{Me\text{-}Im})L^{Me\text{-}Im}_3](ClO_4)_3$ (21)

The ligand **$HL^{Me\text{-}Im}$** (40.5 mg, 0.106 mmol, 1.0 equiv) and NaOtBu (5.30 mg, 0.55 mmol) was dissolved in MeOH (10 mL) under an inert atmosphere of dry argon and stirred for one hour. This solution was added to a solution of $Fe(ClO_4)_2 \cdot 6H_2O$ (28.60 mg, 0.790 mmol) in MeOH (5 mL). The reaction mixture was stirred overnight and then filtered under ambient conditions. The reaction solution was filtered and the majority of the filtrate solvent was removed by rotary evaporation. Crystalline material suitable for further characterization could be obtained by slow diffusion of Et_2O into a solution of the crude product in CH_3CN.

Yield 26.36 mg, 0.016 mmol, 62.5%.

Molecular Weight 1628.4 g mol^{-1}.

ESI-MS (MeCN): m/z (%) = 437.1 (50) $[FeL_2]^{2+}$, 564.8 (100) $[Fe_3(HL)L_3]^{3+}$, 862.2 (5) $[Fe_3L_4]]^{2+}$.

10. Appendix

10.1. NMR Spectroscopy

10.1.1. NMR Spectroscopy of Ligands

3,5-bis(6-(1*H*-pyrazol-1-y) yridine-2-yl)pyrid-2-yl)pyrazole (HL^{Pz})

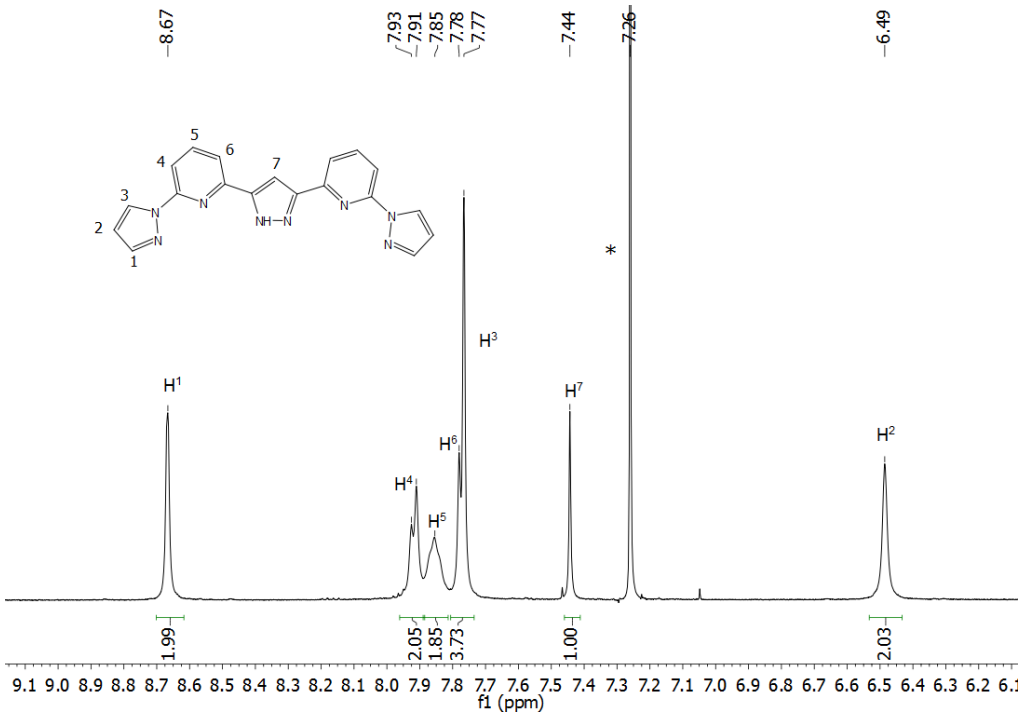

Figure 10.1. ^{1}H NMR spectrum (500 MHz, $CDCl_3$, 298 K) of $\mathbf{HL^{Pz}}$ (*$CHCl_3$).

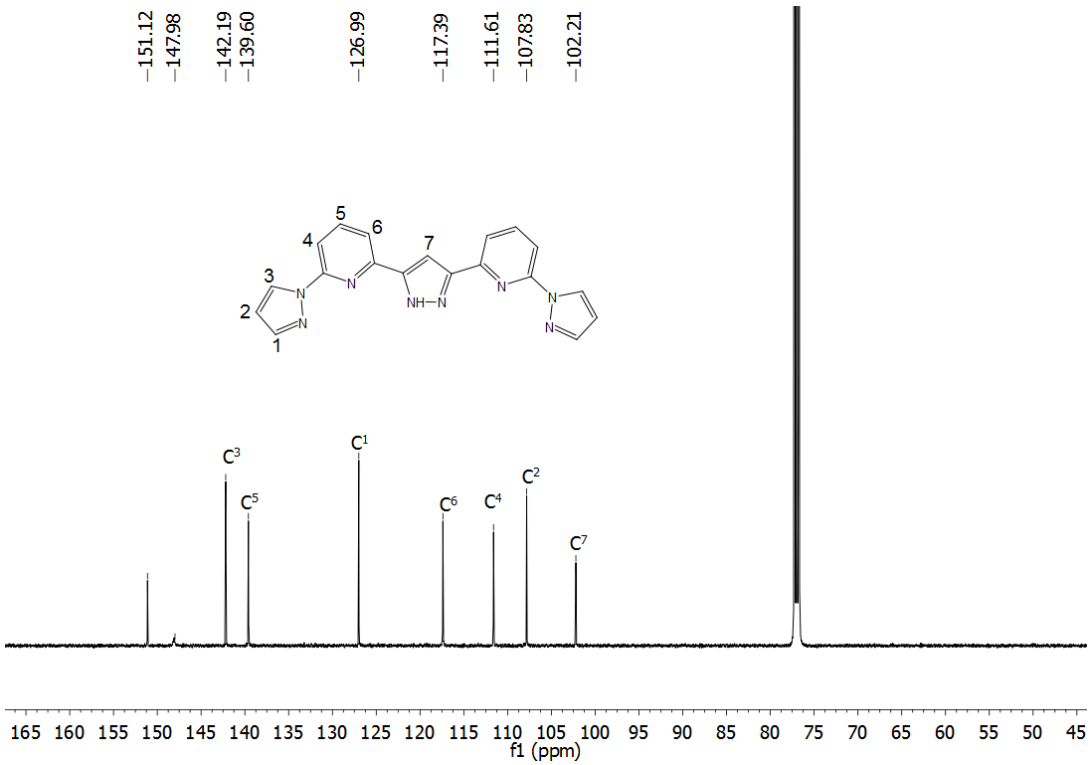

Figure 10.2. $^{13}C\{^{1}H\}$ NMR spectrum (125 MHz, $CDCl_3$, 298 K) of **HL^{Pz}**.

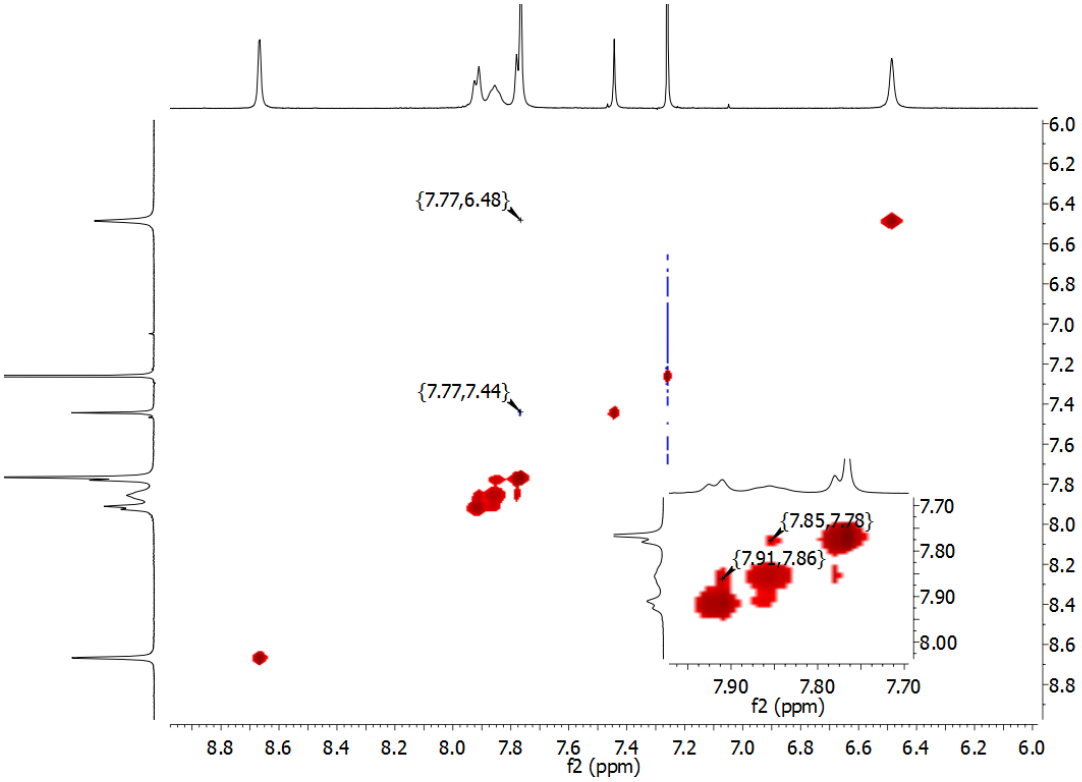

Figure 10.3. ^{1}H-^{1}H-NOESY spectrum (($CDCl_3$, 298 K)) of **HL^{Pz}**.

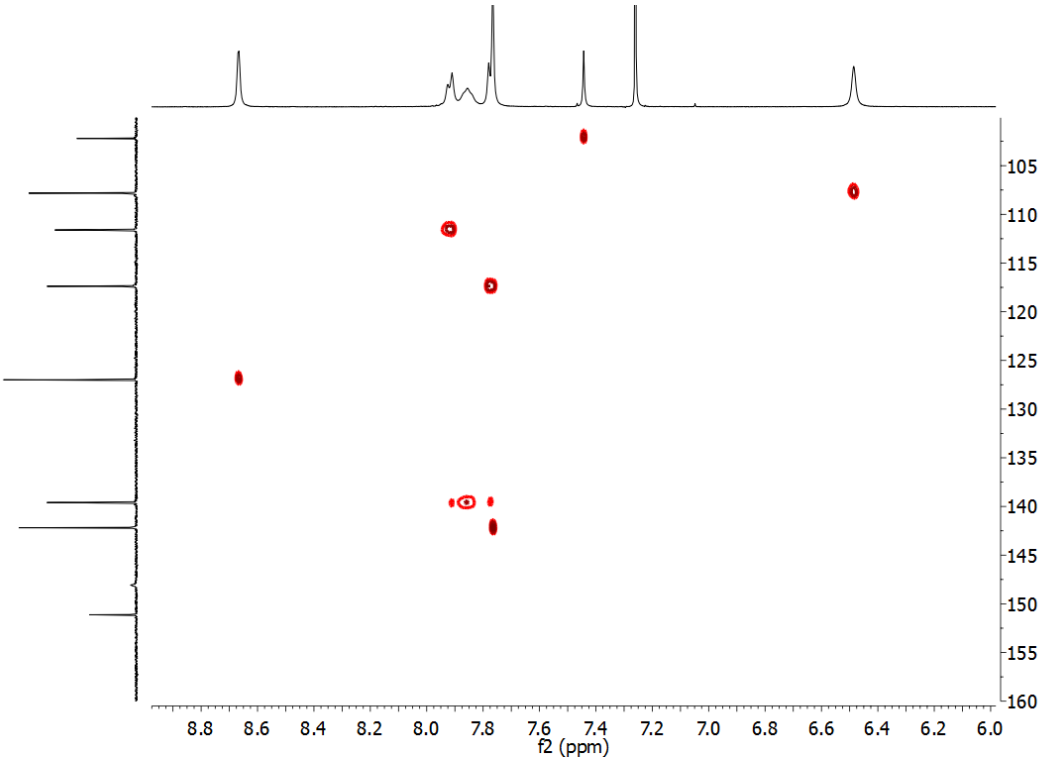

Figure 10.4. ^{1}H-^{13}C-HMQC spectrum ($CDCl_3$, 298 K) of **HL^{Pz}** in the ^{1}H: 6.0 to 9.0 ppm; ^{13}C: 100 to 160 ppm range.

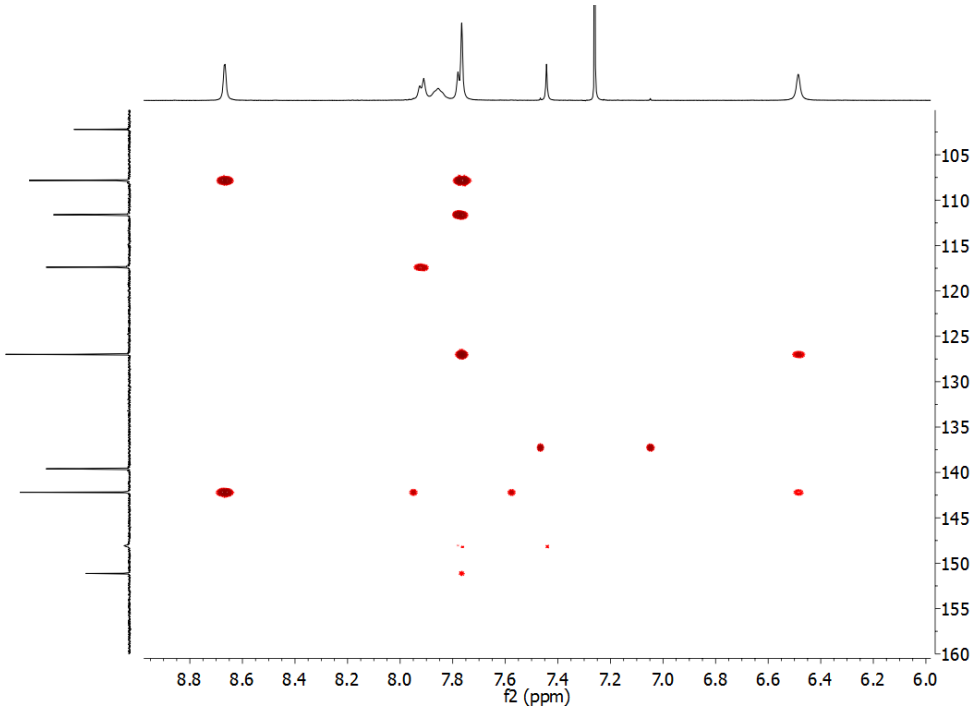

Figure 10.5. ^{1}H-^{13}C-HMBC spectrum ($CDCl_3$, 298 K) of **HL^{Pz}** in the ^{1}H: 6.0 to 9.0 ppm; ^{13}C: 100 to 160 ppm range.

4-methyl-3,5-bis(6-(1*H*-pyrazol-1-y)yridine-2-yl)pyrid-2-yl)pyrazole (HL^{Me-Pz})

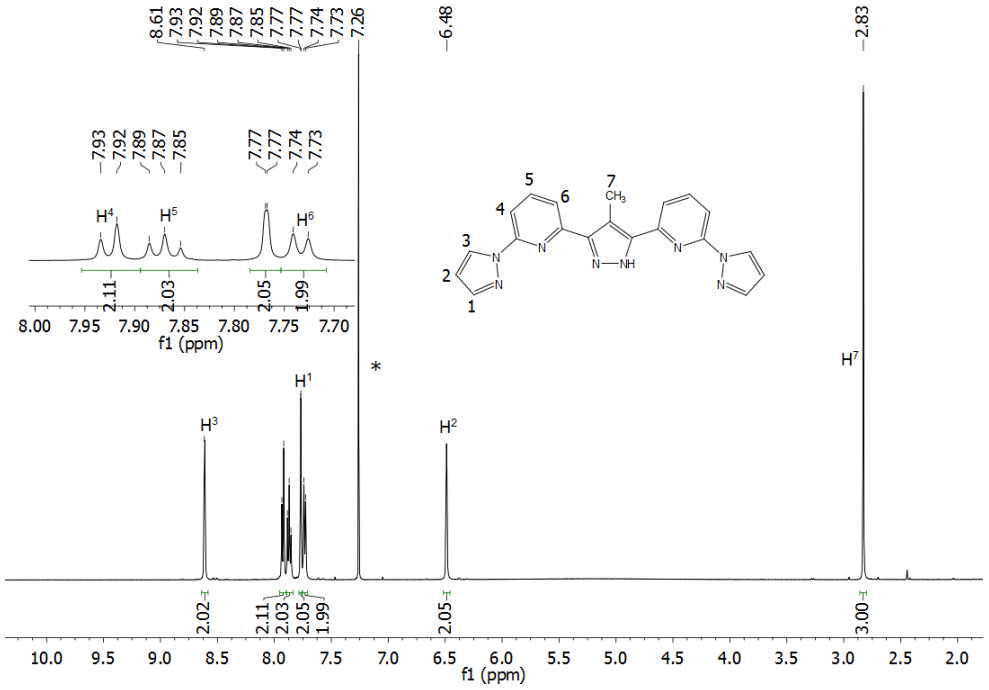

Figure 10.6. ^{1}H NMR spectrum (500 MHz, $CDCl_3$, 298 K)) of **HL^{Me-Pz}** (*$CHCl_3$).

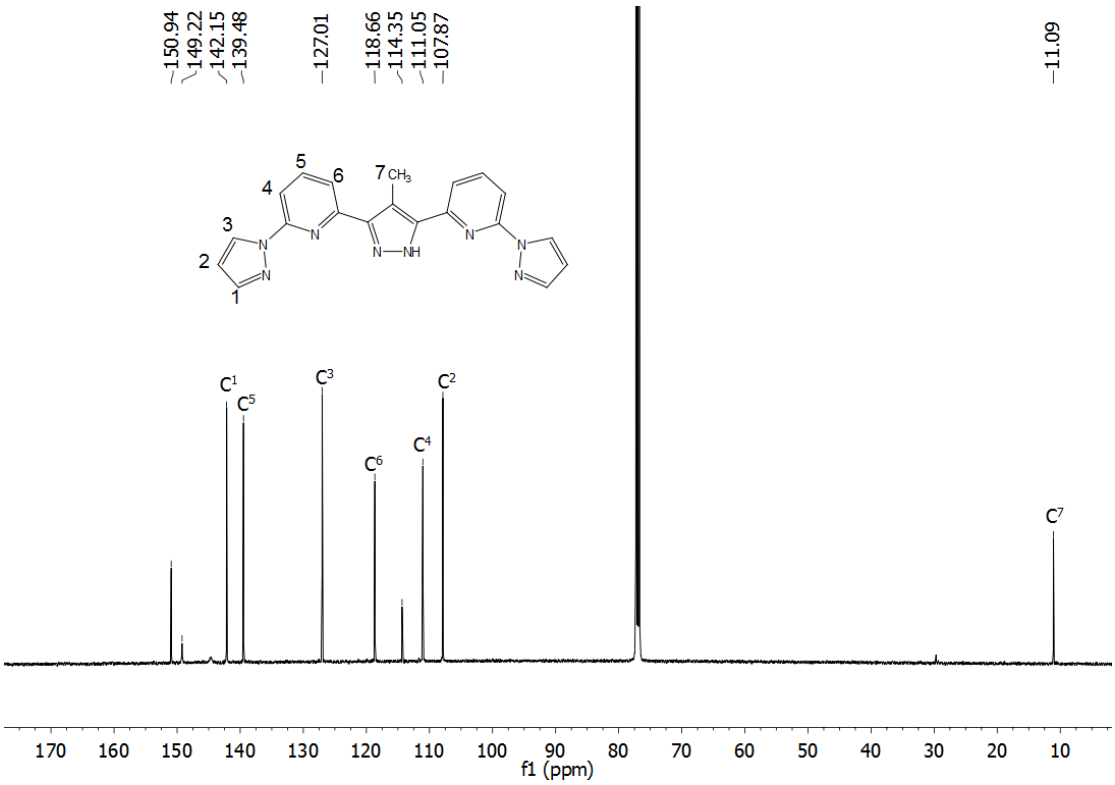

Figure 10.7. $^{13}C\{^{1}H\}$ NMR spectrum (125 MHz, $CDCl_3$, 298 K) of **HL^{Me-Pz}** in the ^{1}H: 10.0 to 170.0 ppm range.

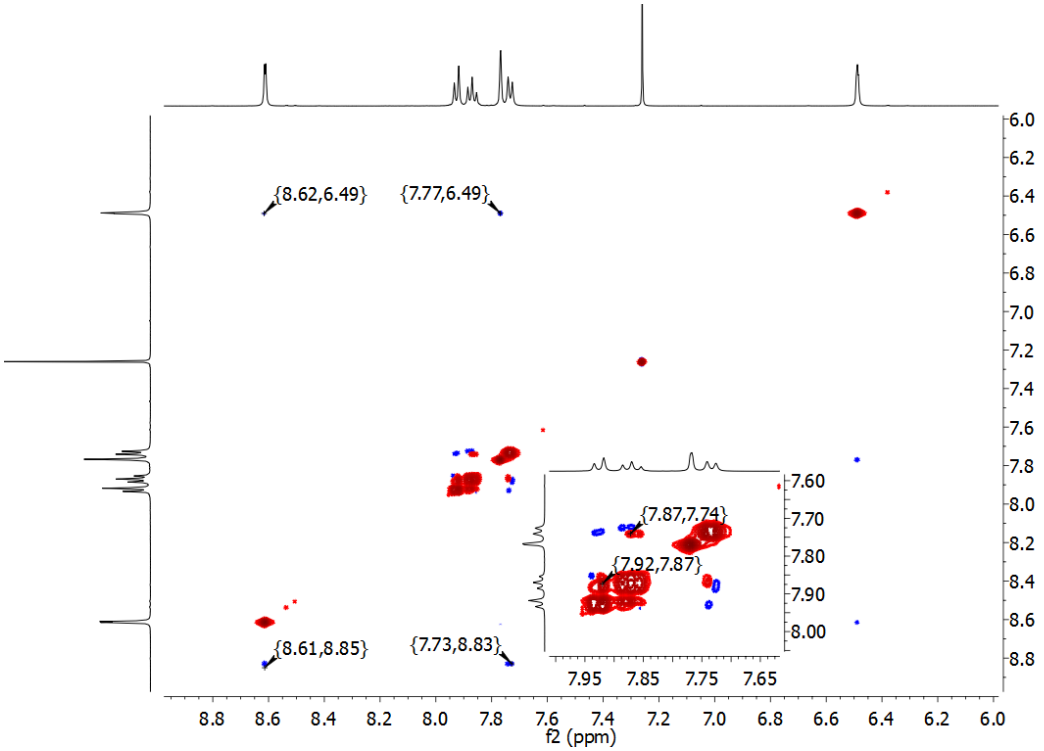

Figure 10.8. ^{1}H-^{1}H-NOESY spectrum ($CDCl_3$, 298 K) of **HL$^{Me\text{-}Pz}$** in the 6.0 to 9.0 ppm range.

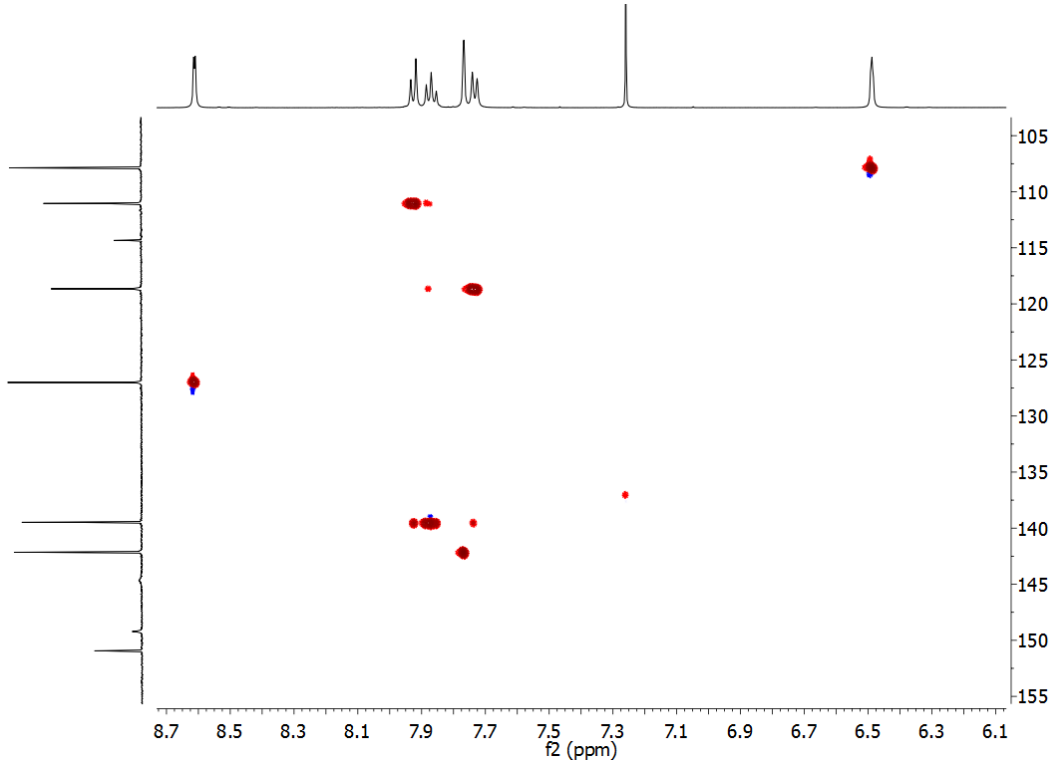

Figure 10.9. ^{1}H-^{13}C-HMQC spectrum ($CDCl_3$, 298 K) of **HL$^{Me\text{-}Pz}$** in the ^{1}H: 6.0 to 9.0 ppm; ^{13}C: 105 to 155 ppm range.

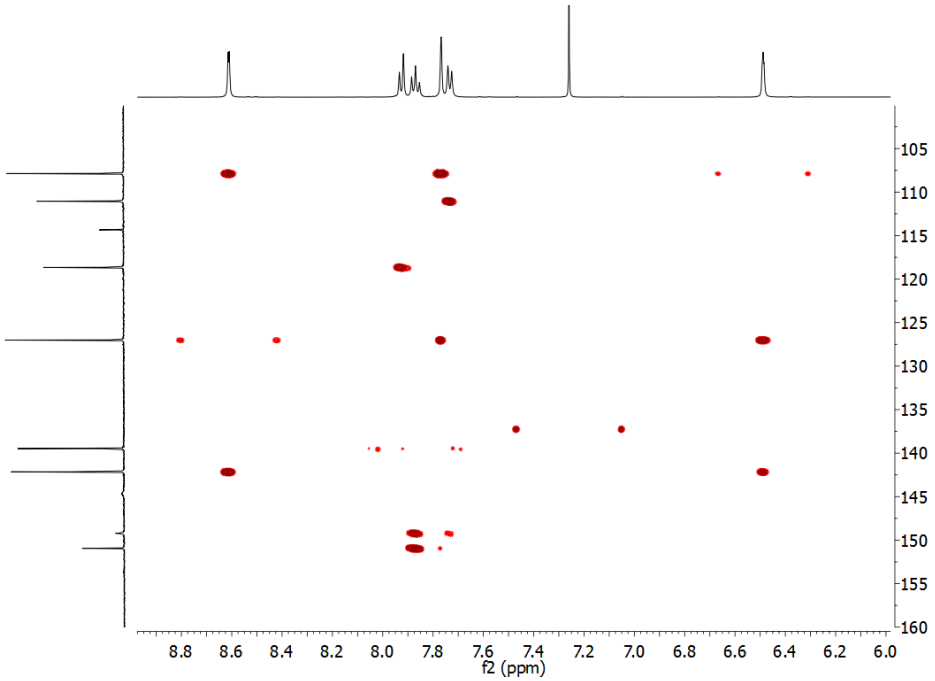

Figure 10.10. ^{1}H-^{13}C-HMBC spectrum ($CDCl_3$, 298 K) of **HL^{Me-Pz}** in the ^{1}H: 6.0 to 9.0 ppm; ^{13}C: 105 to 160 ppm range.

3,5-bis(6-(3,5-dimethyl-1*H*-pyrazol-1-yl)yridine-2-yl)pyrid-2-yl)pyrazole (HL^{Me4-Pz})

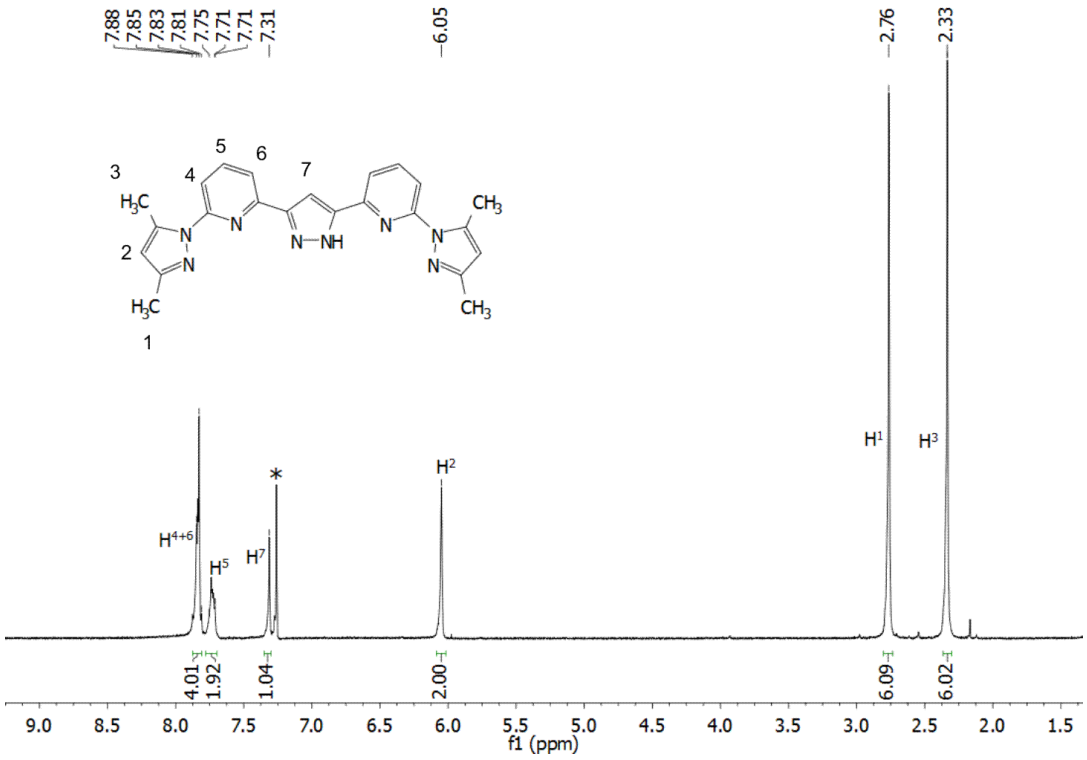

Figure 10.11. ^{1}H NMR spectrum (300 MHz, $CDCl_3$, 298 K) of **HL^{Me4-Pz}** (*$CHCl_3$).

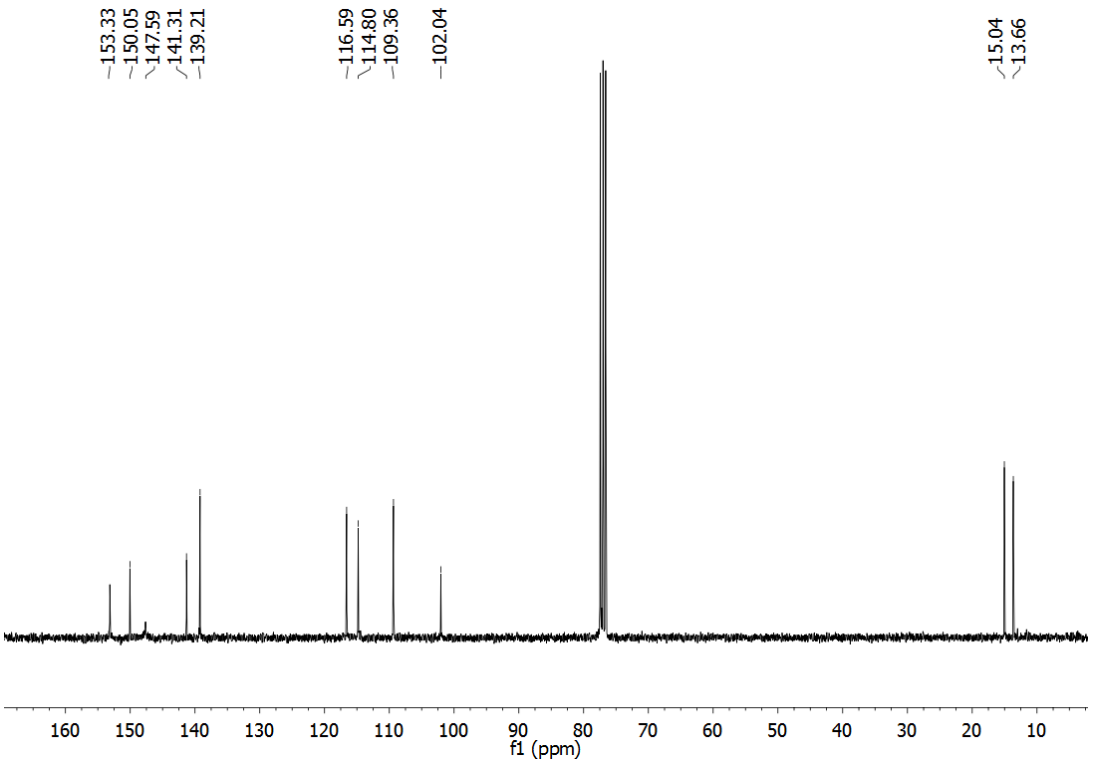

Figure 10.12. $^{13}C\{^{1}H\}$ NMR spectrum (75 MHz, $CDCl_3$, 298 K)) of **HL^{Me4-Pz}**.

2-(3,5-dimethyl-1*H*-pyrazol-1-yl)-6-(3-(6-(3,4,5-trimethyl-1*H*-pyrazol-1-yl)pyridin-2-yl)-1*H*-pyrazol-5-yl)pyridine (HL^{Me5-Pz})

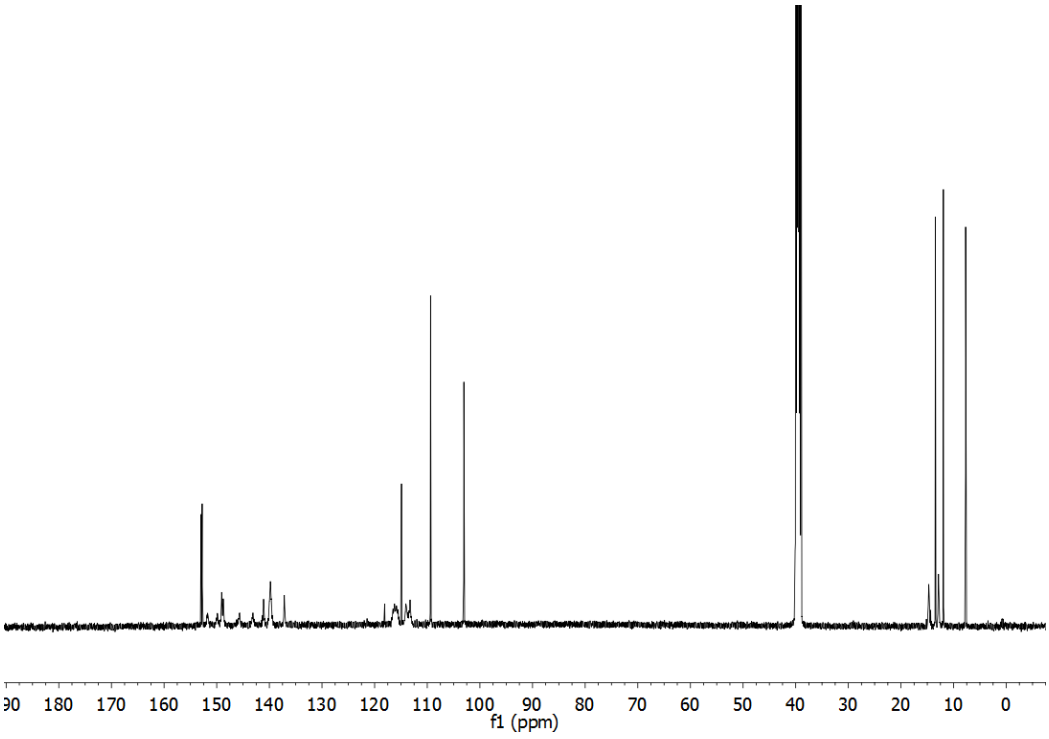

Figure 10.13. $^{13}C\{^{1}H\}$ NMR spectrum (125 MHz, $CDCl_3$, 298 K) of **HL^{Me5-Pz}**.

1,3-bis(6- (1-methyl-1*H*-imidazol-2-yl)yridine-2-yl)pyrazole ($HL^{Me\text{-}Im}$)

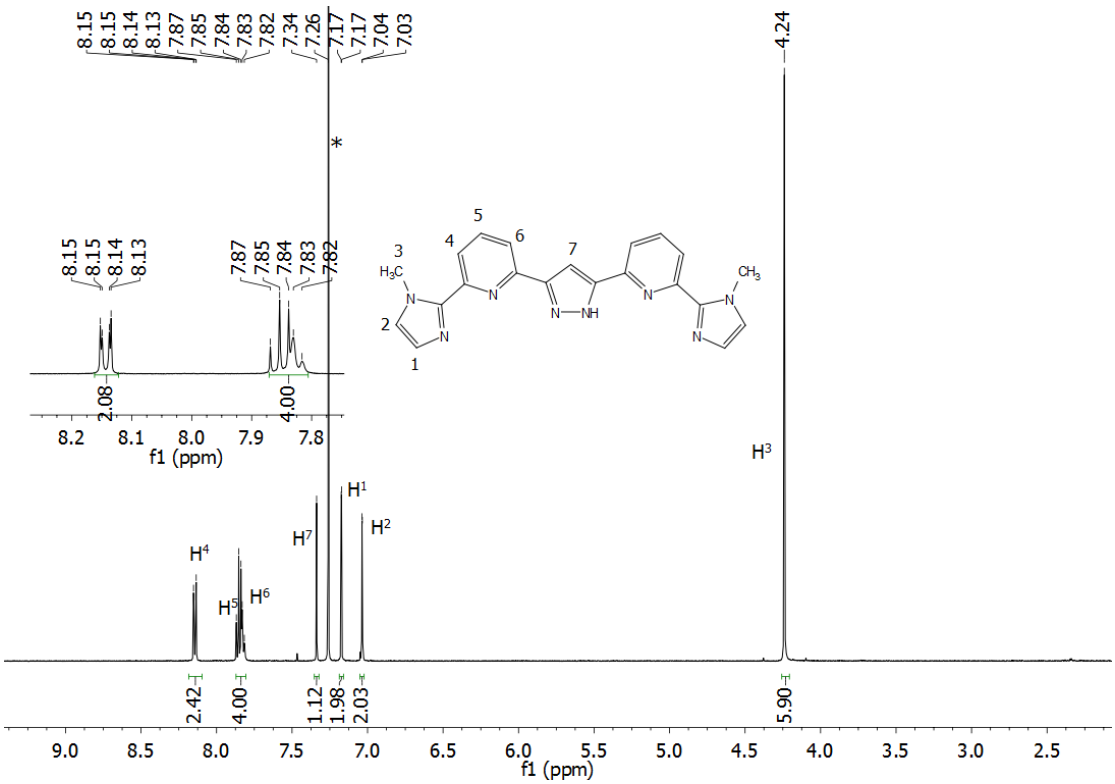

Figure 10.14. ^{1}H NMR spectrum (500 MHz, $CDCl_3$, 298 K) of $HL^{Me\text{-}Im}$ (*$CHCl_3$).

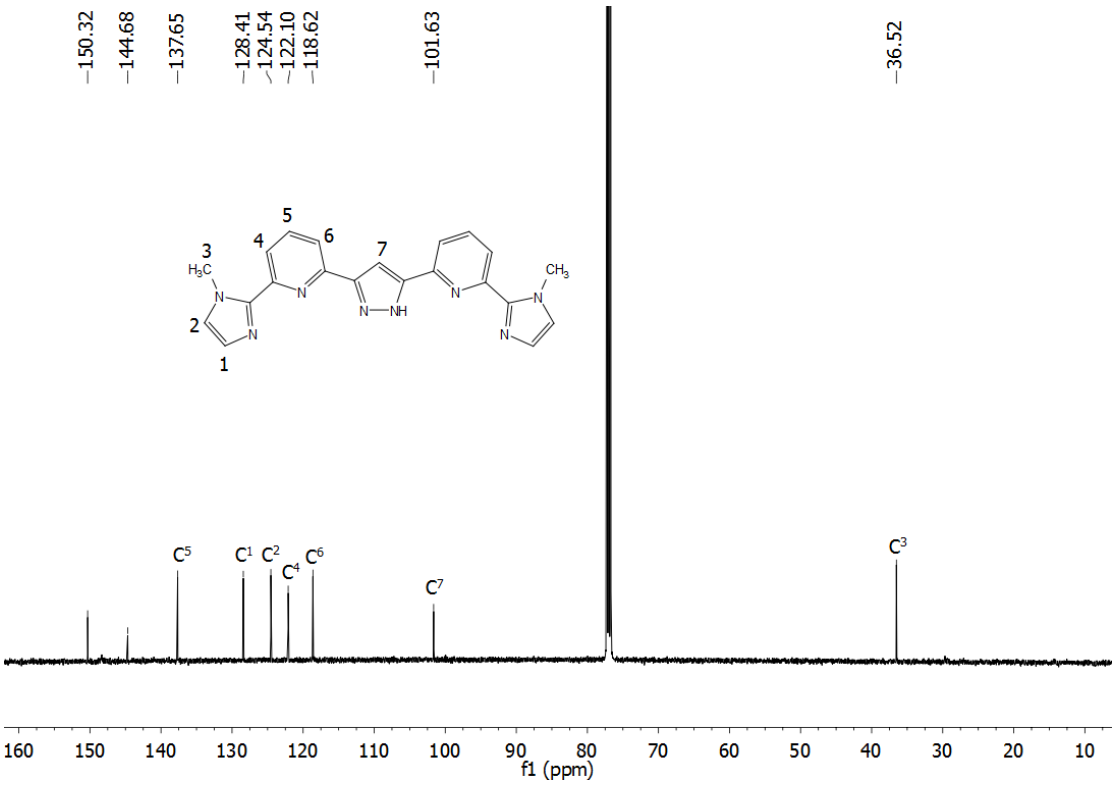

Figure 10.15. $^{13}C\{^{1}H\}$ NMR spectrum (125 Hz, $CDCl_3$, 298 K)) of $HL^{Me\text{-}Im}$.

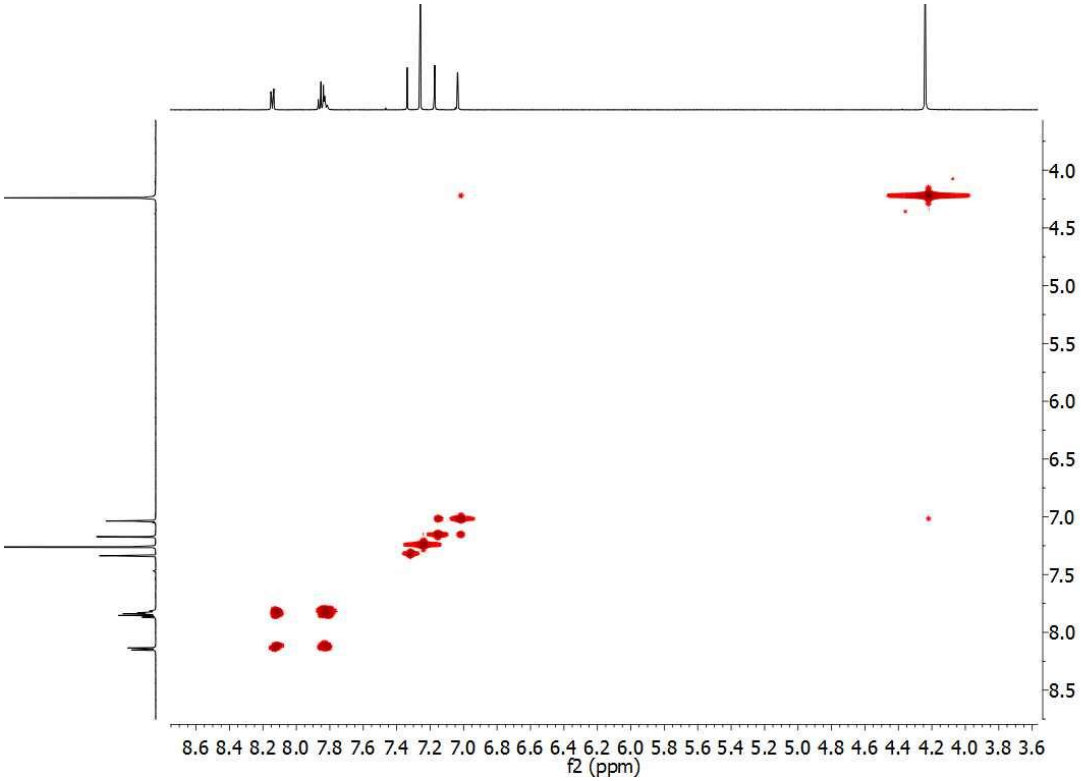

Figure 10.16. ^{1}H-^{13}C-COSY spectrum ($CDCl_3$, 298 K) of **HL$^{Me\text{-}Im}$** in the ^{1}H: 3.5 to 9.0 ppm range.

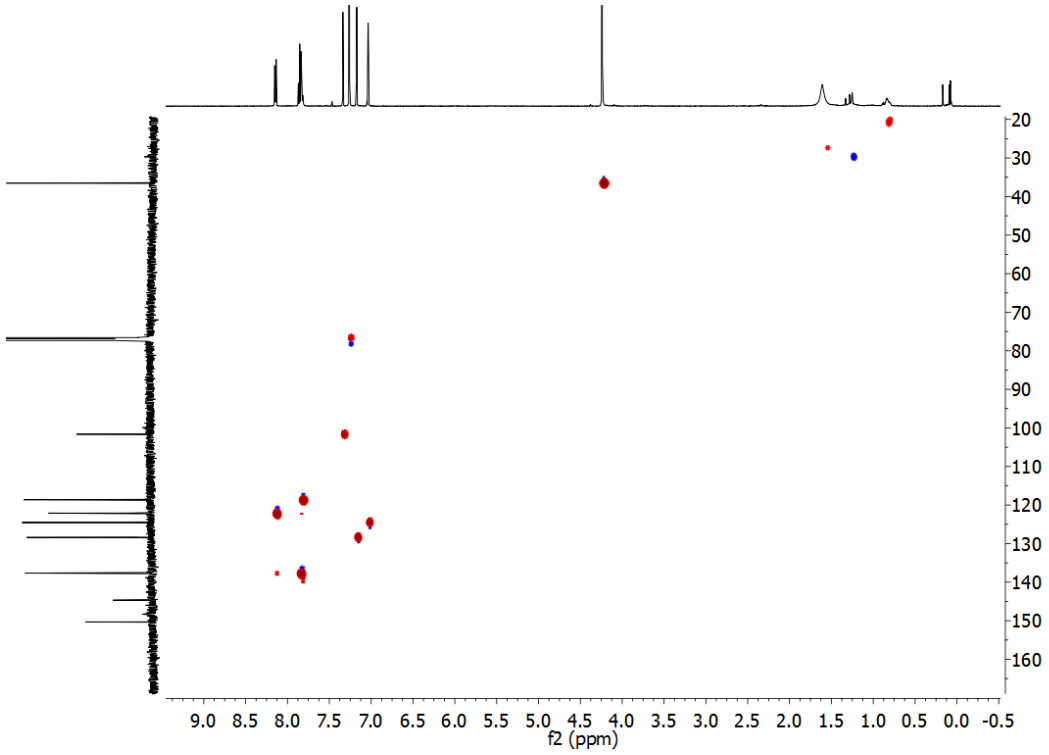

Figure 10.17. ^{1}H-^{13}C-HSQC spectrum ($CDCl_3$, 298 K) of **HL$^{Me\text{-}Im}$** in the ^{1}H: −0.5 to 9.0 ppm; ^{13}C: 20 to 160 ppm range.

4-methyl-1,3-bis(6-(1-methyl-1*H*-imidazol-2-yl)yridine-2-yl)pyrazole (HL$^{Me\text{-}MeIm}$)

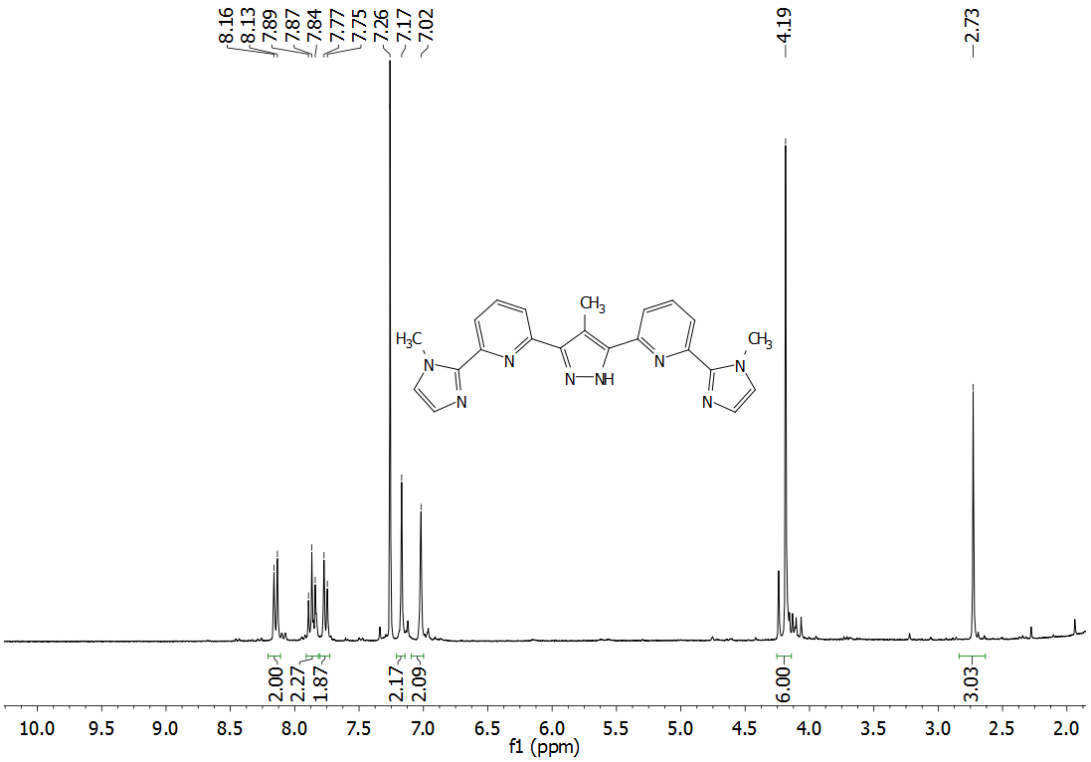

Figure 10.18. ^{1}H NMR spectrum (300 MHz, $CDCl_3$, 298 K) of **HL$^{Me\text{-}MeIm}$** ($CDCl_3$: δ = 7.2 ppm)

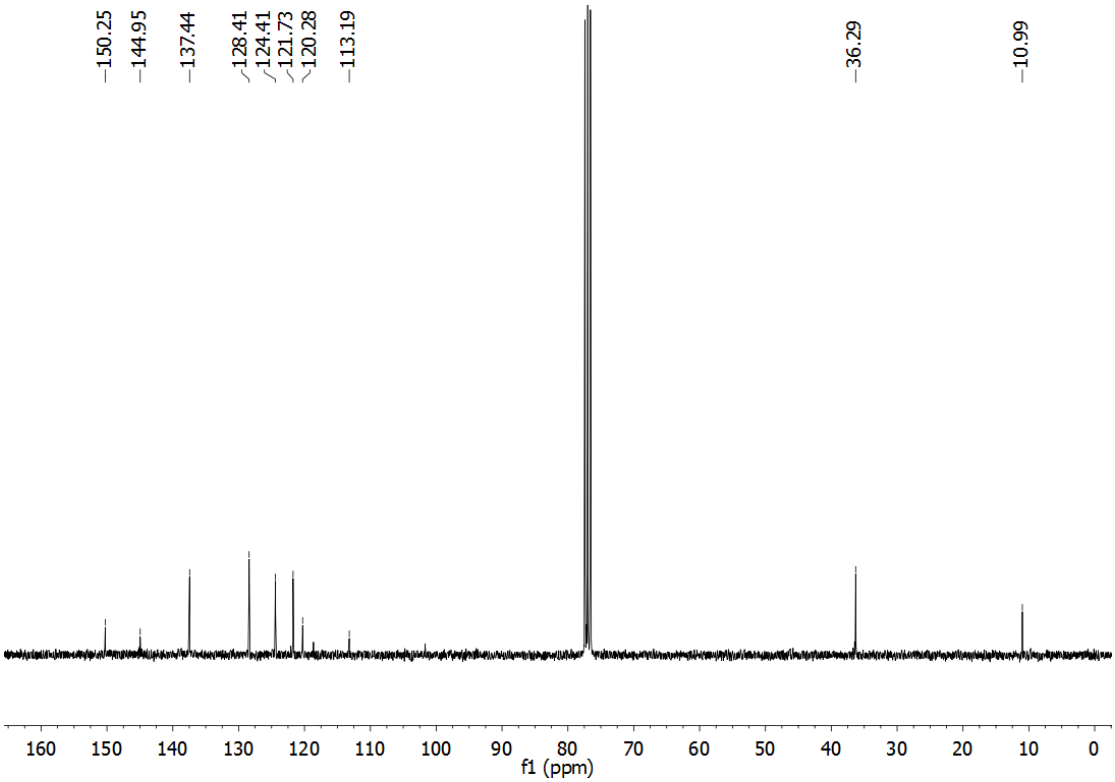

Figure 10.19. ^{13}C NMR spectrum (75 MHz, $CDCl_3$, 298 K) of **HL$^{Me\text{-}MeIm}$**.

1,3-bis(6-(1*H*-imidazol-2-yl)yridine-2-yl)pyrazole (HL^{Im})

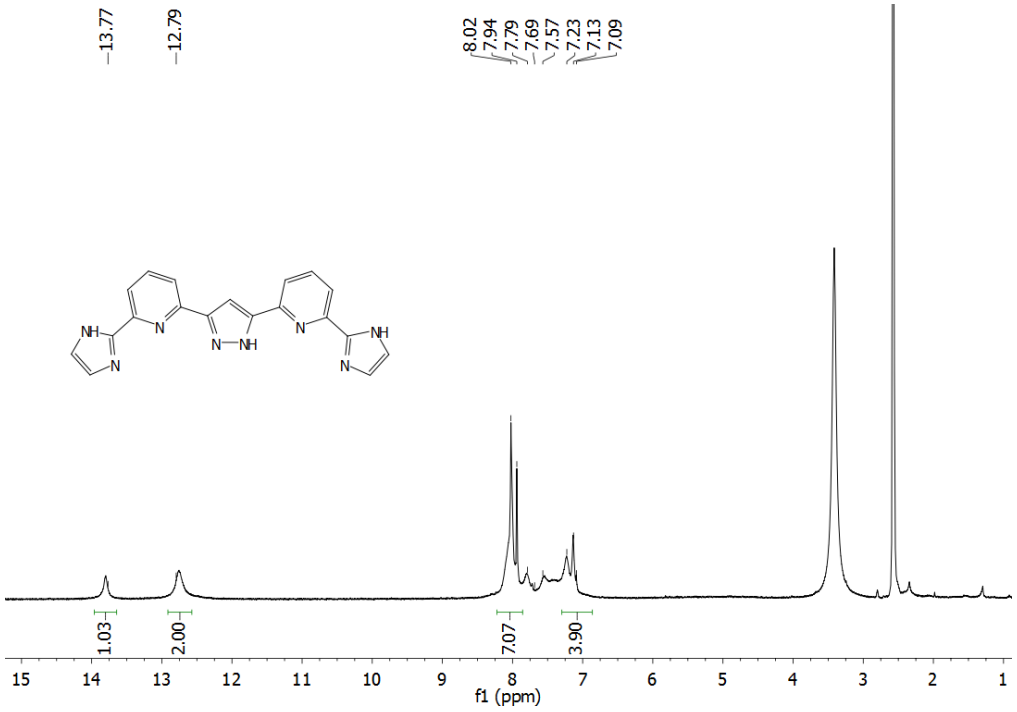

Figure 10.20. ^{1}H NMR spectrum (300 MHz, DMSO-d6, 298 K) of HL^{Im} (DMSO: δ = 2.5 ppm; H_2O: δ = 3.3 ppm).

2,6-bis(3-(6-(1*H*-pyrazol-1-yl)yridine-2-yl)-1*H*-pyrazol-5-yl)pyridine (H_2L^{Pz})

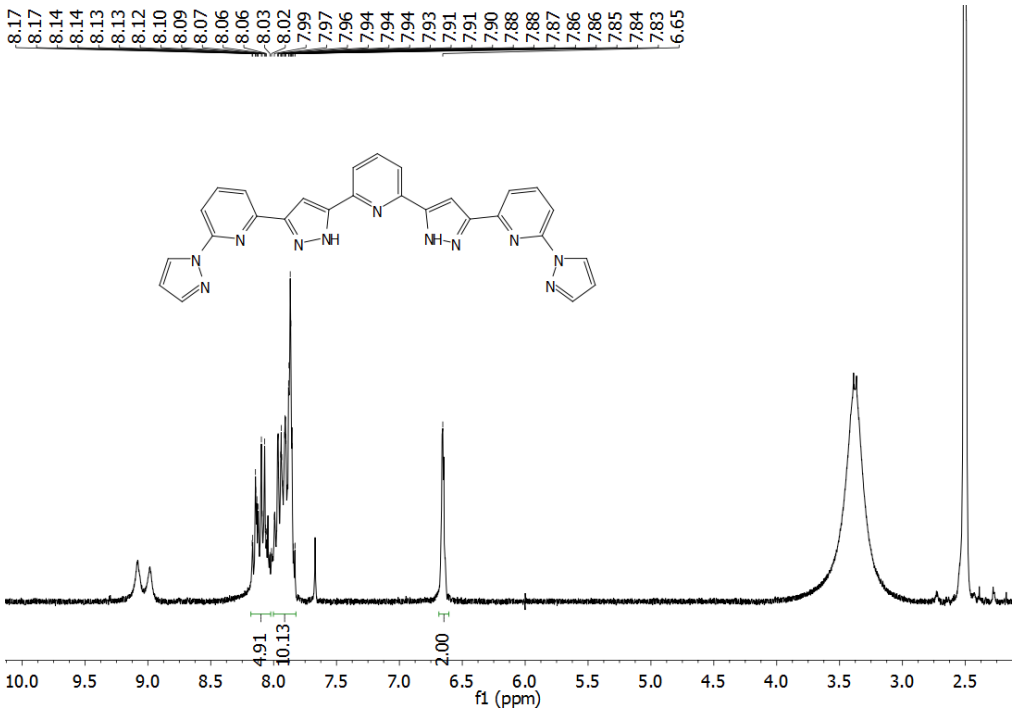

Figure 10.21. ^{1}H NMR spectrum (300 MHz, DMSO-d6, 298 K) of H_2L^{Pz} (DMSO: δ = 2.5 ppm; H_2O: δ = 3.3 ppm).

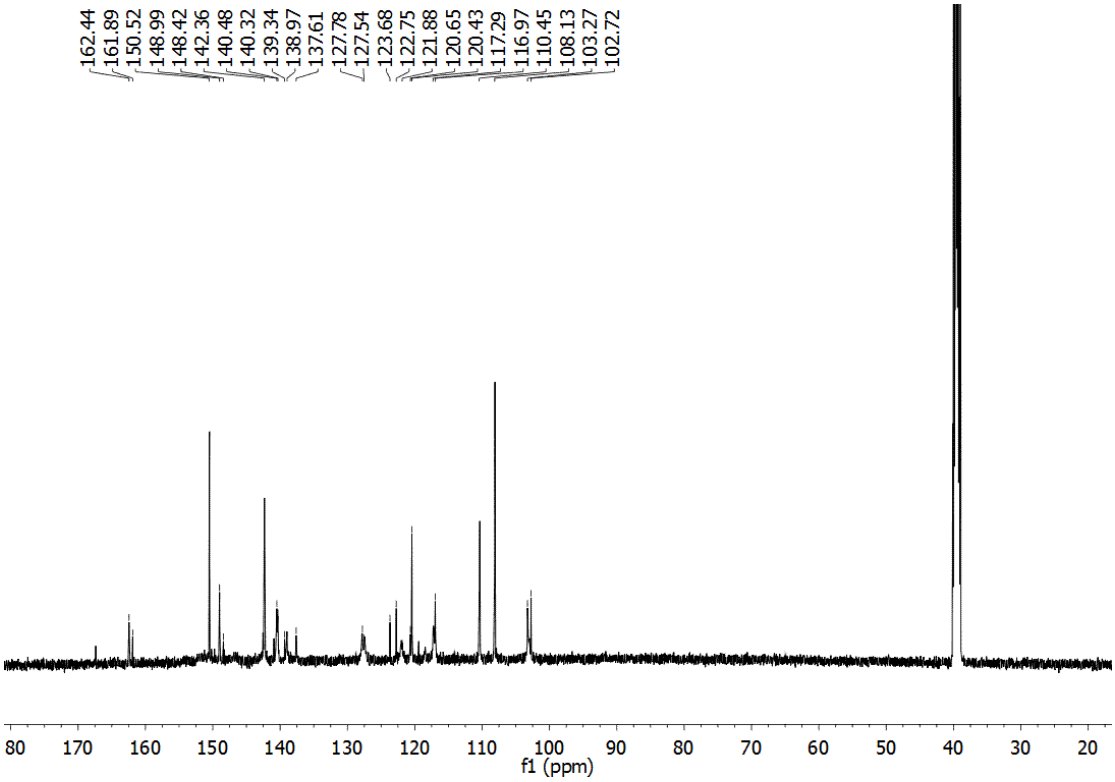

Figure 10.22. ^{13}C NMR spectrum (125 MHz, DMSO-d6, 298 K) of $\mathbf{H_2L^{Pz}}$.

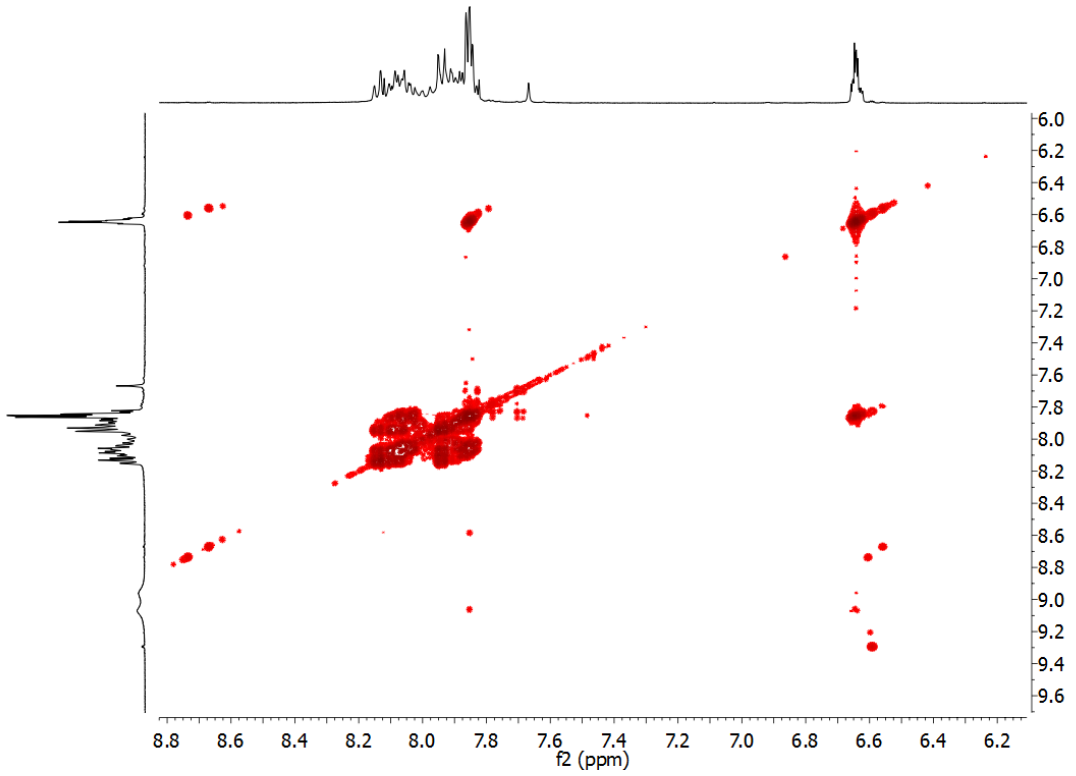

Figure 10.23. ^{1}H-^{1}H-COSY spectrum (DMSO-d_6, 298 K) of $\mathbf{H_2L^{Pz}}$ in the ^{1}H: 6.0 to 9.0 ppm range.

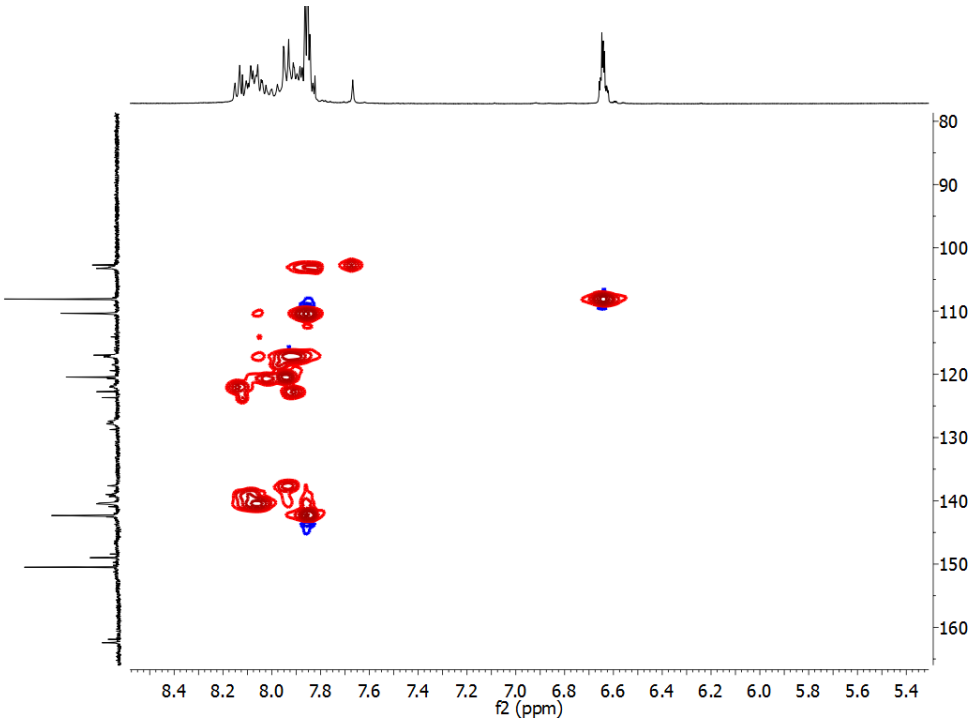

Figure 10.24. ^{1}H-^{13}C-HSQC spectrum (DMSO-d$_6$, 298K) of **H$_2$L^{Pz}** in the ^{1}H: 5.4 to 8.4 ppm; ^{13}C: 80 to 160 ppm range.

2,6-bis(3-(6-(1-methyl-1*H*-imidazol-2-yl)yridine-2-yl)-1*H*-pyrazol-5-yl)pyridine (**H$_2$L^{Me-Im}**)

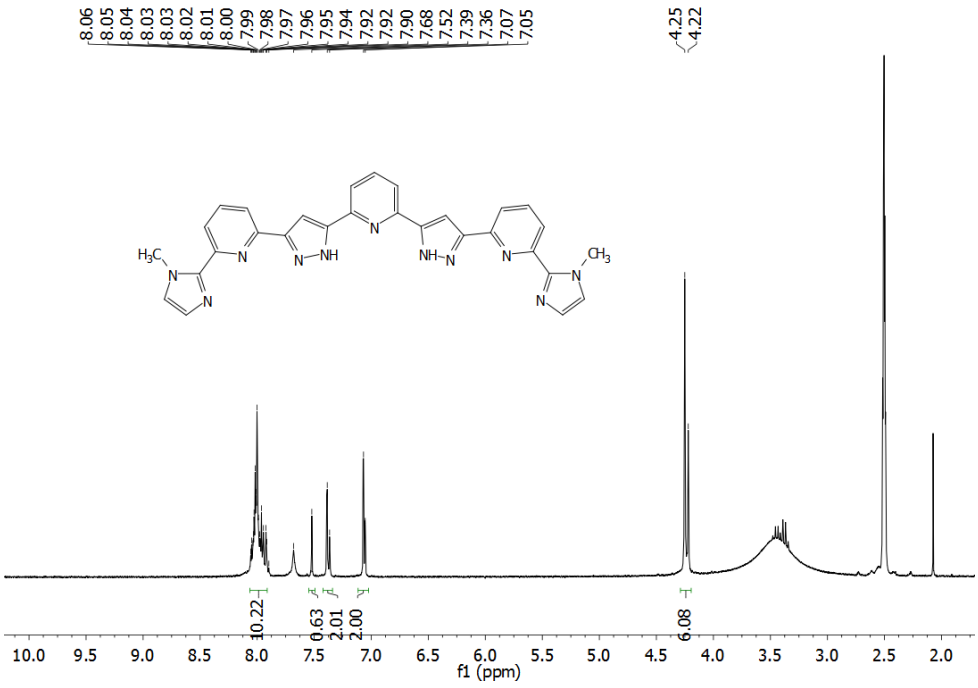

Figure 10.25. ^{1}H NMR spectrum (500 MHz, DMSO-d6, 298 K) of **H$_2$L^{Me-Im}** (DMSO: δ = 2.5 ppm; H$_2$O: δ = 3.3 – 3.5 ppm).

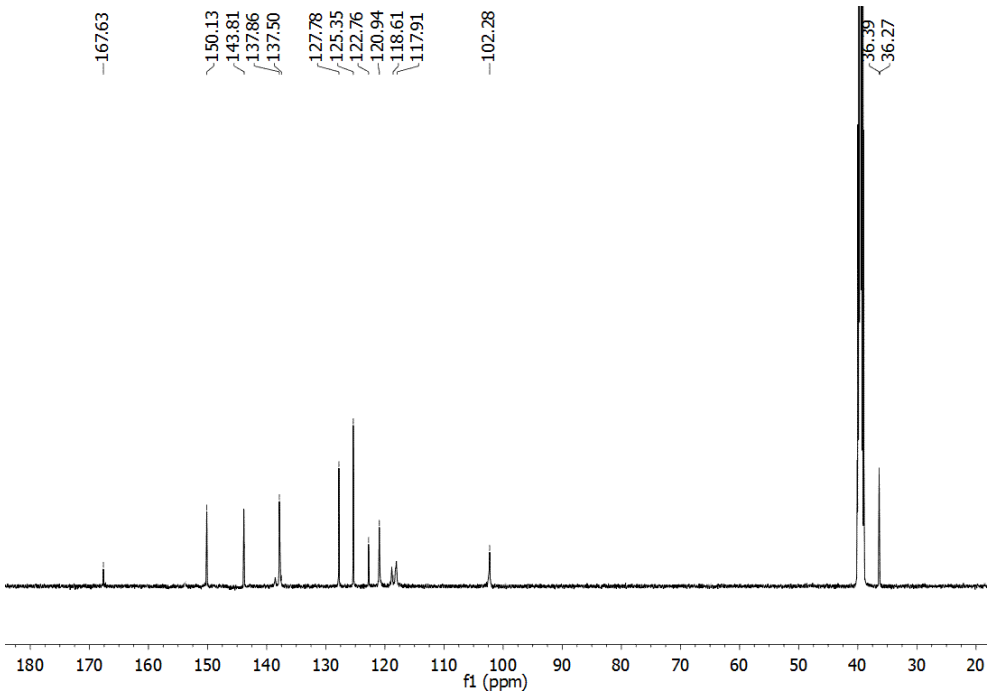

Figure 10.26. ^{13}C NMR spectrum (125 MHz, DMSO-d6, 298 K) of $\mathbf{H_2L^{Me\text{-}Im}}$.

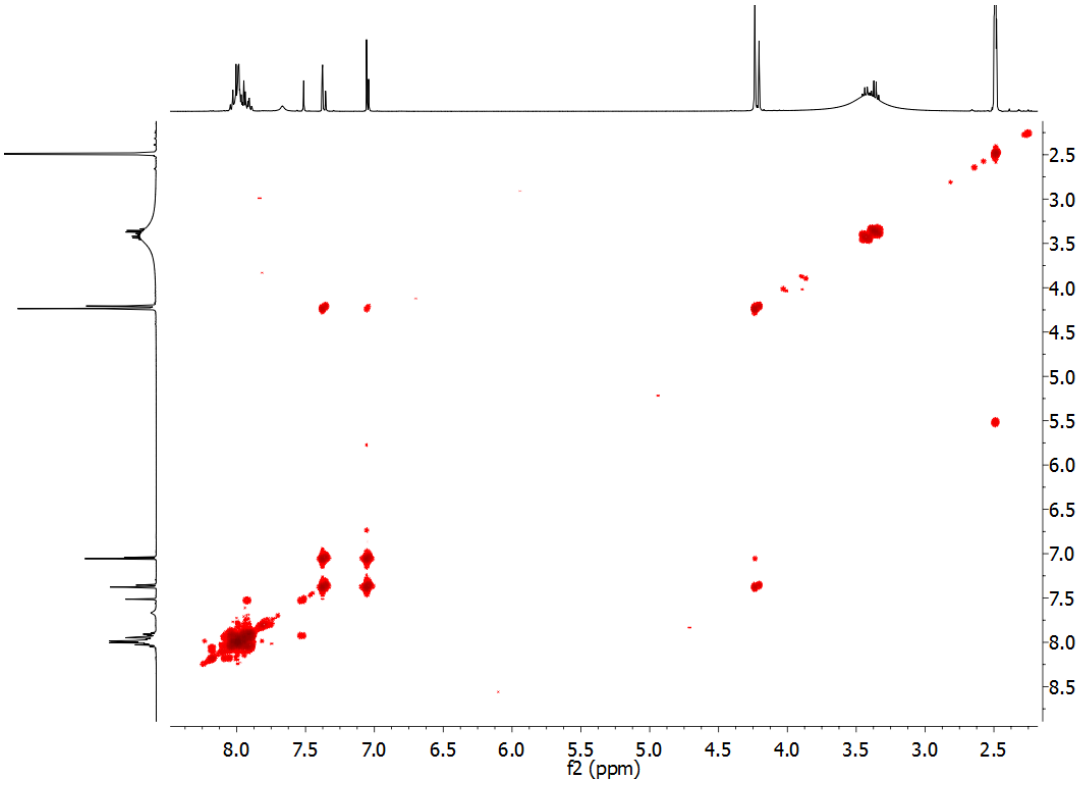

Figure 10.27. ^{1}H-^{1}H-COSY spectrum (DMSO-d_6, 298 K) of $\mathbf{H_2L^{Me\text{-}Im}}$ in the ^{1}H: 2.0 to 9.0 ppm range.

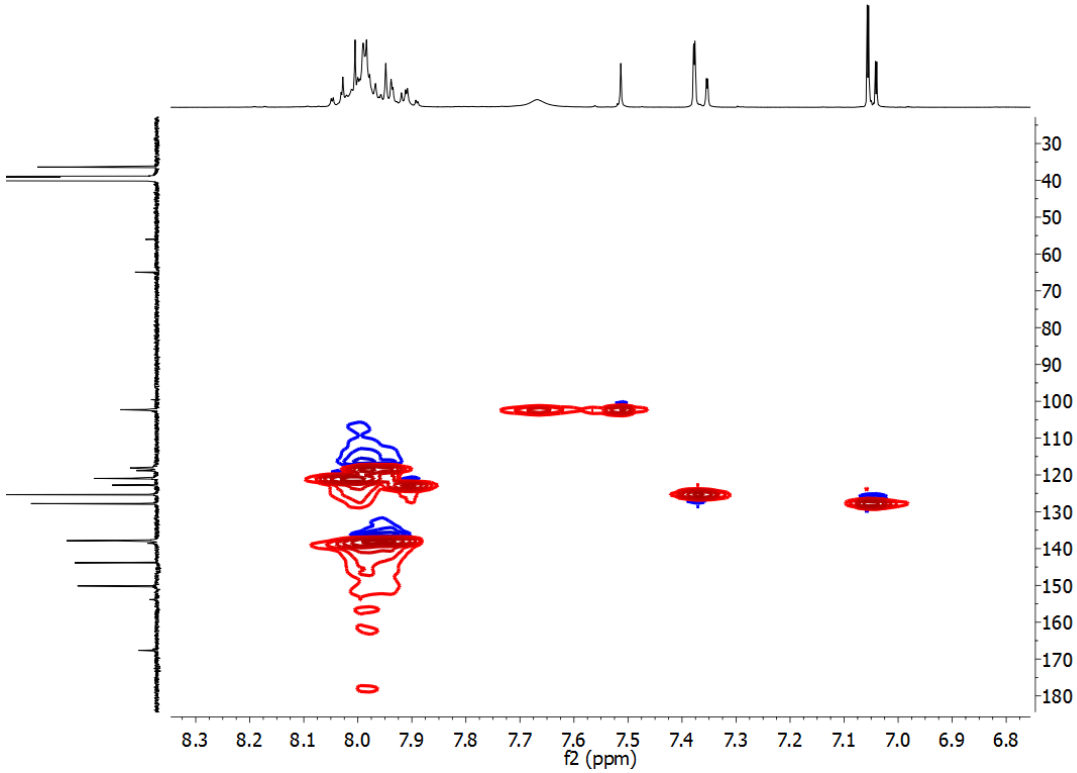

Figure 10.28. ^{1}H-^{13}C-HSQC spectrum (DMSO-d$_6$, 298 K) of **H$_2$L$^{Me\text{-}Im}$** in the ^{1}H: 6.8 to 8.3 ppm; ^{13}C: 30 to 180 ppm range.

2,6-bis(3-(2,2'-bipyridin-6-yl)-1*H*-pyrazol-5-yl)pyridine (H$_2$L^{Py})

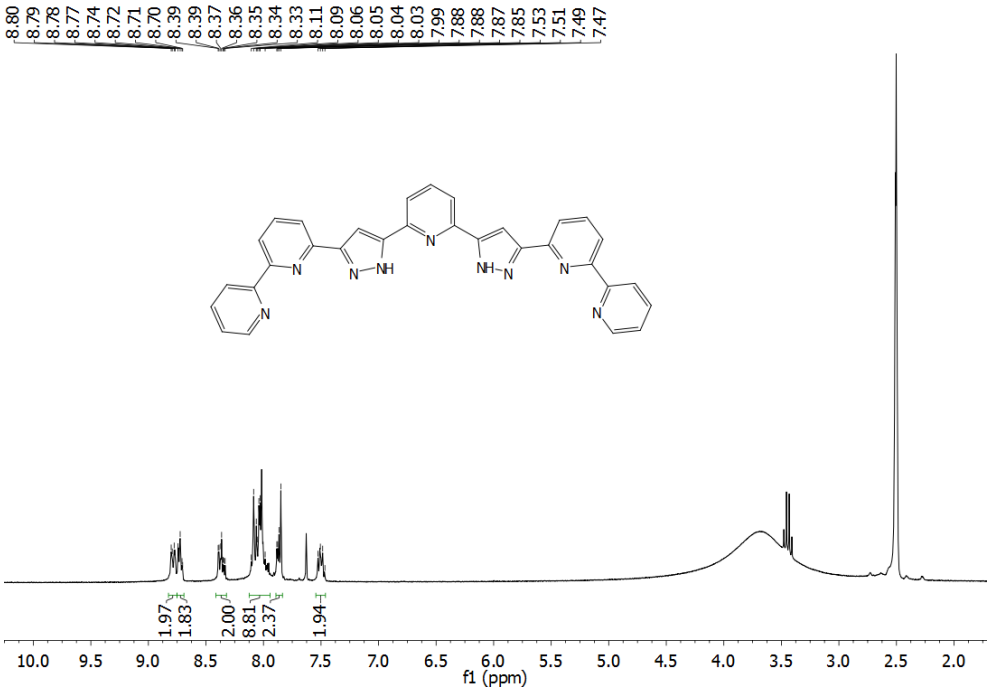

Figure 10.29. ^{1}H NMR spectrum (300 MHz, DMSO-d6, 298 K) of **H$_2$L^{Py}** (DMSO: δ = 2.5 ppm; H$_2$O: δ = 3.3 – 3.8 ppm).

10.1.2. NMR Spectroscopy of Complexes

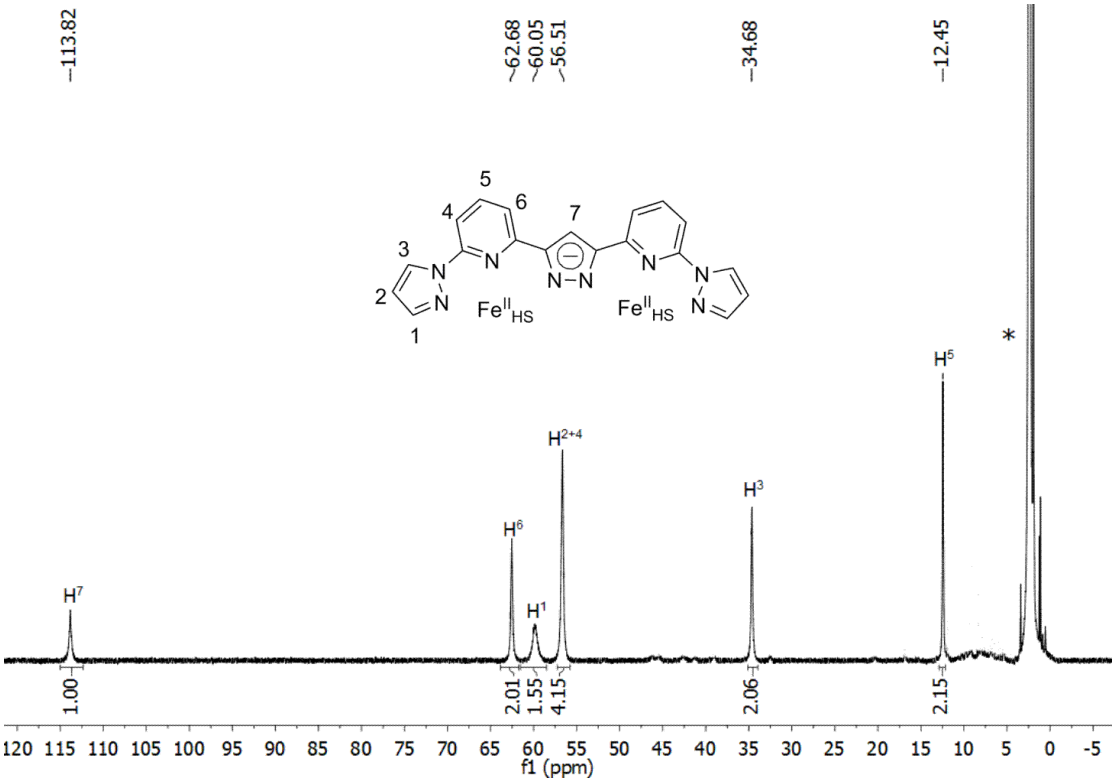

Figure 10.30. ^{1}H NMR spectrum (500 MHz, CD_3CN, 298 K) of $[Fe^{II}_4L^{Pz}_4](BF_4)_4$ (**1**) (*MeCN).

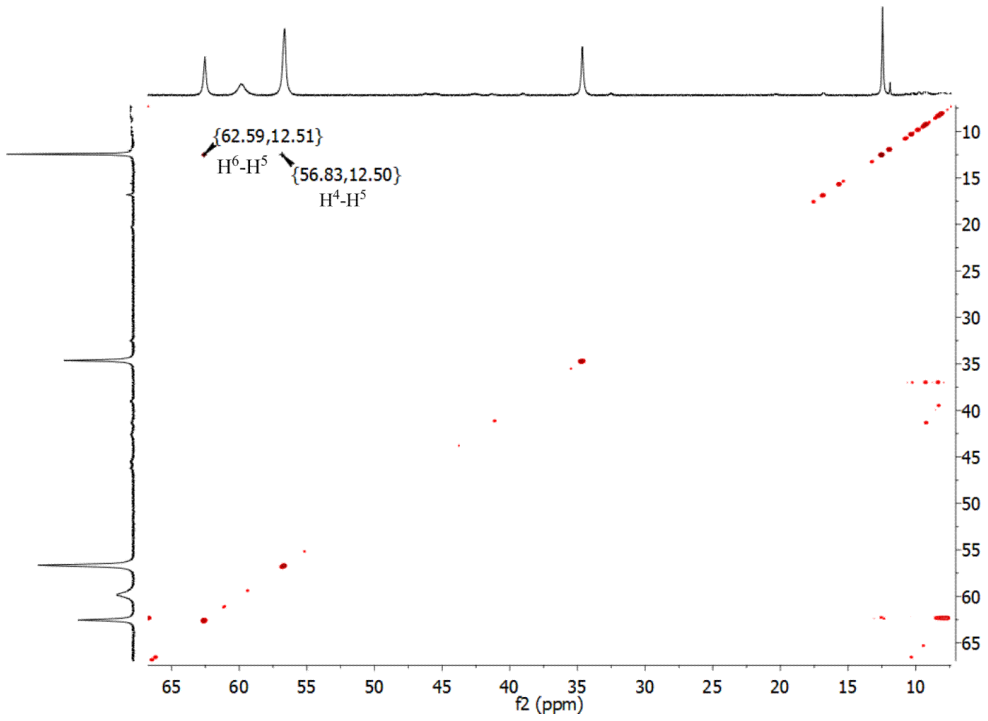

Figure 10.31. ^{1}H-^{1}H COSY spectrum (CD_3CN, 298 K) of $[Fe^{II}_4L^{Pz}_4](BF_4)_4$ (**1**).

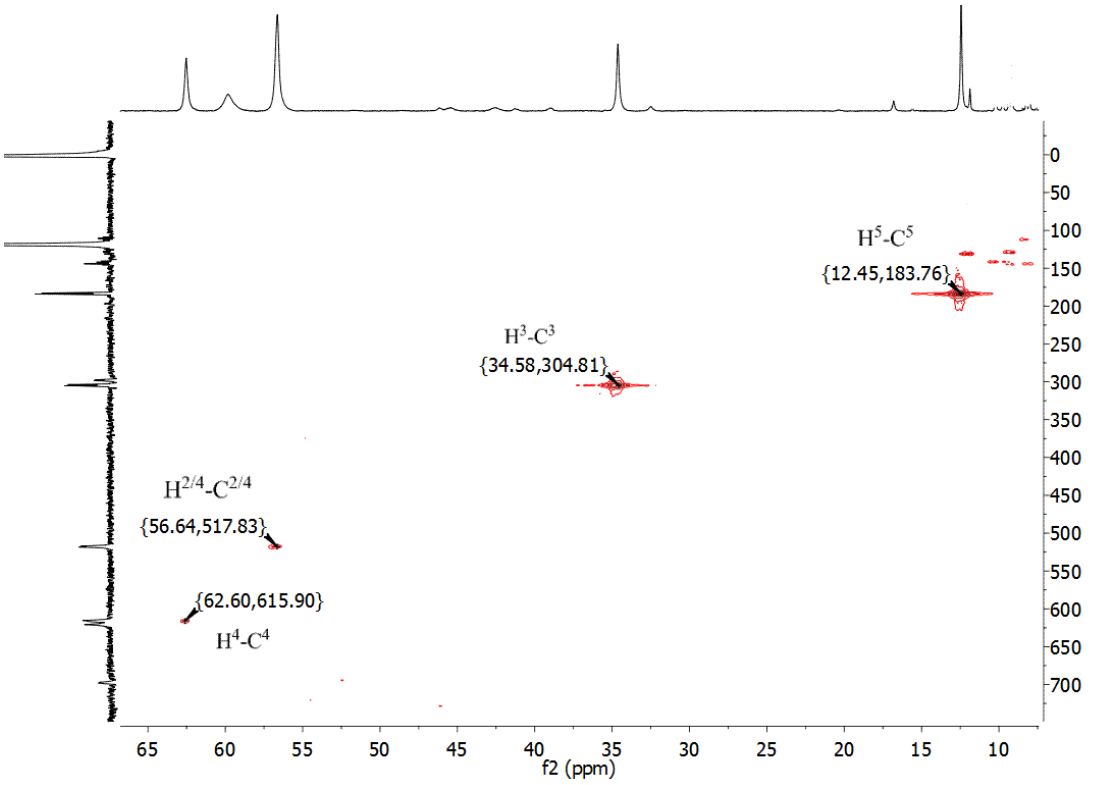

Figure 10.32. ^{1}H-^{13}C HMQC spectrum (CD_3CN, 298 K) of $[Fe^{II}{}_4L^{Pz}{}_4](BF_4)_4$ (**1**).

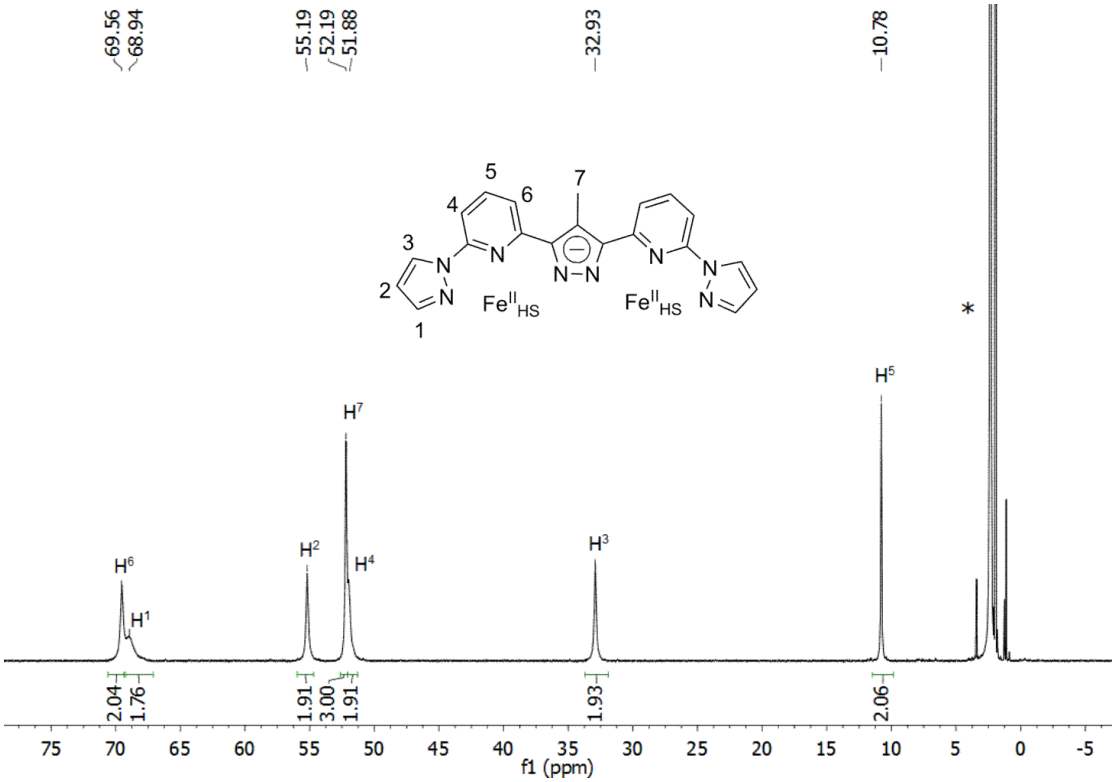

Figure 10.33. ^{1}H NMR spectrum (500 MHz, CD_3CN, 298 K) of $[Fe^{II}{}_4L^{Me\text{-}Pz}{}_4](BF_4)_4$ (**2**)(* MeCN).

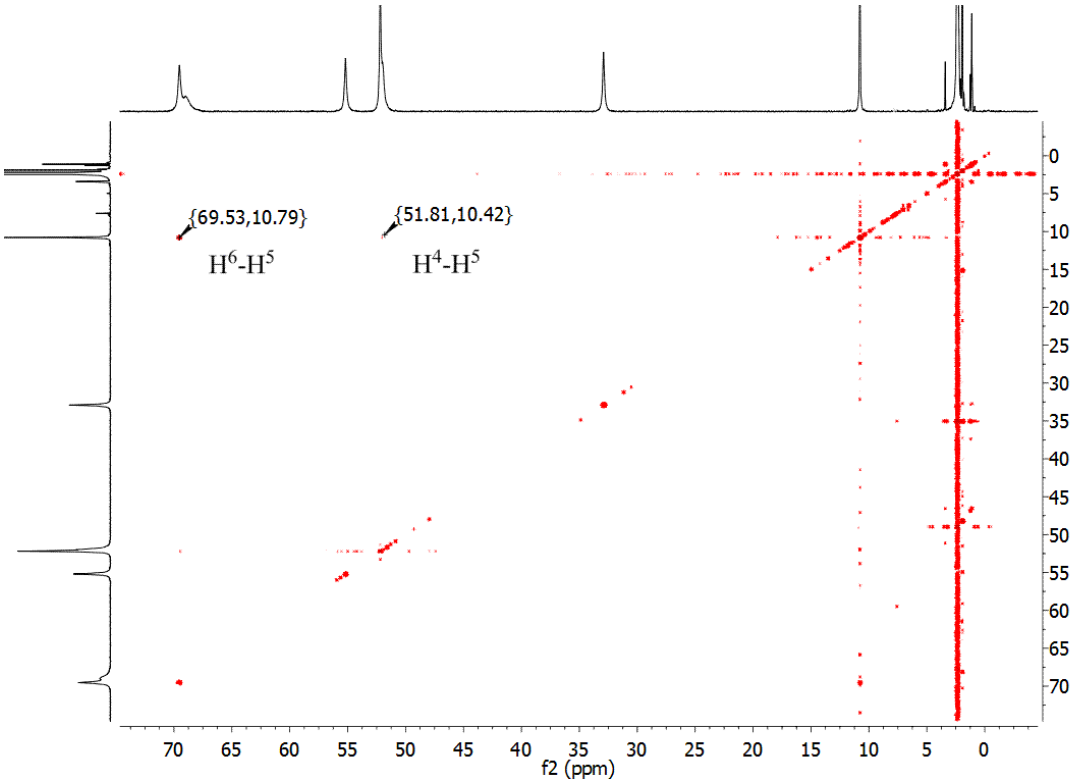

Figure 10.34. ^{1}H-^{1}H COSY spectrum (CD_3CN, 298 K) of $[Fe^{II}_4L^{Me\text{-}Pz}_4](BF_4)_4$ (**2**).

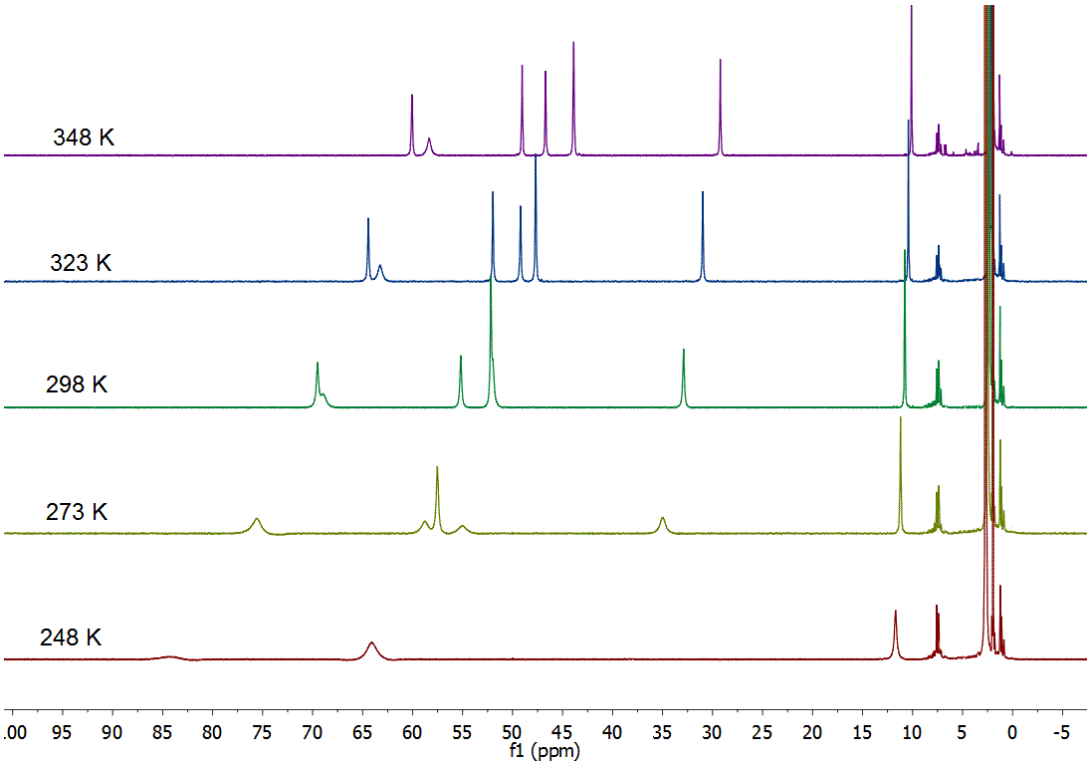

Figure 10.35. Variable-temperature ^{1}H NMR spectra (500 MHz, CD_3CN) of $[Fe^{II}_4L^{Me\text{-}Pz}_4](BF_4)_4$ (**2**).

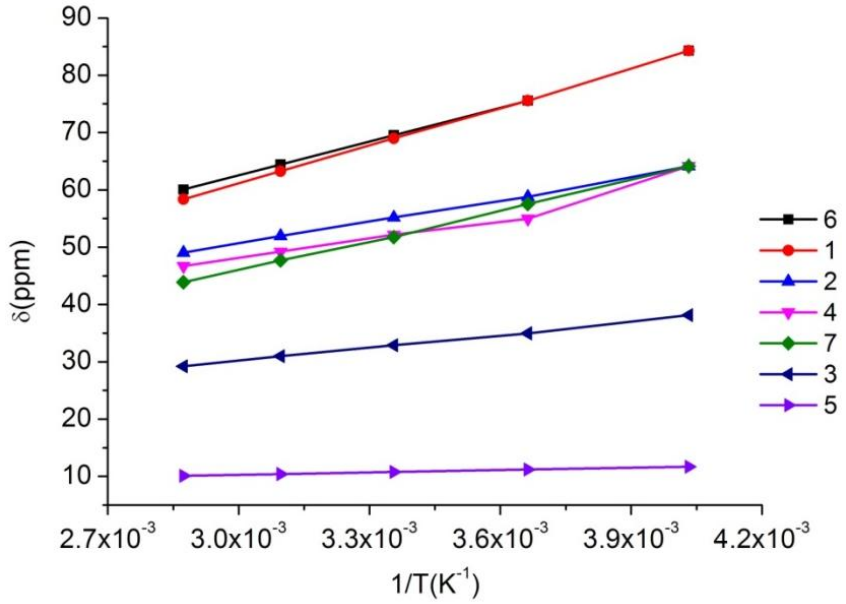

Figure 10.36. Curie plot showing the linear dependence of ^{1}H resonance shifts on the inverse temperature of $[Fe^{II}_4L^{Me\text{-}Pz}_4](BF_4)_4$ (**2**).

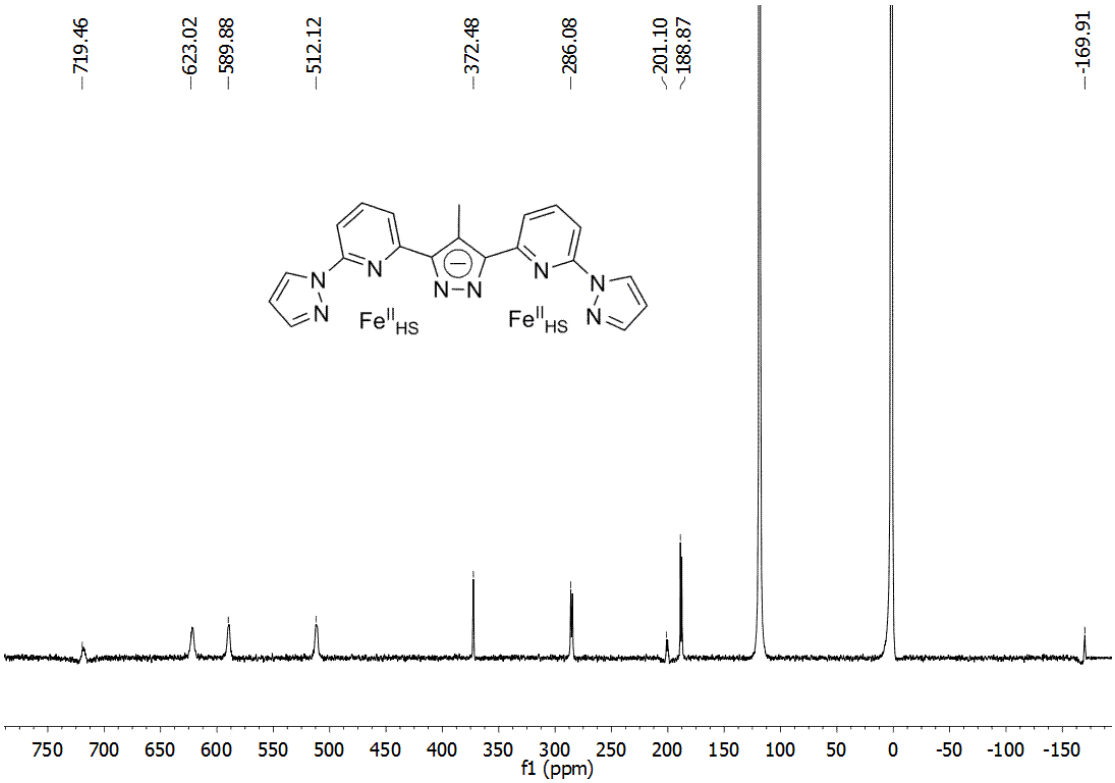

Figure 10.37. ^{13}C NMR spectrum (125 MHz, CD_3CN, 298 K) of $[Fe^{II}_4L^{Me\text{-}Pz}_4](BF_4)_4$ (**2**).

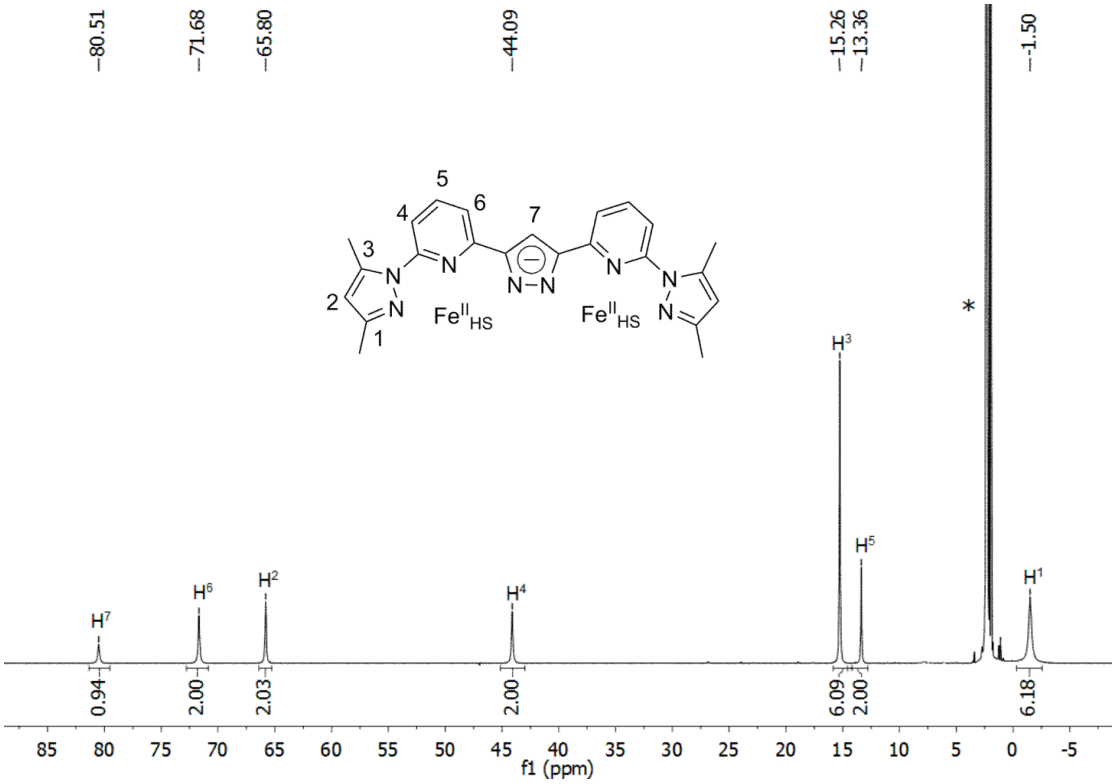

Figure 10.38. ^{1}H NMR spectrum (500 MHz, CD_3CN, 298 K) of $[Fe^{II}_4L^{Me4\text{-}Pz}_4](BF_4)_4$ (**3**) (*MeCN).

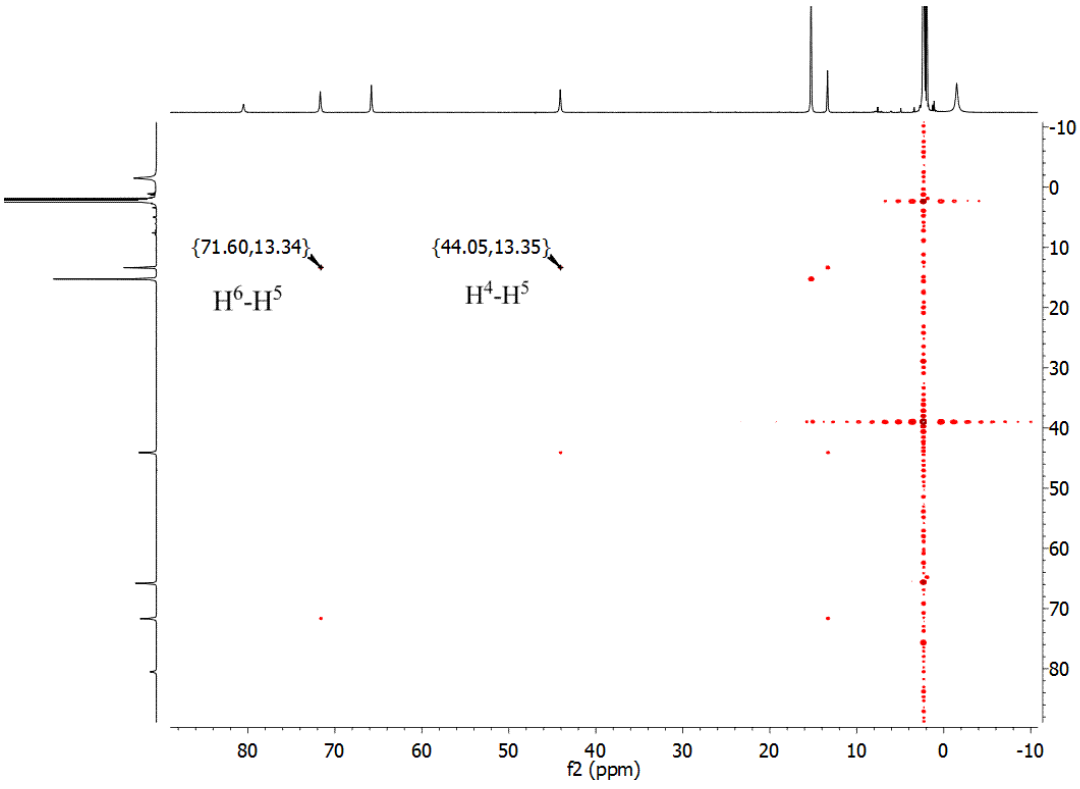

Figure 10.39. ^{1}H-^{1}H COSY spectrum (CD_3CN, 298 K) of $[Fe^{II}_4L^{Me4\text{-}Pz}_4](BF_4)_4$ (**3**).

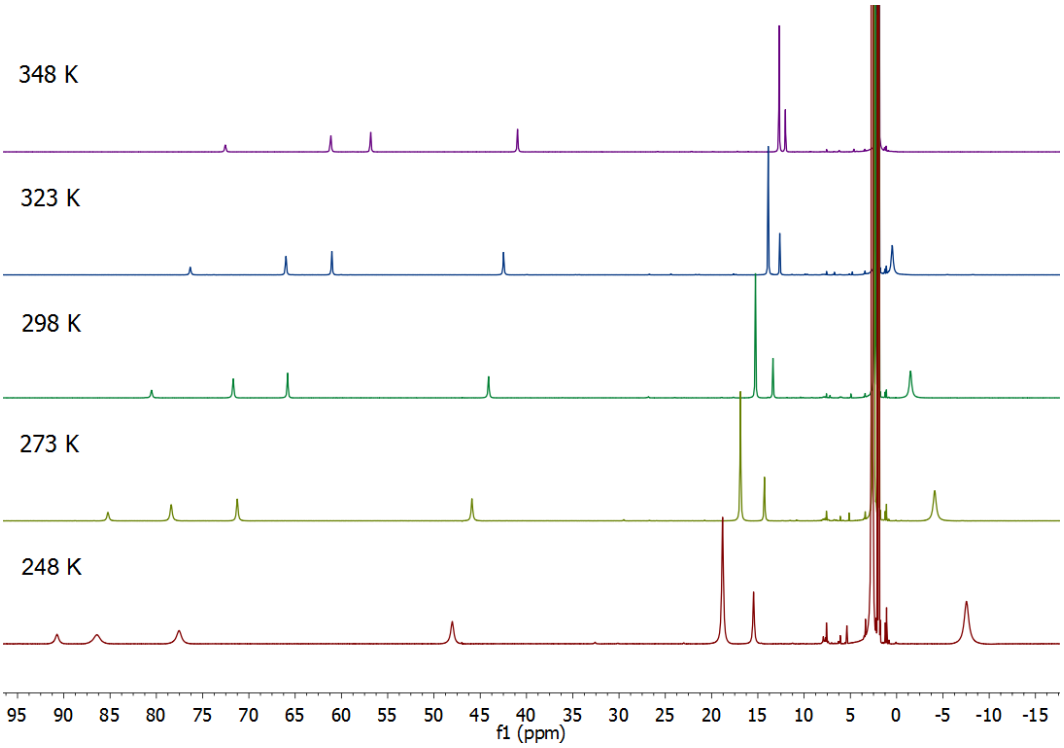

Figure 10.40. Variable-temperature ^{1}H NMR spectra (500 MHz, CD_3CN) of $[Fe^{II}_4L^{Me4\text{-}Pz}_4](BF_4)_4$ (**3**).

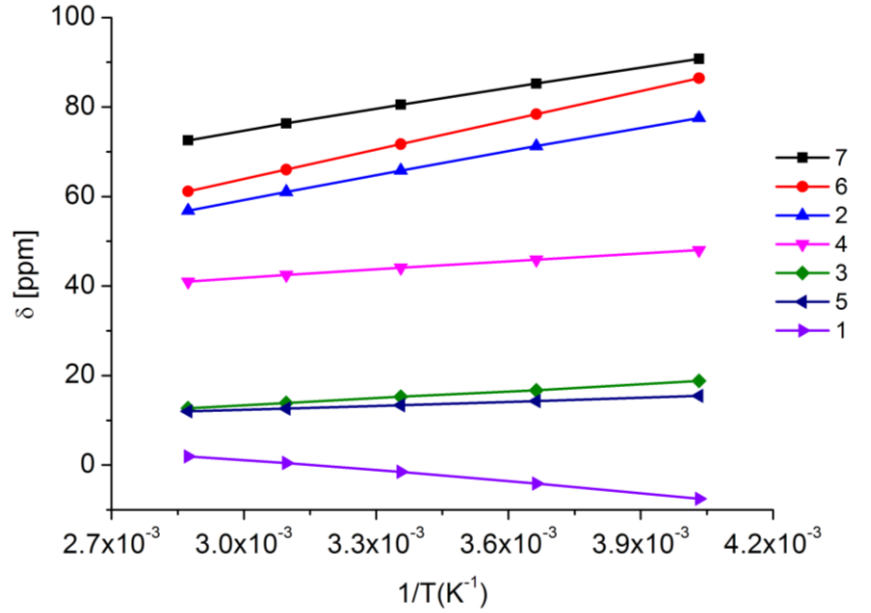

Figure 10.41. Curie plot showing the linear dependence of ^{1}H resonance shifts on the inverse temperature of $[Fe^{II}_4L^{Me4\text{-}Pz}_4](BF_4)_4$ (**3**).

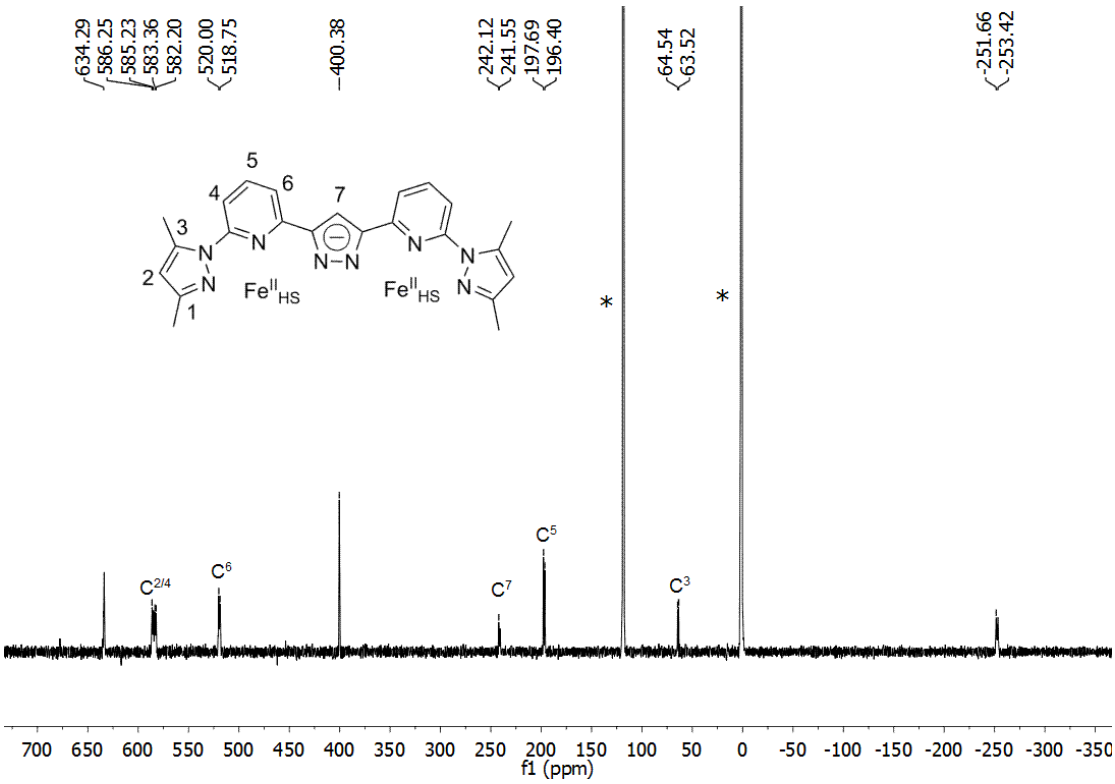

Figure 10.42. ^{13}C NMR spectrum (125 MHz, CD_3CN, 298 K) of $[Fe^{II}_4L^{Me4\text{-}Pz}_4](BF_4)_4$ (**3**) (*MeCN).

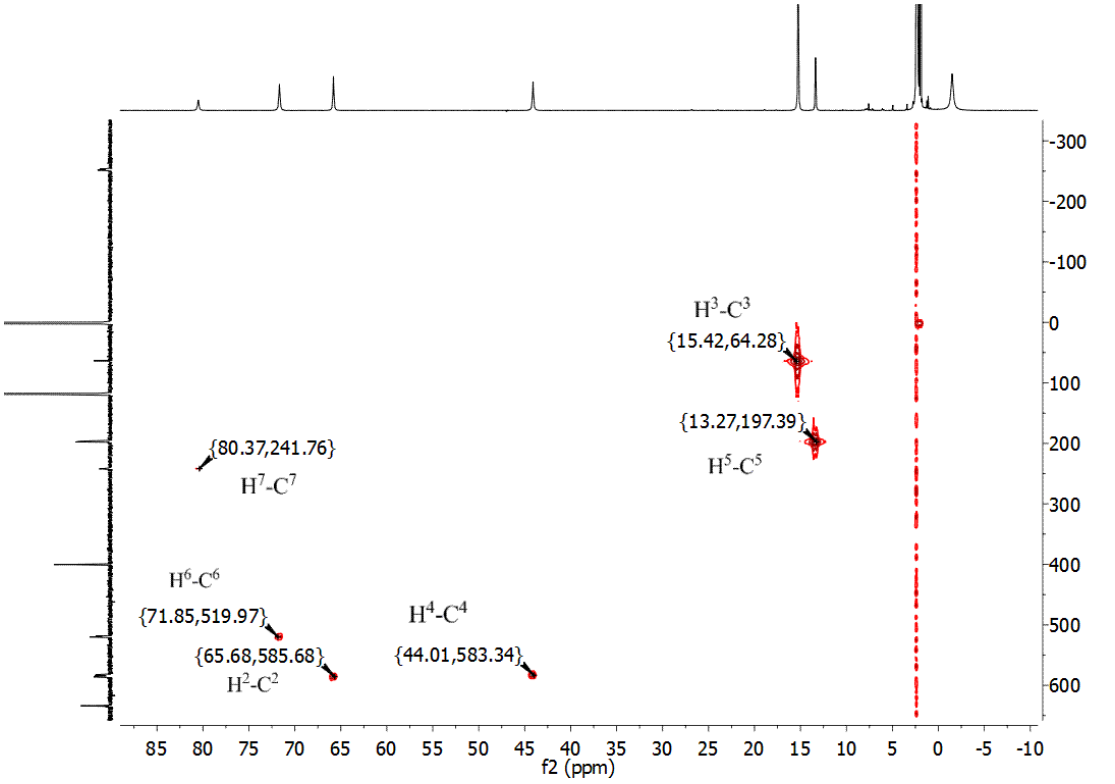

Figure 10.43. ^{1}H-^{13}C HMQC spectrum (CD_3CN, 298 K) of $[Fe^{II}_4L^{Me4\text{-}Pz}_4](BF_4)_4$ (**3**).

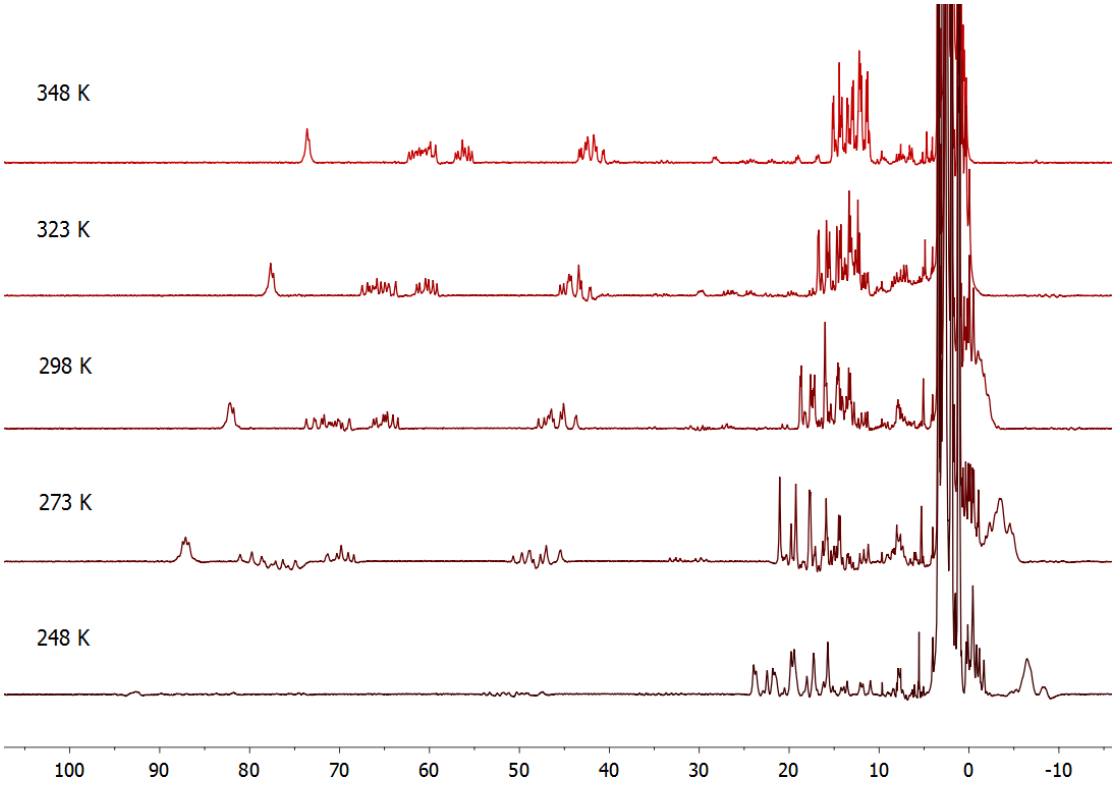

Figure 10.44. Variable-temperature ^{1}H NMR spectra (500 MHz, CD_3CN) of $[Fe^{II}_4L^{Me5\text{-}Pz}_4](BF_4)_4$ (**4**).

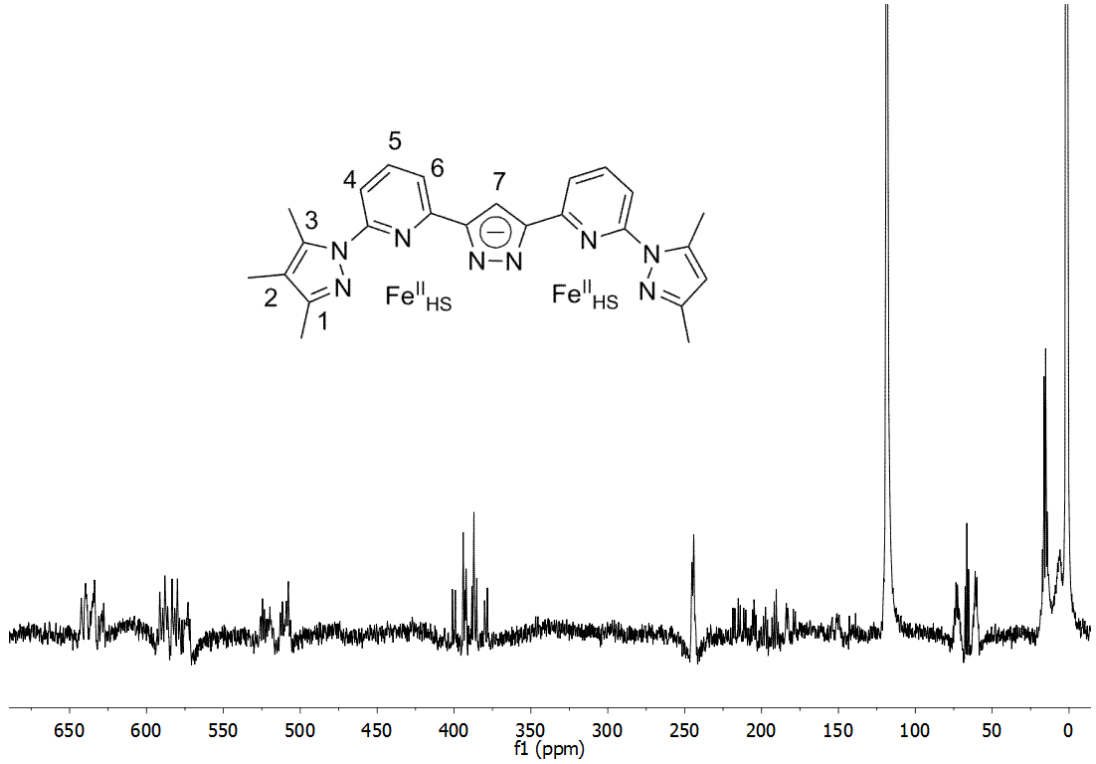

Figure 10.45. ^{13}C NMR spectrum (125 MHz, CD_3CN, 298 K) of $[Fe^{II}_4L^{Me5\text{-}Pz}_4](BF_4)_4$ (**4**).

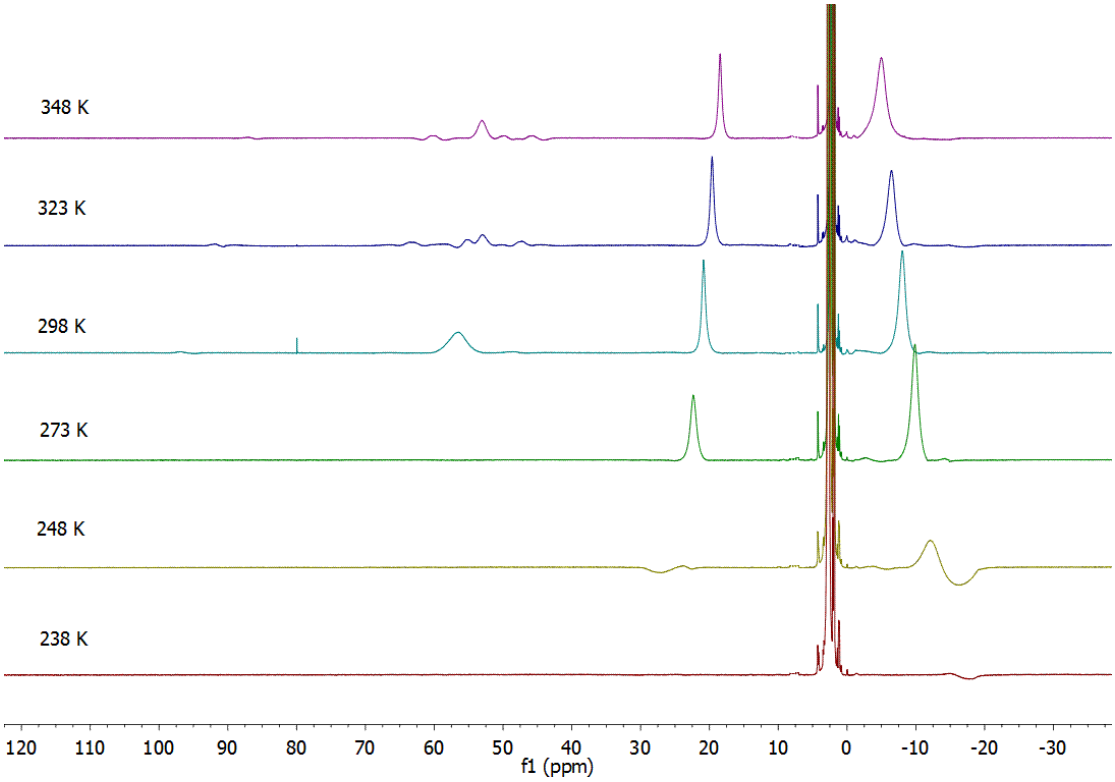

Figure 10.46. Variable-temperature ^{1}H NMR spectra (500 MHz, CD_3CN) of $[Fe^{II}{}_4L^{Me\text{-}Im}{}_4](ClO_4)_4$ (**6**).

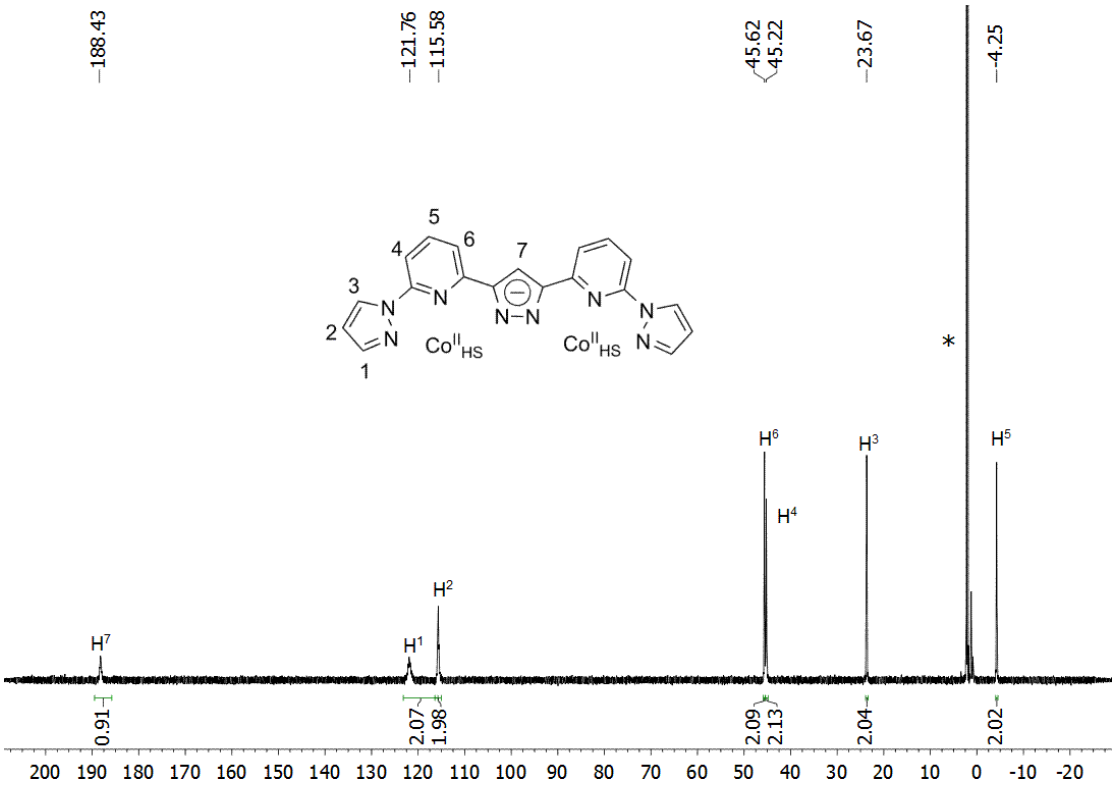

Figure 10.47. ^{1}H NMR spectrum (500 MHz, CD_3CN, 298 K) of $[Co^{II}{}_4L^{Pz}{}_4](BF_4)_4$ (**11**) (*MeCN).

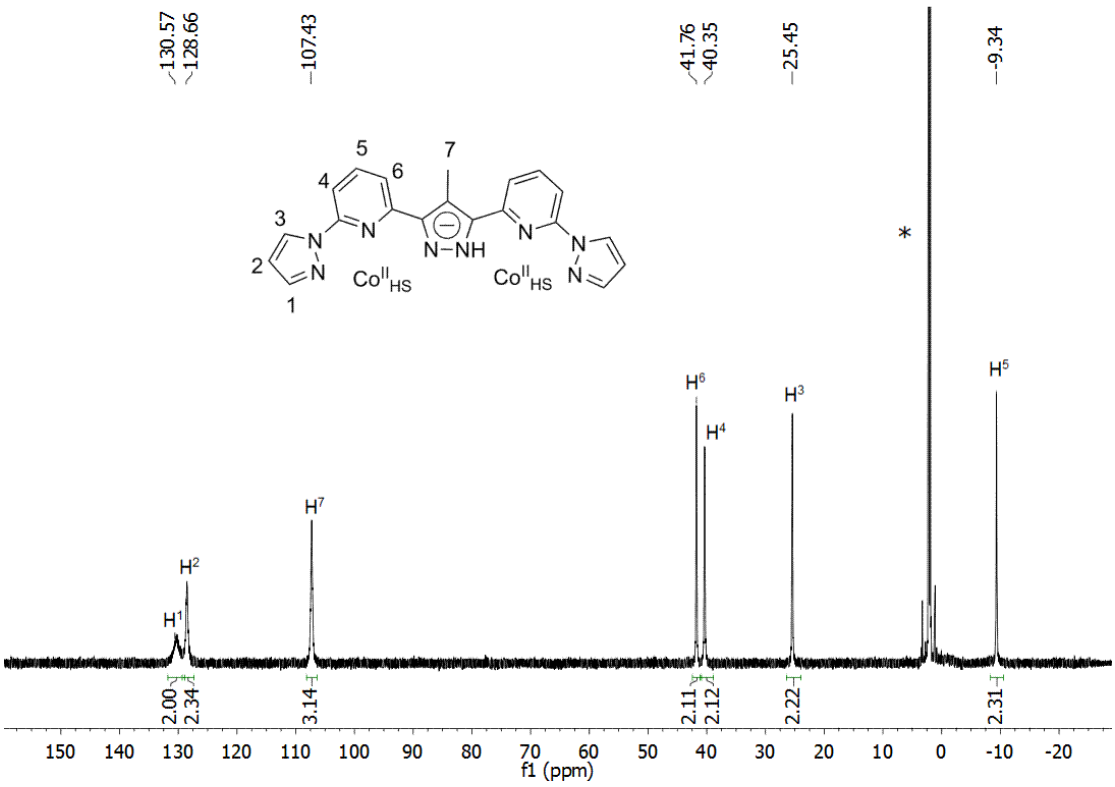

Figure 10.48. ^{1}H NMR spectrum (500 MHz, CD_3CN, 298 K) of $[Co^{II}_4L^{Me\text{-}Pz}_4](BF_4)_4$ (**12**) (*MeCN).

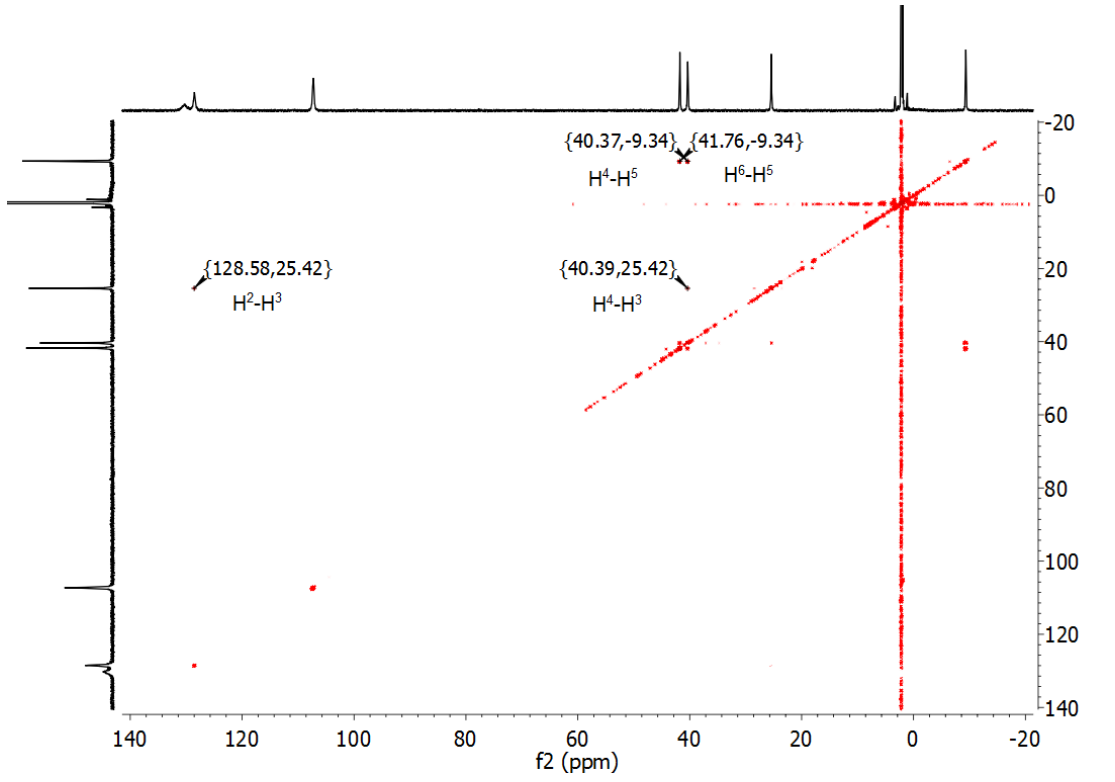

Figure 10.49. ^{1}H-^{1}H COSY spectrum (500 MHz, CD_3CN, 298 K) of $[Co^{II}_4L^{Me\text{-}Pz}_4](BF_4)_4$ (**12**).

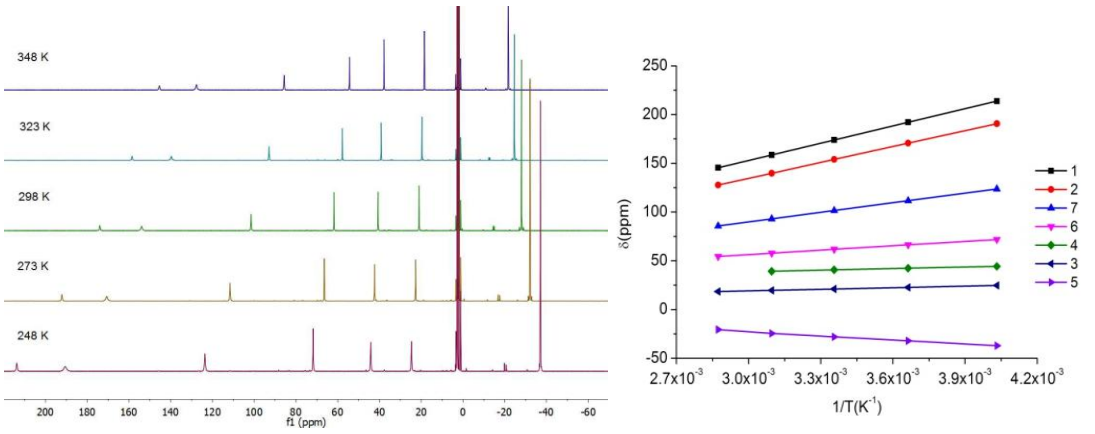

Figure 10.50. Variable-temperature ^{1}H NMR spectra (500 MHz, CD_3CN) of $[Co^{II}{}_4L^{Me\text{-}Pz}{}_4](BF_4)_4$ (**12**) (left); Curie plot showing the linear dependence of ^{1}H resonance shifts on the inverse temperature (right).

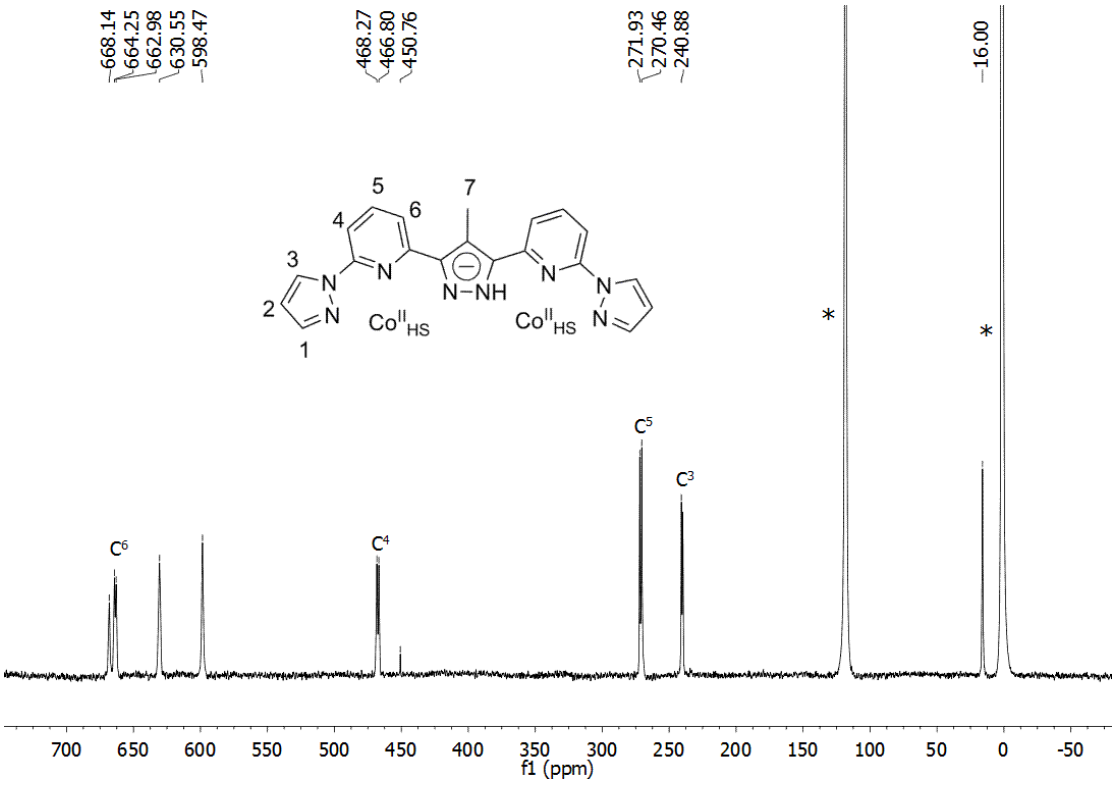

Figure 10.51. ^{13}C NMR spectrum (125 MHz, CD_3CN, 298 K) of $[Co^{II}{}_4L^{Me\text{-}Pz}{}_4](BF_4)_4$ (**12**) (*MeCN).

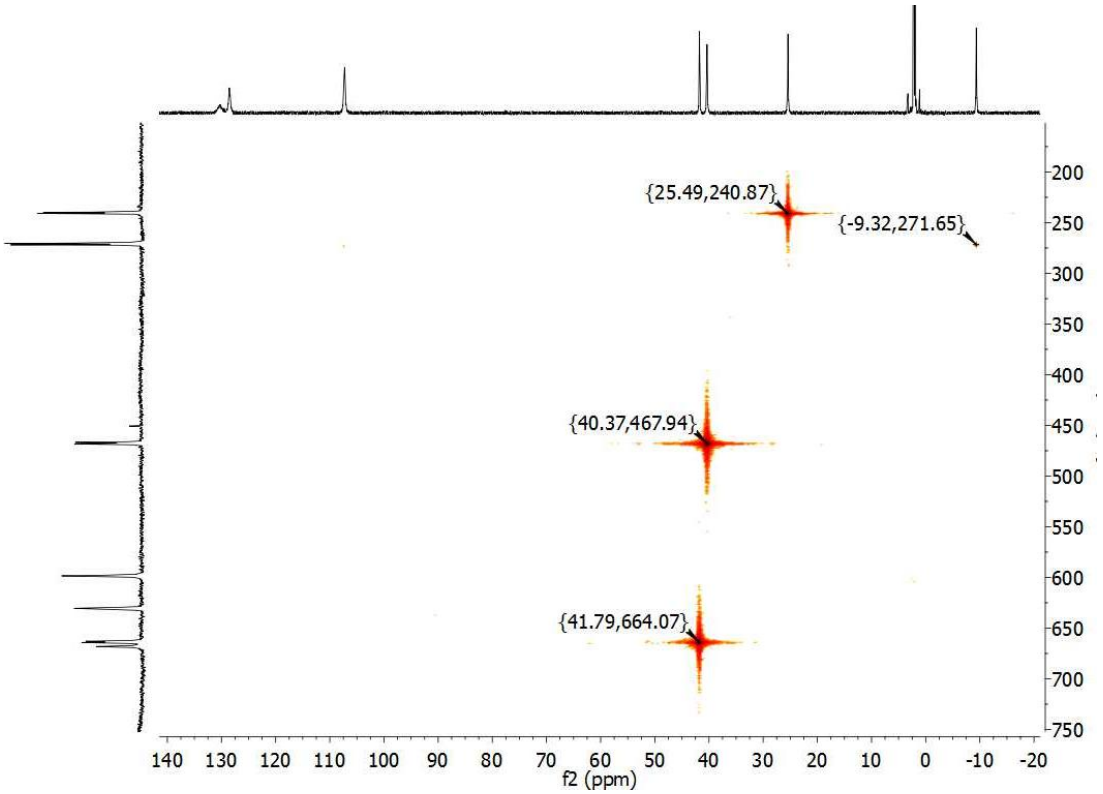

Figure 10.52. ^{1}H-^{13}C HMQC spectrum (CD_3CN, 298 K) of $[Co^{II}{}_4L^{Me\text{-}Pz}{}_4](BF_4)_4$ (**12**).

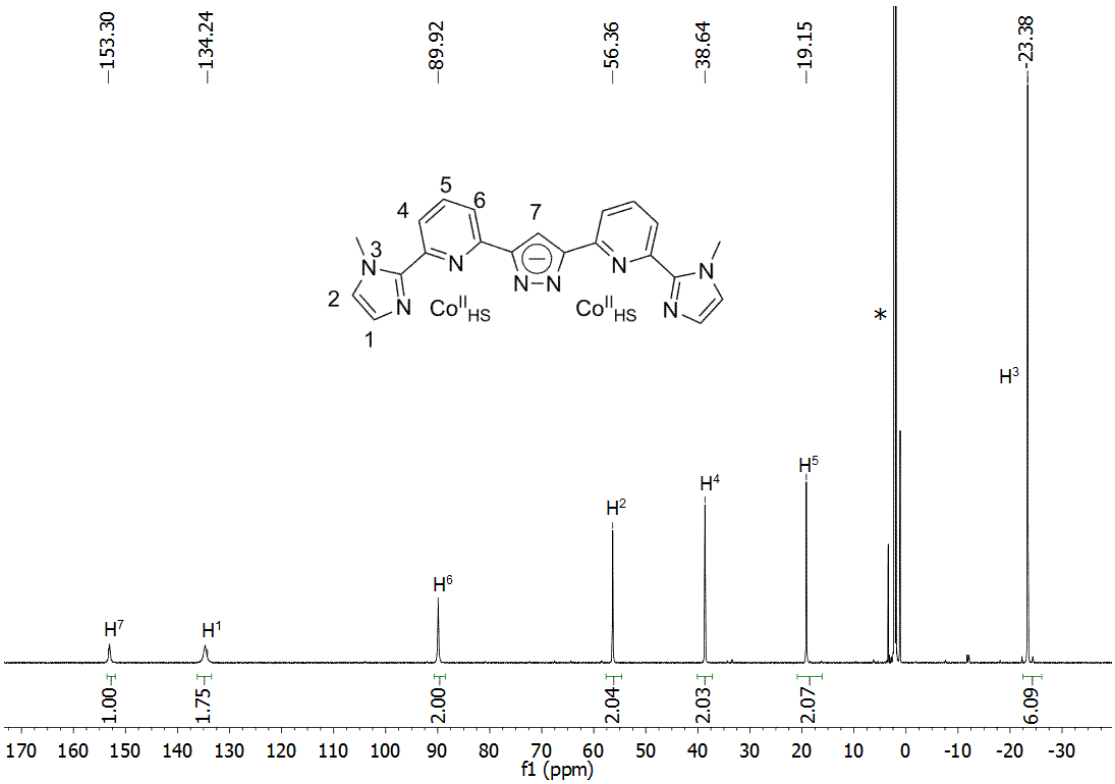

Figure 10.53. ^{1}H NMR spectrum (500 MHz, CD_3CN, 333 K) of $[Co^{II}{}_4L^{Me\text{-}Im}{}_4](BF_4)_4$ (**13**) (*MeCN).

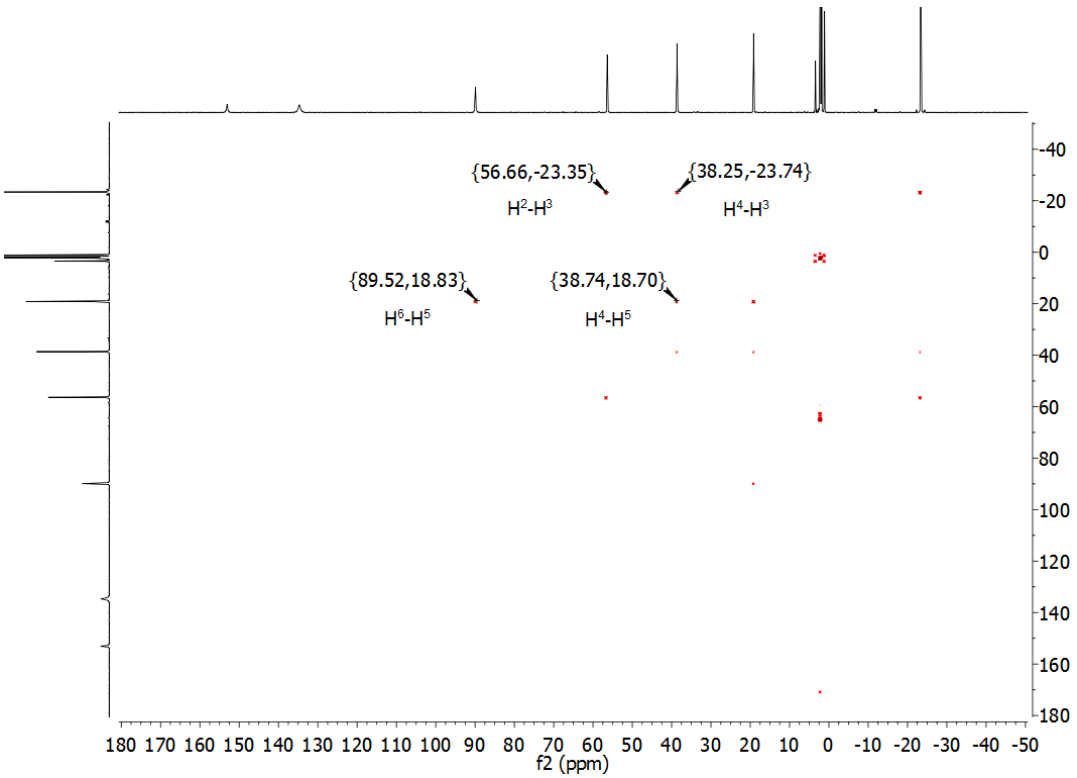

Figure 10.54. ^{1}H-^{1}H NMR spectrum (500 MHz, CD_3CN, 333 K) of $[Co^{II}_4L^{Me\text{-}Im}_4](BF_4)_4$ (**13**).

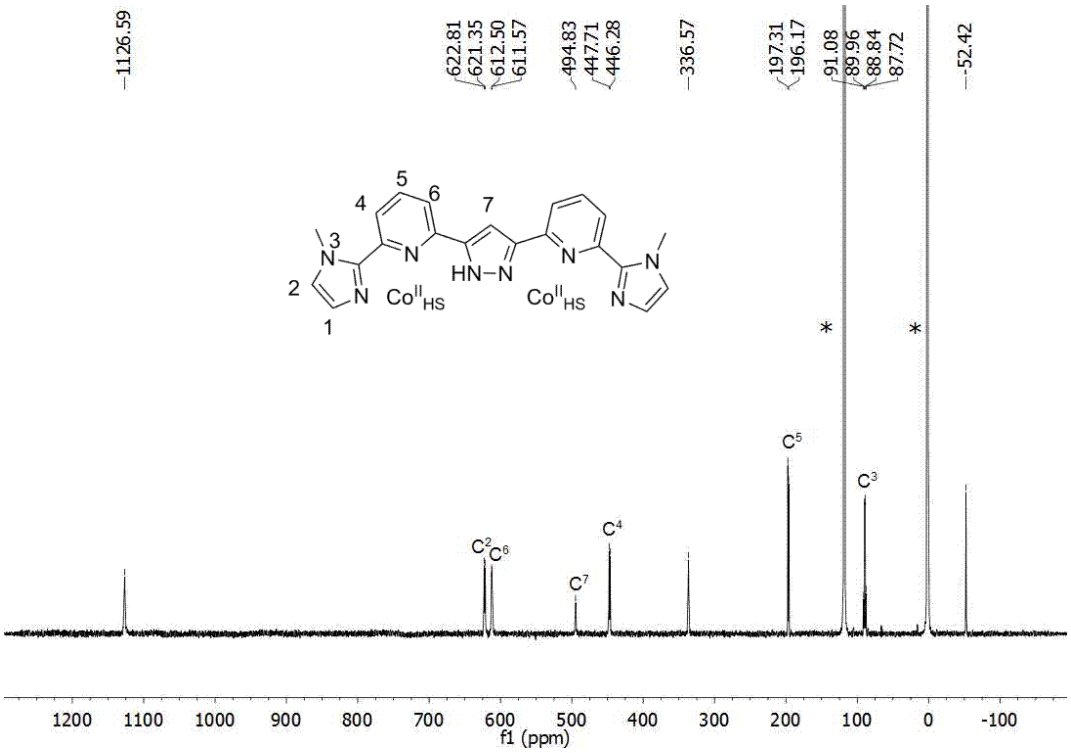

Figure 10.55. ^{13}C NMR spectrum (125 MHz, CD_3CN, 333 K) of $[Co^{II}_4L^{Me\text{-}Im}_4](BF_4)_4$ (**13**) (*MeCN).

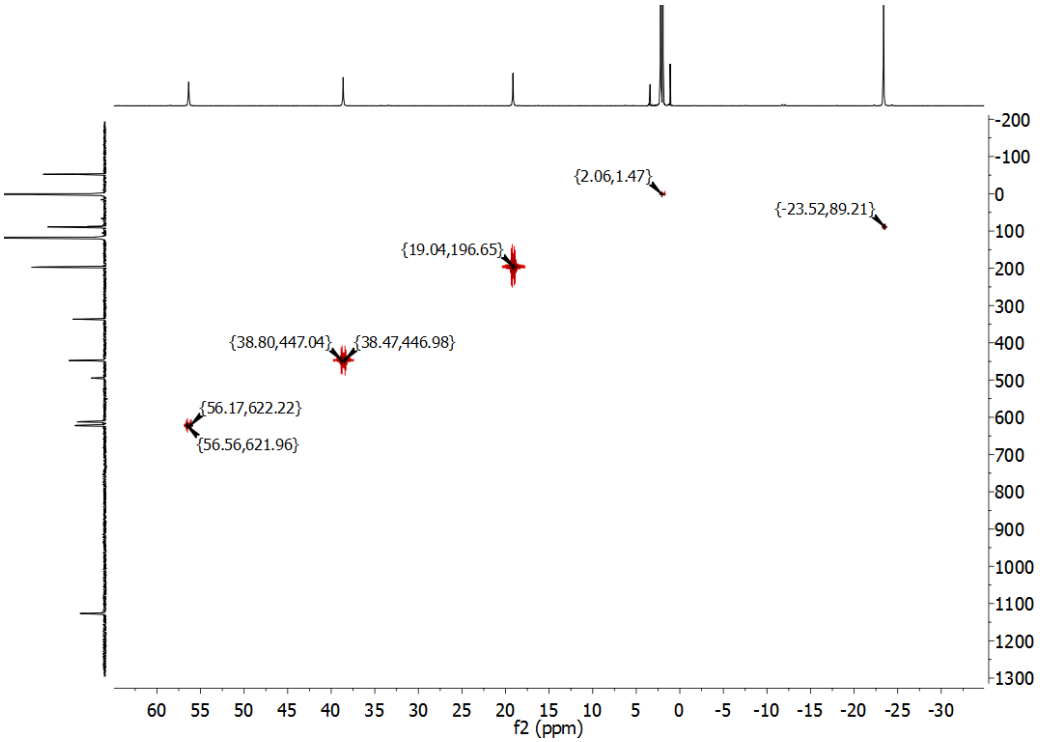

Figure 10.56. ^{1}H-^{13}C HMQC spectrum (500 MHz, CD_3CN, 333 K) of $[Co^{II}_4L^{Me\text{-}Im}_4](BF_4)_4$ (**13**) (^{1}H: −30 − 60 ppm, ^{13}C: −200 − 1300 ppm.).

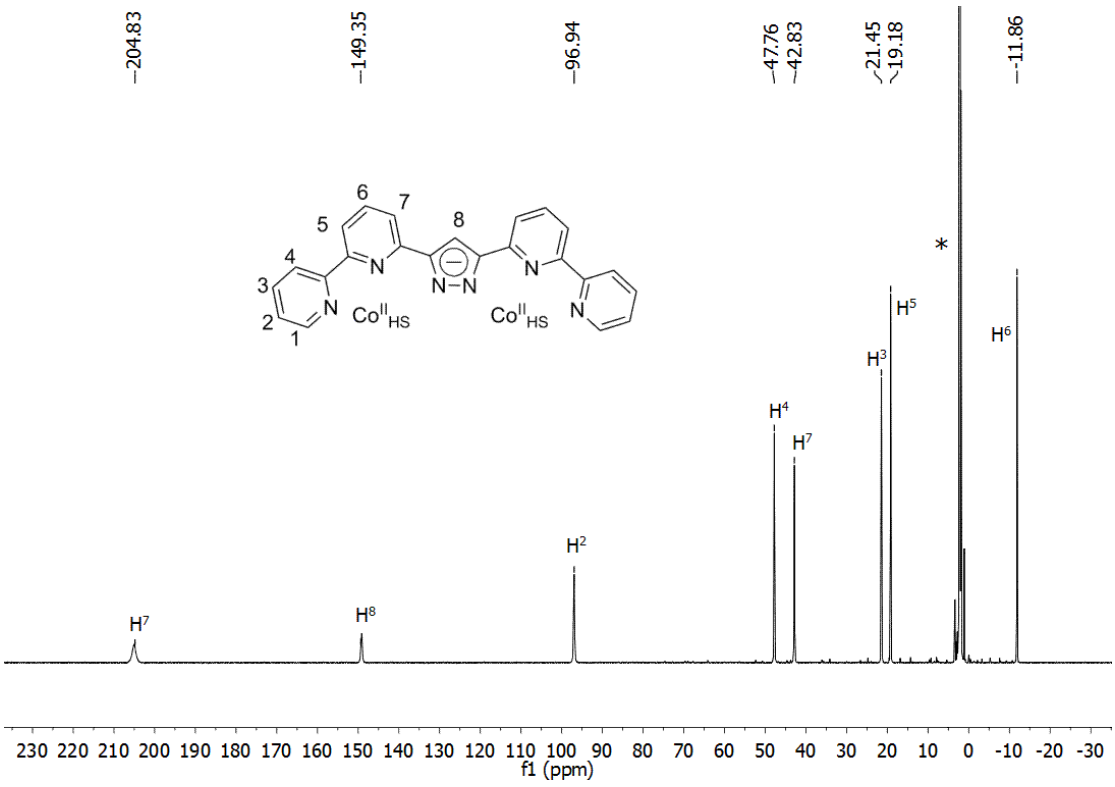

Figure 10.57. ^{1}H NMR spectrum (500 MHz, CD_3CN, 333 K) of $[Co^{II}_4L^{Py}_4](BF_4)_4$ (**14**) (*MeCN).

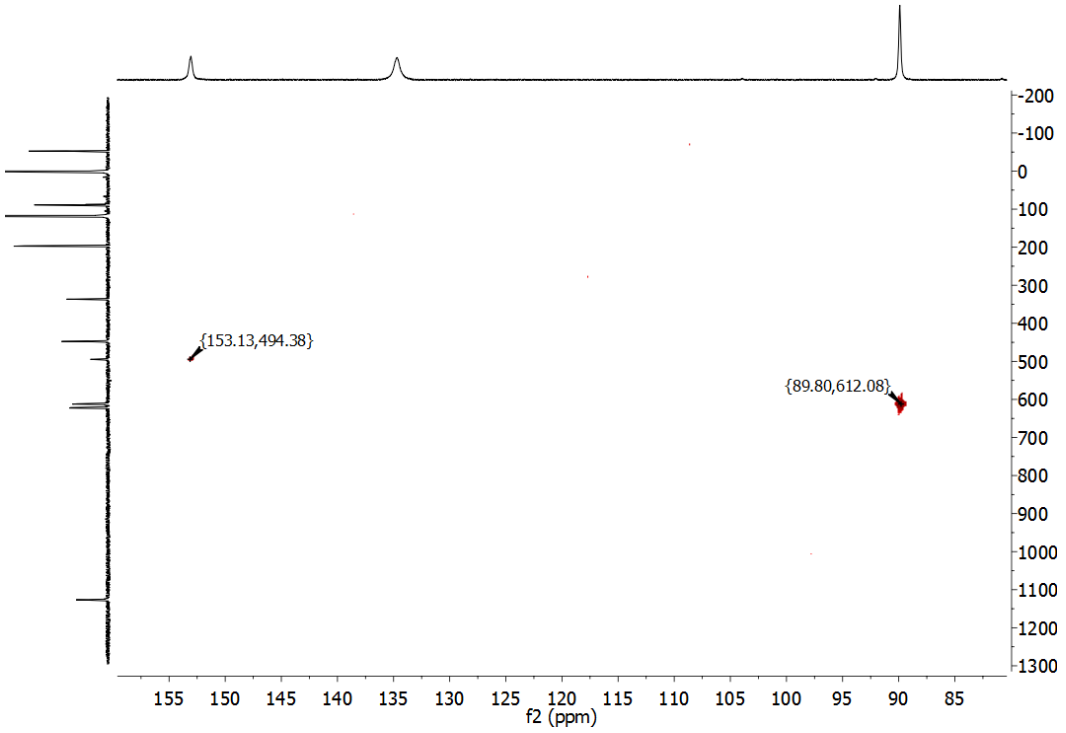

Figure 10.58. ^{1}H-^{13}C HMQC spectrum (500 MHz, CD_3CN, 333 K) of $[Co^{II}_4L^{Me\text{-}Im}_4](BF_4)_4$ (**13**) (^{1}H: 85 – 155 ppm, ^{13}C: –200 – 1300 ppm).

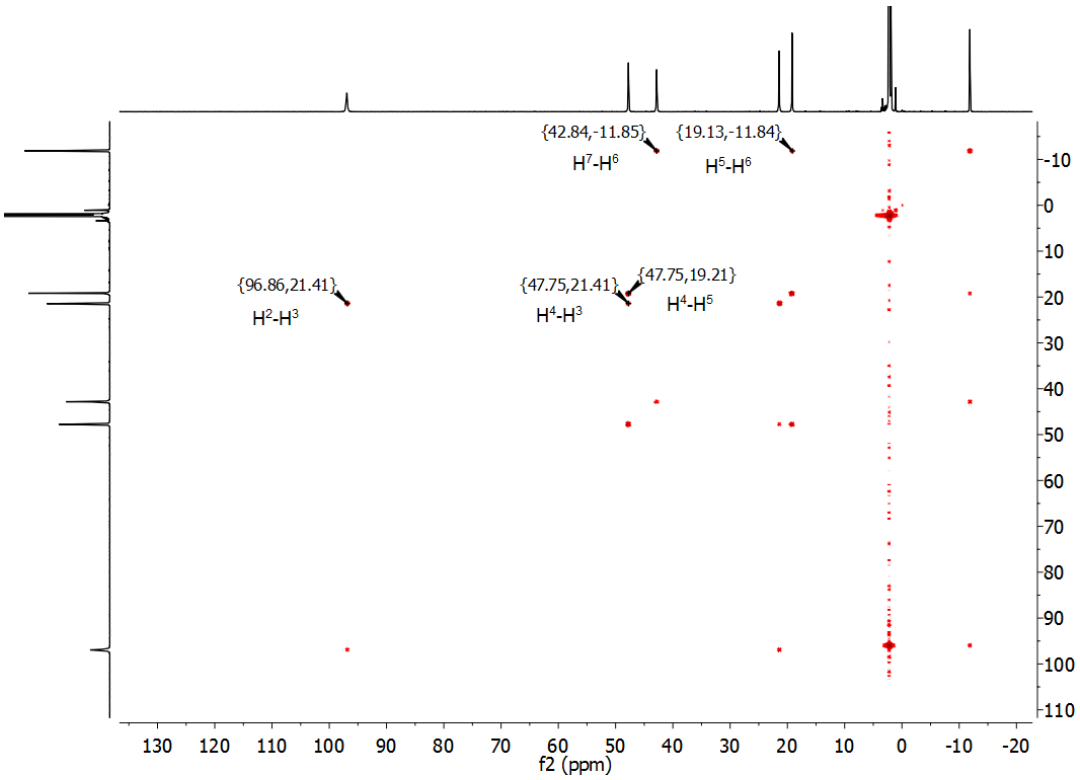

Figure 10.59. ^{1}H-^{1}H COSY spectrum (500 MHz, CD_3CN, 333 K) of $[Co^{II}_4L^{Py}_4](BF_4)_4$ (**14**).

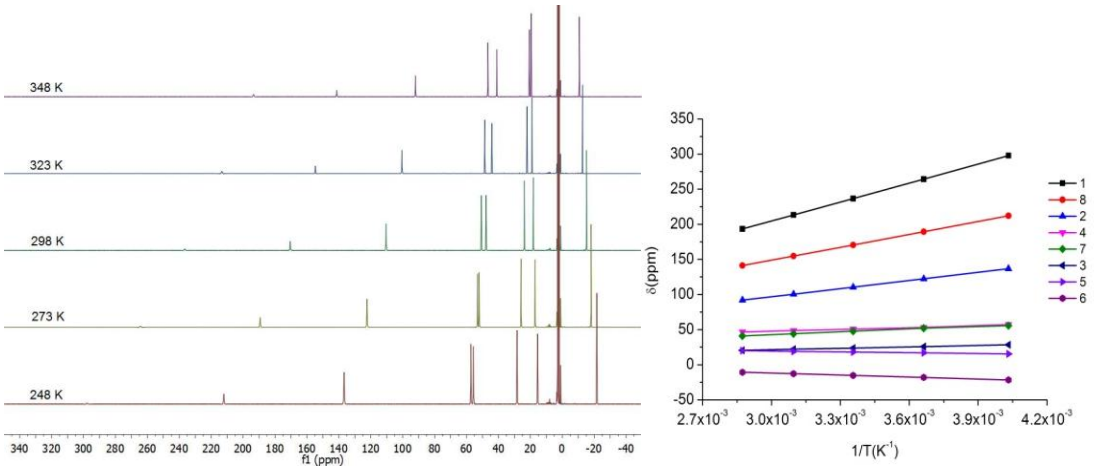

Figure 10.60. Variable-temperature ^{1}H NMR spectra (500 MHz, CD_3CN) of $[Co^{II}{}_4L^{Py}{}_4](BF_4)_4$ (**14**) (left); Curie plot showing the linear dependence of ^{1}H resonance shifts on the inverse temperature (right).

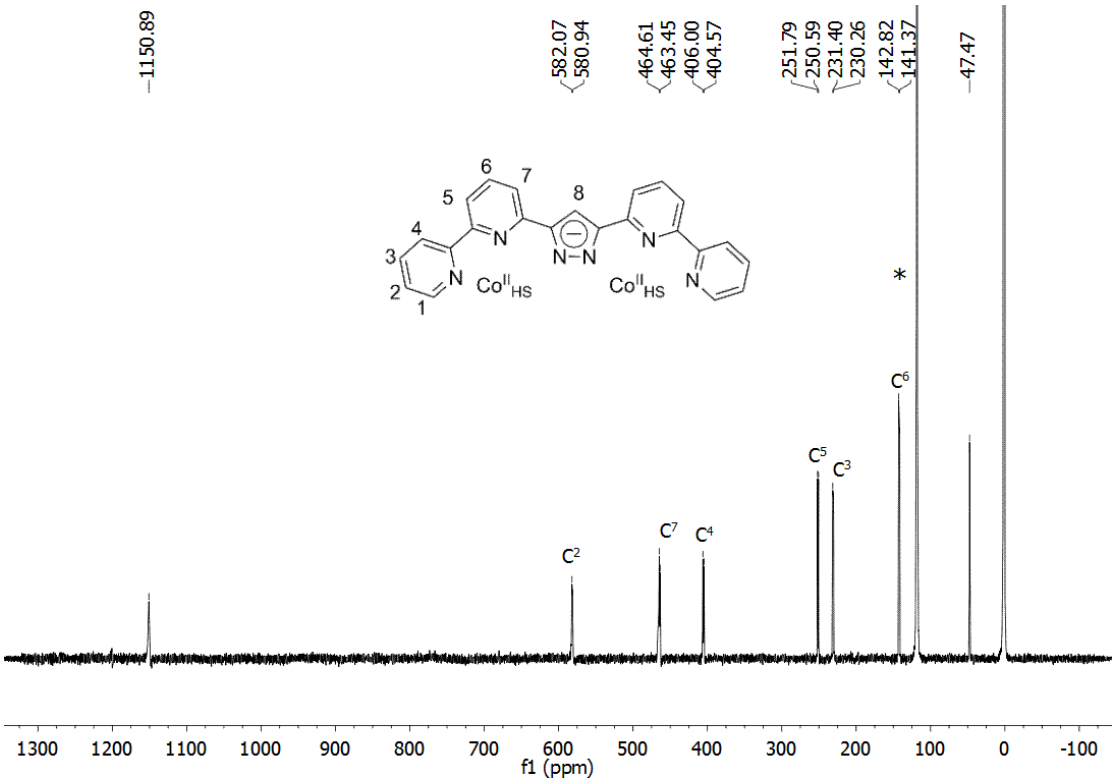

Figure 10.61. ^{13}C NMR spectrum (125 MHz, CD_3CN, 333 K) of $[Co^{II}{}_4L^{Py}{}_4](BF_4)_4$ (**14**) (*MeCN).

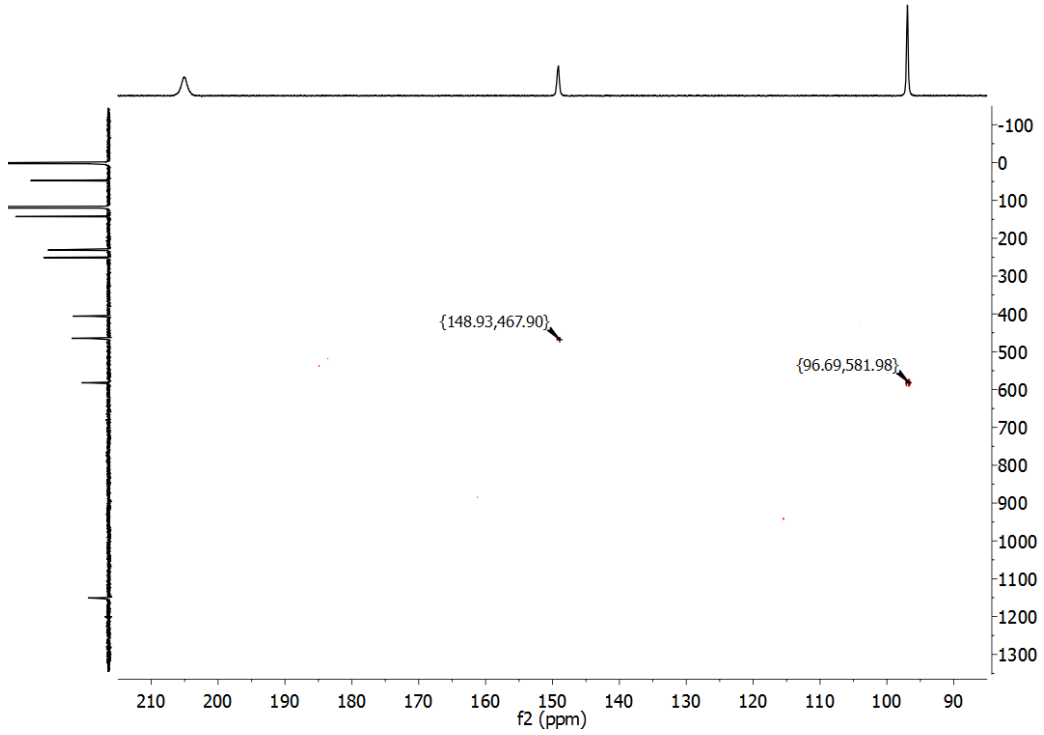

Figure 10.62. ^{1}H-^{13}C HMQC spectrum (CD_3CN, 333 K) of $[Co^{II}{}_4L^{Py}{}_4](BF_4)_4$ (**14**) (^{1}H: 90 – 210 ppm, ^{13}C: –100 – 1300 ppm.).

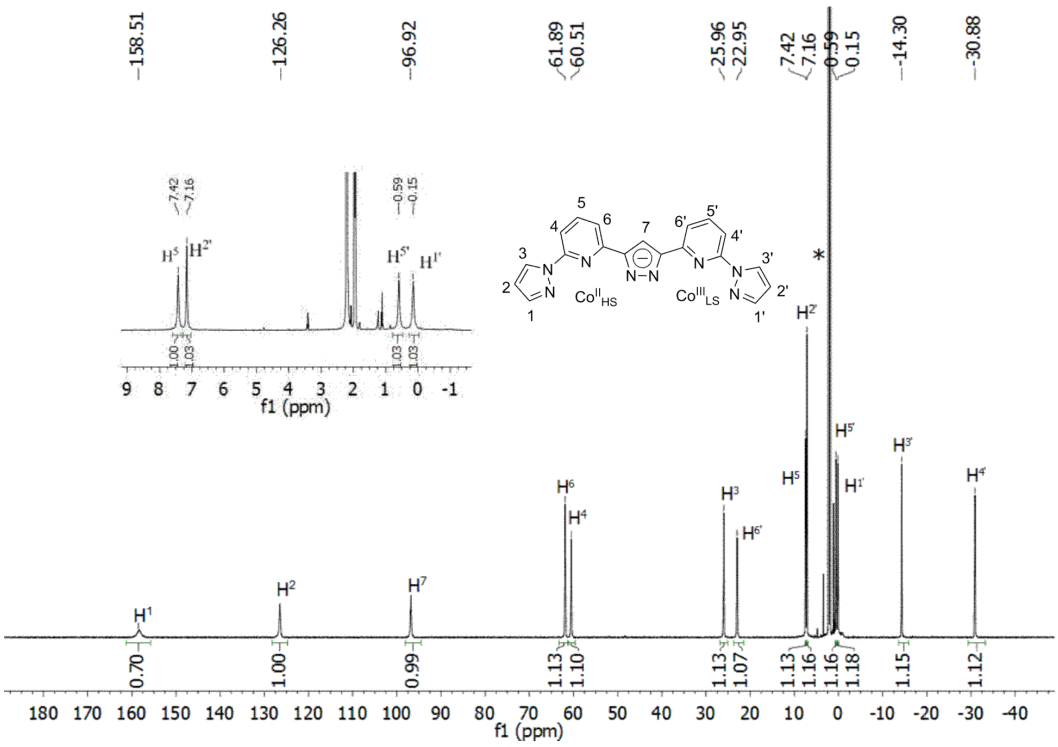

Figure 10.63. ^{1}H NMR spectrum (500 MHz, CD_3CN, 298 K) of $[Co^{II}{}_2Co^{III}{}_2L^{Pz}{}_4](BF_4)_6$ (**15**) (*MeCN).

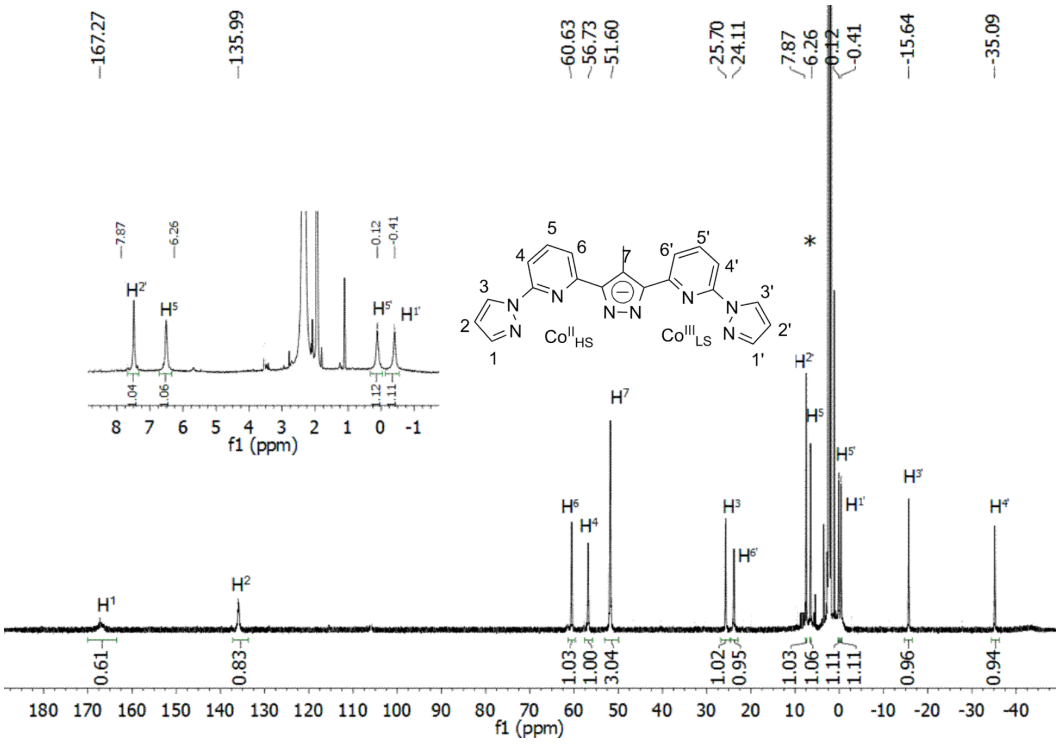

Figure 10.64. ^{1}H NMR spectrum (500 MHz, CD_3CN, 298 K) of $[Co^{II}_2Co^{III}_2L^{Me\text{-}Pz}_4](BF_4)_6$ (**16**) (*MeCN).

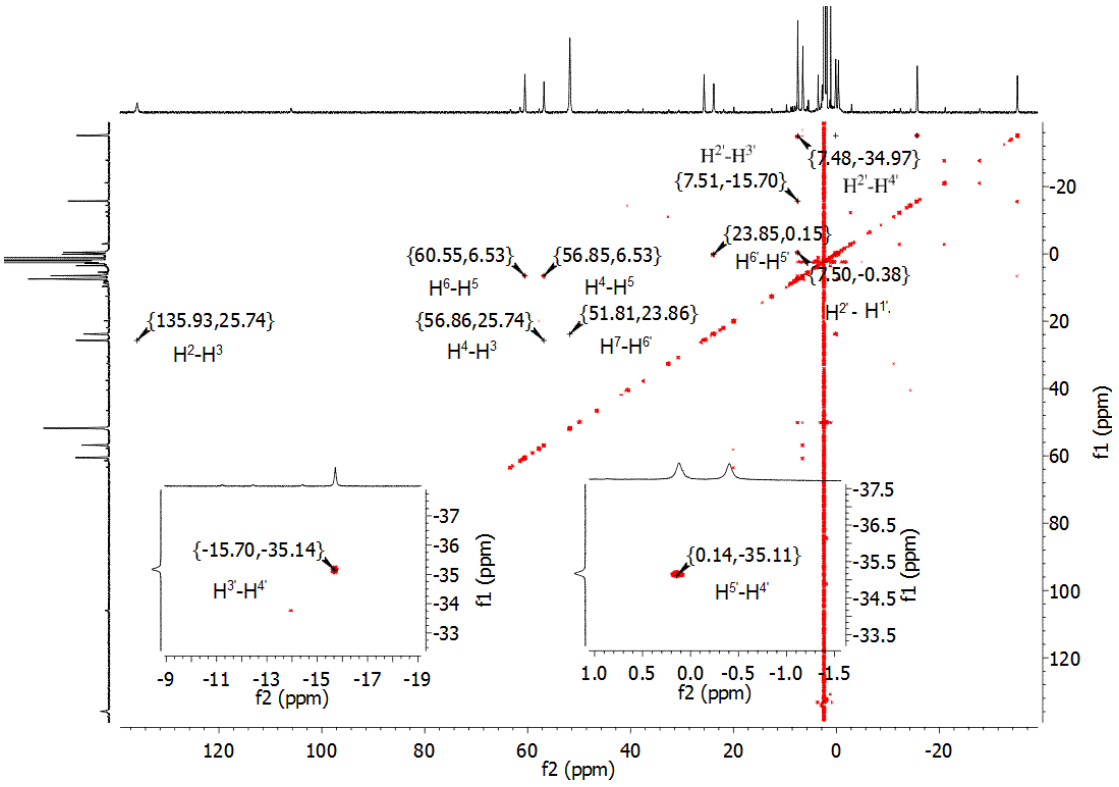

Figure 10.65. ^{1}H-^{1}H COSY spectrum (CD_3CN, 298 K) of $[Co^{II}_2Co^{III}_2L^{Me\text{-}Pz}_4](BF_4)_6$ (**16**).

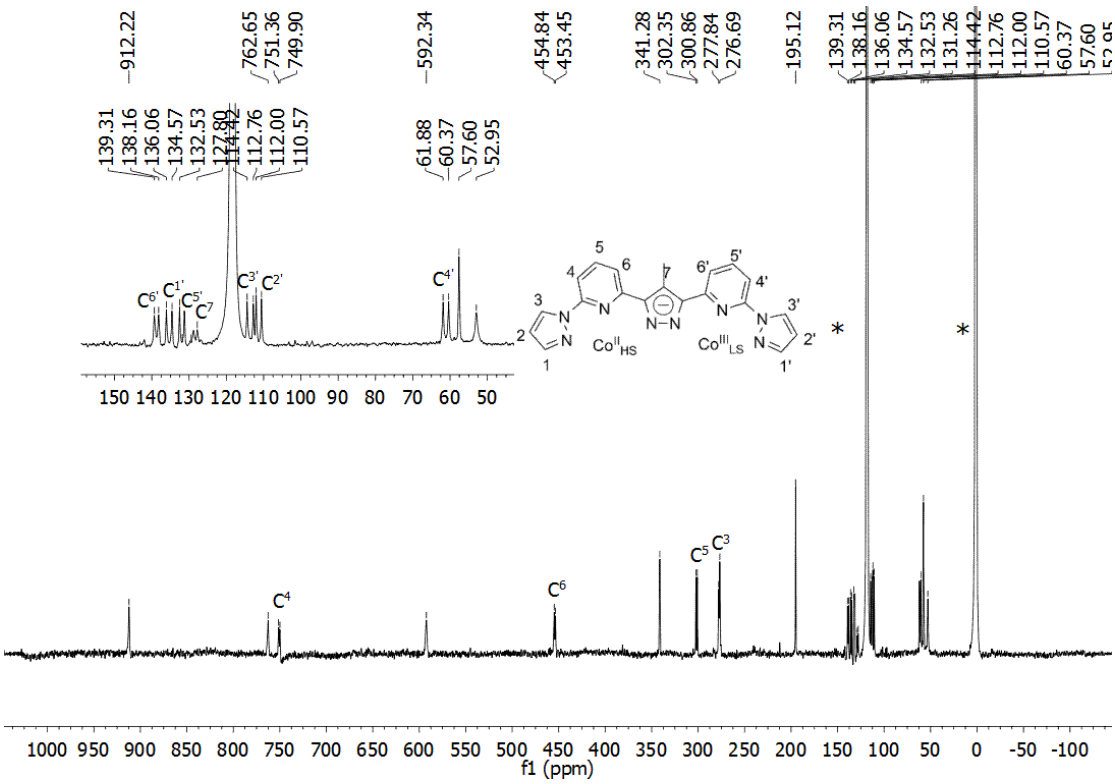

Figure 10.66. ^{13}C NMR spectrum (125 MHz, CD_3CN, 298 K) of $[Co^{II}_2Co^{III}_2L^{Me\text{-}Pz}_4](BF_4)_6$ (**16**) (*MeCN).

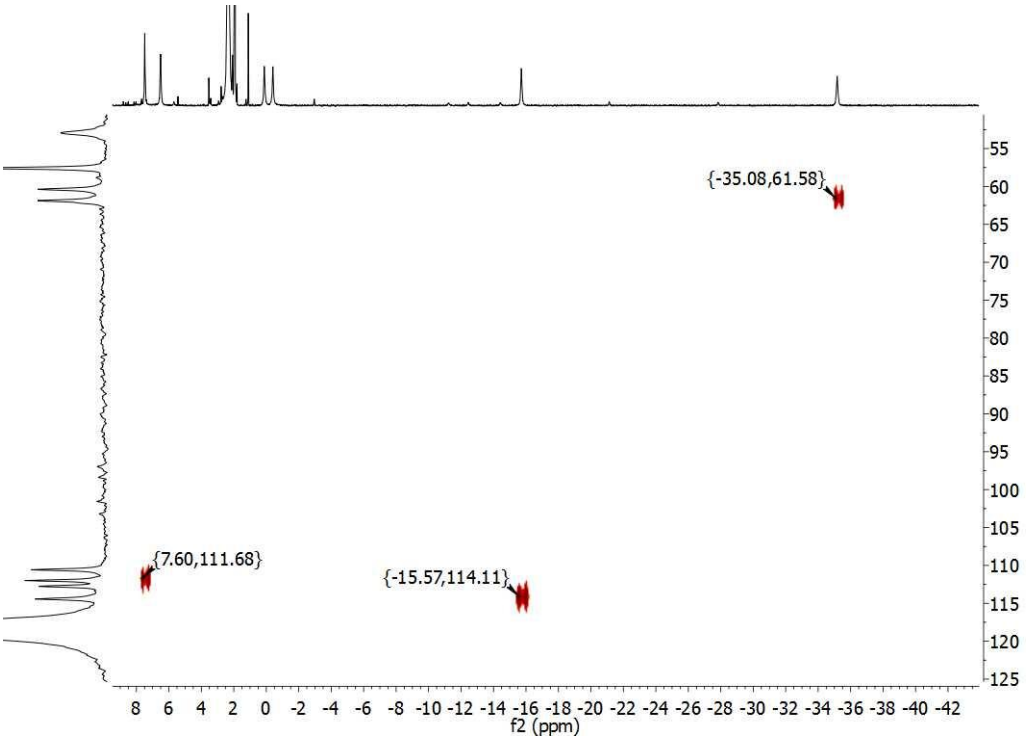

Figure 10.67. ^{1}H-^{13}C HMQC spectrum (CD_3CN, 298 K) of $[Co^{II}_2Co^{III}_2L^{Me\text{-}Pz}_4](BF_4)_6$ (**16**) (^{1}H: –42 to 8 ppm; ^{13}C: 55 to 125 ppm).

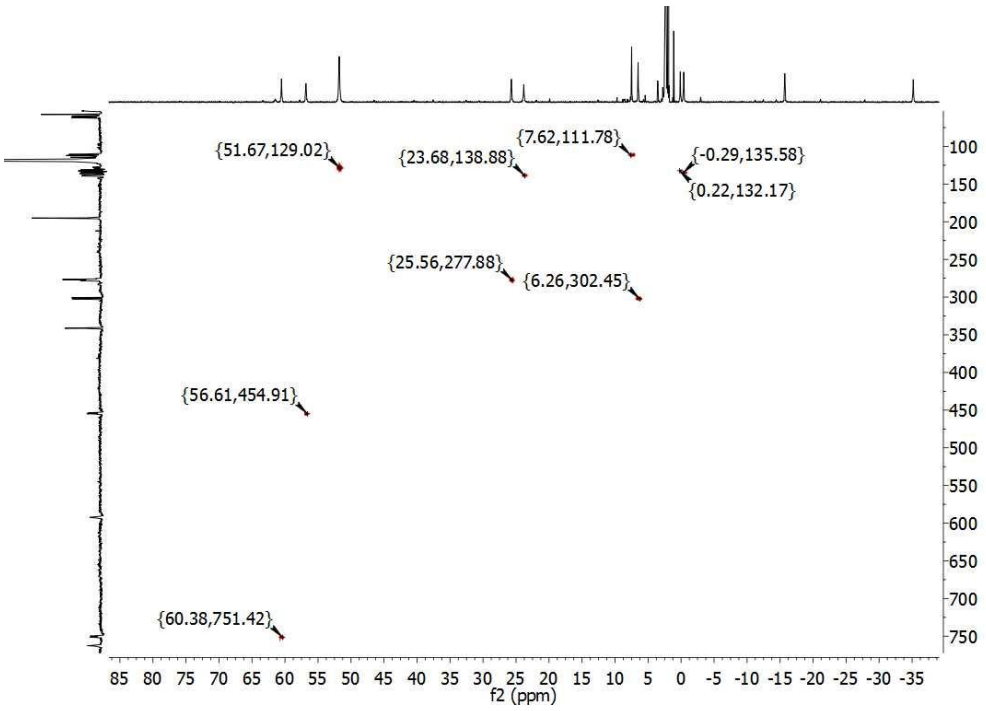

Figure 10.68. ^{1}H-^{13}C HMQC spectrum (CD_3CN, 298 K) of $[Co^{II}_2Co^{III}_2L^{Me\text{-}Pz}_4](BF_4)_6$ (**16**) (^{1}H: −35 to 85 ppm; ^{13}C: 100 to 750 ppm).

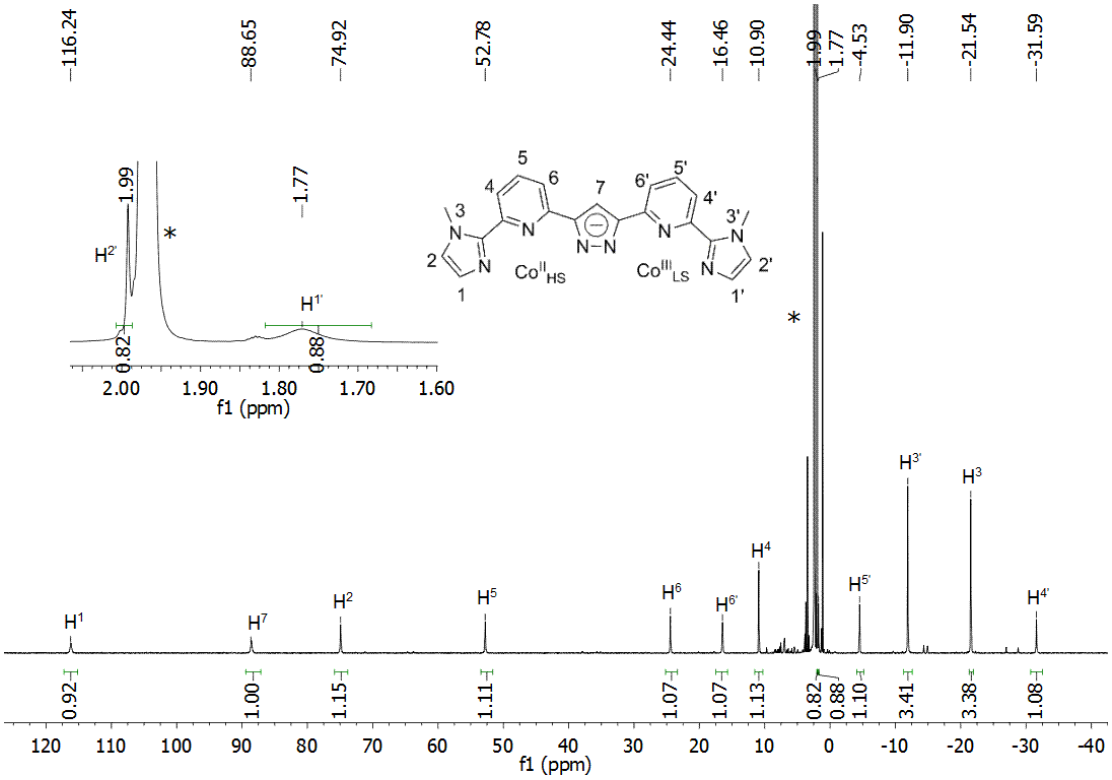

Figure 10.69. ^{1}H NMR spectrum (500 MHz, CD_3CN, 298 K) of $[Co^{II}_2Co^{III}_2L^{Me\text{-}Im}_4](BF_4)_6$ (**17**) (*MeCN).

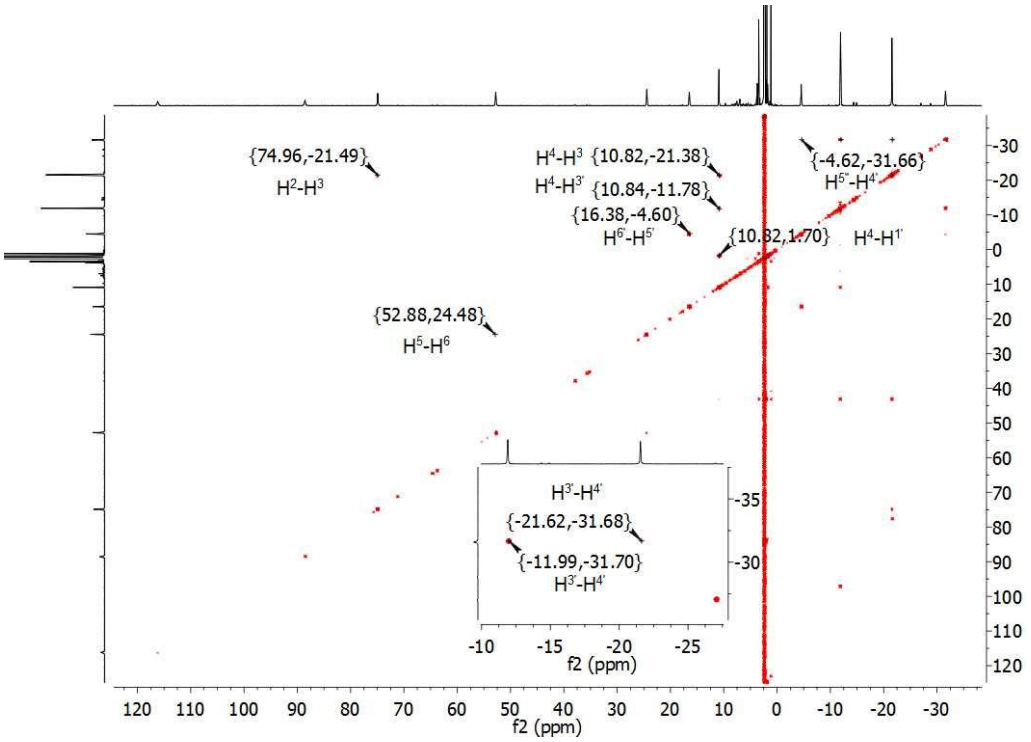

Figure 10.70. ^{1}H-^{1}H COSY spectrum (CD_3CN, 298 K) of $[Co^{II}_2Co^{III}_2L^{Me\text{-}Im}_4](BF_4)_6$ (**17**).

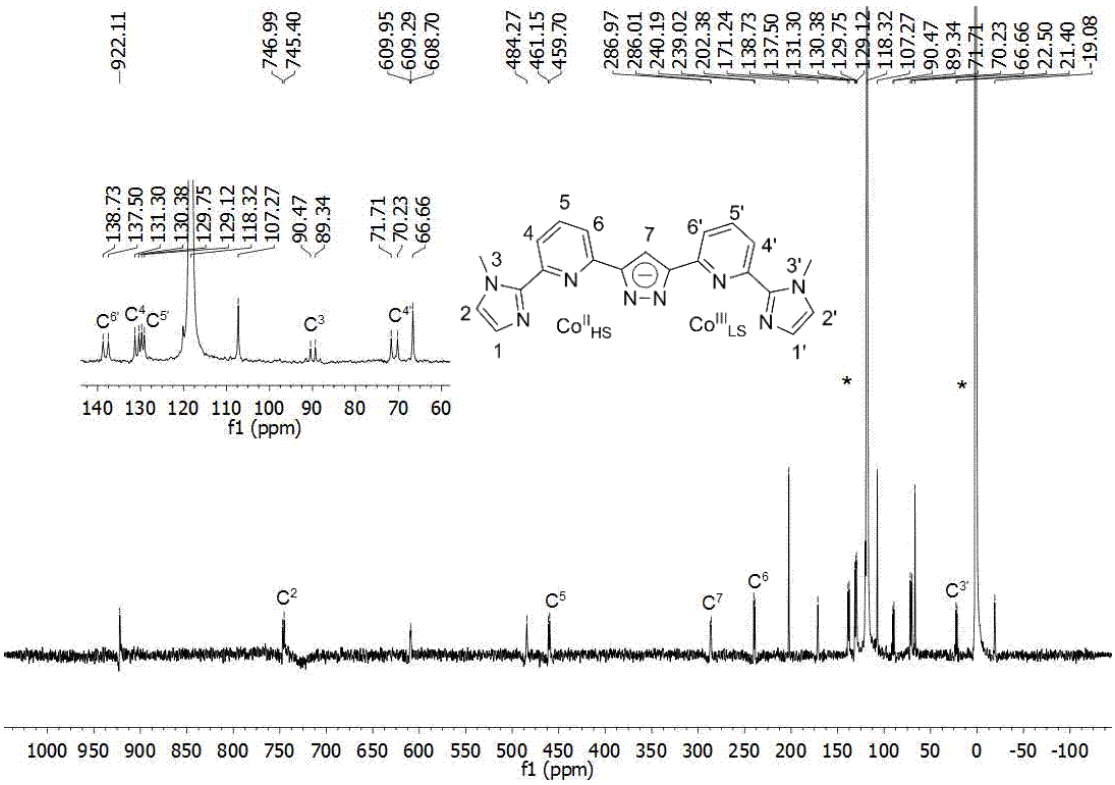

Figure 10.71. ^{13}C NMR spectrum (125 MHz, CD_3CN, 298 K) of $[Co^{II}_2Co^{III}_2L^{Me\text{-}Im}_4](BF_4)_6$ (**17**) (*MeCN).

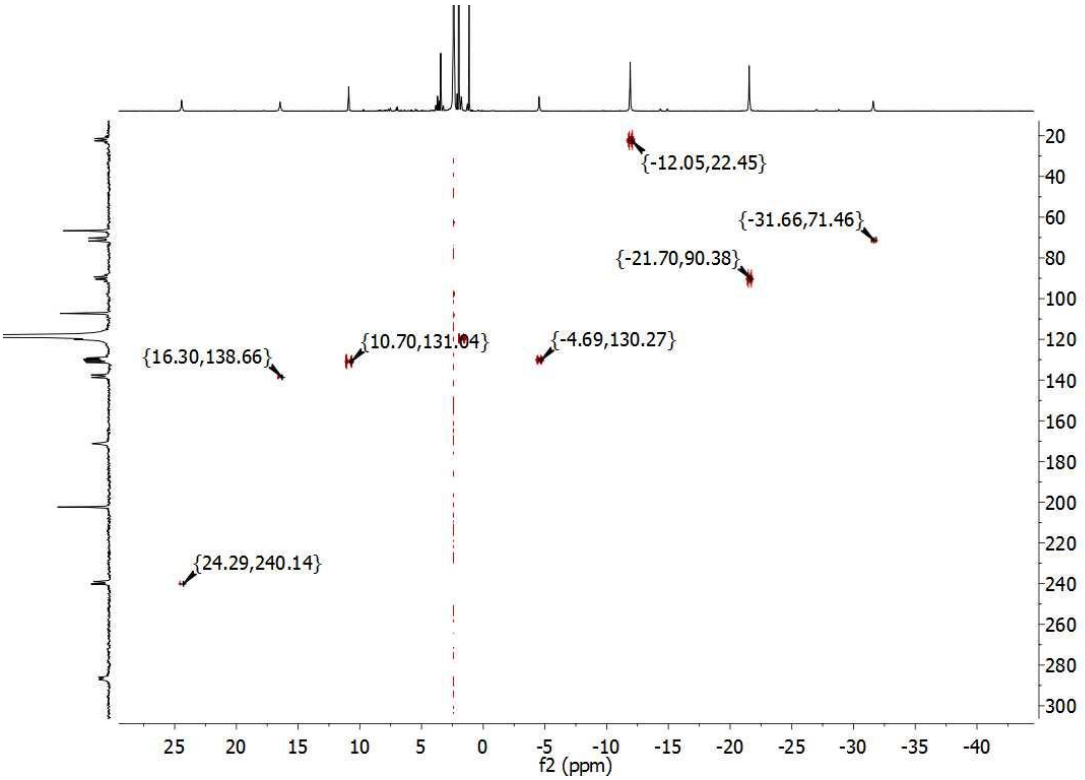

Figure 10.72. ^{1}H-^{13}C HMQC spectrum (CD_3CN, 298 K) of $[Co^{II}_2Co^{III}_2L^{Me\text{-}Im}_4](BF_4)_6$ (**17**) (^{1}H: −40 to 25 ppm; ^{13}C: 20 to 380 ppm).

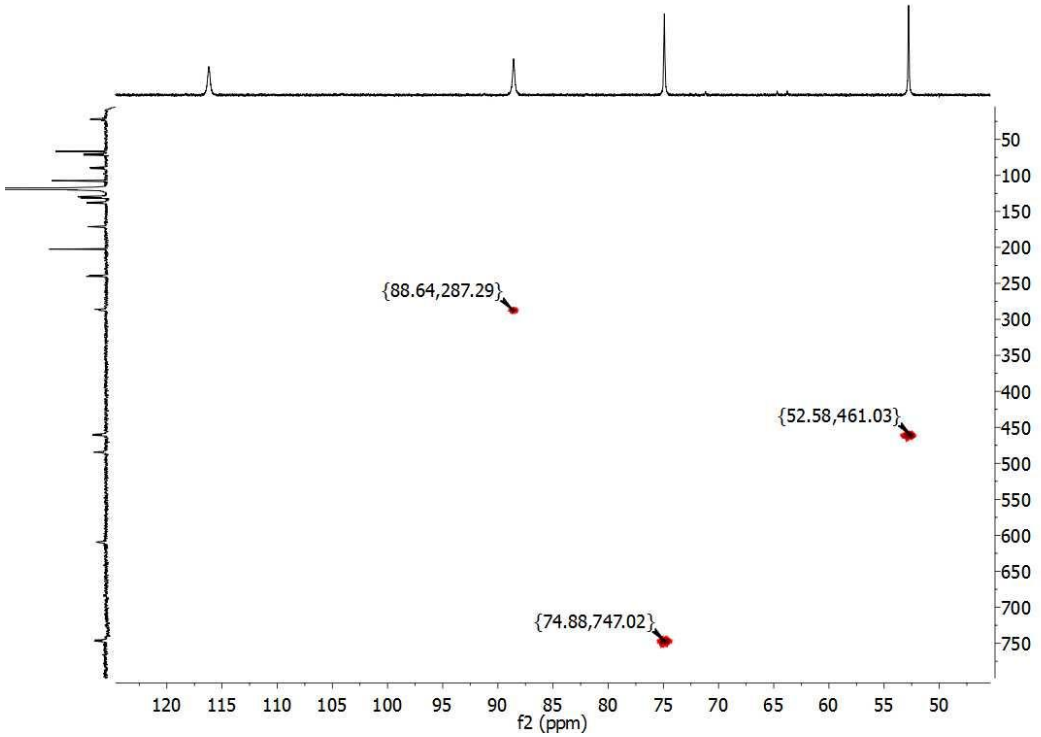

Figure 10.73. ^{1}H-^{13}C HMQC spectrum (CD_3CN, 298 K) of $[Co^{II}_2Co^{III}_2L^{Me\text{-}Im}_4](BF_4)_6$ (**17**) (^{1}H: 50 to 120 ppm; ^{13}C: 100 to 750 ppm).

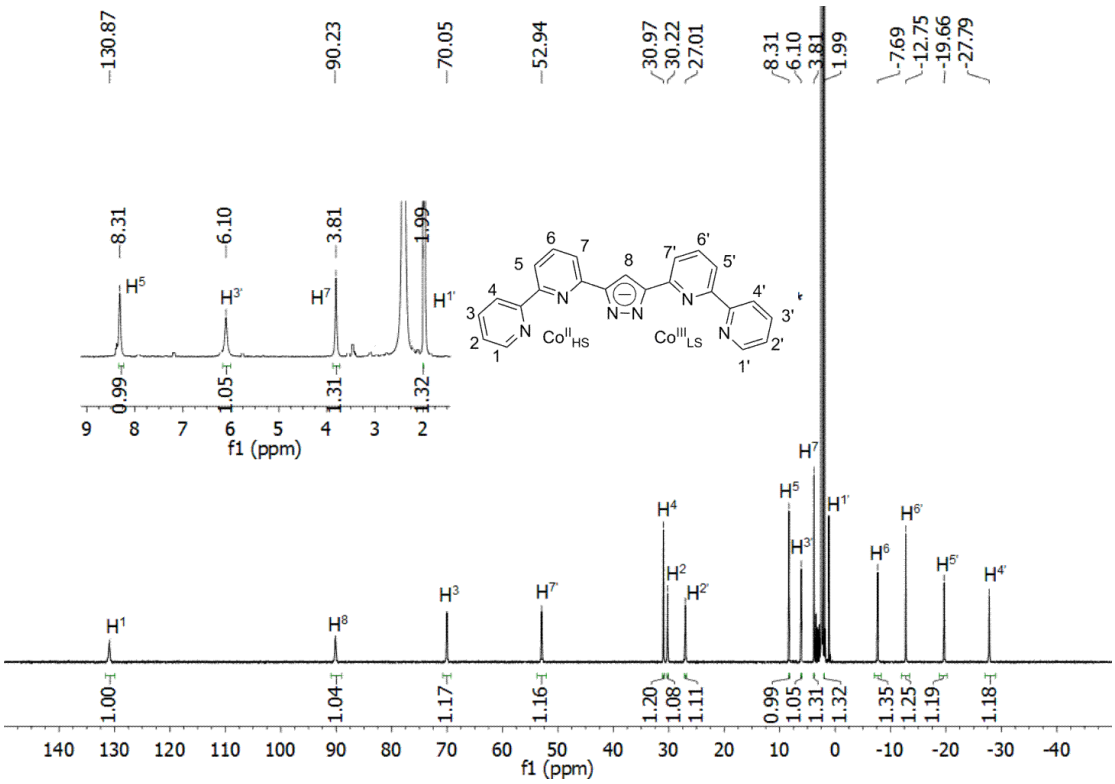

Figure 10.74 ^{1}H NMR spectrum (500 MHz, CD_3CN, 298 K) of $[Co^{II}_2Co^{III}_2L^{Py}_4](BF_4)_6$ (**18**) (*MeCN).

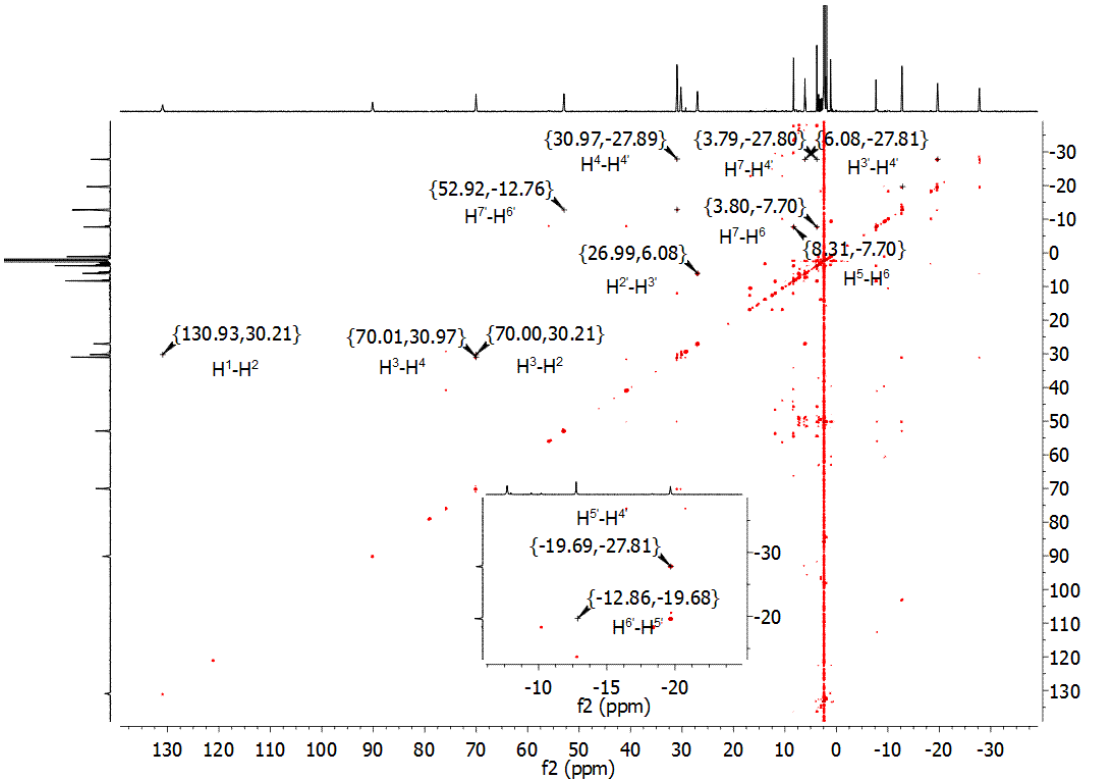

Figure 10.75. ^{1}H-^{1}H COSY spectrum (CD_3CN, 298 K) of $[Co^{II}_2Co^{III}_2L^{Py}_4](BF_4)_6$ (**18**).

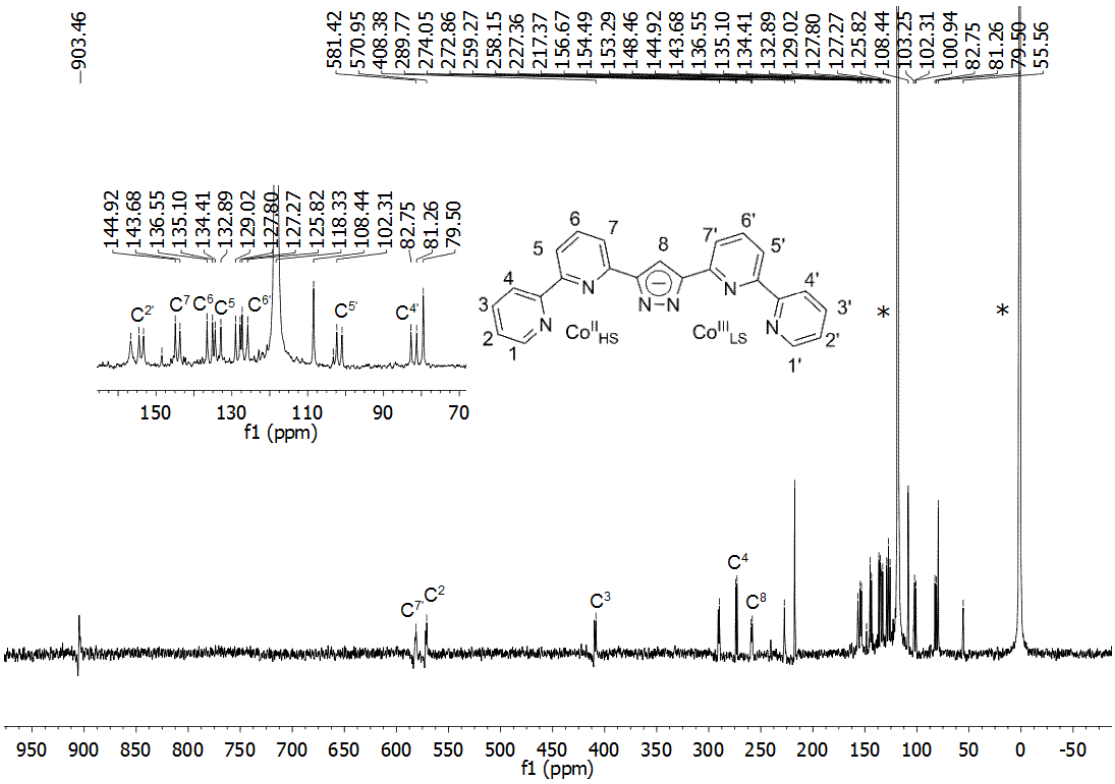

Figure 10.76. ^{13}C NMR spectrum (125 MHz, CD_3CN, 298 K) of $[Co^{II}_2Co^{III}_2L^{Py}_4](BF_4)_6$ (**18**) (*MeCN).

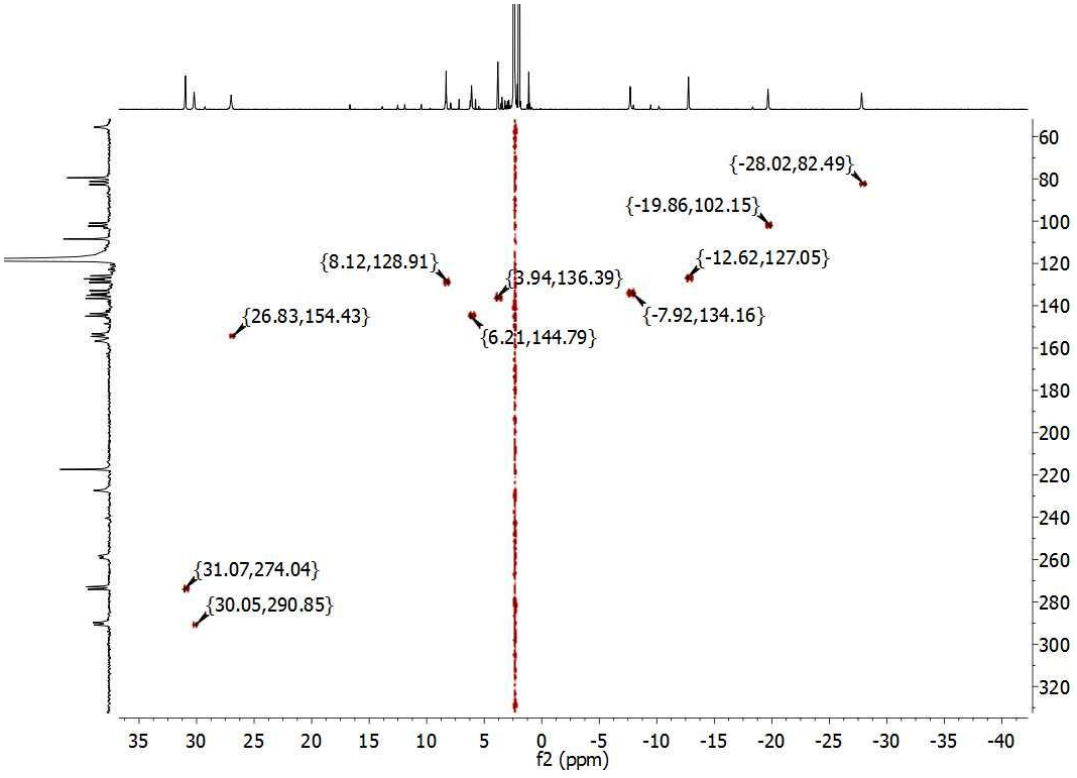

Figure 10.77. ^{1}H-^{13}C HMQC spectrum (CD_3CN, 298 K) of $[Co^{II}_2Co^{III}_2L^{Py}_4](BF_4)_6$ (**18**) (^{1}H: –40 to 35 ppm; ^{13}C: 60 to 320 ppm).

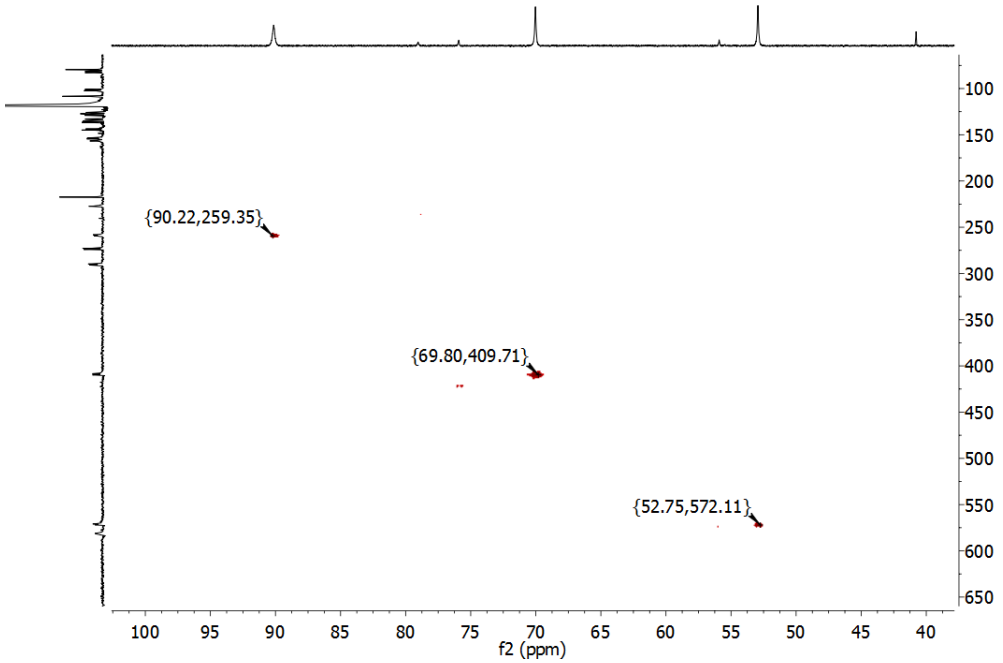

Figure 10.78. ^{1}H-^{13}C HMQC spectrum (CD_3CN, 298 K) of $[Co^{II}_2Co^{III}_2L^{Py}_4](BF_4)_6$ (**18**) (^{1}H: 40 to 100 ppm; ^{13}C: 100 to 650 ppm).

10.2. CV and SWV spectra

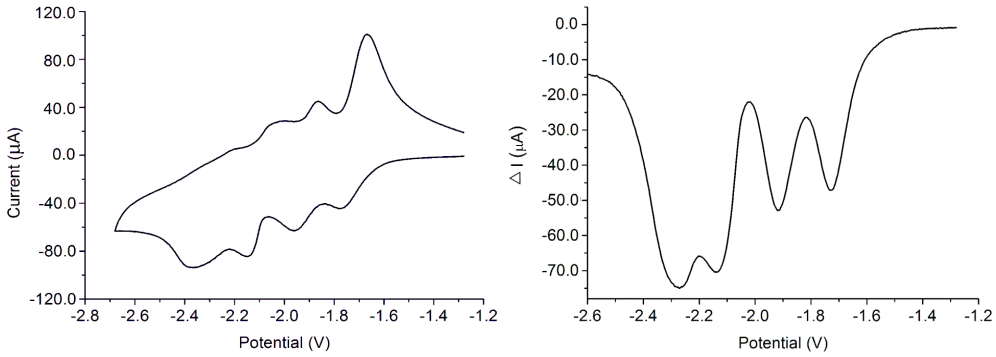

Figure 10.79. Cyclic and square wave voltammograms of $[Fe^{II}{}_4L^{Me\text{-}Pz}{}_4](BF_4)_4$ (**2**) over the potential range −2.68 V to −1.20 V (left) and −2.60 V to −1.20 V (right) (CH_3CN / 0.1M Bu_4NPF_6, scan rate 0.1 V s^{-1}, vs Fc/Fc^+).

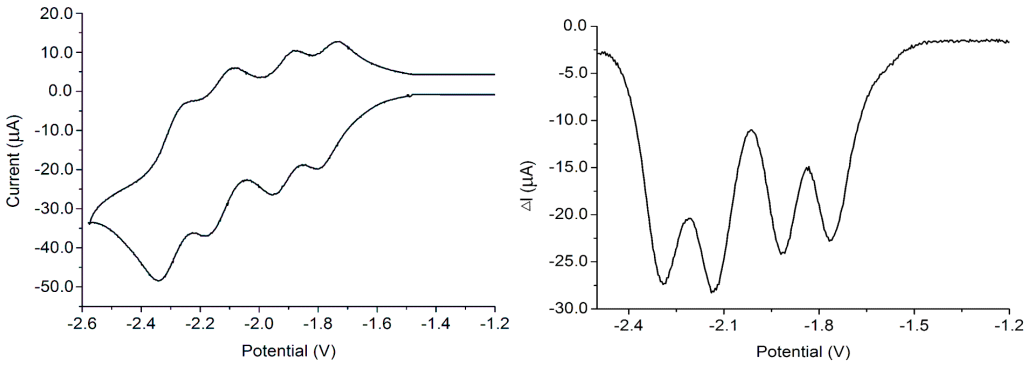

Figure 10.80. Cyclic and square wave voltammograms of $[Fe^{II}{}_4L^{Me4\text{-}Pz}{}_4](BF_4)_4$ (**3**) over the potential range −2.58 V to −1.2 V (left) and −2.55 V to −1.2 V (right) (CH_3CN/0.1M Bu_4NPF_6, scan rate 0.1 V s^{-1}, vs Fc/Fc^+).

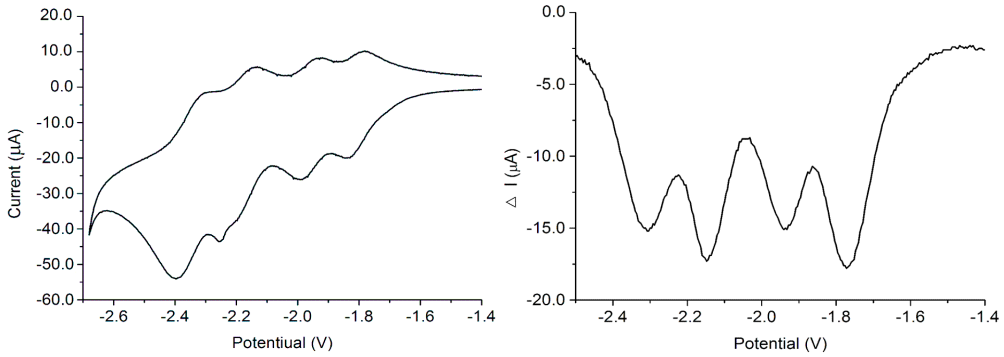

Figure 10.81. Cyclic and square wave voltammograms of $[Fe^{II}{}_4L^{Me5\text{-}Pz}{}_4](BF_4)_4$ (**4**) over the potential range −2.68 V to −1.4 V(left) and −2.50 V to − 1.4 V (right) (CH_3CN/0.1M Bu_4NPF_6, scan rate 0.1 V s^{-1}, vs Fc/Fc^+).

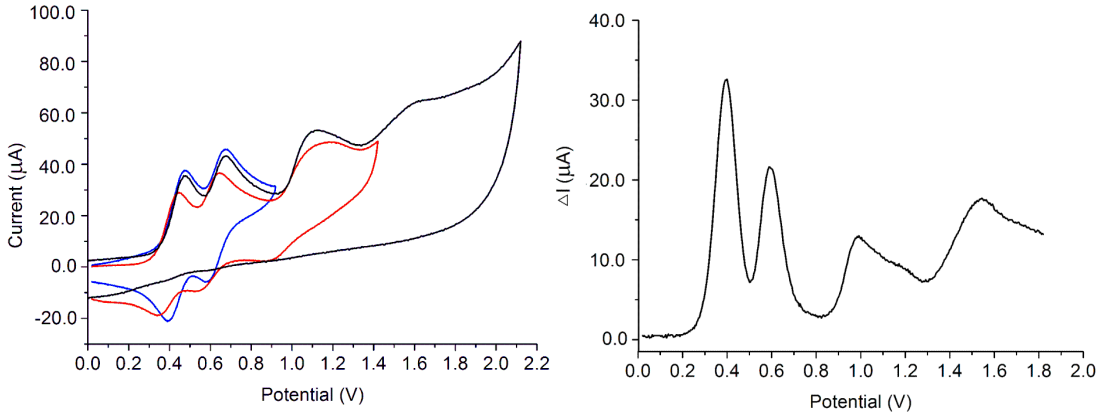

Figure 10.82. Cyclic and square wave voltammograms of $[Fe^{II}_4L^{Me\text{-}Pz}_4](BF_4)_4$ (**2**) over the potential range 0 V to 2.0 V (CH_3CN/0.1M Bu_4NPF_6, scan rate 0.1 V s^{-1}, vs Fc/Fc^+).

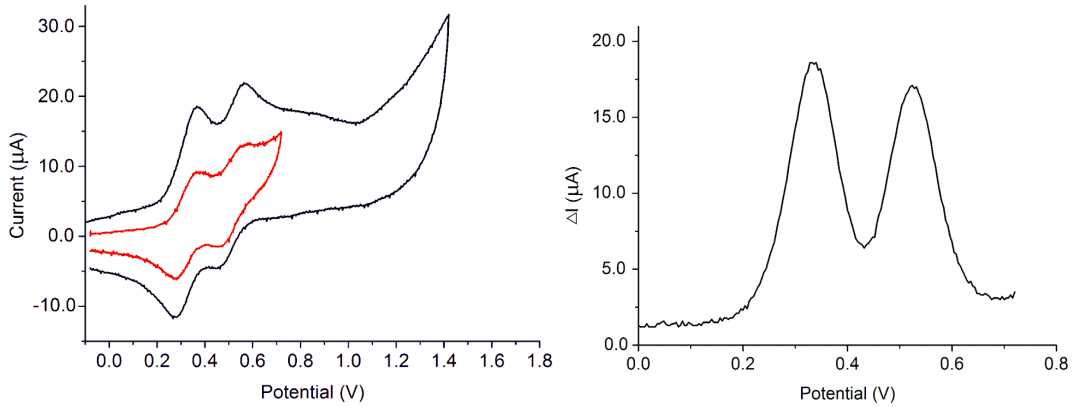

Figure 10.83. Cyclic and square wave voltammograms of $[Fe^{II}_4L^{Me4\text{-}Pz}_4](BF_4)_4$ (**3**) over the potential range 0.0 V to 1.8 V and 0.0 V to 0.8 V (CH_3CN/0.1M Bu_4NPF_6, scan rate 0.1 V s^{-1}, vs Fc/Fc^+).

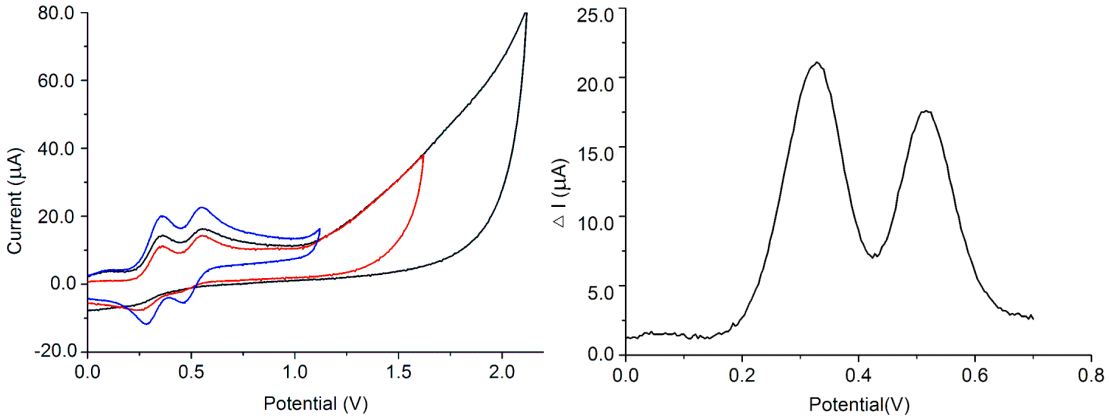

Figure 10.84. Cyclic and square wave voltammograms of $[Fe^{II}_4L^{Me5\text{-}Pz}_4](BF_4)_4$ (**4**) over the potential range 0.0 V to 2.0 V and 0.0 V to 0.8 V (CH_3CN/0.1M Bu_4NPF_6, scan rate 0.1 V s^{-1}, vs Fc/Fc^+).

10.3. Crystallography

X-ray data of suitable single crystals were collected on a *STOE IPDS II* diffractometer with an area detector (graphite monochromated Mo-K_α radiation, λ = 0.71073Å) by use of ω scans at 133K. The structures were solved by direct methods (SHELXS-97 or SHELXS-2014) and refined on F^2 by using all reflections with SHELXL-2015.[199] Most non-hydrogen atoms were refined anisotropically. Most hydrogen atoms were placed in calculated positions and assigned to an isotropic displacement parameter of 1.2/1.5 U_{eq}(C) or 1.5 U_{eq}(O). Face-indexed absorption corrections were performed numerically with the program *X-RED*.[200]

Table 10.1. Crystal data and refinement details of compounds **1**, **2**, and **3**.

	1·6.5MeCN (jin 1)	**2** (jin 31)	**3** (jr a)
empirical formula	$C_{178}H_{143}B_8F_{32}Fe_8N_{77}$	$C_{80}H_{60}B_4F_{16}Fe_4N_{32}$	$C_{92}H_{84}B_4F_{16}Fe_4N_{32}$
formula weight	4501.97	2040.24	2208.55
crystal size [mm³]	0.37 × 0.34 × 0.30	0.50 × 0.22 × 0.19	0.44 × 0.20 × 0.11
crystal system	Triclinic	Tetragonal	Triclinic
space group	*P*–1	$P4_2/n$	*P*–1
a [Å]	13.4127(4)	17.2508(3)	14.7804(5)
b [Å]	14.2138(4)	17.2508(3)	18.1194(6)
c [Å]	26.9440(9)	13.3595(3)	22.5277(8)
α [°]	81.097(3)	90	102.026(3)
β [°]	77.140(2)	90	92.697(3)
γ [°]	86.391(2)	90	103.733(3)
V [Å ³]	4945.4(3)	3975.65(16)	5702.4(4)
Z	1	2	2
ρ[g/cm³]	1.512	1.704	1.286
F(000)	2286	2064	2256
μ [mm^{-1}]	0.673	0.825	0.580
T_{min} / T_{max}	0.7992 / 0.8889	0.7695 / 0.9254	0.7838 – 0.9393
θ range [°]	1.45 – 25.66	1.669 – 25.606	1.332 – 25.669
hkl-range	±16, ±17, ±32	±20, ±20, −16 – 15	±17, −22 – 21, ±27
measured refl.	57055	41859	65102
unique refl. [R_{int}]	18633 [0.0685]	3739 [0.0457]	21463 [0.0835]
obs. Refl. ($I > 2\ \sigma(I)$)	13256	3431	13029
data / res. / param.	18633 / 837 / 1558	3739 / 0 / 336	21463 / 532 / 1561
goodness-of-fit (F^2)	1.018	1.043	1.015
*R*1, *wR*2 ($I > 2\ \sigma(I)$)	0.0674, 0.1725	0.0267, 0.0677	0.0800, 0.1816
*R*1, *wR*2 (all data)	0.0960, 0.1870	0.0304, 0.0694	0.1314, 0.2032
resid. El. Dens. [e/Å ³]	−0.773 / 0.787	−0.232 / 0.277	−0.542 / 1.053

Table 10.2. Crystal data and refinement details of compounds **4**, **5**, and **6**.

	4 (jin 41)	**5**·4MeCN (jin 28)	**6** (jin 5)
empirical formula	$C_{96}H_{92}B_4F_{16}Fe_4N_{32}$	$C_{84}H_{64}B_5F_{20}Fe_4N_{36}$	$C_{84}H_{68}Cl_4O_{16}Fe_4N_{32}$
formula weight	2264.65	2235.16	2146.90
crystal size [mm³]	0.30 × 0.28 × 0.16	0.50 × 0.50 × 0.29	0.50 × 0.29 × 0.20
crystal system	Triclinic	Triclinic	Monoclinic
space group	*P*–1	*P*–1	*C*2/*c*
a [Å]	14.5324(6)	17.604(3)	35.949(7)
b [Å]	14.6957(6)	20.073(4)	18.6544(4)
c [Å]	28.6904(12)	28.837(5)	34.586(8)
α [°]	85.028(3)	106.451(10)	90
β [°]	81.074(3)	96.856(2)	96.944(2)
γ [°]	62.801(3)	106.819(10)	90
V [Å ³]	5382.8(4)	9127.3(3)	23024.3(9)
Z	2	4	8
ρ[g/cm³]	1.397	1.627	1.239
F(000)	2320	4516	8768
μ [mm^{-1}]	0.617	0.825	0.654
T_{min} / T_{max}	0.6724 / 0.8841	1.301 / 25.669	1.141 – 24.748
θ range [°]	1.44 – 26.05	0.632 – 0.806	-
hkl-range	±17, ±18, ±35	±21, ±24, −35 – 34	±42, −20 – 21, −38 – 40
measured refl.	74986	76750	76750
unique refl. [R_{int}]	5275 [0.1061]	19289 [0.0621]	19289 [0.0621]
obs. Refl. ($I > 2\ \sigma(I)$)	45563	14698	14698
data / res. / param.	74986 / 116 / 1372	34373 / 390 / 2739	19289 / 118 / 1305
goodness-of-fit (F^2)	0.963	1.021	1.025
*R*1, *wR*2 ($I > 2\ \sigma(I)$)	0.0780, 0.1737	0.0415, 0.0938	0.0771, 0.2126
*R*1, *wR*2 (all data)	0.1238, 0.1940	0.0608, 0.1003	0.0946, 0.2260
resid. El. Dens. [e/Å ³]	−0.692 / 1.123	−0.803 / 0.928	−0.725 / 1.130

Table 10.3. Crystal data and refinement details of compounds **7**, **8**, and **9**.

	7·2MeCN (jin 3)	**8**·4.5MeCN·MeOH (jin 21)	**9**·2MeCN (jin 16)
empirical formula	$C_{88}H_{74}Cl_5Fe_4N_{34}O_{20}$	$C_{94}H_{85.50}Cl_6Fe_4N_{36.50}O_{25}$	$C_{88}H_{74}Ag_4Cl_6Fe_2N_{34}O_{24}$
formula weight	2328.46	2562.58	2747.69
crystal size [mm³]	0.50 × 0.12 × 0.05	0.47 × 0.37 × 0.15	0.21 × 0.16 × 0.05
crystal system	Triclinic	monoclinic	Triclinic
space group	*P*–1	$P2_1/n$	*P*–1
a [Å]	14.3010(12)	14.0209(3)	16.7818(4)
b [Å]	16.4830(11)	21.5252(6)	17.3735(6)
c [Å]	25.8916(18)	35.1038(7)	22.8606(6)
α [°]	79.919(6)	90	108.442(2)
β [°]	85.507(6)	94.940(2)	105.312(2)
γ [°]	76.093(6)	90	100.604(2)
V [Å ³]	5828.7(7)	10555.1(4)	5831.9(3)
Z	2	4	2
ρ[g/cm³]	1.327	1.613	1.565
F(000)	2378	5244	2748
μ [mm^{-1}]	0.677	0.784	1.118
T_{min} / T_{max}	-	0.6005 / 0.8067	0.5627 / 0.7778
θ range [°]	1.29 – 25.76	1.111 – 24.652	1.292 – 25.629
hkl-range	–17 – 16, ±20, ±31	–14 – 16, ±25, ±41	±20, ±21, ±27
measured refl.	62976	98659	60392
unique refl. [R_{int}]	22048 [0.1401]	17712 [0.1519]	21871 [0.0757]
obs. Refl. ($I > 2\ \sigma(I)$)	8108	14589	14320
data / res. / param.	22048 / 160 / 1359	17712/221/1568	21871/331/1495
goodness-of-fit (F^2)	0.831	1.039	0.965
*R*1, *wR*2 ($I > 2\ \sigma(I)$)	0.0891, 0.2074	0.0923, 0.2367	0.0577, 0.1158
*R*1, *wR*2 (all data)	0.1833, 0.2434	0.1084, 0.2603	0.0988, 0.1284
resid. El. Dens. [e/Å ³]	–0.634 / 1.061	–0.735 / 1.176	–1.338 / 1.192

Table 10.4. Crystal data and refinement details of compounds **10**, **11**, and **12**.

	11·2MeCN (jin 13)	**12** (jin 15)
empirical formula	$C_{80}H_{58}B_4Co_4F_{16}N_{34}$	$C_{80}H_{60}B_4Co_4F_{16}N_{32}$
formula weight	2078.56	2052.56
crystal size [mm³]	0.34 × 0.31 × 0.25	0.50 × 0.20 × 0.10
crystal system	Monoclinic	Tetragonal
space group	$P2_1/c$	$P4_2/n$
a [Å]	14.0340(3)	17.2359(3)
b [Å]	13.3498(2)	17.2359(3)
c [Å]	50.7076(9)	13.2617(2)
α [°]	90	90
β [°]	94.657(1)	90
γ [°]	90	90
V [Å³]	9468.8(3)	3939.74(15)
Z	4	2
ρ[g/cm³]	1.458	1.730
F(000)	4192	2072
μ [mm^{-1}]	0.782	0.938
T_{min} / T_{max}	-	0.6778 / 0.9273
θ range [°]	1.456 – 24.598	1.671 – 25.631
hkl-range	±16, ±15, –58 – 59	±20, ±20, –16 – 13
measured refl.	94032	47837
unique refl. [R_{int}]	15875 [0.0683]	3712 [0.0448]
obs. Refl. ($I > 2\ \sigma(I)$)	12748	3418
data / res. / param.	15875 / 0 / 1243	3712 / 49 / 345
goodness-of-fit (F^2)	1.032	1.080
$R1$, $wR2$ ($I > 2\ \sigma(I)$)	0.0542, 0.1444	0.0314, 0.0751
$R1$, $wR2$ (all data)	0.0682, 0.1528	0.0359, 0.0775
resid. El. Dens. [e/Å³]	–0.479 / 0.648	–0.327 / 0.320

Table 10.5. Crystal data and refinement details of compounds **13**, **14**, and **15**.

	13·2MeOH (jin 6)	**14**·2MeCN·H_2O (jin 39)	**15**·MeCN (jin 26)
empirical formula	$C_{86}H_{76}B_4Co_4F_{16}N_{32}O_2$	$C_{96}H_{66}B_4Co_4F_{16}N_{26}O$	$C_{78}H_{55}B_6Co_4F_{24}N_{33}$
formula weight	2172.74	2182.70	2219.13
crystal size [mm³]	0.41 × 0.26 × 0.21	0.29 × 0.18 × 0.16	0.50 × 0.32 × 0.12
crystal system	Triclinic	Monoclinic	Monoclinic
space group	*P*–1	$P2_1$	$P2_1/n$
a [Å]	15.0505(5)	14.201(3)	12.5051(6)
b [Å]	16.8256(6)	24.221(5)	23.2553(6)
c [Å]	23.5912(8)	14.259(3)	29.4800(12)
α [°]	101.165(3)	90	90
β [°]	90.797(3)	91.14(3)	94.046(4)
γ [°]	106.719(3)	90	90
V [Å³]	5597.8(3)	4903.4(17)	8551.7(6)
Z	2	2	4
[ρ / cm³]	1.289	1.478	1.724
F(000)	2208	2208	4448
μ [mm^{-1}]	0.665	0.758	0.885
T_{min} / T_{max}	-	0.6549 / 0.8677	0.7605 / 0.9098
θ range [°]	1.291 – 25.677	1.428 – 25.647	1.385 – 24.722
hkl-range	±18, ±20, ±28	−17 – 16, ±29, ±17	±14, –27 – 24, ±34
measured refl.	64217	46008	63498
unique refl. [R_{int}]	21076 [0.0537]	18345 [0.0506]	14385 [0.1175]
obs. Refl. ($I > 2\ \sigma(I)$)	15487	15587	11509
data / res. / param.	21076 / 90 / 1323	18345 / 121 / 1385	14385 / 30 / 1331
goodness-of-fit (F^2)	0.988	1.030	1.154
*R*1, *wR*2 ($I > 2\ \sigma(I)$)	0.0482, 0.1126	0.0583, 0.1478	0.0966, 0.2244
*R*1, *wR*2 (all data)	0.0731, 0.1213	0.0304, 0.0694	0.1161, 0.2331
resid. El. Dens. [e/Å³]	–0.457 / 0.493	–0.502 / 0.839	–0.655 / 0.951

Table 10.6. Crystal data and refinement details of compounds **16** and **18**.

	16 (jin 25)	**18**·3MeCN (jin 38)
empirical formula	$C_{80}H_{60}B_6Co_4F_{24}N_{32}$	$C_{98}H_{69}B_6Co_4F_{24}N_{27}$
formula weight	2226.18	2381.38
crystal size [mm³]	0.297 × 0.241 × 0.192	0.264 × 0.168× 0.149
crystal system	Tetragonal	Monoclinic
space group	$I4_1/acd$	$C2/c$
a [Å]	24.7367(4)	22.729(2)
b [Å]	24.7367(4)	21.3408(15)
c [Å]	36.3344(7)	19.8260(19)
α [°]	90	90
β [°]	90	95.201(8)
γ [°]	90	90
V [Å³]	22233.2(8)	9577.0(15)
Z	8	4
[ρ / cm³]	1.330	1.652
F(000)	8944	4800
μ [mm^{-1}]	0.680	0.794
T_{min} / T_{max}	-	0.8023 / 0.9241
θ range [°]	1.616 – 25.705	1.311 – 25.833
hkl-range	–28 – 30, ±30, ±44	±27, –26 – 22, ±24
measured refl.	128964	44739
unique refl. [R_{int}]	5275 [0.0568]	9164 [0.1622]
obs. Refl. ($I > 2\ \sigma(I)$)	4742	4461
data / res. / param.	5275 / 236 / 387	9164 / 113 / 711
goodness-of-fit (F^2)	1.174	0.972
$R1$, $wR2$ ($I > 2\ \sigma(I)$)	0.0738, 0.1527	0.0770, 0.1536
$R1$, $wR2$ (all data)	0.0818, 0.1569	0.1706, 0.1856
resid. El. Dens. [e/Å³]	–0.538 / 0.441	–0.428 / 0.754

10.4. List of Abbreviations

ac	Alternating current
Ac	Acetyl
BL	Bridging ligand
bpy	2,2’-Bipyridine
BVS	Bond valence sums
bypm	2,2’-Bipyrimidin
COSY	Correlation spectroscopy
CSM	Continuous Symmetry Measures
CT	Charge transfer
CTIST	Charge transfer induced spin transitions
CV	Cyclic voltammetry
dc	Direct current
DCM	Dichlormethan
DMSO	Dimethylsulfoxide
DMF	N,N-dimethylformamide
DN	Donor number
EI	Electron ionization

EtOH	Ethanol
eq.	Equation
EPR	Electron paramagnetic resonance
ESI	Electrospray ionization
Et	Ethyl
ETCST	Electron transfer coupled spin transitions
Fc	Ferrocene
HDvV	Heisenberg-Dirac-van-Vleck Hamiltonian
HS	High spin
HMQC	Heteronuclear Multiple Quantum Correlation
im	Imidazole
itp	Ideal trigonal prism
IVCT	Intervalence charge transfer
KHMDS	Potassium bis(trimethylsilyl)amide
L	Ligand
LS	Low spin
LMCT	Ligand-to-metal charge transfer

M	Metal
Me	Methyl
MeIM	N-methylimidazole
MLCT	Metal-to-ligand charge transfer
MS	Mass spectrometry
NIR	Near Infrared
NMR	Nuclear magnetic resonance
phen	1,10-phenanthroline
ppm	Parts per million
py	Pyridine
pz	Pyrazole
QCA	Quantum cellular automata
RT	Room temperature
SCE	Standard calomel electrode
SCO	Spin crossover
SMMs	Single molecule magnets
SQUID	Superconducting quantum interference device

SWV	Square wave voltammetry
^{t}Bu	Tert-buthyl
THF	Tetrahydrofurane
Tp	Peak temperature
Tpa	Tris(2-pyridylmethyl)amin
UV-Vis	Ultraviolette-visible
vs	Versus
VTVH	Variable temperature and variable field
ZFS	Zero field splitting
2D	Two dimention

10.5. Formula Overview

Ligand Precursors

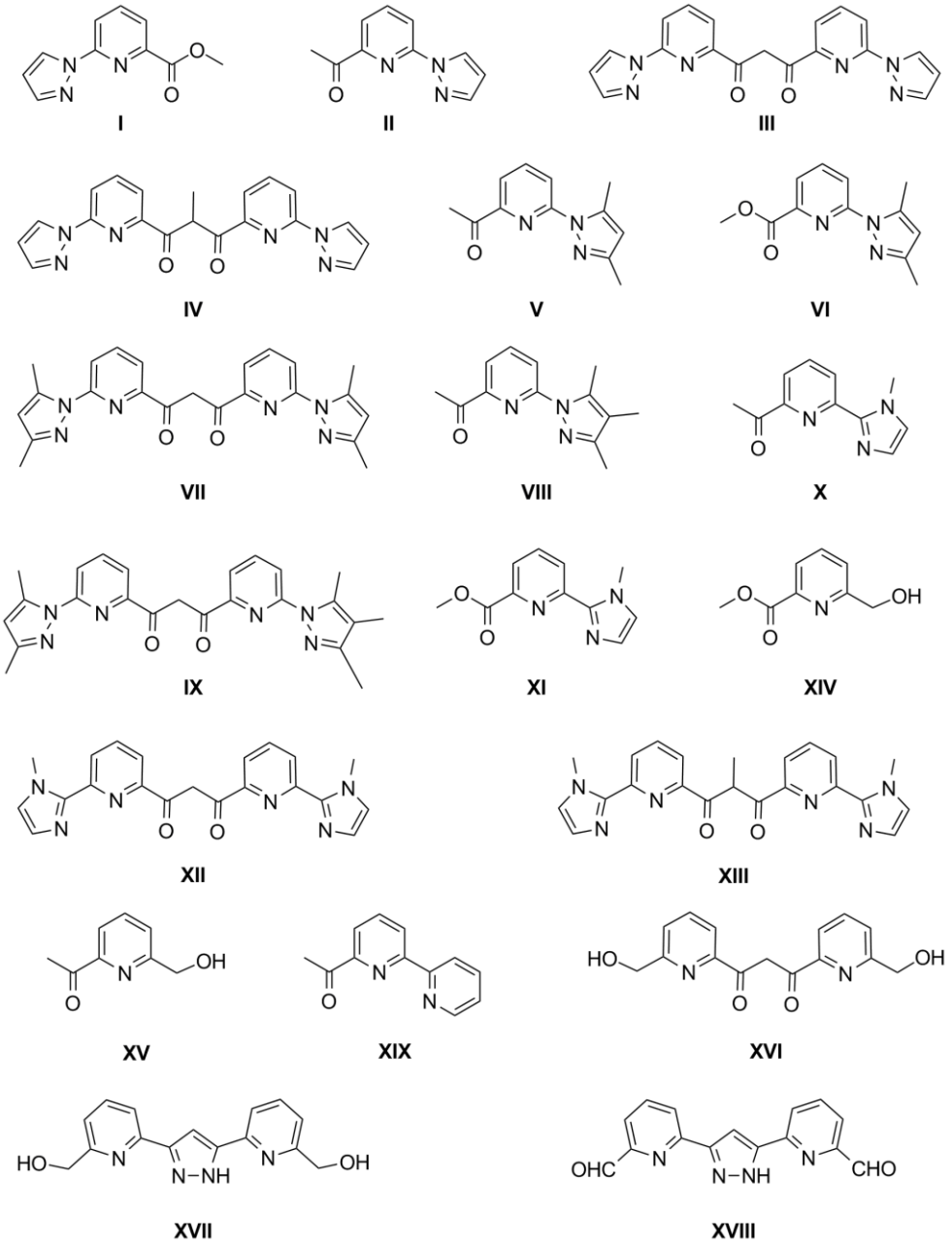

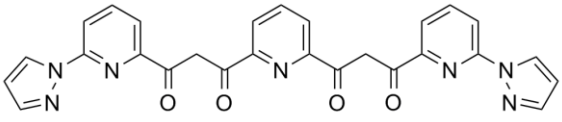

XX

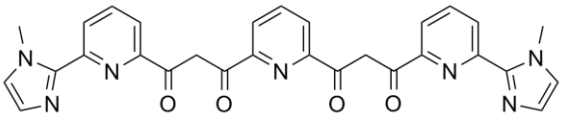

XXI

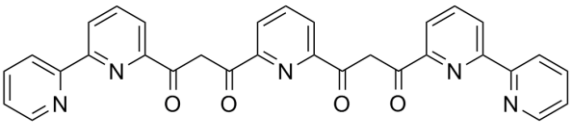

XXII

Ligands

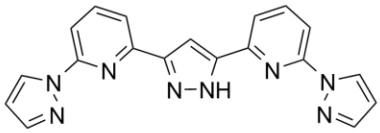

HL^{Pz}

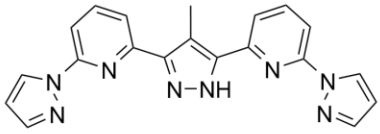

$HL^{Me\text{-}Pz}$

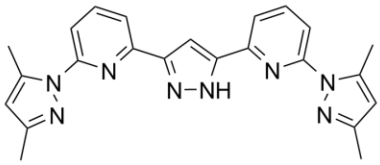

$HL^{Me4\text{-}Pz}$

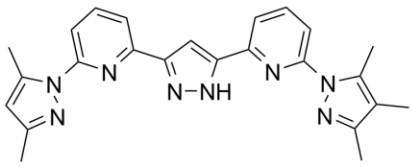

$HL^{Me5\text{-}Pz}$

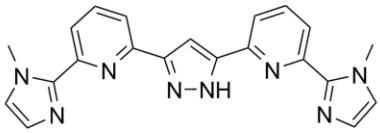

$HL^{Me\text{-}Im}$

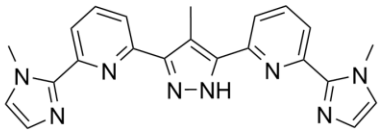

$HL^{Me\text{-}MeIm}$

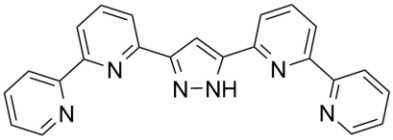

HL^{Py}

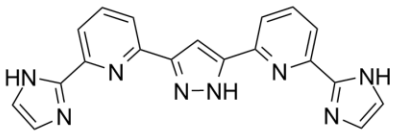

HL^{Im}

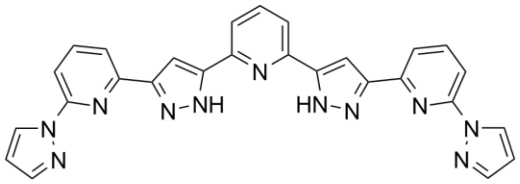

H_2L^{Pz}

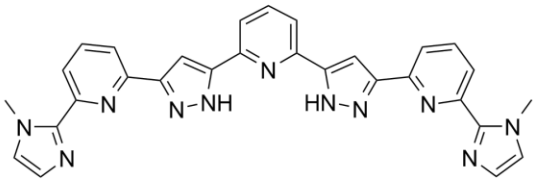

$H_2L^{Me\text{-}Im}$

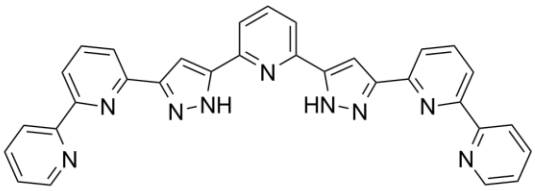

H_2L^{Py}

Complexes

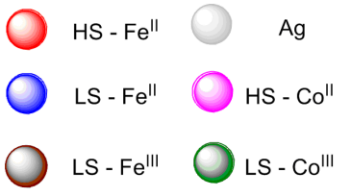

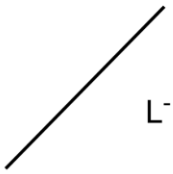

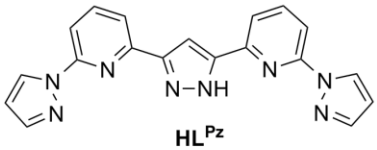

HL^{Pz}

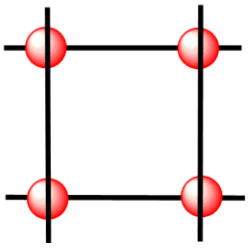

$[Fe^{II}_4L^{Pz}_4](BF_4)_4$ **1**

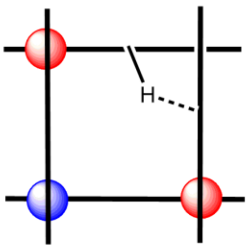

$[Fe^{II}_3(HL^{Pz})L^{Pz}_3](BF_4)_3$ **19**

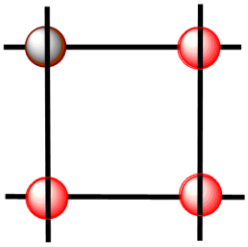

$[Fe^{II}_3Fe^{III}L^{Pz}_4](BF_4)_5$ **5**

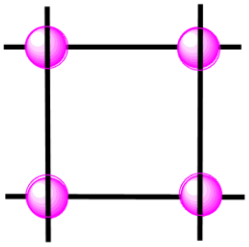

$[Co^{II}_4L^{Pz}_4](BF_4)_4$ **11**

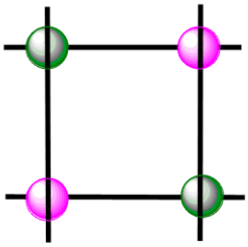

$[Co^{II}_2Co^{III}_2L^{Pz}_4](BF_4)_6$ **15**

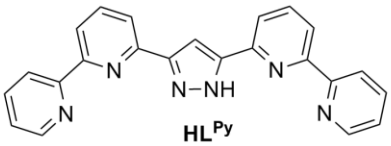

HL^{Py}

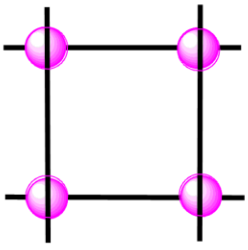

$[Co^{II}_4L^{Py}_4](BF_4)_4$ **14**

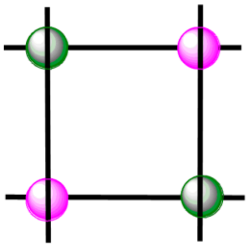

$[Co^{II}_2Co^{III}_2L^{Py}_4](BF_4)_6$ **18**

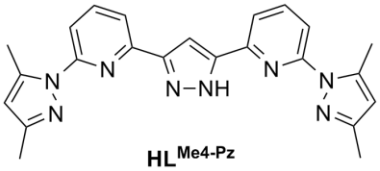

$HL^{Me4\text{-}Pz}$

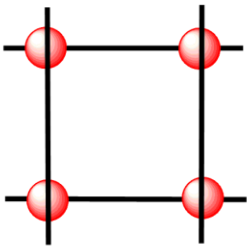

$[Fe^{II}_4L^{Me4\text{-}Pz}_4](BF_4)_4$ **3**

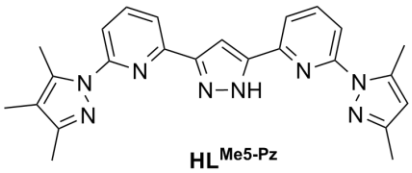

$HL^{Me5\text{-}Pz}$

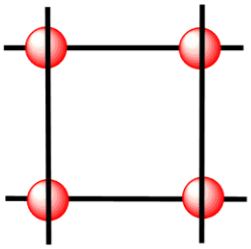

$[Fe^{II}_4L^{Me5\text{-}Pz}_4](BF_4)_4$ **4**

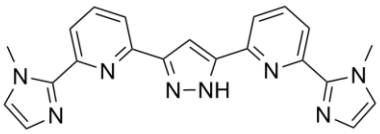

HL^{MeIm}

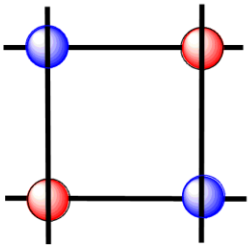

$[Fe^{II}_4L^{MeIm}_4](ClO_4)_4$ **6**

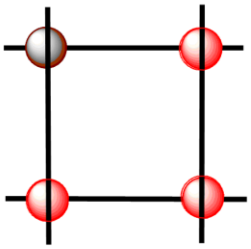

$[Fe^{II}_3Fe^{III}L^{MeIm}_4](ClO_4)_5$ **7**

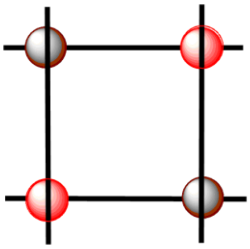

$[Fe^{II}_2Fe^{III}_2L^{MeIm}_4](ClO_4)_6$ **8**

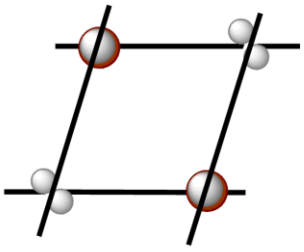

$[Fe^{III}_2Ag^{I}_4L^{MeIm}_4](BF_4)_6$ **9**

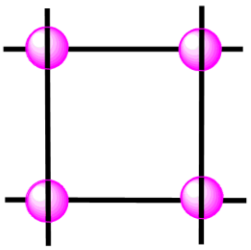

$[Co^{II}_4L^{MeIm}_4](BF_4)_4$ **13**

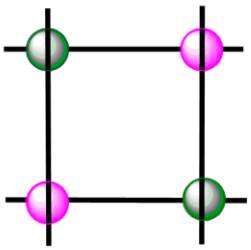

$[Co^{II}_2Co^{III}_2L^{MeIm}_4](BF_4)_6$ **17**

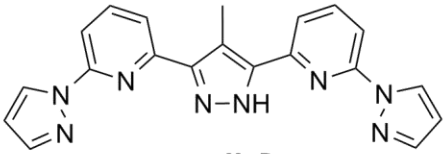

$HL^{Me\text{-}Pz}$

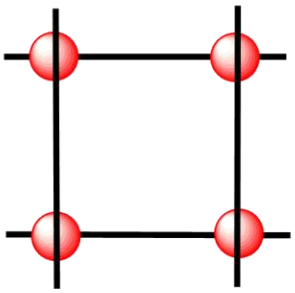

$[Fe^{II}_4L^{Me\text{-}Pz}_4](BF_4)_4$ **2**

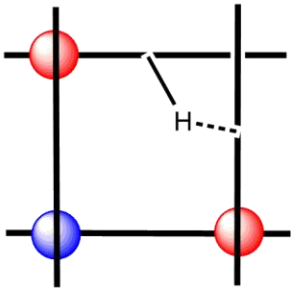

$[Fe^{II}_3(HL^{Me\text{-}Pz})L^{Me\text{-}Pz}_3](BF_4)_3$ **20**

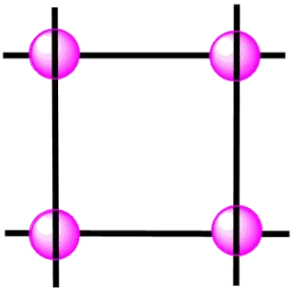

$[Co^{II}_4L^{Me\text{-}Pz}_4](BF_4)_4$ **12**

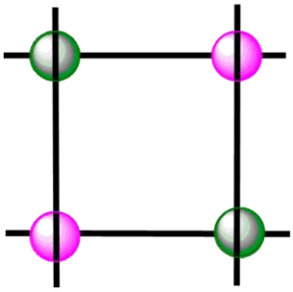

$[Co^{II}_2Co^{III}_2L^{Me\text{-}Pz}_4](BF_6)_6$ **16**

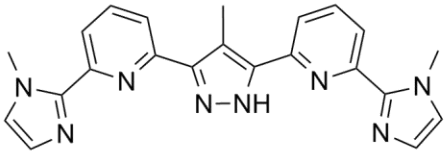

$HL^{Me\text{-}MeIm}$

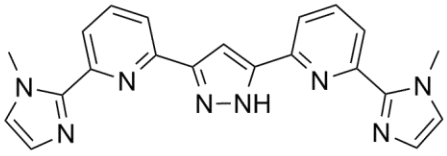

HL^{MeIm}

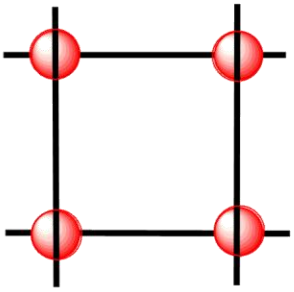

$[Fe^{II}_4L^{Me\text{-}MeIm}_4](BF_4)_4$ **10**

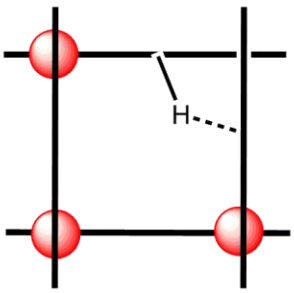

$[Fe^{II}_3(HL^{MeIm})L^{MeIm}_3](ClO_4)_3$ **21**

11. Scientific Contributions

Posters

J. Tong, S. Demeshko, S. Dechert, F. Meyer, Mixed-spin and Mixed-valence [2 × 2] Fe_4 grid complexes, "*6th EuCheMS Conference on Nitrogen Ligands*", Beaune, France, September **2015**.

J. Tong, S. Demeshko, S. Dechert, F. Meyer, Redox-Induced Mixed-Valence: [2 × 2] Co_4 Grid-Type Complexes, "*27th annual conference of GCCCD*", Jena, Germany, August **2015**.

J. Tong, S. Demeshko, S. Dechert, F. Meyer, A family of [2 × 2] Fe_4 grid complexes based on pyrazole-bridged ligands, "*Göttinger Jung Chemiker Forum*", Göttingen, Germany, June, **2015**.

J. Tong, S. Demeshko, S. Dechert, F. Meyer, [2 × 2] Fe_4 grid complexes, "*Methods in Molecular Energy Research: Theory and Spectroscopy Summer School*", Essen, Germany, September, **2013**.

Presentation

J. Tong, S. Demeshko, S. Dechert, F. Meyer, Redox-Induced Mixed-Valence Single-Molecule Magnets: [2 × 2] Co_4 Grid-Type Complexes, "*27th annual conference of GCCCD*", Jena, Germany, August **2015**.

Publications

Jin Tong, Serhiy Demeshko, Michael John, Sebastian Dechert, Franc Meyer, *"Redox-Induced Single-Molecule Magnetism in Mixed-Valent [2 × 2] Co_4 Grid Complexes", Inorg. Chem*. DOI: 10.1021/acs.inorgchem.6b00106.

12. Acknowledgement

First of all, I would like to thank my PhD supervisor Prof. Dr. Franc Meyer, for offering the chance to work in his working group. I appreciated the motivating guidance and the great scientific freedom. Thank you for creating a positive working atmosphere and providing excellent lab equipment. Without his good care and suggestion, this thesis would not be possible. I would like to offer my thanks to my second supervisor Dr. Inke Siewert for her valuable advice during my research.

The other members of my thesis committee and examination board are gratefully acknowledged for spending their precious time with my thesis project.

From our institute, I am very grateful to Dr. Sebstian Dechert, Dr. Nicole Kindermann and Anne Schober for their assistance in collecting X-ray diffraction data, solving the structures and analyzing the results, to Dr. Serhiy Demeshko for dozens of Mössbauer and magnetization measurements, as well as for the detailed explanations, to Jörg Teichgräber for cyclic voltammetry measurements and to Andreas Schwarz for assistance in lab-related questions, to the analytical laboratory for elemental analysis, to Peter Unger, Britta Müller and Dr. Claudia Stückl for the handling of administrative issues. Furthermore, I would like to thank Dr. Michael John for his help in NMR-related concerns. For the maintenance of the ESI-MS spectrometer I would like to thank Dr. Holm Frauendorf.

I would like to say thanks to all the past and present members in Prof. Dr. Meyer's working group, especially to my laboratory mates Dr. Kai Kalz, Dr. Adam Walli, Oliver Mitevski, Stefan Resch, Claudia Kupper for their daily help. I would like to acknowledge Dr. Markus Steinert for his experience and good suggestions to this work.

I am particulary grateful for the financial support from the Chinese Scholarship Council. Finally, I am very grateful to my family and friends for their love. Thanks for your support and encouragement during the preparation of this work!

13. Curriculum Vitae

Personal Data

Name	Jin Tong
Date of birth	09/16/1988
Place of birth	Jiangxi, China
Nationality	Chinese

Education

09/2012 – Present	PhD Candidate, Institute of Inorganic Chemistry, Georg-August University Göttingen, Germany. Supervisor: Prof. Dr. Franc Meyer PhD Thesis: Homo- and Mixed-valence [2 × 2] Grid Complexes
09/2009 – 06/2012	Master, Inorganic Chemistry, Department of Chemistry, Renmin University of China, China. Supervisor: Prof. Shu-Yan Yu Master Thesis: Self-Assembly of Homo- and Hetero-metallic Molecular Quadrangles from Coordination Corners with Pyridyl-pyrazole; Design and Synthesize dipyrazole functional ligand and Coordinate with dimetallic clips via self-assembly
09/2005 – 06/2009	Bachelor, Applied Chemistry, School of Basic Sciences, East China Jiao Tong University, China. Supervisor: Dr. Yun Zhong Bachlor thesis: Synthesis and Fluorescence of Tripodal complexes with Dithiocarboxylic Ligands

Work and Training experience

06/2015 – 07/2015	Teaching assistant for lab course for medical students in the Institute of Organic and Biomolecular Chemistry, Georg-August University Göttingen

09/2014 – 07/2015	Supervisor for bachelor student: The effect of different substituents as electron withdrawing or donating groups on the [2 × 2] iron grid complexes, in Institute of Inorganic Chemistry, Georg-August University Göttingen
09/2013	Summer School of Methods in Molecular Energy Research: Theory and Spectroscopy (including Magnetochemistry, EPR spectroscopy, Mössbauer spectroscopy, UV/Vis and MCD spectroscopy, and X-Ray spectroscopy)
02/2010 – 07/2010	Teaching Assistant for General physical chemistry experiment in department of chemistry, Renmin University of China
Instrument skills	ESI-MS, NMR, IR, UV/Vis, Luminescence and Electrochemistry measurement and data analysis; Mössbauer and SQUID spectroscopy analysis; work in glove-box and Schlenk Technigues

14. References

[1] F. R. Service, *Science*, **2002**, *295*, 2398–2399.

[2] S. M. Sze, *Physics of Semiconductor Devices*, 2nd ed. New York: Wiley, **1981**.

[3] A. Aviram, *Molecular Electronics*: *Science and Technology*, AIP Confer. Proc. New York, **1992**. *262*.

[4] F. L. Carter, *Molecular Electronics Devices II*. New York: M. Dekker, **1987**.

[5] J. M. Lehn, *Angew. Chem. Int. Ed*. **1988**, *27*, 89–112.

[6] J. M. Lehn, *Supramolecular chemistry and self-assembly special feature: Toward cmplex matter:Superamolecular chemistry and self-organization*, *Proc. Nat. Acad. Sci*. USA, **2002**, *99*, 4763–4768.

[7] M. Albrecht, *Naturwissenschaften* **2007**, *94*, 951–966.

[8] N. H. Evans, P. D. Beer, *Angew. Chem. Int. Ed.* **2014**, *53*, 11716–11754.

[9] L. W. Judd, A. P. Davis, *Chem. Commun.* **2010**, *46*, 2227–2229.

[10] S. Ramos, E. Alcalde, G. Doddi, P. Mencarelli, L. Pérez-García, *J. Org. Chem.* **2002**, *67*, 8463–8468.

[11] J. S. Fleming, L. V. Mann-Karen, C. A. Carraz, E. Psillakis, J. C. Jeffery, J. A. McCleverty, M. D. Ward, *Angew. Chem. Int. Ed.* **1998**, *37*, 1279–1281.

[12] Y. Willener, K. M. Joly, C. J. Moody, J. H. R. Tucker, *J. Org. Chem.* **2008**, *73*, 1225–1233.

[13] M. Han, D. M. Engelhard, G. H. Clever, *Chem. Soc. Rev.* **2014**, *43*, 1848–1860.

[14] For a survey of known forms, see P. N. W. Baxter, in J. P. Sauvage, M. W. Hosseini, (Vol. Eds) *Comprehensive Supramolecular Chemistry*, Pergamon/Elsevier Science Ltd., Oxford, **1996**, *9*, 166–211; in particular see also refs 10–14 below.

[15] J. M. Lehn, *Supramolecular Chemistry: Concepts and Perspectives*, VCH, Weinheim, **1995**, Sect. 9.3.

[16] (a) C. Piguet, G. A. Bernardinelli, G. Hopfgartner, *Chem. Rev.* **1997**, *97*, 2005–2062. (b) C. Piguet, M. Borkovec, J. Hamacek, K. Zeckert, *Coord. Chem. Rev.*

2005, *249*, 705–726.

[17] M. Albrecht, *Chem. Soc. Rev.* **1998**, *27*, 281–287; *Chem. Rev.* **2001**, *101*, 3457–3498; *Top. Curr. Chem.* **2004**, *248*, 105–139.

[18] E. C. Constable, in J. P. Sauvage, M. W. Hosseini (Vol. Eds), *Comprehensive Supramolecular Chemistry*, Pergamon/Elsevier Science Ltd, Oxford, **1996**, *9*, 213–252.

[19] (a) M. T. Youinou, N. Rahmouni, J. A. Osborn, *Angew. Chem. Int. Ed.* **1992**, *37*, 733–735. (b) M. Ruben, J. Rojo, F. J. Romero-Salguero, L. H. Uppadine, J. M. Lehn, *Angew. Chem. Int. Ed.* **2004**, *43*, 3644–3662. (c) L. N. Dawe, K. V. Shuvaev, L. K. Thompson, *Chem. Soc. Rev.* **2009**, *38*, 2334–2359. (d) A. M. Stadler, *Eur. J. Inorg. Chem.* **2009**, 4751–4770.

[20] F. Puntoriero, S. Campagna, A. M. Stadler, J. M. Lehn, *Coord. Chem. Rev.* **2008**, *252*, 2480–2492.

[21] (a) M. Fujita, *Chem. Soc. Rev.* **1998**, *27*, 417–425. (b) D. L. Caulder, K. N. Raymond, *Acc. Chem. Res.* **1999**, *32*, 975–982. (c) S. R. Seidel, P. J. Stang, *Acc. Chem. Res.* **2002**, *35*, 972–983. (d) B. Champin, P. Mobian, J. P. Sauvage, *Chem. Soc. Rev.* **2007**, *36*, 358–366.

[22] M. T. Youinou, N. Rahmouni, J. Fischer, J. A. Osborn, *Angew. Chem. Int. Ed. Engl.* **1992**, *31*, 733 – 735;

[23] P. N.W. Baxter, J.-M. Lehn, B. O. Kneisel, D. Fenske, *Chem. Commun*. **1997**, 2231–2232.

[24] P. Van Koningsbruggen, E. Msller, J. G. Haasnoot, J. Reedijk, *Inorg. Chim. Acta*. **1993**, *208*, 37–42.

[25] B. Schneider, S. Demeshko, S. Dechert, F. Meyer, *Angew. Chem. Int. Ed.* **2010**, *49*, 9274–9277.

[26] A. M. Stadler, C. Burg, J. Ramírez, J. M. Lehn, *Chem. Commun.* **2013**, *49*, 5733–5735.

[27] (a) J. Rojo, F. J. Romero-Salguero, J. M. Lehn, G. Baum, D. Fenske, *Eur. J. Inorg. Chem*. **1999**, 1421–1428. (b) V. Patroniak, P. N.W. Baxter, J. M. Lehn, M. Kubicki, M. Nissinen, K. Rissanen, *Eur. J. Inorg. Chem*. **2003**, *22*, 4001–4009.

[28] M. Barbiou, J. M. Lehn, *J. Am. Chem. Soc*. **2003**, *125*, 10257–10265.

[29] (a) G. S. Hanan, PhD thesis, University Louis Pasteur, Strasbourg, **1995**. (b) A. M. Garcia, F. J. Romero-Salguero, D. Bassani, J. M. Lehn, G. Baum, D. Fenske, *Chem. Eur. J*. **1999**, *5*, 1803–1808.

[30] (a) M. Ruben, J. M. Lehn, G. Vaughan, *Chem. Commun*. **2003**, 1338–1339. (b) L. H. Uppadine, J. M. Lehn, *Angew. Chem. Int. Ed*. **2004**, *43*, 240–243.

[31] A. Petitjean, N. Kyritsakas, J. M. Lehn, *Chem. Commun.* **2004**, 1168–1169.

[32] L. H. Uppadine, J. M. Lehn, *Angew. Chem. Int. Ed.* **2004**, *43*, 240–243.

[33] (a) V. Smith, J. M. Lehn, *Chem. Commun*. **1996**, 2733–2734. (b) J. M. Lehn, *Chem. Eur. J*. **2000**, *6*, 2097–2098. (c) D. P. Funeriu, J. M. Lehn,K. M. Fromm,D . Fenske, *Chem. Eur. J*. **2000**, *6*, 2103–2111.

[34] (a) D. Y. Wu, O. Sato, Y. Einaga, C. Y. Duan, *Angew. Chem. Int. Ed*. **2009**, *48*, 1475–1478. (b) E. M. Zueva, E. R. Ryabikh, S. A. Borshch, *Inorg. Chem*. **2011**, *50*, 11143–11151. (c) B. Schneider, S. Demeshko, S. Neudeck, S. Dechert, F. Meyer, *Inorg. Chem*. **2013**, *52*, 13230–13237. (d) D. M. Bassani, J.-M. Lehn, S. Serroni, F. Puntoriero, S. Campagna, *Chem. Eur. J*. **2003**, *9*, 5936. (e) D. M. Bassani, J.-M. Lehn, K. Fromm, D. Fenske, *Angew. Chem. Int. Ed*. **1998**, *37*, 2364.

[35] L. H. Uppadine, J. M. Lehn, *Chem. Eur. J*. **2005**, *11*, 2549–2565.

[36] M. Ruben, J. Rojo, F. J. Romero-Salguero, L. H. Uppadine, J. M. Lehn, *Angew. Chem. Int. Ed*. **2004**, *43*, 3644–3662.

[37] (a) R. K. Rmer, J. M. Lehn, A. Marquis-Rigault, *Proc. Natl. Acad. Sci*. **1993**, *90*, 5394–5398. (b) S. Q. Wu, Y. T. Wang, A. L. Cui, H. Z. Kou, *Inorg. Chem*. **2014**, *53*, 2613–2618. (c) R. Hogg, R .G. Wilkins, *J. Chem. Soc*. **196**2, 341–350.

[38] (a) C. A. Schalley, T. Müller, P. Linnartz, M. Witt, M. Schäfer, A. Lützen, *Chem. Eur. J.* **2002**, *8*, 3538–3551. (b) G. N. Newton, M. Nihei, H. Oshio, *Eur. J. Inorg. Chem.* **2011**, *2011*, 3031–3042. (c) I. Boldog, F. J. Muñoz-Lara, A. B. Gaspar, M. C. Muñoz, M. Seredyuk, J. A. Real, Inorg. *Chem.* **2009**, *48*, 3710–3719. (d) M. Nihei, M. Ui, M. Yokota, L. Han, A. Maeda, H. Kishida, H. Okamoto, H. Oshio,

Angew. Chem. Int. Ed. **2005**, *44*, 6484–6487.

[39] (a) Y. Z. Zhang, P. Ferko, D. Siretanu, R. Ababei, N. P. Rath, M. J. Shaw, R. Clérac, C. Mathonière, S. M. Holmes, *J. Am. Chem. Soc*. **2014**, *136*, 16854−16864. (b) M. Nihei, Y. Okamoto, Y. Sekine, N. Hoshino, T. Shiga, I. P. C. Liu, H. Oshio, *Angew. Chem. Int. Ed*. **2012**, *51*, 6361–6364. (c) G. N. Newton, M. Nihei, H. Oshio, *Eur. J. Inorg. Chem*. **2011**, *2011*, 3031–3042. (d) L. M. C. Beltran, J. R. Long, *Acc. Chem. Res*. **2005**, *38*, 325. (e) L. G. Beauvais, J. R. Long, *J. Am. Chem. Soc*. **2002**, *124*, 12096. (f) J. J. Sokol, M. P. Shores, J. R. Long, *Angew. Chem. Int. Ed*. **2001**, *40*, 236–239. (g) P. A. Berseth, J. J. Sokol, M. P. Shores, J. L. Heinrich, J. R. Long, *J. Am. Chem. Soc*. **2000**, *122*, 9655–9662. (h) H. J. Choi, J. J. Sokol, J. R. Long, *Inorg. Chem*. **2004**, *43*, 1606–1608. (i) O. Hatlevik, W. E. Buschmann, J. Zhang, J. L. Manson, J. S.Miller, *Adv. Mater*. **1999**, *11*, 914–918. (j) Holmes, S. M.; Girolami, G. S. *J. Am. Chem. Soc*. **1999**, *121*, 5593–5594.

[40] E. Pardo, M. Verdaguer, P. Herson, H. Rousselière, J. Cano, M. Julve, F. Lloret, R. Lescouezec, *Inorg. Chem*. **2011**, *50*, 6250–6262.

[41] (a) M. Nihei, Y. Sekine, N. Suganami, K. Nakazawa, A. Nakao, H. Nakao, Y. Murakami, H. Oshio, *J. Am. Chem. Soc*. **2011**, *133*, 3592–3600. (b) N. Shimamoto, S. C. Ohkoshi, O. Sato, K. Hashimoto, *Inorg. Chem*. **2002**, *41*, 678–684.

[42] (a) Y. Zhang, D. Li, R. Clérac, M. Kalisz, C. Mathonière, S. M. Holmes, *Angew. Chem. Int. Ed*. **2010**, *49*, 3752–3756. (b) J. Mercurol, Y. Li, E. Pardo, O. Risset, M. Seuleiman, H. Rousselière, R. Lescouëzec, M. Julve, *Chem. Commun*. **2010**, 8995–8997. (d) M. Nihei, Y. Sekine, N. Suganami, H. Oshio, *Chem. Lett*. **2010**, *39*, 978–979.

[43] (a) P. N. W. Baxter. J. M. Lehn, J. Fischer, M. T. Youinou, *Angew. Chem. Int. Ed.* **1994**, *33*, 2284−2287. (b) L. K. Thompson, T. L. Kelly, L. N. Dawe, H. Grove, M. T. Lemaire, *Inorg. Chem*. **2004**, *43*, 7605−7616. (c) T. Shiga, T. Matsumoto, M. Noguchi, T. Onuki, N. Hoshino, G. N. Newton, M. Nakano, H. Oshio, *Chem.*

Asian J. **2009**, *4*, 1660–1663. (d) G. N. Newton, T. Onuki, T. Shiga, M. Noguchi, T. Matsumoto, J. S. Mathieson, M. Nihei, M. Nakano, L. Cronin, H. Oshio, *Angew. Chem. Int. Ed*. **2011**, *50*, 4844–4848. (e) X. Bao, W. Liu, L. L. Mao, S. D. Jiang, J. L. Liu, Y. C. Chen, M. L. Tong, *Inorg. Chem*. **2013**, *52*, 6233–6235. (f) H. Sato, L. Miya, K. Mitsumoto, T. Matsumoto, T. Shiga, G. N. Newton, H. Oshio, *Inorg. Chem*. **2013**, *52*, 9714–9716. (g) Y. Han, N. F. Chilton, M. Li, C. Huang, H. Xu, H. W. Hou, *Chem. Eur. J*. **2013**, *19*, 6321–6328. (h) M. U. Anwar, L. N. Dawe, S. R. Parsons, S. S. Tandon, L. K. Thompson, S. K. Dey, V. Mereacre, W. M. Reiff, S. D. Bunge, *Inorg. Chem*. **2014**, *53*, 4655−4668.

[44] (a) C. S. Lent, B. Isaksen, M. Lieberman, *J. Am. Chem. Soc*. **2003**, *125*, 1056–1063. (b) M. Lieberman, S. Chellamma, B. Varughese, Y. Wang, C. Lent, G. H. Bernstein,G. Snider, F. C. Peiris, *Ann. N. Y. Acad. Sci*. **2002**, *960*, 225–239. (c) A. O. Orlov, I. Amlani, G. H. Bernstein, C. S. Lent, G. L. Snider, *Science*. **1997**, *277*, 928–930.

[45] G. L.Snider, A. O. Orlov, I. Amlani, G. H. Bernstein, C. S. Lent, J. L. Merz, W. Porod, *Jpn. J. Appl. Phys*. **1999**, *38*, 7227–7229.

[46] C. S. Lent, *Science*. **2000**, *288*, 1597–1599.

[47] (a) J. Y. Jiao, G. J. Long, L. L. Rebbouh, F. Grandjean, A. M. Beatty, T. P. Fehlner, *J. Am. Chem. Soc*. **2005**, *127*, 17819–17831. (b) C. S. Lent, P. D. Tougaw, *J. Appl. Phys*. **1993**, *74*, 6227–6233.

[48] P. Gütlich, H. A. Goodwin. *Spin Crossover in Transition Metal Compounds I*. Springer Berlin. **2004**.

[49] (a) P. Gütlich, H. A. Goodwin, *Top. Curr. Chem*. **2004**, *233*, 1−47. (b) P. Gütlich, A. B. Gaspar, Y. Garcia, J. Beilstein, *Org. Chem*. **2013**, *9*, 342–391. (c) M. A. Halcrow, *Spin-Crossover Materials: Properties and Applications*, 1st ed.; John Wiley & Sons, Ltd: **2013**.

[50] F. A. Cotton, G. Wilkinson, P. L. Gaus, **1995**. *Basic Inorganic Chemistry* (3 ed.). Wiley.

[51] O. Kahn, C. J. Martinez, *Science*, **1998**, *44*, 279.

[52] (a) A. Santoro, L. J. Kershaw Cook, R. Kulmaczewski, S. A. Barrett, O.

Cespedes, M. A. Halcrow, *Inorg. Chem.* **2015**, *54*, 682–693. (b) Fatima Setifi, Eric Milin, Catherine Charles, Franck Thétiot, Smail Triki, Carlos J. Gómez-García, *Inorg. Chem.* **2014**, *53*, 97–104. (c) R. Kulmaczewski, J. Olguín, J. A. Kitchen, H. L. C. Feltham, G. N. L. Jameson, Jeffery L. Tallon, S. Brooker, *J. Am. Chem. Soc*. **2014**, *136*, 878−881. (d) H. Hagiwara, S. Okadab, *Chem. Commun*. **2016**, *52*, 815–818. (e) M. Yamasakia, T. Ishida, *J. Mater. Chem. C*, **2015**, *3*, 7784−7787.

[53] V. V. Zelentsov, *Sov. Sc.i Rev. B. Chem*. **1981**, *81*, 543.

[54] (a) J. Tao, R. J. Wei, R. B. Huang, L. S. Zheng, *Chem. Soc. Rev.* **2012**, *41*, 703−737. (b) B. Li, R. J. Wei, J. Tao, R. B. Huang, L. S. Zheng, Z. Zheng, *J. Am. Chem. Soc*. **2010**, *132*, 1558−1566. (c) R. J. Wei, Q. Huo, J. Tao, R. B. Huang, L. S. Zheng, *Angew. Chem. Int. Ed*. **2011**, *50*, 8940−8943.

[55] (a) L. Cambi, L. B. Szegö, *Dtsch. Chem. Ges*. **1931**, *64*, 2591−2598; *Dtsch. Chem. Ges*. **1933**, *66*, 656−661; *Dtsch. Chem. Ges*. **1937**, *70*, 2067−2078.

[56] P. Gütlich, H. Goodwin, E. J. A. McCleverty, T. J. Meyer, Electronic Spin Crossover (Pergamon, Oxford), **2003**.

[57] (a) A. Bousseksou, G. Molnár, L. Salmon, W. Nicolazzi, *Chem. Soc. Rev*. **2011**, *40*, 3313−3335. (b) A. B. Gaspar, V. Ksenofontov, M. Seredyuk, P. Gütlich, *Coord. Chem. Rev*. **2005**, *249*, 2661–2676. (c) P. Gütlich, A. Hauser, H. Spiering, *Angew. Chem. Int. Ed*. **1994**, *33*, 2024–2054. (d) P. Gütlich, Y. Garcia, H. A. Goodwin, *Chem. Soc. Rev*. **2000**, *29*, 419–427.

[58] (a) M. A. Halcrow, *Chem. Soc. Rev.* **2008**, *37*, 278. (b) K. S. Murray, *Eur. J. Inorg. Chem*. **2008**, 3101–3121.

[59] (a) J. Olguín, S. Brooker, *Coord. Chem. Rev*. **2011**, *255*, 203–240. (b) I. Šalitroš, N. Madhu, R. Bŏca, J. Pavlik, M. Ruben, *Monatsh. Chem*. **2009**, *140*, 695–733.

[60] K. S. Murray, C. J. Kepert, in *Spin Crossover in Transition Metal Compounds I* (Herausgegeben von P. Gütlich, H. Goodwin) (Springer Berlin/Heidelberg), Bd. 233 von Topics in Current Chemistry, **2004**, S. 195–228, S. 195–228.

[61] P. Gütlich, H. A. Goodwin, *Spin Crossover in Transition Metal Compounds IIII*, Nr. 233 in Topics in Current Chemistry (Springer Berlin/Heidelberg), **2004**.

[62] O. Kahn, *Molecular Magnetism* (VCH Publishers, Weinheim), **1993**.

[63] E. Breuning, M. Ruben, J. M. Lehn, F. Renz, Y. Garcia, V. Ksecofontov, P. Gütlich, E. Wegelius, K. Rissanen, *Angew. Chem. Int. Ed.* **2000**, *39*, 2504−2507.

[64] P. Gütlich , R. Link, A. X. Trautwein, *Mössbauer spectroscopy and transition metal chemistry*. *Inorganic Chemistry Concepts Series*. **1978**, *3*, Springer, Berlin Heidelberg New York.

[65] (a) H. A. Goodwin, R. N. Sylva, *Aust. J. Chem*. **1968**, *21*, 83. (b) H. A. Goodwin, E. S. Kucharski, A. H. White, *Aust. J. Chem*. **1983**, *36*, 1115. (c) D. Onggo, J. M. Hook, A. D. Rae, H. A. Goodwin, *Inorganica. Chimica. Acta*, **1990**, *173*, 19–30. (d) M. Ruben, E. Breuning, J. M. Lehn, V. Ksenofontov, F. Renz, P. G. Tlich, G. B. M. Vaughan, *Chem. Eur. J*. **2003**, *9*, 4422–4429.

[66] (a) O. Hietsoi, P.W. Dunk, H. D. Stout, A. Arroyave, K. Kovnir, R. E. Irons, N. Kassenova, R. Erkasov, C.Achim, M. Shatruk, *Inorg. Chem*. **2014**, *53*, 13070−13077. (b) J. S. Costa, S. Rodríguez-Jiménez, G. A. Craig, B. Barth, C. M. Beavers, S. J. Teat, G. Aromí , *J. Am. Chem. Soc*. **2014**, *136*, 3869−3874.

[67] (a) M. Sorai, J. Ensling, P. Gütlich, *Chem. Phys*. **1976**, *18*, 199–209. (b) H, E. Meissner, H. Köppen, W. Müller, P, Gütlich, *Chem. Phys*. **1982**, *68*, 65–71. (c) A. Rotarua, M. M. Dîrtuc, C. Enachescub, R. Tanasab, J. Linaresa, A. Stancub, Y. Garciac, *Polyhedron*, **2009**, *28*, 2531−2536.

[68] (a) M. Affronte, F. Troiani,; A. Ghirri, A. Candini, M. Evangelisti, V. Corradini, S. Carretta, P. Santini, G. Amoretti, F. Tuna, G. Timco, R. E. P. Winpenny, *J. Phys. D: Appl. Phys*. **2007**, *40*, 2999−3004. (b) M. Mannini, F. Pineider, P. Sainctavit, C. Danieli, E. Otero, C. Sciancalepore, A. M. Talarico, M. A. Arrio, A. Cornia, D. Gatteschi, R. Sessoli, *Nat. Mater*. **2009**, *8*, 194−197. (c) L. Bogani, W. Wernsdorfer, *Nat. Mater*. **2008**, *7*, 179−186. (d) M. N. Leuenberger, D. Loss, *Nature*. **2001**, *410*, 789−793.

[69] T. Shiga, T. Matsumoto, M. Noguchi, T. Onuki, N. Hoshino, G. N. Newton, M. Nakano, H. Oshio, *Chem. Asian J*. **2009**, *4*, 1660−1663.

[70] (a) R. Sessoli, H. L. Tsai, A. R. Schake, S. Wang, J. B. Vincent, K. Folting, D. Gatteschi, G. Christou, D. N. Hendrickson, *J. Am. Chem. Soc*. **1993**, *115*, 1804–

1816. (b) R. Sessoli, D. Gatteschi, A. Caneschi, M. A. Novak, *Nature*, **1993**, *365*, 141. (c) H. L. Tsai, H. J. Eppley, N. Devries, K. Folting, G. Christou, D. N. Hendrickson, *J. Chem. Soc. Chem. Commun*. **1994**, 1745–1746. (d) J. R. Friedman, M. P. Sarachik, J. Tejada, R. Ziolo, *Phys. Rev. Lett*. **1996**, *76*, 3830. (e) Z. M. Sun, D. Ruiz, E. Rumberger, C. D. Incarvito, K. Folting, A. L. Rheingold, G. Christou, D. N. Hendrickson, *Inorg. Chem*. **1998**, *37*, 4758–4759. (f) C. Boskovic, E. K. Brechin, W. E. Streib, K. Folting, J. C. Bollinger, D. N. Hendrickson, G. Christou, *J. Am. Chem. Soc*. **2002**, *124*, 3725–3736.

[71] J. D. Rinehart, J. R. Long, *Chem. Sci*. **2011**, *2*, 2078−2085.

[72] (a) J. D. Rinehart, M. Fang, W. J. Evans, J. R. Long, *Nat. Chem*. **2011**, *3*, 538−542. (b) M. Vonci, C. Boskovic, *Aust. J. Chem*. **2014**, *67*, 1542−1552. (c) A. Yamashita, A. Watanabe, S. Akine, T. Nabeshima, M. Nakano, T. Yamamura, T. Kajiwara, *Angew. Chem. Int. Ed*. **2011**, *50*, 4016−4019. (d) T. Kajiwara, M. Nakano, K. Takahashi, S. Takaishi, M. Yamashita, *Chem. Eur. J*. **2011**, *17*, 196−205.

[73] J. M. Zadrozny, D. J. Xiao, M. Atanasov, G. J. Long, F. Grandjean, F. Neese, J. R. Long, *Nat. Chem*. **2013**, *5*, 577–581.

[74] (a) D. E. Freedman, W. H. Harman, T. D. Harris, G. J. Long, C. J. Chang, J. R Long. *J. Am. Chem. Soc*. **2010**, *132*, 1224−1225. (b) P. H. Lin, N. C. Smythe, S. I. Gorelsky, S. Maguire, N. J. Henson, I. Korobkov, B. L. Scott, J. C. Gordon, R. T. Baker, M. Murugesu, *J. Am. Chem. Soc*. **2011**, *133*, 15806−15809. (c) M. Atanasov, J. M. Zadrozny, J. R. Long, F. Neese, *Chem. Sci*. **2013**, *4*, 139–156. (d) C. Mathonière, H. J. Lin, D. Siretanu, R. Clérac, J. M. Smith, *J. Am. Chem. Soc*. **2013**, *135*, 19083−19086. (e) X. Feng, C. Mathonière, I. R. Jeon, M. Rouzières, A. Ozarowski, M. L. Aubrey, M. I. Gonzalez, R. Clérac, J. R. Long, *J. Am. Chem. Soc*. **2013**, *135*, 15880−15884. (f) C. Mathonière, H. J. Lin, D. Siretanu, R. Clèrac, J. M. Smith, *J. Am. Chem. Soc*. **2013**, *135*, 19083−19086.

[75] S. Mossin, B. Tran, D. Adhikari, M. Pink, F. W. Heinemann, J. Sutter, R. K. Szilagyi, K. Meyer, D. J. Mindiola, *J. Am. Chem. Soc*. **2012**, *134*, 13651−13661.

[76] (a) M. Murrie, *Chem. Soc. Rev*. **2010**, *39*, 1986–1995. (b) T. Jurca, A. Farghal, P.

H. Lin, I. Korobkov, M. Murugesu, D. S. Richeson, *J. Am. Chem. Soc*. **2011**, *133*, 15814−15817. (c) J. Vallejo, I. Castro, R. Ruiz-García, J. Cano, M. Julve,; F. Lloret, G. D. Munno, W. Wernsdorfer, E. Pardo, *J. Am. Chem. Soc*. **2012**, *134*, 15704−15707. (d) E. Colacio, J. Ruiz, E. Ruiz, E. Cremades, J. Krzystek, S. Carretta,; J. Cano, T. Guidi, W. Wernsdorfer, E. K. Brechin, *Angew. Chem. Int. Ed*. **2013**, *52*, 9130−9134. (e) S. Gómez-Coca, A. Urtizberea, E. Cremades, P. J. Alonso, A. Camón, E. Ruiz, F. Luis, *Nat. Commun*. **2014**, *5*, 4300. (f) L. Chen, J. Wang, J. M. Wei, W. Wernsdorfer, X. T. Chen, Y. Q. Zhang, Y. Song, Z. L. Xue, *J. Am. Chem. Soc*. **2014**, *136*, 12213−12216. (g) Y. Y. Zhu, T. T. Yin, C. W. Liu, C. Gao, Z. Q. Wu, Y. Q. Zhang, B. W. Wang, S. Gao, *Supramol. Chem*. **2015**, *27*, 401−406. (h) D. Schweinfurth, M. G. Sommer, M. Atanasov, S. Demeshko, S. Hohloch, F. Meyer, F. Neese, B. Sarkar, *J. Am. Chem. Soc*. **2015**, *137*, 1993−2005.

[77] (a) J. M. Zadrozny, J. R. Long, *J. Am. Chem. Soc*. **2011**, *133*, 20732−20734. (b) J. M. Zadrozny, J. Telser, J. R. Long, *Polyhedron*. **201**3, *64*, 209−217. (c) Y. Y. Zhu, C. Cui, Y. Q. Zhang, J. H. Jia, X. Guo, C. Gao, K. Qian, S. D. Jiang, B. W. Wang, Z. M. Wang, S. Gao, *Chem. Sci*. **2013**, *4*, 1802−1806. (d) S. G. Coca, E. Cremades, N. Aliaga-Alcalde, E. Ruiz, *J. Am. Chem. Soc*. **2013**, *135*, 7010−7018. (e) M. S. Fataftah, J. M. Zadrozny, D. M. Rogers, D. E. Freedman, *Inorg. Chem*. **2014**, *53*, 10716−10721.

[78] R. C.Poulten, M. J. Page, A. G. Algarra, J. J. Le Roy, I. López, E. Carter, A. Llobet, S. A. Macgregor, M. F. Mahon, D. M. Murphy, M. Murugesu, M. K. Whittlesey, *J. Am. Chem. Soc*. **2013**, *135*, 13640−13643.

[79] (a) C. J. Milios, A. Vinslava, P. A. Wood, S. Parsons, W. Wernsdorfer, G. Christou, S. P. Perlepes, E. K. Brechin, *J. Am. Chem. Soc*. **2007**, *129*, 8−9. (b) A. R. Tomsa, J. M. Lillo, Y. L. Li, L. M. Chamoreau, K. Boubekeur, F. Farias, M. A. Novak, E. Cremades, E. Ruiz, A. Proust, M. Verdaguer, P. Gouzerh, *Chem. Commun*. **2010**, *46*, 5106–5108. (c) A. Grigoropoulos, M. Pissas, P. Papatolis, V. Psycharis, P. Kyritsis, Y. Sanakis, *Inorg. Chem*. **2013**, *52*, 12869−12871. (d) A.

Grigoropoulos, M. Pissas, P. Papatolis, V. Psycharis, P. Kyritsis, Y. Sanakis, *Inorg. Chem.* **2013**, *52*, 12869−12871. (e) J. Vallejo, A. Pascual-Alvarez, J. Cano, I. Castro, M. Julve, F. Lloret, J. Krzystek, G. D. Munno, D. Armentano, W. Wernsdorfer, R. R. Garcia, E. Pardo, *Angew. Chem. Int. Ed.* **2013**, *52*, 14075−14079. (f) G. A. Craig, J. Marbey, S. Hill, O. Roubeau, S. Parsons, M. Murrie, *Inorg. Chem.* **2015**, *54*, 13−15.

[80] G. A. Craig, M. Murrie, *Chem. Soc. Rev*. **2015**, *44*, 2135−2147.

[81] P. H. Guo, J. Liu, Z. H. Wu, H. Yan, Y. C. Chen, J. H. Jia, M. L. Tong, *Inorg. Chem.* **2015**, *54*, 8087−8092.

[82] (a) M. B. Robin, P. Day, *Mixed Valence ChemistrysA Survey and Classification*. *Adv. Inorg. Chem. Radiochem*. **1967**, *10*, 247–422. (b) K. Prassides, Ed. *Mixed Valency SystemssApplications in Chemistry, Physics and Biology;* Kluwer Academic Publishers: Dordrecht, **1991**.

[83] (a) M. B. Robin, P. Day, *Adv. Inorg. Chem. Radiochem*. **1967**, *10*, 247–422. (b) P. Day, *Int. Rev. Phys. Chem*. **1981**, *1*, 149–193.

[84] (a) J. Woodward, Philos. *Trans. R. Sot. London*, **1724**, *33*, 15. Translated in H.M. *Powell, Proc. Chem. Sot., London*, **1959**, *73*. (b) A. G. Sharpe, *The Chemistry of Cyano-Complexes of the Transition Metals*, Academic Press, New York, **1976**, 99.

[85] (a) N. S. Hush, *Prog. Inorg. Chem.*, **1967**, *8*, 391. (b) M. B. Robin, P. Day, *Adv. Inorg. Chem. Radiochem.*, **1967**, *10*, 247.

[86] M. B.Robin, P. Day, *Adv. Inorg. Chem. Radiochem*. **1967**, *10*, 247–422.

[87] (a) S. F. Nelsen, *Chem. Eur. J*. **2000**, *6*, 581–588. (b) K. D. Demadis, C. M. Hartshorn, T. J. Meyer, *Chem. Rev*. **2001**, *101*, 2655–2685. (c) B. S. Brunschwig, C. Creutz, N. Sutin, *Chem. Soc. Rev.* **2002**, *31*, 168–184.

[88] N. S.Hush, *Prog. Inorg. Chem*. **1967**, 8, 391–444. (b) N. S. Hush, *Electrochim. Acta* **1968**, *13*, 1005–1023.

[89] (a) C. Creutz, *Progr. Inorg. Chem*. **1983**, *30*, 1–73. (b) D. E. Richardson, H. Taube, *Coord. Chem. Rev*. **1984**, *60*, 107–129. (c) R. J. Crutchley, *Adv. Inorg. Chem*. **1994**, *41*, 273–325.

[90] (a) J. A. McCleverty, M. D. Ward, *Acc. Chem. Res*. **1998**, *31*, 842–851. (b) M. Glöckle, W. Kaim, *Angew. Chem. Int. Ed*. **1999**, *38*, 3072–3074.

[91] M. D. Ward, *Chem. Soc. Rev*. **1995**, *34*, 121–134.

[92] (a) D. M. D'Alessandro, F. R.Keene, *Chem. Soc. Rev*. **2006**, *35*, 424–440. (b) B. S. Brunschwig, C. Creutz, N. Sutin, *Chem. Soc. Rev*. **2002**, *31*, 168–184.

[93] (a) N. Hush, *Electrochim. Acta*, **1968**, *13*, 1005–1023. (b) N. S. Hush, *Prog. Inorg. Chem*. **1967**, *8*, 391–444.

[94] (a) E. I. Solomon, T. C. Brunold, M. I. Davis, J. N. Kemsley, S. K. Lee, N. Lehnert, F. Neese, A. J.Skulan, Y. S. Yang, J. Zhou, *Chem. Rev*. **2000**, *100*, 235–349. (b) G. Blondin, J. J. Girerd, *Chem. Rev*. **1990**, *90*, 1359–1376.

[95] (a) E. I. Solomon, T. C. Brunold, M. I. Davis, J. N. Kemsley, S. K Lee, N. Lehnert, F. Neese, A. J. Skulan, Y. S. Yang, J. Zhou, *Chem. Rev*. **2000**, *100*, 235–349. (b) W. Kaim, W. Bruns, J. Poppe, V. Kasack, *J. Mol. Struct*. **1993**, *292*, 221–228. (c) G. Blondin, J. J. Girerd, *Chem. Rev*. **1990**, *90*, 1359–1376. (d) B. Chiari, A. Cinti, O. Crispu, F. Demartin, A. Pasini, O. Piovesana, *J. Chem. Soc*., *Dalton Trans*. **2001**, 3611–3616.

[96] (a) H. Taube, *Angew. Chem. Int. Ed*. **1984**, *23*, 329–338. (b) V. N. Nemykin, Gr. T. Rohde, C. D. Barrett, R. G. Hadt, C. Bizzarri, P. Galloni, B. Floris, I. Nowik, R. H. Herber, A. G. Marrani, R. Zanoni, N. M. Loim, *J. Am. Chem. Soc*. **2009**, *131*, 14969–14978.

[97] N. S. Hush, *Coord. Chem. Rev*. **1985**, *64*, 135–157.

[98] (a) M. D. Ward, *Chem. Soc. Rev*. **1995**, *34*, 121–134. (b) D. Astruc, *Acc. Chem. Res*. **1997**, *30*, 383–391. (c) J. A. McCleverty, M. D. Ward, *Acc. Chem. Res*. **1998**, *31*, 842–851.

[99] A. Bencini, I. Ciofini, C. A. Daul, A. Ferretti, *J. Am. Chem. Soc*. **1999**, *121*, 11418–11424.

[100] (a) S. D. J. McKinnon, B. O. Patrick, A. B. P. Lever, R. G. Hicks , *Inorg. Chem*. **2013**, *52*, 8053−8066. (b) A. I. Gaudette, I. R. Jeon, J. S. Anderson, F. Grandjean, G. J. Long, T. D. Harris, *J. Am. Chem. Soc*. **2015**, 1*37*, 12617−12626. (c) D. Schweinfurth, Y. Rechkemmer, S. Hohloch, N. Deibel, I. Peremykin, J. Fiedler,

R. Marx, P. Neugebauer, J. van Slageren, B. Sarkar, *Chem. Eur. J*. **2014**, *20*, 3475–3486.

[101] (a) Z. Z. He, W. L. Zhang, W. D. Cheng, A. Okazawa, N. Kojima, *Inorg. Chem*. **2012**, *51*, 7469−7471. (b) T. Shiga, M. Noguchi, H. Sato, T. Matsumoto, G. N. Newton, H. Oshio, *Dalton Trans*. **2013**, *42*, 16185–16193. (c) J. B. G. Gluyas, A. J. Boden, S. G. Eaves, H. Yua, P. J. Low, *Dalton Trans.* **2014**, *43*, 6291–6294. (d) M. U. Anwar, L. N. Dawe, S. R. Parsons, S. S. Tandon, L. K. Thompson, S. K. Dey, V. Mereacre,W. M. Reiff, S. D. Bunge, *Inorg. Chem*. **2014**, *53*, 4655−4668.

[102] (a) V. A. Grillo, Z. Sun, K. Folting, D. N. Hendrickson, G. Christou, *Chem. Commun*. **1996**, 2233–2234. (b) Y. Peng, C. B. Tian, H. B. Zhang, Z. H. Li, P. Li, S. W. Du, *Dalton Trans*. **2012**, *41*, 4740–4743. (c) A. M. Ullman, D. G. Nocera, *J. Am. Chem. Soc*. **2013**, *135*, 15053−15061. (d) Q. P. Li, J. J. Qian, C. B. Tian, P. Lin, Z. Z. He, N. Wang, J. N. Shen, H. B. Zhang, T. Chu, D. Q. Yuan, Y. Yang, L. P. Xue, S. W. Du, *Dalton Trans*. **2014**, *43*, 3238–3243. (e) A. Hazari, L. K. Das, R. M. Kadam, A. Bauzá, A. Frontera, A. Ghosh, *Dalton Trans*. **2015**, 44, 3862–3876.

[103] Y. G. Zhao, D. Guo, Y. Liu, C. He, C. Y. Duan, *Chem. Commun*. **2008**, 5725–5727

[104] T. Matsumoto, G. N. Newton, T. Shiga, S.Hayami, Y. Matsui, H. Okamoto, R. Kumai, Y. Murakami, H. Oshio, *Nat. Commun*. **2014**, *5*, 1–8.

[105] (a) F. A. Cotton, C. Lin and C. A. Murillo, *J. Am. Chem. Soc.* **2001**, *123*, 2670–2671. (b) V. C. Lau, L. A. Berben, J. R. Long, *J. Am. Chem. Soc*. **2002**, *124*, 9042–9043. (c) H. Yao, M. Sabat, R. N. Grimes, F. Fabrizi de Biani, P. Zanello, *Angew. Chem. Int. Ed.* **2003**, *42*, 1002–1005. (d) F. A. Cotton, C. Y. Liu, C. A. Murillo and X. Wang, *Chem. Commun*. **2003**, 2190–2191.

[106] (a) P. J. Stang, B. Olenyuk, *Acc. Chem. Res*. **1997**, *30*, 502–518. (b) S. Leininger, B. Olenyuk, P. J. Stang, *Chem. Rev*. **2000**, *100*, 853–908.

[107] J. I. van der Vlugt, S. Demeshko, S. Dechert, F. Meyer, *Inorg. Chem*. **2008**, *47*, 1576−1585.

[108] B. Schneider, S. Demeshko, S. Dechert, F. Meyer, *Angew. Chem. Int. Ed.* **2010**, *49*, 9274−9277.

[109] B. Schneider, S. Demeshko, S. Neudeck, S. Dechert, F. Meyer, *Inorg. Chem.* **2013**, *52*, 13230−13237.

[110] M. Steinert, B. Schneider, S. Dechert, S. Demeshko, F. Meyer, *Inorg. Chem.* **2015,** DOI: 10.1021/acs.inorgchem.5b02762.

[111] M. Steinert, B. Schneider, S. Dechert, S. Demeshko, F. Meyer, *Angew. Chem. Int. Ed*. **2014**, *53*, 6135–6139

[112] (a) B. Schneider, PhD thesis, Georg-August-Universität, Göttingen, **2012**. (b) M. Steinert, PhD thesis, Georg-August-Universität, Göttingen, **2015**.

[113] A. S. Bell; D. A. Roberts, K. S. Ruddock, *Tetrahedron Lett*, **1988**, *29*, 5013.

[114] W. Ye, M. Zhao, Z. Yu, *Chem. Eur. J.* **2012**, *18*, 10843–10846.

[115] R. Zong, P. Thummel, *Inorg. Chem.* **2005**, *44*, 5984–5986.

[116] F. R. Heirtzler, *Synlett*. **1999**, 1203–1206.

[117] F. Teixidor, R. Garcia, J. Pons, J. Casabó, *Polyhedron.* **1988**, *7*, 43–47.

[118] (a) H. Zabrodsky, S. Peleg, D. Avnir, *J. Am. Chem. Soc.* **1992**, *114*, 7843–7851. (b) S. Alvarez, D. Avnir, M. Llunell, M. Pinsky, *New J. Chem.* **2002**, *26*, 996–1009. (c) S. Alvarez, *J. Am. Chem. Soc.* **2003**, *125*, 6795–6802.

[119] P. Gutlich, A. Hauser, H. Spiering, *Angew. Chem. Int. Ed.* **1994**, *33*, 2024–2054.

[120] S. Alvarez, D. Avnir, M. Llunell, M. Pinsky, *New J. Chem.* **2002**, *26*, 996–1009.

[121] H. Zabrodsky, S. Peleg, D. Avnir, *J. Am. Chem. Soc.* **1992**, *114*, 7843–7851; *J. Am. Chem. Soc*. **1993**, *115*, 8278–8289.

[122] L. H. Uppadine, J. P. Gisselbrecht, N. Kyritsakas, K. Naettinen, K. Rissanen, J. M. Lehn, *Chem. Eur. J.* **2005,** *11*, 2549–2565

[123] M. Shatruk, A. Dragulescu-Andrasi, K. E. Chambers, S. A. Stoian, E. L. Bominaar,; C. Achim, K. R. Dunbar, *J. Am. Chem. Soc.* **2007,** *129*, 6104−6116.

[124] *Simulation of the experimental magnetic data with a full-matrix diagonalization*

of exchange coupling and Zeeman splitting was performed with the julX program (Bill, E. Max-Planck Institute for Bioinorganic Chemistry: Mülheim/Ruhr, Germany).

[125] A. R. Stefankiewicz, G. Rogez, J. Harrowfield, M. Drillon, J. M. Lehn, *Dalton Trans*. **2009**, 5787−5802.

[126] P. Gtlich, R. Link, A. Trautwein, *Mössbauer Spectroscopy and Transition Metal Chemistry*, Springer, New York, **1978**.

[127] T. Matsumoto, G. N. Newton, T. Shiga, S. Hayami, Y. Matsui, H. Okamoto, R. Kumai, Y. Murakami, H. Oshio, *Nat. Commun*. **2014**, *5*, 3865/1–3865/8.

[128] (a) F. Little, G. J. Long, *Inorg. Chem.* **1978**, *17*, 3401−3413. (b) W. M. Reiff, G. J. Long, *in Mössbauer Spectroscopy Applied to Inorganic Chemistry*, G. J., Long, Ed. Volume 1, Plenum Press, New York, **1984**, 245–285.

[129] (a) B. Strauss, V. Gutmann, W. Linert, *Monatsh. Chem.* **1993,** 124, 515−522; (b) W. Linert, M. Enamullah, V. Gutmann, R. F. Jameson, *Monatsh. Chem.* **1994,** *125*, 661−670.

[130] J. R. Nitschke, J. M. Lehn, *Proc. Natl. Acad. Sci.* **2003**, *100*, 11970−11974.

[131] I. Bertini, C. Luchinat, G. Parigi, *Solution NMR of Paramagnetic Molecules: Applications to Metallobiomolecules and Models*, Elsevier, Amsterdam, **2001**.

[132] I. Bertini, C. Luchinat, *Coord. Chem. Rev*. **1996**, *150*, 1–292.

[133] M. Kruck, D. C. Sauer, M. Enders, H, Wadepohl, L. H. Gade, *Dalton Trans.* **2011**, *40*, 10406–10415.

[134] No. Elgrishi, M. B. Chambers, V. Arterob, M. Fontecave, *Phys. Chem. Chem. Phys*., **2014**, *16*, 13635−13644.

[135] E. C. Constable, G. Baum, E. Bill, R. Dyson, R. van Eldik, D. Fenske, S. Kaderli, D. Morris, A. Neubrank, M. Neuburger, D. R. Smith, K. Wieghardt, M. Zehnder, A. D. Zuberbhler, *Chem. Eur. J*. **1999**, *5*, 498–508.

[136] T. Ayers, R. Turk, C. Lane, J. Goins, D. Jameson, S. J. Slattery, *Inorg. Chim. Acta*. **2004**, *357*, 202–206.

[137] (a) A. S. Bell, D.A. Roberts, K.S. Ruddock, *Tetrahedron Lett*. **1988**, *29*, 5013–5016. (b) W. Ye, M. Zhao, Z. Yu, *Chem. Eur. J*. **2012**, *18*, 10843–10846. (c) R. Zong, P. Thummel, *Inorg. Chem*. **2005**, *44*, 5984–5986. (d) F. R. Heirtzler, *Synlett*. **1999**, 1203–1206.

[138] J. Olivier, *Molecular Magnetism.* VCH, Weinheim, **1993**.

[139] S. Amedeo, J. K. C. Laurence, K. Rafal, A. B. Simon, C. Oscar, A. H. Malcolm, *Inorg. Chem.* **2015**, *54*, 682–693.

[140] L. H. Uppadine, J. P. Gisselbrecht, N. Kyritsakas, K. Naettinen, K. Rissanen, J. M. Lehn, *Chem. Eur. J.* **2015**, *11*, 2549−2565. (b) T. J. Morin, S. Wanniarachchi, C. Gwengo, V. Makura, H. M. Tatlock, S. V. Linderman, B. Bennett, G. J. Long, F. Grandjean, J. R. Gardinier, *Dalton Trans*. **2011**, *40*, 8024−8034.

[141] S. A. Borshch, E. M. Zueva, *Eur. J. Inorg. Chem*. **2013**, *18*, 1009−1014.

[142] *Full-matrix diagonalization of the spin Hamiltonian for zerofield splitting and Zeeman splitting* was performed with the *julX* program (Max-Planck Institute for Chemical Energy Conversion, Mülheim/Ruhr, Germany).

[143] S. A. Borshch, E. M. Zueva, *Eur. J. Inorg. Chem*. **2013**, *18*, 1009–1014.

[144] M. A. Halcrow, *Chem. Soc. Rev*. **2011**, *40*, 4119−4142.

[145] G. A. Craig, J. S. Costa, O. Roubeau, S. J. Teat, G. Aromí, *Chem. Eur. J*. **2012**, *18*, 11703−11715.

[146] (a) B. Strauss, V. Gutmann, W. Linert, *Monatsh. Chem*. **1993**, *124*, 515−522. (b) W. Linert, M. Enamullah, V. Gutmann, R. F. Jameson, *Monatsh. Chem*. **1994**, *125*, 661−670.

[147] Y. G. Zhao, D. Guo, Y. Liu, C. He, C. Y. Duan, *Chem. Commun*. **2008**, 5725–5727.

[148] (a) D. M. Bassani, J. M. Lehn, S. Serroni, F. Puntoriero, S. Campagna, *Chem. Eur. J*. **2003**, *9*, 5936−5946. (b) M. Ruben, E. Breuning, M. Barboiu, J. Gisselbrecht, J. M. Lehn, *Chem. Eur. J*. **2003**, *9*, 291−299.

[149] W. Kaim, A. Klein, M. Gloeckle, *Acc. Chem. Res*. **2000**, *33*, 755−763

[150] K. Izutsu, *Electrochemistry in Nonaqueous Solutions*. Wiley-VCH: Weinheim, **2002**, Ch.4.

[151] L. H. Uppadine, J. P. Gisselbrecht, Na. Kyritsakas, K. Nättinen, K. Rissanen, J. M. Lehn, *Chem. Eur. J*. **2005**, *11*, 2549–2565.

[152] B. Schneider, S. Demeshko, S. Dechert, F. Meyer, *Inorg. Chem*. **2012**, *51*, 4912−4914.

[153] G. Yang, P. Baran, A. R. Martínez, R. G. Raptis, *Cryst. Growth. Des*. **2013**, *13*, 264−269.

[154] (a) A. N. Khlobystov, A. J. Blake, N. R. Champness, D. A. Lemenovskii, A. G. Majouga, N. V. Zyk, M. Schröder, *Coord. Chem. Rev*. **2001**, *222*, 155−192. (b) M. Mascal, J. Kerdelhué, A. J. Blake, P. A. Cooke, R. J. Mortimer, S. J. Teat, *Eur. J. Inorg. Chem*. **2000**, 485−490.

[155] A. Bondi, *J. Phys. Chem*. **1964**, *68*, 441−451.

[156] P. Gutlich, A. Hauser, H. Spiering, *Angew. Chem. Int. Ed.* **1994**, *33*, 2024–2054.

[157] (a) S. Alvarez, D. Avnir, M. Llunell, M. Pinsky, *New J. Chem*. **2002**, *26*, 996–1009. (b) H. Zabrodsky, S. Peleg, D. Avnir, *J. Am. Chem. Soc.* **1992**, *114*, 7843–7851; *J. Am. Chem. Soc*. **1993**, *115*, 8278–8289.

[158] C. A.Kilner, M. A. Halcrow, *Dalton Trans*. **2010**, *39*, 9008−9012.

[159] (a) A. B. Gaspar, C. M. Munoz, V. Niel, J. A. Real, *Inorg. Chem*. **2001**, *40*, 9−10. (b) R. Hogg, R. G. Wilkins, *J. Chem. Soc*. **1962**, 341−350. (c) J. S. Judge, W. A. Baker, *Inorg. Chim. Acta*. **1967**, *1*, 68−72. (d) H. Z. Kou, O. Sato, *Inorg. Chem*. **2007**, *46*, 9513−9515.

[160] (a) Q. Chen, M. H. Zeng, L. Q. Wei and M. Kurmoo, *Chem. Mater*. **2010**, *22*, 4328−4334. (b) Y. Peng, C. B. Tian, H. B. Zhang, Z. H. Li, P. Lin and S. W. Du, *Dalton Trans*. **2012**, *41*, 4740−4743. (c) S. H. Zhang, Y. Song, H. Liang, M. H. Zeng, *Cryst Eng-Comm*. **2009**, *11*, 865−872.

[161] (a) M. H. Zeng, M. X. Yao, H. Liang, W. X. Zhang, X. M. Chen, *Angew. Chem. Int. Ed*. **2007**, *46*, 1832−1835. (b) Q. Chen, M. H. Zeng, Y. L. Zhou, H. H. Zou,

M. Kurmoo, *Chem. Mater*. **2010**, *22*, 2114−2119. (c) L. Lisnard, F. Tuna, A. Candini, M. Affronte, R. E. P. Winpenny, E. J. L. McInnes, *Angew. Chem. Int. Ed*. **2008**, *47*, 9695−9699. (d) P. Albors, E. Rentschler, *Angew. Chem. Int. Ed*. **2009**, *48*, 9366−9370.

[162] O. Kahn, *Molecular Magnetism*, Wiley-VCH, Publishers Inc.: New York, **1993**, 42.

[163] *Simulation of the experimental magnetic data with a full-matrix diagonalization of exchange coupling and Zeeman splitting* was performed with the julX program (Bill, E. Max-Planck Institute for Bioinorganic Chemistry: Mülheim/Ruhr, Germany).

[164] (a) J. S.Griffith, *Trans. Faraday Soc*. **1958**, *54*, 1109–1116. (b) R. L. Carlin, *Trans. Met. Chem.* **1965**, *1*, 1–32.

[165] E. C. Constable, T. Kulke, M. Neuburger, M. Zehnder, *New J. Chem.* **1997**, *21*, 1091−1102.

[166] E. C. Constable, in *Perspectives in Coordination Chemistry, Education in Advanced Chemistry*, ed. A. M. Trzeciak, P. Sobota, J. J. Ziolkowski, Wydawnictwo Poznanskie, Poznan-Wroclaw, **2000**, vol. 7.

[167] I. Bertini, C. Luchinat, *In NMR of Paramagnetic Substances*. Lever, A. B. P., Ed.; *Coord. Chem. Rev.*; Elsevier: Amsterdam, **1996**, *150*, 29–75.

[168] (a) G. N. LaMar, W. deW. Horrocks, R. H. Holm (ed). *NMR of Paramagnetic Molecules*, Academic Press, New York, **1973**. (b) F. H. Koehler, *Magnetism:Molecules to Materials*, ed. J. S. Miller, M. Drillon, Wiley-VCH, Weinheim, **2001**, 379–430. (c) I. Bertini, C. Luchinat, G. Parigi, *Prog. Nucl. Magn. Reson. Spectrosc.*, **2002**, *40*, 249–273. (d) I. Bertini, C. Luchinat, G. Parigi, R. Pierattelli, *ChemBioChem*, **2005**, 6, 1536–1549. (e) F. Rastrelli, A. Bagno, *Chem. Eur. J.* **2009**, *15*, 7990. (f) M. Kaupp, F. H. Koehler, *Coord. Chem. Rev.*, **2009**, *253*, 2376–2386.

[169] I. Bertini, C. Luchinat, P. Giacome, *Solution NMR of Paramagnetic Molecules, Applications to Metallobiomolecules and Models.* Elsevier:Amsterdam, **2001**, *2*,

168–174.

[170] L. H. Uppadine, J. M. Lehn, *Angew. Chem. Int. Ed*. **2004**, *43*, 240–243.

[171] I. Bertini, C. Luchinat, *NMR of Paramagnetic Molecules in Biological SySubstances*. Lever, A. B. P. Ed. *Coord. Chem. Rev.* Elsevier: Amsterdam, **1996**, *150*, 29–75.

[172] (a) C. Arana, S. Yan, M. Keshavarz-K, T. Potts, H. D. Abruña, *Inorg. Chem*. **1992**, *31*, 3680-3682. (b) N. M. Shavaleev, F. Kessler, M. Grätzel, M. Nazeeruddin, *Inorg. Chim. Acta* **2013**, *407*, 261–268.

[173] (a) L. J. Kershaw Cook, F. Tuna. M. A. Halcrow. *Dalton Trans*. **2013**, *42*, 2254–2265. (b) J. England, E. Bill, T. Weyhermüller, F. Neese, M. Atanasov, Wieghardt, K. *Inorg. Chem.* **2015**, *54*, 12002−12018.

[174] T. Ayers, S. Scott, J. Goins, N. Caylor, D. Hathcock, S. J. Slattery, D. L. Jameson, *Inorg. Chim. Acta.* **2000**, *307*, 7−12.

[175] (a) M. Ruben, E. Breuning, M. Barboiu, J. P. Gisselbrecht, J. M. Lehn. *Chem. Eur. J*. **2003**, *9*, 291–299. (b) M. Ruben, J. Breuning, J. P. Gisselbrecht, J. M. Lehn, *Angew. Chem. Int. Ed.* **2000**, *39*, 4139–4142.

[176] Sapp, S A. Sapp; Elliott, C. M.; Contado, C.; Caramori, S.; Bignozzi, C. A. *J. Am. Chem. Soc.* **2002**, *124*, 11215-11222.

[177] K. Izutsu, *Electrochemistry in Nonaqueous Solutions*. Wiley-VCH: Weinheim, **2002**, Ch.4.

[178] K. G. Alley, R. Bircher, O. Waldmann, S. T. Ochsenbein, H. U. Gudel, B. Moubaraki, K. S. Murray, F. F. Alonso, B. F. Abrahams, C. Boskovic, *Inorg. Chem*. **2006**, *45*, 8950–8957.

[179] T. S. M. Abedin, L. K. Thompson, D. O. Miller, *Chem. Commun*. **2005**, 5512–5514.

[180] N. E. Brese, M. O'Keeffe, *Acta Crystallogr*. **1991**, *B47*, 192–197.

[181] *The Chemical Bond in Inorganic Chemistry*: *The Bond Valence Model*, I. D. Brown, Oxford University Press. **2006**.

[182] (a) M. Okeeffe, N. E. Brese, *J. Am. Chem. Soc*. **1991**, *113*, 3226–3229. (b) I. D.

Brown, D. Altermatt, *Acta Crystallogr*. **1985**, *B41*, 244–247.

[183] S. F. Majed, M. Z. Joseph, M. R. Dylan, E. F. Danna, *Inorg. Chem*. **2013**, *52*, 13230−13237.

[184] (a) T. Jurca, A. Farghal, P. H. Lin, I. Korobkov, M. Murugesu, D. S. Richardson, *J. Am. Chem. Soc*. **2011**, *133*, 15814−15817. (b) J. M. Zadrozny, J. R. Long, *J. Am. Chem. Soc*. **2011**, *133*, 20732−20734.

[185] R. Ruamps, L. J. Batchelor, R. Guillot, G. Zakhia, A. L. Barra, W. Wernsdorfer, N. Guihéry, T. Mallah, *Chem. Sci.* **2014**, *5*, 3418–3424.

[186] (a) G. A. Craig, M. Murrie, *Chem. Soc. Rev*. **2015**, *44*, 2135–2147. (b) A. K. Bar, C. Pichon, J. P. Sutter, *Coord. Chem. Rev*. **2015**, in press. (c) E. Carl, S. Demeshko, F. Meyer, D. Stalke, *Chem. Eur. J*. **2015**, *21*, 10109–10115.

(187) (a) J. Vallejo, I. Castro, R. Ruiz-García, J. Cano, M. Julve, F. Lloret, G. De Munno, W. Wernsdorfer, E. Pardo, *J. Am. Chem. Soc.* **2012**, *134*, 15704–15707. (b) Herchel, R.; Váhovská, L.; Potočňák, I.; Trávníček, Z. *Inorg. Chem.* **2014**, *53*, 5896–5898.

(188) (a) Y.-Y. Zhu, C. Cui, Y.-Q. Zhang, J.-H. Jia, X. Guo, C. Gao, K. Qian, S.-D. Jiang, B.-W. Wang, Z.-M. Wang, S. Gao, *Chem. Sci.* **2013**, *4*, 1802–1806. (b) Y.-Y. Zhu, Y.-Q. Zhang, T.-T. Yin, C. Gao, B.-W. Wang, S. Gao, *Inorg. Chem.* **2015,** *54*, 5475–5486. (c) V. V. Novikov, A. A. Pavlov, Y. V. Nelyubina, M.-E. Boulon, O. A. Varzatskii, Y. Z. Voloshin, R. E. P. Winpenny, *J. Am. Chem. Soc.* **2015**, *137*, 9792–9795.

[189] L. Gregoli, C. Danieli, A. L. Barra, P. Neugebauer, G. Pellegrino, G. Poneti, R. Sessoli, A. Cornia, *Chem. Eur. J*. **2009**, *15*, 6456–6467.

[190] S. A. Borshch, E. M. Zueva, *Eur. J. Inorg. Chem.* **2013**, 1009–1014.

[191] (a) M. H. Klingele, B. Moubaraki, J. D. Cashion, K. S. Murray, S. Brooker, *Chem. Commun.* **2005**, 987–989. (b) C. M. Grunert, S. Reiman, H. Spiering, J. A. Kitchen, S. Brooker, P. Gütlich, *Angew. Chem. Int. Ed.* **2008**, *47*, 2997–2999; (c) A. Y. Verat, N. Ould-Moussa, E. Jeanneau, B. Le Guennic, A. Bousseksou, S. A. Borshch, G. S. Matouzenko, *Chem. Eur. J.* **2009**, *15*, 10070–10082. (d) Y. Klein,

N. F. Sciortino, F. Ragon, C. E. Housecroft, C. J. Kepert, S. M. Neville, *Chem. Commun.* **2014**, *50*, 3838–3840.

[192] E. C. Constable, K. Harris, C. E. Housecroft, M. Neuburger, J. A. Zampese, *Cryst. Eng. Comm*. **2012**, *12*, 2949−2961.

[193] (a) C. Enachescu, I. Krivokapic, M. Zerara, J. A. Real, N. Amstutz, A. Hauser, *Inorg. Chim. Acta*. **2007**, *360*, 3945–3950. (b) J. K. Klosterman, A. Linden, D. K. Frantz, J. S. Siegel, *Dalton Trans*. **2010**, *39*, 1519–1531.

[194] S. Roeser, M. Z. Ertem, C. Cady, R. Lomoth, J. Benet-Buchholz, L. Hammarström, B. Sarkar, W. Kaim, C. J. Cramer, A. Llobet, *Inorg. Chem*. **2012**, *51*, 320–327.

[195] E. Bill, *Mfit*; Max-Planck Institute for Chemical Energy Conversion, Mülheim/Ruhr, Germany, **2008**.

[196] A. S. Bell, D. A. Roberts, K. S. Ruddock, *Tetrahedron Lett.* **1988**, *29*, 5013–5016.

[197] W. Ye, M. Zhao, Z. Yu, *Chem. Eur. J.* **2012**, *18*, 10843–10846.

[198] A. S. Bell, D. A. Roberts, K. S. Ruddock, *Tetrahedron Lett.* **1988**, *29*, 5013–5016.

[199] G. M. Sheldrick, *Acta Cryst.* **2015,** *C71*, 3–8.

[200] G. M. Sheldrick, SHELXL-97: *Program for Crystal Structure Refinement* (Universität Göttingen, Göttingen), **1997**.